BRNO UNIVERSITY OF TECHNOLOGY
VYSOKÉ UČENÍ TECHNICKÉ V BRNĚ

FACULTY OF MECHANICAL ENGINEERING
FAKULTA STROJNÍHO INŽENÝRSTVÍ

ENERGY INSTITUTE
ENERGETICKÝ ÚSTAV

HYDROELASTIC RESPONSE OF HYDROFOIL UNDER CAVITATION CONDITIONS
HYDROELASTICKÁ ODEZVA HYDRAULICKÉHO PROFILU V KAVITUJÍCÍM PROUDĚNÍ

DOCTORAL THESIS
DIZERTAČNÍ PRÁCE

AUTHOR — **Ing. Pavel Čupr**
AUTOR PRÁCE

SUPERVISOR — **doc. Ing. Pavel Rudolf, Ph.D.**
ŠKOLITEL

BRNO 2021

ABSTRACT

This doctoral thesis deals with experimental and numerical research of fluid added effects which act on a hydrofoil. The dynamic response of the hydrofoil was investigated for two types of excitation: Firstly, excitation by the von Kármán vortex shedding and the separation of boundary layer. Secondly, excitation with the use of external mechanical exciter mounted to the hydrofoil. Experimental investigation of hydrofoil dynamic response was carried out in both the non-cavitating and the cavitating flow. The obtained results were used for verification of fluid added effects calculated with the use of numerical modelling.

Key words

Added mass effect, cavitation, dynamic response, Fluid-Structure Interaction, hydrodynamic damping, Modal Work Approach

ABSTRAKT

Tato disertační práce se zabývá experimentálním a výpočtovým výzkumem přídavných účinků od proudu kapaliny na obtékaný hydraulický profil. Dynamická odezva profilu byla analyzována pro dva typy buzení: buzení odtržením mezní vrstvy a Kármánových vírů a dále buzení pomocí externího budiče připojeného k lopatce. Experimentální měření dynamické odezvy profilu na oba typy buzení bylo provedeno pro lopatku umístěnou v kavitujícím a nekavitujícím proudění. Získané výsledky byly použity pro verifikaci přídavných účinků stanovených s využitím numerického modelování.

Klíčová slova

Přídavná hmotnost, kavitace, dynamická odezva, interakce tělesa s tekutinou, hydrodynamické tlumení, Modal Work Approach

BIBLIOGRAPHIC CITATION

ČUPR, Pavel. *Hydroelastic Response of Hydrofoil Under Cavitation Conditions*. Brno, 2021. 267 p. Doctoral thesis. Brno University of Technology, Faculty of Mechanical Engineering, Energy Institute. Available from: https://www.vutbr.cz/studenti/zav-prace/detail/129969 Supervised by doc. Ing. Pavel Rudolf, Ph.D.

STATEMENT OF THE THESIS ORIGINALITY

I honestly declare that this doctoral thesis *Hydroelastic response of hydrofoil under cavitation conditions* was written only by me under the professional leadership of my supervisor and with the use of literature and other information sources, which are all cited in the text and listed at the end of the thesis.

February 26, 2021

…….

Ing. Pavel Čupr

ACKNOWLEDGEMENTS

Undertaking this PhD has been a truly life-changing experience for me and it would not have been possible to do without the support and guidance that I received from many people.

I would first like to thank my patient and supportive supervisor doc. Ing. Pavel Rudolf, Ph.D., who has encouraged and motivated me throughout my postgraduate study. I am very grateful for the opportunity to do the research in the field of Fluid-Structure Interaction.

I would also like to express my deepest appreciation to doc. Ing. Vladimír Habán, Ph.D. for valuable advice and suggestions during our endless hours of consultations. The post-processing of experimental data would have been hardly possible without his expertise in the field of dynamics and experimental measurement.

I would also like to acknowledge my colleagues and Ph.D. students from our department for the friendly atmosphere. Especially, I would like to express my thanks to Ing. Michal Havlásek and Ing. David Štefan, Ph.D. for their help and practical suggestions.

The experimental measurements were carried out in the laboratory at our department. Here, I would like to thank Ing. Martin Hudec for his help with installation of all measurement devices and setting of the recording software and Mr. Bronislav Kusý and Mr. Karel Večeřa for their help to build up the test circuit. Special thanks go to Ing. Lubomír Houfek, Ph.D., who provided us with two LDV vibrometers and to company *Litostroj Engineering a.s.* for design and manufacture of the cavitation tunnel test section.

During my postgraduate study, I spent four months internship at the Methods & Science department of *Voith Hydro Holding GmbH & Co. KG* in Heidenheim, Germany (September – December 2017). I am very grateful to Dr. Jiří Koutník for the internship opportunity. I would also like to extend my gratitude to Dr. Ing. Wilhelm Weber, who patiently supervised me during my internship and Dr. Ing. Björn Hübner for helpful advice.

Finally, I would like to thank my family, especially my parents, for supporting me throughout my whole study life. A special big thank is addressed to my girlfriend Kristina, who stayed patiently by my side for her love, support and understanding.

This thesis is an output of the research supported by the grant no. TH02020705 "Research of turbine blade oscillations with respect to extended regulation range for guarantee of stability and safety of energetic system" of the Technology Agency of the Czech Republic, and specific research project no. FSI-S-20-6235 "The Fluid Mechanics Principle Application as a Sustainable Development Tool".

In addition, the research was supported by the EU project Computer Simulations for Effective Low-Emission Energy funded as project No. CZ.02.1.01/0.0/0.0/16_026/0008392 by Czech Republic Operational Programme: Research, Development and Education, Priority axis 1: Strengthening capacities for high-quality research and the collaboration.

CONTENT

I. INTRODUCTION

1 NEW TRENDS IN TURBINE BLADE DYNAMICS

One of the key innovations in hydropower technology happened in recent decades when hydropower plants became the current best solution to stabilize the power grid efficiently. Consequently, the way of operating water turbines has changed. Originally, the turbines were designed to facilitate base loading with minimum number of starts and to provide the maximum efficiency for a given head and one optimal flow rate. In case the flow rate was not suitable for operating, the turbine was shut down.

Due to the newly introduced regulation requirements, the turbines are now operated for a wide range of flow rates and are started more frequently for only a few hours. However, the more increasing number of shortened start-stop cycles has a negative impact on the lifetime of turbines. Moreover, the requirements on modern hydraulic turbines have rapidly increased. High efficiency in the whole extended operating range, i.e. 10 – 150 % of optimal flow rate is expected. Furthermore, the cavitation in the whole extended operating range should be avoided.

The blade thickness of newly designed turbines has been reduced to ensure high efficiency in the entire operating range. While the blade thickness is being reduced, the water influence on the blade dynamics is rapidly increasing. On the other hand, the blades must stay thick enough to transfer the load from the fluid, which still keeps the same magnitude. Additionally, the blade stiffness and its dynamic response are strongly influenced by the blade thickness. In case the dynamic response to forced oscillations is not properly investigated, the turbine runner fatigue failure, crash and loss of profits may occur. Such contradictory requirements reach physical limits of material and must be considered when designing new turbines.

At present, blade design procedures are based on computational fluid dynamics techniques (CFD) which consider both field dynamics as two separate problems. Various numerical techniques must be used during the design process to satisfy complex requirements. Nevertheless, some unclear crashes of turbines have recently happened due to failure of current design procedures. [1]

The dynamics of the water turbine is a complex problem. Due to periodic excitation forces acting from the fluid on the runner, the investigation of the dynamic runner response is crucial for fatigue failure and runner lifetime prediction. As the requirements on the water turbine operation conditions have changed, the common runner design techniques need to be more developed. The main requirement on the turbine design is to provide constant high efficiency in a wide operating range, i.e. for a wide range of flow rate and various runner speeds. As a consequence, the amplitudes and frequencies of the periodic excitation forces coming from the fluid change and the coincidence between the excitation frequencies and natural frequencies of turbine parts, the so called “resonance”, may occur. If a wide flow rate range (the range of the excitation forces frequency) is required, resonance in the whole operating range cannot be avoided. Such a turbine can be safely operated only with the proper knowledge of both the runner dynamic response and the amount of damping which is present for various natural frequencies of the runner.

Recently, the experimental and numerical investigation of the dynamic response have been widely studied. Due to a strong influence of water on the runner dynamic response, both the fluid dynamics and the runner dynamics have to be considered

as a coupled phenomenon. According to the recent research, the influence of water on the runner dynamics can have three main effects: the added mass, added damping and added stiffness effect.

The main aim of the research presented in this doctoral thesis is to provide greater understanding of the numerical and experimental investigation of the dynamic response for the oscillating structure submerged in the fluid under various flow conditions. The presented results were achieved with the support of grant no. TH02020705 "*Research of turbine blade oscillations with respect to extended regulation range for guarantee of stability and safety of energetic system*" of the Technology Agency of the Czech Republic and of EU project Computer Simulations for Effective Low-Emission Energy funded as project No. CZ.02.1.01/0.0/0.0/16_026/0008392 by Czech Republic Operational Programme: Research, Development and Education, Priority axis 1: Strengthening capacities for high-quality research and the collaboration.

In order to reach the aim, the multiphysics coupled phenomenon is studied considering only one single blade placed into the cavitation tunnel replacing the whole turbine runner (Fig. 1.1). The simplified case can be easily modified and studied in a wide range of conditions, i.e. for various flow rates, angles of attack, hydrofoil geometries and flow regimes. While using the plexiglass walls, the hydrofoil can be observed by optical measurement methods. Moreover, this experimental setup has been studied by engineers who work for water turbine market leaders in cooperation with university scientists. [2]

The doctoral thesis is divided into three main parts. Firstly, the flow behaviour around hydrofoil is introduced, including the description of typical terms which are related to this phenomenon. At the end of this part, the main goals of the doctoral thesis, which have been set in the treatise earlier, are presented. The second part of this thesis contains the governing equations and the study of fluid added effects. Then, the studied case is specified and all experimental and numerical methods which are used in the research are presented. Finally, the third part focuses on all experimental and numerical results.

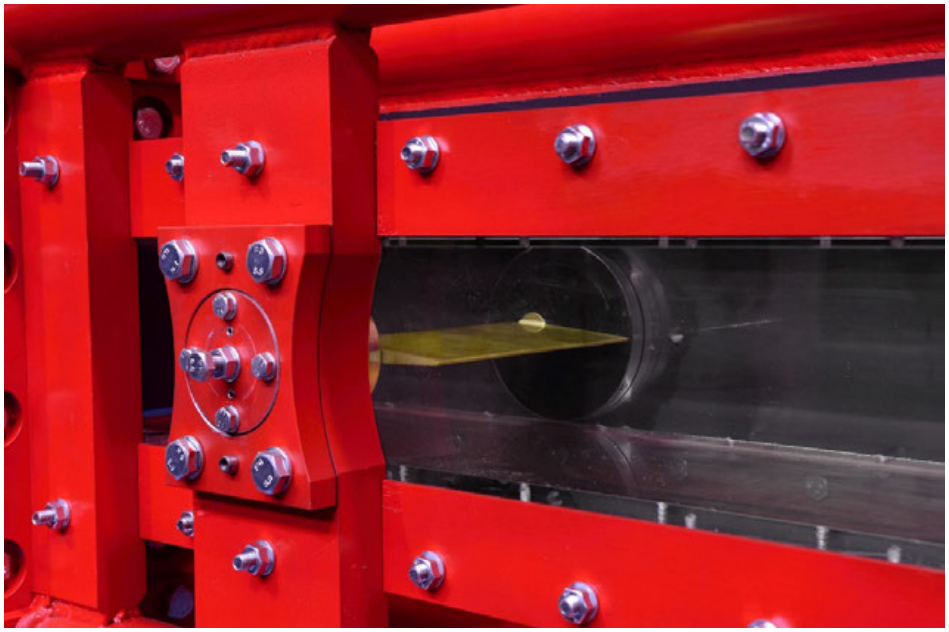

Fig. 1.1 Hydrofoil placed into the cavitation tunnel

2 FLOW BEHAVIOUR AROUND HYDROFOILS

A single profile which is placed into a fluid flow is a basic general case used in the field of fluid mechanics, aerodynamics, aircraft design as well as in the branch of hydromachinery. This simple case can provide a simplified approach to study the flow behaviour instead of analysing complicated structure such as turbine runner. As the shape of the profile has major impact on the flow behaviour, its proper design is crucial for successful development of an aircraft wing or a turbine runner. In many cases, including the branch of hydraulic machines, the geometry of the profiles is based on NACA profiles, which are profiles developed by National Advisory Committee for Aeronautics (NACA). The shapes of these profiles are defined by series of digits, which can be used in equations as parameters, to obtain a proper mathematical description of the profile shape. Since the investigation of dynamic response of a whole turbine runner involves many input parameters, which may result in huge series of investigations, a simple hydrofoil NACA 0005 has been selected for studying of the interaction between the flow dynamics and the hydrofoil dynamics. The detailed description of the test circuit including the test section, hydrofoil mounting and sensors overview can be found in Chapter 6.

2.1 Role of Tangential Forces in Fluid Flow

When a fluid flow is observed, two types of forces are present inside the fluid. Firstly, there are normal forces which result into pressure and secondly, there are tangential forces which are caused by the fluid viscosity and result into shear stresses.

In case of theoretical investigations or numerical modelling of such phenomenon, two types of fluid models are usually considered: the ideal fluid and the real fluid. The ideal fluid is considered to be inviscid and incompressible, which means that only normal forces are present inside the fluid, resulting into pressures. In recent decades, the mathematical theory based on the model of ideal fluid was well developed and provides satisfactory results in many applications. However, there are still many cases where the results remain unacceptable and the fluid needs to be modelled as real fluid. The advantage of the real fluid is that apart from the presence of the normal forces, the tangential forces inside the fluid as well as between the fluid and the walls are present. These tangential or friction forces result into the shear stresses and their existence is related to fluid viscosity. As a consequence, different velocity fields on the boundary between the fluid and a solid body are typical for each of these two models. On the one hand, the ideal fluid slips along the boundary due to the absence of tangential forces. Such boundary is called *free-slip boundary*. On the other hand, the real fluid sticks to the boundary surface due to the presence of tangential forces and the flow velocity on such *no-slip boundary* is equal to zero. [3]

The viscosity of water, which is typical fluid used in the field of hydraulic machines, is very low compared to other liquids such as oil or glycerine. This means that the tangential forces inside the liquid are also very small and the flow of very low viscous liquids is nearly similar to the ideal liquid flow. However, the no-slip boundary condition has significant impact even for low viscous liquids and needs to be considered. Therefore, the modelling of fluid flow in this thesis is based on the assumptions that the water is viscous and incompressible. [3]

2.2 Laminar and Turbulent Flow Regimes

On a microscopic level of view, two different flow regimes, i.e. the laminar flow and the turbulent flow, can be observed depending on the ratio between the inertial and the viscous forces in the fluid. This nondimensional ratio is called Reynolds number Re and is generally defined as:

$$Re = \frac{Inertial\ forces}{Viscous\ forces} = \frac{v \cdot d}{\nu_L} \tag{2.1}$$

where

- v is free stream velocity
- d characteristic length
- ν_L kinematic viscosity.

On the one hand, large values of Reynolds number mean that the inertial forces are large relative to the viscous forces, which results into the turbulent flow. On the other hand, small values of Reynolds number represent flow where viscous forces are large enough to supress the fluctuations and the flow becomes laminar.

The transition between these two regimes occurs over some region of Reynolds numbers in which the flow fluctuates between the laminar and turbulent flow. Once the Reynolds number is higher than its critical value, the flow is considered as turbulent. The value of critical Reynolds number is different for various flow conditions. In case of flow inside a circular pipe, its critical value is equal to $Re_{crit} = 2300$. [3]

2.3 Boundary Layer and its Separation

A thin layer of fluid developing in flows with very high Reynolds numbers, which means that viscosity is low compared to inertial forces, is called boundary layer. Concept of the boundary layer was first published by Ludwig Prandtl [5] and is observed when bodies are placed into high velocity flow or in case of large bodies and moderate flow velocities. If the viscosity of the fluid is low, the friction tangential forces can be neglected in the flow core outside the boundary layer. However, the presence of tangential forces inside the boundary layer cannot be neglected, since the *no-slip boundary condition* plays important role in many cases even for low viscous fluids. Then, based on the Prandtl's concept, two flow regions can be assumed: the one is the inviscid fluid flow core and the other one is the boundary layer where the tangential forces are large. [3][4]

Within the boundary layer, the flow can be laminar or turbulent, i.e. laminar boundary layer or turbulent boundary layer.

In case of boundary layer around a flat plate, both the laminar and the turbulent boundary layers are observed (Fig. 2.1). As the flow moves along the surface, laminar boundary layer develops behind the leading edge of the plate and becomes turbulent further downstream. The position of the transition point x_c can be determined by the critical Reynolds number $Re_{x\,crit}$. In fact, the transition inside the boundary layer is a region of finite length around transition point x_c and is noticeable by a great increase in the boundary layer thickness and in the wall shear stress.

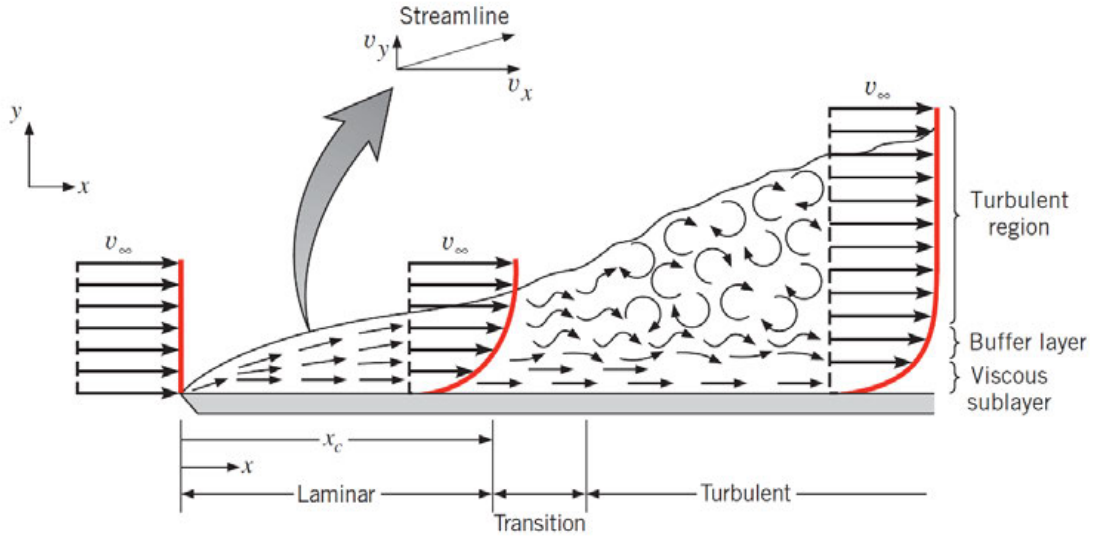

Fig. 2.1 Development of boundary layer thickness along flat plate surface [6]

In the laminar boundary layer, the flow is highly ordered and described by straight streamlines. Downstream from the leading edge, more and more fluid particles are slowed down by friction forces, which results into constant increase of the boundary layer thickness δ along the plate surface (Fig. 2.2). The flow stays laminar until the transition region is reached. Here, the triggering mechanisms coming from fluctuations in the free stream or which are induced by surface roughness result in the development of turbulent boundary layer. [3][6]

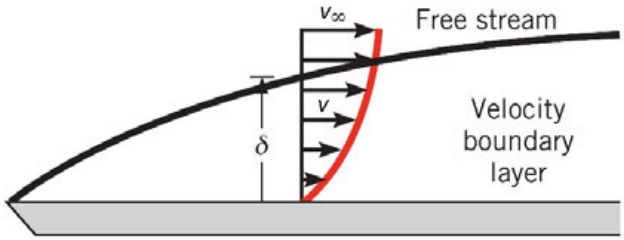

Fig. 2.2 Velocity profile near no-slip wall in laminar boundary layer [6]

Once the flow enters the turbulent boundary layer, it becomes highly irregular and random in all three dimensions. Mixing within the boundary layer causes inception of vortices near the flat plate, which grow and decay in time. As a consequence of this random behaviour, the velocity and pressure fluctuations occur. [3]

Inside the turbulent boundary layer, three main regions may be classified based on the distance from the flat plate surface (Fig. 2.1). Attached to the plate surface, there is a *viscous sublayer* where transport is dominated by diffusion. Further from the plate surface, the mechanism of diffusion and turbulent mixing becomes comparable. This region is called *buffer layer*. As the distance from the surface grows further, turbulent mixing transport is dominant inside the *turbulent region*. [6]

Each region of boundary layer, i.e. laminar and turbulent, has its typical velocity profile (Fig. 2.3). The turbulent velocity profile is relatively flat due to the presence of large velocity gradients within the viscous sublayer and the mixing that occurs inside the buffer layer and turbulent zone.

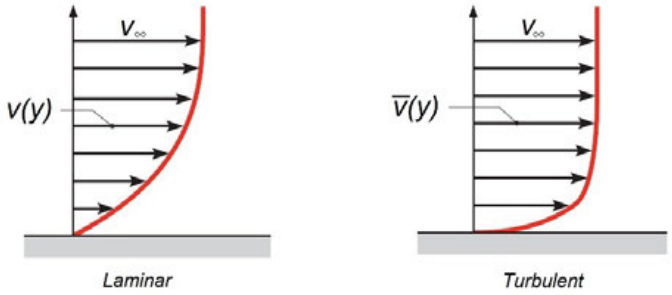

Fig. 2.3 Laminar and turbulent velocity profiles in boundary layer [6]

In case of the flow around a hydrofoil, the shape of its surface influences the flow behaviour. If the incidence angle of the hydrofoil is equal to zero and its thickness is low enough, which is typical for profiles used in hydraulic machines, the boundary layer stays attached to the surface along the whole profile up to the trailing edge. Then, due to the separation of boundary layer at the trailing edge, clockwise and anticlockwise rotating vortices separate behind the hydrofoil and Kármán vortex street can be observed. This phenomenon which is related to flow instability causes existence of periodic force acting from the fluid onto the hydrofoil's body. The shape of the trailing edge has major impact on the vortex shedding.

If the incidence angle is nonzero or the hydrofoil is thick enough, the boundary layer separates from the surface earlier and vortices produced by boundary separation mechanism are observed. This boundary layer separation process is caused by rapid increase of static pressure on the hydrofoil surface in the streamwise direction (Fig. 2.4). Particles which are moving very close to the surface and have lost most of their kinetic energy due to the friction forces, cannot move to this region of increased pressure. As the fluid near the surface decelerates, the velocity gradient on the surface as well as the wall shear stress τ become zero. At this location called separation point, the fluid has lack of momentum to overcome the pressure gradient and the boundary layer separation occurs. The backflow, which can be seen behind the separation point, causes formation of vortices. As vortices separate from the surface and move on downstream, the region filled with vortices follows downstream. Here, the pressure distribution on the hydrofoil surface in the streamwise direction changes and strong pressure drop is present, resulting in drag force acting on the hydrofoil. [3][6]

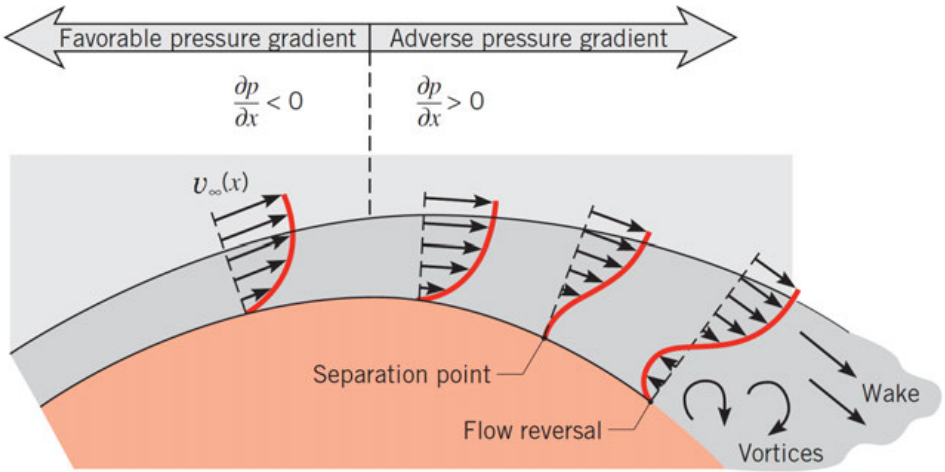

Fig. 2.4 Boundary layer separation [6]

Generally, two different mechanisms, both resulting in periodic force excitation of the hydrofoil, can be present when some fluid flows around a hydrofoil. The first mechanism is caused by boundary layer separation. The other mechanism - Kármán vortex street occurs in case that the boundary layer remains attached to the surface along the whole hydrofoil and separates at the trailing edge (Fig. 2.5), which causes another periodic force excitation of the hydrofoil. Both phenomena are considered as negative and therefore the aim of hydrofoil design for pumps and turbines is to reduce both excitation forces.

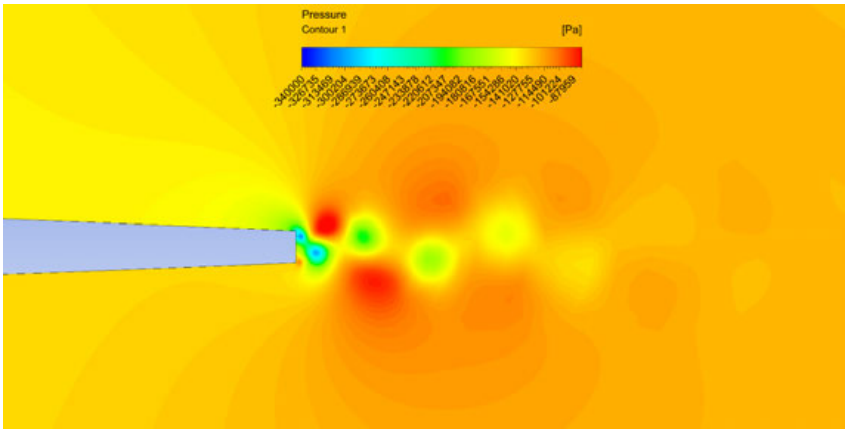

Fig. 2.5 Kármán vortex street – field of static pressure behind a hydrofoil

Most significant Kármán vortex shedding can be observed if the nondimensional Strouhal number St defined in equation (2.2) is equal to its critical value ($St_{crit} = 0.2$ for circular cylinder). Using the critical value of Strouhal number, the Kármán vortex shedding frequency can be estimated.

$$St = \frac{f \cdot d}{v} \tag{2.2}$$

Depending on the shape of the hydrofoil trailing edge, various intensity of vortex shedding as well as various magnitude of force excitation can be reached. The most significant vortex shedding can be observed on the blunt trailing edge (Fig. 2.6 – 01). If the flow flows around a rounded trailing edge (Fig. 2.6 – 02), no fixed separation point of the boundary layer is defined. Therefore, prediction of vortex shedding on such trailing edge using numerical simulation is most difficult. As the angle of top side of the trailing edge is increasing from (Fig. 2.6 – 03) to (Fig. 2.6 – 06) the intensity of vortex shedding is reduced. Due to the fact that the main focus of this doctoral thesis is the dynamic response of hydrofoil, the hydrofoil with blunt trailing edge providing highest intensity of vortex shedding was selected.

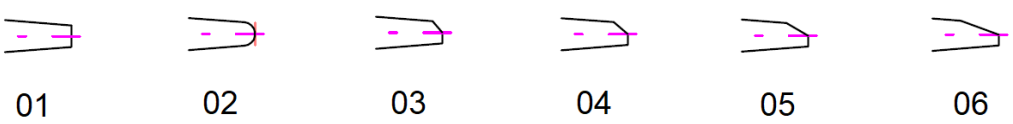

Fig. 2.6 Various shapes of trailing edge on a hydrofoil

2.4 Lock-in

Interaction between the flow and an elastic structure both influencing each other is a multidisciplinary problem and is called Fluid-Structure Interaction (FSI). The frequency of vortex shedding linearly depends on the flow velocity as it can be seen in equation (2.2). As the vortex shedding frequency rises with increasing flow velocity (i.e. with the frequency of force excitation acting on the hydrofoil structure), the coincidence with hydrofoil natural frequency over a range of flow velocity occurs. This effect is called *lock-in* and is a fundamental feature of flow-induced vibration. Lock-in leads to a significant increase of vibration amplitude. Under lock-in conditions, the range of flow velocity vs. the vortex-shedding frequency which is locked to the hydrofoil natural frequency is dependent on oscillation amplitude. The larger the vibration amplitude, the wider the range of the flow velocity. An example of lock-in effect was presented by Ausoni [7] (Fig. 2.7). Here, ratio of vortex shedding frequency and hydrofoil natural frequency is constantly equal to one in a wide range of flow velocity. In this lock-in region, the vortex shedding frequency is locked to the hydrofoil natural frequency. Outside this lock-in region, typical linear dependence of vortex shedding frequency on reduced flow velocity C^* is observed.

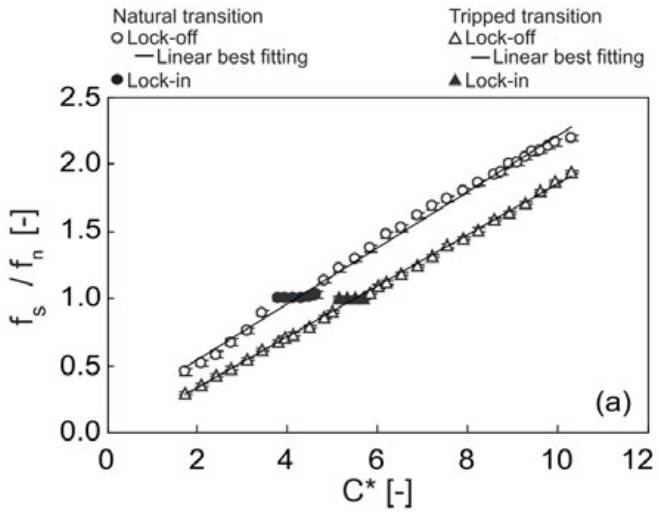

Fig. 2.7 Lock-in effect during flow induced vibration of a hydrofoil [7]

(f_s is vortex shedding frequency, f_n is hydrofoil natural frequency, C^* is reduced velocity)

2.5 Influence of Cavitation on Hydrofoil Dynamics

Cavitation in the fluid flow develops if the pressure in the fluid is lower than its vapour pressure p_V. The vapour pressure is temperature dependent fluid property and its value for water of temperature 20 °C is $p_V = 2.3\ kPa$. The cavitation is a negative phenomenon in almost all the cases especially in hydraulic machines. If the pressure in the flow of liquid drops significantly, the liquid transforms into vapour bubbles which move downstream with the flow. Depending on the flow conditions, various types of cavitation may develop, as described in Chapter 4.3. However, all types of cavitation represent unstable flow behaviour which produces additional force excitation of the hydrofoil. The presence of cavitation also has major impact on the fluid added effects, which are discussed later in this thesis and the dynamic response of the submerged structure. If the cavitation occurs near the surface of such a solid structure, a different density of vapour causes the change of added mass effect and also the change of natural frequency of the structure. Once the vapour bubbles reach a region with higher pressure, they disappear by implosion to itself and the vapour is transformed again to liquid. The cavitation in the hydraulic machines develops usually in off-design operating regimes.

3 GOALS OF THE DOCTORAL THESIS

At the beginning of this doctoral thesis, I would like to present the main goals of this thesis, which were set with regards to scientific research presented in Part II Modelling.

The following goals of the doctoral thesis were set:

- The identification of the added mass effect and the hydrodynamic damping based on the experiment will be carried out.

- The identification of the added effects will be carried out on a hydrofoil which will be excited both by the von Kármán vortex shedding and the separation of boundary layer (5° angle of attack).

- The study of the influence of cavitation on a dynamic response of the hydrofoil with the angle of attack of 5° will be presented.

The outputs of the doctoral thesis can be further used for both the investigation of added effects acting on the whole turbine runner and for study of its dynamic response.

II. MODELLING

4 GOVERNING EQUATIONS

In order to describe behaviour of real mechanical systems, various types of mathematical models are used.

Depending on the number of degrees of freedom (DOF), mechanical behaviour of a material can be assumed as a continuous mass (Eulerian approach) or a discrete system of particles (Lagrangian approach). The continuum has an infinite number of DOF, while the discrete system has a finite number of DOF. As computers can use only discrete values, the numerical methods used for computational simulations are based on the assumption of a discrete system with finite number of DOF.

Mathematical models based on both the Eulerian and Lagrangian approach can be described by linear or nonlinear equations (both time dependent and time independent). According to what kind of equation is used to describe the model, the system is considered as linear or nonlinear.

There are two causes of mechanical system oscillations: the system is not in state of static equilibrium (free oscillations) or some external excitation force is acting on the system (forced oscillations).

The following paragraphs present various mathematical approaches to the description of material behaviour. At first, the motion equations for solid structures are presented. After that, the governing equations used in fluid mechanics are described, i.e. the continuity equation and Navier-Stokes equations. Finally, the equations modelling the cavitation bubbles dynamics and the coupled system of motion equations for fluid-structure interaction problem are shown.

4.1 Solid Mechanics

Since the particles of a solid material do not change its reciprocal positions compared to the liquids, both approaches, i.e. the Lagrangian and Eulerian, are used to describe the mass behaviour in the solid mechanics field. The two mathematical models considering the mass as a continuum (Eulerian approach) and as a system of discrete particles (Lagrangian approach) are described below. The derivations and equations in parts 4.1 and 4.2 are cited and summarized from [8].

4.1.1 Mathematical Model of Continuum Elastodynamic Problem

The governing equation of the dynamic behaviour of a continuum mass is based on the equilibrium (4.1) of mass forces $F_{M,i}$, surface forces $F_{S,i}$ and inertial forces $F_{Inertial,i}$. The symbol $\frac{\mathrm{D}}{\mathrm{D}t}$ represents material derivative.

$$\iiint_V \left(\mathrm{d}F_{M,i} + \mathrm{d}F_{S,i}\right) \mathrm{d}V = \iiint_V \left(\rho \frac{\mathrm{D}^2 u_i}{\mathrm{D}t^2}\right) \mathrm{d}V \tag{4.1}$$

Using formulas (4.2), the equation (4.1) can be written as (4.3):

$$\begin{aligned} \mathrm{d}F_{M,i} &= \rho a_i \\ \mathrm{d}F_{S,i} &= \frac{\partial S_{ij}}{\partial x_j} \\ \mathrm{d}F_{inertial,i} &= \rho \frac{D^2 u_i}{Dt^2} \end{aligned} \tag{4.2}$$

$$\iiint_V \left(\rho a_i + \frac{\partial S_{ij}}{\partial x_j} - \rho \frac{\mathrm{D}^2 u_i}{\mathrm{D}t^2} \right) \mathrm{d}V = 0 \qquad i,j = 1,2,3 \tag{4.3}$$

where

- a_i are components of acceleration
- S_{ij} stress tensor of the structure
- x_j coordinate
- $u_i\ (x_i, t)$ deformation vector component
- t denotes the time.

The equation (4.3) can be applied to any volume V in case the expression inside the integral is equal to zero. By satisfying this condition, the motion equations for continuum mass in general form (4.4) are obtained.

$$\rho \frac{\mathrm{D}^2 u_i}{\mathrm{D}t^2} = \rho a_i + \frac{\partial S_{ij}}{\partial x_j} \quad i,j = 1,2,3 \tag{4.4}$$

These general equations are valid for any type of continuum. Depending on which type of continuum is considered, the stress tensor definition and particle motion ability may vary. Assuming the linearly elastic isotropic continuum, the stress – strain relationship is given by Hook's law (4.5):

$$S_{ij} = \lambda \delta_{ij} \vartheta + 2\mu \varepsilon_{ij} \quad i,j = 1,2,3 \tag{4.5}$$

where

- δ_{ij} is Kronecker delta
- ϑ relative volume change given by (4.6)
- ε_{ij} strain tensor.

$$\vartheta = \varepsilon_{11} + \varepsilon_{22} + \varepsilon_{33} = \frac{\partial u_1}{\partial x_1} + \frac{\partial u_2}{\partial x_2} + \frac{\partial u_3}{\partial x_3} \tag{4.6}$$

Additionally, the two material-dependent Lamé parameters denoted by λ and μ are introduced. The Lamé first parameter λ is defined by equation (4.7), where E refers to Young's modulus and ν is the Poisson's ratio. The Lamé second parameter μ is called shear modulus in the context of elasticity.

$$\lambda = \frac{\nu E}{(1+\nu)(1-2\nu)} \tag{4.7}$$

By using the substitution (4.8) into (4.4), the motion equation for linearly elastic isotropic continuum (4.9) is obtained.

$$\frac{\partial S_{ij}}{\partial x_j} = (\lambda + \mu)\frac{\partial \vartheta}{\partial x_i} + \mu \frac{\partial^2 u_i}{\partial x_j \, \partial x_j} \quad i,j = 1,2,3 \tag{4.8}$$

$$\rho \frac{\mathrm{d}^2 u_i}{\mathrm{d}t^2} = \rho a_i + (\lambda + \mu)\frac{\partial \vartheta}{\partial x_i} + \mu \frac{\partial^2 u_i}{\partial x_j \, \partial x_j} \quad i,j = 1,2,3 \tag{4.9}$$

4.1.2 Mathematical Model of Linear Discrete System Oscillations

Developing the mathematical model of a linear discrete system with *n*-degrees of freedom is based on the Lagrange equations of motion of the second kind (4.10).

$$\frac{\mathrm{d}}{\mathrm{d}t}\left(\frac{\partial E_k}{\partial \dot{q}_\iota}\right) - \frac{\partial E_k}{\partial q_i} = Q_i \quad i = 1, 2, 3, \dots, n \tag{4.10}$$

where

- E_K is kinetic energy
- q_i generalized coordinates
- $Q_i = Q_i(q_1,\ q_2, \dots, q_n, \dot{q_1},\ \dot{q_2}, \dots, \dot{q_n}, t\ )$ generalized forces
- *n* number of DOF.

Assuming a linear system, generalized forces Q_i can be written as a sum of excitation forces $F_i(t)$ dependent on time, conservative potential forces Q_i^P and dissipative (damping) forces Q_i^D.

$$Q_i = Q_i^P(q_1, q_2, \dots, q_n) + Q_i^D(\dot{q_1}, \dot{q_2}, \dots, \dot{q_n}) + F_i(t) \tag{4.11}$$

Generalized conservative forces Q_i^P can be derived from potential energy $E_P(q_1, q_2, \dots, q_n)$.

$$Q_i^P = -\frac{\partial E_P}{\partial q_i} \quad i = 1, 2, 3, \dots, n \tag{4.12}$$

Generalised damping forces can be derived from Rayleigh dissipation function $R(\dot{q_1}, \dot{q_2}, \dots, \dot{q_n})$.

$$Q_i^D = -\frac{\partial R}{\partial \dot{q}_\iota} \quad i = 1, 2, 3, \dots, n \tag{4.13}$$

Excitation forces $F_i(t)$ are defined by virtual work principle:

$$\delta W_i = F_i \delta q_i \quad i = 1, 2, 3, \dots, n \tag{4.14}$$

where δW_i is the virtual work done by all forces (except the conservative and damping force). The virtual displacement δq_i is characterized by virtual change of only one generalized coordinate q_i.

Then the Lagrange equations of motion (4.10) can be rewritten as

$$\frac{\mathrm{d}}{\mathrm{d}t}\left(\frac{\partial E_k}{\partial \dot{\boldsymbol{q}}}\right) - \frac{\partial E_k}{\partial \mathbf{q}} + \frac{\partial E_P}{\partial \mathbf{q}} + \frac{\partial R}{\partial \dot{\boldsymbol{q}}} = \boldsymbol{f}(t) \tag{4.15}$$

using the vector of generalized coordinates $\boldsymbol{q}(t)$ and the vector of excitation forces $\boldsymbol{f}(t)$.

The terms E_k, E_P and R can be substituted by following equations (4.16).

$$E_k = \frac{1}{2}\dot{\boldsymbol{q}}^T \boldsymbol{M_S}\dot{\boldsymbol{q}}, \qquad E_P = \frac{1}{2}\dot{\boldsymbol{q}}^T \boldsymbol{K_S}\dot{\boldsymbol{q}}, \qquad R = \frac{1}{2}\dot{\boldsymbol{q}}^T \boldsymbol{B_S}\dot{\boldsymbol{q}} \tag{4.16}$$

Then, the motion equation of *n-degree-of-freedom* linear system with constant coefficients is obtained and can be written in various forms: (4.17) and (4.18) [8].

$$M_{ij}\ddot{q}_j + B_{ij}\dot{q}_j + K_{ij}q_j = f_i(t) \qquad i,j = 1,2,3,\dots,n \tag{4.17}$$

$$\boldsymbol{M_S}\ddot{\boldsymbol{q}} + \boldsymbol{B_S}\dot{\boldsymbol{q}} + \boldsymbol{K_S}\boldsymbol{q} = \boldsymbol{f}(t) \tag{4.18}$$

where

- $\boldsymbol{M_S}, \boldsymbol{B_S}, \boldsymbol{K_S}$ are real n × n matrices of structural mass, damping and stiffness
- $\boldsymbol{q}, \dot{\boldsymbol{q}}, \ddot{\boldsymbol{q}}$ the column vectors of generalized coordinates and its time derivatives, i.e. generalized velocity and acceleration
- $\boldsymbol{f}(t)$ the column vector of generalized forces.

If the linear system has only one degree of freedom (Fig. 4.1), the equation of motion has a simple form:

$$m_S\ddot{q} + b_S\dot{q} + k_S q = f(t) \tag{4.19}$$

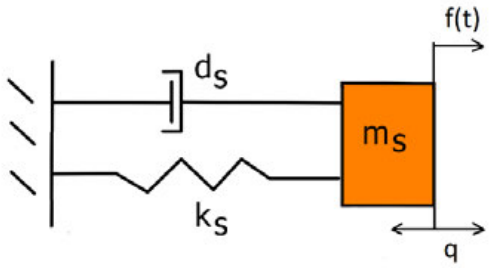

Fig. 4.1 Scheme of SDOF system

4.2 Fluid Mechanics

The general term '*fluids*' involves both the liquids and the gases. Compared to solid structures, fluid particles are not fixed and can move freely. The description of such behaviour for all particles would be very complicated. Therefore, the Eulerian approach describing the whole fluid volume as a continuum is more common. As the presented research is focused on hydraulic machines operating in water, the following paragraphs will be restricted by considering only liquids.

The two main models are used to describe the liquid behaviour: the real liquid and the ideal liquid. The real liquid has two main properties compared to the ideal one: the internal fluid friction, which is the result of cohesive forces acting between liquid particles, and the compressibility of the liquid. The ideal liquid has no internal fluid friction and is incompressible.

4.2.1 Mathematical Model of the Fluid Flow

The Eulerian based system of governing equations which describes the liquid behaviour consists of mass and momentum conservation equations. They correspond to the continuity equation (4.21) and the Navier-Stokes equations. The liquid is considered as real with constant density (4.20) and gravity is neglected.

$$\rho = const. \tag{4.20}$$

$$\frac{\partial v_i}{\partial x_i} = 0 \tag{4.21}$$

The general motion equation of a continuum is given in (4.22).

$$\begin{gathered}\iiint_V \left(\mathrm{d}F_{M,i} + \mathrm{d}F_{S,i}\right)\mathrm{d}V = \iiint_V \left(\rho \frac{\mathrm{D}^2 u_i}{\mathrm{D}t^2}\right)\mathrm{d}V \\ \iiint_V \left(\rho a_i + \frac{\partial \sigma_{ij}}{\partial x_j} - \rho \frac{\mathrm{D}^2 u_i}{\mathrm{D}t^2}\right)\mathrm{d}V = 0 \qquad i,j = 1,2,3\end{gathered} \tag{4.22}$$

Here, the mass forces $F_{M,i}$, the surface forces $F_{S,i}$ and the inertial forces $F_{Inertial,i}$ acting on the continuum are in equilibrium. By satisfying the condition that the expression inside the integral is equal to zero and by using the substitutions given in (4.23), the motion equations for continuum mass in general form (4.24) are obtained.

$$\begin{gathered}\mathrm{d}F_{M,i} = \rho a_i \\ \mathrm{d}F_{S,i} = \frac{\partial \sigma_{ij}}{\partial x_j} \\ \mathrm{d}F_{inertial,i} = \rho \frac{\mathrm{D}^2 u_i}{\mathrm{D}t^2} = \rho\left(\frac{\partial v_i}{\partial t} + v_j \frac{\partial v_i}{\partial x_j}\right)\end{gathered} \tag{4.23}$$

$$\rho a_i + \frac{\partial \sigma_{ij}}{\partial x_j} - \rho\left(\frac{\partial v_i}{\partial \mathrm{t}} + v_j \frac{\partial v_i}{\partial x_j}\right) = 0 \tag{4.24}$$

Various types of continuum are distinguished by the definition of the stress tensor σ_{ij} which is given for a real Newtonian liquid as follows (4.25):

$$\sigma_{ij} = -p\delta_{ij} + \lambda\dot{\vartheta}\delta_{ij} + 2\mu v_{ij} \tag{4.25}$$

where

- $p\ (x_i, t)$ is pressure
- δ_{ij} Kronecker delta
- $\dot{\vartheta}$ volumetric dilatation rate
- v_{ij} strain tensor rate
- λ and μ are the Lamé first and second parameters.

Both volumetric dilatation rate and strain tensor rate can be substituted by (4.26).

$$\dot{\vartheta} = \frac{\partial v_j}{\partial x_j} \qquad v_{ij} = \frac{1}{2}\left(\frac{\partial v_i}{\partial x_j} + \frac{\partial v_j}{\partial x_i}\right) \tag{4.26}$$

The real liquid is defined by the only physical parameter which is the dynamic viscosity μ_D. The Lamé first parameter λ represents the volume viscosity, while the Lamé second parameter μ represents the dynamic viscosity (4.27) in the context of fluid mechanics.

$$\mu = \mu_D \tag{4.27}$$

After the substitution of (4.26) and (4.27) into (4.25), the definition of the stress tensor in the real liquid is obtained (4.28).

$$\sigma_{ij} = \left(-p + \lambda \frac{\partial v_j}{\partial x_j}\right)\delta_{ij} + \mu_D \left(\frac{\partial v_i}{\partial x_j} + \frac{\partial v_j}{\partial x_i}\right) \tag{4.28}$$

Then the definition of the stress tensor (4.28) can be substituted into (4.24). The general equations of motion for the real liquid (4.29), called Navier-Stokes equations, are obtained [8]. Here the mass forces are neglected ($F_{M,i} = 0$) and the incompressible liquid with constant viscosity is assumed. The unknown parameters in the equations are the pressure $p(x_i, t)$ and the velocity fields $v_i(x_i, t)$ defined at each point (x_i) as a function of time *t*.

$$\frac{\partial v_i}{\partial t} + v_j \frac{\partial v_i}{\partial x_j} = -\frac{1}{\rho}\frac{\partial p_i}{\partial x_i} + \nu_L \frac{\partial^2 v_i}{\partial x_j \, \partial x_j} \quad i = 1,2,3 \tag{4.29}$$

The three equations (4.29) describe the laminar flow or instantaneous state of turbulent flow. As most of real fluid flow problems are turbulent, statistical approach needs to be introduced to involve turbulence. The two unknown fields are decomposed as a sum of a mean term, marked with an upper line, and a fluctuating term marked by a prime sign (4.30).

$$\begin{aligned} v_i &= \bar{v}_i + v'_i \\ p &= \bar{p} + p' \end{aligned} \tag{4.30}$$

The governing equations that describe the turbulent flow are obtained by substitution of (4.30) into (4.21) and (4.29). These equations are called Reynolds Averaged Navier-Stokes equations (RANS) and are given in (4.31) and (4.32).

$$\frac{\partial \bar{v}_i}{\partial \mathrm{x}_i} = 0 \tag{4.31}$$

$$\frac{\partial \bar{v}_i}{\partial \mathrm{t}} + \bar{v}_j \frac{\partial \bar{v}_i}{\partial x_j} = -\frac{1}{\rho}\frac{\partial \bar{p}}{\partial x_i} + \nu_L \frac{\partial^2 \bar{v}_i}{\partial x_j \, \partial x_j} + \frac{1}{\rho}\frac{\partial \tau_{t,ij}}{\partial x_j} \tag{4.32}$$

Consequently, a new term $\boldsymbol{\tau_t}$ called Reynolds tensor (4.33) is introduced.

$$\frac{\partial \tau_{t,ij}}{\partial x_j} = -\frac{\partial}{\partial x_j}\left(\rho \bar{v}_i \bar{v}_j\right) \tag{4.33}$$

This tensor is symmetric and has six independent components. In that case, the complete mathematical model consists of four equations (RANS equations) and has ten unknown parameters (three velocity components, pressure and six Reynolds tensor components). As the number of unknown parameters is higher than the number of equations, the system of equations has to be closed with the so-called closure model [9]. There are various types of closure models. Most of them are based on Boussinesq hypothesis (4.34), which enables to model Reynolds stress tensor components in isotropic turbulence.

$$\tau_{t,ij} = \mu_t \left(\frac{\partial \bar{v}_i}{\partial x_j} + \frac{\partial \bar{v}_j}{\partial x_i}\right) - \frac{2}{3}\rho \delta_{ij} k = 2\mu_t \bar{v}_{ij} - \frac{2}{3}\rho \delta_{ij} k \tag{4.34}$$

Boussinesq hypothesis assumes that Reynolds stress tensor components are proportional to the mean strain rate tensor $\bar{v}_{ij}$. The two unknown parameters are the turbulent eddy viscosity μ_t and the turbulent kinetic energy *k* defined as (4.35).

$$k = \frac{1}{2}\overline{v'_J v'_J} \tag{4.35}$$

4.2.2 Turbulence modelling

The most frequently used closure models are the two equation models which close the equation system with two additional equations. Two equation models are widely used due to their good computational accuracy and acceptable numerical effort.

Finally, the completely closed system of equations is established. It consists of four RANS equations and two additional equations obtained by applying Boussinesq hypothesis. As a solution of this equation system, the six unknown parameters (three velocity components, pressure, turbulence eddy viscosity and turbulence kinetic energy) are obtained.

The two basic turbulence models, which use two equations, are the *k-ε turbulence model* and the *k-ω turbulence model*. Each of these two models has different strong sides. The k-ε turbulence model usually overestimates the turbulent eddy viscosity μ_t. As the k-ε turbulence model does not provide integration of the velocity field up to the wall surface, the velocity filed is approximated by the wall functions. Therefore, this turbulence model does not provide good prediction of boundary layer separation. The k-ε turbulence model is recommended for high Reynolds flows, where turbulent Reynolds number Re_t given by equation (4.36) is $Re_t > 300$.

$$Re_t = \frac{y \cdot \sqrt{k}}{\nu_L} \tag{4.36}$$

where

- ν_L is kinematic viscosity
- k turbulence kinetic energy
- y perpendicular distance to the nearest wall.

The k-ε turbulence model uses two model equations, first for turbulence kinetic energy k (4.37) and the other for turbulence dissipation ε (4.38). The turbulent eddy viscosity μ_t is given by Prandtl-Kolmogorov relationship (4.39).

$$\frac{\partial k}{\partial t} + \bar{v}_j \frac{\partial k}{\partial x_j} = \overline{v'}_i \bar{v}_j \frac{\partial \bar{v}_i}{\partial x_j} - \varepsilon + \frac{\partial}{\partial x_j}\left[\left(\nu_L + \frac{\mu_t}{\sigma_k}\right)\frac{\partial k}{\partial x_j}\right] \tag{4.37}$$

$$\frac{\partial \varepsilon}{\partial t} + \bar{v}_j \frac{\partial \varepsilon}{\partial x_j} = \frac{\partial}{\partial x_j}\left(\nu_L \frac{\partial \varepsilon}{\partial x_j} + \frac{\mu_t}{\sigma_e}\frac{\partial \varepsilon}{\partial x_j}\right) + C_{\varepsilon_1}\frac{\varepsilon}{k}\bar{v}_i \bar{v}_j \frac{\partial \bar{v}_i}{\partial x_j} - C_{\varepsilon_2}\frac{\varepsilon^2}{k} \tag{4.38}$$

$$\mu_t = C_\mu \frac{k^2}{\varepsilon} \tag{4.39}$$

where

- k is turbulent kinetic energy
- ε turbulent dissipation
- μ_t turbulent eddy viscosity
- σ_e, σ_k constants
- $C_\mu, C_{\varepsilon_1}, C_{\varepsilon_2}$ constants.

The second turbulence model, Wilcox k-ω turbulence model, is recommended for modelling of low Reynolds flows, where $Re_t < 300$. Here, ω represents the rate of turbulent dissipation (4.40).

$$\omega = \frac{\varepsilon}{k} \tag{4.40}$$

On the one hand, k-ω turbulence model provides better accuracy in modelling of boundary layer separation. On the other hand, the free stream turbulence cannot be well captured by this model. Main advantage of this model is that it can perform the integration up to the wall surface instead of approximation of the solution in the near-wall region by wall functions. However, to provide the solution in the near-wall region, the computational mesh must be fine enough, to ensure that the y^+ value given by (4.41) is less or equal to one. The y^+ is the length scale of the turbulent boundary layer.

$$y^+ = \frac{u_\tau y}{\nu_L} \tag{4.41}$$

$$u_\tau = \sqrt{\frac{\tau_{wall}}{\rho}} \tag{4.42}$$

where

- y is perpendicular distance to the nearest wall
- u_τ friction velocity
- τ_{wall} wall shear stress.

The k-ω turbulence model uses the same model equation for turbulence kinetic energy k (4.37) as the k-ε turbulence model. In addition, the second model equation represents the transk-port of rate of turbulent dissipation ω.

Both the k-ε and the k-ω turbulence models provide good accuracy in different flow regions. Therefore, Menter [9] developed an advanced *Shear Stress Transport (SST) model*. The SST model combines the k-ε turbulence model and the Wilcox k-ω turbulence model with the help of a blending function. The blending function value varies from zero to one depending mainly on the perpendicular distance from the nearest wall. Close to the wall surface, the blending function is equal to one and the Wilcox k-ω turbulence model is used. As the wall distance rises, the value of the blending function decreases up to zero. In this transition region, both models are considered by a proportion that depends on the gradients. Further from the wall surface, the blending function stays equal to zero and the k-ε turbulence model is used for free shear flow modelling.

Due to the combination of two models, SST model is a good compromise between need of very fine computational mesh in whole fluid domain and accuracy of numerical results. The SST model has become very popular in recent years especially in the field of hydraulic machines. Therefore, this model is used in numerical simulations in this doctoral thesis.

4.3 Mathematical Description of Cavitation Dynamics

The presence of cavitation strongly influences the fluid dynamics as well as the dynamic response of the hydrofoil. The three main types of cavitation around hydrofoil as shown in the figure (Fig. 4.2) can be observed: the edge cavitation (a), the sheet cavitation (b) and the supercavitation (c). Once the sheet cavitation develops, the cavitation cloud is periodically shedding from the hydrofoil surface and generates a periodic excitation force acting on the hydrofoil (Fig. 4.3). As the cavitation cloud is filled by vapour and its size is periodically changing, the fluid added effects are strongly affected [11][12].

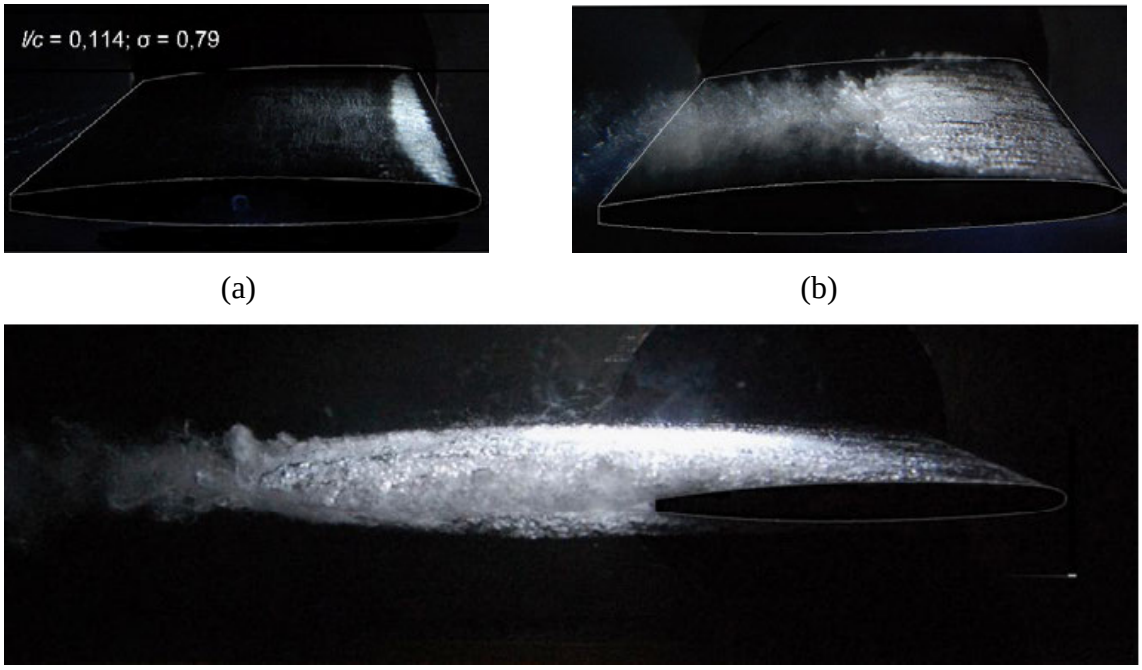

(a) (b)

(c)

Fig. 4.2 Cavitation regimes: a) edge cavitation b) sheet cavitation c) supercavitation [13]

Cavitation phenomenon can be described by nondimensional cavitation number σ defined by equation (4.43):

$$\sigma = \frac{p_\infty - p_V(T_{ref})}{\frac{1}{2}\rho_L v_\infty^2} \tag{4.43}$$

where

- p_∞ free stream pressure
- p_V pressure of saturated vapour (function of temperature)
- T_{ref} reference operating temperature
- ρ_L liquid density
- v_∞ free stream velocity.

This parameter σ can be assigned to any flow. Depending on its value, single-phase or multi-phase flow is observed. If the value of cavitation number is large enough, a single-phase flow occurs. As the value of σ is decreased, cavitation nuclei occur. The cavitation number related to the presence of first cavitation nuclei is called the incipient cavitation number σ_{inc}. Further decrease of cavitation number σ below σ_{inc} leads to more massive forming of vapour bubbles. Such flow is considered of multi-phase flow. [11][12]

The definition of cavitation number σ in experiments is calculated from equation (4.44). Herein, the reference pressure p_2 is measured by sensor no. 2 mounted on the draft tube (Fig. 6.12), the vapour pressure p_V is calculated from equation (4.45), the density of water is calculated from equation (4.46) and the flow rate Q_V is measured by flow meter of cross-section area S_{cross}. The reference temperature T_{ref} is measured by thermometer located inside the water tank.

$$\sigma = \frac{p_2 - p_V(T_{ref})}{\frac{1}{2}\rho_L \left(\frac{Q_V}{S_{cross}}\right)^2} \tag{4.44}$$

$$p_V = 10^{2.7862+0.0312\cdot T_{ref}-0.000104\cdot T_{ref}^2} \tag{4.45}$$

$$\rho_L = 1002 - 0.2716 \cdot T_{ref} + 0.01047 \cdot T_{ref}^2 - 0.00027 T_{ref}^3 \tag{4.46}$$

The computational modelling of cavitation is based on mixture model with Rayleigh-Plesset equation (4.47):

$$\frac{p_b(t) - p_\infty(t)}{\rho_L} = r\frac{\mathrm{d}^2 r}{\mathrm{d}t^2} + \frac{3}{2}\left(\frac{\mathrm{d}r}{\mathrm{d}t}\right)^2 + 4\frac{\nu_L}{R}\frac{\mathrm{d}r}{\mathrm{d}t} + \frac{2S}{\rho_L r} \tag{4.47}$$

where

- p_b is bubble pressure
- p_∞ reference pressure
- ρ_L liquid density
- r radius of the bubble
- ν_L kinematic viscosity of the liquid
- S is surface tension.

Since the integration of the Rayleigh-Plesset equation is very difficult, the simplified fomula (4.48) is usually used.

$$\frac{\mathrm{dr}}{\mathrm{dt}} = \sqrt{\frac{2}{3}\frac{p_b(t) - p_\infty(t)}{\rho_L}} \tag{4.48}$$

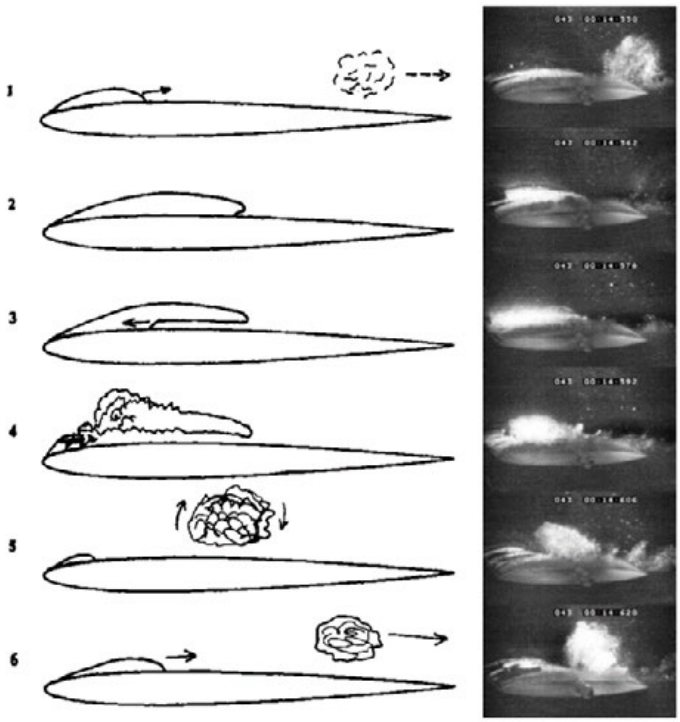

Fig. 4.3 Development of the sheet cavitation [14]

4.4 Motion Equation of Oscillating Body Submerged in Liquid

When a solid body oscillates in the air, its motion can be described by the motion equation (4.18) which assumes small linear oscillations. Here, the force $f(t)$ is a periodic external excitation force acting on the structure (4.49) [8].

$$\boldsymbol{M_S\ddot{q} + B_S\dot{q} + K_S q = f}(t)$$

$$\boldsymbol{f}(t) = f_{max} \cdot e^{i(\omega t)} = f_{max}(\cos \omega t + i \cdot \sin \omega t) \tag{4.49}$$

Considering such oscillating structure submerged into a viscous liquid, its dynamic response is altered by additional force $F_i(t)$. This force acts from the liquid on the surface of the body (4.50) which is in contact with the liquid and is called Fluid-Structure Interface (FSI Interface).

$$\boldsymbol{M_S\ddot{q} + B_S\dot{q} + K_S q = f}(t) + \boldsymbol{F}(t) \tag{4.50}$$

The force $F_i(t)$ is defined as multiplication of the liquid stress tensor σ_{ij} and outward-pointing normal vector n_j integrated over the FSI Interface (4.51).

$$F_i(t) = -\int_A \sigma_{ij} \cdot n_j \mathrm{d}A \tag{4.51}$$

Both the structural field and the fluid field are coupled by the two following conditions that must be satisfied at the FSI Interface:

$$\sigma_{ij} \cdot n_j = S_{ij} \cdot n_j \tag{4.52}$$

$$v_i = \dot{u}_i \tag{4.53}$$

where

- σ_{ij} is stress tensor of the liquid
- S_{ij} stress tensor of the structure
- n_j outward-pointing normal vector
- v_i velocity vector of the liquid at the FSI Interface
- $\dot{u}_i$ is velocity vector of the structure at the FSI Interface.

After substitution (4.51) into the solid body motion equation (4.50), the general motion equation of the oscillating solid body submerged into a liquid is obtained (4.54) [15].

$$(\boldsymbol{M_S} + \boldsymbol{M_{ADD}})\ddot{\boldsymbol{q}} + (\boldsymbol{B_S} + \boldsymbol{B_{ADD}})\dot{\boldsymbol{q}} + (\boldsymbol{K_S} + \boldsymbol{K_{ADD}})\boldsymbol{q} = \boldsymbol{f}(t) \tag{4.54}$$

$$(m_S + m_{ADD})\ddot{q} + (b_S + b_{ADD})\dot{q} + (k_S + k_{ADD})q = f(t) \tag{4.55}$$

In this equation, the force $F(t)$ can be represented by three main added parameters called the added mass $\boldsymbol{M_{ADD}}$, the added damping $\boldsymbol{B_{ADD}}$ and the added stiffness $\boldsymbol{K_{ADD}}$. Alternatively, when a simplified Single Degree of Freedom (SDOF) system is considered (Fig. 4.4), the equation is reduced into (4.55).

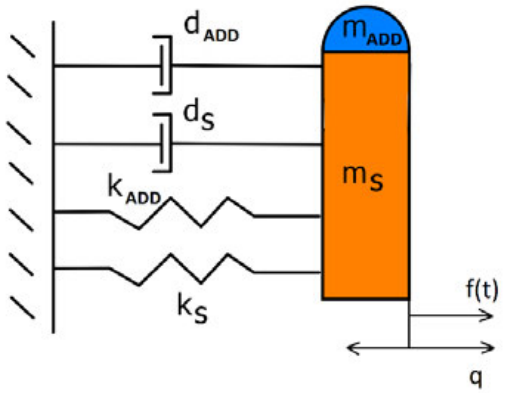

Fig. 4.4 SDOF system of submerged body

5 FLUID ADDED EFFECTS

The dynamic response of an immersed structure is strongly influenced by the presence of the liquid. In order to quantify the influence of the liquid on the dynamic response of the structure, the three main added effects were introduced: the added mass, the added damping and the added stiffness. In the field of hydraulic machinery, the identification of these added effects is crucial for successful design of hydraulic machines. Therefore, many research projects have been focused on the experimental and numerical investigation of the added effects in the hydraulic machines. Despite this massive effort, some phenomena have not been understood yet and many opened questions still remain. The most significant challenge is to properly describe the dynamics of the runner surrounded by water and to predict and quantify all excitations coming from the fluid dynamics [16]. The development of various methods for identification of added effects is often studied on a simple geometry of a hydrofoil placed into cavitation tunnel or on a model runner. The dynamics of such simple geometry submerged in water can be described by equation (4.55). Additionally, a more detailed classification of added effects for SDOF system included into the same equation can be found by Nennemann [17]:

$$(m_S + m_{ADD})\ddot{q} + (b_S + b_W + b_F)\dot{q} + (k_S + k_W + k_F)q = f(t) \tag{5.1}$$

$$b_W + b_F = b_{ADD} \tag{5.2}$$

$$k_W + k_F = k_{ADD} \tag{5.3}$$

where

- m_S is structural modal mass
- m_{ADD} added mass effect
- b_S structural damping of the solid material
- b_W added damping resulting from acoustic radiation and viscous effects
- b_F hydrodynamic (viscous) damping resulting from momentum exchange between the fluid and the structure as a result of the oscillation
- k_S structural stiffness
- k_W added stiffness due to compressibility effects
- k_F fluid added stiffness caused by the fluid flow
- $f(t)$ is external excitation force.

5.1 Added Mass Effect

When natural frequencies of a solid body which performs free oscillations in the air are studied, its first natural frequency $f_{nat,air}$ can be estimated by

$$f_{nat,air} = \frac{1}{2\pi}\sqrt{\frac{k_S}{m_S}} \tag{5.4}$$

However, if a solid body is submerged in a liquid and oscillates, it accelerates and decelerates during the periodic motion. Since the surrounding liquid is present, the solid body must displace some volume of the liquid with it as it moves. Therefore, a virtual inertial force $F_{ADD,MASS}$ which opposes the solid body motion is introduced (5.5) where m_{ADD} is the added mass. [18]

$$F_{ADD,MASS} = -m_{ADD}\ddot{q} \tag{5.5}$$

This virtual force results from pressure loading and viscous shear loading which are acting on the solid body. Both loadings are induced in the liquid by motion of the submerged body and represent a feedback of the liquid on the motion of the solid body. If a SDOF system is described by (4.19) and performs oscillations in a still water which is incompressible and inviscid, the added mass force $F_{ADD,MASS}$ can be implemented into the equation of motion as follows:

$$m_S\ddot{q} + b_S\dot{q} + k_S q = f(t) - F_{ADD,MASS} \tag{5.6}$$

After substitution of (5.5) into (5.6) and reordering the terms, the equation becomes:

$$(m_S + m_{ADD})\ddot{q} + b_S\dot{q} + k_S q = f(t) \tag{5.7}$$

which corresponds to a simple conception that the added mass effect can be modelled as an added mass of liquid which moves (oscillates) with the solid body (Fig. 4.4). Then a new natural frequency $f_{nat,water}$ of the coupled fluid-solid system can be calculated:

$$f_{nat,water} = \frac{1}{2\pi}\sqrt{\frac{k_S}{m_S + m_{ADD}}} \tag{5.8}$$

The ratio between the natural frequency in the air $f_{nat,air}$ and the natural frequency in water $f_{nat,water}$ is written as follows [13]:

$$\frac{f_{nat,air}}{f_{nat,water}} = \frac{\frac{1}{2\pi}\sqrt{\frac{k_S}{m_S}}}{\frac{1}{2\pi}\sqrt{\frac{k_S}{m_S + m_{ADD}}}} = \sqrt{\frac{m_S + m_{ADD}}{m_S}} \tag{5.9}$$

Finally, the added mass of water can be determined as

$$m_{ADD} = m_S \cdot \left[\frac{1}{\left(\frac{f_{nat,water}}{f_{nat,air}}\right)^2} - 1\right] \tag{5.10}$$

The added mass effect m_{ADD} controls the frequency of oscillations and causes the shift of natural frequencies compared to the values measured in the air.

The evaluation of both natural frequencies and added mass effect is usually the first step when a dynamic response of submerged body is investigated. The earliest beginnings of experimental investigation of the added mass effect were studied on cantilever plates [19] - [23]. At first, the natural frequencies of plates in the air were measured. Then, as the plates were partially and at the end also fully submerged into a liquid, the drop of natural frequencies was observed. The results were compared to analytical approaches for estimation of the added mass effect and later also to the numerical results. Additionally, some theoretical studies which were focused on mathematical properties of added mass matrix were also presented [24] [25].

In recent years, many research projects which focused on fluid added effects were carried out in the field of hydraulic turbines. The latest main requirement on the hydraulic turbines is to provide constant high efficiency in a wide operating range instead of designing turbine which provides high efficiency only in one optimal operating point. Consequently, many various excitation forces in such a wide operating range are present. Therefore, the proper determination of natural frequencies of the turbine runner

is necessary as resonance must be avoided. That is why various experimental investigations of the added mass effect acting on the turbine components (especially the turbine runner) were carried out [26] - [32]. Moreover, the detailed experimental and numerical study of the pump-turbine runner and its modal properties was carried out by professor Egusquiza [33].

The rapidly increasing hardware parameters have enabled to develop codes for simulations of various multi-field phenomena. One of them is the modal analysis of solid structure submerged into a liquid. In this analysis, the solid structure is modelled by standard solid elements while the fluid domain is represented by acoustic elements. These elements have one degree of freedom – pressure. The coupling of the two domains is defined at the FSI Interface and is realized by the special acoustic elements attached to this interface which have four degrees of freedom – three components of displacement and pressure. The main output of the acoustic modal analysis are the natural frequencies and corresponding mode shapes for both the submerged structure and the fluid domain. The only restriction of ANSYS software is that acoustic modal analysis can be modelled only with still liquid inside the fluid domain. [34]

The acoustic modal analysis has become a very common tool for investigation of the added mass effect nowadays. Several papers also presenting a good agreement with the experimental results have been published in recent years [34] - [39]. Moreover, advanced research was carried out focusing on the investigation of modal properties of a hydrofoil under cavitation conditions [40] - [42] .

5.2 Hydrodynamic Damping

The total damping of SDOF coupled system submerged into a liquid consists of structural damping b_S and added damping b_{ADD} which can be written as a sum of two contributions b_W and b_F in equation (5.2). The structural damping b_S is usually neglected since it is much lower than the added damping. The first added contribution b_W is the result of the acoustic radiation and of the viscous effects in the liquid. If the natural frequencies of submerged structure are obviously different from the natural frequencies of the fluid domain, i.e. from the nature frequencies of the fluid pressure field, the added damping b_W can be neglected. The other contribution b_F results from momentum exchange between the fluid and the structure. This added damping b_F is called viscous damping or hydrodynamic damping.

In the field of hydraulic machines, the first two contributions b_S and b_W are usually neglected. It is assumed that the total damping of the coupled system is equal to the hydrodynamic damping b_F [17].

If the SDOF mechanical system oscillates in a viscous incompressible liquid, the additional damping force $F_{ADD,DAMP}$ given by (5.11) is present. This force is the result of the viscous effects in the liquid and it is the only damping of the coupled oscillating system by neglecting the added damping b_W.

$$F_{ADD,DAMP} = -b_F \dot{q} \tag{5.11}$$

As the hydrodynamic damping b_F is the only present damping in the mechanical system, the whole dissipated energy from the mechanical system must be equal to the work W_{DISS} done by the damping force $F_{ADD,DAMP}$. [43]

$$W_{DISS} = \int F_{ADD,DAMP}\,\mathrm{d}u = \int_0^T b_F \dot{u}\,\frac{\mathrm{d}u}{\mathrm{d}t}\,\mathrm{d}t = b_F \int_0^T \dot{u}^2\,\mathrm{d}t \qquad (5.12)$$

If the mechanical system performs harmonic oscillations with period T, its deflection u and velocity $\dot{u}$ at time t are given by (5.13) and (5.14).

$$u = U_{MAX}\cos(\omega_0 t) \qquad (5.13)$$

$$\dot{u} = -U_{MAX}\,\omega_0 \sin(\omega_0 t) \qquad (5.14)$$

- u is deflection
- $\dot{u}$ velocity
- U_{MAX} maximal amplitude of deflection
- t time
- ω_0 undamped natural angular frequency
- ω_D is damped natural angular frequency.

After substitution of (5.14) into (5.12) and considering low damped system ($U_{MAX}(t) = U_{MAX}$; $\omega_0 = \omega_D$), the dissipated energy per one oscillation is written as:

$$W_{DISS} = b_F \omega_0^2 \int_0^T U_{MAX}(t)^2 \sin^2(\omega_0 t)\,\mathrm{d}t \qquad (5.15)$$

The integration can be calculated by using the formulas (5.16) and (5.17). Then the final formulation of the dissipated energy W_{DISS} per one oscillation is given by (5.18) . [43]

function	antiderivative
$\sin^2(x)$	$\frac{1}{2}(x - \sin(x)\cdot\cos(x))$
$\cos^2(x)$	$\frac{1}{2}(x + \sin(x)\cdot\cos(x))$

(5.16)

$$\int_0^T \sin^2(\omega_0 t)\,\mathrm{d}t = \int_0^T \cos^2(\omega_0 t)\,\mathrm{d}t = \frac{\pi}{\omega_0} \qquad (5.17)$$

$$W_{DISS} = \pi \omega_0 U_{MAX}^2 b_F \qquad (5.18)$$

The dissipation of energy from the above described SDOF oscillating system can be quantified by the damping coefficient b_F in the equation of motion or by the damping ratio ζ which is very common in the field of hydraulic machines. As described in Chapter 8.3, the damping ratio can be calculated by Modal Work Approach using unsteady CFD simulation.

While the added mass effect controls the frequency of oscillations and causes the shift of natural frequencies, the damping controls the amplitude of oscillations. This behaviour can be illustrated on a characteristic of SDOF system in frequency domain. As the value of damping ratio ζ increases, the amplitude decreases (Fig. 5.1).

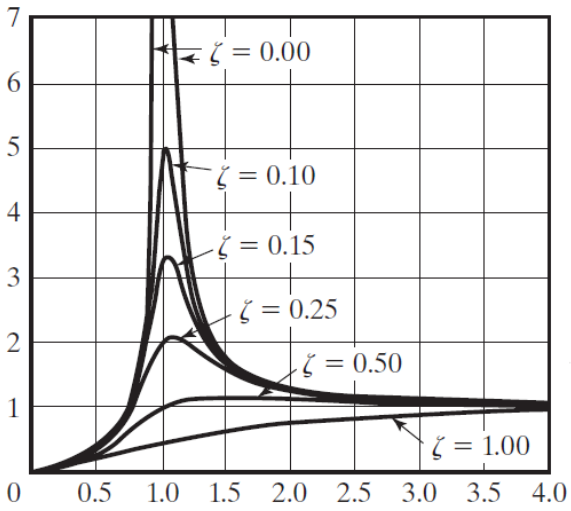

Fig. 5.1 Influence of damping ratio on the amplitude of oscillations [43]

(horizontal axis: normalized natural frequency; vertical axis: amplitude)

Since many excitation forces in the required wide operating range of modern turbines are present, the coincidence between the excitation and natural frequencies cannot be avoided. Therefore, the investigation of hydrodynamic damping for the main dominant modes of turbine components, mainly the runner, is necessary.

The earliest investigations of hydrodynamic damping in the field of hydraulic machines was published by Kaminer, who studied the investigation of added damping in gas turbines [44] as well as in the hydraulic turbines [45]. In recent years, the hydrodynamic damping has been intensively studied in Laboratory for Hydraulic Machines (LMH) at EPFL University in Lausanne in cooperation with UPC University in Barcelona and the main industry partners. The experimental research was carried out on various hydrofoils which were placed into the cavitation tunnel [46]. As the amplitudes of hydrofoil vibrations excited only by vortex shedding were small to observe, two excitation systems were developed. The first system which provides an impulse excitation was presented by Roth[47]: *"A non-intrusive technique, based on a spark generated bubble, is used to generate a wide band mechanical excitation. An underwater electric discharge at the bottom of the test section creates a fast growing and collapsing bubble which generates strong shock waves in the test section. The response of the blade to this excitation impulse is monitored with the help of a digital Laser Doppler Vibrometer*".

The other system provides harmonic excitation and consists of Macro Fibre Composite (MFC) piezoelectric actuators which are bonded to the hydraulic profile [48]. As a sinusoidal signal of voltage is used, the actuators deform. Since they are fully bonded to the hydrofoil surface, the deformation of hydrofoil is excited. This principle can be also used in the opposite direction. If the deformation of the hydrofoil (and also of the MFC actuator) is excited, a voltage is induced in the actuator. Therefore, MFC actuators can be used in pair, one for excitation and the other for measurement of the response, which is their main advantage. Alternatively, the response can be monitored by Laser Doppler Vibrometer (LDV). The MFC actuators have become a very common tool used for the investigation of dynamic response, since they can be also mounted on turbine runners. Various experimental results

of hydrodynamic damping investigation which were measured by the MFC actuators have been presented in recent years[49] - [51]. Further study of the influence of trailing edge shape on the hydrodynamic damping was published by Yao [52]. However, this area remains still not fully understood.

In the field of numerical methods, there are two main procedures which are used for hydrodynamic damping investigation: the two-way FSI coupled analysis [53] - [57] and modal work approach [17], [58], [59] - [61].

As intensive research of the hydrodynamic damping is being carried out and many papers related to this area have already been published, a wide summary of these publications has been presented by Trivedi [2] from NTNU Trondheim. Moreover, NTNU Trondheim organized workshop called *Francis-99* which was focused on the numerical investigation of hydrodynamic damping. The numerical results presented at this workshop [58] [62] [63] were validated by the experimental data provided by NTNU Trondheim [64] [65].

5.3 Fluid Added Stiffness

The total stiffness of the SDOF coupled system consists of three main contributions: the structural stiffness k_S, the added stiffness resulting from the viscous effects and liquid compressibility k_W and the flow induced added stiffness k_F.

The structural stiffness can be easily determined by applying a defined load and by obtaining corresponding deflection in the structural analysis. The added stiffness k_W has significant effect on the dynamic response only if the natural frequencies of submerged structure are obviously different from the natural frequencies of the fluid domain. If not, the added stiffness k_W can be neglected. The last contribution is the flow induced added stiffness k_F. It is present only if the liquid is considered as viscous. While the oscillating elastic body submerged in a liquid deflects, the added stiffness force $F_{ADD,STIFF}$, given by (5.19), starts to influence it. The magnitude of the added stiffness force $F_{ADD,STIFF}$ depends on the velocity of the flow.

$$F_{ADD,STIFF} = -k_F q \tag{5.19}$$

If the hydrofoil placed into the cavitation tunnel is studied, the flow induced stiffness cannot be neglected. Its quantification and degree of its impact can be determined using the visualisation of the flow field and evaluation of the forces acting on the elastic hydrofoil.

In case of such periodic oscillations of hydrofoil in the cavitation tunnel, the investigation of hydrodynamic damping assumes that the whole dissipated energy from the system is equal to work done by the additional damping force $F_{ADD,DAMP}$ given by (5.11). This assumption is only valid if the work done by the total added stiffness force $F_{ADD,STIFF,TOT}$, defined as (5.20), during one hydrofoil oscillation is equal to zero. Assuming that an oscillating displacement and the velocity displacement are given in (5.21) and (5.22), the work $W_{stiffness}$ performed by the added stiffness force $F_{ADD,STIFF,TOT}$ is obtained and given in (5.23).

$$F_{ADD,STIFF,TOT} = -(k_W + k_F)q \tag{5.20}$$

$$u = U_{MAX}\sin(\omega_0 t - \varphi) \tag{5.21}$$

$$\dot{u} = -U_{MAX}\omega_0\cos(\omega_0 t - \varphi) \tag{5.22}$$

$$W_{stiffness} = \int_1^2 F_{ADD,STIFF,TOT}\,\mathrm{d}u = \int_0^T F_{ADD,STIFF,TOT}\frac{\mathrm{d}u}{\mathrm{d}t}\,\mathrm{d}t \tag{5.23}$$

$$W_{stiffness} = \int_0^T (k_W + k_F)\,u\dot{u}\mathrm{d}t =$$

$$= U_{MAX}^2\omega_0(k_W + k_F)\int_0^T \sin(\omega_0 t - \varphi)\cdot\cos(\omega_0 t - \varphi)\,\mathrm{d}t$$

$$= \frac{U_{MAX}^2\omega_0(k_W + k_F)}{2}\left[\sin^2(\omega_0 t - \varphi)\right]_0^T =$$

$$= \frac{U_{MAX}^2\omega_0(k_W + k_F)}{2}(\sin^2(-\varphi) - \sin^2(-\varphi)) = 0$$

- $F_{ADD,STIFF,TOT}$ is total added stiffness force
- k_W and k_F the contributions of added stiffness
- u deflection at time t
- $\dot{u}$ velocity
- U_{MAX} maximal amplitude of the oscillations
- ω_0 undamped natural frequency
- φ phase shift
- $W_{stiffness}$ work done by the total added stiffness force $F_{ADD,STIFF,TOT}$
- T period of oscillation

Since the development of work performed by the hydrodynamic inertia force is similar to (5.23), the only hydrodynamic force performing work during one oscillating period is the hydrodynamic damping force $F_{ADD,DAMP}$.

In recent years, two various approaches to flow induced stiffness investigation have been presented. The first one, presented by Gauthier [60], is based on the static deflection and provides the value of static added stiffness without considering any dynamic behaviour. The other approach is based on the integration of the dissipated energy in time and has been presented by Nennemann [17].

6 CASE DESCRIPTION

This chapter describes the test case which was designed to carry out the investigation of fluid added effects. The research was focused on the field of hydraulic machines. Since the investigation of added effects on the whole turbine runner involves many input parameters, this research was carried out on a single hydrofoil which was placed into the cavitation tunnel.

The doctoral thesis is an output of cooperation with *Litostroj Engineering a. s.* and was supported by joint project no. TH02020705 "*Research of turbine blade oscillations with respect to extended regulation range for guarantee of stability and safety of energetic system*".

The experimental measurements were carried out using a closed test circuit in the hydraulic laboratory of the Viktor Kaplan Department of Fluid Engineering at Brno University of Technology. A special test section, the cavitation tunnel, was designed by *Listostroj Engineering a. s.* and mounted into the test circuit in the hydraulic laboratory at Brno University of Technology.

The main focus of the research project was the study of fluid-structure interaction on a single hydrofoil which is placed into the cavitation tunnel test section. The main output of the research is the investigation of hydrofoil dynamic response.

6.1 Geometry of the Hydrofoil

Geometry of the hydrofoil consists of shaft and hydraulic profile. The two figures below (Fig. 6.1 and Fig. 6.2) show the hydrofoil geometry mounted to a torsion bar according to setup inside the test rig. The hydrofoil is based on NACA profiles, which are profiles developed by National Advisory Committee for Aeronautics (NACA). The selected hydrofoil is symmetric with chord length of 95 mm and thickness of blunt trailing edge of 1.63 mm (Fig. 6.3). The maximal thickness of 5 mm is reached 30 mm behind the leading edge which corresponds to the position of shaft axis. The selected maximal thickness of 5 mm provides enough large deflections during oscillations and sufficient hydrofoil stiffness to protect the hydrofoil from destroying during resonance. This setup corresponds to profile NACA 0005.

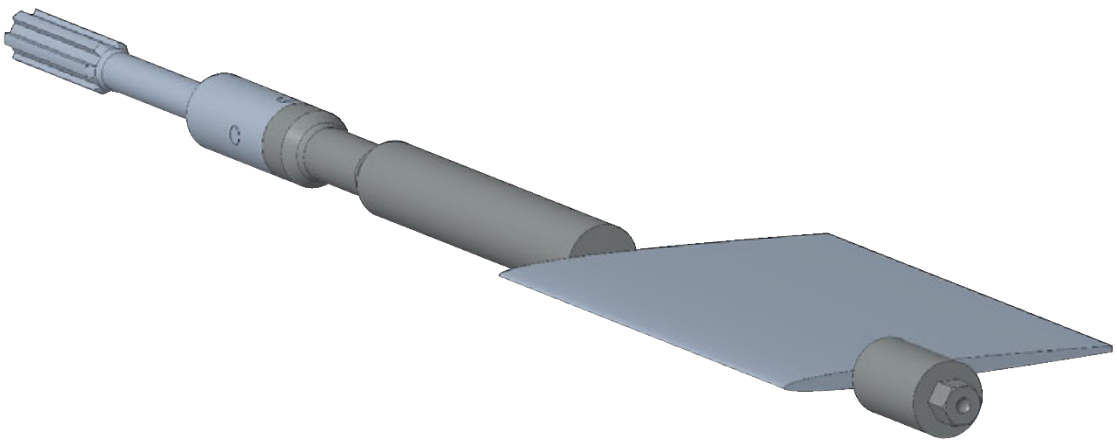

Fig. 6.1 Hydrofoil geometry consisting of hydrofoil and shaft; mounted to torsion bar

Fig. 6.2 Hydrofoil and its shaft without torsion bar

The hydrofoil and its shaft of diameter 20 mm are manufactured from brass as one piece together. Material properties of brass are presented in Table 1. This geometrical configuration is more similar to a guide vane of the water turbine than to runner blades.

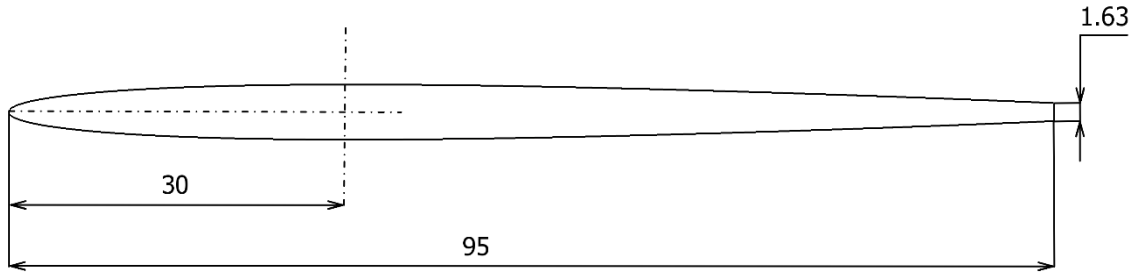

Fig. 6.3 Hydrofoil dimensions in millimetres

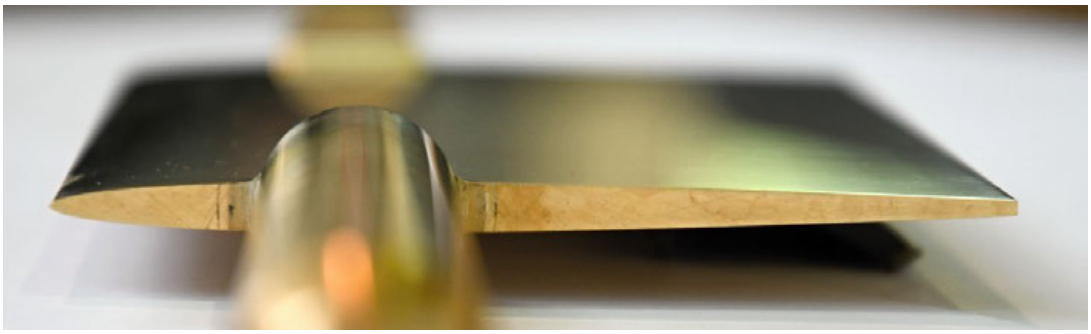

Fig. 6.4 Photo of the hydrofoil made of brass

Table 1 Material properties of brass

ρ	8400 $kg \cdot m^{-3}$
E	96 970 MPa
ν	0.33

6.2 Cavitation Tunnel

The test circuit is designed as a closed loop (Fig. 6.5). Since main parts of the circuit already exist in the hydraulic laboratory, only the test section and its inlet and outlet pipes have been newly designed and manufactured.

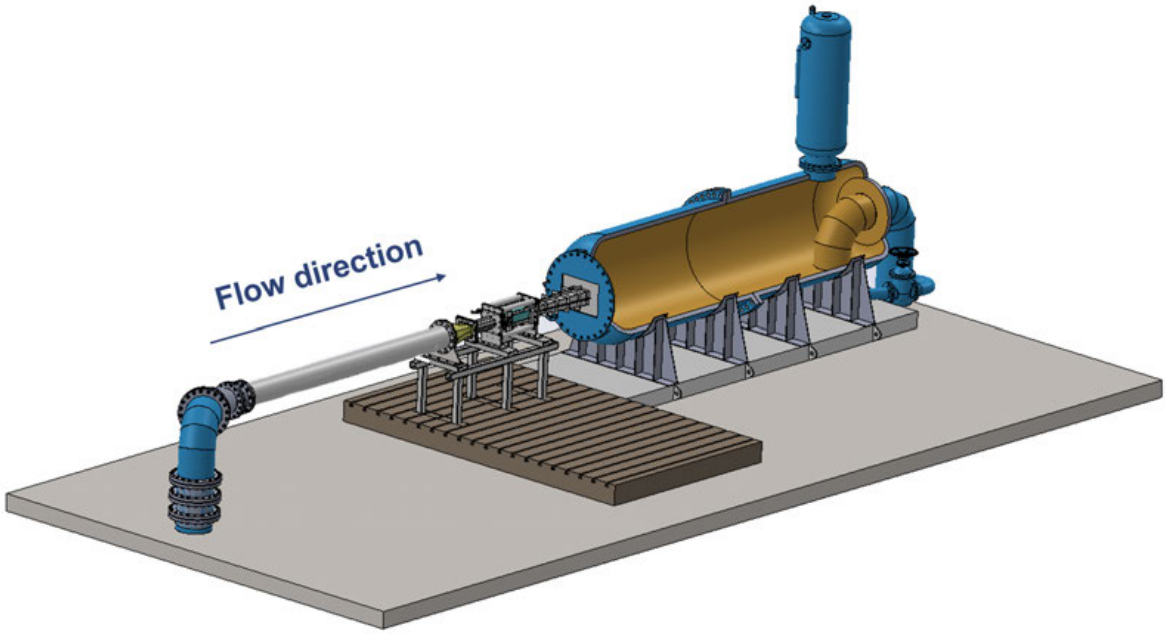

Fig. 6.5 Cavitation tunnel loop

Water comes through a pipe with the diameter of 300 mm which is followed by a 500 mm long contraction nozzle, (see Fig. 6.6 and Fig. 6.7). Its shape continuously changes from the circular inlet to the rectangular outlet. A straight 500 mm long component is installed downstream of the contraction nozzle, which allows the flow to recover before it enters the test section. This section is 750 mm long and has a rectangular cross-section with dimensions of 150 x 100 mm. Downstream of the test section, a 5°-full angle diffuser with rectangular cross-section is mounted and followed by a water tank. The circuit is closed by pipes with circular cross-section of diameter 300 mm. Two pumps located in the basement of the laboratory provide maximal flow rate of 500 l/s which corresponds to the maximal flow velocity of 33 $m \cdot s^{-1}$ in the test rig. The circuit is connected to a vacuum pump to control level of static pressure. All four walls of the test section are made of plexiglass. Three of them are transparent.

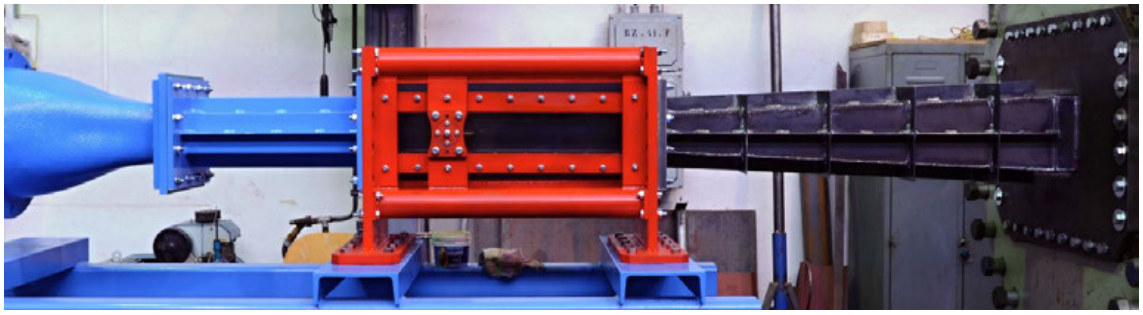

Fig. 6.6 Photo of the cavitation tunnel test section

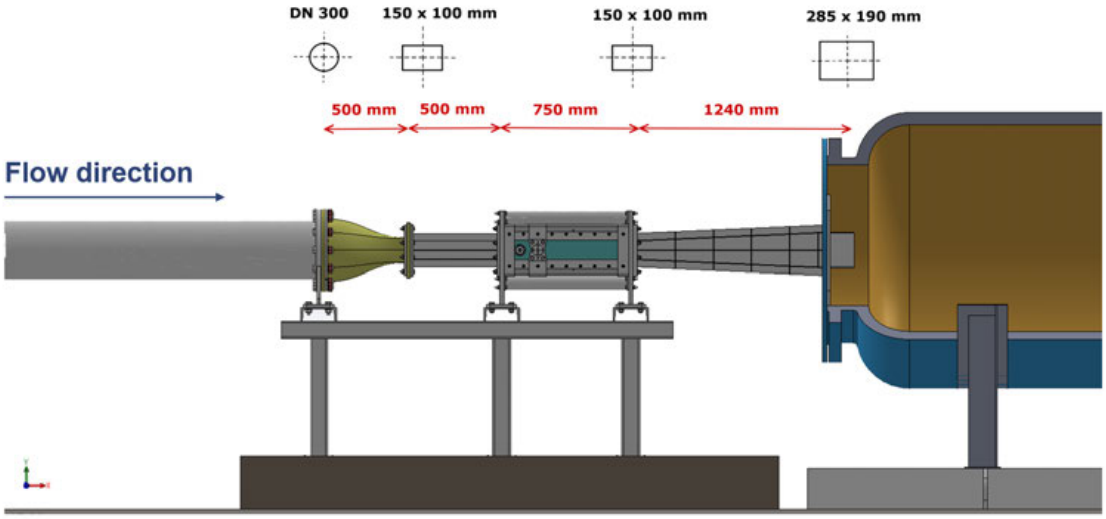

Fig. 6.7 Dimensions of the cavitation tunnel test section

The red coloured test section was designed to enable free torsional oscillations of the hydrofoil shaft. The shorter end of the shaft is fixed in the axial direction by screw with ball end to ensure free rotation around shaft axis (Fig. 6.8). The longer end of the shaft is connected to a torsion bar by pins (Fig. 6.1). Fully fixed mounting of the torsion bar to the test section chasing is ensured by splined end of the torsion bar (Fig. 6.1, Fig. 6.8). This assembly enables the using of torsion bars of various stiffness and thus, the influence of the mounting stiffness on the hydrofoil response can be investigated. However, this investigation was not realized due to the wide range of measurements and only one torsion bar was used.

The hydrofoil shaft is fitted to the chasing by three ball bearings (see Fig. 6.8): one bearing on the shorter end and two small bearings on the longer end.

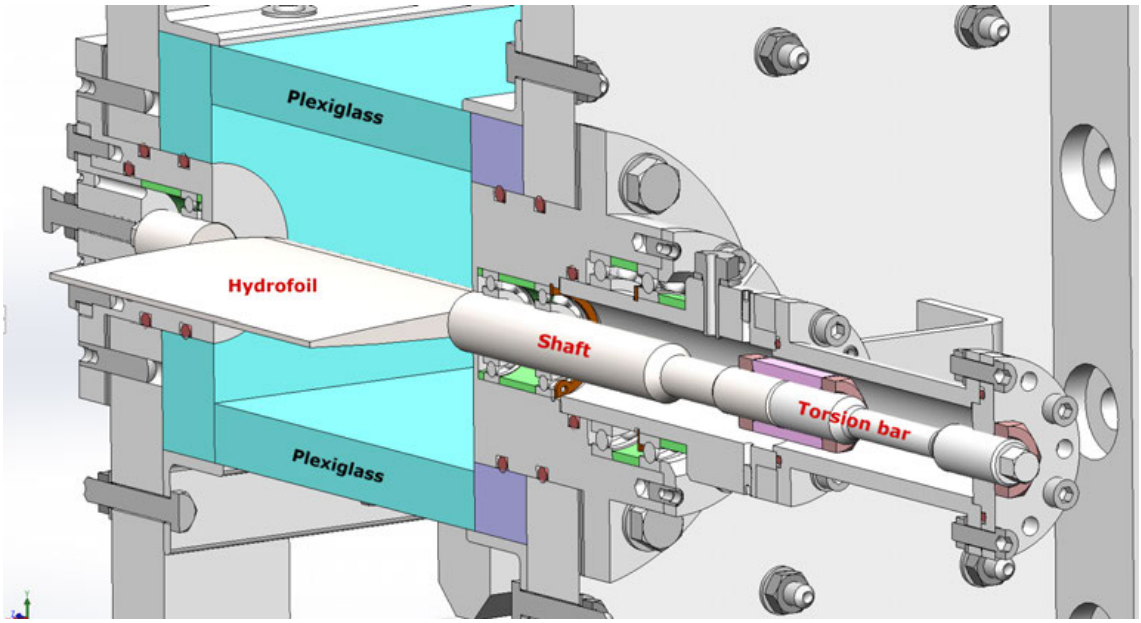

Fig. 6.8 Mounting of the hydrofoil inside the test section [66]

Since the assembly which consists of hydrofoil, its shaft and torsion bar is mounted to an external bar, various angles of attack can be set by this external bar (Fig. 6.9 and Fig. 6.10).

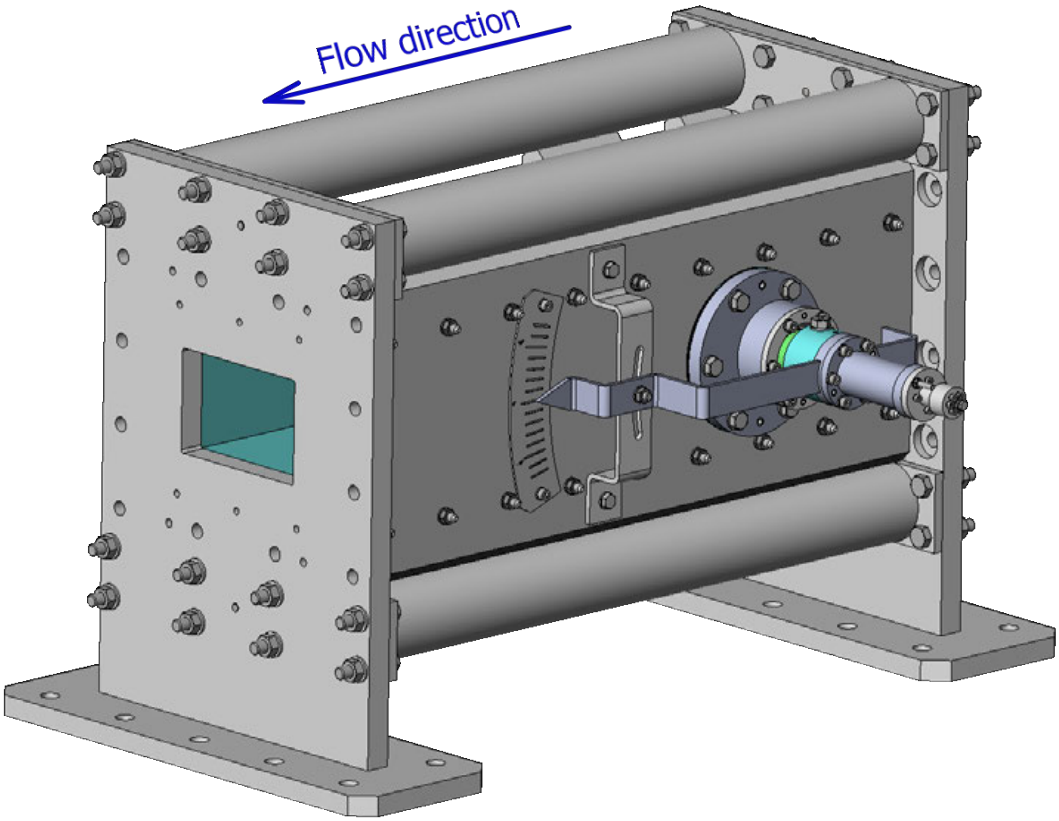

Fig. 6.9 Rear view of the test section – model [66]

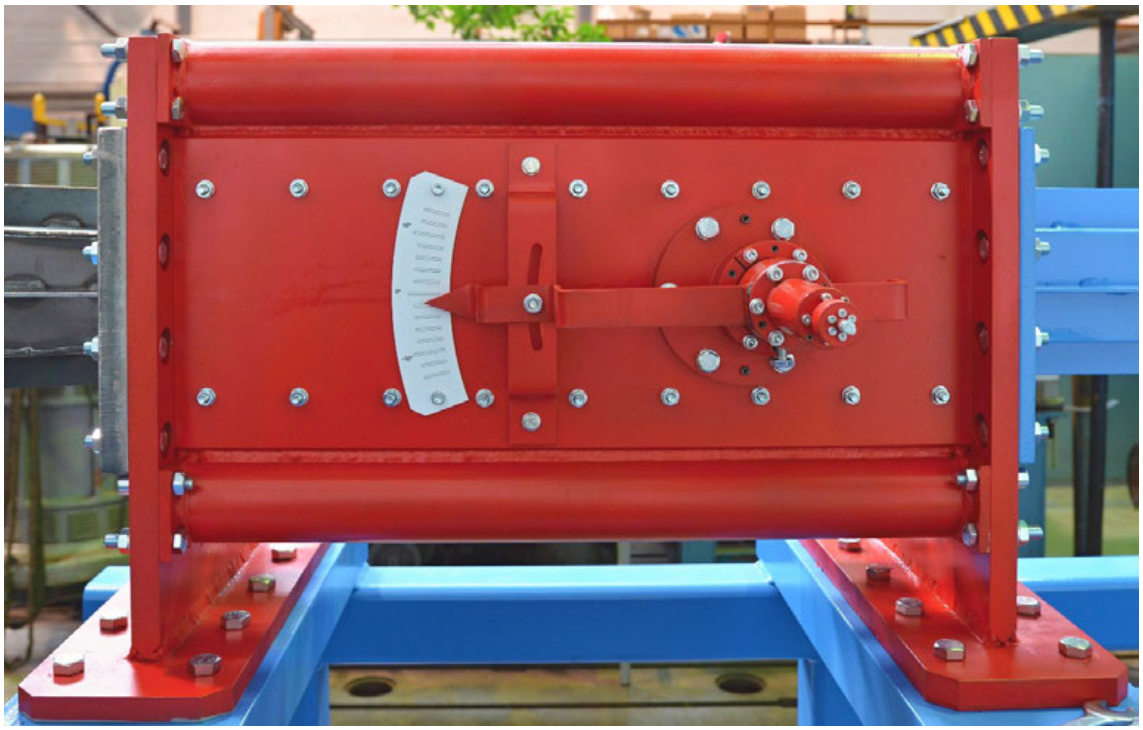

Fig. 6.10 Rear view of the test section - photo

6.3 Experimental Setup

The test circuit is equipped with various sensors which are used for monitoring of operation conditions, observing vortex structures behind trailing edge and measurements of hydrofoil response. All sensors and equipment which were used for experimental measurements are presented in the following tables. Photos which follow the tables show most of the installed sensors. These sensors are schematically numbered regarding to the list in tables. Data from all presented sensors including optical methods were collected synchronously.

The flow rate in the test circuit was measured by electromagnetic flowmeter. The absolute pressure was monitored inside the water tank and at the inlet and the outlet of the test section (Fig. 6.12, Fig. 6.15). Moreover, a piezoelectric pressure sensor, which is the dynamic pressure transducer, was located 95 mm behind the trailing edge of the hydrofoil in the top wall of the test section (Fig. 6.12). Such distance corresponds to the hydrofoil chord length. Additionally, a microphone was installed on the draft tube to monitor acoustic emission (Fig. 6.12).

Two kinds of hydrofoil excitation were used. In the first case, the hydrofoil was excited only by separation of boundary layer and vortex shedding. Frequency of such excitation was controlled by change of flow rate. In the second case, an external mechanical exciter was connected to the external bar (red coloured) on the test section (Fig. 6.13). As the external bar was firmly connected to the torsion bar, the vibrations of the exciter were transmitted on the hydrofoil. The input signal was a sinus wave generated by LabVIEW software. This continuous discretized signal was amplified by power amplifier (Fig. 6.14) and sent to the external exciter. Additional accelerometers were installed on the exciter membrane as well as on the external bar to control the real excited signal (Fig. 6.13). Another accelerometer was installed on the outer surface of the draft tube (Fig. 6.12).

Since three out of four test section walls are transparent, the hydrofoil can be easily observed by two optical methods. The first one is the *Laser Doppler Vibrometer* (LDV) which was used to measure the hydrofoil response (Fig. 6.18). Two laser beams of LDV vibrometers were pointed to corners of the hydrofoil near the trailing edge. These locations enabled to capture various mode shapes and were selected according to the results obtained from acoustic modal analysis. The other one is the *Particle Image Velocimetry* (PIV). PIV enables to visualise the vortex structures behind the trailing edge of the hydrofoil (Fig. 6.17, Fig. 6.18). The experimental measurement with PIV method was carried out at the beginning of eight-week long session of measurements. Once the data were post-processed, it turned out that the joint between the torsion bar and the test section had low stiffness due to the presence of micromovements. This issue was solved by applying a glue which filled small gaps in the joint. This improvement resulted in the increase of the mounting stiffness. All the measurements were repeated, but without the PIV method. This was caused by the lack of time and complicated transport of PIV equipment. Therefore, the results of PIV measurement are not included in this thesis.

In addition, a strain gauge was installed on the hydrofoil shaft to measure the torsional oscillations (Fig. 6.11). During the measurements, it turned out that due to too small measured values, these strain gauges were not suitable for response measurements.

Following tables summarize all applied sensors and their main characteristics. Most of them are also shown on the photos which were taken during the measurements.

- **Flowmeter**

1	Electromagnetic Flowmeter		
Manufacturer:	Krohne	Range of measurement:	$3000\ m^3/h$
Type:	ALTOFLUX 4100	Output:	$0-20\ mA$
Accuracy:	± 0.2 % of measured value		

- **Pressure Sensors**

2	Pressure Transducers (in water tank and at the outlet of test section)		
Manufacturer:	BD SENSORS	Range of measurement:	$0-4\ bar$
Type:	DMP 331	Output:	$0-20\ mA$
Accuracy:	± 0.25 % of range of measurement		
Variable:	Absolute pressure		

3	Pressure Transducer (at the inlet of test section)		
Manufacturer:	BD SENSORS	Range of measurement:	$0-6\ bar$
Type:	DMP 331	Output:	$0-20\ mA$
Accuracy:	± 0.25 % of range of measurement		
Variable:	Absolute pressure		

4	Piezoelectric Pressure Sensor (pressure tap in plexiglass)		
Manufacturer:	KISTLER	Range of measurement:	$0-3.5\ bar$
Type:	211B6	Output:	$1450\ mV/bar$
Accuracy:	± 1.0 % of range of measurement		
Variable:	Relative pressure		

- **Accelerometers**

5	Accelerometer (external bar, exciter)		
Manufacturer:	PCB PIEZOTRONICS	Range of measurement:	$\pm 500\ g$
Type:	352C03	Range of measurement:	$0.5Hz-10kHz$
		Output:	$10\ mV/g$

6	Accelerometer (draft tube)		
Manufacturer:	PCB PIEZOTRONICS	Range of measurement:	$\pm 500\ g$
Type:	352A60	Range of measurement:	$0.5Hz - 60kHz$
		Output:	$10\ mV/g$

7	Accelerometer (water resistant)		
Manufacturer:	PCB PIEZOTRONICS	Range of measurement:	$\pm 5000\ g$
Type:	W352B10	Range of measurement:	$0.5Hz - 10kHz$
		Output:	$10\ mV/g$

- **Strain Gauges**

8	Strain Gauge		
Manufacturer:	HBM		
Type:	1.5 / 120XY21		
Resistance:	$120\ \Omega\ \pm 0.35\%$	Gauge factor:	$1.91\ \pm 1\%$
Temperature coefficient of gauge factor:			$95\ ppm/K$
Temperature compensation (steel):			$\alpha = 11\ ppm/K$
Variable:			

- **Optical Methods**

9	Laser Doppler Vibrometer (LDV)		
Manufacturer:	OMETRON	Range of measurement:	$\pm 500\ mm/s$
Type:	VH-1000-D	Range of measurement:	$0.5Hz - 22kHz$
Laser type:	Helium neon	Output:	$0 - 5\ V$
Wavelength:	$633\ nm$	Laser class:	2

10	Time Resolved Particle Image Velocimetry (TR PIV)		
Laser:	Litron FDY300	Pulse frequency:	$1000\ Hz$
Camera:	Dantec Dynamics, Speed Sense Camera		
Resolution:	$1280 \times 800\ px$		
Software:	DynamicStudio (Dantec Dynamics)		

- **Power Supplies**

11	Laboratory Power Supply (DC)		
Manufacturer:	Tesla Brno	Output Voltage:	$0 - 20\ V / 1A$
Type:	BK 123		

12	Laboratory Power Supply (DC)		
Manufacturer:	Statron	Output Voltage:	$0 - 24\ V / 6A$
Type:	2224.1		

- **Mechanical Exciter Used for Enforced Vibrations of Hydrofoil**

13	External Mechanical Exciter		
Manufacturer:	VEB Robotron-Meßelektronik „Otto Schön“ Dresden		
Type:	11077		

14	Power Amplifier		
Manufacturer:	VEB Metra Mess – und Frequenztechnik Radebeul		
Type:	LV 102	Power Voltage:	$220\ V$
		Frequency Range:	$3Hz - 40kHz$

- **Thermometer**

15	Thermometer		
Manufacturer:	RAWET	Range of measurement:	$0 - 50°C$
Type:	PT 100	Output:	$4 - 20\ mA$
Accuracy:	± 0.3 %		

- **Microphone**

16	Microphone		
Manufacturer:	G.R.A.S.	Range of measurement:	$0 - 100\ Pa$
Type:	40PH	Range of measurement:	$10Hz - 20kHz$
		Output:	$50\ mV/Pa$

- **Devices Used for Data Collection**

- Real-Time system NI PXIe-1078 chassis
- Real Time controller NI PXIe-8135
- PXI Sound and Vibration Module NI PXIe-4492
  - 8 simultaneously sampled input channels
  - Maximal sample rate 204.8 kS/s
  - A/D converter resolution 24 bits
  - Range of measurement ±5 V
- PXI Multifunction I/O Module NI PXIe-6356
  - 8 simultaneously sampled input channels
  - Maximal sample rate 1.25 MS/channel
  - A/D converter resolution 16 bits
  - Range of measurement ±10 V
- Software: LabVIEW 2019
- Power relay output board with resistance 1x500 Ω
  - (accuracy 0.1%)

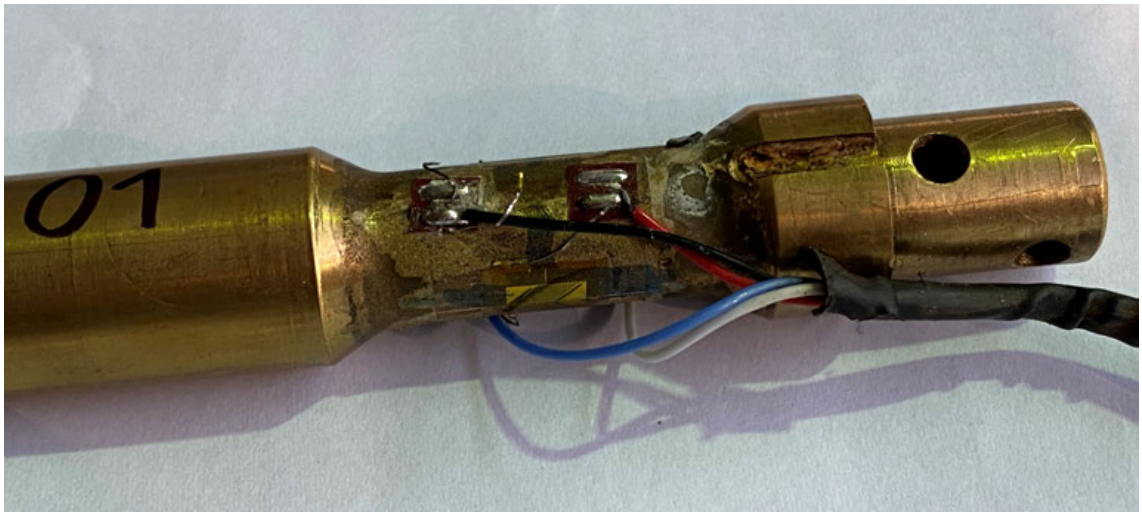

Fig. 6.11 Strain gauge on the hydrofoil shaft

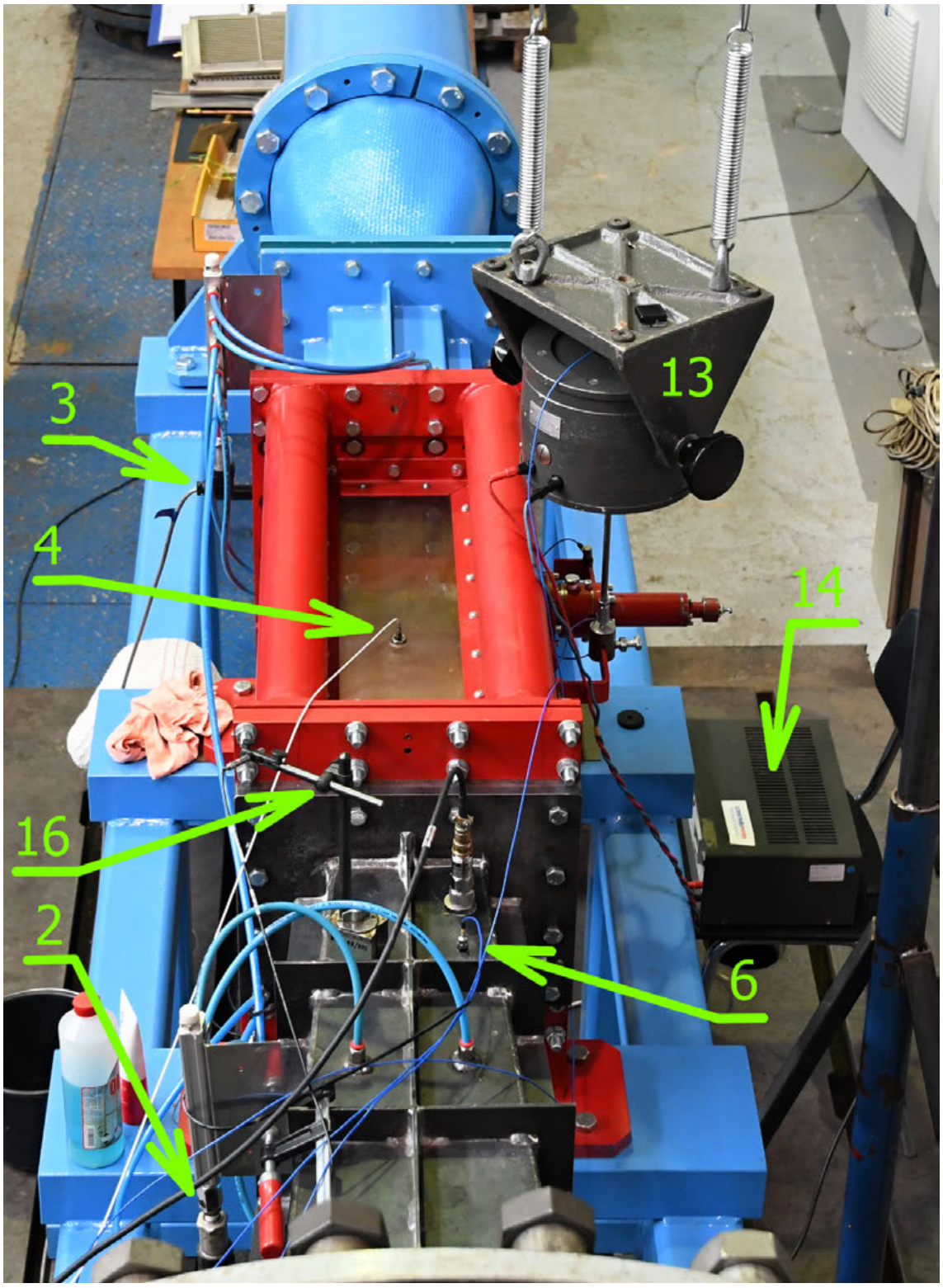

Fig. 6.12 General overview of all sensors

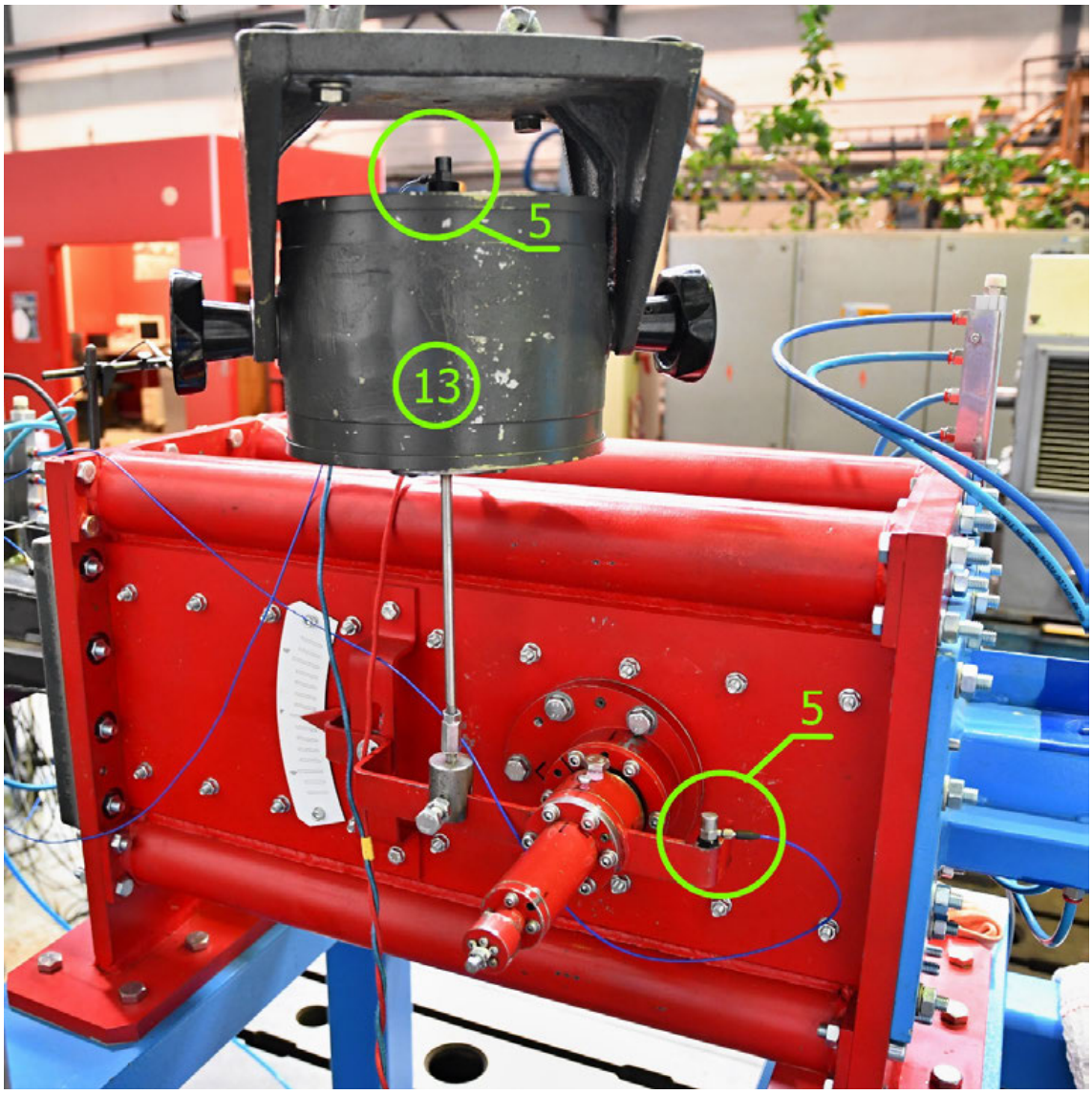

Fig. 6.13 External mechanical exciter mounted to the test section

Fig. 6.14 Power Amplifier which amplifies the input signal of external exciter

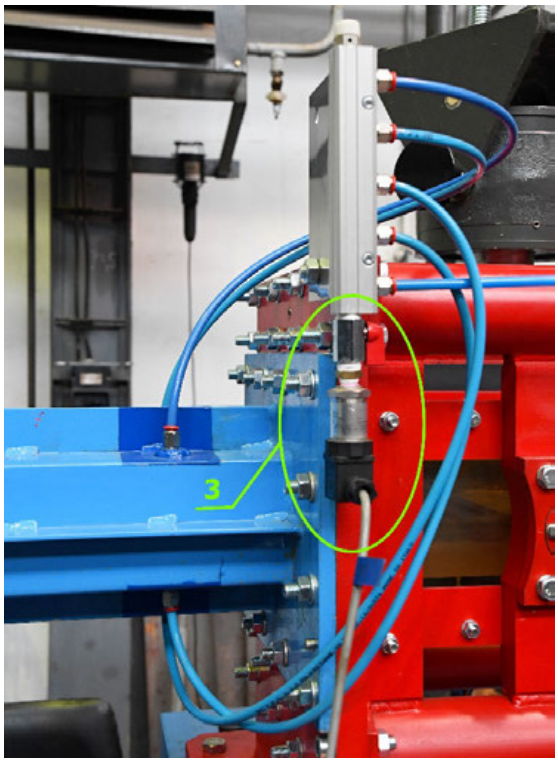

Fig. 6.15 Pressure transducer at the inlet of the test section

Fig. 6.16 Laboratory Power Supplies

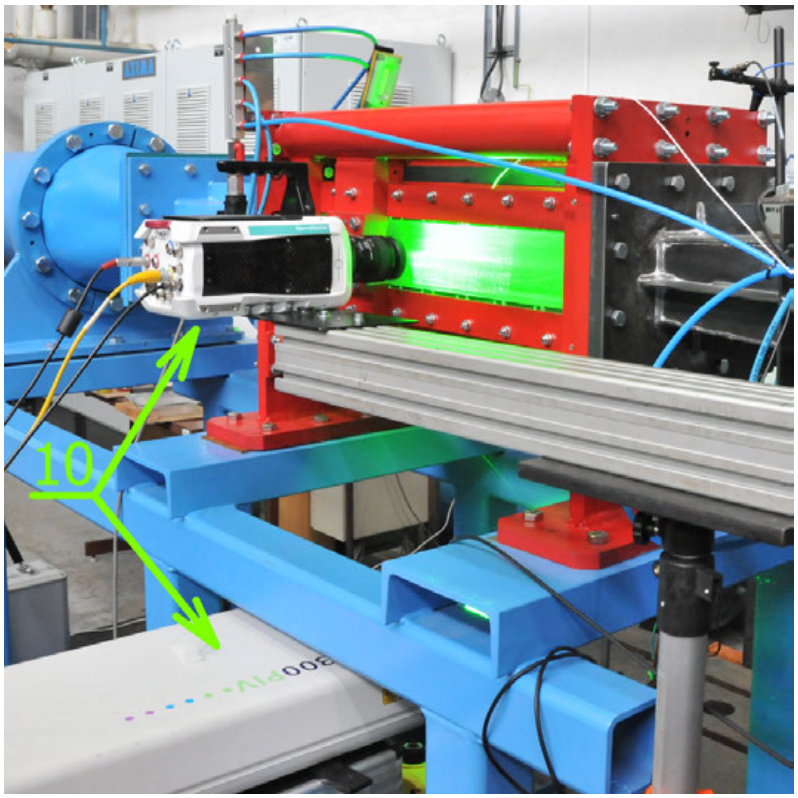

Fig. 6.17 High speed camera and laser used for PIV

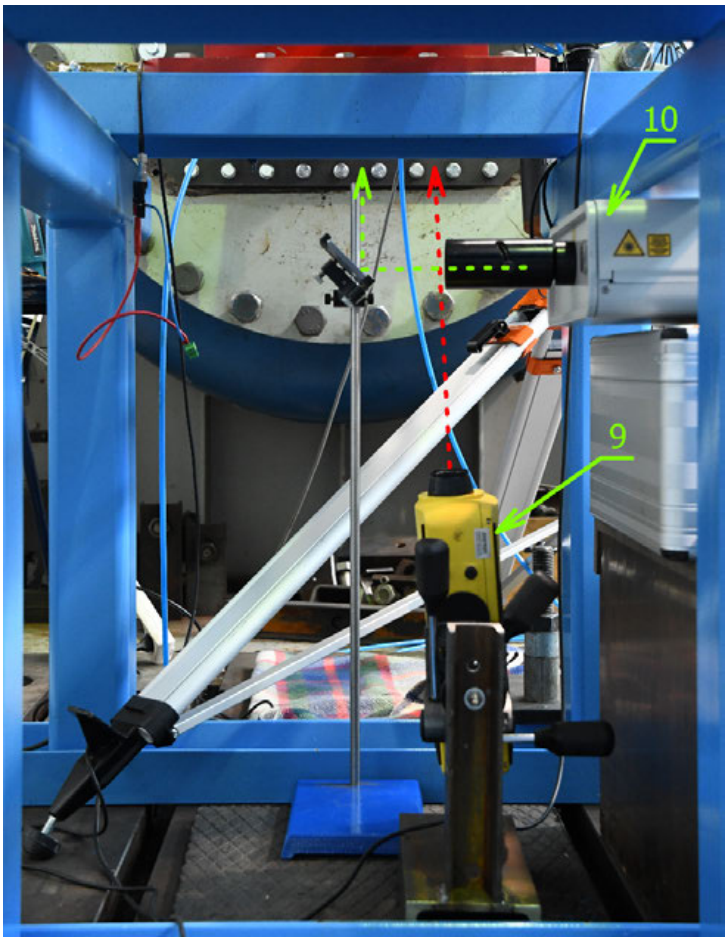

Fig. 6.18 LDV laser beam (red); PIV laser (green) - a mirror creates laser plane

7 EXPERIMENTAL METHODS

As the doctoral thesis contains wide range of experimental measurements which were carried out as a part of the research project, this separate chapter describes all applied experimental methods and main steps of data post-processing for each method. Firstly, the algorithm of measurement procedure is described. Secondly, two methods which were used for evaluation of hydrofoil response to enforced vibrations are presented. Then, the identification of natural frequencies as well as measurement of flow induced vibrations is described. Finally, at the end of this chapter, two methods used for damping ratio calculation are mentioned.

7.1 Measurement of Harmonic Response of the Hydrofoil

The response of the hydrofoil was measured for two different types of excitation. Firstly, the hydrofoil was excited by external exciter which was mounted to the test section. Secondly, the flow induced vibrations of the hydrofoil were analysed. In both cases, the hydrofoil response was measured by two LDV vibrometers denoted as "LDV 1" and "LDV 2". Each vibrometer was pointed to a different corner of the hydrofoil trailing edge to measure the hydrofoil response (Fig. 7.1). These locations of expected highest deflections were selected according to mode shapes obtained from numerical modal analysis. The vibrometers were placed below the test section and pointed on the bottom surface of the hydrofoil. This enabled to measure the hydrofoil response even in presence of cavitation on the top surface of the hydrofoil.

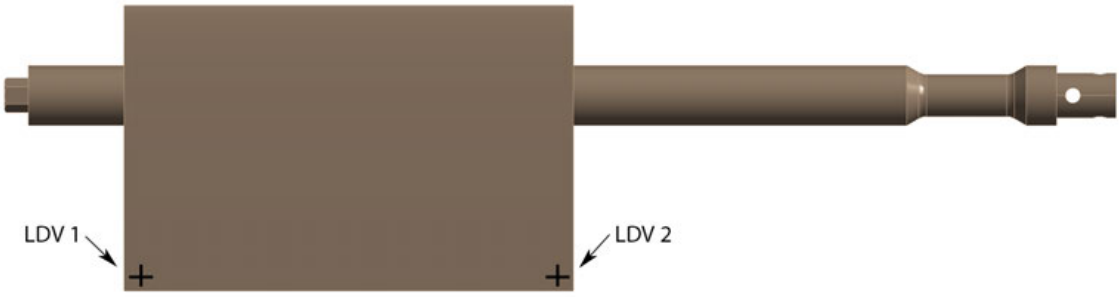

Fig. 7.1 Location of LDV laser beams which were focused on hydrofoil bottom surface

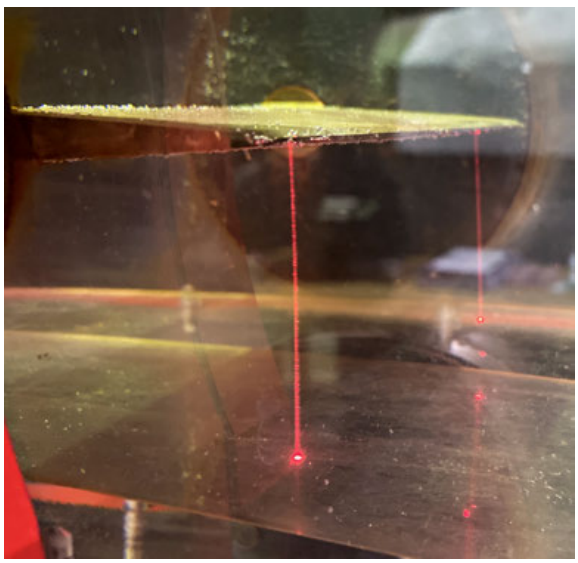

Fig. 7.2 Two LDV laser beams pointing on the bottom surface of the hydrofoil

The hydrofoil response to the enforced vibrations was post-processed from data obtained from series of measurements. The measurement process was executed in a loop controlled by LabVIEW. At the beginning of the measurement, a set of input parameters had to be defined: the range of excitation frequency, increment of excitation frequency, sampling frequency and length of signal which is saved from all sensors. Then, an automatic loop controlled by LabVIEW software (Fig. 7.3) went through the whole range of excitation frequency and executed a measurement of hydrofoil response to each excitation frequency in the defined range. Data from each measurement were saved to a separate file.

The process of measurement (Fig. 7.3) started by definition of current excitation frequency f_{EXCT} and generation of harmonic sinus signal in LabVIEW. This generated signal was amplified by power amplifier (Fig. 6.14) and sent to the mechanical exciter (Fig. 6.13) to excite the hydrofoil. As the excitation frequency varied in each iteration of the measurement process, a waiting time $\Delta t = 5s$ was set before the experimental data were measured by LDV vibrometers. During this time delay Δt, the hydrofoil response recovered after the change of excitation frequency at the beginning of the iteration. Then, two seconds long signal of hydrofoil response was measured by LDV vibrometers and the data were saved to a file. The sampling frequency was 50 kHz. Once the data were saved, next iteration of measurement process started by selection of new excitation frequency.

The whole process was repeated until the last value of excitation frequency was reached. The data from rest of sensors including the hydraulic parameters were saved synchronously with data from LDV to the same text file.

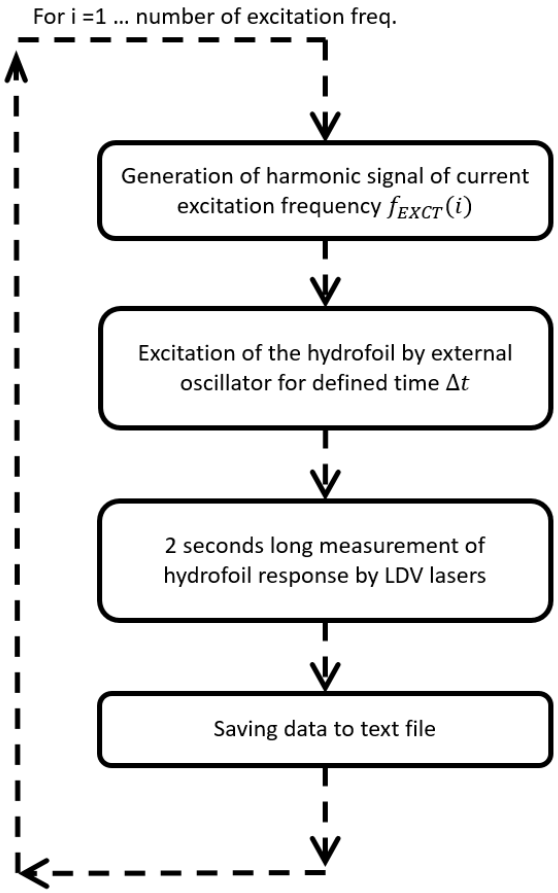

Fig. 7.3 Algorithm of measurement controlled by LabVIEW

7.2 Evaluation of Harmonic Response from Experiment

Once the measurements were finished in whole range of excitation frequency, the response were calculated by post-processing of measured data.

The test case was designed to be as similar as possible to the real conditions in a Francis turbine. Construction of the test section was based on the requirements of our industrial partner *Listostroj Engineering a. s.* Since the blade was mounted on the shaft, its behaviour corresponded more to the turbine guide vane than the runner blade. As the mechanism which held the blade in the test case consisted of many components, the measurement was influenced by various effects which propagated from different parts of the test section and influenced the blade behaviour. Moreover, the parameters of the mounting such as bearing stiffness cannot be accurately quantified.

Various methods of post-processing were tested to evaluate the hydrofoil response to the enforced vibrations. As a result, two different methods were used in this thesis to obtain the response of hydrofoil. The first method is based on optimisation of length of input signal to obtain maximal amplitude value on the analysed excitation frequency. The calculated response was then obtained in the units of analysed sensor (response from LDV vibrometer is obtained in [ms^{-1}]). The second method is more straightforward and simply calculates FFT from the imported data for each value of excitation frequency. In this case, the obtained response from LDV vibrometer was divided by response obtained from accelerometer located on the membrane of the mechanical exciter. Such obtained response is nondimensional and represents Frequency Response Function (FRF) of the hydrofoil.

Both methods of data post-processing were coded in MATLAB R2019a. Since a separate file was saved for each value of excitation frequency during the measurement, the post-processing of both methods was organized as a series of operations executed for each file in a loop. After post-processing of all files, i.e. data for all excitation frequencies, the response of the hydrofoil was obtained.

7.2.1 Method 1 – Optimisation of length of input signal

The post-processing loop (Fig. 7.4) starts with the import of a file which contains synchronously measured data from all sensors for one value of excitation frequency. Main focus of post-processing is concentrated on data obtained by two LDV vibrometers and by accelerometer which was mounted on the membrane of the mechanical exciter (Fig. 6.13, sensor no. 5 in the upper part of the photo). The signal measured by this accelerometer represents a real excitation provided by exciter which is transmitted by the external bar from the exciter to the hydrofoil. A short segment of this harmonic excitation signal is selected from the middle of two-second long measurement (blue coloured signal in diagram Fig. 7.4). The length of this segment is ten periods of the current excitation frequency f_{EXCT} which corresponds to the number of samples L_{INIT}. The amplitude-frequency spectrum of the selected segment of signal is obtained by applying the Fast Fourier Transformation (FFT). A dominant peak which corresponds to the current value of excitation frequency is observed. As the amplitude value of this peak is influenced by the length of the input signal (number of samples), the optimal length of the input signal segment $L_{OPTIMAL}$ was investigated to obtain maximal amplitude value [67]. The ten periods long segment of signal was consecutively shortened by one sample until one period of excitation frequency was removed (which means that the segment of the signal analysed by FFT was at the end of investigation nine periods long). After each removing of one sample a new amplitude-frequency spectrum was

calculated and the amplitude value which corresponds to the current excitation frequency was saved including the corresponding number of removed samples N from the input signal. [43]

Finally, the maximal value of this amplitude was found (AMP_{MAX}). The optimal length of the segment of the input signal $L_{OPTIMAL}$ is calculated by subtracting the corresponding number of removed samples N from initial number of samples L_{INIT}. Once the optimal length of the signal segment is known, the second part of the process can be executed. Here, a new segment of length $L_{OPTIMAL}$ (marked by green) is cut from each signal (blue coloured – accelerometer, black coloured – LDV). An amplitude-frequency spectrum is then obtained by FFT for each sensor. After that, the amplitude value which corresponds to the current excitation frequency is detected and stored to build response in whole range of excitation frequency. The detected amplitude is marked by small red circle in the amplitude-frequency characteristic. This whole process is repeated for each value of excitation frequency. Finally, the dependence of detected amplitude on the excitation frequency can be plotted.

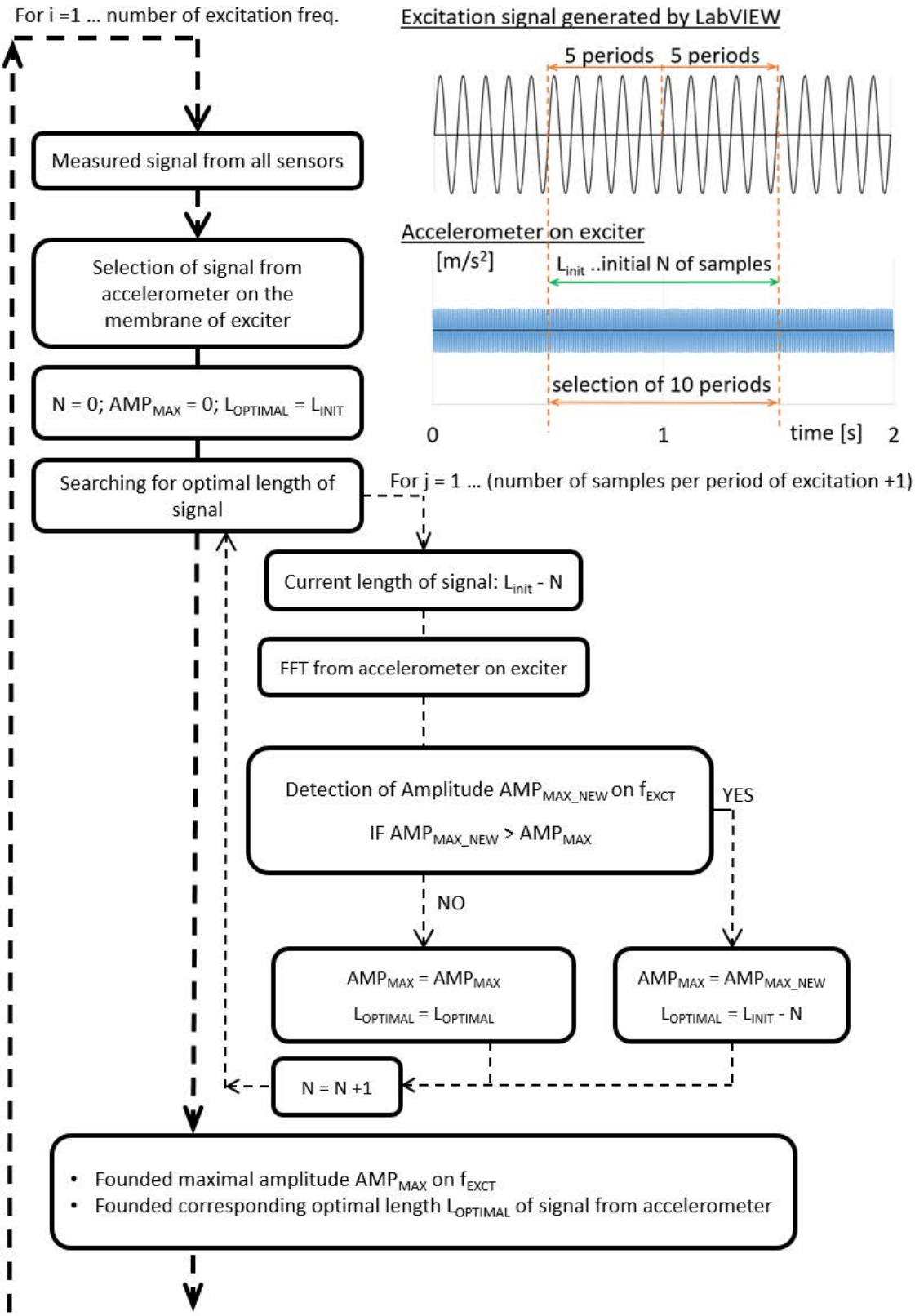
For i =1 … number of excitation freq.
Measured signal from all sensors
Selection of signal from accelerometer on the membrane of exciter
N = 0; AMP_MAX = 0; L_OPTIMAL = L_INIT
Searching for optimal length of signal
For j = 1 … (number of samples per period of excitation +1)
Current length of signal: L_init - N
FFT from accelerometer on exciter
Detection of Amplitude AMP_MAX_NEW on f_EXCT
IF AMP_MAX_NEW > AMP_MAX
YES
NO
AMP_MAX = AMP_MAX
L_OPTIMAL = L_OPTIMAL
AMP_MAX = AMP_MAX_NEW
L_OPTIMAL = L_INIT - N
N = N +1
• Founded maximal amplitude AMP_MAX on f_EXCT
• Founded corresponding optimal length L_OPTIMAL of signal from accelerometer
Excitation signal generated by LabVIEW
5 periods 5 periods
Accelerometer on exciter
[m/s²]
L_init ..initial N of samples
selection of 10 periods
0
1
time [s]
2

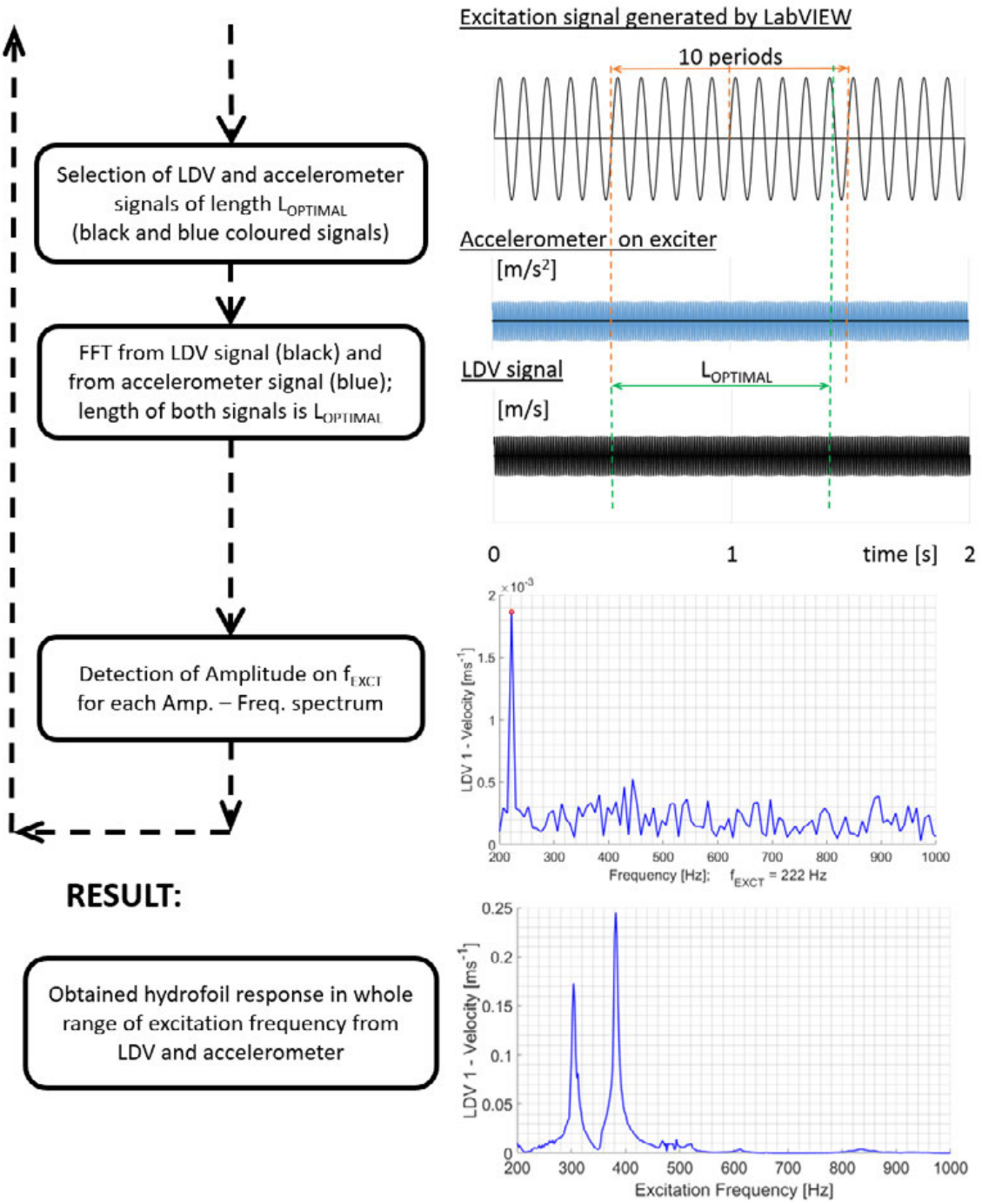

Fig. 7.4 Diagram of data post-processing by optimisation of length of input signal

7.2.2 Method 2 – Calculation of Frequency Response Function

The main differences from the first method are skipping the optimization process and determining the final hydrofoil response as a nondimensional Frequency Response Function (FRF).

The procedure (Fig. 7.5) starts by importing a data file which contains synchronously measured two-second long signals from all sensors. A separate file was previously saved for each value of excitation frequency during the measurement. A short segment is selected from the middle of each analysed signal, i.e. signals measured by LDV vibrometers (black coloured in diagram Fig. 7.5) and by accelerometer (blue coloured) which was mounted on the exciter. The length of these short segments L_{INIT} is for all sensors ten periods of the current excitation frequency f_{EXCT}. Then the amplitude-frequency spectrum of selected segment is obtained for each sensor.

As a dominant peak is observed on the current excitation frequency, its position in the spectrum (index of sample $i_{AMP-MAX}$) is detected from the accelerometer by searching the maximal amplitude value ±3 samples around the excitation frequency. Once the maximal amplitude value AMP_{MAX} and corresponding index $i_{AMP-MAX}$ are detected from accelerometer spectrum, the amplitude value on same position $i_{AMP-MAX}$ is stored from all spectrums (accelerometer and LDV). This procedure is repeated in a loop until all excitation frequencies are analysed. Then, the dependence of detected amplitude on the excitation frequency can be plotted for all analysed sensors.

Since the FRF is defined as a nondimensional ratio between the input and the output of the system [43], the dependence of detected amplitude on the excitation frequency obtained from LDV must be divided by the same characteristic measured by accelerometer mounted on the exciter (represents input excitation of the system). This characteristic represents acceleration and must be transformed to velocity in frequency domain. Then, a nondimensional Frequency Response Function can be calculated and used for identification of further dynamic parameters of the system.

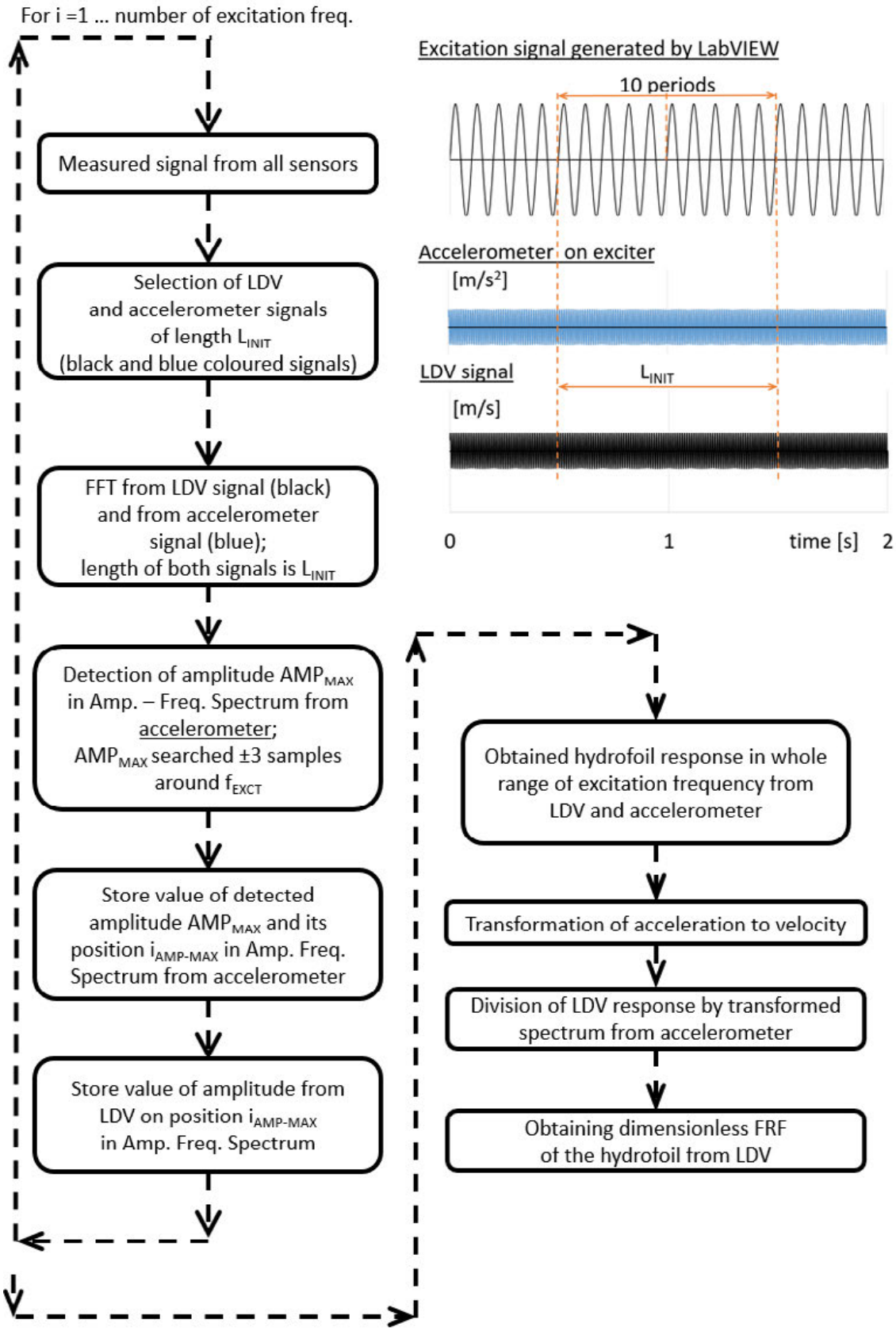

Fig. 7.5 Diagram of data post-processing by calculating nondimensional FRF

7.3 Identification of Natural Frequencies

Natural frequencies of the hydrofoil which was mounted inside the test section were investigated both in air and in still water. Since the test section was a part of closed circuit of pipes, it was not possible to place an accelerometer on the hydrofoil surface to investigate the natural frequencies. Therefore, the natural frequencies were evaluated from the hydrofoil response which was measured and calculated according to the steps described in previous paragraphs. The natural frequencies of hydrofoil submerged in water were investigated in fully flooded test section with zero relative pressure and still water.

Since the identification of first mode of the hydrofoil was most important, two separate measurements were executed. The first measurement was measured only around the first natural frequency with step of frequency $\Delta f_{EXCT} = 1Hz$. The other modes of the hydrofoil in the range 200 – 1000 Hz were investigated in the second measurement with step of $\Delta f_{EXCT} = 2Hz$. This approach was used for both environments, i.e. air and water.

7.4 Hydrofoil Response to Flow Induced Vibrations

When a hydrofoil is placed into the flow inside the cavitation tunnel test section, two periodic forces may excite the hydrofoil. The first periodic force is induced by the boundary layer separation near the hydrofoil surface. The second excitation force may occur under certain circumstances and results from vortex shedding behind the trailing edge of the hydrofoil.

The boundary layer of symmetric hydrofoil with zero angle of attack can separate along its surface or can stay attached up to the trailing edge. If the hydrofoil thickness varies significantly along the chord line, massive boundary layer separation occurs and the flow does not remain attached to hydrofoil surface. In this case, the hydrofoil is excited by both the boundary layer separation and the vortex shedding. If the hydrofoil geometry is thin enough, the boundary layer stays attached to the hydrofoil surface after its separation and vortices behind the trailing edge form periodically. Then, the hydrofoil is excited only by excitation force induced by vortex shedding.

Since the angle of attack changes the flow conditions around the hydrofoil, both types of excitation forces are influenced by its value. As the value of the incidence angle is increasing, the vortex shedding phenomenon continuously disappears while the boundary layer separation along the profile becomes more dominant. If the angle of attack is enough far from zero, the hydrofoil is excited only by massive separation of boundary layer.

The identification of excitation frequencies related to flow induced vibrations is important to avoid of resonance during the operation time of hydraulic machines.

Experimental investigation of hydrofoil response to flow induced vibrations was carried out for wide range of inlet mean flow velocities v_{inlet}. The flow velocity varied in the range 1 ms^{-1} – 17.5 ms^{-1} with smooth step Δv = 0.5 ms^{-1}. The hydrofoil response was measured by two LDV vibrometers with sampling frequency of 50 kHz, each pointed to two different corners of the trailing edge (Fig. 7.2). These positions were selected according to the mode shapes obtained from numerical modal analysis. The 10-second long signals obtained from each of two lasers were post-processed by FFT to obtain the amplitude-frequency spectra. All measurements were carried out for angle of attack 0° and 5°.

7.5 Damping Ratio Investigation

As the wide range of operating regimes of hydraulic machines is required, the coincidence between the excitation frequencies and runner natural frequencies cannot be always avoided. In such situations, the parameter which controls the amplitudes of deflection is the damping. Damping of a mechanical oscillating system is usually represented by damping ratio ζ.

Experimental investigation of damping ratio can be done using various methods. These methods can be divided into two groups. The first group of methods is developed for analysing Single Degree of Freedom (SDOF) systems while the other group is used for Multi Degree of Freedom (MDOF) systems. In fact, a SDOF system does not exist in real life and all mechanical systems are of type MDOF. However, due to the fact that the Frequency Response Function (FRF) of MDOF system can be described by superposition of more SDOF, the SDOF methods can be used for analysing MDOF systems. The restriction of this approach is that the natural frequencies must be well-separated. When the damping ratio related to the selected vibration mode is evaluated from FRF, it is assumed that whole amplitude is excited almost only by the vibration mode, which natural frequency is the nearest. However, the FRF of MDOF system consists mainly from contribution of the nearest vibration mode, but there are also contributions from further vibration modes. The SDOF methods can be used for analysing of MDOF systems only if the vibration modes are not too close to each other. Then, the contributions of further vibration modes can be considered as very small and can be neglected. [43] [68]

The most common SDOF methods are the peak-amplitude method, the circle-fit method, the logarithmic decrement approach or an exponential envelope of free damped vibrations. The MDOF methods are usually based on curve fitting procedure or complex exponential methods. [68]

In this thesis, the main goal of the experiments was the investigation of damping ratio ζ for the first mode of the hydrofoil under various flow conditions.

7.5.1 Investigation of Various Damping Ratio Contributions

The assumed mathematical model of hydrofoil which oscillates in the fluid flow is based on description of SDOF system (Chapter 4.4). As the hydrofoil is submerged in a fluid, namely water, additional force effects (Chapter 5) affect the hydrofoil behaviour. The equation of motion (5.1) contains three damping contributions: the structural damping b_S and two fluid added damping contributions (b_W - contribution from acoustic radiation and viscous effects; b_F – hydrodynamic damping). The total damping in the coupled SDOF system b_{TOT} is then given as a sum of these three contributions in equation (7.1).

$$b_{TOT} = b_S + b_W + b_F \tag{7.1}$$

The presented mathematical description enables to easily separate these three damping contributions. However, the only damping which can be measured during the hydrofoil oscillations in a fluid flow is the total damping b_{TOT}. The structural damping b_S can be measured during the enforced oscillations of hydrofoil in air. Then, the fluid added damping b_{ADD} can be estimated as a difference between b_{TOT} and b_S. The experimental investigation of only b_W or only b_F is not possible. Since water can be considered as incompressible liquid, it can be assumed that the contribution b_W is very small and can be neglected. Then, the total damping b_{TOT} consists of only two main contributions which can be separated from the experimental measurement.

7.5.2 SDOF Response Fit Method

SDOF Response Fit Method approximates the complex FRF of the MDOF system which is obtained from experimental measurement by a curve. This curve represents the FRF of the SDOF system and is function of undamped natural angular frequency ω_0, damping ratio ζ and a constant C. [43] [69] [70]

Mathematical description of this approximation is derived from the equation of motion of SDOF system which is excited by harmonic force F_0.

$$m_S\ddot{x} + b_S\dot{x} + k_S x = F_0 e^{i\omega t} \tag{7.2}$$

If the initial conditions $x(0) = 0;\ \dot{x}(0) = 0$ are considered, the following FRF of this SDOF system is obtained by applying Laplace transform:

$$x_{SDOF} = \frac{\frac{F_0}{k_s} e^{i\omega t}}{1 - \eta^2 + i2\zeta\eta} \tag{7.3}$$

Here, the frequency ratio η and damping ratio ζ are defined as:

$$\eta = \frac{\omega}{\omega_0} \tag{7.4}$$

$$\zeta = \frac{b_s}{2\omega_0 m_s} \tag{7.5}$$

By introducing the substitutions (7.6) - (7.8), the equation (7.3) can be rewritten as (7.9) and (7.10) respectively.

$$C = C_{Re} + iC_{Im} = \frac{F_0}{k_s} e^{i\omega t} \tag{7.6}$$

$$a = 1 - \eta^2 \tag{7.7}$$

$$b = 2\zeta\eta \tag{7.8}$$

$$x_{SDOF} = \frac{C_{Re} + iC_{Im}}{a + ib} \tag{7.9}$$

$$x_{SDOF} = \frac{aC_{Re} + bC_{Im}}{a^2 + b^2} + i\frac{aC_{Re} - bC_{Im}}{a^2 + b^2} \tag{7.10}$$

The following four unknown parameters ζ, ω_0, C_{Re} and C_{Im} are obtained by approximation of FRF from experiment by x_{SDOF} with the use of least squares method:

$$min = \sum_{i=1}^{n} |x_i - x_{SDOF}|^2 \tag{7.11}$$

Here, x_i is the FRF from experiment, x_{SDOF} is the curve which approximates the experimental data and is defined by equation (7.10) and n is the number of points around the natural frequency in experimental FRF which are approximated by x_{SDOF}. Index i varies in the range 1 – n.

The iterative procedure of the method can be programmed as a script. In the first step, the experimental data which will be approximated must be defined. The program requires to load the complex FRF obtained from experimental measurement.

Then, the frequency range which is approximated by x_{SDOF} is selected: the number of approximated points n in FRF and the point which is closest to the top of the peak in FRF are defined.

In the second step, the initial estimated values of parameters ζ, ω_0, C_{Re} and C_{Im} are defined including the target residual value. Then, the best approximation of experimental data is searched by iterative process with the use of least squares method. The procedure ends when the residual value calculated according to equation (7.11) reaches the required value. Finally, the values of parameters ζ, ω_0, C_{Re} and C_{Im} are obtained. The damped natural (angular) frequency ω_D and $f_{NAT,SDOF}$ which correspond to the top of the peak (orange colour) can be then obtained.

$$\omega_D = \omega_0 \cdot \sqrt{1 - \zeta^2} \tag{7.12}$$

$$f_{NAT,SDOF} = \frac{\omega_D}{2\pi} \tag{7.13}$$

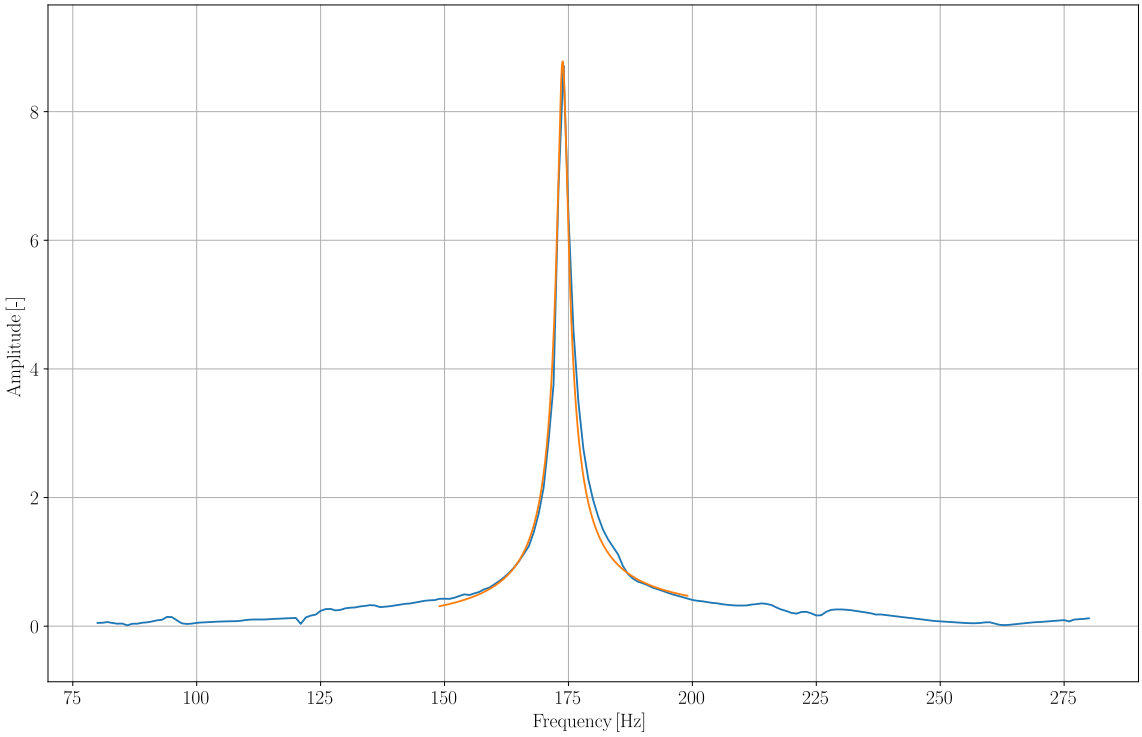

Fig. 7.6 Example of FRF approximation by SDOF Response Fit method (LDV 1)

7.6 List of All Measurements

As the experimental part of the research involved wide range of measurements, the complete list of all measured flow regimes is summarized in following tables.

Two types of hydrofoil excitation were used during the experiments. In case of flow induced vibrations, the hydrofoil was excited only by boundary layer separation along the profile and by vortex shedding behind the trailing edge. In the second case, the forced vibrations of hydrofoil were excited by external mechanical exciter. However, the excitation forces due to the boundary layer separation and the vortex shedding were still present.

An extra additional excitation was present during the presence of cavitation. Formation and collapse of cavitation bubbles cause unstable flow behaviour which produces additional force excitation of the hydrofoil. This excitation is strongly stochastic and cannot be well-quantified. Therefore, it is considered as a part of flow environment instead of controlled excitation mechanism.

Three sets of measurements were carried out for each kind of hydrofoil excitation. Each set consisted of measurements for various flow velocities. The first two sets were measured with the incidence angle 0° and 5° without presence of cavitation. The last set was carried out with the presence of cavitation and 5° incidence angle. For each flow velocity, measurements for three different values of cavitation number σ were carried out. Since the sheet cavitation was attached to the hydrofoil surface, these three cases reflected different percentage of hydrofoil surface covered by the cavitation cloud (one third of hydrofoil top surface behind the leading edge, two thirds and whole top surface). Due to the technical limits of the test circuit, it was not possible to observe the cavitation cloud over whole hydrofoil surface for lower flow velocities. Therefore, only two cavitation regimes were measured for flow velocities below 8 ms^{-1}.

An additional measurement of hydrofoil forced vibrations in air was carried out to investigate the natural frequencies and structural damping. In this case, the hydrofoil with 0° incidence angle was placed into empty test section filled by air.

The Reynolds number Re which is defined for the test section of the cavitation tunnel is calculated from the following equation:

$$Re = \frac{v \cdot d_h}{\nu_L} \tag{7.14}$$

$$d_h = \frac{4 \cdot S_{cross}}{L_c} \tag{7.15}$$

where

- v is free stream flow velocity at the inlet of the test section
- d_h hydraulic diameter calculated from equation (7.15)
- ν_L kinematic viscosity
- S_{cross} cross-section area of the test section
- L_c circumference of the cross-sectional area.

Table 2 Experiments: flow induced vibrations; 0° incidence angle; no cavitation

Flow Induced Vibrations of Hydrofoil					
	Angle of Attack	Flow Rate	Mean Flow Velocity at the Inlet of Test Section	Reynolds Number	Cavitation Number
	$[deg]$	$Q_V[l \cdot s^{-1}]$	$v_{inlet}\ [m \cdot s^{-1}]$	$Re\ [-]$	$\sigma\ [-]$
1	0	15	1.0	119 522	No cavitation
2	0	37.5	2.5	298 805	No cavitation
3	0	45	3.0	358 566	No cavitation
4	0	52.5	3.5	418 327	No cavitation
5	0	60	4.0	478 088	No cavitation
6	0	67.5	4.5	537 849	No cavitation
7	0	75	5.0	597 610	No cavitation
8	0	82.5	5.5	657 371	No cavitation
9	0	90	6.0	717 131	No cavitation
10	0	97.5	6.5	776 892	No cavitation
11	0	101.25	6.75	806 773	No cavitation
12	0	105	7.0	836 653	No cavitation
13	0	112.5	7.5	896 414	No cavitation
14	0	120	8.0	956 175	No cavitation
15	0	127.5	8.5	1 015 936	No cavitation
16	0	135	9.0	1 075 697	No cavitation
17	0	142.5	9.5	1 135 458	No cavitation
18	0	150	10.0	1 195 219	No cavitation
19	0	157.5	10.5	1 254 980	No cavitation
20	0	165	11.0	1 314 741	No cavitation
21	0	172.5	11.5	1 374 502	No cavitation
22	0	180	12.0	1 434 263	No cavitation
23	0	187.5	12.5	1 494 024	No cavitation
24	0	195	13.0	1 553 785	No cavitation
25	0	202.5	13.5	1 613 546	No cavitation
26	0	210	14.0	1 673 307	No cavitation
27	0	217.5	14.5	1 733 068	No cavitation
28	0	225	15.0	1 792 829	No cavitation
29	0	232.5	15.5	1 852 590	No cavitation
30	0	240	16.0	1 912 351	No cavitation
31	0	247.5	16.5	1 972 112	No cavitation
32	0	255	17.0	2 031 873	No cavitation
33	0	262.5	17.5	2 091 633	No cavitation

Table 3 Experiments: flow induced vibrations; 5° incidence angle; no cavitation

Flow Induced Vibrations of Hydrofoil					
	Angle of Attack	Flow Rate	Mean Flow Velocity at the Inlet of Test Section	Reynolds Number	Cavitation Number
	$[deg]$	$Q_V[l \cdot s^{-1}]$	$v_{inlet}\ [m \cdot s^{-1}]$	$Re\ [-]$	$\sigma\ [-]$
1	5	37.5	2.5	298 805	No cavitation
2	5	45	3.0	358 566	No cavitation
3	5	52.5	3.5	418 327	No cavitation
4	5	60	4.0	478 088	No cavitation
5	5	67.5	4.5	537 849	No cavitation
6	5	75	5.0	597 610	No cavitation
7	5	82.5	5.5	657 371	No cavitation
8	5	90	6.0	717 131	No cavitation
9	5	97.5	6.5	776 892	No cavitation
10	5	101.25	6.75	806 773	No cavitation
11	5	105	7.0	836 653	No cavitation
12	5	112.5	7.5	896 414	No cavitation
13	5	120	8.0	956 175	No cavitation
14	5	127.5	8.5	1 015 936	No cavitation
15	5	135	9.0	1 075 697	No cavitation
16	5	142.5	9.5	1 135 458	No cavitation
17	5	150	10.0	1 195 219	No cavitation
18	5	157.5	10.5	1 254 980	No cavitation
19	5	165	11.0	1 314 741	No cavitation
20	5	172.5	11.5	1 374 502	No cavitation
21	5	180	12.0	1 434 263	No cavitation
22	5	187.5	12.5	1 494 024	No cavitation
23	5	195	13.0	1 553 785	No cavitation
24	5	202.5	13.5	1 613 546	No cavitation
25	5	210	14.0	1 673 307	No cavitation
26	5	217.5	14.5	1 733 068	No cavitation
27	5	225	15.0	1 792 829	No cavitation

Table 4 Experiments: flow induced vibrations; 5° incidence angle; cavitation

Flow Induced Vibrations of Hydrofoil under Cavitation Conditions					
	Angle of Attack	Flow Rate	Mean Flow Velocity at the Inlet of Test Section	Reynolds Number	Cavitation Number
	$[deg]$	$Q_V[l \cdot s^{-1}]$	$v_{inlet}\ [m \cdot s^{-1}]$	$Re\ [-]$	$\sigma\ [-]$
1	5	75	5.0	597 610	1.860
2	5	75	5.0	597 610	2.583
3	5	90	6.0	717 131	1.768
4	5	90	6.0	717 131	2.480
5	5	105	7.0	836 653	1.813
6	5	105	7.0	836 653	2.326
7	5	112.5	7.5	896 414	2.181
8	5	112.5	7.5	896 414	2.823
9	5	120	8.0	956 175	1.538
10	5	120	8.0	956 175	1.751
11	5	120	8.0	956 175	2.295
12	5	135	9.0	1 075 697	1.458
13	5	135	9.0	1 075 697	1.761
14	5	135	9.0	1 075 697	2.301
15	5	150	10.0	1 195 219	1.615
16	5	150	10.0	1 195 219	1.770
17	5	150	10.0	1 195 219	2.198
18	5	165	11.0	1 314 741	1.497
19	5	165	11.0	1 314 741	1.850
20	5	165	11.0	1 314 741	2.134
21	5	180	12.0	1 434 263	1.514
22	5	180	12.0	1 434 263	1.774
23	5	180	12.0	1 434 263	2.241
24	5	187.5	12.5	1 494 024	1.664
25	5	187.5	12.5	1 494 024	1.806
26	5	187.5	12.5	1 494 024	2.533

Table 5 Experiment: forced vibrations of hydrofoil mounted in test section

Hydrofoil Oscillations Forced by Mechanical Exciter				
			Angle of attack	$0\ deg$
	Range of Excitation Frequency	Environment	Step of Excitation Frequency Δf	Excitation
	$[Hz]$		$[Hz]$	
1	$80 - 280\ Hz$	Air	1	Mechanical exciter
2	$200 - 1000\ Hz$	Air	2	Mechanical exciter
3	$200 - 1000\ Hz$	Water	2	Mechanical exciter

Table 6 Experiments: forced vibrations; 0° incidence angle; no cavitation

Hydrofoil Oscillations Forced by Mechanical Exciter				
			Angle of attack	$0\ deg$
			Range of Excitation Frequency	$60 \div 200Hz$
			Step of Excitation Frequency	$\Delta f = 1Hz$
	Flow Rate	Mean Flow Velocity at the Inlet of Test Section	Reynolds Number	Cavitation Number
	$Q_V[l \cdot s^{-1}]$	$v_{inlet}\ [m \cdot s^{-1}]$	$Re\ [-]$	$\sigma\ [-]$
1	0	0.0	0	No cavitation
2	15	1.0	119 522	No cavitation
3	30	2.0	239 044	No cavitation
4	45	3.0	358 566	No cavitation
5	60	4.0	478 088	No cavitation
6	75	5.0	597 610	No cavitation
7	90	6.0	717 131	No cavitation
8	105	7.0	836 653	No cavitation
9	120	8.0	956 175	No cavitation
10	135	9.0	1 075 697	No cavitation
11	150	10.0	1 195 219	No cavitation

Table 7 Experiments: forced vibrations; 5° incidence angle; no cavitation

Hydrofoil Oscillations Forced by Mechanical Exciter				
			Angle of attack	$5\ deg$
			Step of Excitation Frequency	$\Delta f = 2Hz$
	Mean Flow Velocity at the Inlet of Test Section	Reynolds Number	Cavitation Number	Range of Excitation Frequency
	$v_{inlet}\ [m \cdot s^{-1}]$	$Re\ [-]$	$\sigma\ [-]$	$[Hz]$
1	0	0	No cavitation	$50 - 1000\ Hz$
2	2.5	298 805	No cavitation	$50 - 1000\ Hz$
3	5.0	597 610	No cavitation	$50 - 1000\ Hz$
4	7.5	896 414	No cavitation	$50 - 1000\ Hz$
5	10.0	1 195 219	No cavitation	$50 - 2000\ Hz$
6	12.5	1 494 024	No cavitation	$50 - 2000\ Hz$

Table 8 Experiments: forced vibrations; 5° incidence angle; cavitation

Hydrofoil Oscillations Forced by Mechanical Exciter under Cavitation Conditions				
			Angle of attack	$5\ deg$
			Step of Excitation Frequency	$\Delta f = 2Hz$
	Mean Flow Velocity at the Inlet of Test Section	Reynolds Number	Cavitation Number	Range of Excitation Frequency
	$v_{inlet}\ [m \cdot s^{-1}]$	$Re\ [-]$	$\sigma\ [-]$	$[Hz]$
1	5.0	597 610	1.942	$50 - 1000\ Hz$
2	5.0	597 610	2.690	$50 - 1000\ Hz$
3	7.5	896 414	2.114	$50 - 1000\ Hz$
4	7.5	896 414	2.430	$50 - 1000\ Hz$
5	10.0	1 195 219	1.651	$50 - 2000\ Hz$
6	10.0	1 195 219	1.970	$50 - 2000\ Hz$
7	10.0	1 195 219	2.398	$50 - 2000\ Hz$
8	12.5	1 494 024	1.718	$50 - 2000\ Hz$
9	12.5	1 494 024	1.830	$50 - 2000\ Hz$
10	12.5	1 494 024	2.533	$50 - 2000\ Hz$

8 NUMERICAL MODELLING

Various mechanical and fluid properties of the hydrofoil case were investigated using numerical modelling. The numerical simulations were carried out with the use of commercial software ANSYS 19.1. which includes ANSYS Mechanical and ANSYS CFX solvers. The structural and acoustic meshes were created in ANSYS Meshing, while the fluid mesh was created in ANSYS ICEM CFD.

Three types of numerical modal analysis were carried out as a part of this research. At the beginning, the modal analysis of the hydrofoil and its shaft was carried out to obtain the natural frequencies and the corresponding mode shapes. The boundary conditions were set according to the mounting of the shaft in the test section. In the next step, the acoustic domain was created around the hydrofoil and the acoustic modal analysis was calculated. The acoustic domain represented the test section filled by water. As a result, the natural frequencies of the hydrofoil submerged in still water were obtained. Then, the added mass effect was evaluated. If the cavitation regime of the flow around the hydrofoil is operated, a two-phase flow composed of water and its vapour is present near the hydrofoil top surface (Fig. 4.2). Since the density of the liquid has major impact on the drop of hydrofoil natural frequencies, the presence of cavitation sheet attached to the hydrofoil surface influences its natural frequencies. Therefore, a subdomain filled by mixture of water and vapour was created inside the acoustic domain. The influence of both the subdomain dimensions and the mixture density on the hydrofoil modal properties was studied. [71]

As the fluid flows around the hydrofoil, the boundary layer separation and also the vortex shedding behind the trailing edge occur. These phenomena result in periodic force excitation of the hydrofoil. A transient CFD analysis of the flow around the hydrofoil was carried out to capture these both phenomena and to identify the main excitation frequencies.

The main focus of numerical simulations was concentrated on the identification of the damping. Since the fluid added damping depends on the flow velocity, its value was investigated for various values of flow velocity. As described later in this chapter, two approaches of numerical modelling are available: the two-way FSI coupled transient simulation and the Modal Work Approach. However, only results obtained from the Modal Work Approach are presented in this thesis. The two main reasons for this restriction are the occurred difficulties which extended the time spent on the experimental part of the research and the complicated time consuming debugging of two-way FSI coupled analysis.

It should be noted that the transient two-way FSI coupled simulation was set and calculated for another hydrofoil geometry with simplified boundary conditions [72]. This simulation was part of the same research project. In this case, the hydrofoil was fully fixed on its both sides to the walls of the test section without any shaft. The maximal thickness of the hydrofoil was 3 millimetres. Unfortunately, the results of this coupled analysis were not validated by experiment. The fixed mounting of the hydrofoil on its both sides simplifies both the setting of mesh motion as well as the applying of initial deflection at the beginning of the simulation. If the hydrofoil with its shaft is assumed, its mode shape involves deformation of both hydrofoil sides. Keeping continuous connection of the structural and fluid meshes during the simulation time is difficult and the simulation often crashes due to the presence of cells with negative volume.

This chapter is divided into three parts. The first part describes various types of structural simulations which were carried out during the research. The second part focuses on numerical investigation of vortex shedding behind the hydrofoil. The last part of the chapter deals with description of numerical approaches for calculation of damping ratio.

8.1 MECHANICAL ANALYSES

Evaluation of the added mass effect is based on the comparison of natural frequencies of the hydrofoil placed in the air and submerged in the liquid. Therefore, the following modal analyses were carried out.

8.1.1 Modal Analysis in Air

The model of geometry which was involved into the modal analysis (see Fig. 6.1) consisted from the hydraulic profile with the shaft (both manufactured as a one piece together from brass) and the torsion bar (manufactured from stainless steel). Both materials were modelled as linear elastic. The corresponding material properties can be found in Table 1 and Table 9.

Table 9 Material properties of stainless steel

ρ	7800 $kg \cdot m^{-3}$
E	210 000 MPa
ν	0.33

The computational mesh was created with the use of quadratic elements and consisted of 100 000 elements (290 000 nodes). Detailed view of the mesh is presented in the following pictures (Fig. 8.1 - Fig. 8.3).

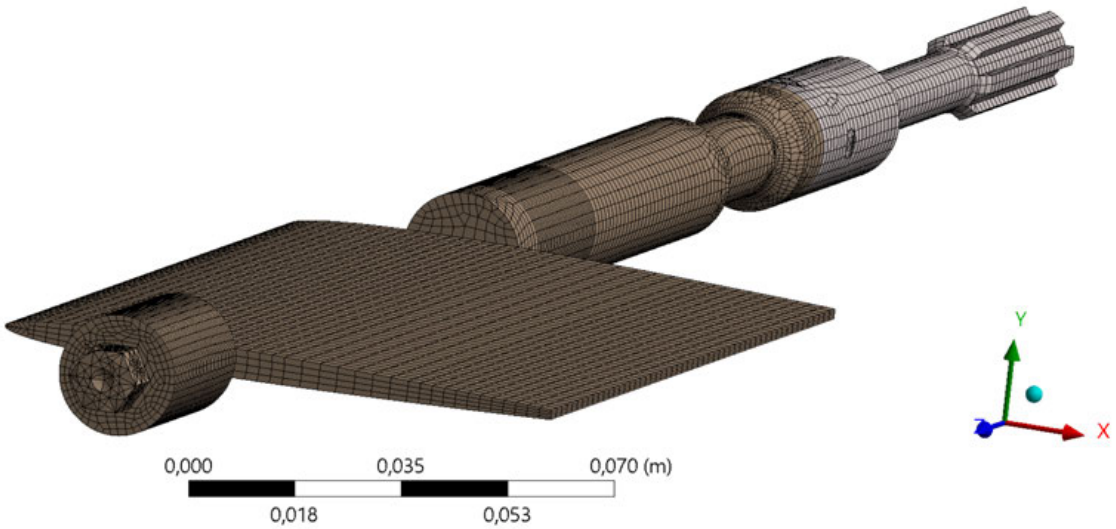

Fig. 8.1 Structural mesh

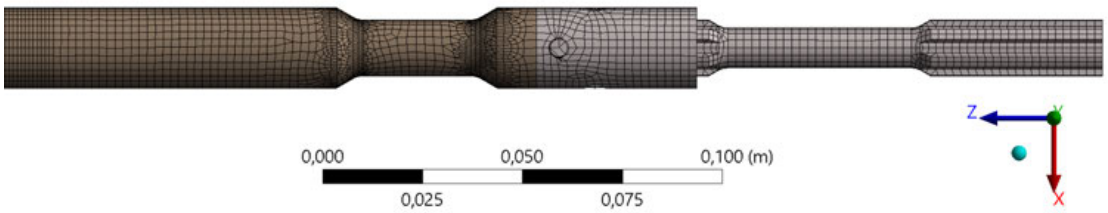

Fig. 8.2 Structural mesh

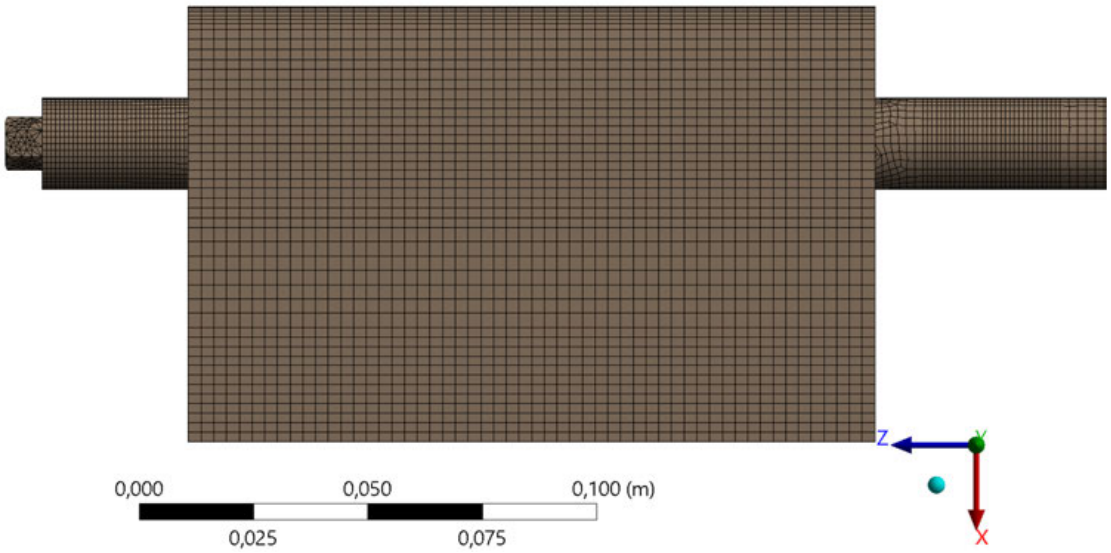

Fig. 8.3 Structural mesh

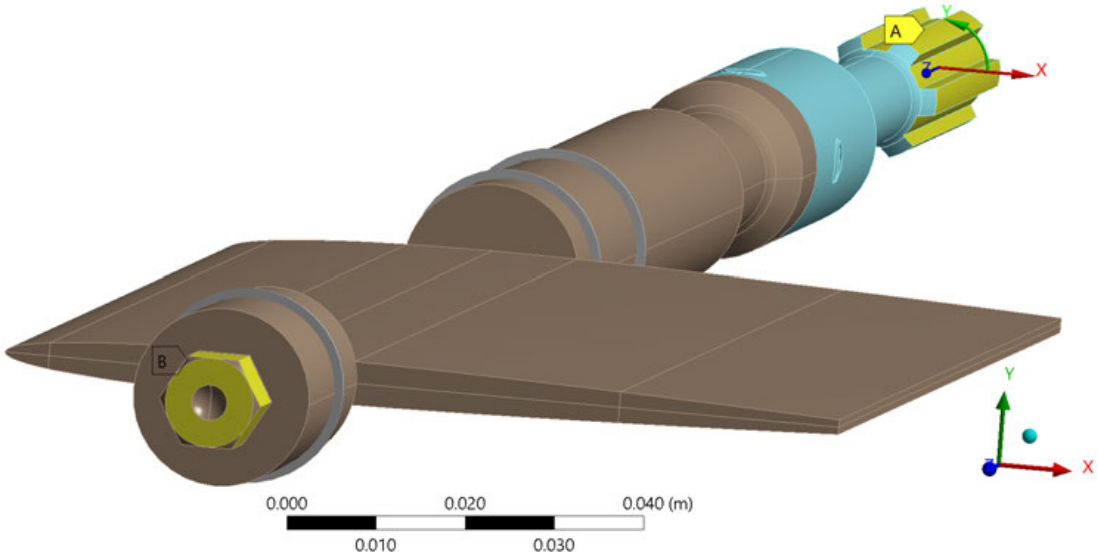

Fig. 8.4 Boundary conditions applied on the hydrofoil

The boundary conditions were applied according to the mounting of the hydrofoil inside the test section as shown in the figure (Fig. 8.4). The shaft of the hydrofoil is mounted by three ball bearings to the test section. Each of these bearings is marked by grey circle around the shaft (one bearing on the short part of the shaft and another two bearings on the longer side of the shaft). The "*Bearing*" boundary condition was applied on each of these three cross-sections of the shaft with the stiffness value of $1 \cdot 10^{15} N/m$. An additional cylindrical coordinate system was defined to apply the "*Displacement*" boundary conditions (see Fig. 8.4). Zero values of all three displacements were applied on the yellow coloured end of the torsion bar (letter "A"). On the short end of the shaft (letter "B"), the free rotation in y-direction (green axis of the cylindrical coordinate system) is applied together with zero displacement in the two remaining axis directions of this coordinate system. This set of boundary conditions corresponds to the mounting of the hydrofoil in the test section.

8.1.2 Acoustic Modal Analysis

Since the presence of liquid affects the natural frequencies of the structure, the acoustic modal analysis was carried out to calculate the modal properties of the hydrofoil which is submerged in still water.

An additional acoustic domain was created around the structural parts which were involved into the modal analysis in air (Fig. 8.5 - Fig. 8.6). This acoustic domain represented the test section filled by water. As all three bearings are flooded by water which comes from the test section, the cavities around bearings were also involved into the acoustic domain.

The domain was meshed by acoustic elements FLUID 220 and FLUID 221 which have one degree of freedom – pressure. The acoustic mesh consisted of 60 000 elements (400 000 nodes).

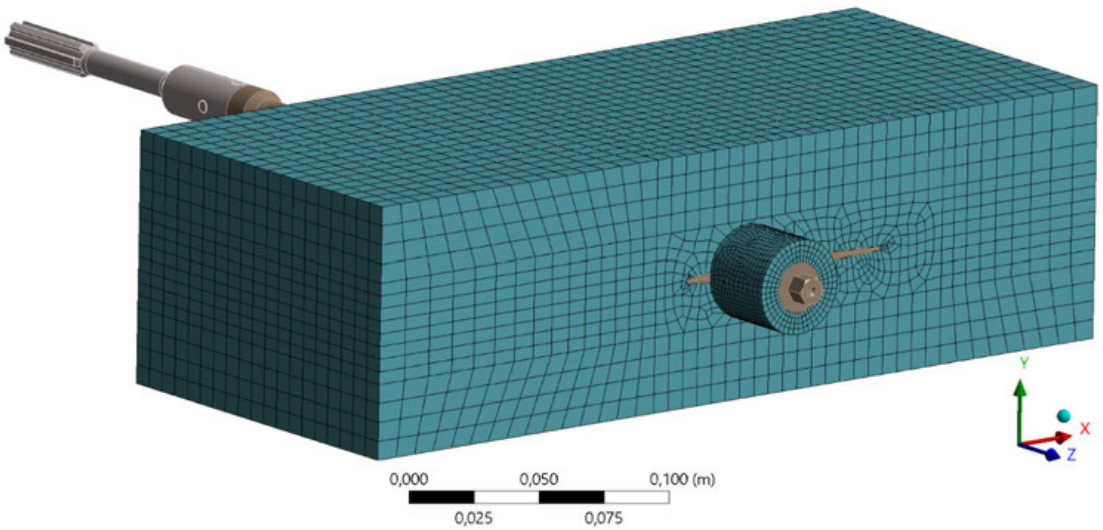

Fig. 8.5 Acoustic mesh

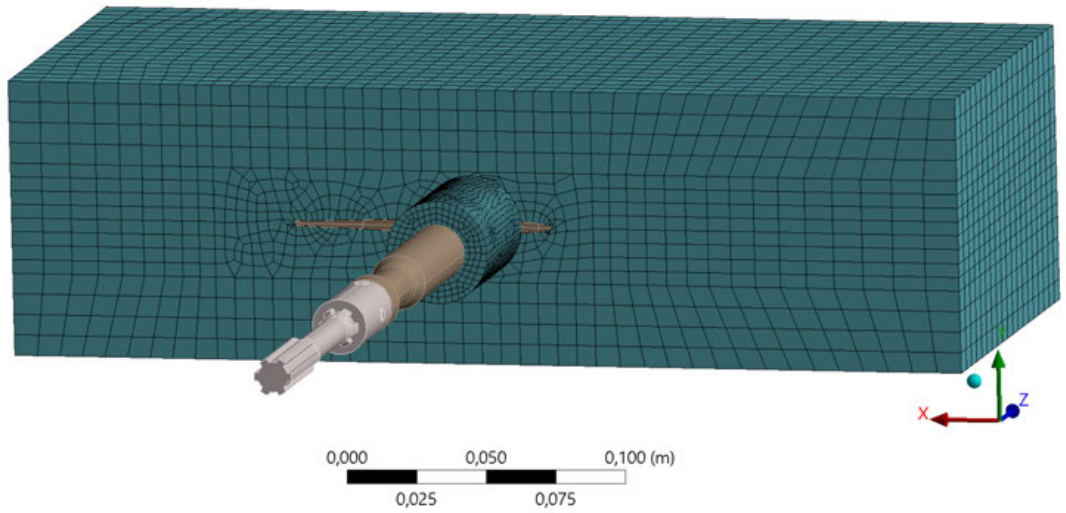

Fig. 8.6 Acoustic mesh

The mounting of the hydrofoil to the test section was modelled by the same boundary conditions as in the modal analysis in air. Additionally, the "*FSI Interface*" boundary condition was applied on the surface of hydrofoil and shaft which was in contact with water (Fig. 8.7). Since the acoustic and structural meshes are continuously connected, all nodes which were located on the interface had four degrees of freedom: the acoustic pressure p and three components of structural displacement u_s. Such special mathematical definition in these nodes enables coupling of the numerical solution in the acoustic domain and in the structure by following equations:

$$S_{ij}(u_s) \cdot n_j + p \cdot n_j = 0 \tag{8.1}$$

$$n_j \cdot u_s - n_j \cdot u_F = 0 \tag{8.2}$$

where

- S_{ij} is stress tensor of the structure
- p acoustic pressure
- u_s displacement in solid structure
- u_F displacement in acoustic fluid
- n_j outward normal unit vector of acoustic domain.

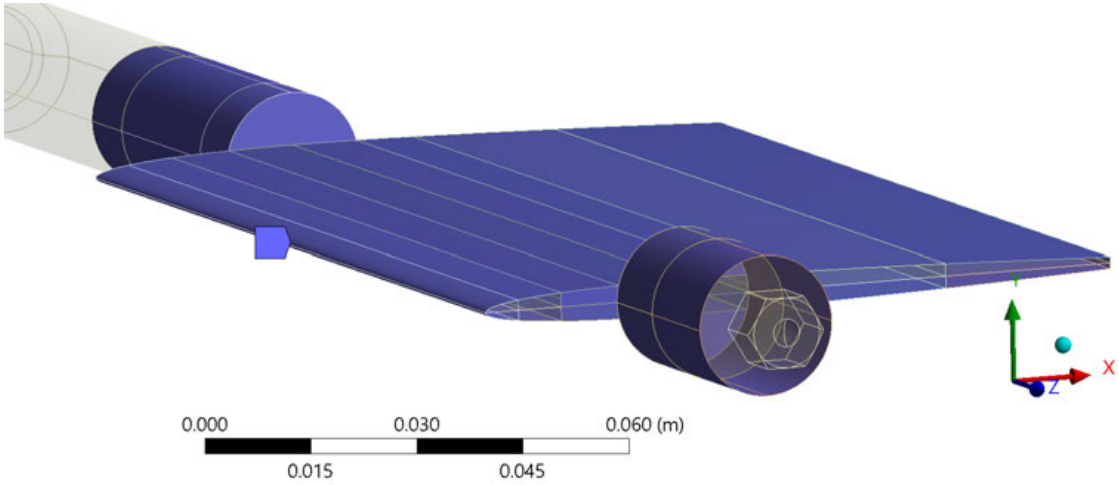

Fig. 8.7 FSI Interface boundary condition applied on the hydrofoil surface

The numerical solution in the fluid-acoustic domain is based on the wave equation and the linearized Navier-Stokes equation and is restricted by following assumptions:

- The fluid is compressible.
- The fluid is potential.
- The pressure disturbance of the fluid is small.
- There is no viscous stress.

Therefore, only potential flow of an inviscid fluid with no shear stress effects can be modelled. The fluid inside the acoustic domain, i.e. the water, was defined by its two main properties: the density and the speed of sound (see Table 10). Zero acoustic pressure was applied at the inlet and the outlet of the acoustic domain.

Table 10 Properties of water applied into acoustic modal analysis

ρ_w	$998.2\ kg \cdot m^{-3}$
c_w	$1482.1\ m \cdot s^{-1}$

8.1.3 Acoustic Modal Analysis under Cavitation Conditions

The modal properties of a hydrofoil oscillating in water are strongly influenced by fluid added effects compared to the oscillation of the same profile in air. It is generally known that the added mass effect, which primarily causes change in the natural frequencies of the body submerged in a liquid, depends on the density of the liquid and on the geometric configuration of the submerged body (shape and dimensions).

The flow velocity around guide vanes and runner blades inside Francis turbines can reach values up to 30 ms^{-1}. Therefore, cavitation during the operation of water turbine in off-design operating regimes may occur. The cavitation on the blades usually occurs in the form of a cavitation cloud, which is periodically shedding from the surface of the hydrofoil (Fig. 4.3). Due to changes in the velocity and pressure fields around the blade, the pressure behind the leading edge of the blade drops below the value of the saturated vapour pressure p_V. Then, bubbles filled with saturated vapour are formed and further carried by the flow along the hydrofoil surface to the area of higher pressure, where these bubbles disappear in the form of implosion.

The presence of a cavitation cloud attached to surface of the blade, whose properties (dimensions and density of the mixture of saturated vapour and water) change over time, has a fundamental effect on the added mass effect. From a microscopic point of view, the cavitation cloud is filled by a mixture of very small bubbles of saturated vapour and water droplets. Since the flow in the cavitation cloud region is a strongly non-stationary process and the size of the cavitation cloud itself changes over time, it is very difficult to quantify the added mass effect for a hydrofoil surrounded by a cavitating flow.

Effect of cavitation cloud on the modal properties of the hydrofoil can be estimated from acoustic modal analysis. Computational model consists of the hydrofoil structure, the cavitation cloud and the water inside the test section. The acoustic domain which represents the water inside the test section has same parameters and dimensions as described in previous analysis. The cavitation cloud is modelled as a subdomain inside the acoustic domain and is attached to the top surface of the hydrofoil.

However, this approach is only approximation of a real strongly non-stationary process under the following simplified assumptions [71]:

- The added mass effect does not depend on the flow velocity around the hydrofoil.
- The size and dimensions of the cavitation cloud does not change over time.
- The cavitation cloud is filled by homogeneous mixture of saturated vapour and liquid water; the physical properties of this mixture are defined for various percentage of saturated vapour in this mixture.
- The influence of non-stationary processes is not considered (formation and collapse of cavitation bubbles, tearing of the boundary layer and change in the size of the cavitation cloud over time).

In a real experiment, the increase of flow velocity usually results in change of hydrofoil natural frequencies. This behaviour is caused mainly by added mass and added stiffness effects (m_{ADD} and k_{ADD}). Since these two added forces act on the body in phase, it is not clear which of them has a dominant effect on the change in natural frequency. In order to quantify each of these effects separately, it is assumed that the drop of natural frequencies by submerging the structure into still water is caused only by the added mass effect and does not depend on the flow velocity. The observed change of natural frequencies which occurs by increase of the flow velocity is then considered as a result of the fluid added stiffness.

- **Geometry**

The modal properties of hydrofoil with attached cavitation cloud were studied with the use of acoustic modal analysis. The acoustic domain filled by water was created as shown in previous analysis (Fig. 8.5). Inside this domain, five different configurations of cavitation cloud were created. Two different values of cloud length (25 mm and 60 mm) and of cloud thickness (0.5 mm and 2.0 mm) resulted in four analysed cases (Fig. 8.8 - Fig. 8.9). The fifth configuration was created to represent shape of the sheet cavitation which can typically be observed on hydraulic profiles (Fig. 8.10). All five cloud configurations were designed according to the cavitation behaviour which was observed during our experiments.

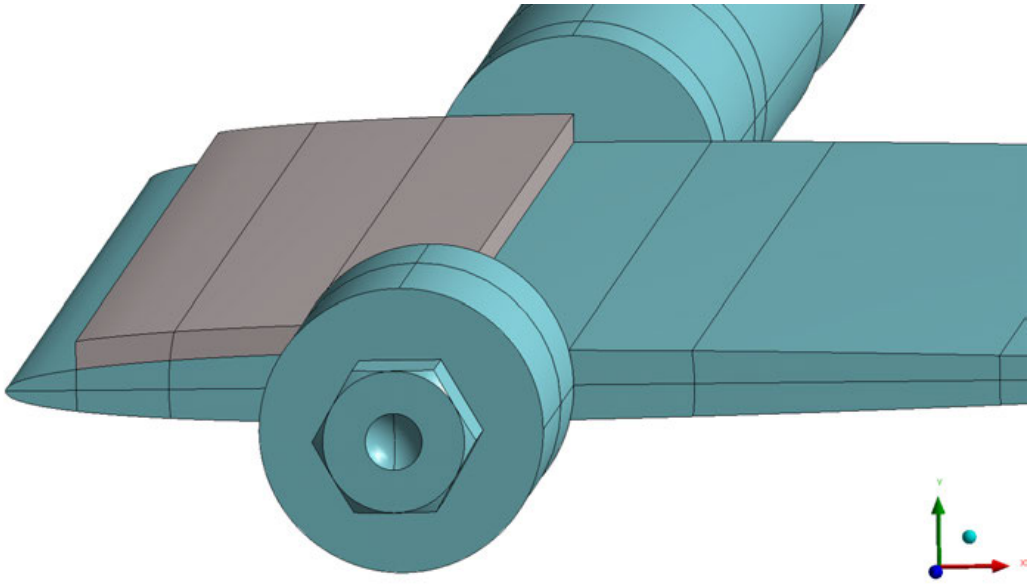

Fig. 8.8 Cavitation cloud: Length 25 mm; constant thickness 0.5 mm or 2.0 mm

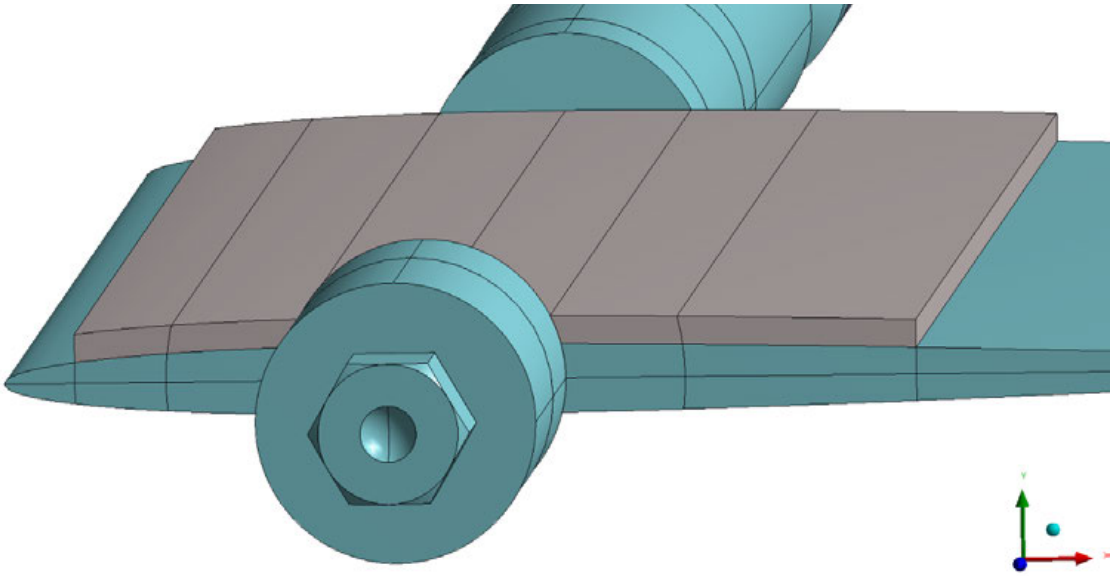

Fig. 8.9 Cavitation cloud: Length 60 mm; constant thickness 0.5 mm or 2.0 mm

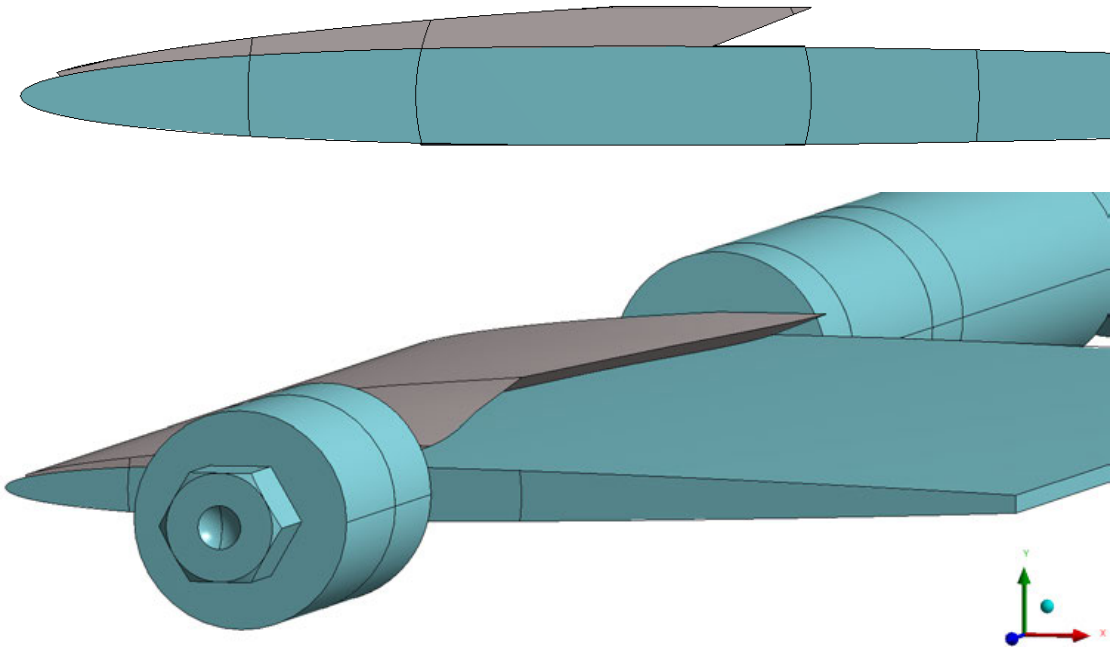

Fig. 8.10 *"Real"* cavitation cloud; variable thickness in the range 0.5 – 2.0 mm

- **Physical Properties of Cavitation Cloud**

Physical properties of both the liquid water and the saturated vapour can be found in Table 11. The properties of water inside the acoustic domain of the test section were set to constant values. It is assumed that the cavitation cloud is filled by homogenous mixture of water and saturated vapour. Ten different settings of physical properties inside this cavitation cloud were considered for each cloud geometry. Each of the settings corresponded to different percentage of vapour inside the cloud in the range 0 – 100 % of vapour. From all calculations, the first five natural frequencies and the corresponding mode shapes were evaluated.

Table 11 Physical properties of water and saturated vapour

	Water	Saturated Vapour
Speed of Sound	$c_w = 1482.1\ m \cdot s^{-1}$	$c_{vap} = 340\ m \cdot s^{-1}$
Density	$\rho_w = 998.2\ kg \cdot m^{-3}$	$\rho_{vap} = 0.174\ kg \cdot m^{-3}$

Physical properties of the mixture inside the cavitation cloud can be calculated from the two following equations [12]:

$$\rho_{mix} = \alpha_w \rho_w + \alpha_{vap} \rho_{vap} \tag{8.3}$$

$$\frac{1}{{c^2}_{mix}} = \left(\alpha_w . \rho_w + \alpha_{vap} \cdot \rho_{vap}\right) \cdot \left[\frac{\alpha_{vap}}{\rho_{vap} {c^2}_{vap}} + \frac{\alpha_w}{\rho_w {c^2}_w}\right] \tag{8.4}$$

where

- ρ_{mix} is density of the mixture inside the cavitation cloud
- ρ_w density of water
- ρ_{vap} density of saturated vapour
- α_w volume fraction of water
- α_{vap} volume fraction of saturated vapour
- c_{mix} speed of sound of the mixture inside the cavitation cloud
- c_w speed of sound of water
- c_{vap} speed of sound of saturated vapour.

The physical properties of the mixture calculated by equations (8.3) and (8.4) are presented in Table 12 and in the two following figures (Fig. 8.11 - Fig. 8.12). The acoustic modal analysis was calculated for each value of volume fraction α_{vap}in the table.

The applied boundary conditions remain same as in the previous analyses described in Chapters 8.1.1 and 8.1.2.

Table 12 Physical properties of the mixture inside the cavitation cloud

α_w	α_{vap}	ρ_{mix}	c_{mix}
$[-]$	$[-]$	$[kg \cdot m^{-3}]$	$[m \cdot s^{-1}]$
1.00	0.00	998.20	1482.10
0.90	0.10	898.31	14.96
0.80	0.20	798.51	11.22
0.70	0.30	698.72	9.80
0.60	0.40	598.93	9.16
0.50	0.50	499.14	8.98
0.40	0.60	399.34	9.16
0.30	0.70	299.55	9.79
0.20	0.80	199.76	11.22
0.10	0.90	99.97	14.95
0.00	1.00	0.17	340.00

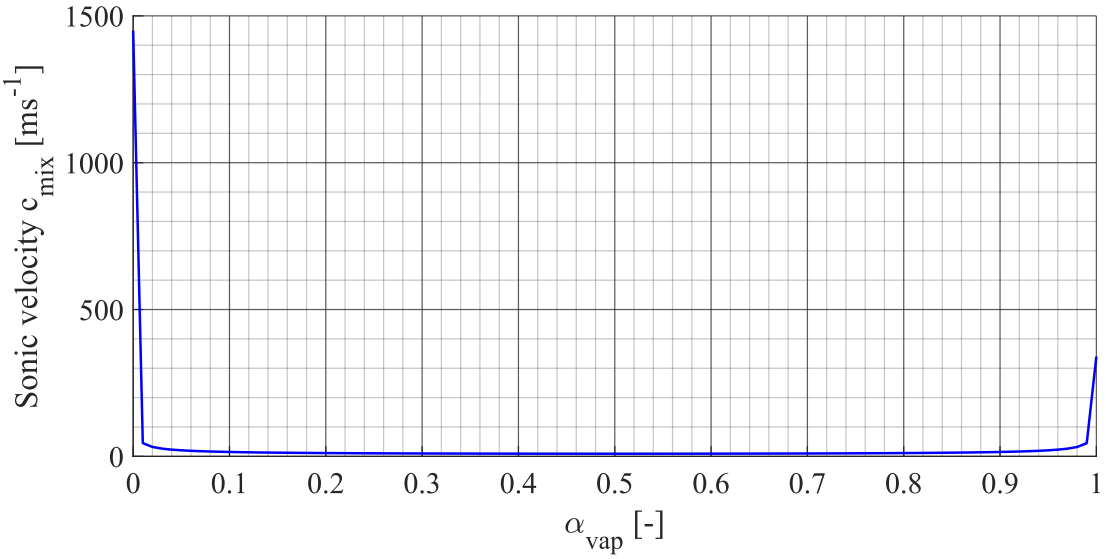

Fig. 8.11 Dependence of speed of sound on vapour volume fraction

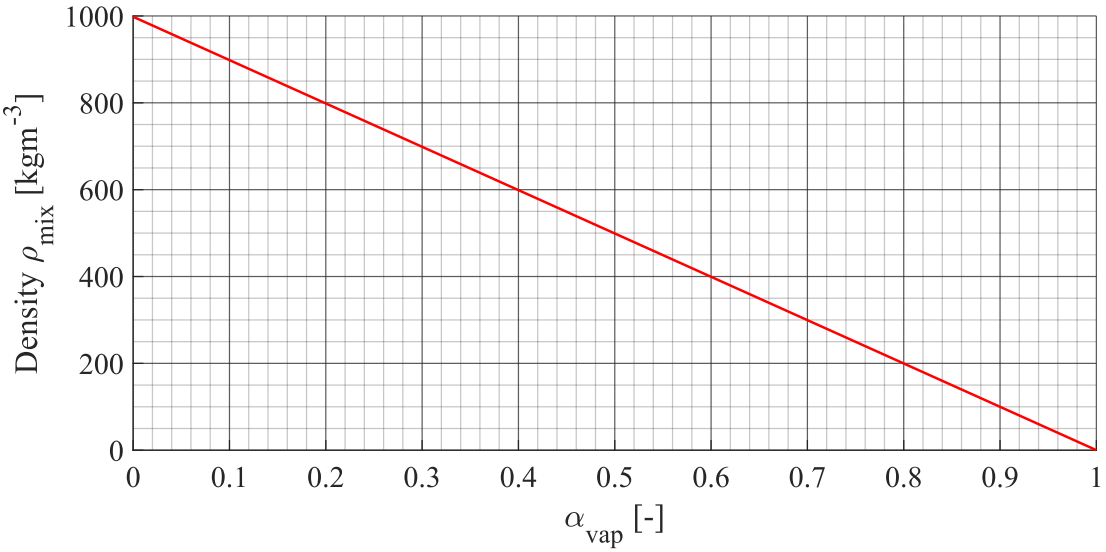

Fig. 8.12 Dependence of density on vapour volume fraction

8.2 NUMERICAL INVESTIGATION OF VORTEX SHEDDING

The unsteady CFD analysis was calculated in ANSYS CFX to simulate the boundary layer separation from the hydrofoil surface as well as to capture the frequencies of vortex shedding behind the trailing edge. The computational domain consisted of three main parts (see Fig. 6.6 and Fig. 8.13): the red coloured test section, the straight pipe upstream of the test section and the 5°-full angle diffuser with rectangular cross-section. In order to obtain better convergence, the diffuser was extended by 1 meter long straight pipe of rectangular cross-section.

Fig. 8.13 Fluid domain in CFD simulation

8.2.1 CFD Mesh

Three different computational mesh resolutions were tested as a part of the mesh-sensitivity study. The final mesh which was used for the presented simulations consisted of 14.25 million hexahedral cells (14.4 million nodes) as described in Table 13. The boundary layer refinement was created to satisfy $y^+ < 1$ on the hydrofoil surface as well as on the walls of the test section for maximal mean velocity $v_{inlet} = 20\ ms^{-1}$ at the inlet of the domain. As it can be seen in figure (Fig. 8.14), the maximal value of y^+ on hydrofoil surface at $v_{inlet} = 20\ ms^{-1}$ is $y^+ \approx 1.05$ on the trailing edge. The region of higher values of y^+ behind the leading edge reaches value $y^+ \approx 0.85$. Details of the computational mesh are shown in the figures below (Fig. 8.15 - Fig. 8.17).

This computational mesh was used for two different CFD analyses: the unsteady analysis of flow around rigid hydrofoil to capture vortex shedding and the investigation of viscous damping using unsteady analysis with prescribed motion of the hydrofoil.

Table 13 Mesh size of the fluid domains

	Nodes	Cells
Straight Pipe	1 mil.	1 mil.
Test Section	9 mil.	9 mil.
Diffuser	4.4 mil.	4.5 mil.
Total	14.4 mil.	14.5 mil.

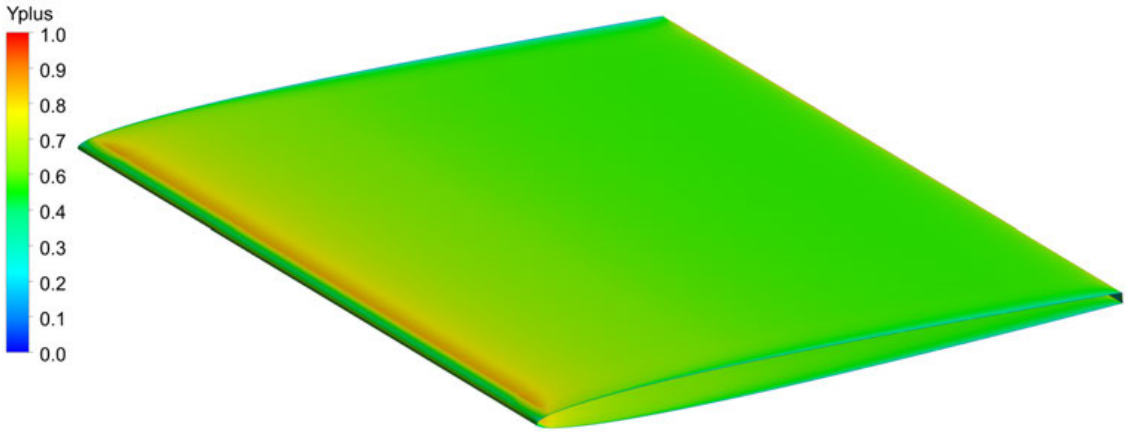

(a)

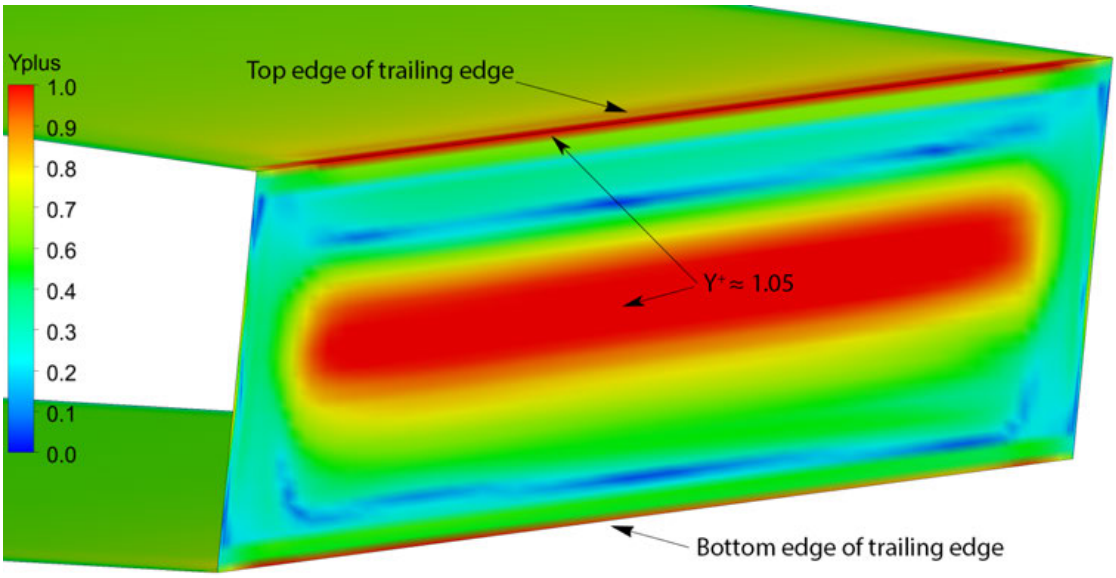

(b)

Fig. 8.14 Contours of y^+ on hydrofoil surface: (a) view on leading edge, (b) view on trailing edge

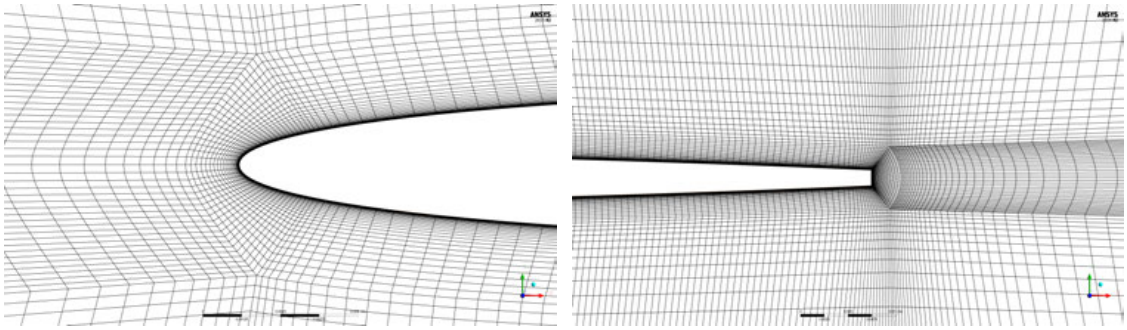

(a) (b)

Fig. 8.15 Detail of mesh resolution near the leading edge (a), Detail of mesh resolution near the trailing edge (b)

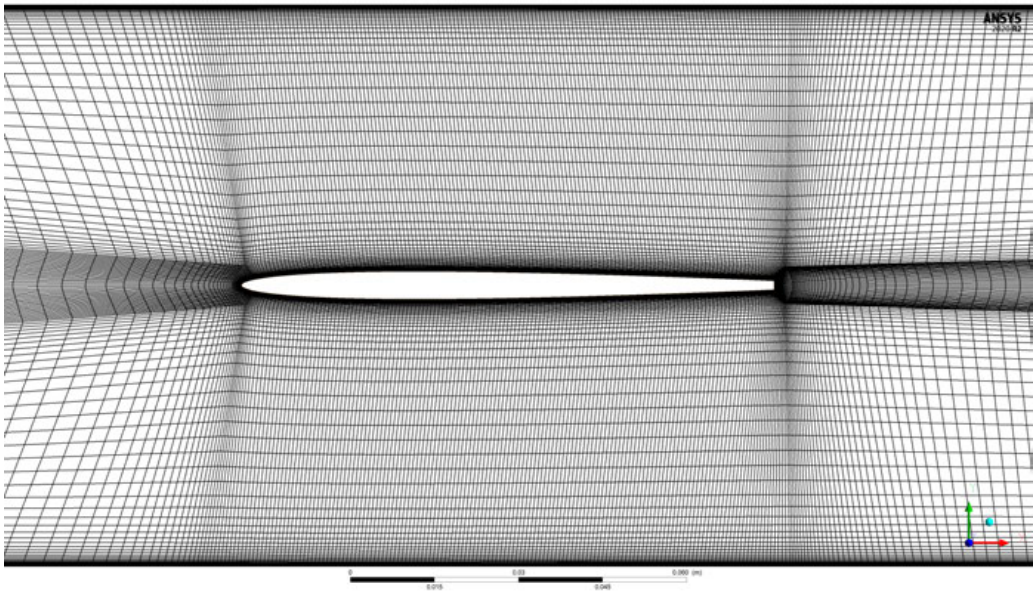

Fig. 8.16 CFD mesh in the test section

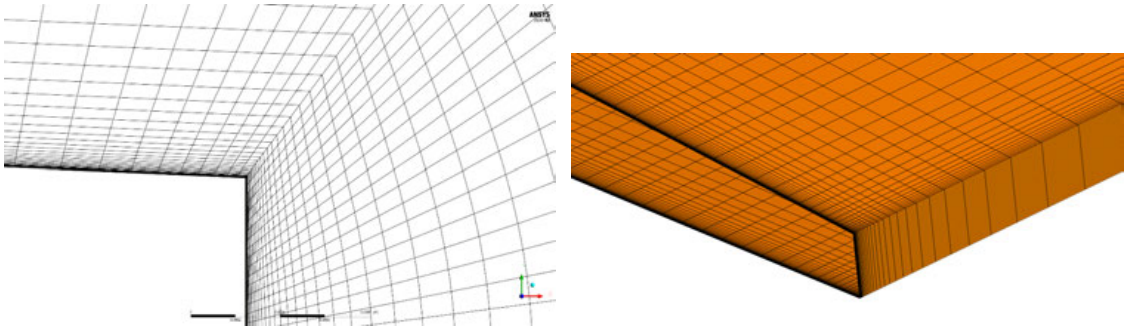

(a) (b)

Fig. 8.17 CFD mesh at the top side of the trailing edge (a), Surface mesh on the hydrofoil (b)

8.2.2 Boundary Conditions and Solver Settings

The phenomenon of vortex shedding behind the hydrofoil trailing edge occurs, if the boundary layer stays attached to the hydrofoil surface even after its separation. These flow conditions can be achieved by very thin profile with zero incidence angle. Then, periodic formation of vortices behind the trailing edge is observed and von Kármán vortex street develops. Such flow behaviour produces periodic force which excites the hydrofoil vibrations.

In order to estimate the vortex shedding frequency, an unsteady CFD simulation of the flow behaviour inside the test section was carried out. The above described computational domain and mesh were used in the simulation. Since the domain inlet is located at the outlet of a contraction nozzle in the test circuit, a velocity profile boundary condition was applied at the inlet of the computational domain. This velocity profile was obtained from additional CFD steady state analysis of the flow inside the contraction nozzle for each analysed flow velocity. An example of the applied velocity profile at $v_{inlet} = 10\ ms^{-1}$ is shown in the following figure (Fig. 8.18). The vortex shedding

frequency was analysed numerically for inlet mean velocities in the range 2.5 ms^{-1} – 20 ms^{-1} with a step of 2.5 ms^{-1}. The no-slip boundary condition was applied on the walls of the test section as well as on the hydrofoil surface. At the outlet of the domain, zero static pressure was applied.

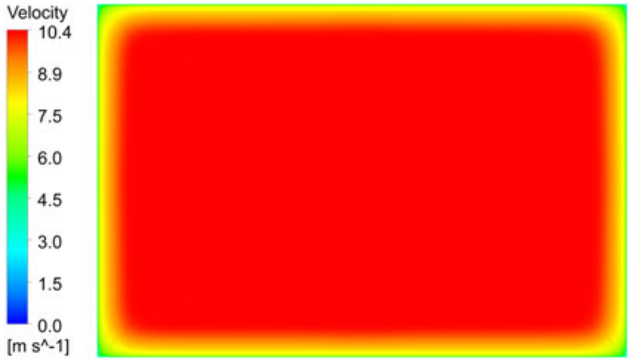

Fig. 8.18 Velocity profile at inlet of the domain at $v_{inlet} = 10\ ms^{-1}$

Two-equation SST k-ω turbulence model was employed for all CFD simulations in this thesis. The initial values for unsteady simulations were obtained from steady-state solution for each value of mean velocity. All unsteady simulations were executed using Second Order Backward Euler Transient Scheme. High-Resolution Scheme was applied for advection. Two types of turbulence schemes were tested, i.e. the First Order Scheme and the High-Resolution Scheme. The High-Resolution Scheme did not provide any significant improvement. Therefore, the First Order Scheme was applied for turbulence which provided lower values of residuals and better convergence.

The pressure fluctuations were monitored in six points (P1 – P6) located behind the trailing edge (Fig. 8.19). Additionally, the lift and drag forces acting on the hydrofoil were monitored. The vortex shedding frequency was evaluated from amplitude-frequency spectra of the monitored variables obtained by Fast Fourier Transformation (FFT).

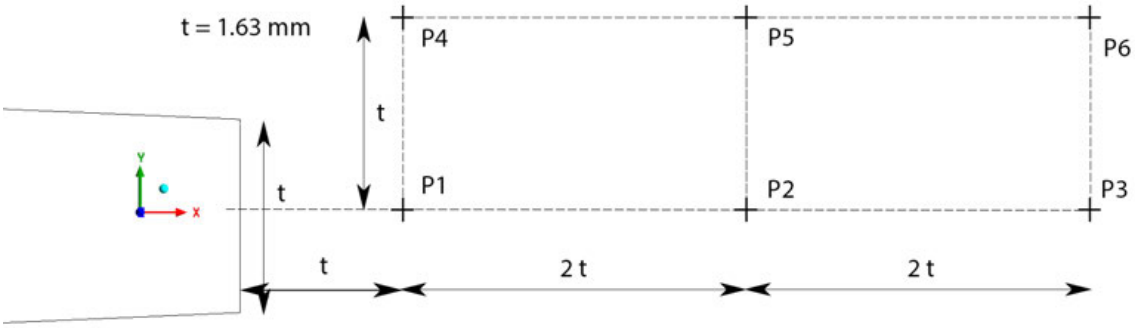

Fig. 8.19 Monitors of pressure (P1 - P6) behind trailing edge

Since the time-step *dt* has influence on the vortex shedding frequency, the time-independent study was performed at maximal mean velocity $v_{inlet} = 20\ ms^{-1}$. By consecutive decreasing of the time-step size, it was found out that the vortex shedding frequency does not change for time-step size which is equal to or smaller than $dt = 2.20e^{-6}s$. Therefore, this time-step size was used for all values of mean velocities.

8.3 NUMERICAL INVESTIGATION OF DAMPING RATIO

In recent years, two main numerical approaches of damping ratio estimation became common and popular in the field of hydraulic machines. Considering forced oscillations of a fixed hydrofoil submerged into water, as shown in the photo (Fig. 1.1), physics of both fields are strongly coupled. Therefore, the first approach is the fully coupled transient two-way FSI analysis [73][74]. Details of the two-way FSI approach as well as the obtained results for a simplified case were presented in a journal proceeding [72]. The two-way coupled FSI analysis is a highly complicated algorithm. Setting up and debugging such complicated analysis is very time consuming and the CPU time requirements are enormously demanding. Therefore, less sophisticated numerical methods need to be developed providing enough accurate results. Focusing on the hydrodynamic damping investigation for the oscillating hydrofoil immersed into the water, the second approach is the recently developed Modal Work Approach. This very effective algorithm is often used for damping ratio investigation which is documented by several publications [17][58][60][75].

In this thesis, the damping ratio is calculated with the use of modified Modal Work Approach. This technique was developed during the author's internship in Voith Hydro Holding GmbH & Co. KG in Heidenheim, Germany and presented in a conference paper [76]. Main steps of the Modal Work Approach are described in the following chapter and compared to the modified technique presented in [76].

8.3.1 Procedure of Modal Work Approach

The Modal Work Approach was developed to calculate damping ratio of a structure which performs harmonic oscillations and is submerged in a liquid. Due to simplified assumptions, the Modal Work Approach enables to model a multi-field problem by using only a single field solver, which is the fluid solver. By using this approach, the damping ratio for the chosen mode shape can be calculated. The following assumptions are considered:

- The hydrofoil performs small linear periodic oscillations.
- The oscillation frequency is equal to the chosen natural frequency (for example the first natural frequency of the submerged hydrofoil).
- The hydrofoil deformation during oscillations is determined by the corresponding mode shape.
- The mode shape is damped weakly and therefore the effect of damping on frequency and mode shape is negligible.
- The mode shapes of the hydrofoil in the air and submerged into the water are identical. This assumption simplifies the solution procedure without any significant impact on the results but is not generally applicable as shown by Escaler in [77].
- The numerical model assumes hydrofoil oscillations with a constant amplitude U_{MAX}.
- The hydrofoil deformation during the oscillation is elastic and structural damping is neglected.
- The natural frequencies of the fluid domain are obviously different from the natural frequencies of the submerged structure. Therefore, the added effects b_W and k_W in equation (5.1) can be neglected and the hydrodynamic damping b_F is the only present damping.

- The only force which performs work during periodic oscillations of the structure is the damping force $F_{ADD,DAMP}$ (see Chapter 5.2). Therefore, all dissipated energy is equal to the work W_{DISS} done by the damping force. The work done by the stiffness force during one period of oscillation is equal to zero as shown in Chapter 5.3.

The submerged oscillating structure, i.e. the hydrofoil, is considered as a single degree-of-freedom (SDOF) oscillator. Its motion is described by equation of motion

$$m_S\ddot{q} + b_S\dot{q} + k_S q = F(t) \tag{8.5}$$

where

- m_S is mass of the structure
- b_S structural damping
- k_S stiffness of the structure
- $F(t)$ fluid force acting from the liquid on the structure.

The equation can be rewritten as (8.6), where the added effects introduced in Chapter 5 are present. According to the above described assumptions the equation is simplified to the final formulation (8.7).

$$(m_S + m_{ADD})\ddot{q} + (b_S + b_W + b_F)\dot{q} + (k_S + k_W + k_F)q = 0 \tag{8.6}$$

$$(m_S + m_{ADD})\ddot{q} + b_F\dot{q} + (k_S + k_F)q = 0 \tag{8.7}$$

The hydrofoil modal properties, i.e. the natural frequencies and corresponding mode shapes, are obtained as a result of acoustic modal analysis. The selected mode shape, of which damping ratio is investigated, must be normalized to the mass matrix $\boldsymbol{M_S}$ and exported. The displacement components U_X, U_Y and U_Z are exported only for nodes attached to the hydrofoil surface which is in contact with water (FSI Interface between solid and fluid). The fluid solver is not able to solve the equations describing the structural behaviour of the hydrofoil. However, the assumption of small linear periodic oscillations with constant amplitude U_{MAX} enables to model the hydrofoil oscillations as a prescribed periodic motion of the hydrofoil surface walls in the fluid domain. The displacements obtained from the acoustic modal analysis are imported to the fluid solver. The motion of the FSI Interface which represents the hydrofoil oscillations in the fluid solver is prescribed according to:

$$u(x, y, z, t) = U_{MAX} \cdot \Phi(x, y, z) \cdot \sin(\omega_0 \cdot t), \tag{8.8}$$

where

- u is deflection
- U_{MAX} $[m]$ hydrofoil amplitude (scaling factor)
- Φ normalized mode shape deflection
- ω_0 undamped natural angular frequency
- t is time.

Such a prescribed hydrofoil motion satisfies the assumption of hydrofoil oscillation on the chosen natural frequency and corresponding mode shape. Using the transient approach for determining the modal work, the influence of two main parameters, which is the prescribed amplitude U_{MAX} and the time-step size, needs to be studied. Typically, the amplitude U_{MAX} is set up in the range of 0.5 – 2 % of the chord length and ca. 250 time steps per oscillation period are applied [78]. The dissipated

energy W_{DISS}, which is exchanged between hydrofoil and fluid (also called "*modal work*") during a single blade oscillation period, is evaluated (8.9) [79]:

$$W_{DISS} = \int_{t_0}^{t_0+T} \oiint_A \left(p\delta_{ij}n_j + \tau_{ij}n_j\right) \cdot \dot{u}_i(t)\, \mathrm{d}A\mathrm{d}t \tag{8.9}$$

where

- p is pressure
- δ_{ij} Kronecker delta
- n_j surface normal vector (pointing into the fluid)
- τ_{ij} wall shear stress tensor
- $\dot{u}_i$ mode shape velocity vector (mesh velocity in fluid solver)
- t time
- A surface area
- T blade oscillation period.

As the scalar product between wall shear stress tensor τ_{ij} and the surface normal vector n_j is along the hydrofoil surface equal to zero, the contribution from τ_{ij} to the dissipated energy W_{DISS} is significant only at free edges where τ_{ij} is aligned with the surface normal vector n_j. According to [17], the contribution from τ_{ij} on Francis turbine blades is 2-3 orders of magnitude smaller than the pressure contribution and is usually neglected.

Consequently, the estimation of damping ratio ζ according to the following equation (8.10) [58] is performed:

$$\zeta = \frac{W_{DISS}}{2\pi M \omega_0^2 U_{MAX}^2} \tag{8.10}$$

where

- W_{DISS} is modal work exchanged between structure and fluid
- M modal mass
- ω_0 undamped natural angular frequency in still water
- U_{MAX} is modal reference amplitude.

Using ANSYS CFX, the area integral of variable *Wall Power Density* over moving walls of prescribed mode shape might be monitored during one period T of mode cycle [79]. Using the time integration, the modal work W_{DISS} is then calculated in the same way as defined by (8.9) and the damping ratio can be calculated using the formula (8.10).

The obtained damping ratio can be positive or negative. Depending on the type of analysed FSI system, the sign may have different meanings. Considering FSI system which consists of a hydrofoil placed into a flow, the following explanation was presented by Nennemann and Monette [61]: If a hydraulic profile is placed into a flow of high flow velocity and in absence of von Kármán vortices, the damping is expected to be generally positive. However, in presence of von Kármán vortices, both signs of damping may be obtained. The positive sign of damping means that the natural vibration amplitude (the amplitude which will result as a consequence of energy balance) will be smaller than the prescribed amplitude U_{MAX} in the numerical simulation. The negative sign of damping indicates that the natural vibration amplitude will be larger than the prescribed

amplitude U_{MAX}. In case of other analysed phenomena such as pump turbine guide vane flutter or air foil flutter, the negative value of damping indicates self-excitation of the system. In such situations the limit vibration amplitude may not exist and the only limitation of a real system's vibration amplitude is a contact with other nearby structure. [61]

In the FSI system which is analysed in this thesis, the sign of the damping is expected to be positive since the surface normal n_j is oriented into the fluid domain. The positive sign of dissipated energy means that the energy is transferred from the structure to the fluid and the hydrofoil oscillations are damped by the water.

The Modal Work Approach has the same requirements on hardware and CPU time as the standard unsteady CFD analysis and is therefore much more effective compared to the two-way FSI coupled analysis. Additional time savings can be reached by solving the CFD analysis in frequency domain instead of time domain. The solution of the flow field in the frequency domain can be obtained by Harmonic Balance Method [80] - [83], which has been implemented into ANSYS CFX recently.

In this thesis, the damping ratio is calculated with the use of modified Modal Work Approach which was presented in [76]. This technique follows the already described general steps. The modification consists in calculation of damping ratio by comparing the dissipated energy W_{DISS} and the elastic strain energy E_{TOT} calculated by static structural analysis:

$$\zeta = \frac{W_{DISS}}{4\pi E_{TOT}} \tag{8.11}$$

The following two assumptions must be satisfied in addition to the above mentioned assumptions:

- When the hydrofoil reaches its maximum deflection during the periodic motion, the total energy E_{TOT} of the oscillation (potential and kinetic energy) is accumulated into deformation, i.e. E_{TOT} is equal to the elastic strain energy.
- The hydrofoil deformation during the oscillation is elastic and structural damping is neglected.

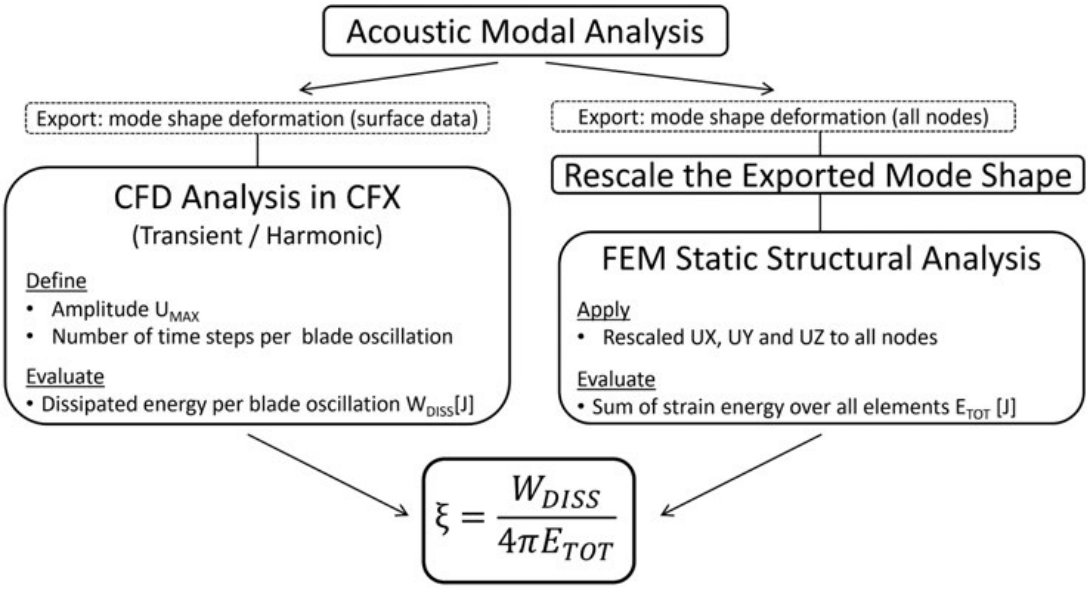

Fig. 8.20 Diagram of modified Modal Work Approach

The main steps of the modified Modal Work Approach are shown in the scheme above (Fig. 8.20). Once the natural frequencies and mode shapes of the submerged hydrofoil are obtained from acoustic modal analysis, the chosen mode shape is normalized to the mass matrix and exported in two ways: First, the deformations UX, UY and UZ are exported only for nodes attached to the hydrofoil surface which is in contact with water (interface between solid and fluid). Secondly, the mode shape deformation is exported for all nodes including the nodes inside the hydrofoil volume. The first set of surface data is used to prescribe a harmonic motion in ANSYS CFX, while the second set of volume deformation is used to calculate the elastic strain energy in a static structural analysis. In the second case, the exported mode shape must be rescaled to the same maximal amplitude U_{MAX} which is applied in the fluid solver in equation (8.8).

Considering the hydrofoil as SDOF system, its total energy E_{TOT} is given by the sum of potential and kinetic energy. When the oscillation reaches its maximal deflection, the total energy is equal to the potential energy being accumulated in terms of elastic strain energy which is calculated by a static analysis based on nodal displacements scaled with the mode shape amplitude U_{MAX}.

8.3.2 Unsteady CFD Analysis

The dissipated energy per one blade oscillation W_{DISS} was calculated by unsteady CFD analysis in ANSYS CFX. The same computational mesh which was created for unsteady simulation of vortex shedding was used. In order to reduce the amount of equations which were solved to calculate the mesh displacement, the original mesh was divided into two domains: an inner domain around the hydrofoil and an outer domain involving the rest of the model. The mesh displacement equations were then solved only in the inner domain which significantly reduced the CPU time. These two domains consisted of same number of cells as the original mesh and were connected together at the interface (Fig. 8.21).

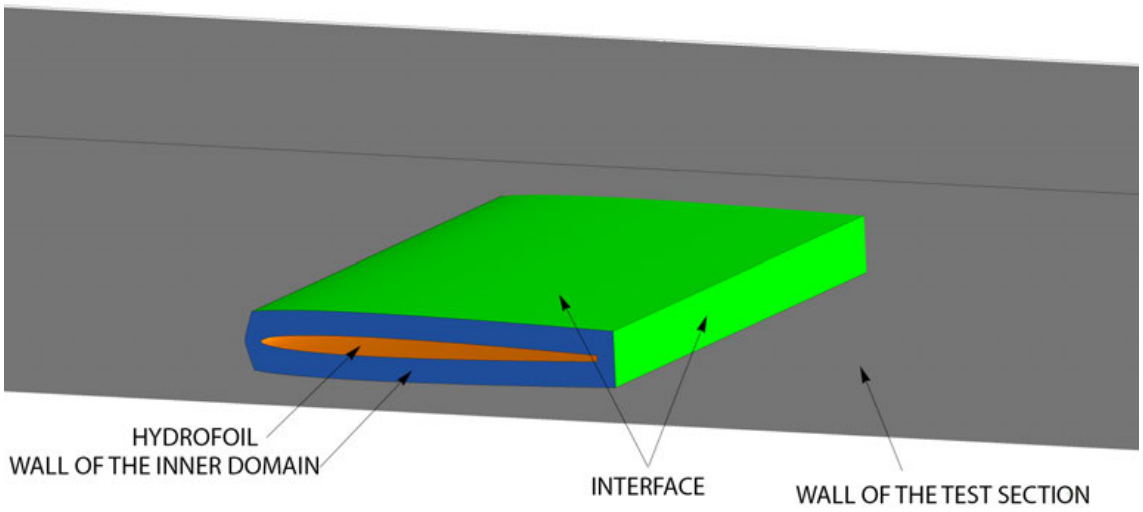

Fig. 8.21 Inner and outer domain around the hydrofoil

The same boundary conditions and solver settings were applied as described in Chapter 8.2.2 except the hydrofoil surface. Here, the no-slip boundary condition was applied with mesh motion specified as "*periodic displacement*". This option defines the prescribed harmonic motion of the wall which represents hydrofoil surface according to equation (8.8). Once the normalised mode shape $\Phi(x, y, z)$ is imported (considered only hydraulic profile without shaft), the corresponding natural frequency and scaling factor U_{MAX} must be defined. The initial values for unsteady simulations were obtained

from steady-state solution for all values of mean velocity v_{inlet}. The time duration of the unsteady simulation was defined by number of (blade) periods per simulation which was selected to fifteen periods. The main output parameter is dissipated energy per blade oscillation W_{DISS}. This variable can be obtained by user defined expression of equation (8.9). Another possibility is to monitor *Wall Work Density* in ANSYS CFX which can be calculated from "*Full Period Integration*" with respect to the hydrofoil periods of motion or from "*Moving Interval*" which calculates dissipated energy from moving interval of recent time-steps. Generally, no significant difference between these two definitions was observed.

Two main parameters influence the accuracy of the analysis: the time-step size and the scaling factor U_{MAX}. By using the tool "*Transient Blade Row Models*", which is available even for single profile, the time-step size is defined by number of time-steps per one blade oscillation. The influence of time-step size dt on dissipated energy W_{DISS} was studied in the range of 200 – 400 time-steps per blade oscillation at maximal mean velocity $v_{inlet} = 20\ ms^{-1}$. The obtained results are presented in the figure (Fig. 8.22). It can be seen that number of time-steps per oscillation has no significant influence on the value of dissipated energy and the dissipated energy varies less than 2 %. Therefore, 300 time-steps per blade oscillation were selected according to the recommendation in [78].

The influence of prescribed amplitude U_{MAX} on dissipated energy W_{DISS} was tested at $v_{inlet} = 20\ ms^{-1}$ and 300 time-steps per blade oscillation. As the prescribed amplitude decreases, the dissipated energy is getting smaller. Several values of U_{MAX} were tested in the range from 1.0 e^{-5} m to 1.0 e^{-3} m. The obtained results are summarized in the figure (Fig. 8.23) and table (Table 14). According to the sensitivity study and by analysing maximal measured hydrofoil deflections in the experiments, the damping ratio was calculated with prescribed amplitude $U_{MAX} = 1e^{-5}\ m$ for all values of mean velocity.

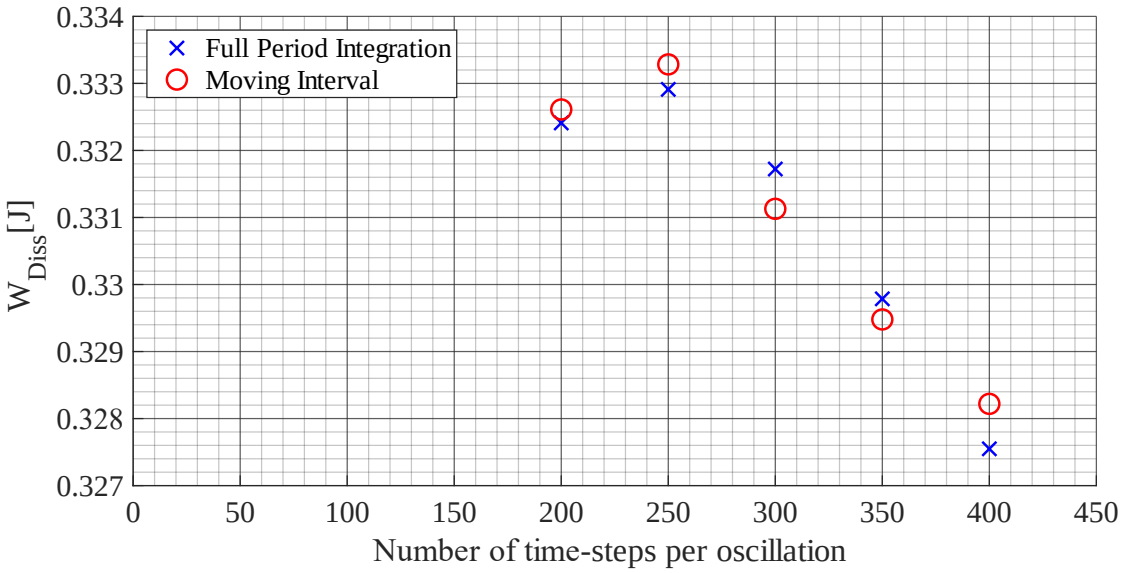

Fig. 8.22 Influence of time-step size dt on dissipated energy W_{DISS} at $v_{inlet} = 20\ ms^{-1}$

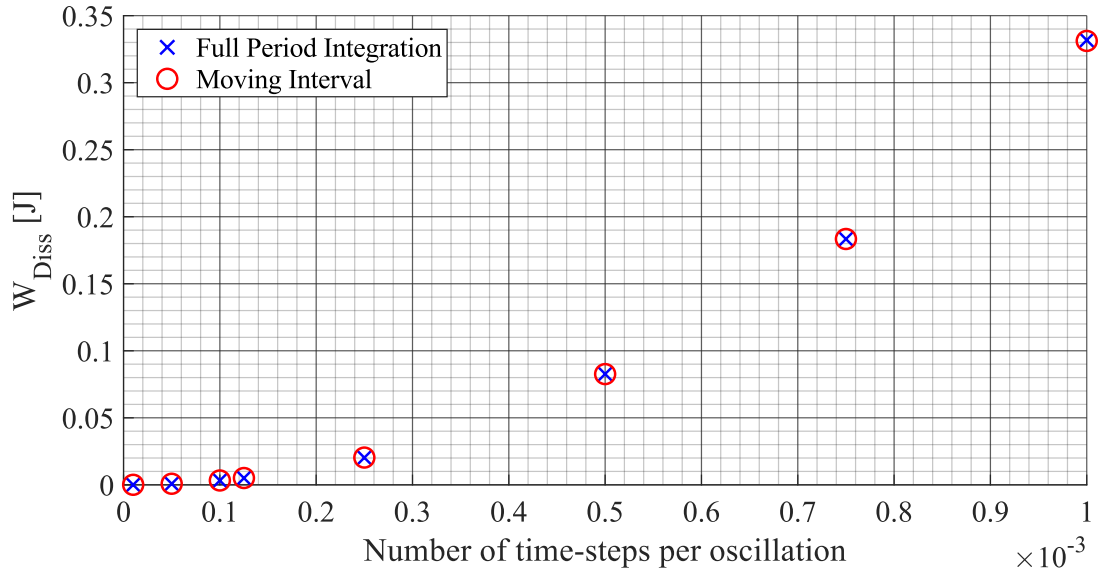

Fig. 8.23 Influence of amplitude U_{MAX} on dissipated energy W_{DISS} at $v_{inlet} = 20\ ms^{-1}$

Table 14 Summary of sensitivity study for settings of unsteady CFD simulation

Influence of time-step on W_{DISS}			Influence of prescribed amplitude on W_{DISS}		
Time-steps per oscillation	W_{DISS}		U_{MAX}	W_{DISS}	
	Full Period	Moving Interval		Full Period	Moving Interval
[1]	[J]	[J]	[m]	[J]	[J]
200	0.3324	0.3326	1.0 e^{-3}	0.3317	0.3311
250	0.3329	0.3333	7.5 e^{-4}	0.1834	0.1834
300	0.3317	0.3311	5.0 e^{-4}	0.0827	0.0826
350	0.3298	0.3295	2.5 e^{-4}	0.0203	0.0204
400	0.3275	0.3282	1.25 e^{-4}	0.0050	0.0051
			1.0 e^{-4}	0.0032	0.0033
			5.0 e^{-5}	0.00079	0.00081
			1.0 e^{-5}	0.000035	0.000033

8.3.3 Calculation of Elastic Strain Energy

By considering the assumptions given in Chapter 8.3.1, the total energy of the hydrofoil oscillation can be calculated as a sum of elastic strain energy in static analysis. Once the normalized mode shape is exported from the acoustic modal analysis, it must be manually rescaled to maximal deflection U_{MAX} which has the same value as applied in the fluid solver. The structural model of the hydrofoil and its shaft is then loaded by rescaled nodal displacement. In order to calculate correctly the elastic strain energy, the nodal displacement must be applied into all nodes, not only into the surface nodes. Then, the elastic strain energy from all elements can be obtained. In this analysis, the hydrofoil is fixed by the boundary conditions which corresponds to the mounting in the test section (see Chapter 8.1.1).

III. RESULTS

9 IDENTIFICATION OF NATURAL FREQUENCIES

Identification of natural frequencies is usually the first step which is carried out when a mechanical system is analysed. In this case, the natural frequencies of the hydrofoil mounted into the test section were investigated for both the empty test section filled by air and the test circuit fully flooded by still water. For each environment, two separate measurements were performed. The first measurement with step of excitation frequency $\Delta f_{EXCT} = 1Hz$ was focused on identification of the first mode of the hydrofoil. The second measurement was carried out to identify higher modes of the hydrofoil in frequency range from 200 Hz to 1000 Hz with step of $\Delta f_{EXCT} = 2Hz$.

The natural frequencies obtained from experiment were compared to modal properties calculated by finite element modal analyses. Finally, the added mass effect, which cause the drop of natural frequencies of hydrofoil submerged in water, was quantified.

9.1 Hydrofoil in Air

9.1.1 Finite Element Modal Analysis

The modal properties of the hydrofoil mounted into the empty test section were obtained from finite element modal analysis. Detailed description of the analysis settings is presented in Chapter 8.1.1. First eight natural frequencies of the hydrofoil in air $f_{NAT,AIR,FEM}$ are presented together with the corresponding mode shapes in tables below (Table 15 and Table 16). The first mode, which is more deeply investigated in following measurements, is the torsion mode. Its calculated natural frequency is $f_{NAT,AIR,FEM} = 178.25\ Hz$. The deformed shape of the hydrofoil is caused by presence of the shaft. The second mode is the first bending mode with frequency $f_{NAT,AIR,FEM} = 559.62\ Hz$. The corresponding mode shape is characterized by large deflections in the middle of the trailing edge. Further modes are shown in Table 16.

Table 15 Natural frequencies of hydrofoil in air; simulation

Mode	$f_{NAT,AIR,FEM}\ [Hz]$	Mode	$f_{NAT,AIR,FEM}\ [Hz]$
1	178.25	5	1293.1
2	559.62	6	1476.1
3	638.57	7	1789.8
4	909.29	8	2110

Table 16 Mode shapes of the hydrofoil in air

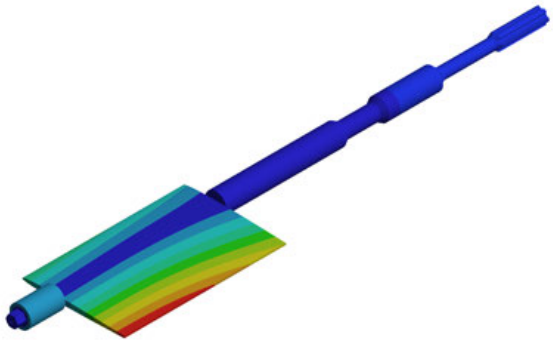

Mode 1, Frequency 178.25 Hz

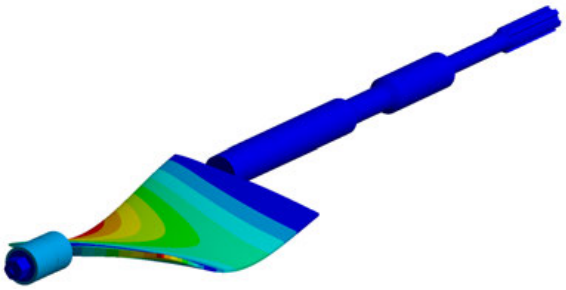

Mode 2, Frequency 559.62 Hz

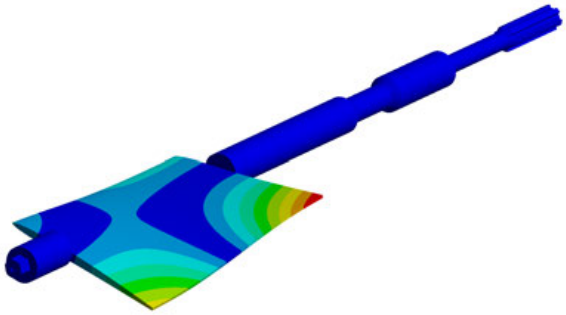

Mode 3, Frequency 638.57 Hz

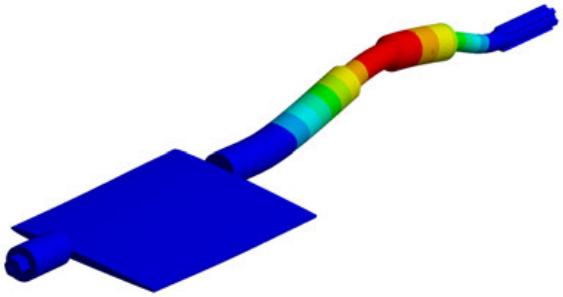

Mode 4, Frequency 909.29 Hz

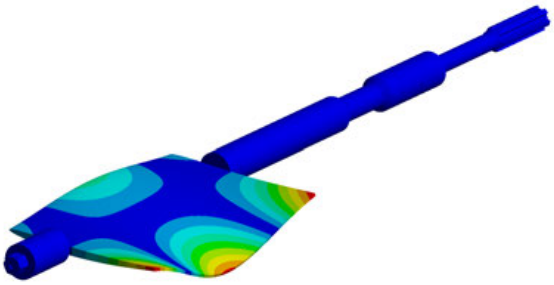

Mode 5, Frequency 1293.1 Hz

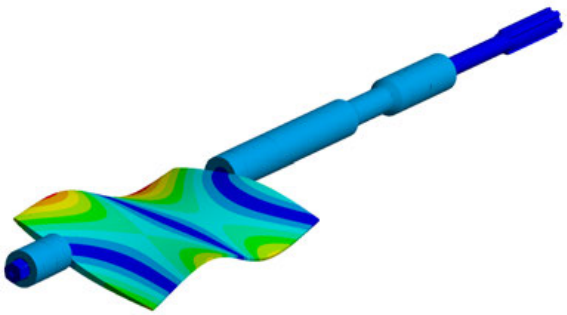

Mode 6, Frequency 1476.1 Hz

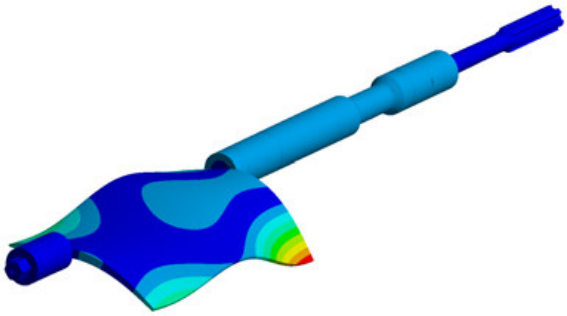

Mode 7, Frequency 1789.8 Hz

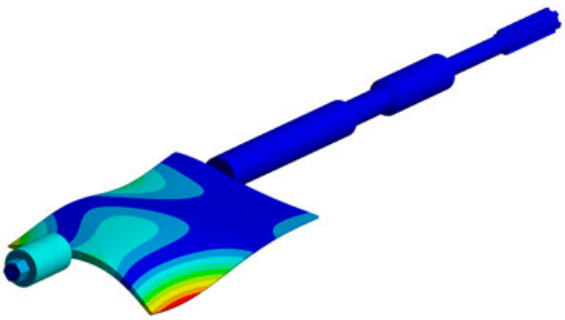

Mode 8, Frequency 2110 Hz

9.1.2 Experiment

Natural frequencies of the hydrofoil were investigated from hydrofoil response to the enforced vibrations. The hydrofoil was mounted into the test section with no water inside the pipes. Harmonic signal which was generated in LabVIEW and sent to the mechanical exciter was used to excite the hydrofoil. Two LDV vibrometers, one in each corner of the hydrofoil trailing edge, were used to measure the hydrofoil response (see Fig. 7.2).

Identification of hydrofoil natural frequencies was divided into two separate measurements. The first measurement was carried out in the range of excitation frequency f_{EXCT} from 80 Hz to 280 Hz with a smooth step of 1 Hz. The second measurement was carried out in the range of excitation frequency f_{EXCT} from 200 Hz to 1000 Hz with a step of 2 Hz. The procedure of measurement was controlled by LABVIEW, see Chapter 7.1.

Postprocessing of the measured data was executed using own scripts created in MATLAB. As the test case which was designed for this research project was very similar to real conditions of the guide vane of Francis turbine, the properties of hydrofoil mounting are not clearly defined (mainly the stiffness of bearings). Therefore, various methods of data postprocessing were tested. As a result, two methods described in Chapter 7.2 were used in this research. In case of hydrofoil in air, both measurements were post-processed by the second method which calculates the nondimensional frequency response function (see Chapter 7.2.2).

The frequency response function obtained from the first measurement is shown in the following figure (Fig. 9.1). A detail view on amplitude as well as on phase around the peak which corresponds to the first natural frequency is shown in the figure Fig. 9.2. The presented phase is related to the phase shift from mechanical exciter to the hydrofoil. As it can be seen, the difference in detected natural frequencies is 1 Hz. The FRF from both vibrometers are in phase which corresponds to behaviour of the first mode in numerical simulation. The blue coloured response is obtained from vibrometer which was pointed to location of the largest deflection of the first mode. The frequency detected from this sensor differs from the calculated value ($f_{NAT,AIR,FEM} = 178.25\ Hz$) by 2.4 %.

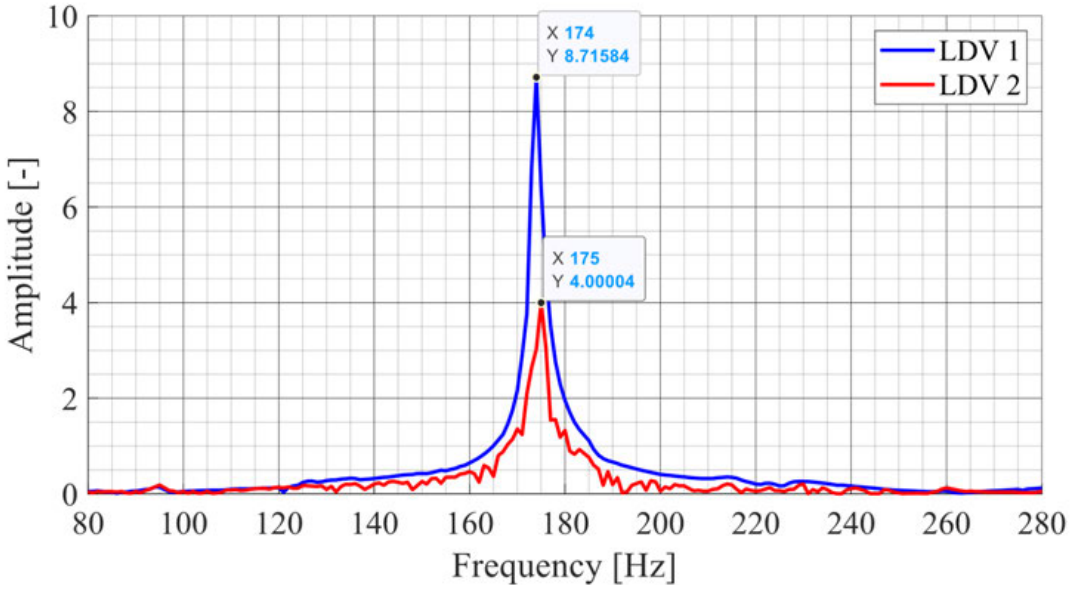

Fig. 9.1 FRF around first mode for hydrofoil in air

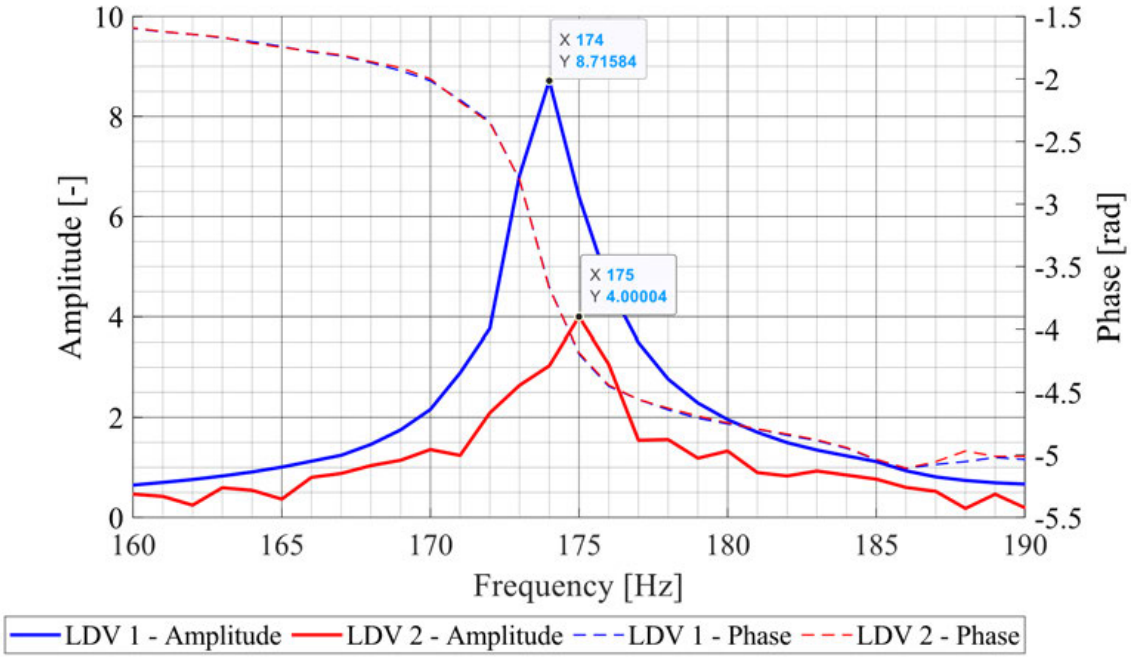

Fig. 9.2 Amplitude and phase around first natural frequency in air

The higher modes of the hydrofoil were investigated in the second measurement. In this case, the frequency response function was measured in the range 200 Hz – 1000 Hz with a step of $\Delta f_{EXCT} = 2\ Hz$. Three dominant peaks were observed in the obtained FRF as shown in the figure bellow (Fig. 9.3).

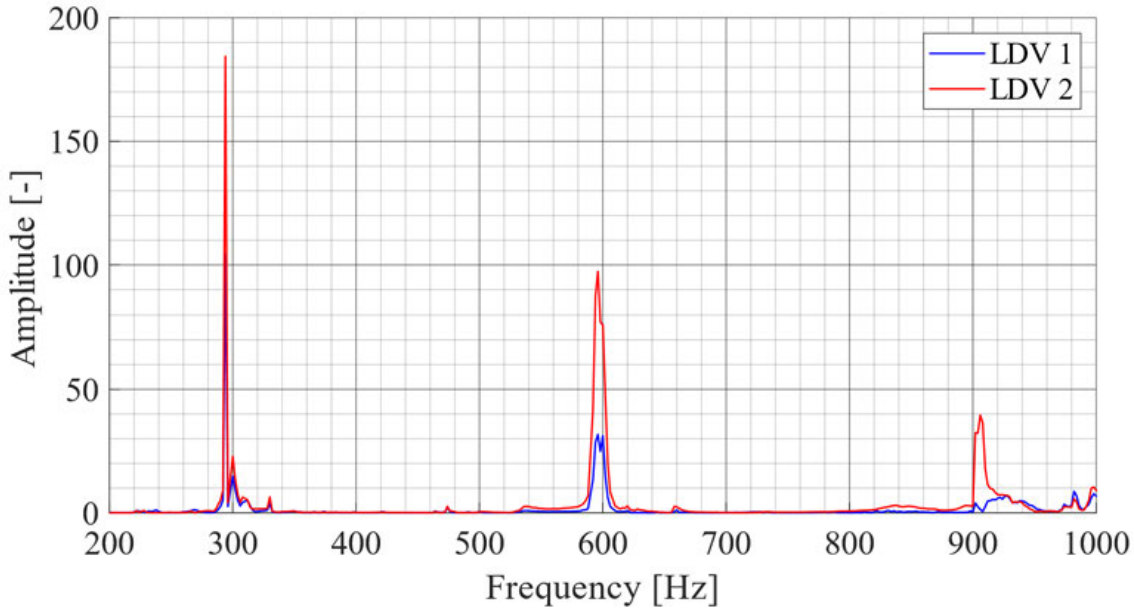

Fig. 9.3 FRF in the range 200 Hz – 1000 Hz for hydrofoil in air

The first detected peak at frequency 294 Hz was not assigned to any mode shape of the hydrofoil. This frequency may be related to vibrations of the external bar which connects membrane of the exciter to the hydrofoil shaft.

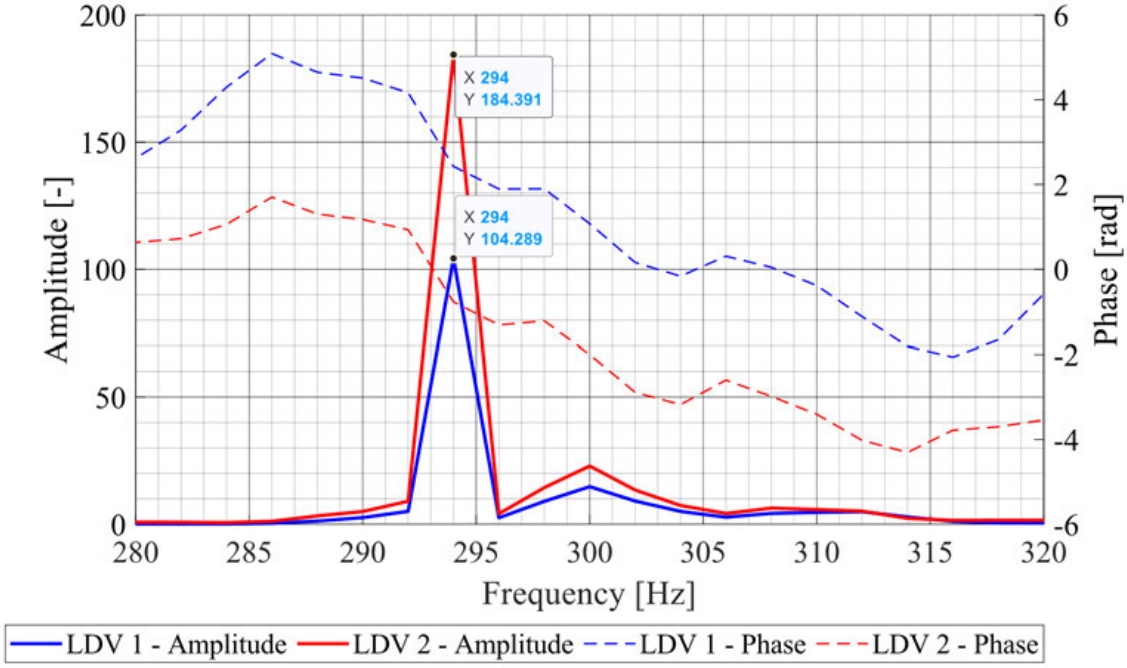

Fig. 9.4 Detail of FRF around peak at $f_{EXCT} = 292\ Hz$ for hydrofoil in air

The second significant peak was detected at frequency 596 Hz. As the two obtained responses are in phase, this frequency is assigned to the second mode of the hydrofoil which is the first bending mode. Difference between the measured frequency ($f_{NAT,AIR,EXP} = 596\ Hz$) and its value calculated by modal analysis is 6.1 %. ($f_{NAT,AIR,FEM} = 559.62\ Hz$)

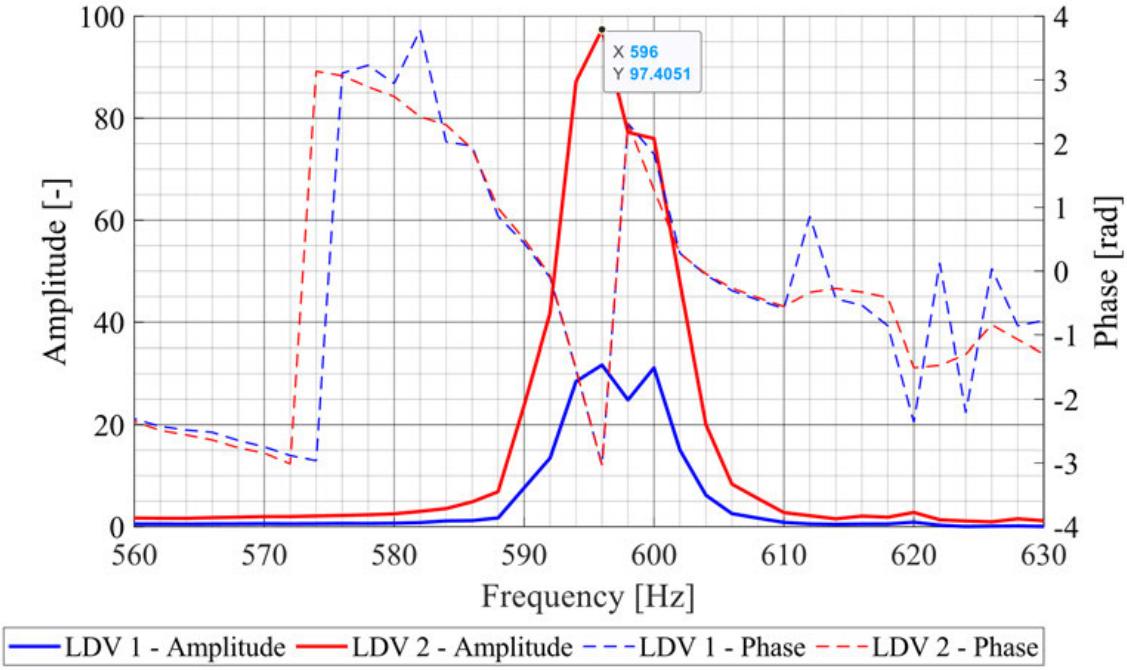

Fig. 9.5 Detail of FRF around peak at $f_{EXCT} = 596\ Hz$ for hydrofoil in air

The third mode of the hydrofoil which was obtained from modal analysis at frequency $f_{NAT,AIR,FEM} = 638.57\ Hz$ was not well excited in the experiment. Its calculated mode shape is characterized by out of phase oscillations of two trailing edge corners. A small peak was detected at frequency $f_{EXCT} = 658\ Hz\ (660\ Hz)$ from both responses. As the measured responses are out of phase, this peak might be related to the third mode.

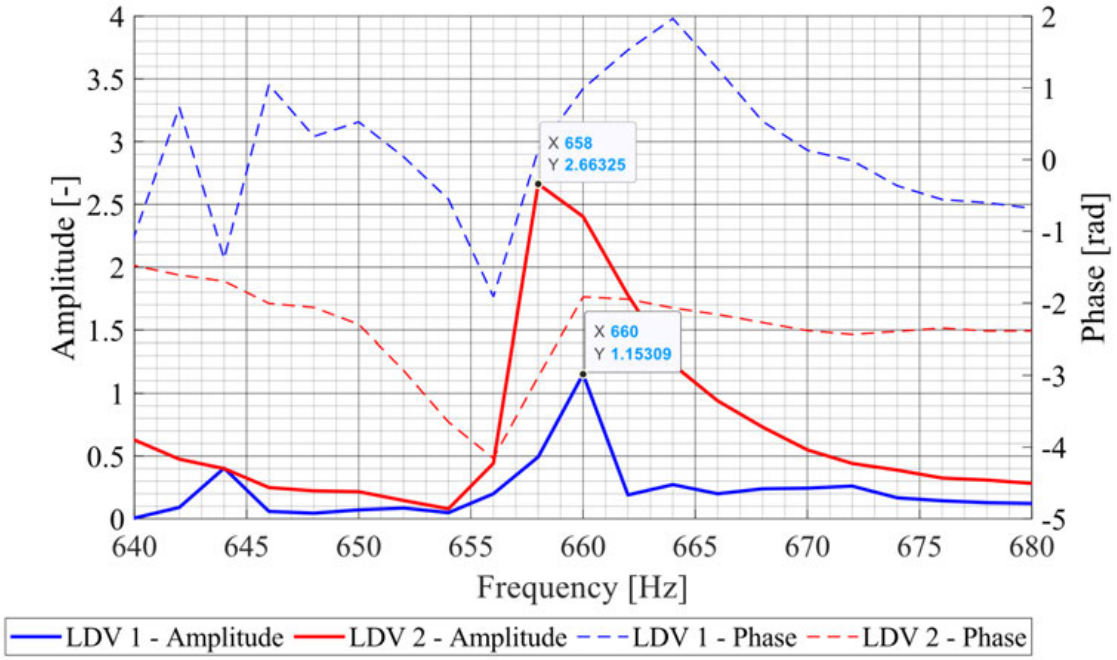

Fig. 9.6 Detail of FRF around peak at $f_{EXCT} = 658\ Hz$ for hydrofoil in air

The last dominant peak was detected at frequency 906 Hz only by vibrometer LDV 2 which was located on the side with long shaft of the hydrofoil. As the peak was detected only by one vibrometer, this frequency can be assigned to the fourth mode of the hydrofoil. Its mode shape is bending of the hydrofoil shaft. The difference between calculated frequency $f_{NAT,AIR,FEM} = 909.29\ Hz$ and the measured value is less than 1 %.

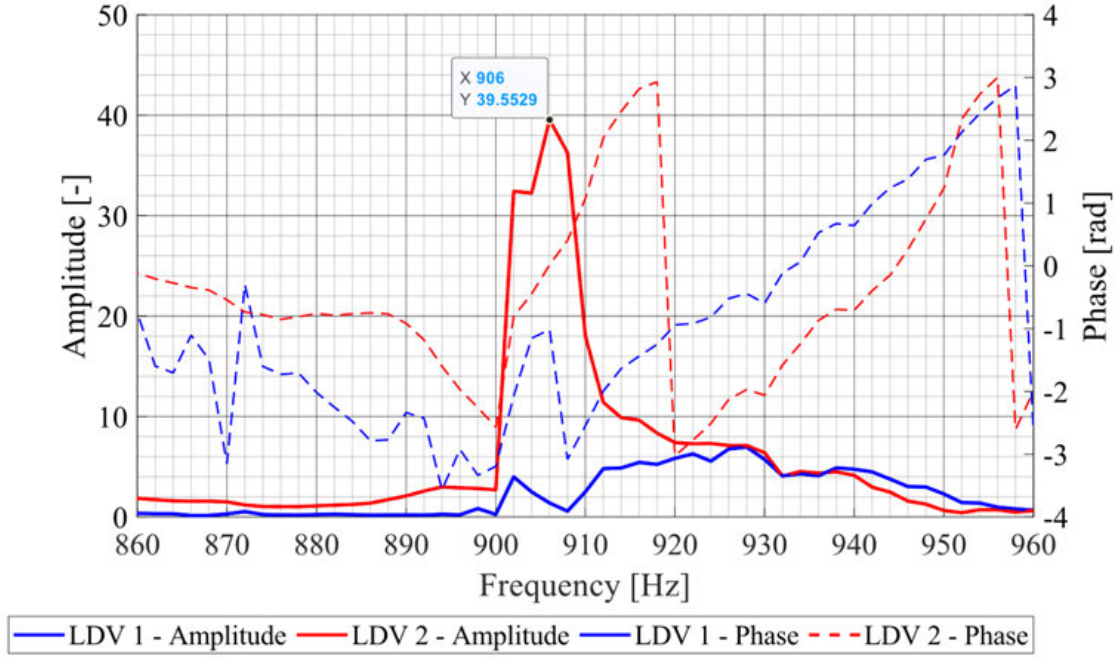

Fig. 9.7 Detail of FRF around peak at $f_{EXCT} = 906\ Hz$ for hydrofoil in air

9.2 Hydrofoil in Water

9.2.1 Acoustic Modal Analysis

The natural frequencies of the hydrofoil submerged in still water were calculated by acoustic modal analysis. Mounting of the hydrofoil into the test section was modelled by similar boundary conditions as in previous modal analysis. The presence of still water inside the test section was modelled by acoustic elements. Further details of analysis setup are described in Chapter 8.1.2.

The first eight natural frequencies and mode shapes are presented in following tables (Table 17 and Table 19).

Table 17 Natural frequencies of hydrofoil in water; simulation

Mode	$f_{nat,SW,FEM}[Hz]$	Mode	$f_{nat,SW,FEM}[Hz]$
1	104.15	5	909.4
2	356.4	6	1077.6
3	410.7	7	1491
4	896.1	8	1589.8

By comparing mode shapes from both modal analyses, the natural frequencies calculated in water can be assigned to values obtained for hydrofoil in air (Table 18). The change of order is observed by two pairs of modes. In the first case, the natural frequency of the fourth mode $f_{nat,AIR,FEM} = 909.29\ Hz$ is not affected by presence of water and its value keeps constant value in both cases. This behaviour is caused by deformation of the assigned mode shape. As the hydrofoil which is in contact with water does not deform, the added mass effect has no influence on this mode. Therefore, the value of natural frequency is not shifted by presence of water which results in change of modes order. The second pair of modes with changed order was detected by the eighth mode. As the mode shapes of hydrofoil in water were analysed, the additional ninth mode had to be considered. Its calculated natural frequencies in both environments were added to the table below.

A comparison of the mode shapes from both analyses shows that deformations of corresponding mode shapes are similar in both environments.

Table 18 Assignment of hydrofoil modes

Mode in air	$f_{nat,AIR,FEM}[Hz]$	Mode in water	$f_{nat,SW,FEM}[Hz]$
1	178.25	1	104.15
2	559.62	2	356.4
3	638.57	3	410.7
4	909.29	5 ↑	909.4
5	1293.1	4 ↓	896.1
6	1476.1	6	1077.6
7	1789.8	7	1491
8	2110	9 ↑	1702.9
9	(2202)	8 ↓	1589.8

Table 19 Mode shapes of the hydrofoil submerged in still water

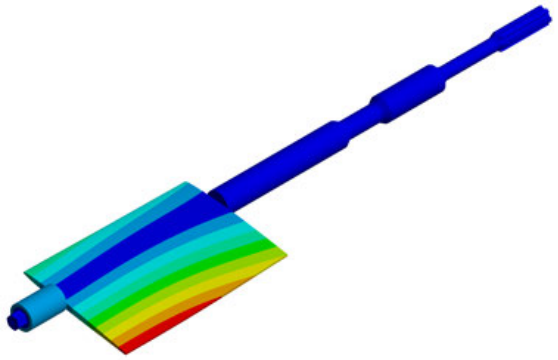

Mode 1, Frequency 104.15 Hz

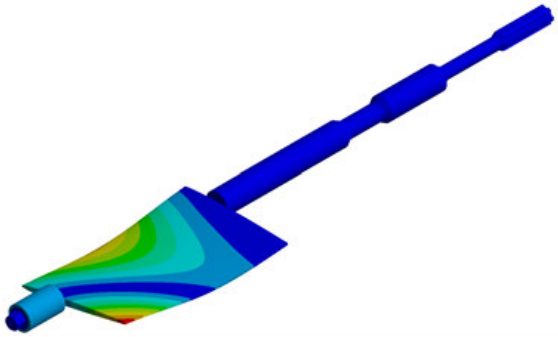

Mode 2, Frequency 356.39 Hz

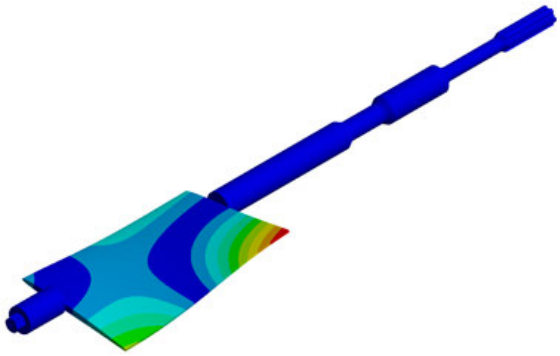

Mode 3, Frequency 410.7 Hz

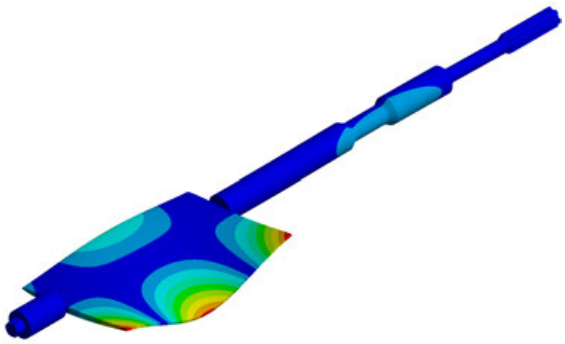

Mode 4, Frequency 896.1 Hz

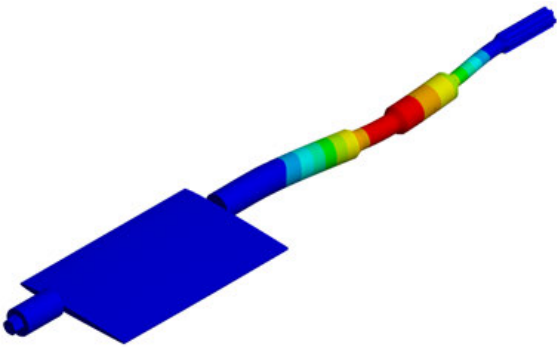

Mode 5, Frequency 909.4 Hz

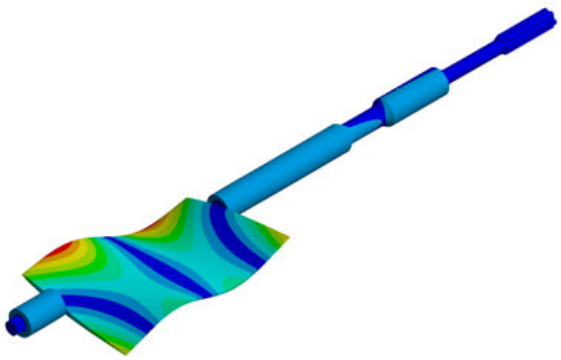

Mode 6, Frequency 1077.6 Hz

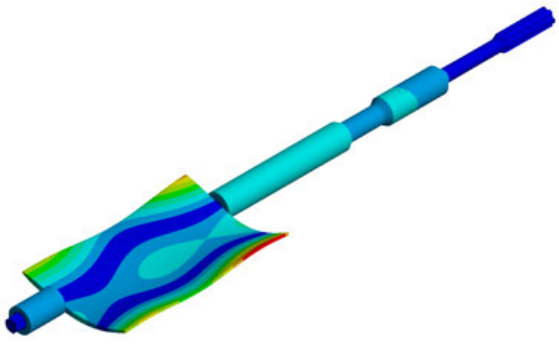

Mode 7, Frequency 1491 Hz

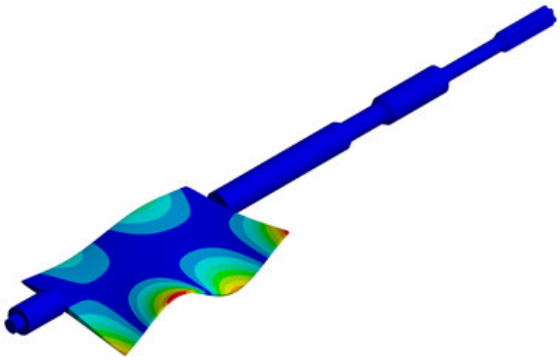

Mode 8, Frequency 1589.8 Hz

The shift of natural frequencies is caused by added mass and added stiffness effects. Since the incompressible fluid with zero flow velocity is considered, the influence of added stiffness on the drop of natural frequencies is negligible. The acoustic modal analysis does not consider any damping induced by presence of water. Therefore, the only effect which causes drop of natural frequencies is the added mass effect.

The added mass effect can be represented by two main parameters. The first parameter is the added mass of water m_{ADD} which represents volume of water displaced by vibrations of the hydrofoil and can be calculated from equation (5.10). This mass of water is proportional to the virtual inertial force $F_{ADD,MASS}$ which opposes the hydrofoil motion. The second parameter is ratio of natural frequencies for each mode. Value of the ratio differs for each analysed mode and depends on deformation of the mode shape. By comparing value of this ratio for all considered modes, the highest drop of natural frequency is observed by the first mode (42 % decrease of frequency). The frequency drop observed by the second and third modes is slightly smaller (36 %) than by the first mode. For higher modes, the drop of frequency is less than 30 % except the fourth mode which is not affected by the added mass effect. Quantification of added mass effect for all considered modes is presented in the table below (Table 20).

Table 20 Comparison of natural frequencies in air and in water

	Mode:	1	2	3	4	5	6	7	8
$f_{nat,AIR,FEM}$	[Hz]	178.3	559.6	638.6	909.3	1293.1	1476.1	1790	2110
$f_{nat,SW,FEM}$	[Hz]	104.2	356.4	410.7	909.4	896.1	1077.6	1491	1703
$\frac{f_{nat,SW,FEM}}{f_{nat,AIR,FEM}}$	[1]	58.4 %	63.7 %	64.3 %	100 %	69.3 %	73.0 %	83.3 %	80.7 %
Added mass m_{ADD}	[kg]	0.810	0.615	0.595	0	0.455	0.368	0.185	0.225
$\frac{\text{added mass}}{\text{profile mass}}$	[1]	1.93	1.47	1.42	0	1.08	0.88	0.44	0.54

9.2.2 Experiment

Natural frequencies of hydrofoil submerged in still water were identified from two separate measurements. The first measurement was carried out in the range of excitation frequency f_{EXCT} from 50 Hz to 200 Hz with a smooth step of 1 Hz. The second measurement was carried out in the range of excitation frequency f_{EXCT} from 200 Hz to 1000 Hz with a step of 2 Hz. Relative pressure in the circuit was set to 0 Pa during both experiments.

The first measurement which was focused on identification of the first natural frequency in the range 50 Hz – 200 Hz was post-processed by the second method. The nondimensional frequency response function of the hydrofoil was calculated according to the steps described in Chapter 7.2.2. The obtained frequency response function is shown in the following figure (Fig. 9.8). A detail view on amplitude as well as on phase around the peak which corresponds to the first natural frequency is shown in the figure Fig. 9.9.

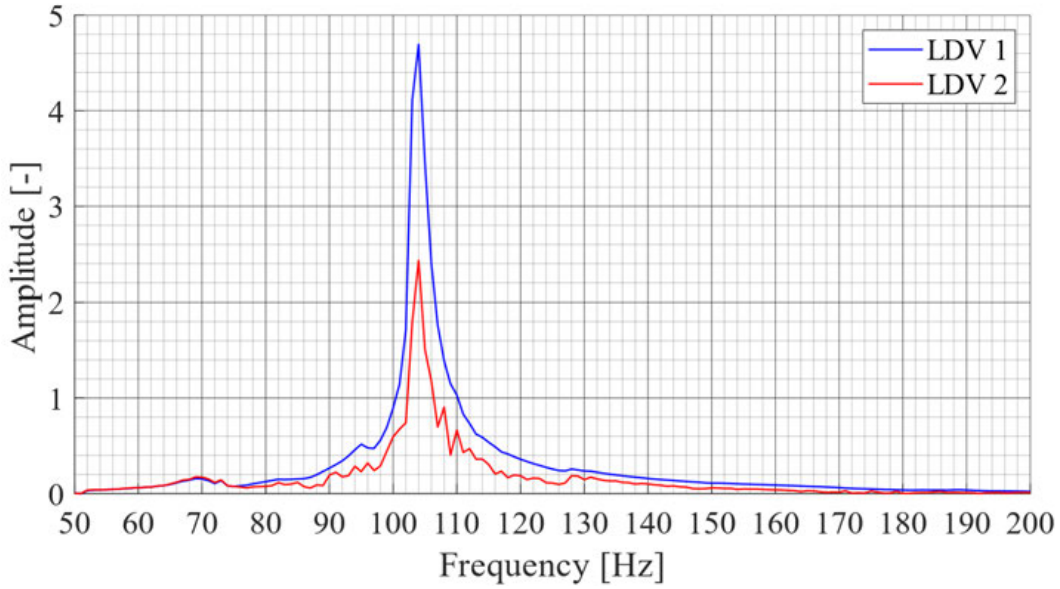

Fig. 9.8 FRF around first mode for hydrofoil in water

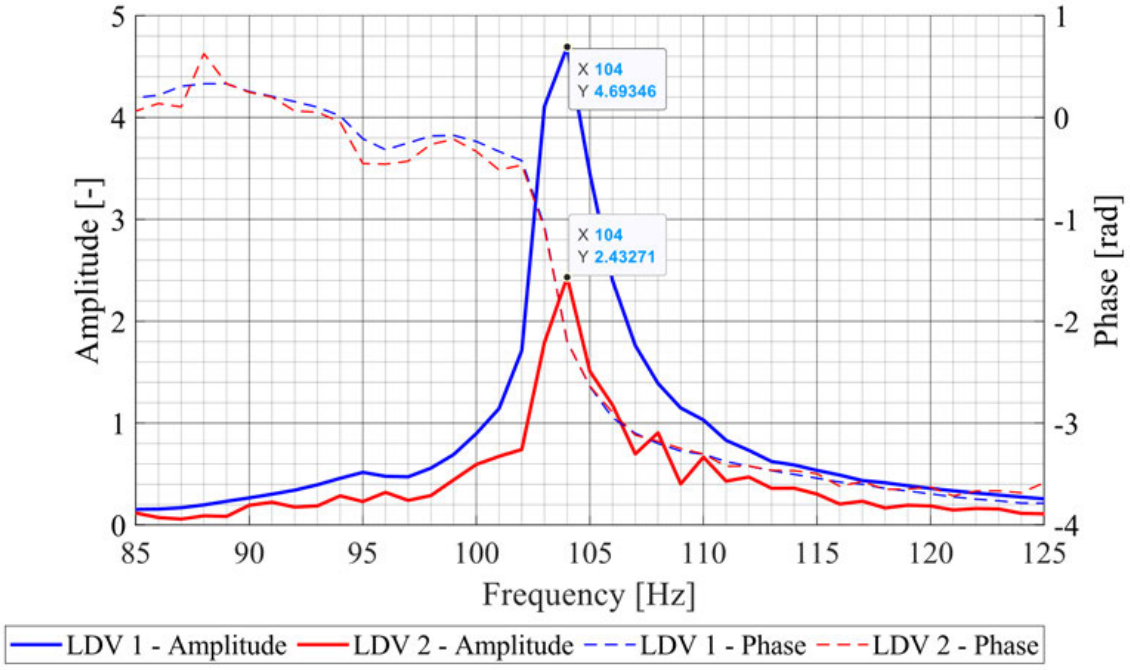

Fig. 9.9 Amplitude and phase around first natural frequency in water

The detected value of natural frequency $f_{nat,SW,EXP} = 104\,Hz$ from both vibrometers is equal to value calculated by acoustic modal analysis $f_{nat,SW,FEM} = 104.15\,Hz$. The FRF from both vibrometers is in phase which is in agreement with calculated mode shape.

Higher modes of the hydrofoil were investigated by the second measurement in the range from 200 Hz – 1000 Hz with a step of 2 Hz. Due to the difficulties which occurred during the measurement, this experiment was post-processed by the first method. In this case, the influence of length of input signal was tested as described in Chapter 7.5.1.

The hydrofoil response calculated by this method is not dimensionless and does not represent the exact Frequency Response Function (FRF). Therefore, it is called in the text

only "*hydrofoil response*" instead of "*frequency response function*". The obtained phase does not represent phase shift from the exciter to the hydrofoil. Therefore, the phase difference between the vibrometers is additionally plotted. The calculated result of this response is shown in the figure bellow (Fig. 9.10). Two dominant peaks at frequencies 304 Hz and 382 Hz are observed.

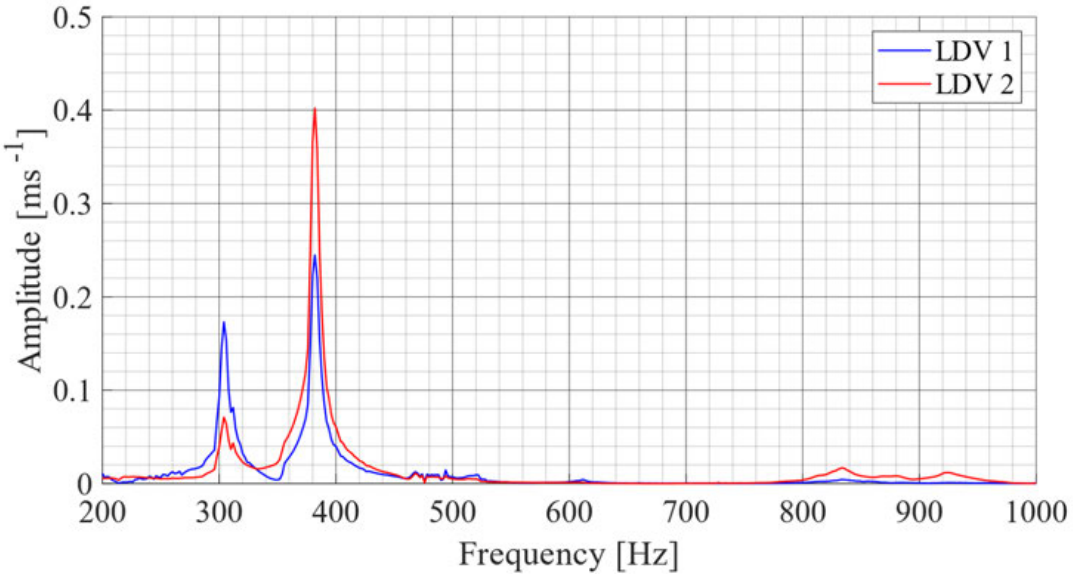

Fig. 9.10 Response of hydrofoil in water in the range 200 Hz – 1000 Hz

The first dominant peak was detected at frequency 304 Hz. Responses obtained from both vibrometers are in phase (Fig. 9.11). Two possible modes calculated by acoustic modal analysis can be assigned to this peak: the second mode (356.4 Hz) and the third mode (410.7 Hz). The deflection in corners of the trailing edge is in phase by the second mode but out of phase by the third mode (see Table 19). A comparison of the frequency values and of the in-phase deflections shows that the frequency $f_{nat,SW,EXP} = 304\ Hz$ corresponds to the second mode ($f_{nat,SW,FEM} = 356.4\ Hz$). The difference between measured frequency and calculated value is 17.2 %.

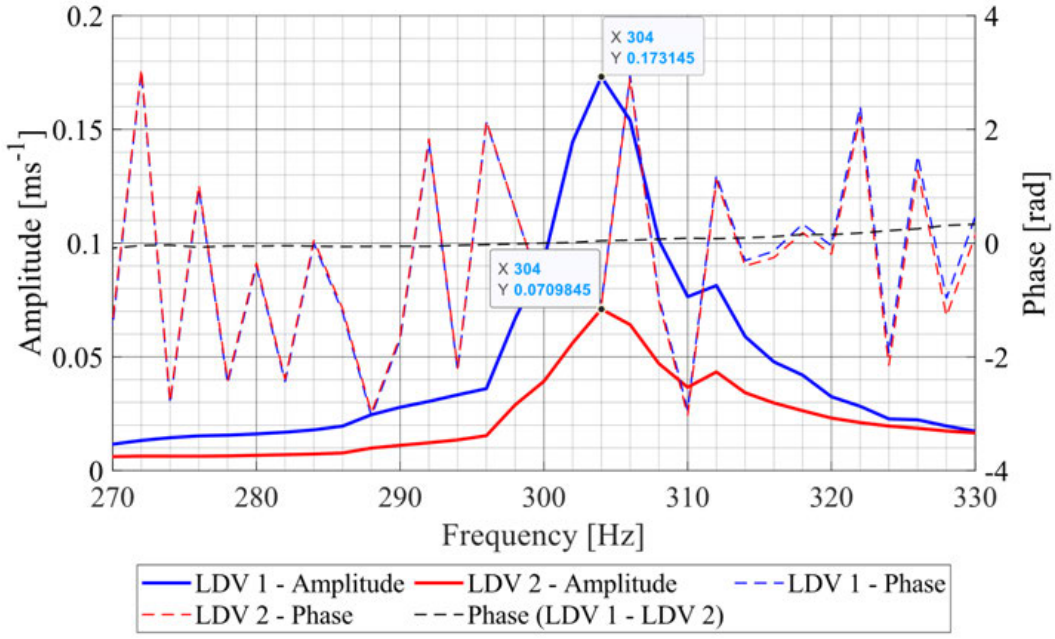

Fig. 9.11 Detail of response of hydrofoil in water around peak at $f_{EXCT} = 304\ Hz$

The second dominant peak was detected at frequency 382 Hz. In this case, the deflections of the two corners is out of phase which is illustrated by the phase difference (black coloured curve in Fig. 9.12). Therefore, this frequency is assigned to the third mode ($f_{nat,SW,FEM} = 410.7\ Hz$). The difference between the calculated and measured frequencies is 7.5 %.

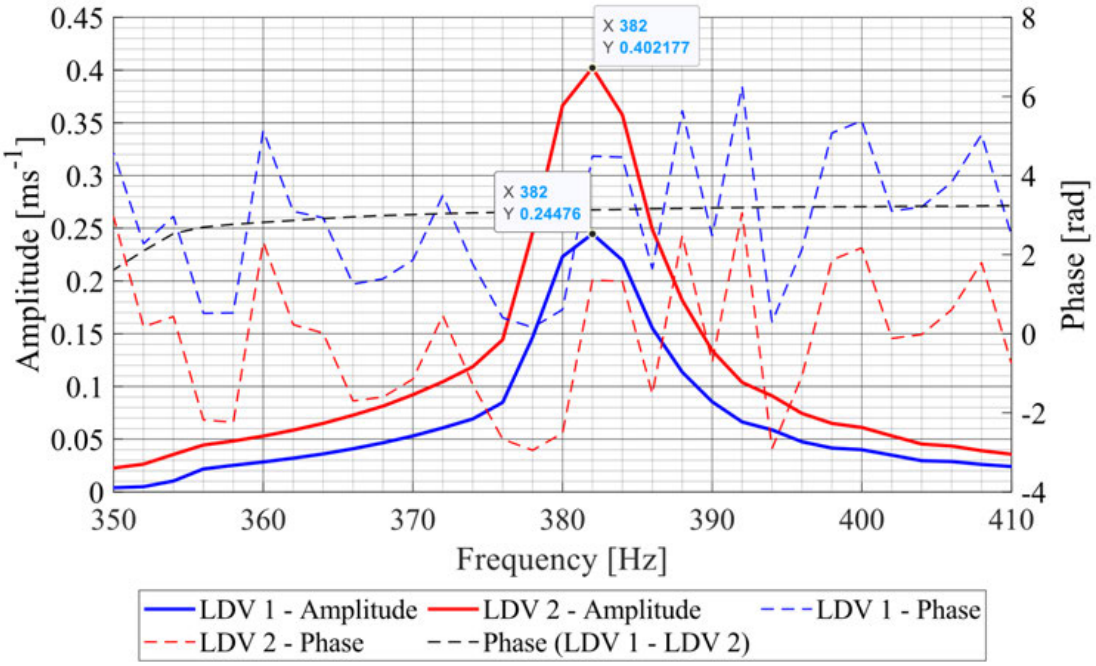

Fig. 9.12 Detail of response of hydrofoil in water around peak at $f_{EXCT} = 382\ Hz$

The fourth mode of the hydrofoil in water was not well excited in the experiment. Its calculated natural frequency is $f_{nat,SW,FEM} = 896.1\ Hz$. Detailed analysis in region of higher amplitudes between 800 Hz and 950 Hz showed, that two peaks with small amplitudes can be identified at frequencies 834 Hz and 925 Hz (Fig. 9.13).

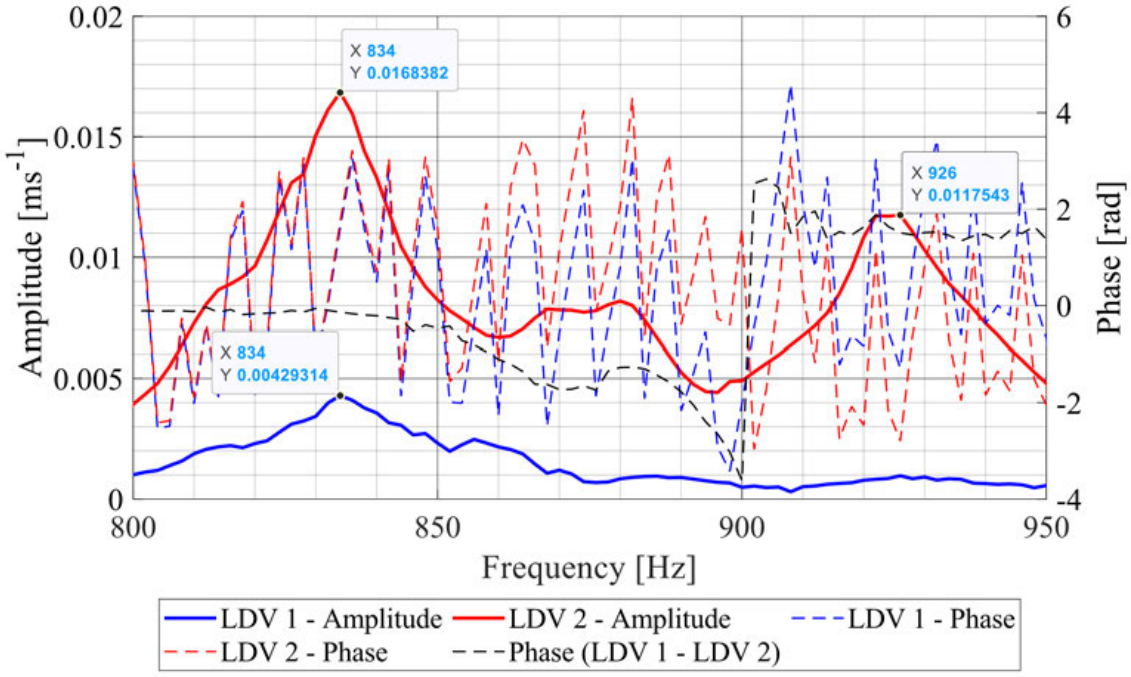

Fig. 9.13 Detail of response of hydrofoil in water in the range $f_{EXCT} = 800 - 950\ Hz$

The oscillations of the hydrofoil corners around the first peak (834 Hz) are in phase. As the excitation frequency rises, the phase difference is increasing up to the region of the second peak (925 Hz). By comparing phase behaviour and the values of calculated ($f_{nat,SW,FEM} = 896.1\ Hz$) and detected ($f_{nat,SW,EXP} = 834\ Hz$) frequencies, this peak can be assigned to the fourth mode of the hydrofoil in water. The frequency difference is 7.5 %. The top of the second peak is not well captured by the coarse step of the measurement $\Delta f_{EXCT} = 2\ Hz$. Since this peak is detected only by one vibrometer, it corresponds to the fifth mode of the hydrofoil in water, which is deformation of the shaft. The detected value of frequency differs from the calculated value ($f_{nat,SW,FEM} = 909.4\ Hz$) by 1.8 %.

9.3 Partial Conclusion – Modal Properties of The Hydrofoil

Modal properties of hydrofoil which was mounted inside the test section of cavitation tunnel were investigated for two different conditions: the empty test section filled by air and the test section fully flooded by still water. Both cases were analysed by experimental measurement and numerical modal analysis.

Experimental measurement of hydrofoil response in air was carried out in range of excitation frequency 50 Hz – 1000 Hz. The response of hydrofoil on harmonic excitation was measured by two LDV vibrometers. Dominant peaks which were detected in the hydrofoil response were compared to the results of finite element modal analysis. The first four natural frequencies were identified by comparing mode shapes of hydrofoil obtained from modal analysis and responses measured by two vibrometers. The natural frequencies calculated by modal analysis show good agreement with the experimental results. The calculated first natural frequency 178.25 Hz differs by 2.44 % from the measured value 174 Hz. Maximal difference 6.10 % was observed by the second mode of the hydrofoil. An additional dominant peak was detected at frequency 294 Hz. This peak was not assigned to any mode shape of the hydrofoil and may be related to vibrations of the external bar which connected membrane of the mechanical exciter to the hydrofoil shaft.

Table 21 Comparison of hydrofoil natural frequencies in air

Mode in air	$f_{nat,AIR,FEM}$	$f_{nat,AIR,EXP}$	Δf
	[Hz]	[Hz]	[1]
1	178.25	174	2.44 %
2	559.62	596	6.10 %
3	638.57	658	2.95 %
4	909.29	906	0.36 %

$$\Delta f = \frac{\left| f_{nat,FEM} - f_{nat,EXP} \right|}{f_{nat,EXP}} \cdot 100\ \% \tag{9.1}$$

Natural frequencies of the hydrofoil which was submerged into still water are lower compared to the values measured in air. This drop of natural frequencies is caused by the added mass effect. The first five natural frequencies were identified from experimental measurement and compared to the results of acoustic modal analysis. The calculated value of the first natural frequency 104.15 Hz is in good agreement with the measured value 104 Hz (40 % decrease). Natural frequencies obtained by numerical simulation do not differ from the experimental results more than 8 % except the second mode (17 %).

Table 22 Comparison of hydrofoil natural frequencies in still water

Mode in water	$f_{nat,SW,FEM}$	$f_{nat,SW,EXP}$	Δf
	[Hz]	[Hz]	[1]
1	104.15	104	0.14 %
2	356.4	304	17.24 %
3	410.7	382	7.51 %
4	896.1	834	7.45 %
5	909.4	926	1.79 %

10 FLOW INDUCED VIBRATIONS

Identification of frequencies which are related to excitation forces induced by flow behaviour is important to avoid of resonance during the operation time of hydraulic machines. Since the main excitation force which acts on the hydrofoil is induced by vortex shedding, the frequency of vortex shedding at zero incidence angle was investigated by both the unsteady CFD simulation and the experimental measurement. The obtained results are presented and compared in this chapter.

Depending on the angle of attack, the hydrofoil can be excited by vortex shedding, boundary layer separation along the profile or by both these phenomena at the same time. Therefore, an additional measurement was carried out with 5° angle of attack to investigate which type of hydrofoil excitation is present. The obtained results are presented at the end of this chapter.

10.1 Unsteady Numerical Simulation

Numerical prediction of vortex shedding frequency was carried out from unsteady CFD simulation. The flow behaviour around hydrofoil with zero incidence angle was analysed for inlet mean velocity in the range 2.5 ms^{-1} – 20 ms^{-1} with a step of 2.5 ms^{-1}. Detailed description of computational mesh, boundary conditions and solver settings can be found in Chapter 8.2.

Two following figures present the pressure field (Fig. 10.1) and the velocity field (Fig. 10.2) around the hydrofoil at maximal mean velocity 20 ms^{-1}. The vortex shedding behind the hydrofoil trailing edge can be observed in both figures. Additionally, this vortex structures can be visualised in form of iso-surface of vorticity component which is perpendicular to the mean flow (Fig. 10.3) and of iso-surface of Q-criterion.

Q-criterion enables to visualise vortex structures based on the second invariant of the velocity gradient tensor. Its definition is given by equations (10.1) and (10.2)

$$\omega_{ij} = \frac{1}{2}\left(\frac{\partial v_i}{\partial x_j} - \frac{\partial v_j}{\partial x_i}\right) \tag{10.1}$$

$$Q = \left(\left\|\omega_{ij}\right\|^2 - \left\|v_{ij}\right\|^2\right) \tag{10.2}$$

where

- ω_{ij} is tensor of vorticity
- v_{ij} strain tensor rate defined in equation (4.26)
- v_i, v_j flow velocity components
- x_i, x_j are coordinates.

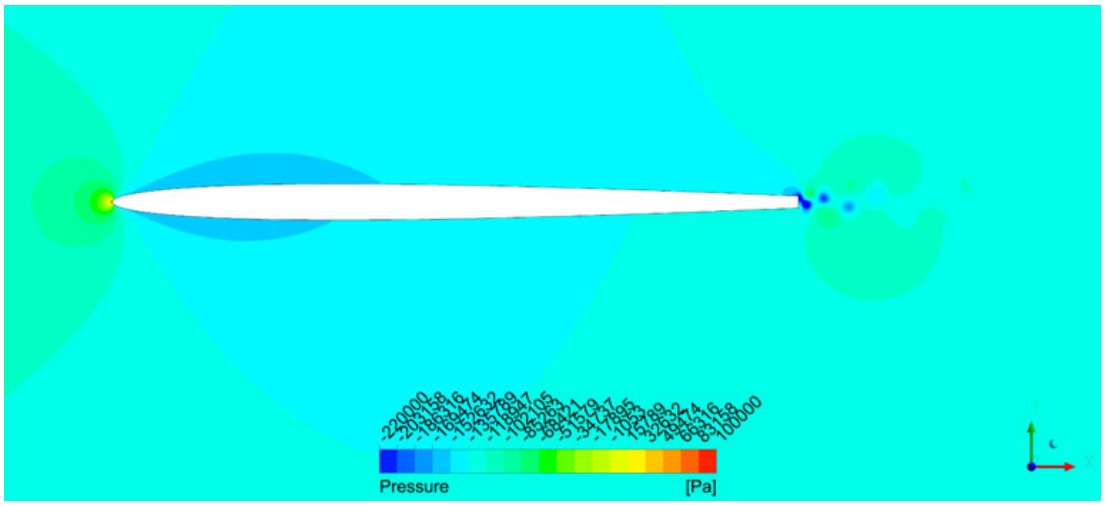

Fig. 10.1 Pressure field around hydrofoil at $v_{inlet} = 20\ ms^{-1}$

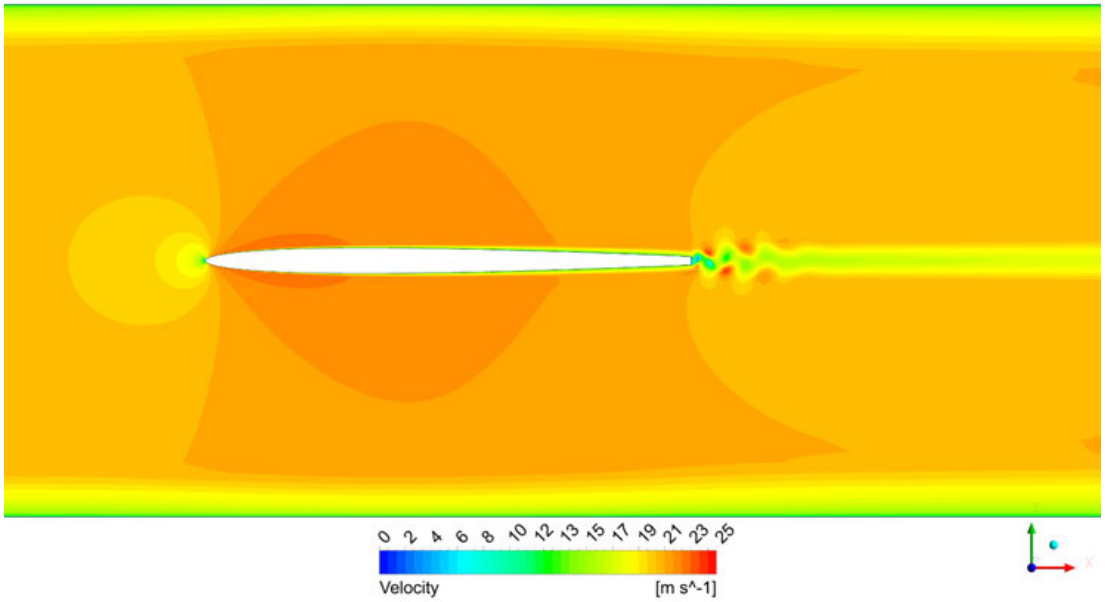

Fig. 10.2 Velocity field around hydrofoil at $v_{inlet} = 20\ ms^{-1}$

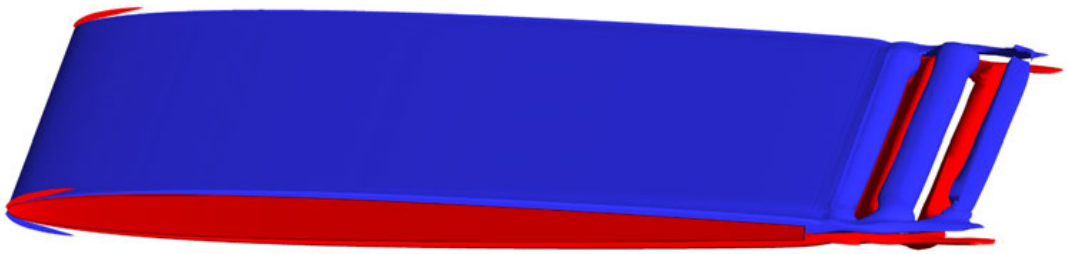

Fig. 10.3 Vortex shedding at $v_{inlet} = 20\ ms^{-1}$ visualised by iso-surface of vorticity component perpendicular to the mean flow (-2500 s^{-1} is blue, 2500 s^{-1} in red)

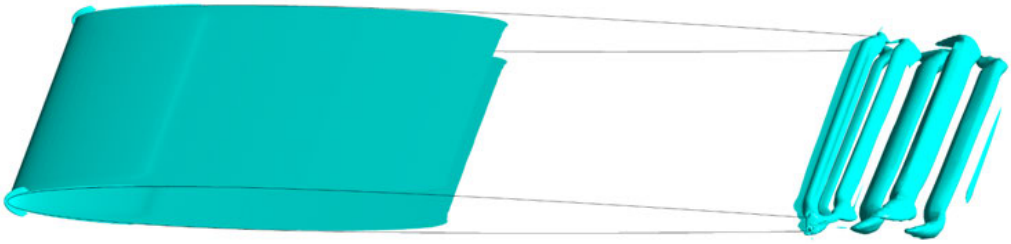

Fig. 10.4 Vortex shedding at $v_{inlet} = 20\ ms^{-1}$ visualised by iso-surface of Q-criterion for value $2.5 \cdot 10^{6}\ s^{-2}$

As the fluid flows around the hydrofoil, vortices are alternately generated on the top and bottom surfaces of the blunt trailing edge. These low-pressure regions are moved downstream by the flow and form von Kármán vortex street. The periodic pressure fluctuations near the trailing edge cause fluctuating force which excites the hydrofoil. The vortex shedding frequency was evaluated from both the lift force acting on the hydrofoil and the pressure fluctuations in all six points P1 – P6 as described in figure (Fig. 8.19). Since the points P1 – P3 lie on the axis of symmetry of the blade, the pressure fluctuations in these points are caused by vortices induced on both sides of the hydrofoil. However, this behaviour is not observed at points P4 – P6, where the pressure fluctuations are induced only by vortices which are shedding from top surface of the hydrofoil. Therefore, the frequency of pressure fluctuations at points P1 – P3 is two times higher than at points P4 – P6. As the vortices are periodically shedding, the lift force which excites the hydrofoil is generated. The frequency of the lift force, which is the main excitation frequency, has half value than at points P1 – P3. The observed pressure fluctuations at points P1 and P4 are compared in the figure bellow (Fig. 10.5). Additionally, the dependence of lift force on time is plotted (Fig. 10.6).

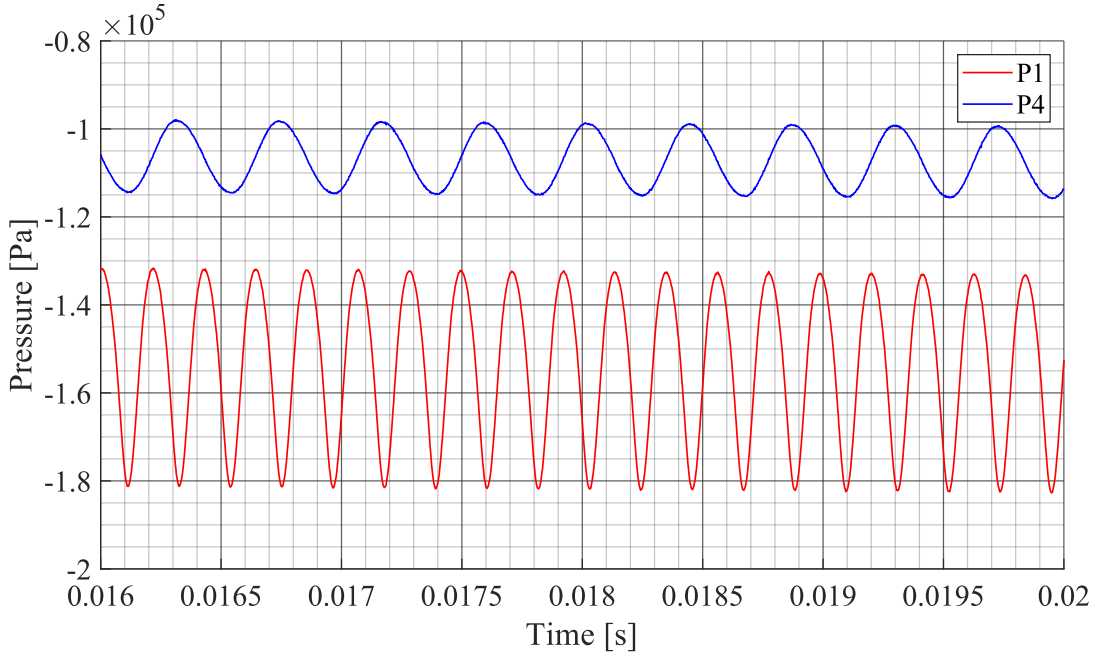

Fig. 10.5 Monitors of pressure at points P1 and P4 at $v_{inlet} = 20\ ms^{-1}$

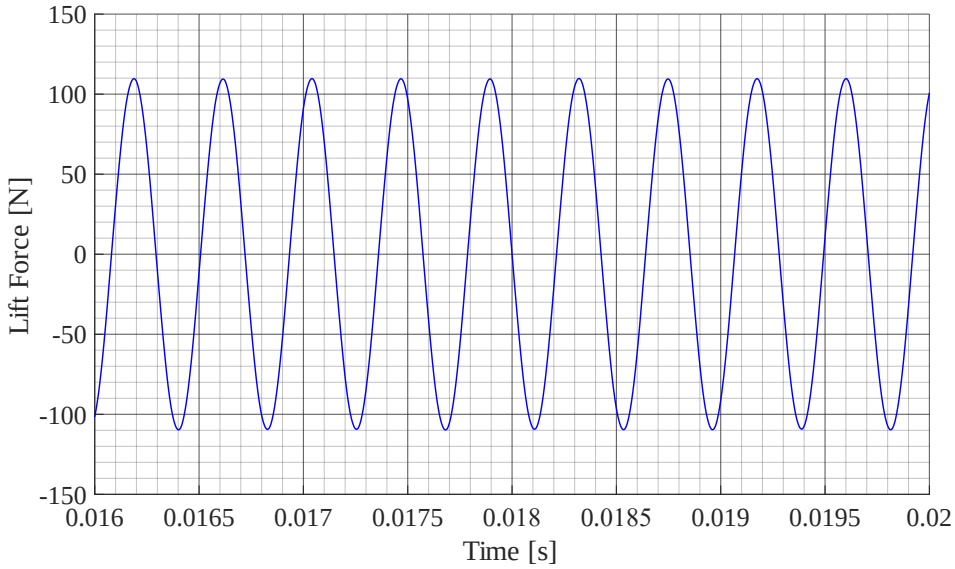

Fig. 10.6 Lift force in time which acts on the hydrofoil at $v_{inlet} = 20\ ms^{-1}$

The vortex shedding frequency was detected from amplitude-frequency spectra calculated from pressure fluctuations at points P1 – P6 and two forces. The equal values of frequency were obtained in two groups of points: P1 – P3 and P4 – P6. Therefore, results only at one point from each group are presented (P1 and P4). The amplitude-frequency spectra of both the pressure fluctuations and lift force are shown in the following figure (Fig. 10.7). The amplitude-frequency spectra calculated for lower mean velocities can be found in the Appendix A.2.

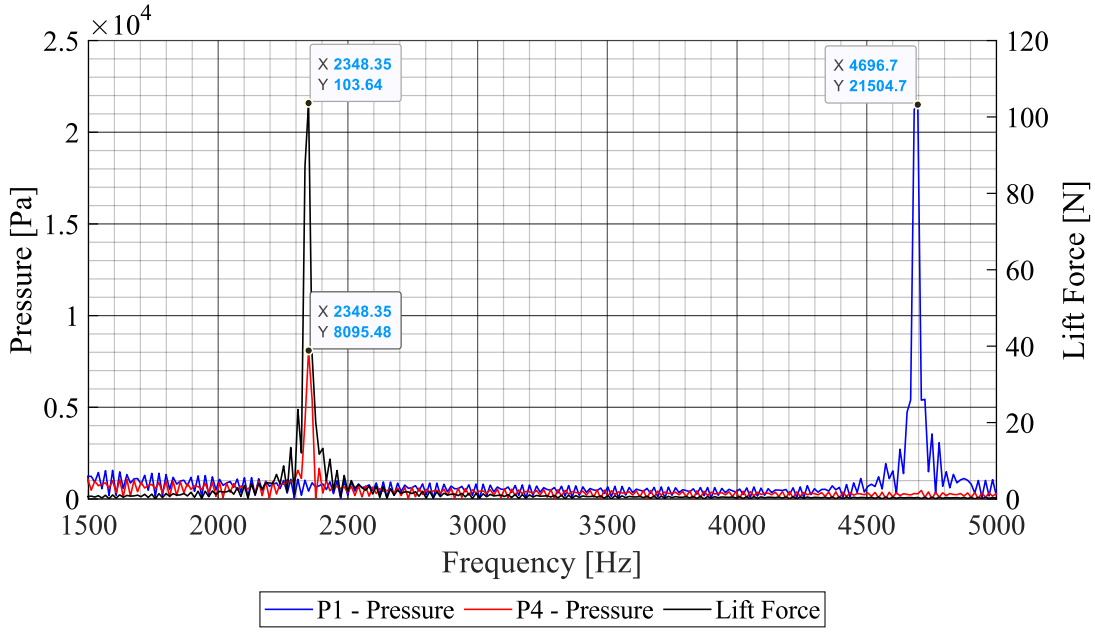

Fig. 10.7 Amplitude-frequency spectra of vortex shedding at $v_{inlet} = 20\ ms^{-1}$

The excitation frequencies detected from fluctuations of lift force at all values of mean velocity are presented in table below (Table 23). The results obtained from CFD analysis are compared to values which were estimated with the use of empirical formula and Strouhal number *St*. By assuming critical value of Strouhal number $St = 0.2$ and characteristic dimension equal to thickness of the trailing edge $d = 0.00163\ m$,

vortex shedding frequency can be estimated from equation (10.3). Additionally, the Reynolds number Re_{TE} which is related to the thickness of the trailing edge is introduced by equation (10.4). In this equation, the considered value of kinematic viscosity is $\nu_L = 1.004 \cdot 10^{-6}\, m^2 s^{-1}$.

$$f_{Karman,St} = \frac{St \cdot v_{inlet}}{d} \tag{10.3}$$

$$Re_{TE} = \frac{v_{inlet} \cdot d}{\nu_L} \tag{10.4}$$

Table 23 Vortex shedding frequency based on lift force from unsteady CFD

Inlet mean velocity	Vortex shedding frequency			
v_{inlet}	$f_{Karman,CFD}$	$f_{Karman,St}$	St	Re_{TE}
[ms^{-1}]	[s^{-1}]	[s^{-1}]	[1]	[1]
2.5	253	307	0.165	4 059
5.0	550	614	0.179	8 118
7.5	830	920	0.180	12 176
10.0	1126	1227	0.184	16 235
12.5	1401	1534	0.183	20 294
15.0	1730	1841	0.188	24 353
17.5	2005	2147	0.187	28 411
20.0	2348	2454	0.191	32 470

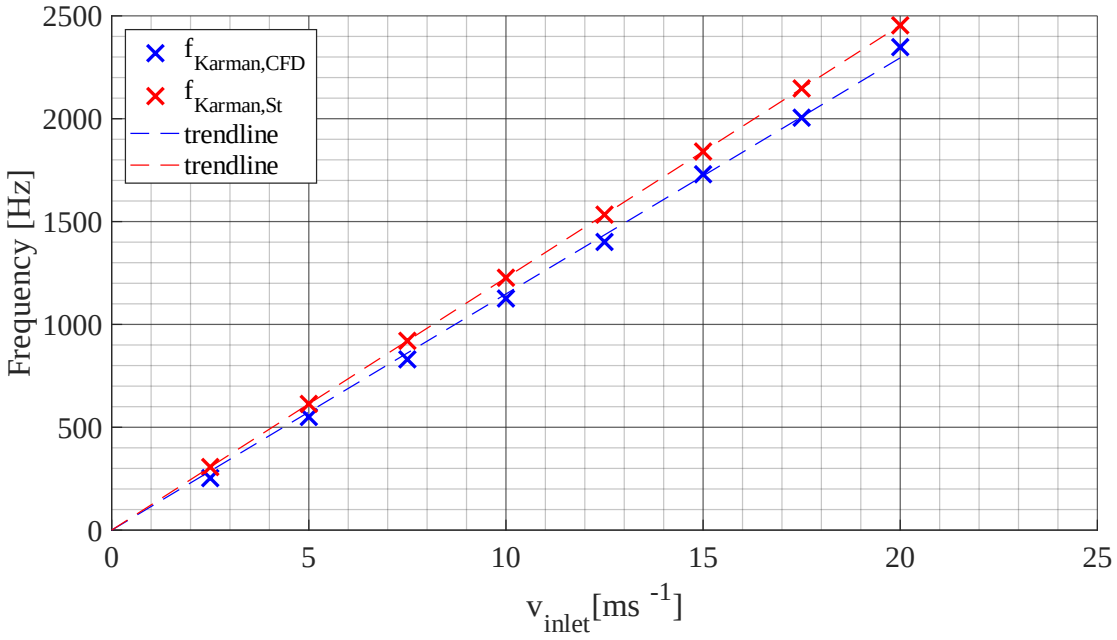

Fig. 10.8 Comparison of vortex shedding frequency from CFD and theoretical values

The dependence of vortex shedding frequency calculated from unsteady CFD simulation on flow velocity shows a linear trend (Fig. 10.8). The maximal difference between the theoretical and calculated value of frequency is 21 % at $v_{inlet} = 2.5\, ms^{-1}$. As the flow velocity is increasing, the difference is getting smaller up to 4.5 % at maximal velocity $v_{inlet} = 20\, ms^{-1}$. The calculated values are verified by experimental results later in this chapter.

10.2 Experiment – Angle of Attack 0°

The experimental measurement was carried out for two different angles of attack: 0° (1 – 17.5 ms^{-1}) and +5° (2.5 – 14.5 ms^{-1}). Both configurations were measured with step of flow velocity Δv = 0.5 ms^{-1}. Vibrations of the hydrofoil were measured by two LDV vibrometers with sampling frequency of 50 kHz which were pointed to the same locations as in previous cases (Fig. 7.1). The 10-second long signals obtained from each vibrometer were post-processed by FFT.

The obtained amplitude-frequency spectra for all values of flow velocity are shown in the following figures (Fig. 10.9 and Fig. 10.10).

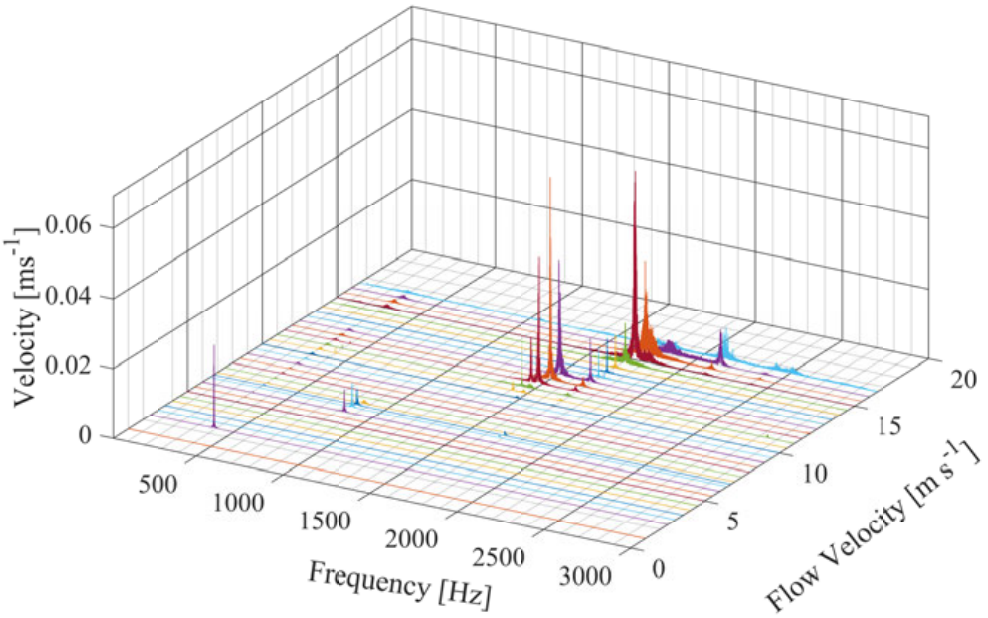

Fig. 10.9 Flow induced vibrations – LDV 1 ($\alpha_{inc} = 0°$)

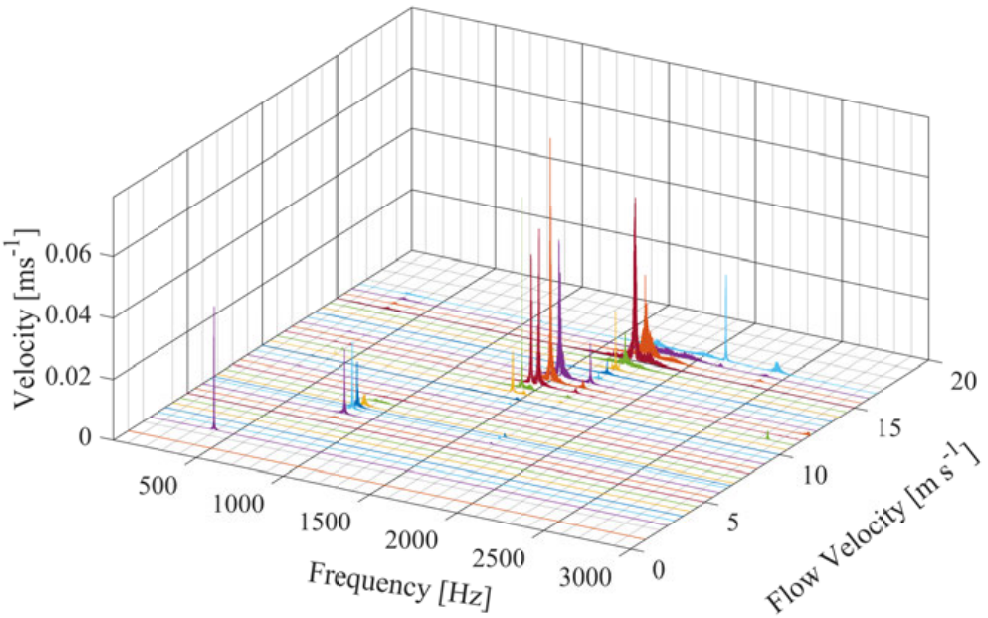

Fig. 10.10 Flow induced vibrations – LDV 2 ($\alpha_{inc} = 0°$)

The expected linear dependence of vortex shedding frequency on increasing flow velocity can be observed by both vibrometers. Since the basic physical quantity measured by LDV vibrometer is velocity, the amplitudes in both figures represent velocity of hydrofoil vibrations. The size of real deflection of the hydrofoil was estimated by transformation of spectra from velocity to displacement in frequency domain. The peaks observed in both figures (Fig. 10.9 and Fig. 10.10) have amplitude of deflection in order $1 \cdot 10^{-5}$ m.

As the flow velocity is increasing, the amplitude values of detected peaks are getting higher. This trend is observed by both vibrometers. The amplitude values at lower flow velocities below 10 ms^{-1} are much lower than at higher flow velocities. This is caused by slower vortex shedding which results in lower amplitudes of the excitation force on the hydrofoil. However, dominant peaks in the near of expected values of vortex shedding frequency were observed and manually detected in each spectrum. The overview of detected values $f_{Karman,EXP1,2}$ from both vibrometers is shown in the following table. Experimental values of vortex shedding frequency are compared to frequencies of the lift force calculated by unsteady CFD simulation (see Fig. 10.11).

Table 24 Experimental values of vortex shedding frequency ($\alpha_{inc} = 0°$)

Inlet mean velocity	Vortex shedding frequency				
v_{inlet}	$f_{Karman,EXP1}$	$f_{Karman,EXP2}$	v_{inlet}	$f_{Karman,EXP1}$	$f_{Karman,EXP2}$
[ms^{-1}]	[s^{-1}]	[s^{-1}]	[ms^{-1}]	[s^{-1}]	[s^{-1}]
1	108.2	108.2	10.0	1224.6	1226.9
2.5	316.5	316.5	10.5	1219.9	1219.9
3.0	388.5	388.5	11.0	1416.9	1416.9
3.5	399.9	397.6	11.5	1423	1423
4.0	530.6	482.4	12.0	1483.4	1483.4
4.5	570.3	537.7	12.5	1504.5	1504.5
5.0	609.3	609.3	13.0	1511.5	1511.5
5.5	836.8	836.8	13.5	1697	1696.8
6.0	823.9	823.9	14.0	1703.1	1702.7
6.5	839.4	839.4	14.5	1708.7	1708.7
6.75	841.7	841.7	15.0	1720.5	1722.2
7.0	847.5	847.5	15.5	1737.2	1737.2
7.5	867.1	872.6	16.0	1750.6	1750.6
8.0	899.2	899.2	16.5	1824.8	1843.1
8.5	972.5	974.7	17.0	2131.8	2132.2
9.0	1063.3	1052.6	17.5	2142.33	2142.17
9.5	1136	1091.9			

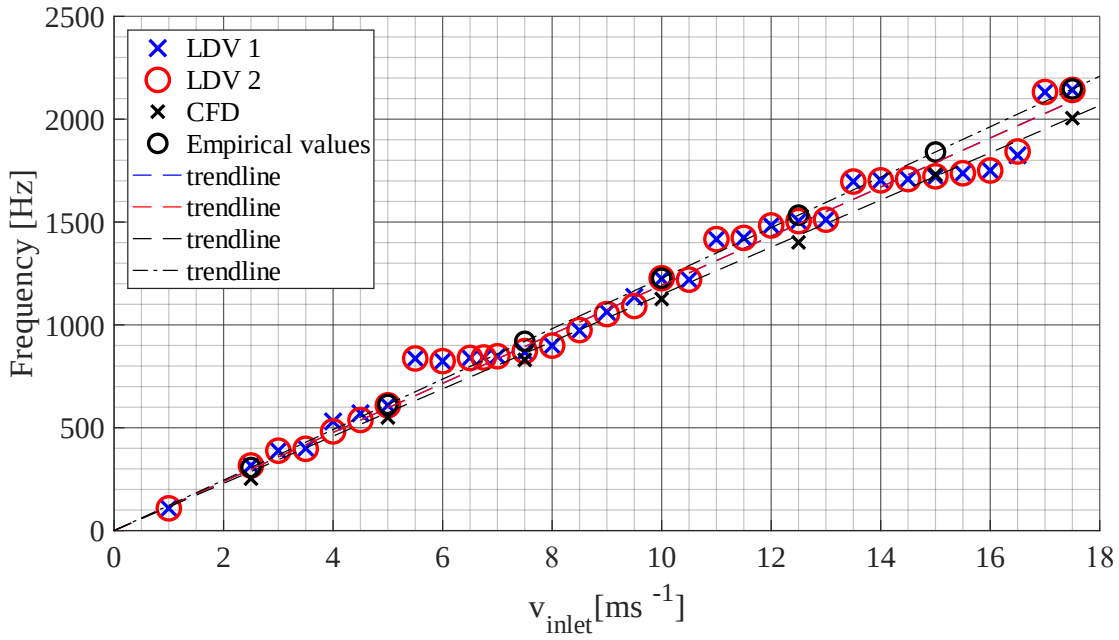

Fig. 10.11 Comparison of vortex shedding frequency results

Experimental results have a linear increasing trend which is in good agreement with theoretical values calculated from equation (10.3). Three regions with constant vortex shedding frequency can be found in the graph: 4.5 – 7.0 ms^{-1} (839 Hz), 12.0 – 13.0 ms^{-1} (1511 Hz) and 13.5 – 16.0 ms^{-1} (1722 Hz). This behaviour is caused by coupling of the vortex shedding frequency to a natural frequency of the structure and is called "lock-in". The lock-in region occurs in a close range of flow velocity, where vortex shedding frequency passes through the hydrofoil natural frequency. The vortex shedding frequency is locked to the hydrofoil natural frequency and has constant value in whole lock-in region. An example can be found in the range of flow velocity between 4.5 - 7.0 ms^{-1} where the measured vortex shedding frequency has constant value of 839 Hz which is almost equal to the fourth natural frequency identified in experiment ($f_{nat,SW,EXP} = 834\ Hz$).

The unsteady CFD simulation was verified by comparison of the amplitude-frequency spectra of the lift force to the experimental values of vortex shedding frequency (see Table 25). The difference between the experimental and numerical results was calculated by formula (10.5). The numerical results underestimate the experimental values up to 10 % except the lowest mean velocity 2.5 ms^{-1} with difference of 20 %. As the flow velocity rises, the difference between the numerical and experimental values is getting smaller. The amplitude-frequency spectra of the lift force were compared to the spectra obtained from both vibrometers. The comparison of obtained spectra at $v_{inlet} = 15\ ms^{-1}$ is shown in the graph (Fig. 10.12). This comparison was plotted for all values of flow velocity and can be found in Appendix A.3.

The dependence of Strouhal number St on Reynolds number Re_{TE} is shown in figure Fig. 10.13. The values of Strouhal number for turbulent flow should keep constant value 0.2. [1]

$$\Delta f_{1,2} = \frac{\left| f_{Karman,EXP1,2} - f_{Karman,CFD} \right|}{f_{Karman,EXP1,2}} * 100\ \% \qquad (10.5)$$

Table 25 Comparison of vortex shedding frequency from CFD and experiment

Inlet mean velocity	Vortex shedding frequency				
	Experiment		CFD Simulation		
v_{inlet}	$f_{Karman,EXP1}$	$f_{Karman,EXP2}$	$f_{Karman,CFD}$	Δf_1	Δf_2
	LDV 1	LDV 2	Lift Force		
[ms^{-1}]	[s^{-1}]	[s^{-1}]	[s^{-1}]	[%]	[%]
2.5	316.5	316.5	253	20.06	20.06
5.0	609.3	609.3	550	9.73	9.73
7.5	867.1	872.6	830	4.28	4.88
10.0	1224.6	1226.9	1126	8.05	8.22
12.5	1504.5	1504.5	1401	6.88	6.88
15.0	1720.5	1722.2	1730	0.55	0.45
17.5	2142.33	2142.17	2005	6.41	6.40

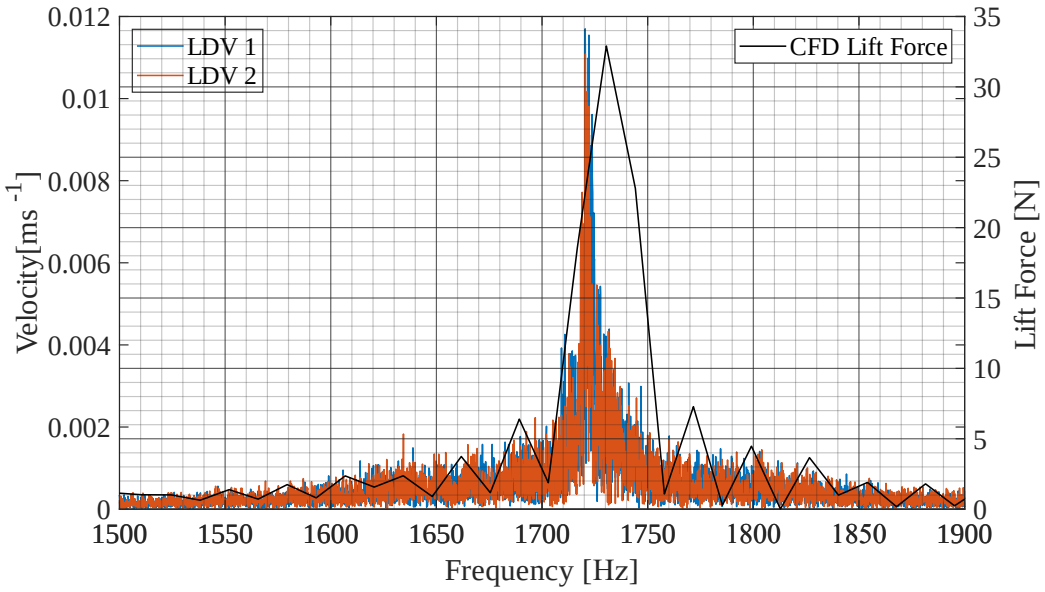

Fig. 10.12 Amp.-freq. spectra: CFD lift force and vibrometers at $v_{inlet} = 15ms^{-1}$

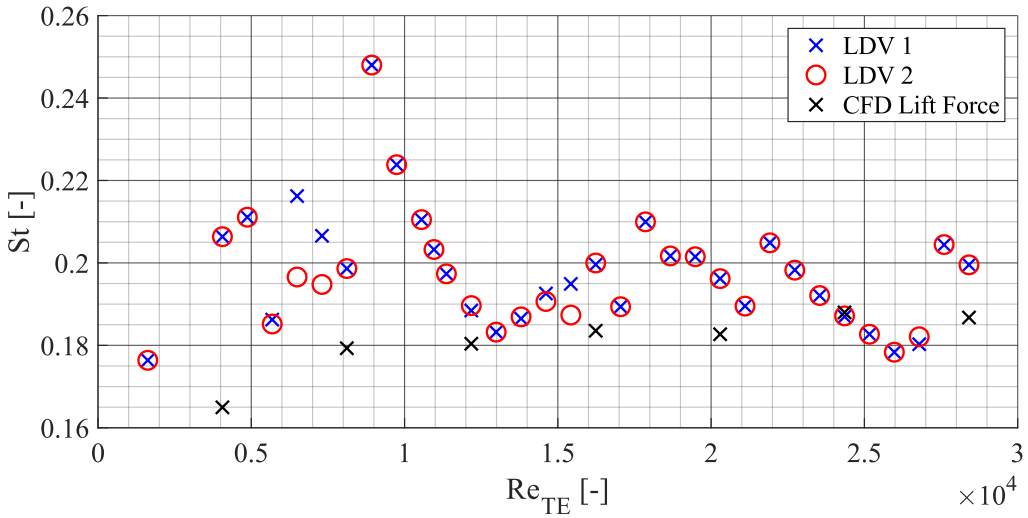

Fig. 10.13 Comparison of Strouhal number for experiment and CFD simulation

10.3 Experiment – Angle of Attack 5°

Experimental investigation of flow induced vibrations was also measured for incidence angle of 5° in the range of mean velocity 2.5 ms^{-1} – 14.5 ms^{-1}. The maximal mean velocity was limited by presence of cavitation which occurred at 15 ms^{-1}. Post-processing of the measurement was executed by same procedure as in case of zero angle of attack. The obtained amplitude-frequency spectra from both vibrometers are shown in the following graphs (Fig. 10.14 and Fig. 10.15). In this case, no linear trend of vortex shedding frequency was observed. Frequencies of the detected peaks does not vary with the change of the flow velocity. However, the amplitudes of the peaks at constant frequency are increasing as the flow velocity rises. This behaviour indicates that the detected peaks correspond to the natural frequencies of the structure and as the flow velocity is getting higher, the amplitudes increase due to larger excitation force.

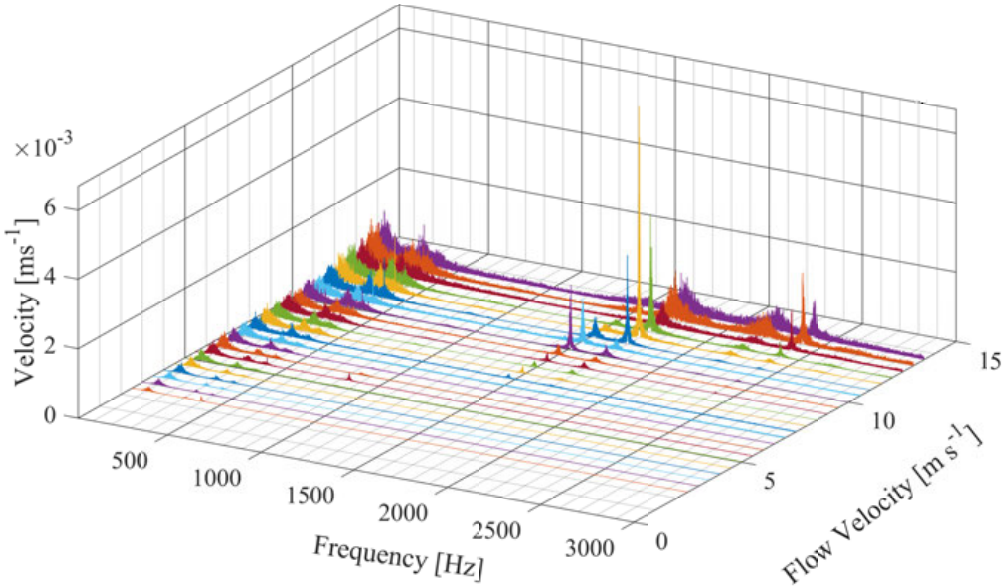

Fig. 10.14 Flow induced vibrations – LDV 1 ($\alpha_{inc} = 5°$)

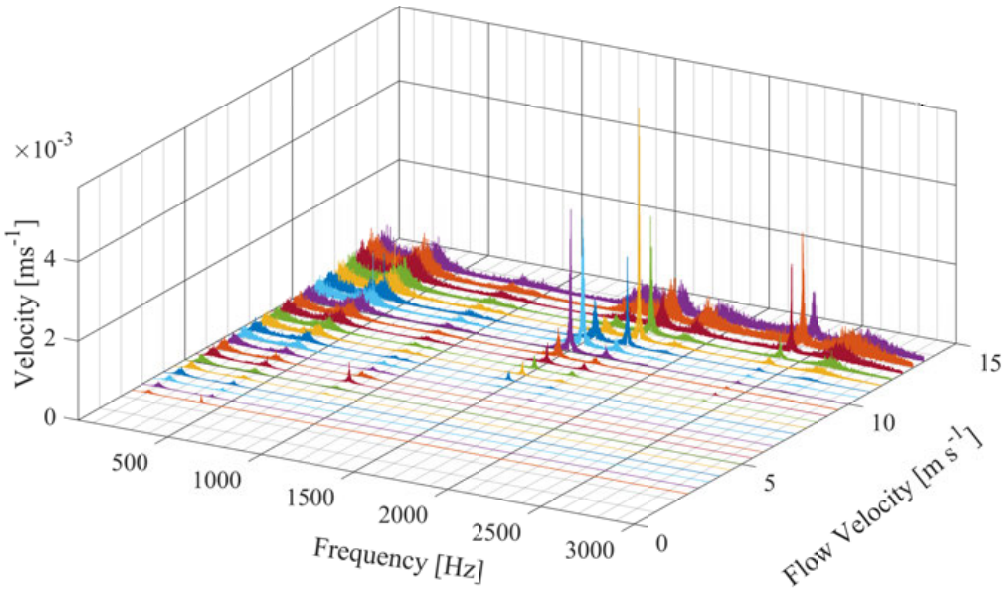

Fig. 10.15 Flow induced vibrations – LDV 2 ($\alpha_{inc} = 5°$)

Comparison of detected frequencies and natural frequencies measured in still water can be carried out in the range 0 Hz – 1000 Hz. This range of the above presented figures is shown in detail (Fig. 10.16 and Fig. 10.17). Four dominant frequencies can be identified by both vibrometers. They correspond to the measured values of natural frequencies $f_{nat,SW,EXP} = 104\ Hz, 304\ Hz, 382\ Hz$ and $834\ Hz$.

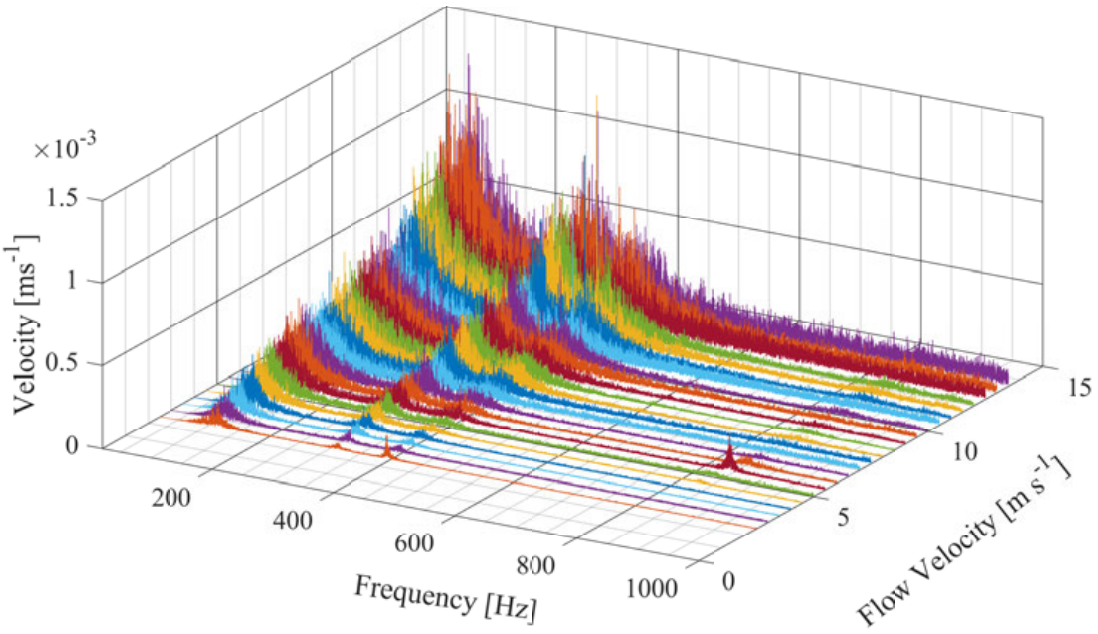

Fig. 10.16 Flow induced vibrations in range 0 – 1000 Hz (LDV 1; $\alpha_{inc} = 5°$)

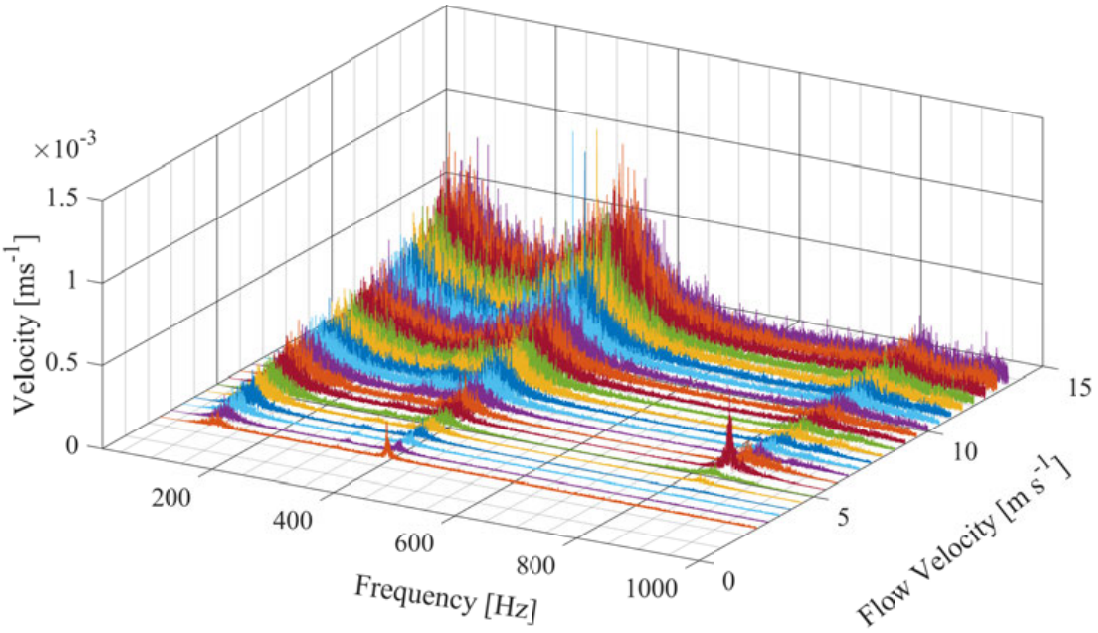

Fig. 10.17 Flow induced vibrations in range 0 – 1000 Hz (LDV 2; $\alpha_{inc} = 5°$)

10.4 Partial Conclusion – Flow Induced Vibrations

Flow induced vibrations of the hydrofoil were investigated by experimental measurement for two values of angle of attack: 0° and 5°. In addition, unsteady CFD analysis of vortex shedding was calculated for zero angle of attack.

The frequency of vortex shedding at zero angle of attack was measured in range of flow velocity 1 ms^{-1} – 17.5 ms^{-1} with step of 0.5 ms^{-1}. A linear increase of Kármán frequency was observed in the whole range of flow velocity except the lock-in regions which occurred when the vortex shedding frequency was close to natural frequency of the hydrofoil. The experimental results obtained from the two vibrometers do not differ in whole range of measurements.

Numerical investigation of vortex shedding frequency was carried out in range of flow velocity 2.5 ms^{-1} - 20 ms^{-1} with a step of 2.5 ms^{-1}. The amplitude-frequency spectra obtained by Fast Fourier Transformation from the lift force were compared to the experimental values. The numerical results do not differ more than 10 % from the experimental values except the flow velocity 2.5 ms^{-1}. At this flow velocity, the numerical result underestimates the experimental value by 20 %.

The experimental measurement of flow induced vibrations at 5° angle of attack did not capture the frequency of vortex shedding. The only observed dominant peaks in the amplitude-frequency spectra were related to the natural frequencies of the hydrofoil.

11 HYDROFOIL OSCILLATIONS FORCED BY EXTERNAL EXCITER

Measurement of enforced vibrations enables to calculate the Frequency Response Function (FRF) of the hydrofoil. In this chapter, the FRF was used for evaluation of damping ratio for the first mode of the hydrofoil. The experimental results were used for verification of damping ratio calculated by modified Modal Work Approach.

11.1 Experiment

The experimental investigation of damping ratio ζ of the first hydrofoil mode was carried out in range of flow velocity 0 ms^{-1} – 10 ms^{-1} with a step of 1 ms^{-1}. The FRF of the hydrofoil was obtained by post-processing of measured data. Procedure of both the data post-processing and the calculation of FRF is described in Chapter 7.2.2 and denoted as "Method 2". Damping ratio of the hydrofoil was evaluated by SDOF Response Fit method which approximates calculated FRF of MDOF system by a curve. This curve represents FRF of a SDOF system (see Chapter 7.5.2).

11.1.1 Structural Damping

The first step of experimental investigation was evaluation of damping ratio for hydrofoil in air. Damping ratio was post-processed from the same measurement as the first natural frequency in Chapter 9.1.2 (range of excitation frequency 80 Hz – 280 Hz, step of 1 Hz). The FRF obtained by both vibrometers (Fig. 11.1) were approximated by SDOF Response Fit method. The figures below (Fig. 11.2 – Fig. 11.5) show a fitted curve of amplitude and phase (orange colour) of SDOF system on the measured FRF which is marked by blue colour. The obtained values of both the damping ratio and the damped first natural frequency $f_{NAT,SDOF}$ of the hydrofoil are presented in the table (Table 26). As it can be seen, the difference in calculated natural frequency is less than 1 % while the difference of damping ratio from the two vibrometers is 37 %. The vibrometer LDV 1 was pointed to the location of maximal deflections of the first mode, while the other vibrometer LDV 2 was located in region of very low deflections. Consequently, the FRF obtained by vibrometer LDV 2 is not as smooth as the FRF obtained by the first vibrometer. Therefore, the values obtained by vibrometer LDV 1 are more accurate.

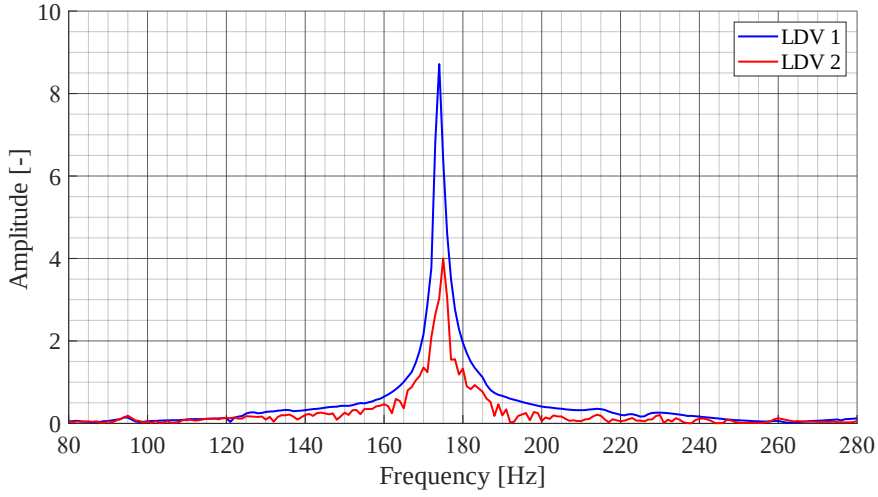

Fig. 11.1 FRF of hydrofoil in air from both vibrometers LDV 1 and LDV 2 ($\alpha_{inc} = 0°$)

Table 26 Structural damping calculated by SDOF Response Fit method

LDV 1		LDV 2		
$f_{NAT,SDOF,1}$	$\zeta_{SDOF,LDV1}$	$f_{NAT,SDOF,2}$	$\zeta_{SDOF,LDV2}$	$\Delta\,\zeta$
[Hz]	[1]	[Hz]	[1]	[%]
173.82	0.00639	174.22	0.00875	36.9

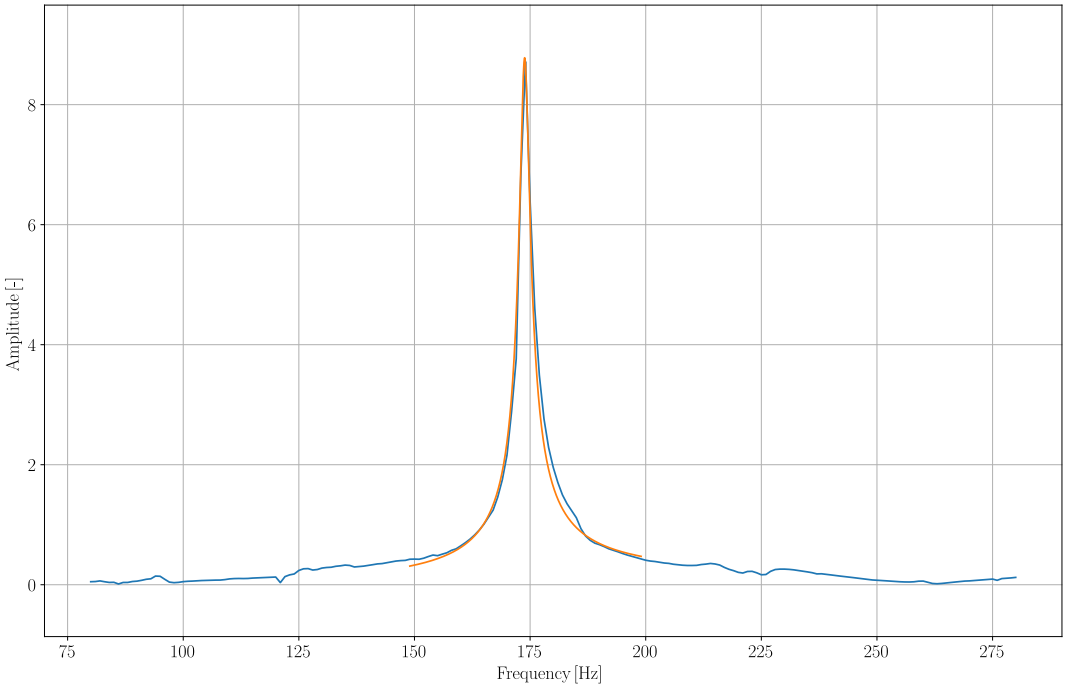

Fig. 11.2 Approximation of FRF by SDOF Response Fit method – amplitude LDV 1

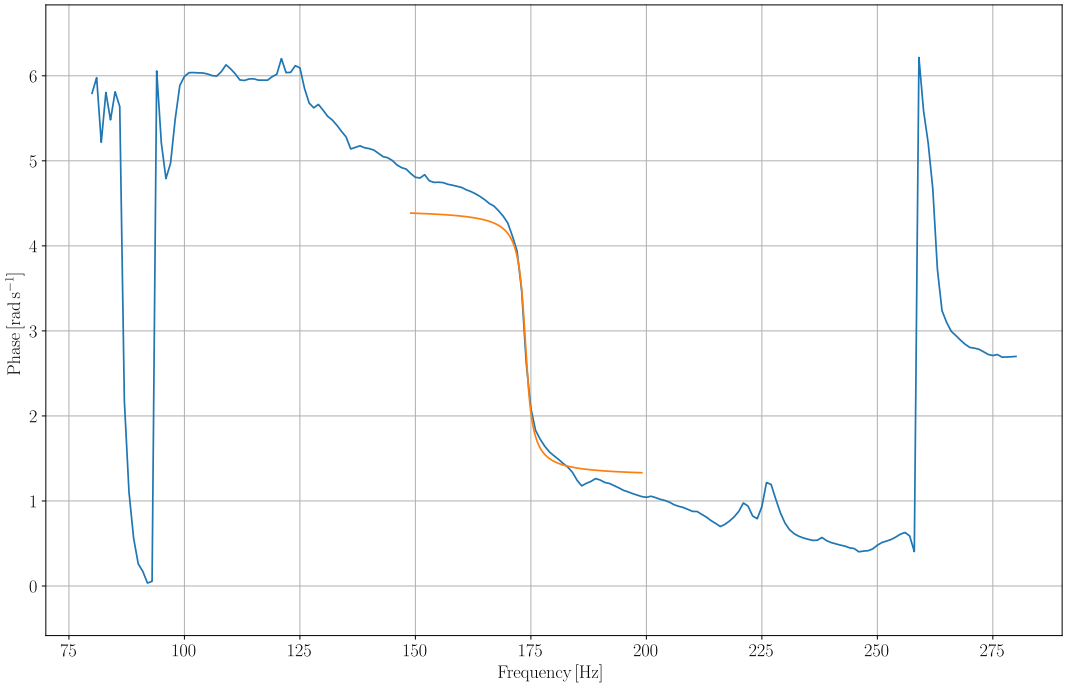

Fig. 11.3 Approximation of FRF by SDOF Response Fit method – phase LDV 1

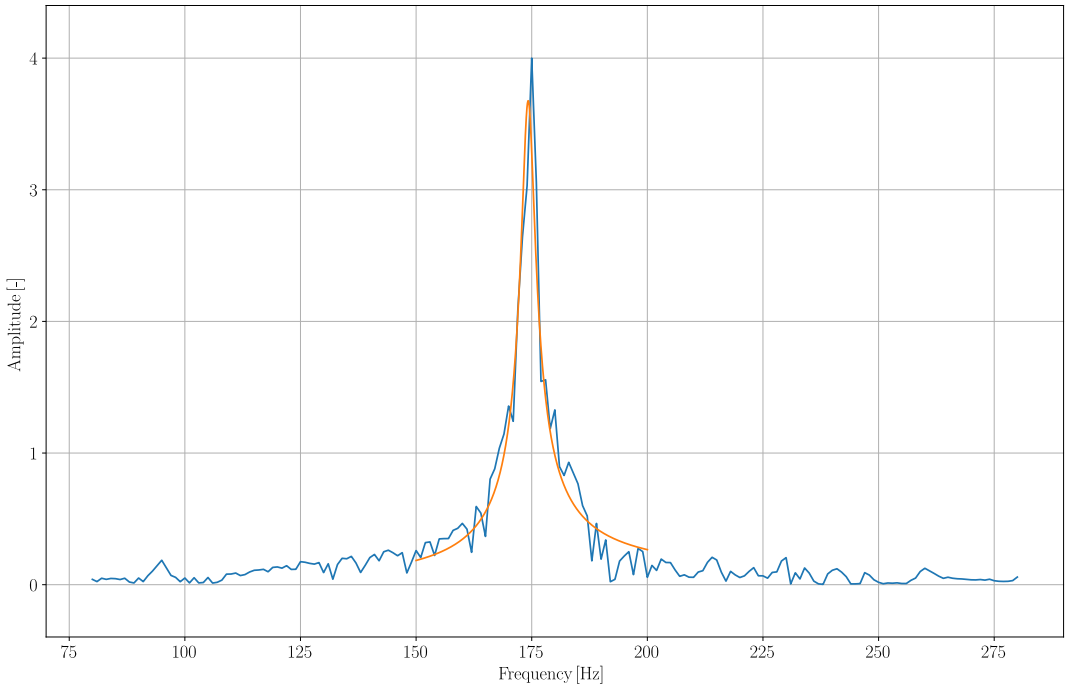

Fig. 11.4 Approximation of FRF by SDOF Response Fit method – amplitude LDV 2

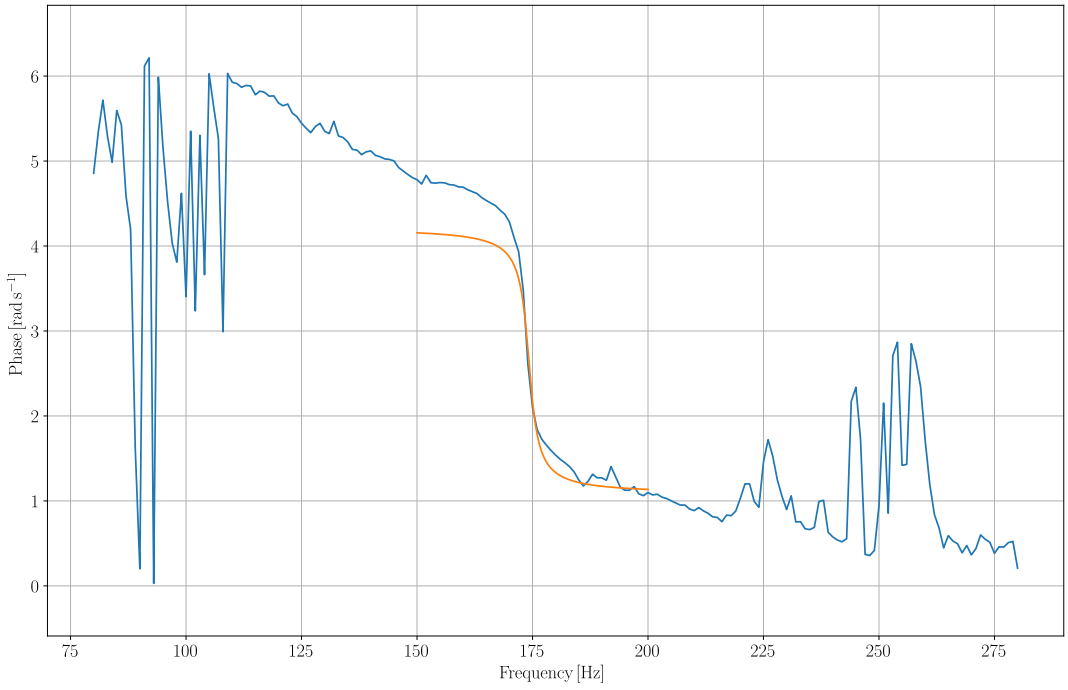

Fig. 11.5 Approximation of FRF by SDOF Response Fit method – phase LDV 2

11.1.2 Experiment - Angle of Attack 0°

Experimental investigation of hydrodynamic damping was carried out in range of flow velocity 0 ms^{-1} – 10 ms^{-1} with a step of 1 ms^{-1}. As the expected value of the natural frequency was around 104 Hz, the excitation frequency varied in range 50 Hz – 200 Hz with a step of 1 Hz. In context of considerations about various damping contributions in Chapter 7.5.1 the damping ratio measured in this chapter is related to the total damping of the system b_{TOT}. However, since the structural damping is very low and the water can be considered as incompressible ($b_W \approx 0$), the main contribution of the total damping is from the viscous – hydrodynamic damping b_F.

The values of damping ratio were obtained by SDOF Response Fit method. In addition, estimation of damping ratio based on value of *magnification factor* is presented. [43]

The FRF, which is non-dimensional, is obtained by dividing the hydrofoil response from vibrometer by signal measured on the exciter. The signal which was measured by accelerometer mounted on the membrane of the exciter must be first transformed from acceleration to velocity in frequency domain. Such calculated FRF can also be interpreted as a *magnification factor* A_{MAG} [1] between the hydrofoil response (output of mechanical system) and the excitation (input). By introducing non-dimensional excitation force F_0 given by equation (11.1) the damping ratio can be then evaluated from formula (11.2). [43]

$$F_0 = 2\zeta \cdot A_{MAG} \tag{11.1}$$

$$\zeta = \frac{F_0}{2 \cdot A_{MAG}} \tag{11.2}$$

The non-dimensional excitation force F_0 is first calculated by multiplication of damping ratio ζ and magnification factor A_{MAG} (equation (11.1)). Here, the damping ratio is obtained by SDOF response Fit method for hydrofoil in still water. The value of magnification factor A_{MAG} corresponds to the value at the first natural frequency (104 Hz). Once the value of F_0 is calculated, the same value is used for estimation of damping ratio at higher values of flow velocity. This estimation of damping ratio can be used by assuming a linear low damped system with modes which are well separated and do not affect each other.

The figure Fig. 11.6 shows FRF of hydrofoil submerged in still water. As it can be seen, the amplitude of the FRF (which is the amplification factor A_{MAG}) measured by vibrometer LDV 1 is higher than by vibrometer LDV 2. This behaviour was observed at all values of flow velocity and corresponds to the analysed mode shape. The amplitudes by vibrometer LDV 1 were ca. 10 – 50 % higher than by LDV 2. FRF obtained for other values of flow velocity can be found in Appendix A.4. The obtained FRF are smooth only at very low flow velocities. By increasing the flow velocity, the calculated FRF are not represented by a smooth curve. This fact may influence the results. Alternatively, the FRF might be approximated by a curve before applying the SDOF Response method. However, the data in this thesis are directly post-processed with no additional filtering or improvements.

The values of damping ratio $\zeta_{SDOF,LDV1,2}$ and damped natural frequency $f_{NAT,SDOF,1,2}$ calculated by SDOF Response Fit method are presented in Table 27. The approximated FRF are presented in Appendix A.5. The maximal difference between values of damping ratio calculated from two vibrometers is 8.37 %. The values

of damping ratio measured in still water differ from the structural damping by 22 % (LDV 1) and 8 % (LDV 2). As the flow velocity rises in range 0 ms^{-1} – 7 ms^{-1}, the difference between the values of damped natural frequency from the two vibrometers is slightly increasing up to 2.5 %. In flow velocity range 8 ms^{-1} – 10 ms^{-1}, higher difference up to 10.3 % is observed.

The estimated values of damping ratio calculated by introducing the non-dimensional excitation force F_0 are summarized in Table 28. The obtained values of damping ratio are sensitive to the input values which are used for initial calculation of the non-dimensional force F_0. In this case, the values at $v_{inlet} = 1\ ms^{-1}$ were used in equation (11.1). On the one hand, this approach does not provide accurate damping ratio for hydrofoil in still water. On the other hand, good agreement with the results of SDOF Response Fit method is observed in range of flow velocity 1 ms^{-1} – 7 ms^{-1} (maximal difference 22 %).

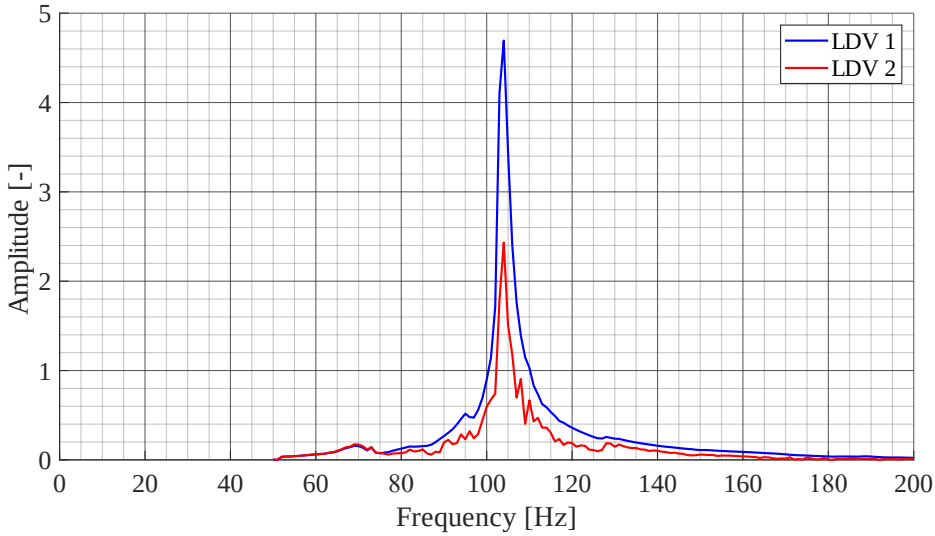

Fig. 11.6 FRF of hydrofoil at $v_{inlet} = 0\ ms^{-1}$ ($\alpha_{inc} = 0°$)

Table 27 Results of SDOF Response Fit method ($\alpha_{inc} = 0°$)

	LDV 1		LDV 2			
v_{inlet}	$f_{NAT,SDOF,1}$	$\zeta_{SDOF,LDV1}$	$f_{NAT,SDOF,2}$	$\zeta_{SDOF,LDV2}$	Δf	$\Delta \zeta$
[ms^{-1}]	[Hz]	[1]	[Hz]	[1]	[%]	[%]
0	103.71	0.00819	103.76	0.00813	0.05	0.74
1	103.21	0.02542	103.03	0.02582	0.17	1.58
2	103.41	0.04530	102.83	0.04377	0.56	3.38
3	100.58	0.07319	100.60	0.07620	0.01	4.12
4	103.07	0.07824	101.69	0.08243	1.34	5.36
5	101.77	0.09038	100.83	0.09794	0.92	8.37
6	103.55	0.11140	100.48	0.10821	2.97	2.87
7	101.47	0.11840	99.05	0.12548	2.39	5.98
8	109.48	0.14149	98.24	0.13706	10.27	3.13
9	106.22	0.14685	98.74	0.14334	7.04	2.39
10	100.52	0.14183	96.69	0.14710	3.81	3.71

$$\Delta\,\zeta = \frac{\left|\zeta_{SDOF,LDV2} - \zeta_{SDOF,LDV1}\right|}{\zeta_{SDOF,LDV1}} \cdot 100\ \% \tag{11.3}$$

$$\Delta\,f = \frac{\left|f_{NAT,SDOF,2} - f_{NAT,SDOF,1}\right|}{f_{NAT,SDOF,1}} \cdot 100\ \% \tag{11.4}$$

Table 28 Results of damping ratio calculated by magnification factor ($\alpha_{inc} = 0°$)

	LDV 1		LDV 2			
v_{inlet}	A_{MAG}	$\zeta_{MAG,LDV1}$	A_{MAG}	$\zeta_{MAG,LDV2}$	$\Delta\,A_{MAG}$	$\Delta\,\zeta$
[ms^{-1}]	[1]	[1]	[1]	[1]	[%]	[%]
0	4.7	0.03082	2.45	0.04215	47.87	36.74
1	5.7	0.02542	4	0.02582	29.82	1.58
2	3.5	0.04139	2.6	0.03972	25.71	4.04
3	2.3	0.06299	1.6	0.06454	30.43	2.47
4	1.8	0.08049	1.3	0.07944	27.78	1.30
5	1.5	0.09658	1.05	0.09835	30.00	1.83
6	1.2	0.12073	0.9	0.11474	25.00	4.96
7	1	0.14487	0.78	0.13240	22.00	8.61
8	0.75	0.19317	0.68	0.15186	9.33	21.38
9	0.68	0.21305	0.6	0.17211	11.76	19.21
10	0.66	0.21951	0.55	0.18776	16.67	14.46

Table 29 Comparison of two methods of damping ratio evaluation

	LDV 1			LDV 2		
v_{inlet}	$\zeta_{SODF,LDV1}$	$\zeta_{MAG,LDV1}$	$\Delta\,\zeta$	$\zeta_{SODF,LDV2}$	$\zeta_{MAG,LDV2}$	$\Delta\,\zeta$
[ms^{-1}]	[1]	[1]	[%]	[1]	[1]	[%]
0	0.00819	0.03082	276.31	0.00813	0.04215	418.45
1	0.02542	0.02542	0.00	0.02582	0.02582	0.00
2	0.04530	0.04139	8.63	0.04377	0.03972	9.25
3	0.07319	0.06299	13.94	0.07620	0.06454	15.30
4	0.07824	0.08049	2.88	0.08243	0.07944	3.63
5	0.09038	0.09658	6.86	0.09794	0.09835	0.42
6	0.11140	0.12073	8.38	0.10821	0.11474	6.03
7	0.11840	0.14487	22.36	0.12548	0.13240	5.51
8	0.14149	0.19317	36.53	0.13706	0.15186	10.80
9	0.14685	0.21305	45.08	0.14334	0.17211	20.07
10	0.14183	0.21951	54.77	0.14710	0.18776	27.64

$$\Delta\,\zeta = \frac{\left|\zeta_{SDOF,LDV} - \zeta_{MAG,LDV}\right|}{\zeta_{SDOF,LDV}} \cdot 100\% \tag{11.5}$$

Values of damping ratio calculated by both methods from both vibrometers are presented in the following figure (Fig. 11.7). The results obtained by SDOF Response Fit method (marked by crosses) perform linear trend in range 0 ms^{-1} – 8 ms^{-1}. The values of damping ratio from both vibrometers at 3 ms^{-1} do not copy the linear trend and are very close to the values at 4 ms^{-1}. This behaviour is caused by presence of lock-in region which was observed in measurement of vortex shedding frequency (the third mode of hydrofoil $f_{nat,SW,EXP} = 382\ Hz$). At higher flow velocity in range 8 ms^{-1} – 10 ms^{-1}, values of damping ratio keep constant value. In this case, the measured vortex shedding frequency has a linear increasing trend and no lock-in region is present. Results from both vibrometers are in good agreement with maximal difference 8.37 %.

The value of damping ratio calculated with the use of magnification factor (marked by circles) at 0 ms^{-1} does not match the value obtained by SDOF Response Fit method. Since the non-dimensional force F_0 was calculated from damping ratio at flow velocity 1 ms^{-1}, no difference between the two methods is observed at this flow velocity. A good agreement between the two methods is observed at higher flow velocities in range 2 ms^{-1} – 7 ms^{-1} with maximal difference 22 %. By further increase of flow velocity, the values calculated by non-dimensional force F_0 overestimate the SDOF Response Fit method up to 55 %. Maximal difference between the values from two vibrometers is 21 % except the case in still water (37 %).

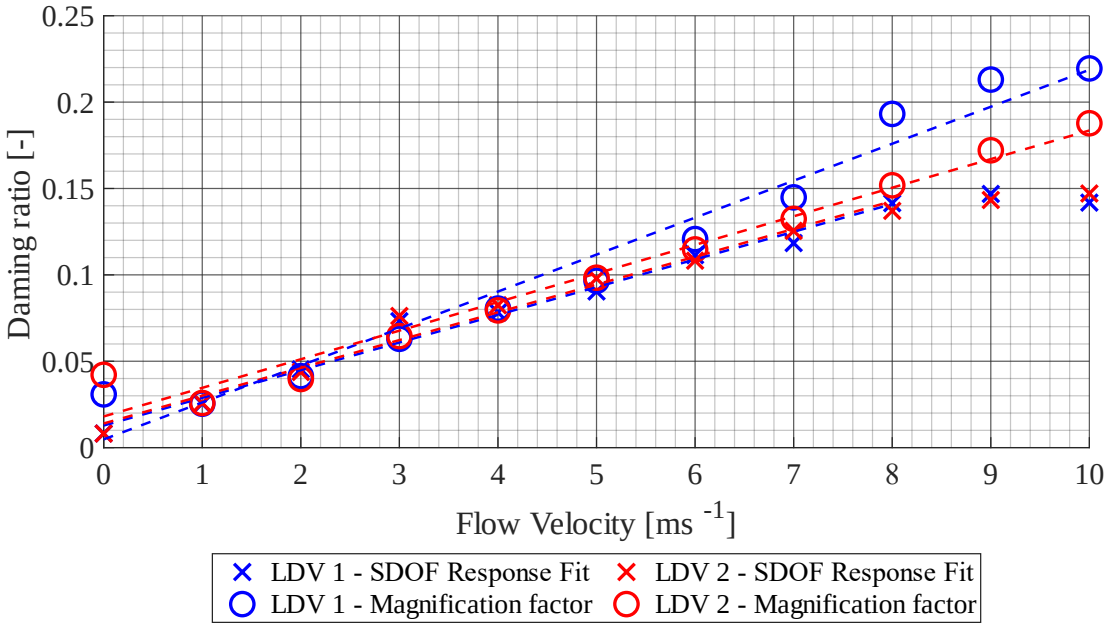

Fig. 11.7 Overview experimental values of damping ratio ($\alpha_{inc} = 0°$)

The values of the damped natural frequency $f_{NAT,SDOF,1,2}$ obtained from both vibrometers are significantly decreasing with increase of flow velocity (Fig. 11.8). This behaviour may be caused by increase of added mass effect m_{ADD} or decrease of fluid added stiffness k_F. As the mechanical system is analysed with the use of linearized models, the observed drop of the first natural frequency may be result of nonlinear behaviour of the analysed system.

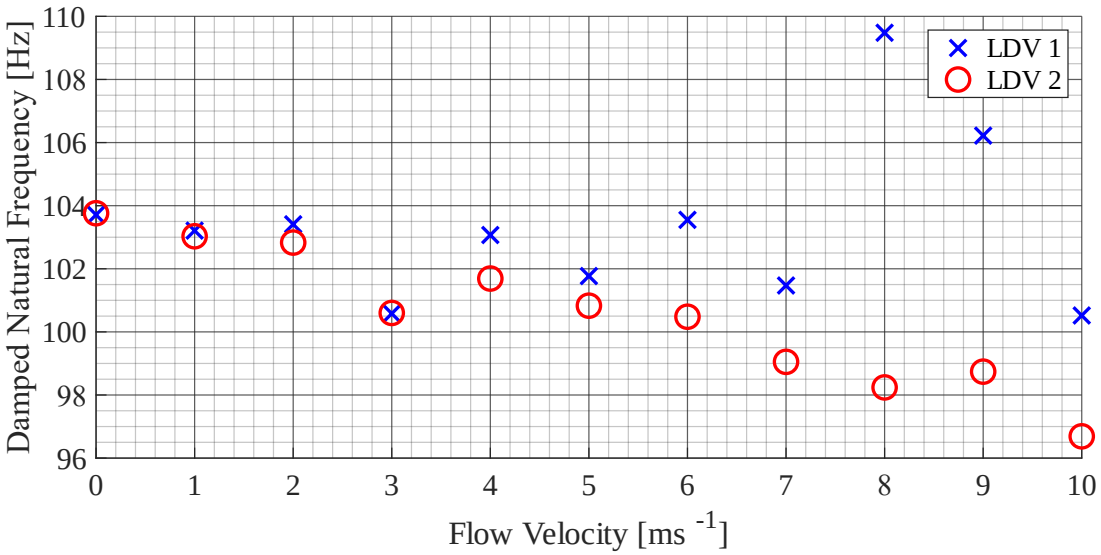

Fig. 11.8 Damped natural frequency $f_{NAT,SDOF,1,2}$ ($\alpha_{inc} = 0°$)

The response of the hydrofoil was measured by two LDV vibrometers. Experimental data were also collected from four additional sensors which were mounted on the test section: accelerometer on the external bar (sensor no. 5 in the right bottom corner; Fig. 6.13), accelerometer on the draft tube (sensor no. 6; Fig. 6.12), pressure tap located in the top wall of the test section behind the hydrofoil trailing edge (sensor no. 4; Fig. 6.12) and microphone (sensor no. 16; Fig. 6.12). Data from all above mentioned sensors were time-synchronously collected during each measurement and post-processed by same procedure as the vibrometers. An example of results obtained from four additional sensors at flow velocity 10 ms^{-1} is illustrated in the four figures below (Fig. 11.9 – Fig. 11.12). The figures show data which were not divided by response from mechanical exciter and therefore do not represent exact FRF.

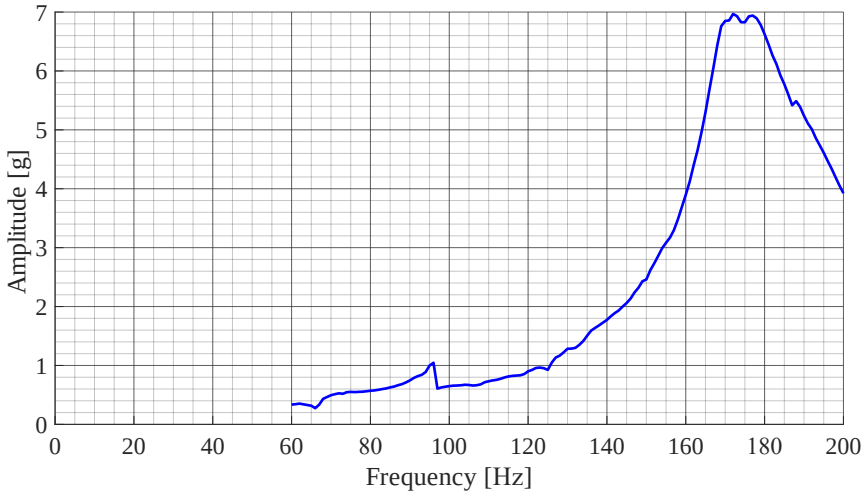

Fig. 11.9 Response measured by accelerometer on external bar at $v_{inlet} = 10\ ms^{-1}$

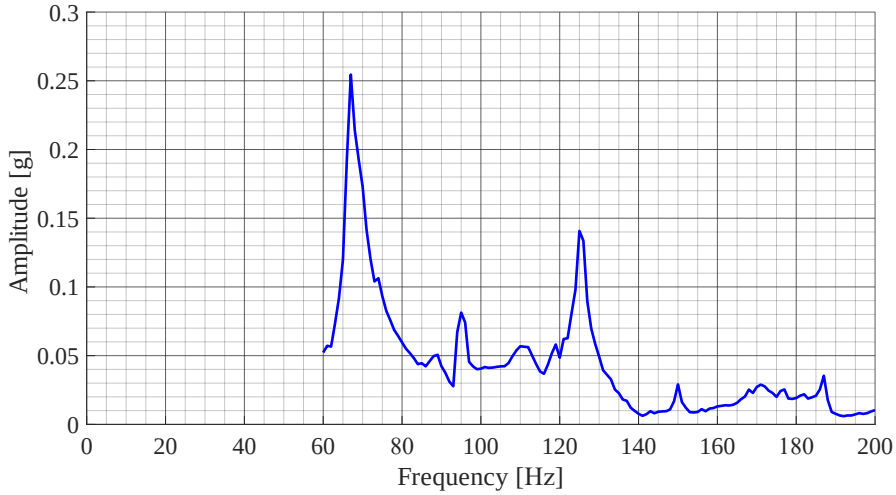

Fig. 11.10 Response measured by accelerometer on draft tube at $v_{inlet} = 10\ ms^{-1}$

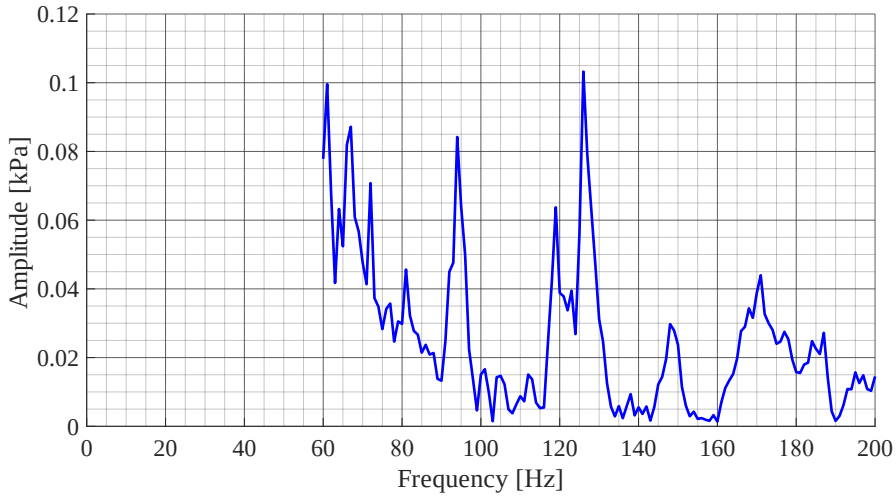

Fig. 11.11 Response measured by pressure tap in test section at $v_{inlet} = 10\ ms^{-1}$

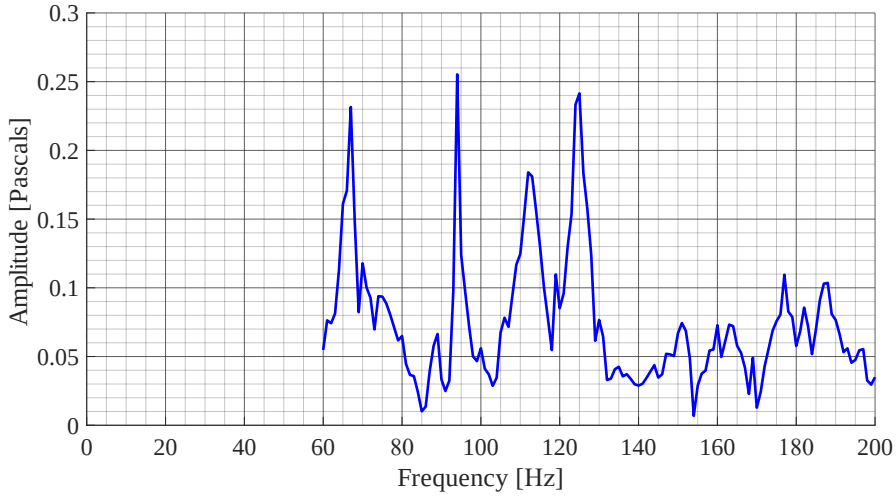

Fig. 11.12 Response measured by microphone on the draft tube at $v_{inlet} = 10\ ms^{-1}$

11.1.3 Experiment - Angle of Attack 5°

Experimental investigation of damping ratio was also carried out for hydrofoil with 5° angle of attack. The 5° incidence angle was the highest acceptable value of angle due to the significant increase of hydrofoil vibration amplitudes. Further increase of incidence angle may result in damage of both the hydrofoil and the test section. As the angle of attack was increased, the flow becomes strongly turbulent and massive boundary layer separation was observed. Therefore, the hydrofoil response was measured in limited range of flow velocity 0 ms^{-1} – 12.5 ms^{-1} with a step of 2.5 ms^{-1} with no presence of cavitation. In addition, the measurement of hydrofoil response in air was performed. The non-dimensional FRF of the hydrofoil was calculated by same procedure as in previous measurement (see Chapter 7.2.2). The results are presented in the following figures (Fig. 11.13 – Fig. 11.19). Due to the strongly turbulent flow and high vibration amplitudes, the evaluation of damping ratio was not possible at all measured flow velocities. Therefore, only results from one vibrometer LDV 1 are presented in range of flow velocity 0 ms^{-1} – 10 ms^{-1}.

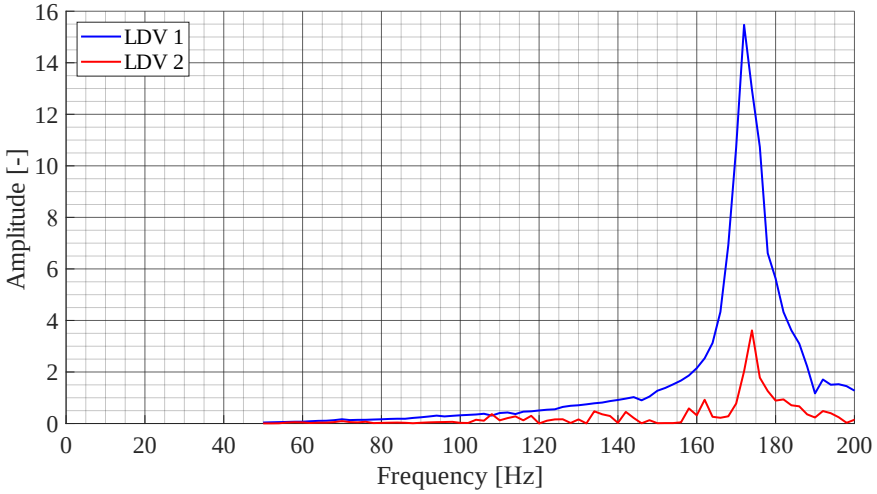

Fig. 11.13 FRF of hydrofoil in air ($\alpha_{inc} = 5°$)

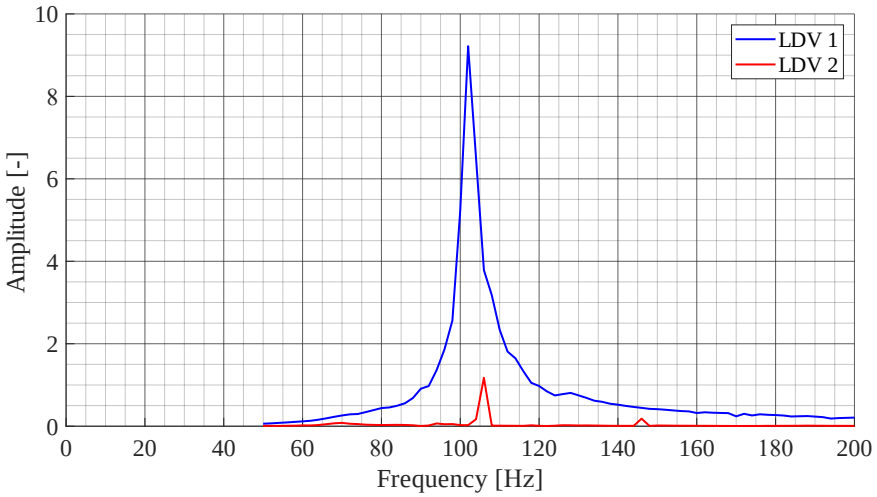

Fig. 11.14 FRF of hydrofoil at $v_{inlet} = 0\ ms^{-1}$ ($\alpha_{inc} = 5°$)

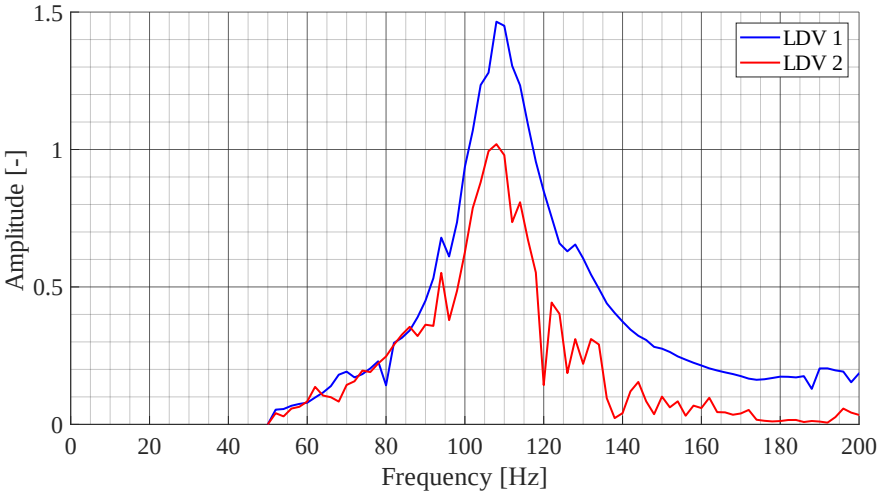

Fig. 11.15 FRF of hydrofoil at $v_{inlet} = 2.5\ ms^{-1}$ ($\alpha_{inc} = 5°$)

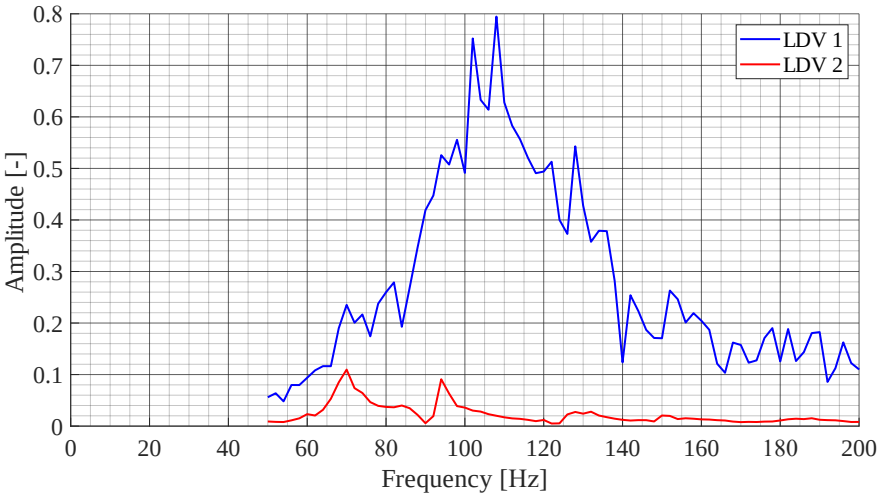

Fig. 11.16 FRF of hydrofoil at $v_{inlet} = 5\ ms^{-1}$ ($\alpha_{inc} = 5°$)

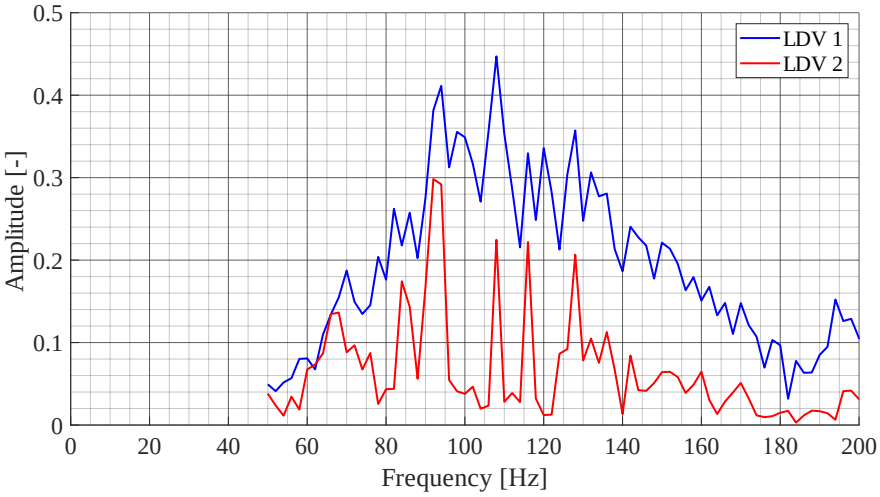

Fig. 11.17 FRF of hydrofoil at $v_{inlet} = 7.5\ ms^{-1}$ ($\alpha_{inc} = 5°$)

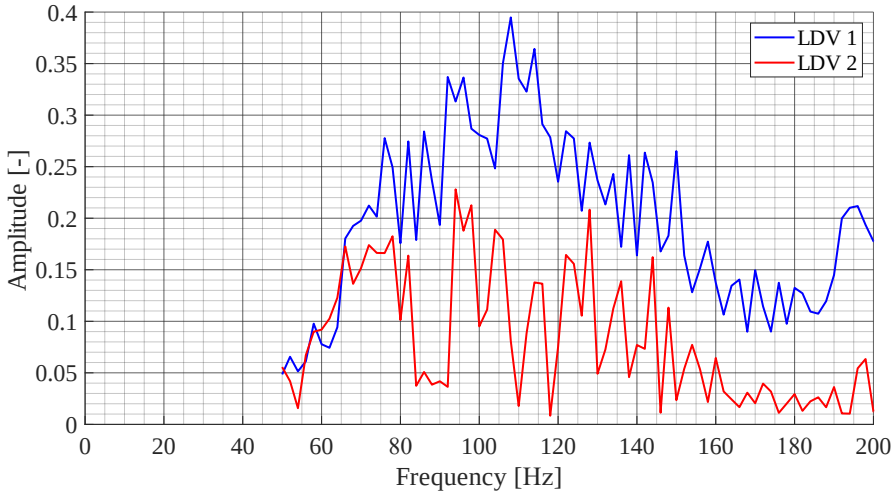

Fig. 11.18 FRF of hydrofoil at $v_{inlet} = 10\ ms^{-1}$ ($\alpha_{inc} = 5°$)

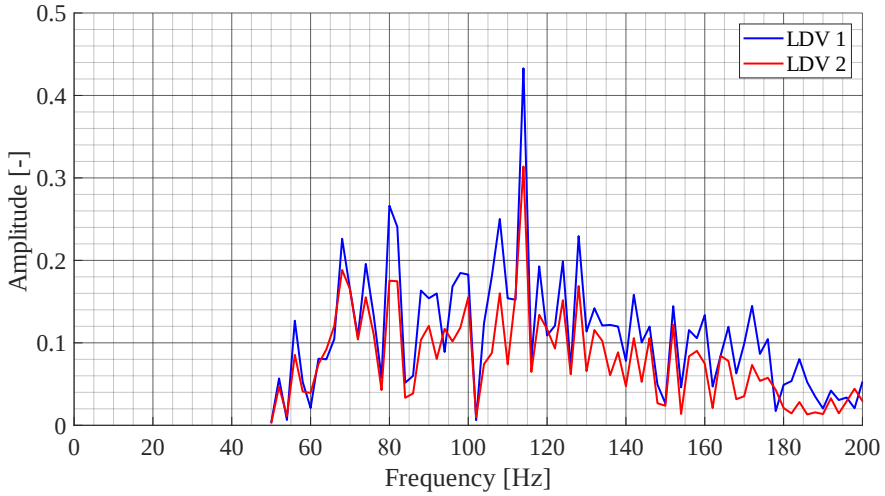

Fig. 11.19 FRF of hydrofoil at $v_{inlet} = 12.5\ ms^{-1}$ ($\alpha_{inc} = 5°$)

The obtained FRF of the hydrofoil were approximated by SDOF Response Fit method. As the post-processed FRF were highly influenced by the dynamics of the flow, the evaluation of damping ratio was not possible for all cases. Main results were obtained from vibrometer LDV 1 which was pointed to location of highest mode shape deflections.

The structural damping obtained by vibrometer LDV 1 is two times higher than the value measured by same vibrometer at zero incidence angle while the value measured by the other vibrometer LDV 2 increased only about 7.5 %. The identified value of damped natural frequency in air does not differ from the values measured at zero angle of attack (see Table 30).

Two following figures (Fig. 11.20, Fig. 11.21) show approximation of FRF by SDOF Response Fit method at zero flow velocity. Approximation of all evaluated cases can be found in Appendix A.6. The obtained values of both the damping ratio and the damped natural frequency are summarized in Table 31 and figure Fig. 11.22.

Table 30 Structural damping calculated by SDOF Response Fit method

LDV 1		LDV 2		
$f_{NAT,SDOF,1}$	$\zeta_{SDOF,LDV1}$	$f_{NAT,SDOF,2}$	$\zeta_{SDOF,LDV2}$	$\Delta\,\zeta$
[Hz]	[1]	[Hz]	[1]	[%]
172.74	0.01337	173.75	0.00941	29.61

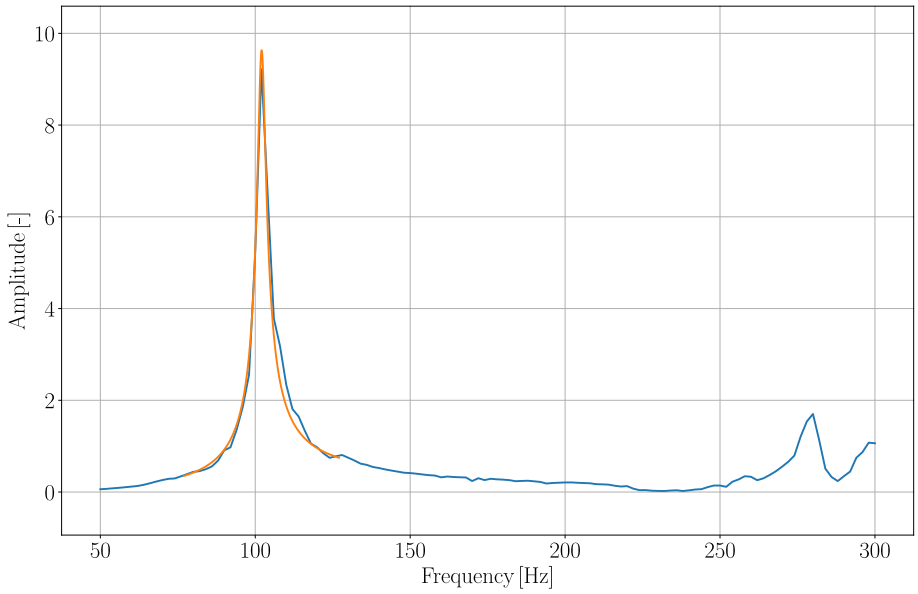

Fig. 11.20 Approximation of FRF at $v_{inlet} = 0\ ms^{-1}$ – amplitude LDV 1 ($\alpha_{inc} = 5°$)

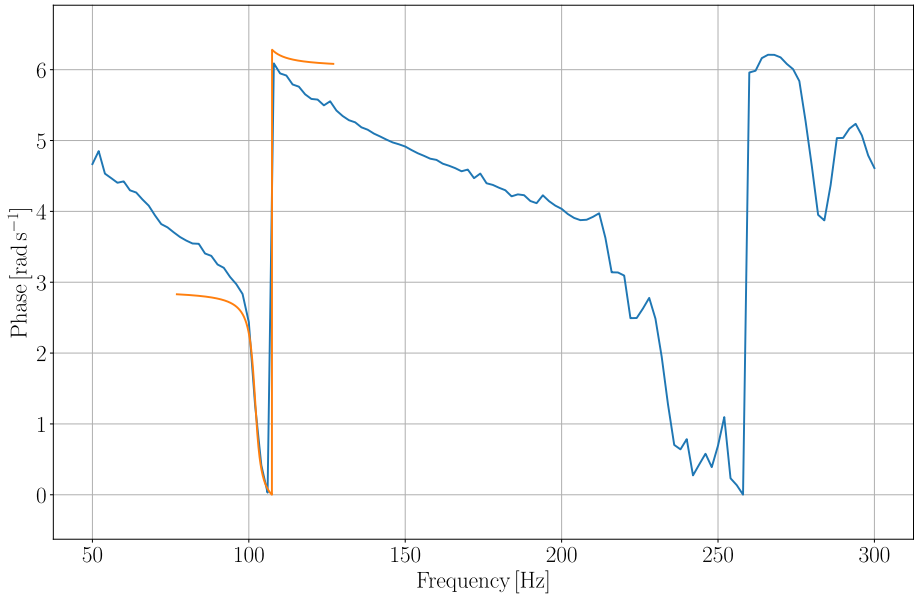

Fig. 11.21 Approximation of FRF at $v_{inlet} = 0\ ms^{-1}$ – phase LDV 1 ($\alpha_{inc} = 5°$)

Table 31 Results of SDOF Response Fit method ($\alpha_{inc} = 5°$)

	LDV 1		LDV 2			
v_{inlet}	$f_{NAT,SDOF,1}$	$\zeta_{SDOF,LDV1}$	$f_{NAT,SDOF,2}$	$\zeta_{SDOF,LDV2}$	Δf	$\Delta \zeta$
[ms^{-1}]	[Hz]	[1]	[Hz]	[1]	[%]	[%]
0	102.04	0.01379	106.11	0.00034	3.99	97.53
2.5	108.56	0.04798	107.41	0.04751	1.05	0.99
5	106.46	0.07891	-	-	-	-
7.5	101.90	0.12204	-	-	-	-
10	101.28	0.13809	-	-	-	-
12.5	-	-	-	-	-	-

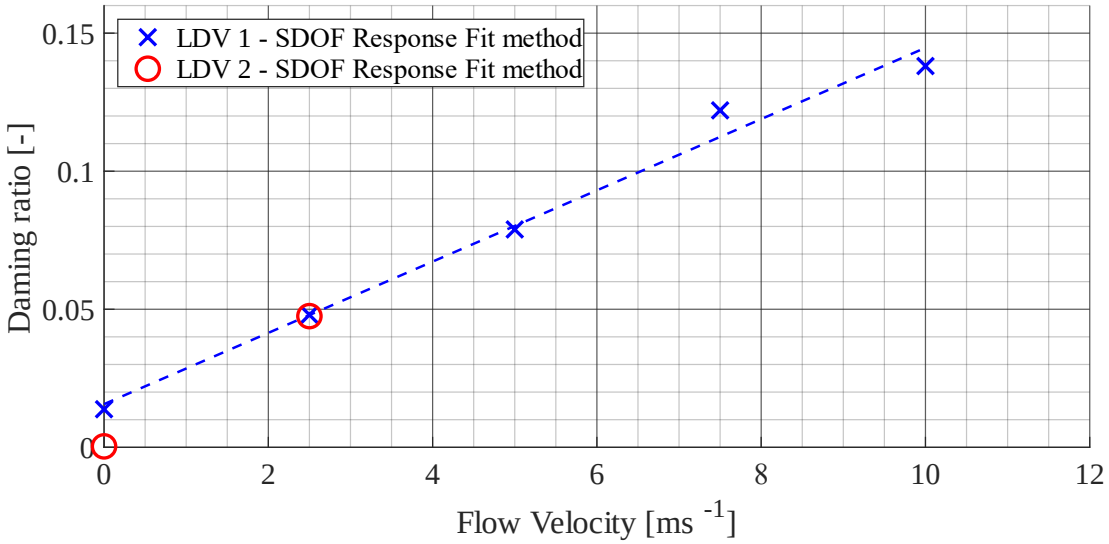

Fig. 11.22 Overview of experimental values of damping ratio ($\alpha_{inc} = 5°$)

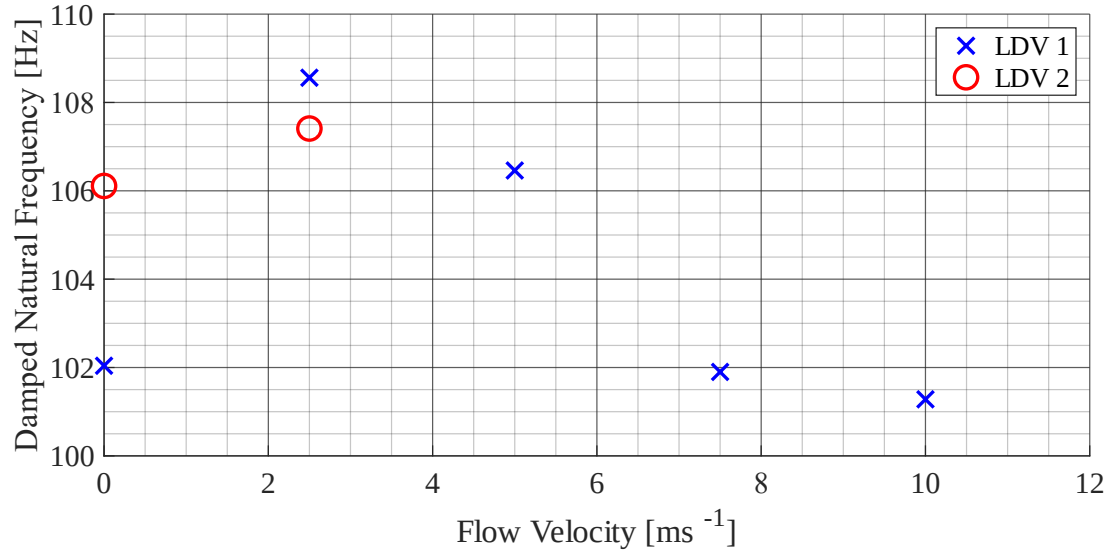

Fig. 11.23 Damped natural frequency $f_{NAT,SDOF,1,2}$ ($\alpha_{inc} = 5°$)

The values of damping ratio obtained by vibrometer LDV 1 have a linear increasing trend in whole measured range of flow velocity. The corresponding values measured by the other vibrometer LDV 2 are available only in still water and at flow velocity 2.5 ms^{-1}. In case of still water, the vibrometer LDV 2 underestimates the first vibrometer by 97.5 %. This discrepancy is a result of very low amplitude values measured by vibrometer LDV 2. This was probably caused by some technical issue such as contact between the hydrofoil and wall of the test section. In the second case (2.5 ms^{-1}), both vibrometers provide same value of damping ratio measured with maximal difference 1 %. Unfortunately, the evaluation of results from vibrometer LDV 2 at higher values of flow velocity was not possible. The identified values of damped natural frequency do not show any significant trend (Fig. 11.23).

The comparison of damping ratio obtained by SDOF Response Fit method from both vibrometers shows that the angle of attack 5° has no significant impact on the values of damping ratio. Both configurations of incidence angle perform same linear increasing trend (Fig. 11.24).

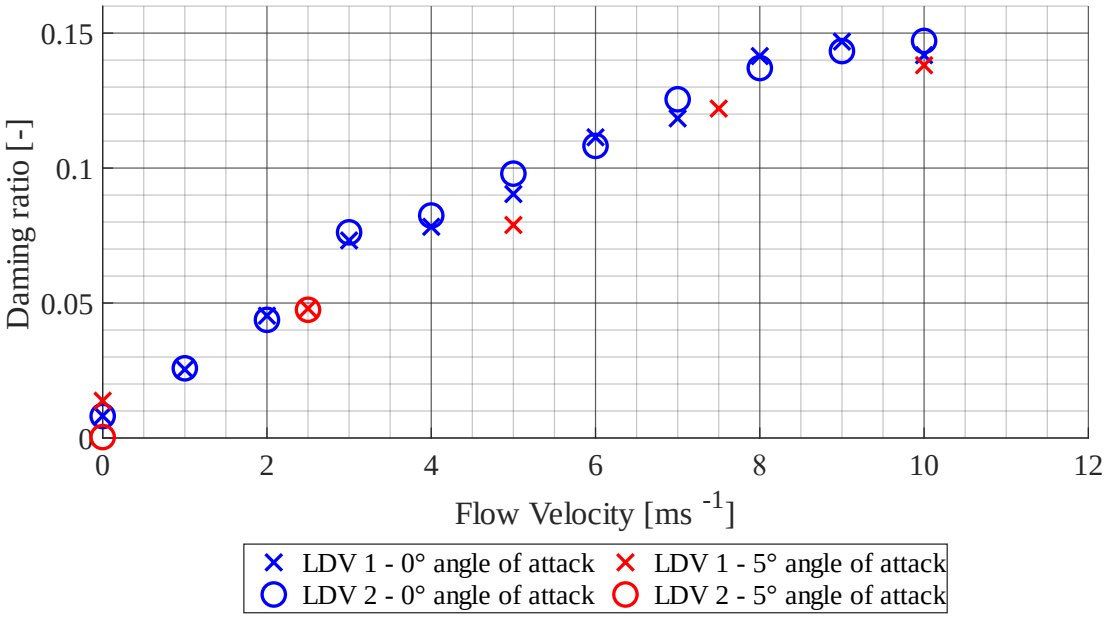

Fig. 11.24 Comparison of damping ratio calculated by SDOF Response Fit method

11.2 Numerical Simulation

Numerical investigation of damping ratio was carried out with the use of modified Modal Work Approach which involved both the unsteady CFD analysis and the static structural analysis. The first natural mode shape of the hydrofoil (Fig. 11.25) was prescribed as a periodic motion with maximal amplitude $U_{MAX} = 1e^{-5}\, m$ and corresponding frequency $f_{nat,SW,FEM} = 104.15\, Hz$ to the hydrofoil surface in the CFD analysis. Main output of the calculation was the dissipated energy W_{DISS} which is energy exchanged between hydrofoil and fluid (also called "*modal work*") during a single blade oscillation period. Then, the elastic strain energy was calculated by applying deformation load on the hydrofoil in steady structural analysis. The deformed shape corresponded to the analysed mode shape with same maximal amplitude U_{MAX} as prescribed in the unsteady CFD simulation. This approach simulates moment of maximum deflection during the periodic motion, when the total energy E_{TOT} of the oscillation (potential and kinetic energy) is accumulated into deformation, i.e. E_{TOT} is equal to the elastic strain energy. The damping ratio ζ was calculated as a ratio of dissipated energy W_{DISS} and elastic strain energy E_{TOT}. Numerical investigation of damping ratio was calculated with flow velocity 0 ms^{-1} – 20 ms^{-1}. The pressure field behind the hydrofoil trailing at 10 ms^{-1} is shown in figure Fig. 11.26 (pressure field at all other analysed flow velocities can be found in Appendix A.7). Detailed description of Modal Work Approach and analyses settings can be found in Chapter 8.3.

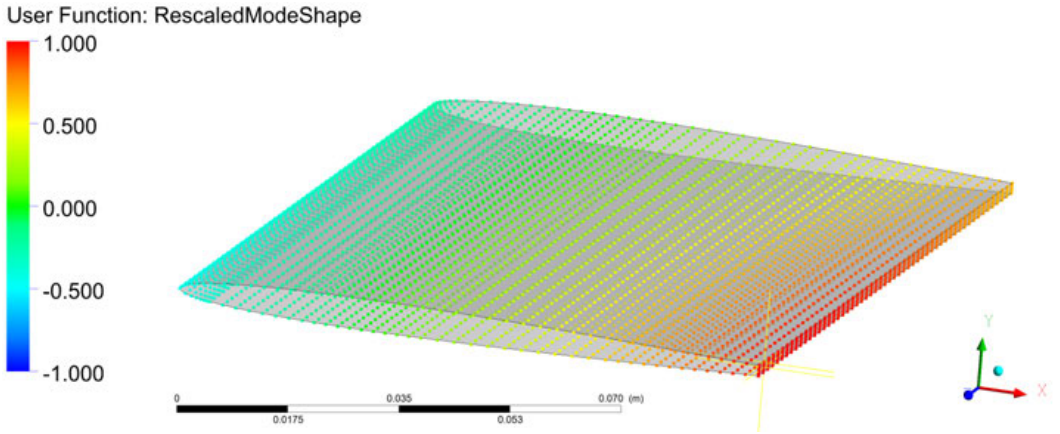

Fig. 11.25 Normalized y-component of prescribed mode shape;$f_{nat,SW,FEM} = 104.15\, Hz$

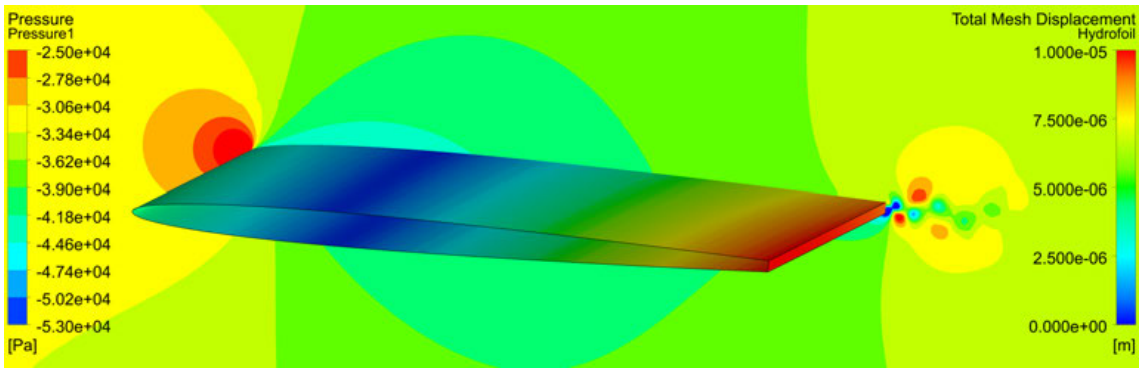

Fig. 11.26 Pressure field from unsteady CFD with prescribed motion at $v_{inlet} = 10\, ms^{-1}$

Typical behaviour of dissipated energy in time can be seen in the figure (Fig. 11.27). The prescribed oscillations of hydrofoil are marked by red colour. The dissipated energy calculated by "*Full Period Interval*" has constant value which changes at the end of each blade oscillation. The blue coloured values are obtained by integration of "*Moving Interval*" which integrates a moving window of last 300 time-steps during the blade motion. This behaviour was also observed by Nennemann [61]. Average values of dissipated energy during last five blade periods from the total of fifteen calculated periods were used to calculate the damping ratio.

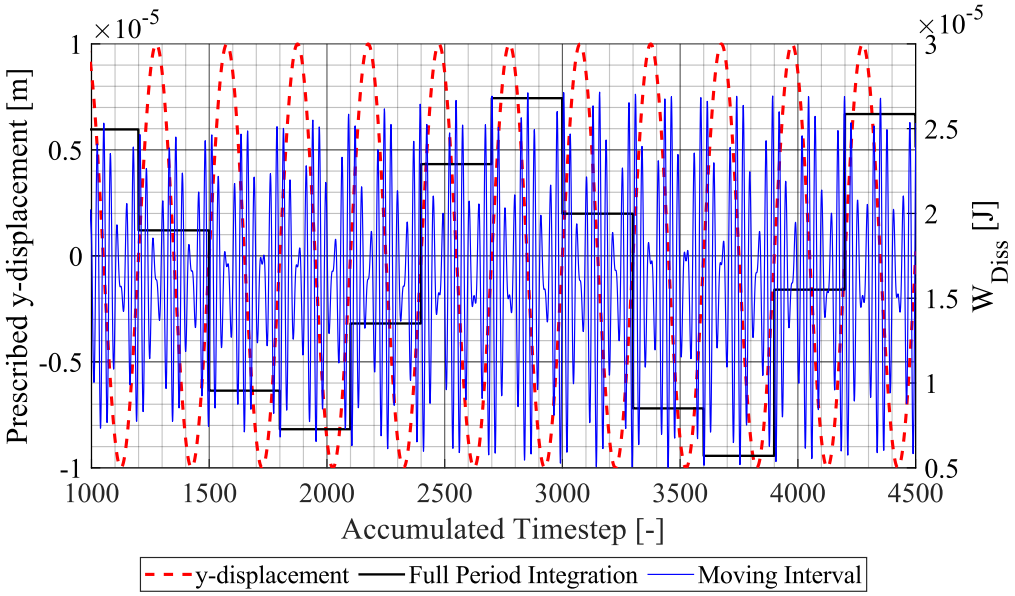

Fig. 11.27 Dissipated Energy (modal work) as a function of time at $v_{inlet} = 10\ ms^{-1}$

The values of dissipated energy W_{DISS} calculated by both types of integration were positive throughout the simulated time at all values of flow velocity. The only case when the values of W_{DISS} were temporarily negative was observed at flow velocity 1 ms^{-1} (see Fig. 11.28). In this figure, the negative value of W_{DISS} is observed in the range of time-steps 2400 – 3300.

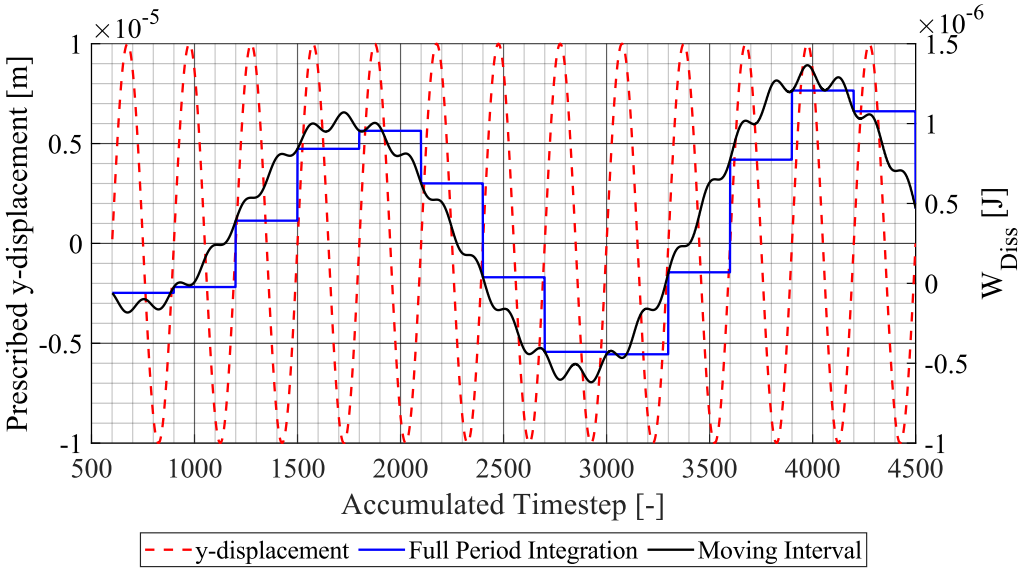

Fig. 11.28 Dissipated Energy (modal work) as a function of time at $v_{inlet} = 1\ ms^{-1}$

This temporary negative value of dissipated energy occurs when the ratio of vortex shedding frequency and frequency of prescribed hydrofoil motion $f_{Kármán}/f_{Prescribed}$ is very close or equal to the value of 1. A sudden drop in damping ratio which decreased to negative values was observed by Miyagawa [84] in 2-way coupled simulation for ratio $f_{Kármán} / f_{Prescribed} = 1$. The negative value of damping and presence of high vibration amplitudes were interpreted as a result of self-excitation.

A detailed investigation of the energy transfer between the hydrofoil structure and the flow was carried out by Nennemann [61]. The presented sensitivity study of stay vane damping on three main parameters (flow velocity, prescribed amplitude U_{MAX} and prescribed hydrofoil frequency $f_{Prescribed}$) resulted in the following conclusion: The transfer of dissipated energy from the oscillating hydrofoil to the fluid in the presence of von Kármán vortices results generally in positive damping. Based on the presented hypothesis, one of the main mechanisms of energy transfer from the hydrofoil to the fluid is very similar to von Kármán vortices. As the hydrofoil performs the prescribed harmonic motion, vortices with frequency $f_{Prescribed}$ are formed behind the trailing edge. These vortices were observed in unsteady CFD simulation in [61]. As the wave length $v_{inlet} / f_{Prescribed}$ of hydrofoil oscillations is getting close to the wave length of von Kármán vortices $v_{inlet} / f_{Kármán}$, the damping ratio becomes very strongly dependent on amplitude U_{MAX} and varies from negative to positive values. Then the excitation and dissipation arise from two very similar phenomena – shedding of vortices. It is assumed that an apparent hydrodynamic damping $\zeta_{Kármán}$ is exhibited by the system. This damping $\zeta_{Kármán}$ is a function of both the frequency ratio and the prescribed amplitude and makes the system non-linear $\zeta_{Kármán} = f\,(f_{Kármán} / f_{Prescribed};\ U_{MAX})$. When $f_{Kármán} / f_{Prescribed} = 1$, the increasing vibration amplitude U_{MAX} causes the increase of the hydrodynamic damping until a limit value of amplitude U_{MAX} is reached. [61]

The vortex shedding frequency at flow velocity 1 ms^{-1} can be estimated by equation (10.3) $f_{Karman,St} = 122.7\ Hz$ and compared to the measured value $f_{Karman,EXP1} = 108.2\ Hz$. Both of these values are very close to the prescribed frequency $f_{Prescribed} = 104.15\ Hz$. The presence of negative value of dissipated energy is only temporary and mean values of W_{DISS} are positive at all simulated flow velocities. Since the first natural frequency of the hydrofoil was very low (104.15 Hz), the vortex shedding at this frequency was measured at flow velocity below 1 ms^{-1}. The amplitudes of both the pressure and the hydrofoil oscillations were very low. Moreover, due to the low flow velocity it was not possible to investigate the damping ratio in the region of flow velocity below the lock-in. For the above mentioned technical reasons, further investigation of damping ratio in the lock-in region was not possible.

The second step of modified Modal Work Approach was calculation of elastic strain energy E_{TOT}. The normalized components of displacement *UX*, *UY* and *UZ* of the hydrofoil first mode shape were exported from all nodes in the volume of the hydraulic profile except the shaft on both sides of the hydrofoil. As the shaft is not present in the unsteady CFD analysis, the harmonic oscillations in CFD analysis are prescribed only to the hydraulic profile. Therefore, the displacement load in the steady structural analysis was applied only to the nodes of the hydraulic profile.

The exported mode shape was rescaled to satisfy the following condition in the node with maximal total displacement $\sqrt{U_X^2 + U_Y^2 + U_Z^2} = U_{MAX}$. Here, the maximal value of total displacement must be equal to the prescribed amplitude in unsteady CFD analysis ($U_{MAX} = 1 \cdot 10^{-5}\ m$).

Since the mesh in the CFD analysis which is attached to the vertical walls of the test section cannot move in axial direction of the shaft (displacement *UZ*), the same boundary condition *UZ* = 0 was applied on both sides of the hydrofoil structure except the shaft cross-sections. The mounting of the hydrofoil in the test section was simulated by same boundary conditions as in modal analyses (i.e. three bearings and two displacement boundary conditions each applied at one end of the shaft – see Fig. 8.4).

Deformed shape of the hydrofoil calculated by the steady structural analysis corresponds to the hydrofoil mode shape obtained by modal analyses (Fig. 11.29). The maximal value of equivalent stress was 4 MPa (Fig. 11.32, Fig. 11.33). The elastic strain energy was calculated for two different regions (Fig. 11.30, Fig. 11.31). In the first case, the sum of elastic strain energy was calculated over the elements of hydraulic profile (damping ratio $\zeta_{CFD,P}$). This corresponds to the harmonic motion in the unsteady CFD analysis which was prescribed only to the profile. In the second case, the sum of elastic strain energy was calculated over all elements of both the profile and the shaft (damping ratio $\zeta_{CFD,PS}$). Then, the damping ratio was calculated by equation (8.11). The obtained values of damping ratio for both two cases are presented in Table 32 and compared to the experimental values.

Additionally, the damping ratio $\zeta_{CFD,MOD}$) was evaluated by equation (8.10). Here, the modal mass M = 1 kg·m^2 [58], ω_0 is undamped natural angular frequency in still water and $U_{MAX} = 1 \cdot 10^{-5}\, m$. The obtained values are presented in Table 33 and compared to the results of modified Modal Work Approach in the graph (Fig. 11.34).

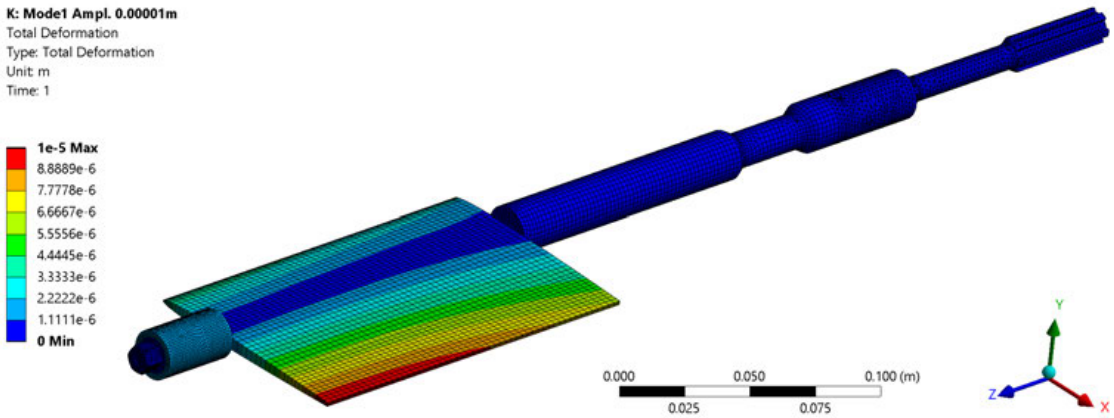

Fig. 11.29 Deformed shape of hydrofoil obtained from steady structural analysis

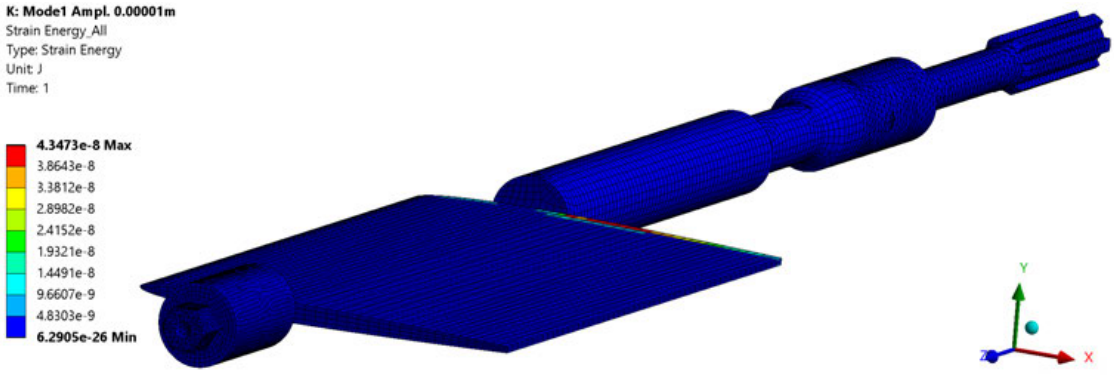

Fig. 11.30 Elastic strain energy E_{TOT} of the hydrofoil ($U_{MAX} = 1 \cdot 10^{-5}\, m$)

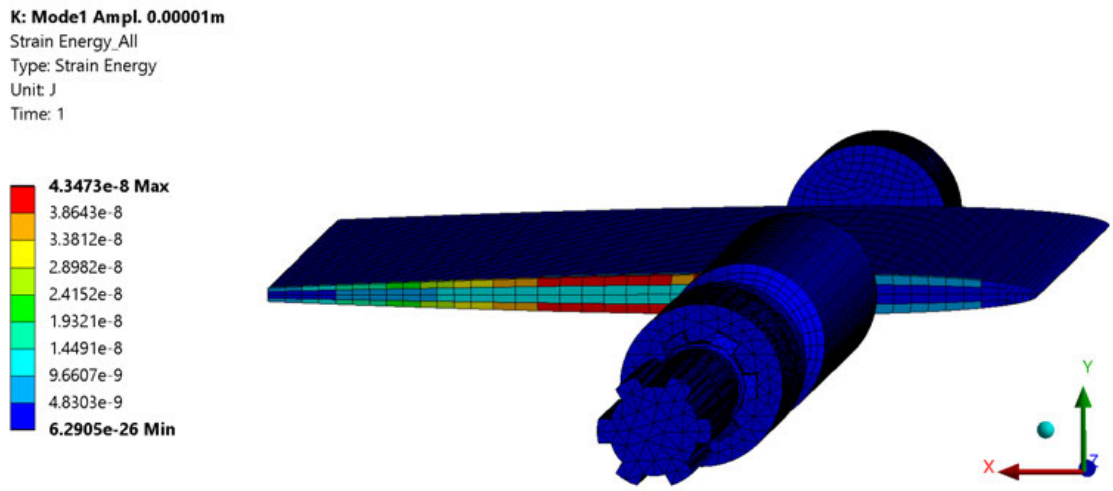

Fig. 11.31 Elastic strain energy E_{TOT} of the hydrofoil ($U_{MAX} = 1 \cdot 10^{-5}\ m$)

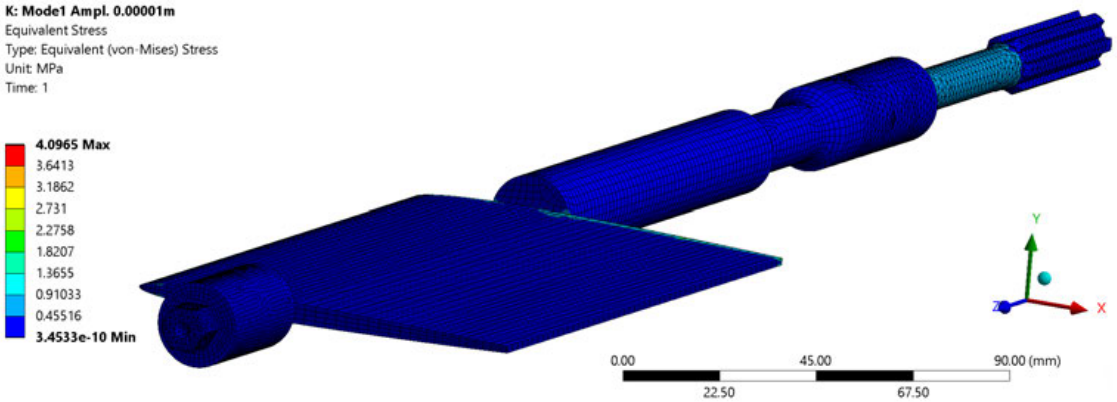

Fig. 11.32 Distribution of equivalent stress on the hydrofoil ($U_{MAX} = 1 \cdot 10^{-5}\ m$)

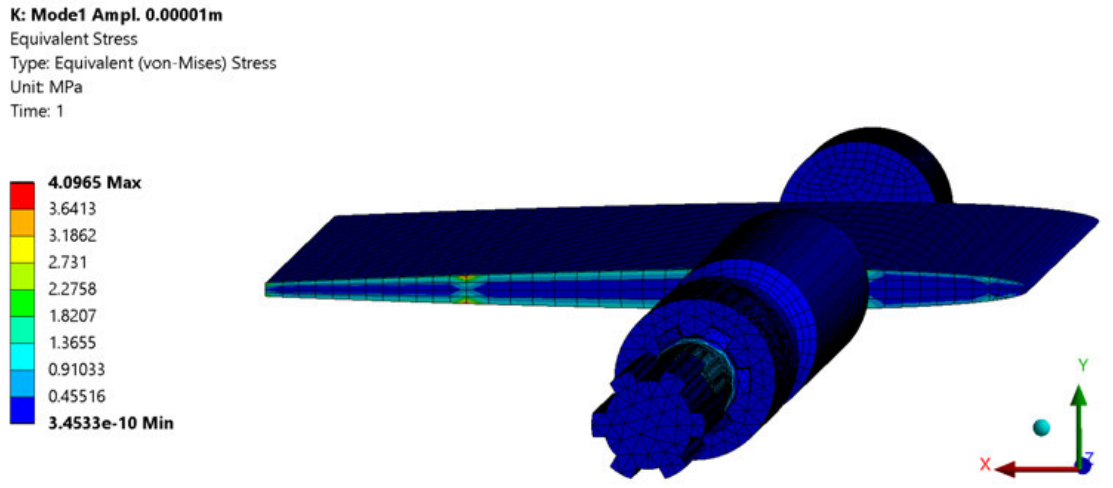

Fig. 11.33 Distribution of equivalent stress on the hydrofoil ($U_{MAX} = 1 \cdot 10^{-5}\ m$)

Table 32 Damping ratio calculated by modified Modal Work Approach ($\alpha_{inc} = 0°$)

E_{TOT}:	Only profile		Profile and shaft		Experiment	
v_{inlet}	$\zeta_{CFD,P}$	$\Delta\,\zeta$	$\zeta_{CFD,PS}$	$\Delta\,\zeta$	$\zeta_{SDOF,LDV1}$	$\zeta_{SDOF,LDV2}$
[ms^{-1}]	[1]	[%]	[Hz]	[%]	[1]	[1]
0	0.00637	22.24	0.00389	52.46	0.00819	0.00813
1	0.00794	68.77	0.00485	80.91	0.02542	0.02582
2	0.05691	25.63	0.03479	23.19	0.04530	0.04377
2.5	0.07328	-	0.04480	-	-	-
3	0.09596	31.11	0.05866	19.85	0.07319	0.07620
4	0.13026	66.49	0.07964	1.79	0.07824	0.08243
5	0.16584	83.49	0.10139	12.18	0.09038	0.09794
6	0.19932	78.92	0.12186	9.39	0.11140	0.10821
7	0.23005	94.30	0.14065	18.79	0.11840	0.12548
7.5	0.24469	-	0.14959	-	-	-
8	0.25826	82.53	0.15789	11.59	0.14149	0.13706
9	0.30237	105.90	0.18486	25.88	0.14685	0.14334
10	0.33421	135.64	0.20433	44.07	0.14183	0.14710
12.5	0.41169	-	0.25169	-	-	-
15	0.49674	-	0.30369	-	-	-
17.5	0.59555	-	0.36410	-	-	-
20	0.67522	-	0.41281	-	-	-

$$\Delta\,\zeta = \frac{\left|\zeta_{CFD,P(S)} - \zeta_{SDOF,LDV1}\right|}{\zeta_{SDOF,LDV1}} \cdot 100\ \% \qquad (11.6)$$

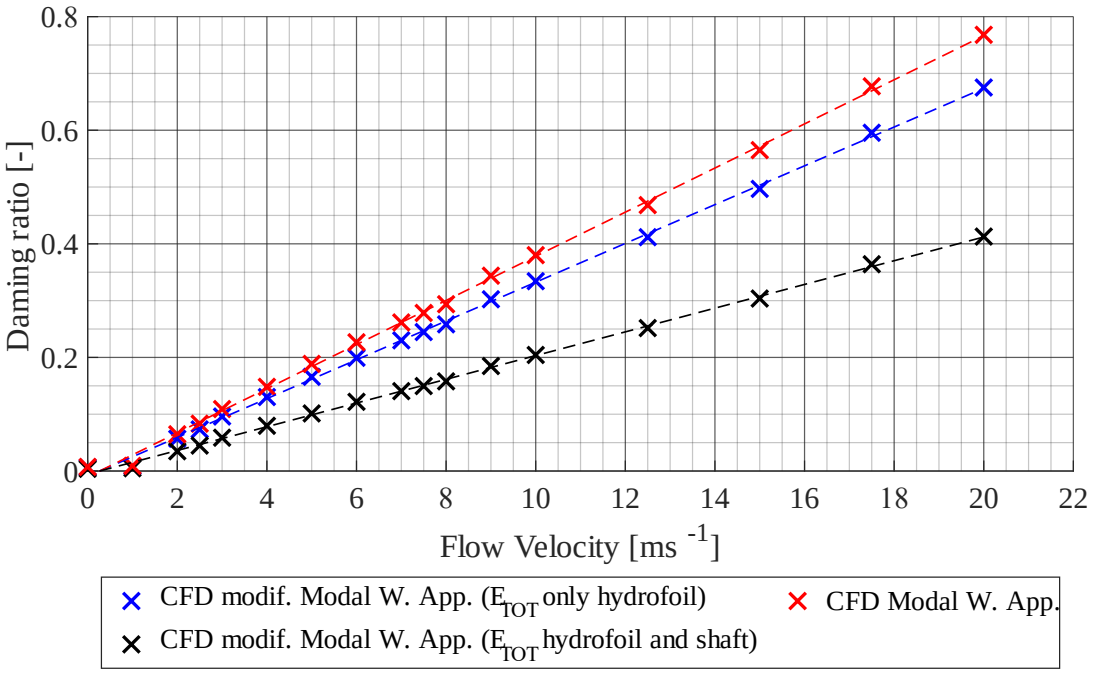

Fig. 11.34 Damping ratio calculated from unsteady CFD analysis ($\alpha_{inc} = 0°$)

Table 33 Damping ratio calculated by Modal Work Approach ($\alpha_{inc} = 0°$)

E_{TOT}:	Modal Work App.		Experiment	
v_{inlet}	$\zeta_{CFD,MOD}$	$\Delta\,\zeta$	$\zeta_{SDOF,LDV1}$	$\zeta_{SDOF,LDV2}$
[ms^{-1}]	[1]	[%]	[1]	[1]
0	0.00724	11.56	0.00819	0.00813
1	0.00903	64.48	0.02542	0.02582
2	0.06473	42.89	0.04530	0.04377
2.5	0.08335	-	-	-
3	0.10913	49.11	0.07319	0.07620
4	0.14815	89.36	0.07824	0.08243
5	0.18861	108.69	0.09038	0.09794
6	0.22670	103.50	0.11140	0.10821
7	0.26165	120.99	0.11840	0.12548
7.5	0.27829	-	-	-
8	0.29373	107.60	0.14149	0.13706
9	0.34389	134.18	0.14685	0.14334
10	0.38011	168.01	0.14183	0.14710
12.5	0.46823	-	-	-
15	0.56496	-	-	-
17.5	0.67734	-	-	-
20	0.76795	-	-	-

$$\Delta\,\zeta = \frac{\left|\zeta_{CFD,MOD} - \zeta_{SDOF,LDV1}\right|}{\zeta_{SDOF,LDV1}} \cdot 100\ \% \qquad (11.7)$$

All three procedures of damping ratio evaluation provide results with linear increasing trend. The values calculated by sum of elastic strain energy only over hydrofoil highly overestimates the experimental values from both vibrometers. The same behaviour is observed by results of Modal Work Approach without considering the steady structural analysis.

The best agreement between the experimental and numerical results is achieved by values of damping ratio calculated from a sum of elastic strain energy over both the hydrofoil and the shaft (Fig. 11.35). The calculated value of damping ratio for hydrofoil submerged in still water underestimates the experimental value by 52 %. The maximal difference between this approach and experimental results is observed at 1 ms^{-1} (81 %). It should be noted that vortex shedding frequency at this flow velocity is very close to the hydrofoil first natural frequency. This difference may be caused by nonlinear behaviour of the hydrofoil in the lock-in region. Numerical values underestimate the experimental values in the range of flow velocity 2 ms^{-1} – 3 ms^{-1} by 20 – 23 %. The experimental values at 3 ms^{-1} are significantly influenced by lock-in at frequency 839 Hz which was observed in the experimental investigation of vortex shedding frequency. However, as the hydrofoil structure was not present in the numerical model, this behaviour cannot be captured in the simulation. By further increasing of the flow velocity above 4 ms^{-1} (difference about 1.8 %) the numerical results overestimate the experimental values up to 44 % (10 ms^{-1}). The higher difference between

the experimental and numerical results at 9 ms^{-1} – 10 ms^{-1} is caused by change of linear trend in experimental values.

Significant differences in various numerical techniques of damping ratio investigation show that the numerical results are very sensitive to the applied boundary conditions. The model of guide vane which was analysed in this research was designed to study a realistic behaviour of the blade. The modified Modal Work Approach was developed and tested on a single hydrofoil which was fully fixed on its both sides. The obtained results on such simple case were in very good agreement with the experimental values. As a further step, this technique was applied on a realistic model of guide vane in this research project. The obtained results showed that the applied boundary conditions have major impact on the obtained values. Therefore, further investigation of this technique may improve its accuracy.

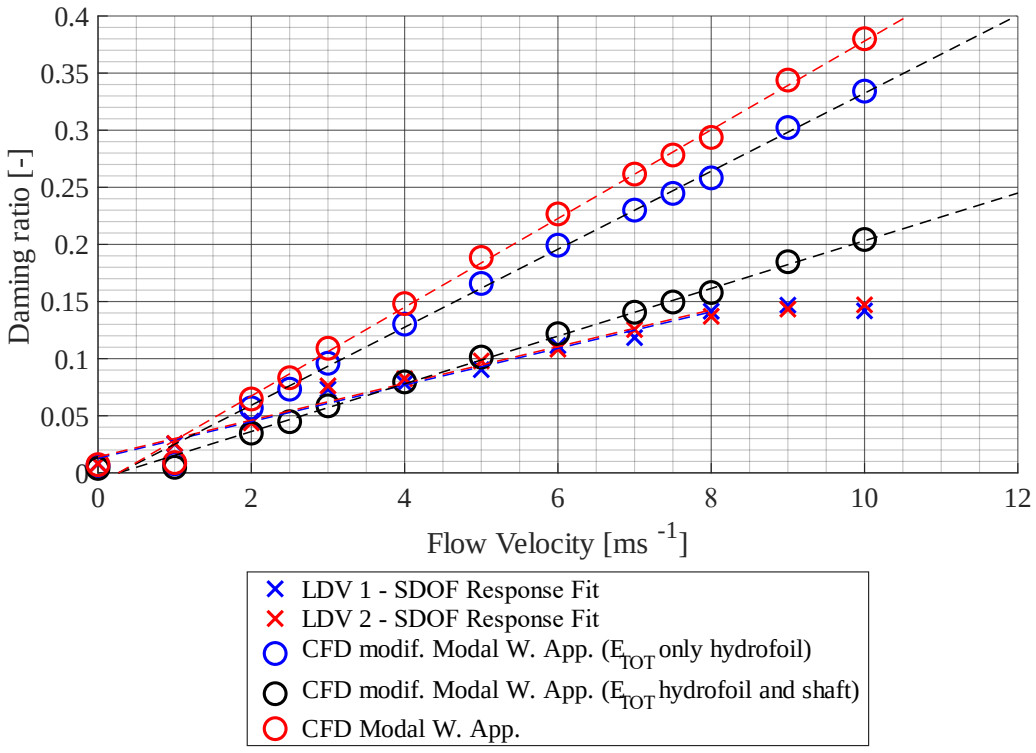

Fig. 11.35 Comparison of damping ratio from experiment and numerical analysis

11.3 Partial Conclusion - Hydrodynamic Damping

The total damping of hydrofoil b_{TOT} which oscillates in a fluid flow consists of three main contributions: the structural damping b_S, the hydrodynamic damping b_F and b_W which results from the acoustic radiation and from the viscous effects in the liquid. Experimental measurement enables to measure the structural damping b_S (enforced vibrations of the hydrofoil in air) or the total damping b_{TOT} (enforced vibrations of the hydrofoil in a fluid flow). Since the structural damping is very low and the water can be considered as incompressible ($b_W \approx 0$), the main contribution of the total damping is from the viscous – hydrodynamic damping b_F. Therefore, the experimental value of total damping was compared to the hydrodynamic damping calculated by unsteady CFD simulation with prescribed harmonic motion of the hydrofoil.

Experimental measurement of hydrofoil response on harmonic excitation was used for calculation of Frequency Response Function (FRF). The damping ratio of the hydrofoil first mode was evaluated by approximation of FRF by SDOF Response Fit Method. In addition, the damping ratio was estimated by introducing a non-dimensional excitation force with the use of amplification factor. However, the accuracy of this approach depends on the calibration of the non-dimensional excitation force and cannot be used as a separate method.

The structural damping of the first mode of the hydrofoil was evaluated from the measurement of hydrofoil enforced vibrations in air. This measurement was carried out for two values of angle of attack: 0° and 5°. The obtained values of the damping ratio from two vibrometers at zero angle of attack differ by 37 % (LDV 1: 0.6 %; LDV 2: 0.9 %), while the results measured at 5° incidence angle differ by 30 % (LDV 1: 1.3 %; LDV 2: 0.9 %). The difference between the damping ratio measured for various values of incidence angle is probably caused by different properties of the mounting caused by manipulation with the hydrofoil.

The measured value of hydrodynamic damping at zero angle of attack in still water is 0.8 %. This value was measured by both vibrometers and is comparable with the value of structural damping. As the flow velocity rises, the damping ratio has linear increasing trend in range of flow velocity 1 ms^{-1} – 8 ms^{-1}. Then a constant value of damping ratio 0.14 is observed in range of flow velocity 8 ms^{-1} – 10 ms^{-1}. The values of the damped natural frequency obtained by both vibrometers are significantly decreasing with increase of flow velocity. This behaviour may be caused by the increase of added mass effect m_{ADD} or the decrease of fluid added stiffness k_F. As the mechanical system is analysed with the use of linearized models, the observed drop of the first natural frequency may be the result of nonlinear behaviour of the analysed system.

Experimental measurement of hydrodynamic damping at 5° incidence angle showed that the incidence angle of 5° has no significant impact on the hydrodynamic damping in whole range of flow velocity 0 ms^{-1} – 10 ms^{-1}. The evaluated values of damping ratio do not significantly differ from the values obtained at zero angle of attack. The same linear increasing trend is observed.

Numerical investigation of hydrodynamic damping was carried out for hydrofoil with zero angle of attack. In the first step, the dissipated energy per blade oscillation was calculated by unsteady CFD analysis with prescribed harmonic motion of the hydrofoil. Then total energy of the hydrofoil which is a sum of kinetic and potential energy was calculated by steady structural analysis. Here the elastic strain energy was summed over

the hydrofoil and its shaft. Finally, the damping ratio of the first mode of the hydrofoil was calculated as a ratio of the dissipated energy and the total energy of the motion.

This approach is sensitive to the applied boundary conditions in the structural analysis and proper calculation of elastic strain energy. On the one hand, the sum of elastic strain energy over hydrofoil except the shaft resulted in highly overestimated values of damping ratio. On the other hand, the sum of elastic strain energy over hydrofoil and its shaft provide results which correspond with the experimental values. Additionally, the damping ratio was evaluated from the same unsteady CFD analysis by Modal Work Approach. The obtained values of damping ratio highly overestimated the experimental results.

12 HYDROFOIL OSCILLATIONS UNDER CAVITATION CONDITIONS

The presence of cavitation has a negative impact on the hydraulic parameters of turbines and may result in cavitation damage of turbine components. Modern hydraulic turbines are designed to provide high efficiency in wide operating range, i.e. 10 – 150 % of optimal flow rate. The presence of cavitation in such wide operating range cannot be avoided. Therefore, the influence of cavitation on dynamic response of turbine components needs to be studied.

In this chapter, two types of experimental measurements are presented. The first measurement was focused on the investigation of flow induced vibrations under cavitation conditions, while the other measurement was carried out to study enforced vibrations of hydrofoil and investigation of hydrodynamic damping. Both measurements were carried out in range of flow velocity 5 ms^{-1} – 12.5 ms^{-1} with angle of attack 5°. This range of flow velocity resulted from minimal and maximal values of pressure which were possible to maintain in the test circuit. Three different values of cavitation number σ were selected at each flow velocity. These three cases corresponded to three sizes of sheet cavitation: one third and two thirds of the chord length behind the leading edge and sheet cavitation over whole hydrofoil.

The influence of cavitation on hydrofoil modal properties was calculated by acoustic modal analysis. The key parameters which control the added mass effect are the size of cavitation cloud and its physical properties (density and speed of sound of a mixture inside the cavitation cloud). The presented approach is based on simplified assumptions and estimates the change of modal properties for various physical and geometrical parameters of the cavitation cloud.

12.1 Flow Induced Vibrations – Angle of Attack 5°

Flow induced vibrations were investigated in range of flow velocity 5 ms^{-1} – 12.5 ms^{-1} with step of 1 ms^{-1}. Due to the limits of vacuum pump, it was not possible to observe sheet cavitation over whole hydrofoil at flow velocity below 8 ms^{-1}. Therefore, only two measurements are presented at lower values of flow velocity.

The experimental setup remained same as in the previous measurements. Vibrations of the hydrofoil were measured by two LDV vibrometers which were pointed to two corners of the trailing edge (Fig. 7.1). Since wide range of flow regimes was investigated, results only from vibrometer LDV 1 are presented. The measured data were post-processed by FFT as described in Chapter 7.4. The four following figures (Fig. 12.1 – Fig. 12.4) present comparison of amplitude-frequency spectra at 10 ms^{-1} for three cavitation regimes. In addition, the spectrum measured for non-cavitating regime at same flow velocity and incidence angle is presented. This spectrum was obtained in measurement presented in Chapter 10.3 (Fig. 10.16). Each cavitation regime is visualised by photo which were taken during the measurement. In these photos, the hydrofoil leading edge is located at the top of the photo, while the trailing edge is located at the bottom. The obtained amplitude-frequency spectra for all values of flow velocity are presented in Appendix A.8.

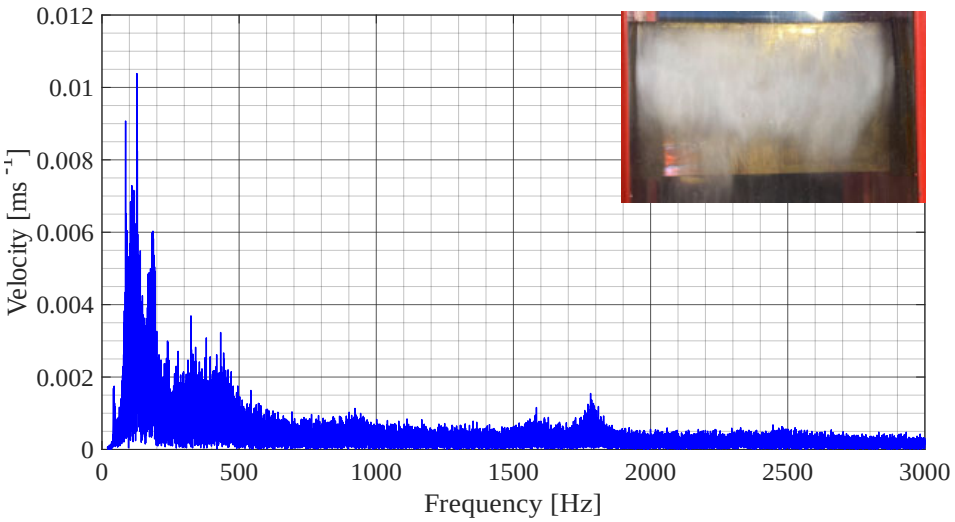

Fig. 12.1 Flow induced vibrations at $v_{inlet} = 10\ ms^{-1}$ σ = 1.615 (LDV 1)

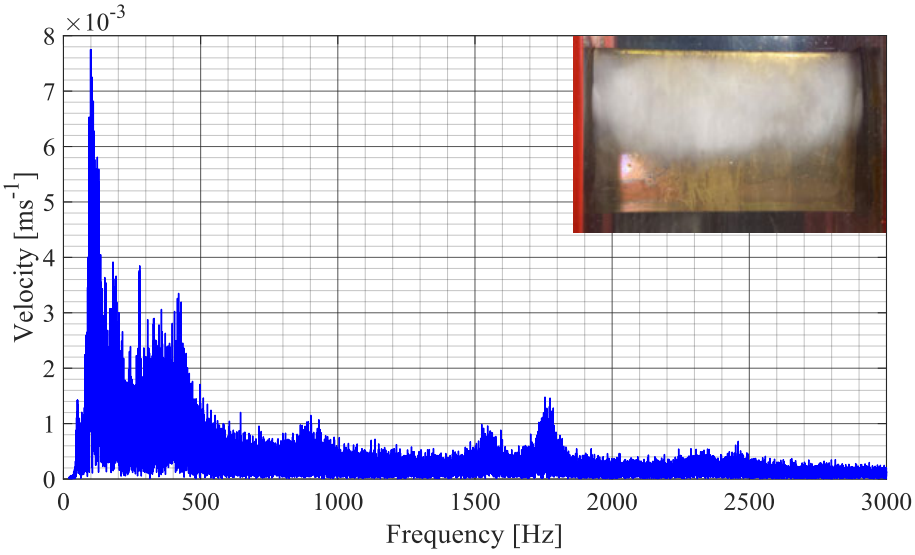

Fig. 12.2 Flow induced vibrations at $v_{inlet} = 10\ ms^{-1}$ σ = 1.770 (LDV 1)

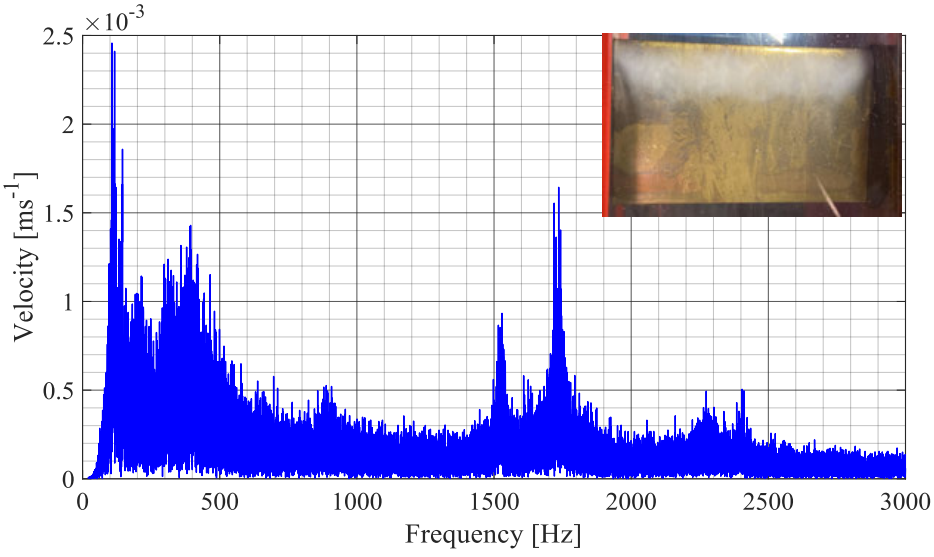

Fig. 12.3 Flow induced vibrations at $v_{inlet} = 10\ ms^{-1}$ σ = 2.198 (LDV 1)

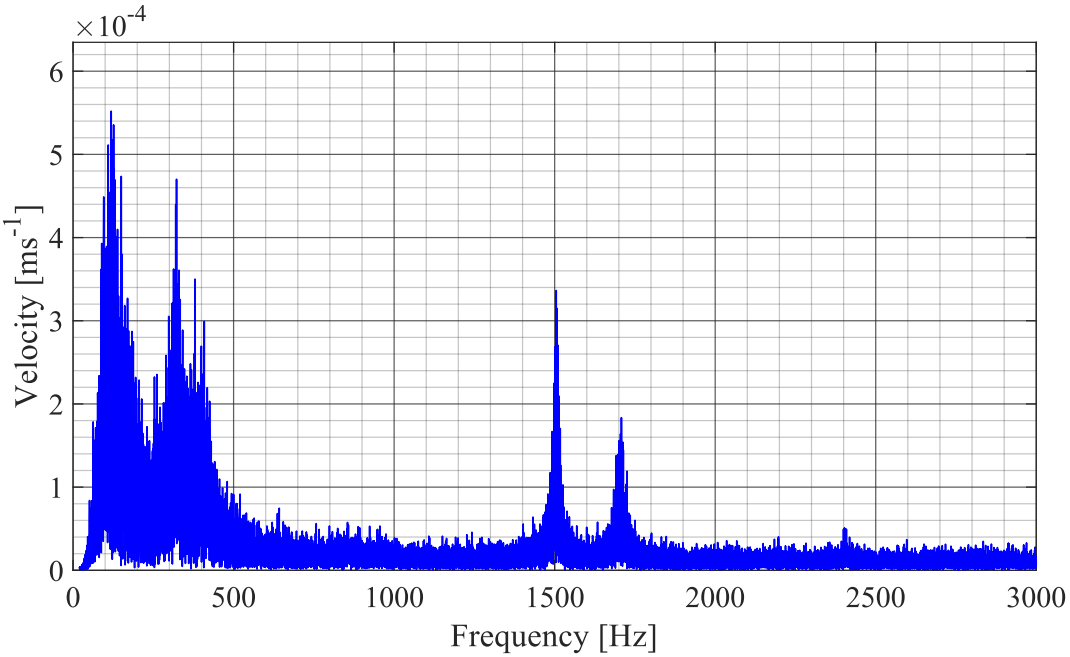

Fig. 12.4 Flow induced vibrations at $v_{inlet} = 10\ ms^{-1}$ no cavitation (LDV 1, $\alpha_{inc} = 5°$)

As it can be seen from the figures above, the amplitude-frequency spectra measured under cavitation conditions contain more detected peaks then observed by non-cavitating flow. By increasing cavitation intensity (decreasing cavitation number) at constant flow velocity, the values of amplitudes are getting higher. Generally, the amplitudes measured under cavitation conditions are higher in whole frequency range, then in case of flow without presence of cavitation. A dominant peak was observed on the first natural frequency of the hydrofoil ($f_{nat,SW,EXP} = 104\ Hz$) by all analysed flow regimes. The other dominant peaks can be compared to the measured values of natural frequencies. Since the cavitation is strongly non-stationary phenomenon and excites the hydrofoil on wide range of frequencies, the observed peaks cannot be assigned to one exact value of frequency and compared to values of natural frequencies. However, the increased values of amplitudes can be found near all measured natural frequencies in range 0 Hz – 1000 Hz. The frequency of vortex shedding was not identified which corresponds to the results of same measurement in non-cavitating flow ($\alpha_{inc} = 5°$).

12.2 Enforced Vibrations – Angle of Attack 5°

The enforced vibrations of hydrofoil under cavitation conditions were studied in the same range of flow velocity as previous investigation of flow induced vibrations with step of 2.5 ms^{-1}. The angle of attack was set to 5° which enabled to observe sheet cavitation on the hydrofoil top surface and measure its response by vibrometers pointed to the bottom surface. Experimental settings remained same as in previous measurement. The hydrofoil was excited by mechanical exciter in range of excitation frequency 50 Hz – 1000 Hz with step of 2 Hz. The hydrofoil response, which was measured by two LDV vibrometers, was strongly influenced by presence of cavitation. Since the cavitation is strongly non-stationary and stochastic phenomena, wide peaks with rapidly changing amplitudes were obtained from both methods of post-processing described in Chapter 7.2. The calculation of FRF provided spectra with more significant peaks then the first method. Therefore, the dimensionless response of hydrofoil is presented (Fig. 12.5). The FRF for all measured cavitation regimes can be found in Appendix A.9. Each cavitation regime is documented by attached photo. Here, the leading edge of the hydrofoil is located at the top of the photo, while the trailing edge is located at the bottom. As it can be seen from the attached figures, the responses measured by vibrometer LDV 2 have significantly lower amplitudes. This behaviour was observed also by the previous measurement of flow induced vibrations.

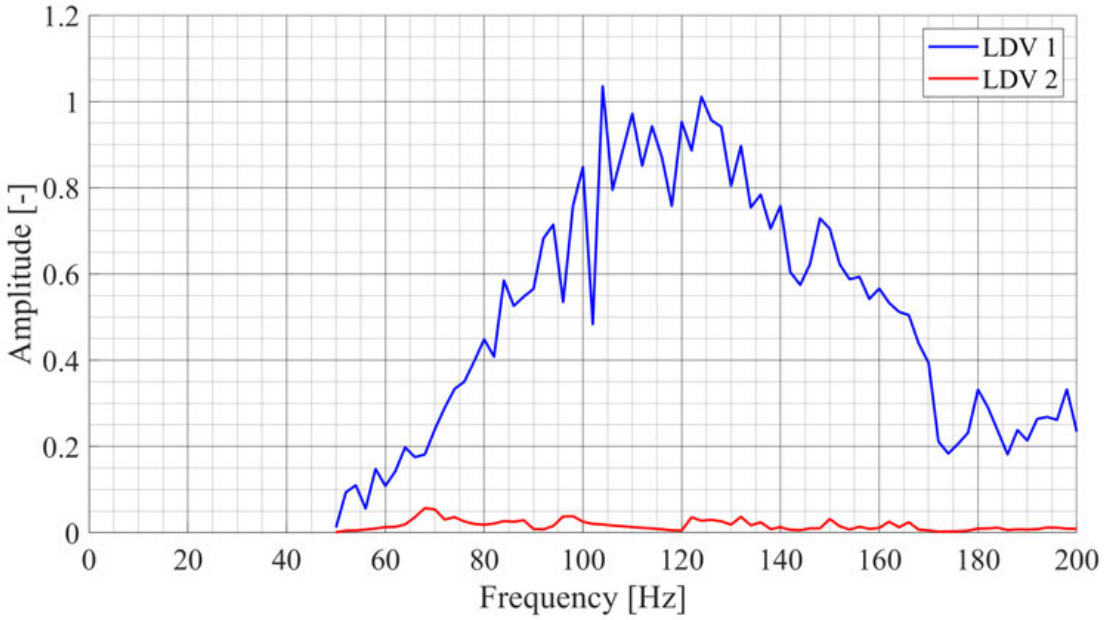

Fig. 12.5 FRF of hydrofoil at $v_{inlet} = 5.0\ ms^{-1}$; σ = 1.942 ($\alpha_{inc} = 5°$)

The damping ratio was evaluated by SDOF Response Fit Method (see Appendix A.10). The rapidly changing values of amplitudes which were observed by all analysed cavitation regimes negatively influenced the results of the method. Therefore, it was not possible to evaluate damping ratio for flow regimes with higher cavitation intensity (only flow regimes with cavitation cloud attached to one third of the hydrofoil chord length were successfully evaluated). The measurement with higher cavitation intensity was successfully evaluated only at low flow velocity 5.0 ms^{-1} (cavitation cloud attached to two thirds of chord length). The calculated results are presented in the following table (Table 34) and compared to the values measured at same flow velocity without presence of cavitation (Table 35).

Table 34 Hydrofoil damping ratio under cavitation conditions ($\alpha_{inc} = 5°$)

LDV 1 – cavitation flow regimes ($\alpha_{inc} = 5°$)						
v_{inlet}	σ	Length of sheet cavitation*	$f^{\sigma}_{NAT,SDOF,1}$	$\zeta^{\sigma}_{SDOF,LDV1}$	Δf	$\Delta \zeta$
[ms^{-1}]	[1]	[1]	[Hz]	[1]	[%]	[%]
5	2.690	1/3	106.33	0.07665	0.12	2.86
5	1.942	2/3	114.49	0.13513	7.54	71.25
7.5	2.430	1/3	96.05	0.07381	5.74	39.52
7.5	2.114	2/3	-	-	-	-
10	2.398	1/3	110.07	0.09995	8.68	27.62
10	1.970	2/3	-	-	-	-
10	1.651	3/3	-	-	-	-
12.5	2.533	1/3	126.10	0.11910	-	-
12.5	1.830	2/3	-	-	-	-
12.5	1.718	3/3	-	-	-	-

*length of sheet cavitation represents what part of hydrofoil surface is covered by cavitation cloud

$$\Delta \zeta = \frac{\left|\zeta^{\sigma}_{SDOF,LDV1} - \zeta_{SDOF,LDV1}\right|}{\zeta_{SDOF,LDV1}} \cdot 100\% \tag{12.1}$$

$$\Delta f = \frac{\left|f^{\sigma}_{NAT,SDOF,1} - f_{NAT,SDOF,1}\right|}{f_{NAT,SDOF,1}} \cdot 100\% \tag{12.2}$$

Table 35 Hydrofoil damping ratio in non-cavitating flow ($\alpha_{inc} = 5°$)

LDV 1 – no cavitation ($\alpha_{inc} = 5°$)		
v_{inlet}	$f_{NAT,SDOF,1}$	$\zeta_{SDOF,LDV1}$
[ms^{-1}]	[Hz]	[1]
0	102.04	0.01379
2.5	108.56	0.04798
5	106.46	0.07891
7.5	101.90	0.12204
10	101.28	0.13809
12.5	-	-

The following figure compares values of damping ratio according to cavitation regimes (Fig. 12.6). As it can be seen from the figure, the sheet cavitation over one third of hydrofoil surface at 5.0 ms^{-1} has no significant influence on hydrodynamic damping (3 % decrease compared to non-cavitating regime), while the presence of cavitation on two thirds of hydrofoil surface results in increase of damping ratio by 71 %. The presence of cavitation attached to one third of hydrofoil cause decrease of damping ratio by 28 % – 40 % at higher values of flow velocity (7.5 ms^{-1} and 10.0 ms^{-1}). The values of damping ratio in this range of flow velocity have linear increasing trend which is similar to the trend of damping ratio measured for non-cavitating flow regime. The damping ratio at maximal flow velocity 12.5 ms^{-1} follows the linear trend observed in range 7.5 ms^{-1} – 10.0 ms^{-1}. However, this value cannot be compared to the measurement without presence of cavitation.

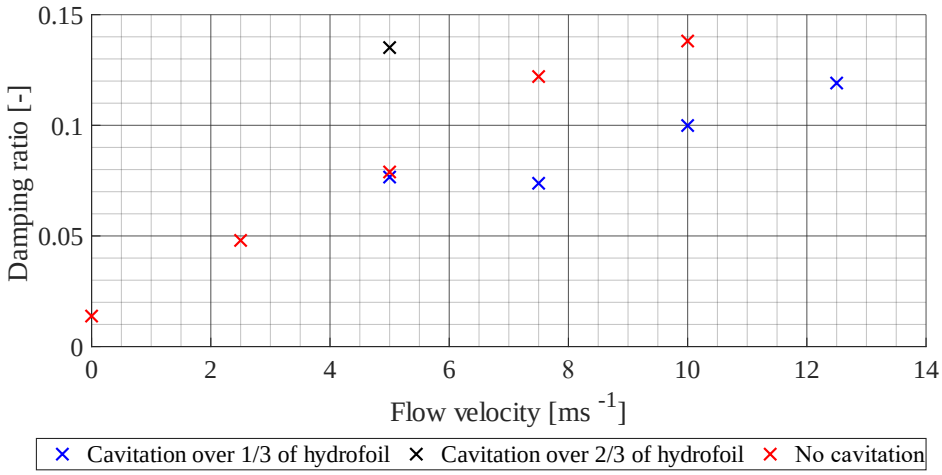

Fig. 12.6 Damping ratio under cavitation conditions ($\alpha_{inc} = 5°$)

The same comparison based on the size of cavitation cloud was carried out for values of damped natural frequency (Fig. 12.7). The following figure shows that the damped natural frequency at 5.0 ms^{-1} follows the behaviour of damping ratio. The presence of sheet cavitation over one third of hydrofoil surface has no influence on damped natural frequency (difference 0.12 %). By increasing the size of cavitation cloud to two thirds of hydrofoil, an increase of natural frequency is observed (7.5 %). This indicates that enlarging of cavitation cloud from one to two thirds of hydrofoil surface at constant flow velocity results in decrease of added mass effect, while the hydrodynamic damping rises. Since the flow velocity is constant by both flow regimes, the fluid added stiffness is expected to be constant as well.

The damped natural frequency measured with cavitation cloud attached to one third of hydrofoil surface performs significant linear increase in range of higher values of flow velocity (7.5 ms^{-1} – 12.5 ms^{-1}). Since the size of sheet cavitation is constant, this behaviour is probably caused by increase of flow induced stiffness which linearly depends on the flow velocity. More detailed analysis of fluid added effects under cavitation conditions would require experimental measurements in range of low flow velocities (5.0 ms^{-1} – 10.0 ms^{-1}) with smooth step of 0.5 ms^{-1} and selection of more cavitation regimes at each value of flow velocity. Unfortunately, this detailed study was not carried out due to the lack of time which resulted from difficulties during testing and modifying of the two post-processing methods.

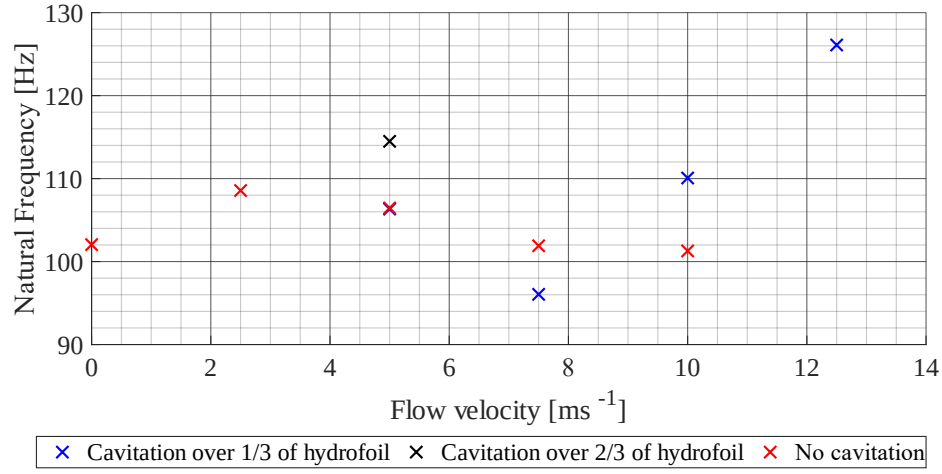

Fig. 12.7 Damped natural frequency under cavitation conditions ($\alpha_{inc} = 5°$)

12.3 Influence of Cavitation on Modal Properties

Modal properties of the hydrofoil, i.e. the natural frequencies and corresponding mode shapes, are influenced by presence of water. Significant drop of natural frequencies which was observed by hydrofoil submerged in water is caused by added mass effect. The main parameters which influence the added mass effect are the density of water and the hydrofoil geometry (shape and dimensions).

If the hydrofoil is placed into cavitating flow, a cavitation cloud which is filled by mixture of water and saturated vapour is attached to the hydrofoil surface. The physical properties of the mixture inside the cavitation cloud differ from the physical properties of the water. Therefore, the presence of cavitation which is attached to the hydrofoil surface strongly influences its modal properties.

The influence of sheet cavitation on the modal properties of hydrofoil were studied with the use of acoustic modal analysis. This approach is based on simplified assumptions which are described in Chapter 8.1.3. The cavitation cloud was modelled as a subdomain inside the acoustic region which represented water inside the test section. Since the size of cavitation cloud changes over time, five different geometries of cavitation cloud were tested. In addition, all combinations of physical properties in Table 12 were tested for tested. The first five natural frequencies were evaluated for each analysed case. As the natural frequencies depend on the value of volume fraction of saturated vapour α_{vap}, the change of natural frequencies was quantified by Frequency Reduction Ratio *FRR* given by following equation [71] [85]:

$$FRR_i = \frac{f_{i,\alpha_{vap}=1} - f_{i,\alpha}}{f_{i,\alpha_{vap}=1}} \cdot 100\% \tag{12.3}$$

where

- $f_{i,\alpha_{vap}=1}$ is *i-th* natural frequency calculated for cavitation cloud filled only by saturated vapour
- $f_{i,\alpha}$ *i-th* natural frequency calculated for cavitation cloud filled by mixture of water and saturated vapour $\alpha_{vap} = 0 - 1$
- FRR_i (Frequency Reduction Ratio).

Five different geometries of the cavitation cloud were selected according to the flow regimes which were also selected for experimental measurements. The first case represented cavitation cloud which is attached to one third of chord length behind the leading edge ($L_{cloud} = 25\ mm$). In the second case, the cavitation cloud was attached to the hydrofoil on two thirds of the chord length ($L_{cloud} = 60\ mm$). Two different values of cloud thickness were analysed for both cases ($H_{cloud} = 0.5\ mm; 2.0\ mm$). The last configuration, denoted as "*real cavitation*" represented a cavitation cloud in the moment of shedding from the hydrofoil surface. This is captured by specific shape of the cloud.

It should be noted that the cavitation cloud occurs on both the top and the bottom surfaces of the hydrofoil with incidence angle $\alpha_{inc} = 0°$. However, the computational model was simplified by modelling of cavitation cloud only on the hydrofoil top surface. This corresponds to flow behaviour which was observed at incidence angle $\alpha_{inc} = 5°$. Since the fluid flow is not involved into the model, this simplification has no impact on the calculated results.

12.3.1 Sensitivity on Physical Properties

As a first step, the sensitivity study of the natural frequencies on two physical properties was carried out with the geometry of "*real cavitation*" (Fig. 8.10). In the first case, the constant value of speed of sound was applied, while the density of the mixture varied. The obtained results are summarized in the following table and figure. The obtained results show that the influence of mixture density on the natural frequencies is negligible. The only observed changes of natural frequencies was observed in range of values 0 kg·m^{-3} – 100 kg·m^{-3}.

Table 36 Sensitivity study of natural frequencies on mixture density

ρ_{mix}	f_1	f_2	f_3	f_4	f_5
$[kgm^{-3}]$	$[Hz]$	$[Hz]$	$[Hz]$	$[Hz]$	$[Hz]$
998.1	104.1	356.4	410.7	896.1	909.4
898.3	104.1	357	410.7	896.2	909.4
798.5	104.2	357.2	410.8	896.3	909.4
698.7	104.2	357.4	410.9	896.4	909.4
598.9	104.2	357.6	411.0	896.5	909.4
499.1	104.3	357.9	411.1	896.6	909.4
399.3	104.3	358.2	411.3	896.7	909.4
299.5	104.4	358.5	411.5	896.8	909.4
199.8	104.5	359.1	411.9	896.9	909.4
100	104.8	360.2	412.1	897.1	909.4
0.17	96.6	108	380.1	420.7	900.8

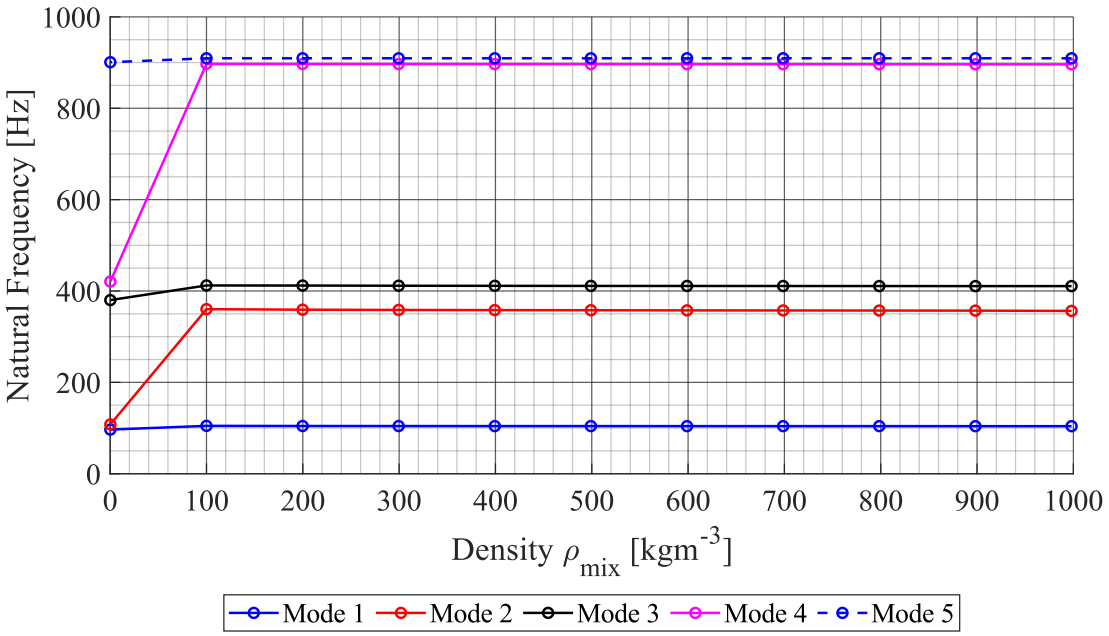

Fig. 12.8 Sensitivity study of natural frequencies on mixture density

In the second step, the value of mixture density was set to value 0.17 kg·m^{-3} which corresponds to cavitation cloud fully filled by saturated vapour ($\alpha_{vap} = 1$). The values of speed of sound varied in range 10 ms^{-1} – 1450 ms^{-1}. The obtained results are presented in the figure below (all calculated values of calculated natural frequencies can be found in Appendix A.11).

As it can be seen in the figure, the speed of sound has significant impact on the hydrofoil natural frequencies. A linear increase of the natural frequencies is observed by all modes. This linear increase is called "*mode transition line*" [71] and describes change of natural frequency from lower to a new higher constant value of natural frequency.

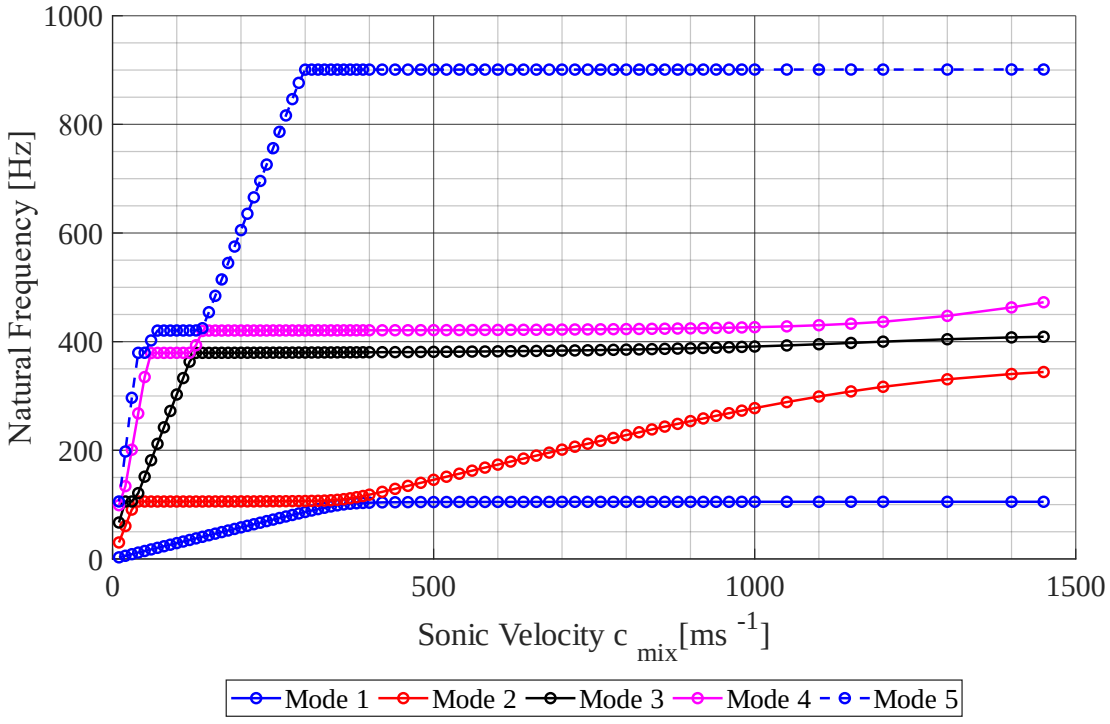

Fig. 12.9 Sensitivity study of natural frequencies on speed of sound

12.3.2 Cavitation Cloud of Length 25 mm

The obtained values of first five natural frequencies for 25 mm long cavitation cloud of thickness 0.5 mm and 2.0 mm are presented in the following tables and figures. The obtained mode shapes of the hydrofoil which correspond to $\alpha_{vap} = 0.5$ and 1 can be found in Appendix A.12.

Table 37 Cavitation cloud ($L_{cloud} = 25\ mm$; $H_{cloud} = 0.5\ mm$)

Mode	1		2		3		4		5	
α_{vap}	f_1	FRR_1	f_2	FRR_2	f_3	FRR_3	f_4	FRR_4	f_5	FRR_5
[−]	[Hz]	[%]	[Hz]	[%]	[Hz]	[%]	[Hz]	[%]	[Hz]	[%]
0.0	104.1	0.79	356.4	-111.9	410.7	-8.2	896.1	-113.9	909.4	-0.3
0.1	104.1	0.8	345.0	-105.3	407.2	-7.4	557.7	-33.3	743.8	17.4
0.2	104.1	0.8	319.3	-89.9	399.3	-5.4	438.8	-4.8	546.4	39.3
0.3	104.1	0.8	283.6	-68.7	385.5	-1.7	415.7	0.7	452.6	49.7
0.4	104.1	0.8	252.9	-50.5	375.2	1.0	390.4	6.7	413.8	54.1
0.5	104.1	0.8	229.7	-36.6	351.7	7.2	367.2	12.3	406.1	54.9
0.6	104.1	0.8	211.5	-25.8	322.9	14.8	355.5	15.1	398.0	55.8
0.7	104.1	0.8	197.1	-17.3	300.9	20.6	341.7	18.4	391.2	56.6
0.8	104.1	0.8	185.6	-10.4	284.2	25.0	329.2	21.4	386.2	57.11
0.9	104.2	0.7	176.2	-4.8	272.9	28.0	322.8	22.9	383.9	57.36
1.0	105.0	0.0	168.1	0.0	379.0	0.0	418.6	0.0	900.4	0.00

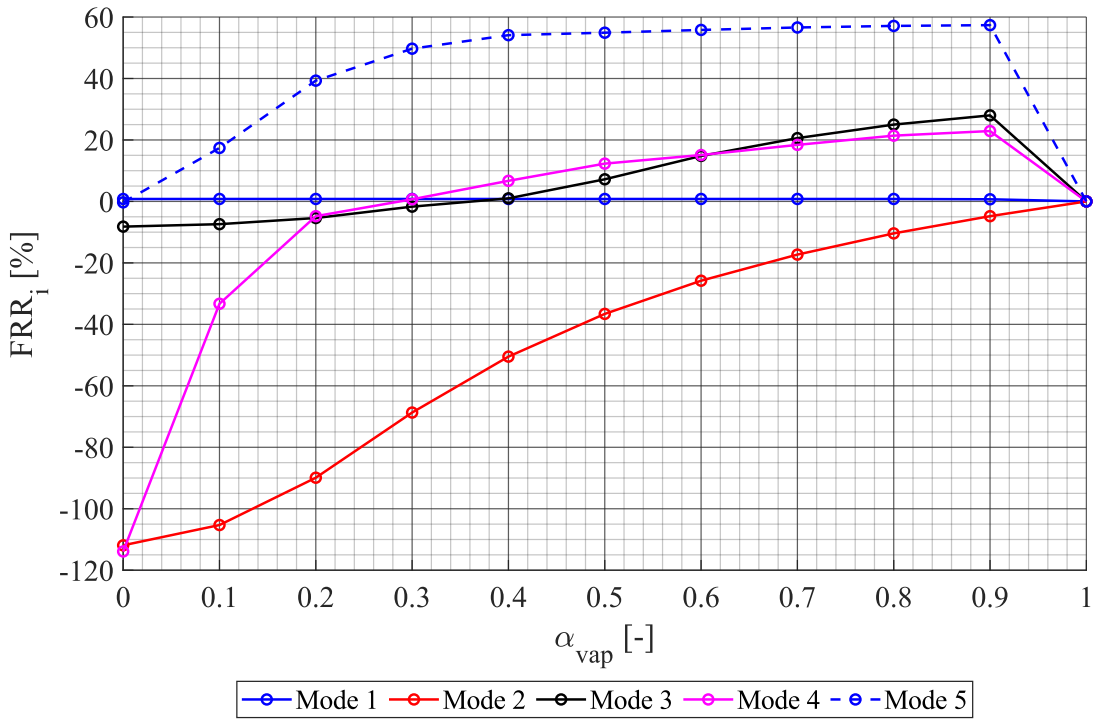

Fig. 12.10 Cavitation cloud ($L_{cloud} = 25\ mm$; $H_{cloud} = 0.5\ mm$)

Table 38 Cavitation cloud ($L_{cloud} = 25\ mm$; $H_{cloud} = 2.0\ mm$)

Mode	1		2		3		4		5	
α_{vap}	f_1	FRR_1	f_2	FRR_2	f_3	FRR_3	f_4	FRR_4	f_5	FRR_5
$[-]$	$[Hz]$	[%]	$[Hz]$	[%]	$[Hz]$	[%]	$[Hz]$	[%]	$[Hz]$	[%]
0.0	104.1	-20.9	356.4	-237.4	410.7	-8.6	896.1	-114.0	909.4	-0.3
0.1	104.1	-20.8	255.5	-142.0	375.9	0.4	397.7	4.9	416.6	53.7
0.2	104.0	-20.8	186.6	-76.8	286.6	24.1	330.8	20.9	386.5	57.1
0.3	103.9	-20.6	154.0	-45.9	235.9	37.5	279.7	33.1	322.7	64.2
0.4	103.7	-20.4	134.3	-27.2	205.6	45.5	246.1	41.2	283.2	68.6
0.5	103.3	-20.0	121.2	-14.8	185.4	50.9	223.5	46.6	257.8	71.4
0.6	101.8	-18.8	112.1	-6.2	170.8	54.8	207.5	50.4	240.5	73.3
0.7	99.0	-15.5	107.3	-1.6	160.0	57.6	196.5	53.0	229.8	74.5
0.8	94.6	-10.3	105.8	-0.2	152.5	59.6	190.7	54.4	226.6	74.8
0.9	90.2	-5.2	105.4	0.1	149.6	60.4	194.9	53.4	240.4	73.3
1.0	85.7	0.0	105.6	0.0	377.5	0.0	418.2	0.0	900.5	0.0

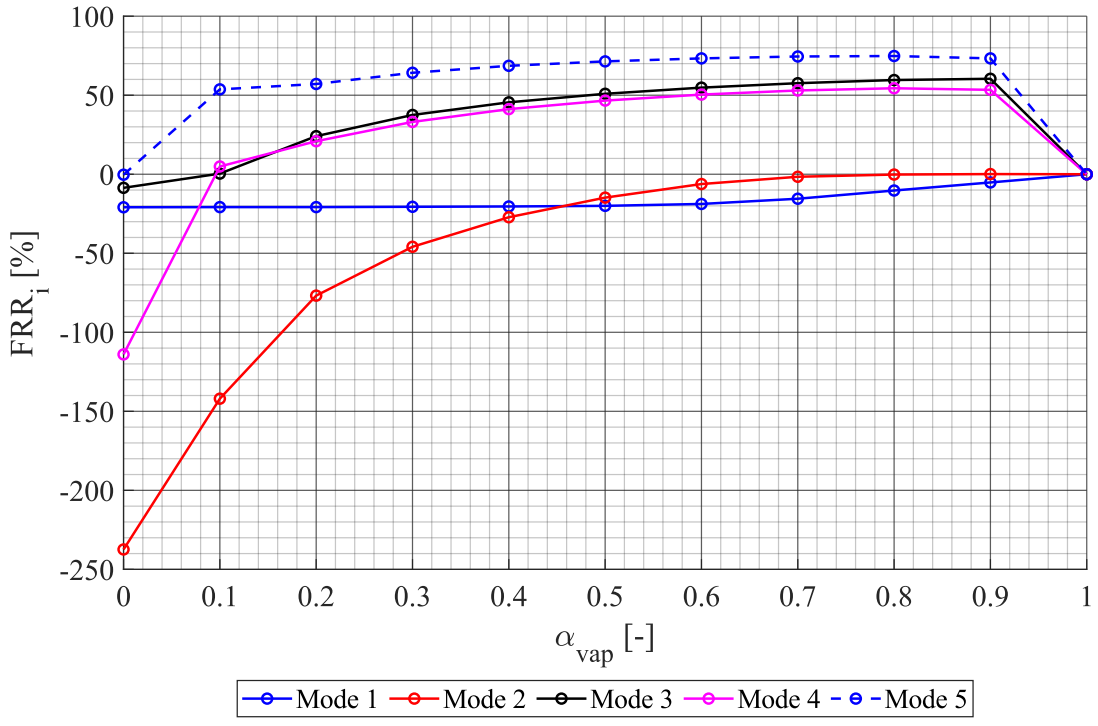

Fig. 12.11 Cavitation cloud ($L_{cloud} = 25\ mm$; $H_{cloud} = 2.0\ mm$)

12.3.3 Cavitation Cloud of Length 60 mm

The obtained values of first five natural frequencies for 60 mm long cavitation cloud of thickness 0.5 mm and 2.0 mm are presented in the following tables and figures. The obtained mode shapes of the hydrofoil which correspond to $\alpha_{vap} = 0.5$ and 1 can be found in Appendix A.12.

Table 39 Cavitation cloud ($L_{cloud} = 60\ mm$; $H_{cloud} = 0.5\ mm$)

Mode	1		2		3		4		5	
α_{vap}	f_1	FRR_1	f_2	FRR_2	f_3	FRR_3	f_4	FRR_4	f_5	FRR_5
[−]	[Hz]	[%]	[Hz]	[%]	[Hz]	[%]	[Hz]	[%]	[Hz]	[%]
0.0	104.1	-0.3	356.4	-178.5	410.7	-5.1	896.1	-102.6	909.4	-0.1
0.1	103.3	0.0	320.2	-150.5	392.1	-0.5	428.2	3.1	614.0	31.9
0.2	103.0	0.3	253.4	-98.2	362.2	7.2	386.3	12.5	463.7	48.6
0.3	102.7	0.6	211.8	-65.7	329.6	15.5	361.3	18.2	417.6	53.7
0.4	102.3	1.0	185.4	-45.0	294.4	24.5	342.1	22.6	393.1	56.4
0.5	101.9	1.4	167.4	-30.9	267.1	31.5	322.4	27.0	372.2	58.7
0.6	101.4	1.9	154.0	-20.5	246.0	37.0	303.3	31.3	353.0	60.9
0.7	100.8	2.4	143.8	-12.5	229.6	41.1	287.1	35.0	336.5	62.7
0.8	100.2	3.1	136.1	-6.5	217.4	44.3	275.3	37.7	324.5	64.0
0.9	99.7	3.5	130.3	-1.9	210.0	46.2	271.6	38.5	322.8	64.2
1.0	103.8	0.0	127.8	0.0	390.1	0.0	441.7	0.0	901.9	0.0

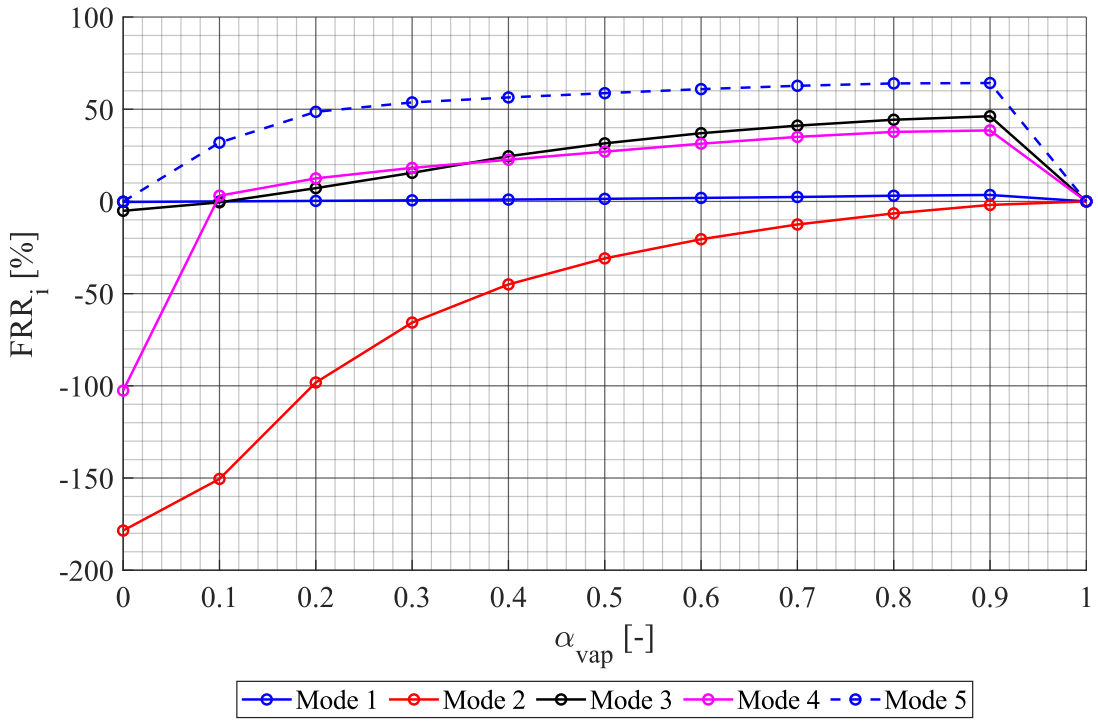

Fig. 12.12 Cavitation cloud ($L_{cloud} = 60\ mm$; $H_{cloud} = 0.5\ mm$)

Table 40 Cavitation cloud ($L_{cloud} = 60\ mm$; $H_{cloud} = 2.0\ mm$)

Mode	1		2		3		4		5	
α_{vap}	f_1	FRR_1	f_2	FRR_2	f_3	FRR_3	f_4	FRR_4	f_5	FRR_5
$[-]$	$[Hz]$	[%]	$[Hz]$	[%]	$[Hz]$	[%]	$[Hz]$	[%]	$[Hz]$	[%]
0.0	104.1	-75.1	356.4	-237.3	410.7	-5.0	896.1	-102.0	909.4	-0.1
0.1	102.3	-73.0	186.4	-76.6	298.1	23.7	345.5	22.0	397.8	55.9
0.2	99.9	-68.8	136.2	-29.0	217.1	44.4	274.0	38.2	323.2	64.2
0.3	94.7	-60.1	117.5	-11.3	179.2	54.1	229.5	48.2	271.7	69.9
0.4	87.0	-47.1	110.8	-5.0	156.4	60.0	201.9	54.5	239.4	73.5
0.5	79.7	-34.7	108.3	-2.6	141.2	63.8	183.6	58.6	218.4	75.8
0.6	73.7	-24.5	107.2	-1.5	130.3	66.6	170.9	61.4	204.0	77.4
0.7	68.8	-16.3	106.7	-1.1	122.5	68.6	162.7	63.3	195.0	78.4
0.8	64.9	-9.7	106.8	-1.2	117.7	69.9	159.6	64.0	192.1	78.7
0.9	61.8	-4.5	108.1	-2.5	117.8	69.8	167.8	62.2	202.7	77.5
1.0	59.2	0.0	113.7	-7.7	390.6	0.0	443.2	0.0	901.9	0.0

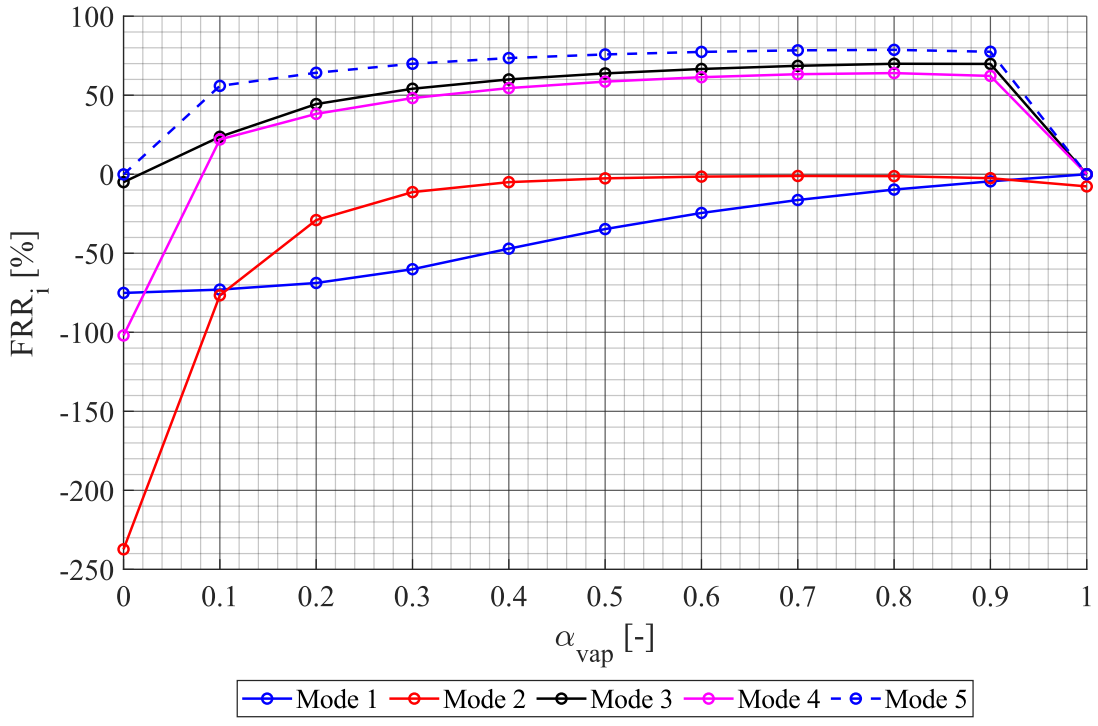

Fig. 12.13 Cavitation cloud ($L_{cloud} = 60\ mm$; $H_{cloud} = 2.0\ mm$)

12.3.4 "Real" Cavitation Cloud

The obtained values of first five natural frequencies for "*real*" cavitation cloud of variable thickness are presented in the following tables and figures. The obtained mode shapes of the hydrofoil which correspond to $\alpha_{vap} = 0.5$ and 1 can be found in Appendix A.12.

Table 41 "*Real*" cavitation cloud with variable thickness

Mode	1		2		3		4		5	
α_{vap}	f_1	FRR_1	f_2	FRR_2	f_3	FRR_3	f_4	FRR_4	f_5	FRR_5
$[-]$	$[Hz]$	[%]	$[Hz]$	[%]	$[Hz]$	[%]	$[Hz]$	[%]	$[Hz]$	[%]
0.0	104.1	-3.0	356.4	-229.1	410.7	-7.9	896.1	-112.9	909.4	-0.2
0.1	104.0	-2.9	292.8	-169.4	383.2	-0.8	410.1	2.6	448.5	50.2
0.2	103.9	-2.8	218.5	-100.6	312.6	17.8	353.1	16.1	403.1	55.2
0.3	103.8	-2.7	180.9	-65.8	257.7	32.3	312.7	25.7	364.6	59.5
0.4	103.6	-2.5	157.8	-44.3	224.5	41.0	278.2	33.9	319.4	64.5
0.5	103.4	-2.3	142.2	-29.9	202.3	46.8	253.6	39.7	290.1	67.8
0.6	103.1	-2.0	130.7	-19.3	186.2	51.1	235.6	44.0	270.0	70.0
0.7	102.3	-1.6	122.2	-11.4	174.3	54.2	223.0	47.0	257.1	71.5
0.8	101.6	-0.8	116.1	-5.8	166.1	56.4	216.2	48.7	252.3	72.0
0.9	100.6	0.2	112.1	-2.0	162.8	57.2	220.1	47.7	264.8	70.6
1.0	100.8	0.0	109.9	0.0	380.3	0.0	420.8	0.0	900.8	0.0

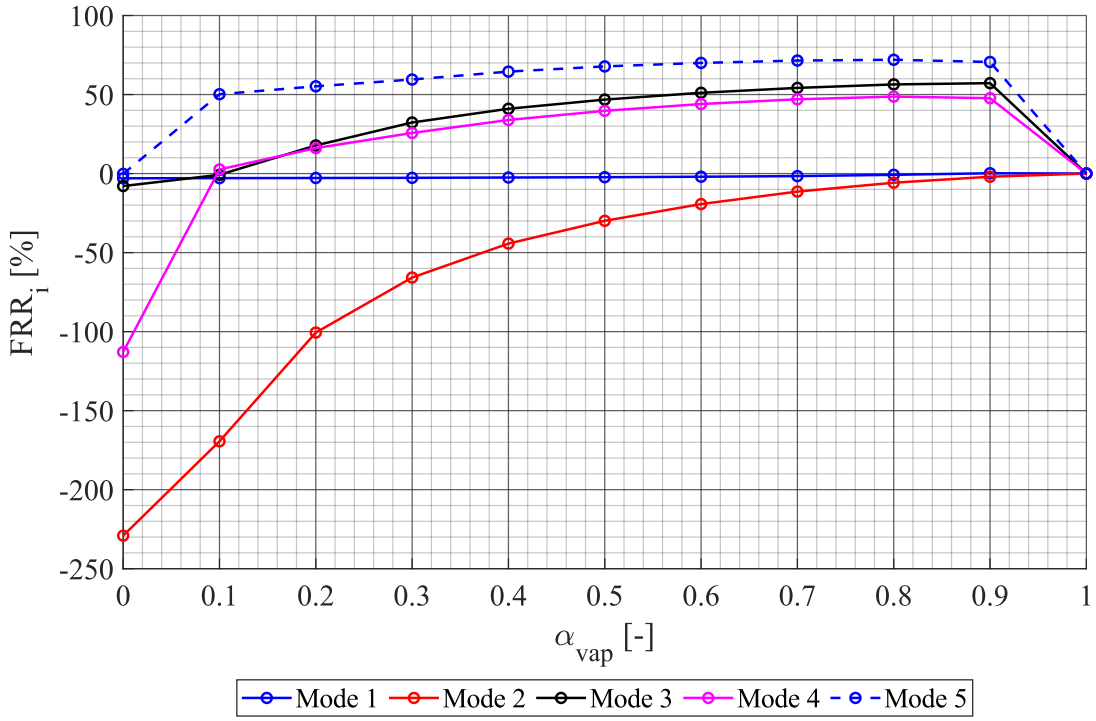

Fig. 12.14 "*Real*" cavitation cloud with variable thickness

12.4 Partial Conclusion – Influence of Cavitation

The influence of cavitation on dynamic response of the hydrofoil was investigated in two experimental measurements. Both the measurements were carried out at 5° angle of attack. Three cavitation regimes were investigated at each analysed flow velocity. These cavitation regimes were selected to observe sheet cavitation on one third of the hydrofoil surface, two thirds and on the whole surface of the hydrofoil.

The first measurement was focused on the study of flow induced vibrations under cavitation conditions. The response of hydrofoil was measured by two LDV vibrometers. The amplitude-frequency spectra of the response were calculated by Fast Fourier Transformation. These spectra contain more detected peaks than the spectra observed by non-cavitating flow at same value of incidence angle. The higher values of amplitudes are observed by increasing cavitation intensity (decreasing cavitation number) at constant flow velocity. The frequency of vortex shedding was not identified, which corresponds to the results of same measurement in non-cavitating flow.

The other experimental measurement was carried out to study the response of hydrofoil on enforced vibrations. Due to the strong influence of cavitation, the damping ratio was evaluated only for flow regimes with sheet cavitation attached to one third of hydrofoil surface. The FRF, obtained for flow regimes with higher cavitation intensity, contained wide peaks with rapidly changing values of amplitudes. Therefore the approximation of the FRF by SDOF Response Fit Method was not possible.

The only measurement with evaluated damping ratio for sheet cavitation on two thirds of hydrofoil surface was at flow velocity 5.0 ms^{-1}. At this flow velocity, the sheet cavitation over one third of hydrofoil surface had no significant influence on hydrodynamic damping (3 % decrease), while the presence of cavitation on two thirds of hydrofoil surface resulted in an increase of damping ratio by 71 %.

At higher values of flow velocity (7.5 ms^{-1} and 10.0 ms^{-1}), the presence of cavitation attached to one third of hydrofoil caused a decrease of damping ratio by 28 % – 40 %. The values of damping ratio in this range of flow velocity had linear increasing trend which was similar to the trend of damping ratio measured for non-cavitating flow regime.

The influence of cavitation on modal properties of the hydrofoil was investigated with the use of acoustic modal analysis. Five different geometries of cavitation cloud were analysed, based on the experience from experimental measurements. The influence of length and thickness of the cavitation cloud was studied by four of total of five cases. The last case was designed to simulate moment of shedding of the cloud from the hydrofoil surface. In this case, the cloud thickness varied along the chord length.

Since physical properties of the mixture inside the cavitation cloud have major impact on the modal properties of the hydrofoil, the sensitivity study of natural frequencies on density and on speed of sound was performed. While one of the two parameters was constant, the other parameter varied in selected range. This approach does not correspond to a real situation, but enables to quantify the influence of each parameter separately. It was found that the density of the mixture has almost no influence on hydrofoil natural frequencies. The only significant changes of natural frequencies were observed in range 0 – 100 $kg \cdot m^{-3}$. However, the speed of sound strongly influences the modal properties of the hydrofoil. Dependence of all first five natural frequencies on the speed of sound was observed in range of speed of sound 10 ms^{-1} – 1450 ms^{-1}. A linear increase of the natural frequencies from lower to a new higher constant value

of natural frequency was observed by all analysed modes. This significant increase is called "*mode transition line*" [71].

On the one hand, the modal properties of the first mode are not influenced by the presence of cavitation. As the volume fraction of saturated vapour changes, the first natural frequency and corresponding mode shape remain the same by all five geometrical shapes of the cavitation cloud. On the other hand, the modal properties, i.e. the natural frequencies and the mode shapes of higher modes, are strongly influenced by presence of cavitation. The most significant changes are observed by the second, the fourth and the third modes. The fifth mode is characterized by deformation of only shaft and therefore the only change of natural frequency is observed.

The comparison of various geometrical shapes of the cavitation cloud showed that the change of cloud thickness has stronger influence on natural frequencies than the change of the cloud length.

13 GLOBAL CONCLUSIONS

The main aim of the thesis was the investigation of dynamic response of hydrofoil under various flow conditions including the presence of cavitation and the investigation of fluid added effects which act on the hydrofoil.

This study of Fluid-Structure Interaction was carried out with the use of cavitation tunnel which was designed and manufactured as a part of research project in cooperation with *Litostroj Engineering a. s.* In contrast to the typical cavitation tunnels with fully fixed hydrofoil on its both sides, this cavitation tunnel was designed as small scaled model of turbine guide vane. The hydrofoil was manufactured as a one piece together with its shaft and mounted by three ball bearings in the test section. This setup enabled to model realistic behaviour of a turbine guide vane.

The first part of the thesis introduces general terms and equations in the field of fluid and solid dynamics which are related to Fluid-Structure Interaction in hydraulic machines. This overview is followed by the description of fluid added effects which includes the summary of recently published results of their experimental and numerical investigation. Finally, the experimental setup of the cavitation tunnel including detailed description of all experimental and numerical methods used in this thesis is presented.

The second part of the thesis deals with experimental and numerical investigation of hydrofoil dynamic response:

- Natural frequencies of the hydrofoil were investigated by harmonic excitation of the hydrofoil with the use of mechanical exciter. The hydrofoil response was measured by two LDV vibrometers. Experimental values of natural frequencies were identified by comparison of detected peaks to modal properties obtained by finite element modal analysis. The first four natural frequencies of hydrofoil in air were measured. The numerical results do not differ more than 6 %. In case of hydrofoil submerged in still water, the first five natural frequencies calculated by acoustic modal analysis do not differ more than 7.5 % except the second mode (17 %).

- Experimental investigation of flow induced vibrations was carried out for two values of incidence angle: 0° and 5°. A linear increase of vortex shedding frequency was observed at zero value of angle of attack in whole range of flow velocity 1 ms^{-1} – 17.5 ms^{-1} except the lock-in regions which occurred when the vortex shedding frequency was close to natural frequency of the hydrofoil. The frequency of vortex shedding was also evaluated from amplitude-frequency spectra of the lift force calculated by unsteady CFD analysis. The numerical results do not differ more than 10 % from the experimental values except the flow velocity 2.5 ms^{-1} (20 %). The experimental study of flow induced vibrations at 5° angle of attack showed that the only dominant peaks which were detected in the amplitude-frequency spectra are related to the natural frequencies of the hydrofoil. The vortex shedding was not captured in this measurement.

- Total damping of the oscillating hydrofoil which is placed in a fluid flow consists of three main contributions: the structural damping, the viscous – hydrodynamic damping and the damping which is the result of the acoustic radiation and from the viscous effects in the liquid. Since water can be considered incompressible, the last damping contribution can be neglected. Then the total damping consists of only two contributions, where the structural damping is considered to be very low compared to the hydrodynamic damping. This assumption was confirmed by measured value of structural damping ratio 0.6 % related to the first mode which is significantly lower than the value of damping ratio 14 % measured in range of flow velocity 8 ms^{-1} – 10 ms^{-1}.

- Experimental investigation of damping ratio was carried out for the first mode of the hydrofoil at zero angle of attack. The enforced vibrations excited by external mechanical exciter were measured in range of flow velocity 1 – 10 ms^{-1}. The damping ratio was calculated by approximation of Frequency Response Function by SDOF Response Fit Method. The evaluated values of damping ratio show a linear increasing trend in range of flow velocity in range of flow velocity 1 ms^{-1} – 8 ms^{-1}. Then a constant value of damping ratio 0.14 is observed in range of flow velocity 8 ms^{-1} – 10 ms^{-1}. The values of the damped natural frequency obtained by both vibrometers are significantly decreasing with increase of flow velocity. This behaviour may be caused by the increase of added mass effect m_{ADD} or the decrease of fluid added stiffness k_F. As the mechanical system is analysed with the use of linearized models, the observed drop of the first natural frequency may be the result of nonlinear behaviour of the analysed system.

- Experimental measurement of hydrodynamic damping at 5° incidence angle showed that the incidence angle of 5° has no significant impact on the hydrodynamic damping in whole range of flow velocity 0 ms^{-1} – 10 ms^{-1}. The evaluated values of damping ratio do not differ from the values obtained at zero angle of attack and keep the same linear increasing trend.

- Numerical investigation of hydrodynamic damping was carried out with the use of modified Modal Work Approach. This method is based on the standard Modal Work Approach and was tested and developed during the internship in *Voith Hydro Holding GmbH & Co. KG*. The standard Modal Work Approach calculates the damping ratio as a ratio of the dissipated energy per hydrofoil oscillation and the total energy of the hydrofoil motion. The modified approach calculates the total energy of the hydrofoil motion as a sum of elastic strain energy over all structural elements of the hydrofoil. However, this method is sensitive to boundary conditions in the structural analysis and to proper calculation of the sum of elastic strain energy. The sum of elastic strain energy over hydrofoil and its shaft provide results which correspond with the experimental values, while the sum of elastic strain energy over hydrofoil without shaft provides highly overestimated values of damping ratio. Alternatively, the values of damping ratio calculated by standard Modal Work Approach highly overestimated the experimental results.

- The dynamic response of the hydrofoil under cavitation conditions was measured for flow induced vibrations and for enforced vibrations excited by external mechanical exciter. Both measurements were carried out at 5° angle of attack. Three cavitation regimes were investigated at each analysed flow velocity. These cavitation regimes were selected to observe sheet cavitation on one third of the hydrofoil surface, two thirds and on the whole surface of the hydrofoil. The obtained amplitude-frequency spectra contain more detected peaks than the spectra observed by non-cavitating flow at the same value of flow velocity and of incidence angle. As the cavitation intensity and also the area covered by sheet cavitation are enlarging, the amplitudes in the obtained spectra are increasing.

- The influence of cavitation on the damping ratio of the first hydrofoil mode was studied from Frequency Response Function of the hydrofoil. However, due to the rapidly changing values of amplitudes caused by strong influence of cavitation, the damping ratio was evaluated only for flow regimes with sheet cavitation attached to one third of hydrofoil surface. The only measurement with evaluated damping ratio for sheet cavitation on two thirds of hydrofoil surface was at flow velocity 5.0 ms^{-1}. As the sheet cavitation over one third of hydrofoil surface had no significant influence on hydrodynamic damping, the cavitation over two thirds of hydrofoil surface resulted in increase of damping ratio by 71 %. The presence of cavitation attached to one third of hydrofoil caused decrease of damping ratio by 28 % – 40 % at higher values of flow velocity (7.5 ms^{-1} and 10.0 ms^{-1}).

- The numerical study of modal properties of the hydrofoil under cavitation conditions was performed by acoustic modal analysis. However, the results were not validated by experimental values. The sensitivity study showed that the density of the mixture inside the cavitation cloud has almost no influence on hydrofoil natural frequencies. The only significant changes of natural frequencies were observed in range 0 $kg \cdot m^{-3}$ – 100 $kg \cdot m^{-3}$. However, the speed of sound strongly influences the modal properties of the hydrofoil. A linear increase of the natural frequencies from lower to a new higher constant value of natural frequency was observed by gradual increasing of speed of sound from 10 ms^{-1} to 1450 ms^{-1}. This significant increase is called "*mode transition line*" [71]. The modal properties of the first mode were not influenced by presence of cavitation. As the volume fraction of saturated vapour changed, the first natural frequency and corresponding mode shape kept constant value by all five geometrical shapes of the cavitation cloud. The modal properties of higher modes were strongly influenced by presence of cavitation. The most significant changes were observed by the second, the fourth and the third modes. The comparison of various cloud geometrical shapes showed that the change of cloud thickness has stronger influence on the natural frequencies than the change of the cloud length.

The main thesis outcomes:

- Developing of modified Modal Work Approach and its application on geometry of a guide vane.
- Finding of reliable procedure of calculation of Frequency Response Function.
- Experimental investigation of hydrodynamic damping under cavitation conditions.
- Numerical investigation of hydrodynamic damping at 5° angle of attack in both the cavitating and non-cavitating flow.
- Numerical study of hydrofoil modal properties under cavitation conditions.

Suggestions and recommendations for further investigation:

- The first natural frequency of the submerged hydrofoil should be in range 300 Hz – 600 Hz. This will enable investigation of damping ratio in the lock-in region. Since the vortex shedding frequency 104 Hz which corresponded to the first natural frequency was induced close to flow velocity 1 ms^{-1}, it was not possible to perform detailed study in the lock-in region of the first mode.
- More detailed analysis of fluid added effects under cavitation conditions in range of low flow velocities (5.0 ms^{-1} – 10.0 ms^{-1}) with smooth step of 0.5 ms^{-1} and selection of more cavitation regimes at each value of flow velocity. The Frequency Response Function measured at lower cavitation intensity will be suitable for approximation by SDOF Response Fit Method.
- The excitation of the hydrofoil can be realized by piezoelectric patches mounted on the hydrofoil surface. These patches may excite directly the hydrofoil instead of other components of the test section which may reduce the vibrations of the test section and result in better response measured by vibrometers.

LITERATURE

[1] DÖRFLER, Peter, Mirjam SICK and André COUTU. Flow-induced pulsation and vibration in hydroelectric machinery: engineer's guidebook for planning, design and troubleshooting. New York: Springer, 2013. ISBN 978-1-4471-4251-5.

[2] TRIVEDI, Chirag. A review on fluid structure interaction in hydraulic turbines: A focus on hydrodynamic damping: A focus on hydrodynamic damping. *Engineering Failure Analysis*. Elsevier, 2017, **77**, 1-22. DOI: 10.1016/j.engfailanal.2017.02.021.

[3] SCHLICHTING, Hermann and Klaus GERSTEN. *Boundary-Layer Theory*. 9th ed. 2017. Berlin, Heidelberg: Springer Berlin Heidelberg, 2017. ISBN 978-3-662-52917-1.

[4] ÇENGEL, Yunus A. and John M. CIMBALA. *Fluid mechanics: fundamentals and applications*. 3rd ed. New York: McGraw-Hill. ISBN 978-0-07-338032-2.

[5] PRANDTL, Ludwig. *Über Flüssigkeitsbewegnugen bei sehr kleiner Reibung*. Verhandlg. III. Intern. Math. Kongr. Heidelberg, 484–491. 1904

[6] BERGMAN, Theodore L., Adrienne S. LAVINE, Frank P. INCROPERA and David P. DE WITT. *Fundamentals of Heat and Mass Transfer*. 8th edition. USA: Wiley, 2018, 992 s. ISBN 978-1-119-32042-5.

[7] AUSONI, Philippe. *Turbulent vortex shedding from a blunt trailing edge hydrofoil*. Lausanne, 2009. PhD thesis. EPFL Lausanne.

[8] BRDIČKA, Miroslav, Ladislav SAMEK and Bruno SOPKO. *Mechanika kontinua*. 4th Edition. Praha: Academia, 2011. Gerstner. ISBN 978-80-200-2039-0.

[9] VERSTEEG, H.K and W. MALALASEKERA. *An introduction to computational fluid dynamics: the finite volume method*. Harlow: Longman, 1995. ISBN 0-582-21884-5.

[10] MENTER, F. R. Two-equation eddy-viscosity turbulence models for engineering applications. *AIAA Journal*. 1994, **32**(8), 1598-1605. DOI: 10.2514/3.12149. ISSN 0001-1452.

[11] FRANC, Jean-Pierre and Jean-Marie MICHEL. *Fundamentals of cavitation*. Boston: Kluwer Academic Publishers, 2004. ISBN 14-020-2232-8.

[12] BRENNEN, Christopher E. *Cavitation and bubble dynamics*. New York: Oxford University Press, 1995. ISBN 01-950-9409-3.

[13] DE LA TORRE, Oscar et al. Experimental investigation of added mass effects on a hydrofoil under cavitation conditions. *Journal of Fluids and Structures*. Elsevier, 2013, **39**, 173-187. DOI: 10.1016/j.jfluidstructs.2013.01.008. ISSN 08899746.

[14] LANGE, D.F. de and G.J. de BRUIN. Sheet cavitation and cloud cavitation, re-entrant jet and three-dimensionality. *Applied Scientific Research*. Springer Verlag, 1998, **58**, 91-114. DOI: https://doi.org/10.1023/A:1000763130780. ISSN 1573-1987.

[15] PAIDOUSSIS, M. P., Stuart PRICE and Emmanuel de LANGRE. *Fluid-structure interactions: cross-flow-induced instabilities*. 2nd edition. New York: Cambridge University Press, 2011. ISBN 978-0-521-11942-9.

[16] NENNEMANN, B., T. C. VU and M. FARHAT. CFD prediction of unsteady wicket gate-runner interaction in Francis turbines: A new standard hydraulic design procedure. In: *EPFL Lib*. 2005, s. 1-9.

[17] NENNEMANN, Bernd, Christine MONETTE and Joël CHAMBERLAND-LAUZON. Hydrodynamic damping and stiffness prediction in Francis turbine runners using CFD. *IOP Conference Series: Earth and Environmental Science*. IOP Publishing, 2016, **49**, 1-10. DOI: 10.1088/1755-1315/49/7/072006. ISSN 1755-1315.

[18] PAIDOUSSIS, M. P. *Fluid-structure interactions: slender structures and axial flow*. Second edition. Kidlington, Oxford: Academic Press is an imprint of Elsevier, 2014. ISBN 978-0-12-397312-2.

[19] LINDHOLM, Ulric S., Daniel D. KANA, Wen-Hwa CHU and Norman ABRAMSON. Elastic Vibration Characteristics of Cantilever Plates in Water. *Journal of Ship Research*. New York: Society of Naval Architects and Marine Engineers, 1965, p. 11-36. ISSN 0022-4502.

[20] YADYKIN, Y, V TENETOV and D LEVIN. The added mass of a flexible plate oscillating in a fluid. *Journal of Fluids and Structures*. 2003, **17**(1), 115-123. DOI: 10.1016/S0889-9746(02)00100-7. ISBN 8489925704.

[21] LIANG, Cho Chung, Ching Chao LIAO, Yuh Shiou TAI and Wen Hao LAI. The free vibration analysis of submerged cantilever plates. *Ocean Engineering*. 2001, **28**(9), 1225-1245. DOI: 10.1016/S0029-8018(00)00045-7.

[22] ERGIN, A. and B. UĢURLU. Linear vibration analysis of cantilever plates partially submerged in fluid. *Journal of Fluids and Structures*. 2003, **17**(7), 927-939. DOI: 10.1016/S0889-9746(03)00050-1. ISBN 9021228564.

[23] MOTLEY, Michael R., Matthew R. KRAMER and Yin Lu YOUNG. Free surface and solid boundary effects on the free vibration of cantilevered composite plates. *Composite Structures*. Elsevier, 2013, **96**, 365-375. DOI: 10.1016/j.compstruct.2012.09.023.

[24] BRENNEN, C. E. *A Review of Added Mass and Fluid Inertial Forces*. Department of the Navy, Port Hueneme, CA, USA, 1982. ISBN N62583-81-MR-554. Available at: http://authors.library.caltech.edu/233/

[25] CONCA, C., A. OSSES and J. PLANCHARD. Added mass and damping in fluid-structure interaction. *Computer Methods in Applied Mechanics and Engineering*. 1997, **146**(3-4), 387-405. DOI: 10.1016/S0045-7825(96)01246-7.

[26] LIANG, Q. W., et al. Modal Response of Hydraulic Turbine Runners. In: *Proceedings of the 23rd IAHR Symposium on Hydraulic Machinery and Systems, Yokohama, Japan*. Yokohama, Japan, 2006, s. 1-9. ISBN 4819018094.

[27] PRESAS, Alexandre, et al. On the detection of natural frequencies and mode shapes of submerged rotating disk-like structures from the casing. *ANSYS Systems and Signal Processing*. 2015, **60-61**, 547-570. DOI: 10.1016/j.ymssp.2015.01.013. ISSN 08883270.

[28] PRESAS, Alexandre, et al. Experimental analysis of the dynamic behaviour of a rotating disk submerged in water. *IOP Conference Series: Earth and Environmental Science*. 2014, **22**(3), 547-570. DOI: 10.1088/1755-1315/22/3/032043. ISSN 1755-1307.

[29] PRESAS, Alexandre, et al. Influence of the rotation on the natural frequencies of a submerged-confined disk in water. *Journal of Sound and Vibration*. 2015, **337**, 161-180. DOI: 10.1016/j.jsv.2014.10.032. ISSN 0022460X.

[30] RODRIGUEZ, C. G., et al. Experimental investigation of added mass effects on a Francis turbine runner in still water. *Journal of Fluids and Structures*. 2006, **22**(5), 699-712. DOI: 10.1016/j.jfluidstructs.2006.04.001. ISSN 0889-9746.

[31] VALENTÍN, D., et al. Influence of the added mass effect and boundary conditions on the dynamic response of submerged and confined structures. *IOP Conference Series: Earth and Environmental Science*. 2014, **22**(3), 1-11. DOI: 10.1088/1755-1315/22/3/032042. ISSN 1755-1307.

[32] LAIS, S., Q. LIANG, U. HENGGELER, T. WEISS, X. ESCALER and E. EGUSQUIZA. Dynamic Analysis of Francis Runners- Experiment and Numerical Simulation. *International Journal of Fluid Machinery and Systems*. 2009, **2**(4), 303-314. DOI: 10.5293/IJFMS.2009.2.4.303. ISSN 1882-9554.

[33] EGUSQUIZA, Eduard et al. Fluid Added Mass Effect in the Modal Response of a Pump-Turbine Impeller. *Volume 1: 22nd Biennial Conference on ANSYS Vibration and Noise, Parts A and B*. ASME, 2009, 2009, p. 715-724. DOI: 10.1115/DETC2009-86830. ISBN 978-0-7918-4898-2.

[34] ANSYS. ANSYS 19.1 Documentation: Acoustic Analysis Guide. 2018

[35] DE LA TORRE, et al. Numerical and experimental study of a nearby solid boundary and partial submergence effects on hydrofoil added mass. *Computers and Fluids*. Elsevier, 2014, **91**, 1-9. DOI: 10.1016/j.compfluid.2013.12.003. ISSN 0045-7930.

[36] RODRIGUEZ, C. G., et al. Capability of structural-acoustical FSI numerical model to predict natural frequencies of submerged structures with nearby rigid surfaces. *Computers and Fluids*. Elsevier, 2012, **64**, 117-126. DOI: 10.1016/j.compfluid.2012.05.011. ISSN 00457930.

[37] VALENTÍN, D., et al. Influence of the boundary conditions on the natural frequencies of a Francis turbine. *28th AHR Symposium on Hydraulic Machinery and Systems, Grenoble, July 4-8*. 2016, p. 365-372. DOI: 10.1088/1755-1315/49/7/072004.

[38] LIANG, Q., et al. Numerical simulation of fluid added mass effect on a francis turbine runner. *Computers & Fluids*. 2007, **36**(6), 1106-1118. DOI: 10.1016/j.compfluid.2006.08.007. ISSN 0045-7930.

[39] WEBER, Wilhelm and SEIDEL, Ulrich. Analysis of natural frequencies of disc-like structures in water environment by coupled fluid-structure-interaction simulation. In: *6th IAHR International Meeting of the Workgroup on Cavitation and Dynamic Problems in Hydraulic Machinery and Systems. (Cited on page 41.)*. 2015.

[40] HUANG, Xingxing and Xavier ESCALER. Added Mass Effects on a Francis Turbine Runner with Attached Blade Cavitation. *Fluids*. 2019, **4**(2), 1-19. DOI: 10.3390/fluids4020107. ISSN 2311-5521.

[41] ESCALER, X, O DE LA TORRE and M FARHAT. Review of parameters influencing the structural response of a submerged body under cavitation conditions. *Journal of Physics: Conference Series*. 2015, **656**. DOI: 10.1088/1742-6596/656/1/012150. ISSN 1742-6588.

[42] BENAOUICHA, Mustapha and Jacques-André ASTOLFI. Analysis of added mass in cavitating flow. *Journal of Fluids and Structures*. 2012, **31**, 30-48. DOI: 10.1016/j.jfluidstructs.2012.03.003. ISSN 08899746.

[43] RAO, Singiresu S. *Mechanical vibrations*. Sixth edition. Hoboken: Pearson, 2017. ISBN 978-0-134-36130-7.

[44] KAMINER, A. A. and N. Ya. NASTENKO. Aerodynamic damping of turbine blade oscillations in air flow. *Strength of Materials*. 1974, **6**(6), 709-712. DOI: 10.1007/BF01528071. ISSN 0039-2316.

[45] KAMINER, A. A. and B. M. KAVITSKII. Experimental investigation of hydrodynamic damping during bending oscillations of blade profiles in water flow. *Strength of Materials*. 1976, **8**(1), 25-27. DOI: 10.1007/BF01528208. ISSN 0039-2316.

[46] AVELLAN, Francois, Pierre HENRY and Inge L. RYHMING. A new high speed cavitation tunnel for cavitation studies in hydraulic machinery. In: *Proceedings of International Cavitation Research Facilities and Techniques, ASME Winter Annual Meeting*. Boston, 1987, p. 1-25.

[47] ROTH, Steven, et al. Hydrodynamic damping identification from an impulse response of a vibrating blade. In: Proceedings of the 3rd IAHR International Meeting of the Workgroup on Cavitation and Dynamic Problems in Hydraulic Machinery and Systems. Brno University of Technology, 2009. p. 253-260.

[48] SEELEY, Charles et al. Determination of Hydrofoil Damping Due to Fluid Structure Interaction Using MFC Actuators. *54th AIAA/ASME/ASCE/AHS/ASC Structures, Structural Dynamics, and Materials Conference*. Reston, Virginia: American Institute of Aeronautics and Astronautics, 2013, 2013-04-08. DOI: 10.2514/6.2013-1910. ISBN 978-1-62410-223-3.

[49] COUTU, A. et al. Damping measurements in flowing water. *IOP Conference Series: Earth and Environmental Science*. 2012, **15**(6), 062060-062060. DOI: 10.1088/1755-1315/15/6/062060.

[50] PRESAS, A. et al. Feasibility of using PZT actuators to study the dynamic behaviour of a rotating disk due to rotor-stator interaction. *Sensors (Basel, Switzerland)*. Multidisciplinary Digital Publishing Institute, 2014, **14**(7). DOI: 10.3390/s140711919.

[51] SEELEY, C. et al. Characterization of hydrofoil damping due to fluid–structure interaction using piezocomposite actuators. *Smart Materials and Structures*. 2012, **21**(3), 35027-35027. DOI: 10.1088/0964-1726/21/3/035027.

[52] YAO, Z., F. WANG, M. DREYER and M. FARHAT. Effect of trailing edge shape on hydrodynamic damping for a hydrofoil. *Journal of Fluids and Structures*. Elsevier, 2014, **51**, 189-198. DOI: 10.1016/j.jfluidstructs.2014.09.003

[53] LIAGHAT, T., et al. Two-Way Fluid-Structure Coupling in Vibration and Damping Analysis of an Oscillating Hydrofoil. *Volume 4A: Dynamics, Vibration, and Control*. ASME, 2014, 2014-11-14, 1-10. DOI: 10.1115/IMECE2014-38441. ISBN 978-0-7918-4647-6.

[54] HÜBNER, B., U. SEIDEL and S. ROTH. Application of fluid-structure coupling to predict the dynamic behaviour of turbine components. *IOP Conference Series: Earth and Environmental Science*. 2010, **12**, 012009-012009. DOI: 10.1088/1755-1315/12/1/012009. ISSN 1755-1315.

[55] HÜBNER, B., U. SEIDEL, and J. KOUTNIK. Assessing the dynamics of turbine components using advanced fluid-structure interaction HYDRO 2012 (Bilbao). 2012.

[56] HU, Shiliang, Chuanjing LU and Yousheng HE. Fluid-structure interaction simulation of three-dimensional flexible hydrofoil in water tunnel. *Applied Mathematics and Mechanics*. 2016, **37**(1), 15-26. DOI: 10.1007/s10483-016-2011-9. ISSN 0253-4827.

[57] DOMPIERRE, F and M SABOURIN. Determination of turbine runner dynamic behaviour under operating condition by a two-way staggered fluid-structure interaction method. *IOP Conference Series: Earth and Environmental Science*. 2010, **12**. DOI: 10.1088/1755-1315/12/1/012085. ISSN 1755-1315.

[58] TENGS, E. O., et al. Numerical simulation of the hydrodynamic damping of a vibrating hydrofoil. *IOP Conference Series: Earth and Environmental Science*. 2019, **240**, 1-10. DOI: 10.1088/1755-1315/240/6/062002. ISSN 1755-1315.

[59] GAUTHIER, J.P., A.M. GIROUX, S. ETIENNE and F.P. GOSSELIN. A numerical method for the determination of flow-induced damping in hydroelectric turbines. *Journal of Fluids and Structures*. 2017, **69**, 341-354. DOI: 10.1016/j.jfluidstructs.2017.01.004. ISSN 08899746.

[60] GAUTHIER, J. P., A. M. GIROUX, S. ETIENNE and F. P. GOSSELIN. CFD evaluation of added damping due to fluid flow over a hydroelectric turbine blade. *IOP Conference Series: Earth and Environmental Science*. 2016, **49**(7), 1-10. DOI: 10.1088/1755-1315/49/7/072003. ISSN 1755-1315.

[61] NENNEMANN, B. and C. MONETTE. Prediction of vibration amplitudes on hydraulic profiles under von Karman vortex excitation. *IOP Conference Series: Earth and Environmental Science*. 2019, **240**, 062004-062004. DOI: 10.1088/1755-1315/240/6/062004.

[62] TENGS, Erik, Johannes EINZINGER and Pål-Tore STORLI. Two-way coupled simulation of the Francis-99 hydrofoil using model order reduction. *Journal of Physics: Conference Series*. 2019, **1296**. DOI: 10.1088/1742-6596/1296/1/012001. ISSN 1742-6588.

[63] ČUPR, P., D. ŠTEFAN, V. HABÁN and P. RUDOLF. FSI analysis of francis-99 hydrofoil employing SBES model to adequately predict vortex shedding. *Journal of Physics: Conference Series*. 2019, **1296**. DOI: 10.1088/1742-6596/1296/1/012002. ISSN 1742-6588.

[64] BERGAN, C. W., E. O. TENGS, B. W. SOLEMSLIE and O. G. DAHLHAUG. An experimental investigation of the hydrodynamic damping of vibrating hydrofoils. *IOP Conference Series: Earth and Environmental Science*. 2019, **240**. DOI: 10.1088/1755-1315/240/6/062008. ISSN 1755-1315.

[65] SAGMO, K. F., E. O. TENGS, C. W. BERGAN and P. T. STORLI. PIV measurements and CFD simulations of a hydrofoil at lock-in. *IOP Conference Series: Earth and Environmental Science*. 2019, **240**. DOI: 10.1088/1755-1315/240/6/062006. ISSN 1755-1315.

[66] Technical drawing no. 1-ENR-2-2839 created by *Litostroj Engineering a.s.* as an output of grant no. TH02020705

[67] COLEMAN, Brendan, Pat MEEHAN, John REEDY and Pat WEEKS. Coherent sampling helps when specifying DSP A/D converters. *EDN*. October 15 1987, 145-152. ISSN 00127515.

[68] EWINS, D.J. Modal testing: theory, practice and application. England: Research Studies Press, 1986. Mechanical engineering research studies. ISBN 0-86380 036X.

[69] LIEVEN, N. A. J., D. J. EWINS, N. M. M. MAIA and J. M. M. SILVA. Modal analysis identification techniques. *Philosophical Transactions of the Royal Society of London. Series A: Mathematical, Physical and Engineering Sciences*. 2001, **359(1778)**, 29-40. ISSN 1364-503X. DOI:10.1098/rsta.2000.0712

[70] LITTLER, J.D. An assessment of some of the different methods for estimating damping from full-scale testing. *Journal of Wind Engineering and Industrial Aerodynamics*. 1995, **57**(2-3), 179-189. ISSN 01676105. DOI:10.1016/0167-6105(94)00109-Q

[71] WANG, Wei, et al. Numerical Investigation into the Effect of Sound Speed in Attached Cavitation on Hydrofoil Modes of Vibration. *Energies*. 2019, **12(9)**. DOI: 10.3390/en12091758. ISSN 1996-1073.

[72] ČUPR, Pavel, Pavel RUDOLF and Vladimír HABÁN. Numerical investigation of added mass and damping effects on a hydrofoil in cavitation tunnel. *WASSERWIRTSCHAFT*. 2019, **109(S1)**, 6-11. DOI: 10.1007/s35147-019-0216-2 ISSN 0043-0978.

[73] ANSYS. ANSYS 19.1 Documentation: Coupled-Field Analysis Guide. 2018

[74] LIAGHAT, T., et al. Two-Way Fluid-Structure Coupling in Vibration and Damping Analysis of an Oscillating Hydrofoil. *Volume 4A: Dynamics, Vibration, and Control*. ASME, 2014, 2014-11-14, 1-10. DOI: 10.1115/IMECE2014-38441. ISBN 978-0-7918-4647-6.

[75] MONETTE, C., et al. Hydro-dynamic damping theory in flowing water. *IOP Conference Series: Earth and Environmental Science*. 2014, **22**(September), 1-10. DOI: 10.1088/1755-1315/22/3/032044. ISSN 1755-1315.

[76] ČUPR, P., W. WEBER and B. HÜBNER. Investigation on the hydrodynamic damping using prescribed blade motion techniques. *IOP Conference Series: Earth and Environmental Science*. 2019, **405**. DOI: 10.1088/1755-1315/405/1/012017. ISSN 1755-1315.

[77] ESCALER, Xavier and Oscar DE LA TORRE. Axisymmetric vibrations of a circular Chladni plate in air and fully submerged in water. *Journal of Fluids and Structures*. 2018, **82**, 432-445. DOI: 10.1016/j.jfluidstructs.2018.07.017. ISSN 08899746.

[78] TENGS, E. O., et al. Numerical simulation of the hydrodynamic damping of a vibrating hydrofoil. *IOP Conference Series: Earth and Environmental Science*. 2019, **240**, 1-10. DOI: 10.1088/1755-1315/240/6/062002. ISSN 1755-1315.

[79] ANSYS. ANSYS 19.1 Documentation: ANSYS CFX-Solver Modeling Guide. 2018

[80] FREY, Christian, et al. A Harmonic Balance Technique for Multistage Turbomachinery Applications. *Volume 2B: Turbomachinery*. ASME, 2014, 2014-6-16, 1-14. DOI: 10.1115/GT2014-25230. ISBN 978-0-7918-4561-5.

[81] GOPINATH, Arathi and Antony JAMESON. Time Spectral Method for Periodic Unsteady Computations over Two- and Three- Dimensional Bodies. In: *43rd AIAA Aerospace Sciences Meeting and Exhibit*. Reston, Virigina: American Institute of Aeronautics and Astronautics, 2005, p. 1-14. DOI: 10.2514/6.2005-1220. ISBN 978-1-62410-064-2.

[82] HALL, Kenneth et al. Computation of Unsteady Nonlinear Flows in Cascades Using a Harmonic Balance Technique. *AIAA Journal*. 2002, **40**(5), 879-886. DOI: 10.2514/2.1754. ISSN 0001-1452.

[83] GONG, Yiming and Weiwei ZHANG. Efficient Aeroelastic Solution Based on Time-Spectral Fluid–Structure Interaction Method. *AIAA Journal*. 2019, **57**(7), 3014-3025. DOI: 10.2514/1. J057628. ISSN 0001-1452.

[84] MIYAGAWA, K., S. Fukao and Y. Kawata. Study on stay vane instability due to Vortex shedding *22th IAHR Symposium on Hydraulic Machinery and Systems, Stockholm,* 2004

[85] LIU, Xin, Zhengwei WANG, Xavier ESCALER and Lingjiu ZHOU. Numerical evaluation of cavitation void ratio significance on hydrofoil dynamic response. *Journal of Physics: Conference Series* [online]. 2015, **656**. DOI: 10.1088/1742-6596/656/1/012159. ISSN 1742-6588.

NOMENCLATURE

Greek

Acronym	Unit	Description
α	[1]	Relaxation parameter
α_{inc}	deg	Angle of attack of hydrofoil
α_{vap}	[1]	Volume fraction of saturated vapour
α_w	[1]	Volume fraction of water
δ	[1]	Thickness of boundary layer
δ_{ij}	[1]	Kronecker delta
ε	$m^2 s^{-3}$	Turbulent dissipation
ε_{ij}	[1]	Strain tensor
ζ	[1]	Damping ratio
$\zeta_{SDOF,LDV1,2}$	[1]	Damping ratio calculated by SDOF Response Fit method
ϑ	[1]	Relative volume change
$\dot{\vartheta}$	s^{-1}	Volumetric dilatation rate
Λ	[1]	Logarithmic decrement
λ		Lamé first parameter
ν	[1]	Poisson's ratio
ν_L	$m^2 \cdot s^{-1}$	Kinematic viscosity of liquid
μ		Lamé second parameter
μ_D	$Pa \cdot s$	Dynamic viscosity
μ_t	$m^2 \cdot s^{-1}$	Turbulence eddy viscosity
ρ	$kg \cdot m^{-3}$	Density
ρ_L	$kg \cdot m^{-3}$	Liquid density
ρ_{mix}	$kg \cdot m^{-3}$	Density of mixture inside cavitation cloud
ρ_{vap}	$kg \cdot m^{-3}$	Density of saturated vapour
ρ_w	$kg \cdot m^{-3}$	Water density
σ	[1]	Cavitation number
σ_e, σ_k	[1]	Constants of the turbulent models
σ_{inc}	[1]	Incipient cavitation number
$\boldsymbol{\sigma}$ σ_{ij}	Pa	Fluid stress tensor

$\boldsymbol{\tau}\ \tau_{ij}$	Pa	Wall shear stress tensor
$\boldsymbol{\tau_t}\ \tau_{t,ij}$	Pa	Reynolds tensor
τ_{wall}	MPa	Wall shear stress
Φ	[1]	Normalized mode shape deflection
φ	deg, rad	Phase shift
ω	$rad \cdot s^{-1}$	Angular frequency
ω	s^{-1}	Rate of turbulent dissipation (in Chapter 4.2.1)
ω_0	$rad \cdot s^{-1}$	Undamped natural angular frequency
ω_D	$rad \cdot s^{-1}$	Damped natural angular frequency

Latin

A	m^2	Surface area
A_{MAG}	[1]	Magnification factor
a	$m \cdot s^{-2}$	Acceleration
$\boldsymbol{B_{ADD}}$	$kg \cdot s^{-1}$	Modal matrix of added damping
$\boldsymbol{B_S}\ B_{ij}$	$kg \cdot s^{-1}$	Modal damping matrix of structure
b_{ADD}	$kg \cdot s^{-1}$	Modal added damping of SDOF system
b_f	$kg \cdot s^{-1}$	Hydrodynamic damping coefficient
b_S	$kg \cdot s^{-1}$	Modal structural damping of SDOF system
b_{TOT}	$kg \cdot s^{-1}$	Total damping
b_W	$kg \cdot s^{-1}$	Added damping coefficient (contribution from acoustic radiation and viscous effects)
$C_\mu, C_{\varepsilon_1}, C_{\varepsilon_2}$	[1]	Constants of the turbulence models
c	$m \cdot s^{-1}$	Speed of sound
c_{mix}	$m \cdot s^{-1}$	Speed of sound of mixture inside cavitation cloud
c_{vap}	$m \cdot s^{-1}$	Speed of sound in saturated vapour
c_w	$m \cdot s^{-1}$	Speed of sound in water
d	m	Characteristic length
d_h	m	Hydraulic diameter
E	Pa	Young modulus
E_K	J	Kinetic energy
E_P	J	Potential energy
$\boldsymbol{F}\ F_i$	N	Vector of force
F_0	[1]	Non-dimensional excitation force

$F_{ADD,DAMP}$	N	Contribution of the total fluid added damping force from the hydrodynamic damping
$F_{ADD,DAMP,TOT}$	N	Total fluid added damping force
$F_{ADD,MASS}$	N	Added mass force
$F_{ADD,STIFF}$	N	Contribution of the total fluid added stiffness force from the flow induced stiffness
$F_{ADD,STIFF,TOT}$	N	Total fluid added stiffness force
$\boldsymbol{F_{Inertial}}$ $F_{Inertial,i}$	N	Vector of inertial force
$\boldsymbol{F_M}$ $F_{M,i}$	N	Vector of mass force
$\boldsymbol{F_S}$ $F_{S,i}$	N	Vector of surface force
$\boldsymbol{f}$ f_i	N	Vector of excitation forces
f	N	Excitation force
$f_{Karman,CFD}$	s^{-1}	Vortex shedding frequency calculated from CFD unsteady analysis
$f_{Karman,St}$	s^{-1}	Vortex shedding frequency estimated with the use of Strouhal number
f_{MAX}	N	Amplitude of the excitation force
$f_{nat,air}$	s^{-1}	Natural frequency in air
$f_{NAT,AIR,EXP}$	s^{-1}	Natural frequency of hydrofoil in air obtained from experiment
$f_{NAT,AIR,FEM}$	s^{-1}	Natural frequency of hydrofoil in air obtained from finite element modal analysis
$f_{NAT,SDOF,12}$	s^{-1}	Natural frequency of hydrofoil obtained by SDOF Response Fit method
$f_{NAT,SW,EXP}$	s^{-1}	Natural frequency of hydrofoil in still water obtained from experiment
$f_{NAT,SW,FEM}$	s^{-1}	Natural frequency of hydrofoil in still water obtained from acoustic modal analysis
$f_{nat,water}$	s^{-1}	Natural frequency in water
H_{cloud}	m	Height (thickness) of the cavitation cloud
$\boldsymbol{K_{ADD}}$	$kg \cdot s^{-2}$	Modal matrix of added stiffness
$\boldsymbol{K_S}$ K_{ij}	$kg \cdot s^{-2}$	Modal stiffness matrix of structure
k	$J \cdot kg^{-1}$	Turbulence kinetic energy
k_{ADD}	$kg \cdot s^{-2}$	Modal added stiffness of SDOF system
k_F	$kg \cdot s^{-2}$	Added stiffness coefficient (contribution from the fluid flow)
k_S	$kg \cdot s^{-2}$	Modal structural stiffness of SDOF system

k_W	$kg \cdot s^{-2}$	Added stiffness coefficient (contribution from acoustic radiation and viscous effects
L_c	m	Circumference of the cross-sectional area
L_{cloud}	m	Length of the cavitation cloud
M	kg	Modal mass
$\boldsymbol{M_{ADD}}$	kg	Modal matrix of added mass
$\boldsymbol{M_S}$ M_{ij}	kg	Modal mass matrix of structure
m_{ADD}	kg	Modal added mass of SDOF system
m_S	kg	Modal structural mass of SDOF system
$\boldsymbol{n}$ n_j	[1]	Outward-pointing normal vector
p	Pa	Pressure
$\bar{p}$	Pa	Mean pressure
p'	Pa	Pressure fluctuations
p_b	Pa	Bubble pressure
p_V	Pa	Pressure of saturated vapour
p_∞	Pa	Reference pressure
Q	N	Generalized force
Q^D	N	Dissipative (damping) force
Q^P	N	Conservative potential force
Q_V	$m^3 \cdot s^{-1}$	Flow rate
q	*m, rad*	Generalized coordinate
$\boldsymbol{q}$ q_i	*m, rad*	Vector of generalized coordinates
$\dot{q}$	*m, rad*	Generalized velocity
$\dot{\boldsymbol{q}}$ $\dot{q}_i$	*m, rad*	Vector of generalized velocities
$\ddot{q}$	*m, rad*	Generalized acceleration
$\ddot{\boldsymbol{q}}$ $\ddot{q}_i$	*m, rad*	Vector of generalized acceleration
R	J	Rayleigh dissipation function
Re	[1]	Reynolds number
Re_{crit}	[1]	Critical value of Reynolds number
$Re_{x\,crit}$	[1]	Critical value of Reynolds number for transition inside boundary layer
Re_t	[1]	Turbulent Reynolds number
Re_{TE}	[1]	Reynolds number related to the thickness of hydrofoil trailing edge
r	m	Radius of bubble

S	$N \cdot m^{-1}$	Surface tension
S_{cross}	m^2	Cross-section area
$\boldsymbol{S}\ S_{ij}$	Pa	Stress tensor of the structure
St	[1]	Strouhal number
St_{crit}	[1]	Critical value of Strouhal number
T	s	Period of oscillation
T_{ref}	$°C$	Reference operating temperature
t	s	Time
$\boldsymbol{U}$	m	Vector of displacement
U_{MAX}	m	Maximal amplitude of oscillations
$\boldsymbol{u}\ u_i$	m	Vector of deformation / deflection
u_τ	$m \cdot s^{-1}$	Friction velocity
v	$m \cdot s^{-1}$	Velocity
v_{inlet}	$m \cdot s^{-1}$	Mean velocity at the inlet of the CFD domain
v_f	$m \cdot s^{-1}$	Free stream velocity of the flow
v_∞	$m \cdot s^{-1}$	Reference flow velocity
$\boldsymbol{v}\ v_i$	$m \cdot s^{-1}$	Vector of velocity
$\overline{\boldsymbol{v}}_{\boldsymbol{i}}\ \bar{v}_i$	$m \cdot s^{-1}$	Vector of mean velocity
$\boldsymbol{v'}_{\boldsymbol{i}}\ v'_i$	$m \cdot s^{-1}$	Vector of velocity fluctuations
v_{ij}	s^{-1}	Strain tensor rate
$\bar{v}_{ij}$	s^{-1}	Mean strain rate tensor
V	m^3	Volume
W	J	Work
W_{DISS}	J	Modal work exchanged between fluid and structure
x	m	Coordinate in space
x_c	m	Position of transition point inside boundary layer
$\boldsymbol{x}\ x_i$	m	Vector of space coordinates
y^+	[1]	Wall distance (length scale)

ABBREVIATIONS

CFD	Computational Fluid Dynamics
CPU	Central processor unit
DOF	Degree of freedom
EMA	Experimental Modal Analysis
EPFL	L'Ecole polytechnique fédérale de Lausanne
FFT	Fast Fourier Transformation
FRF	Frequency Response Function
FSI	Fluid Structure Interaction
LDV	Laser Doppler Vibrometer
LMH	Laboratory for Hydraulic Machines
MDOF	Multi Degree of Freedom
MFC actuators	Macro Fibre Composite actuators
NACA	National Advisory Committee for Aeronautics
NTNU	Norwegian University of Science and Technology
PIV	Particle Image Velocimetry
SDOF	Single Degree of Freedom
TR PIV	Time Resolved Particle Image Velocimetry
RANS equations	Reynolds Averaged Navier-Stokes equations
UPC	Universitat Politècnica de Catalunya

LIST OF PUBLICATIONS

2019

ČUPR, P., D. ŠTEFAN, V. HABÁN and P. RUDOLF. FSI analysis of francis-99 hydrofoil employing SBES model to adequately predict vortex shedding. *Journal of Physics: Conference Series*. 2019, 1296. DOI: 10.1088/1742-6596/1296/1/012002. ISSN 1742-6588.

ČUPR, Pavel, Pavel RUDOLF and Vladimír HABÁN. Numerical investigation of added mass and damping effects on a hydrofoil in cavitation tunnel. *WASSERWIRTSCHAFT*. 2019, 109(S1), 6-11. DOI: 10.1007/s35147-019-0216-2 ISSN 0043-0978.

ČUPR, P., W. WEBER and B. HÜBNER. Investigation on the hydrodynamic damping using prescribed blade motion techniques. *IOP Conference Series: Earth and Environmental Science.* 2019, 405. DOI: 10.1088/1755-1315/405/1/012017. ISSN 1755-1315.

STAREČEK, Jakub, Pavel ČUPR and Miloslav HALUZA. Design of a high-specific speed turbine with non-uniform blade cascade. *EPJ Web of Conferences*. 2019, 213. DOI: 10.1051/epjconf/201921302078. ISSN 2100-014X.

2018

ČUPR, Pavel, Mateus DA SILVA CARDOSO and Pavel RUDOLF. Design of a new cavitation tunnel at Brno University of Technology for FSI testing. In: *Engineering Mechanics 2018*. 2018, p. 173-176. DOI: 10.21495/91-8-173. ISBN 978-80-86246-91-8. ISSN 1805-8248.

STAREČEK, Jakub, Pavel ČUPR and Miloslav HALUZA. Hydraulický návrh vysokoprůtočné turbíny na lokalitě MVE Lužnice In *Hydroturbo 2018.* 2018. p. 37-52. ISBN 978-80-227-4829-2.

2016

POCHYLÝ, F., RUDOLF, P., HALUZA, M., HABÁN, V., HUDEC, M., ŠTEFAN, D. and ČUPR, P. Vývoj vírové turbíny v násoskovém uspořádání. In *Hydroturbo 2016 - Sborník abstraktů.* 2016. p. 28-29.

RUDOLF, P., MACH, J., ČUPR, P. and POCHYLÝ, F. Hydraulic and structural optimization of very low head siphon propeller turbine (swirl turbine). In *Proceeding 19th International Seminar on Hydropower Plants.* Vienna, AUSTRIA: 2016. p. 1-10

APPENDIX

A.1 Visualisation of Vortex Shedding from CFD Analysis

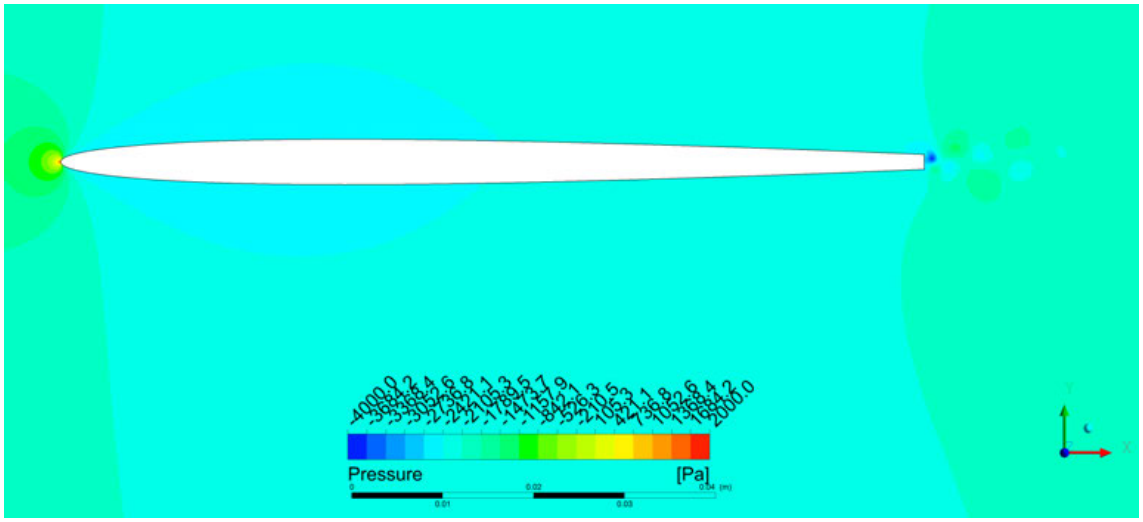

A 1.1 Pressure field around hydrofoil at $v_{inlet} = 2.5\ ms^{-1}$

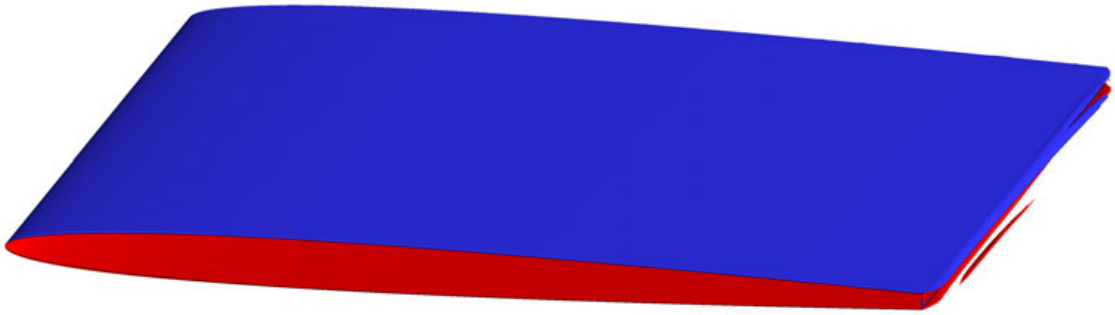

A 1.2 Vortex shedding at $v_{inlet} = 2.5\ ms^{-1}$ visualised by iso-surface of vorticity component perpendicular to the mean flow (-3500 s^{-1} is blue, 3500 s^{-1} in red)

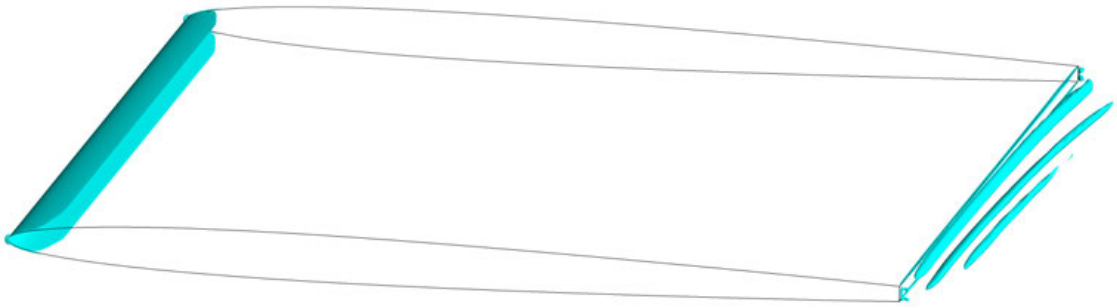

A 1.3 Vortex shedding at $v_{inlet} = 2.5\ ms^{-1}$ visualised by iso-surface of Q-criterion for value $0.8 \cdot 10^6\ s^{-2}$

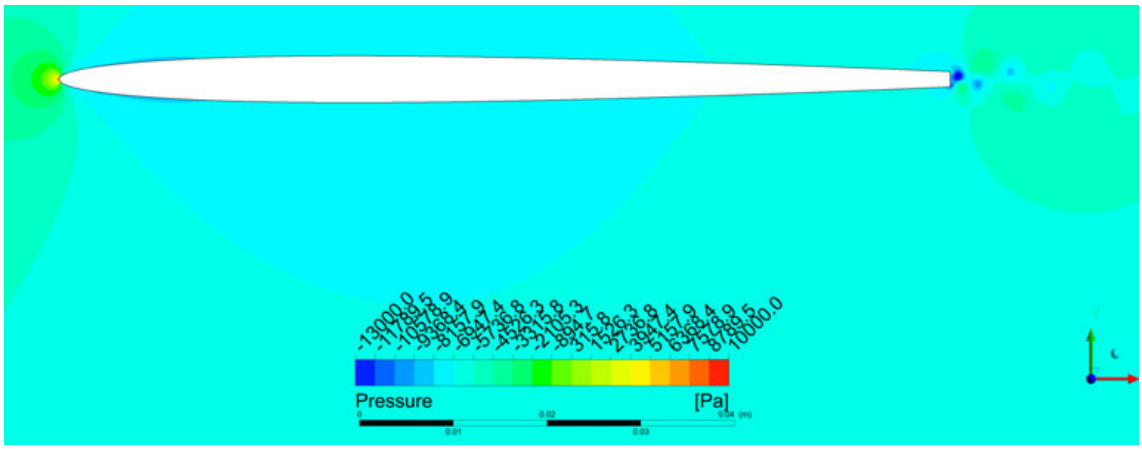

A 1.4 Pressure field around hydrofoil at $v_{inlet} = 5\ ms^{-1}$

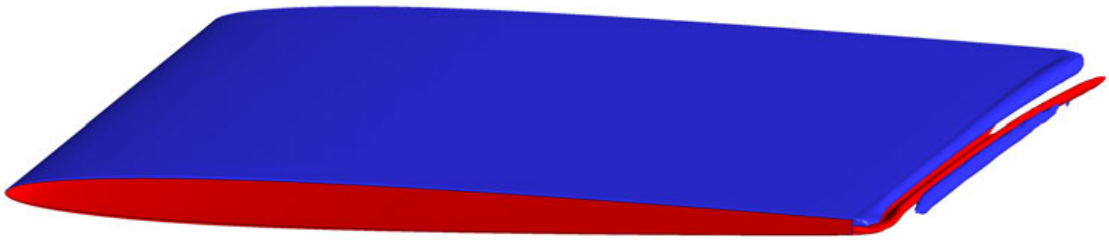

A 1.5 Vortex shedding at $v_{inlet} = 5\ ms^{-1}$ visualised by iso-surface of vorticity component perpendicular to the mean flow (-3500 s^{-1} is blue, 3500 s^{-1} in red)

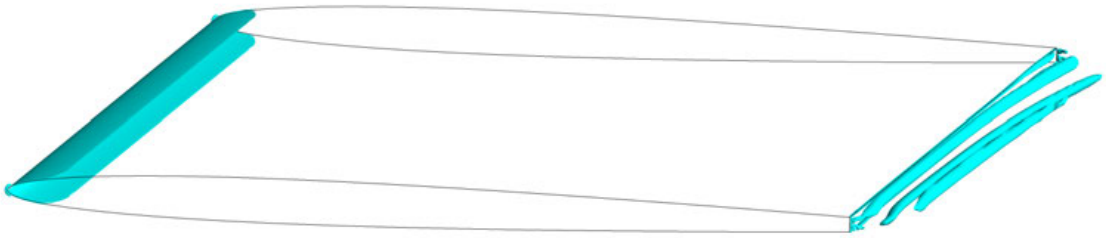

A 1.6 Vortex shedding at $v_{inlet} = 5\ ms^{-1}$ visualised by iso-surface of Q-criterion for value $2.5 \cdot 10^6\ s^{-2}$

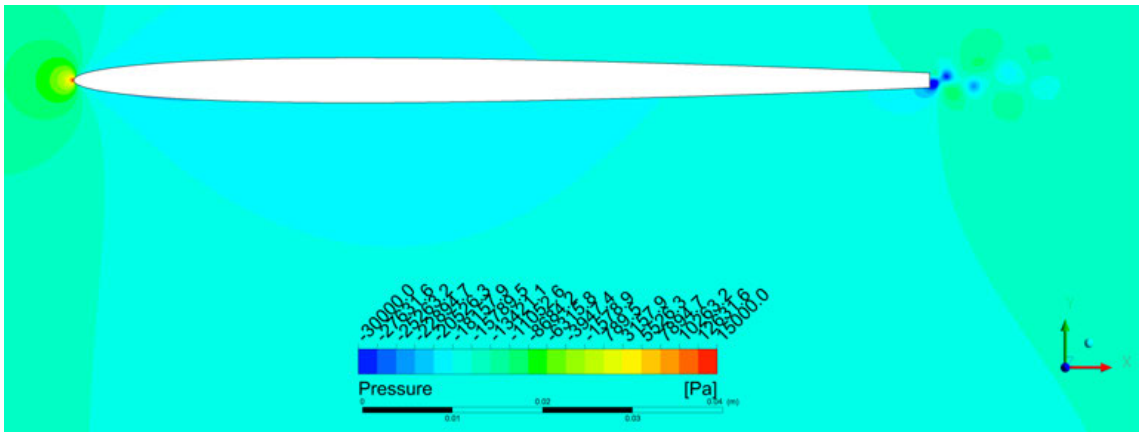

A 1.7 Pressure field around hydrofoil at $v_{inlet} = 7.5\ ms^{-1}$

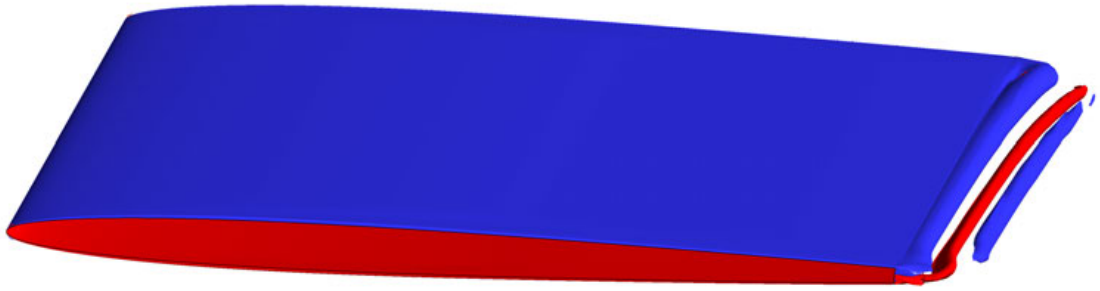

A 1.8 Vortex shedding at $v_{inlet} = 7.5\ ms^{-1}$ visualised by iso-surface of vorticity component perpendicular to the mean flow (-3500 s^{-1} is blue, 3500 s^{-1} in red)

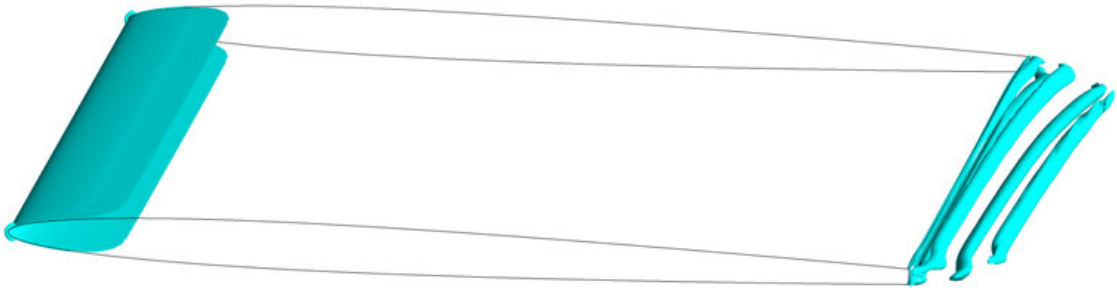

A 1.9 Vortex shedding at $v_{inlet} = 7.5\ ms^{-1}$ visualised by iso-surface of Q-criterion for value $2.5 \cdot 10^6\ s^{-2}$

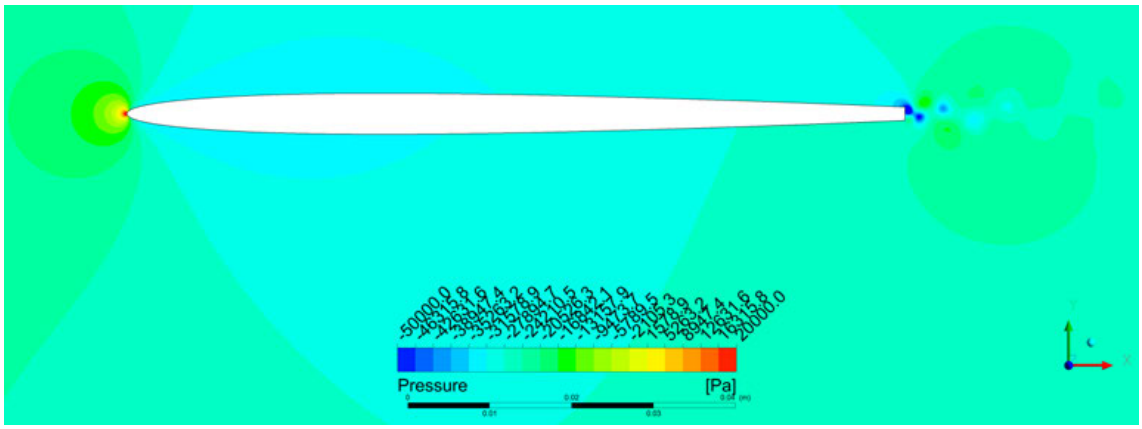

A 1.10 Pressure field around hydrofoil at $v_{inlet} = 10\ ms^{-1}$

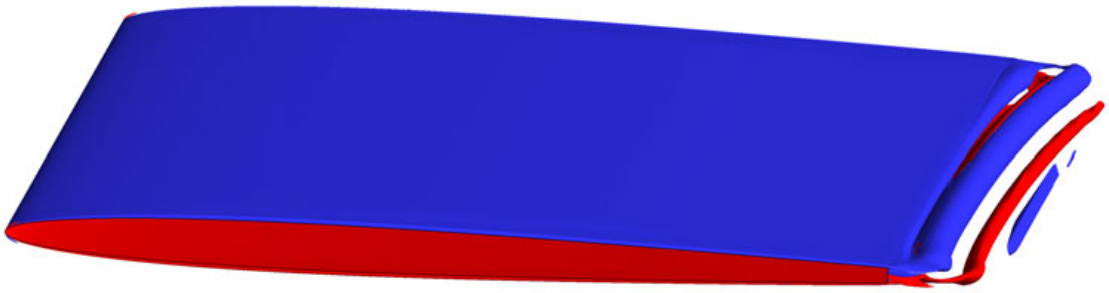

A 1.11 Vortex shedding at $v_{inlet} = 10\ ms^{-1}$ visualised by iso-surface of vorticity component perpendicular to the mean flow (-3500 s^{-1} is blue, 3500 s^{-1} in red)

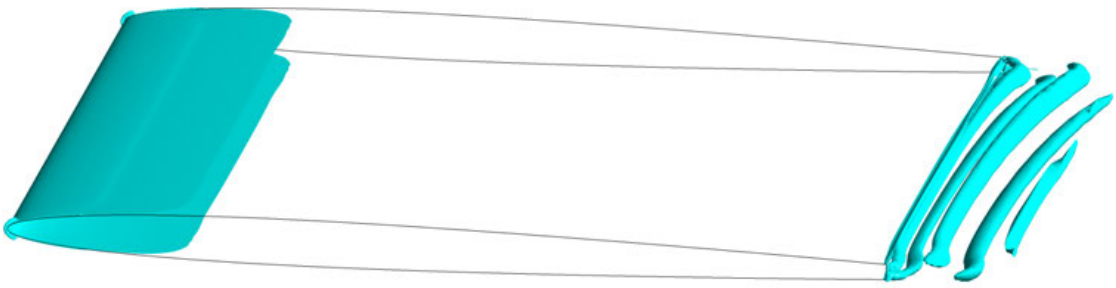

A 1.12 Vortex shedding at $v_{inlet} = 10\ ms^{-1}$ visualised by iso-surface of Q-criterion for value $2.5 \cdot 10^6\ s^{-2}$

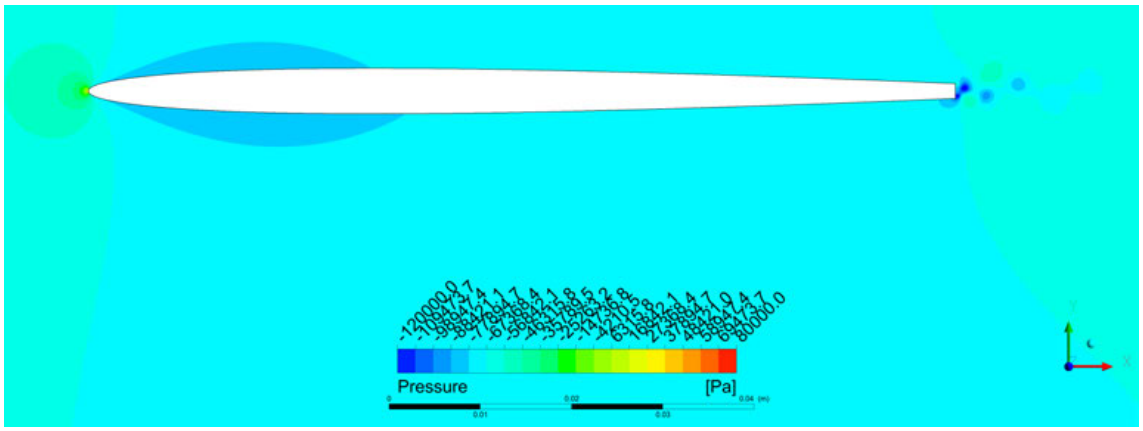

A 1.13 Pressure field around hydrofoil at $v_{inlet} = 12.5\ ms^{-1}$

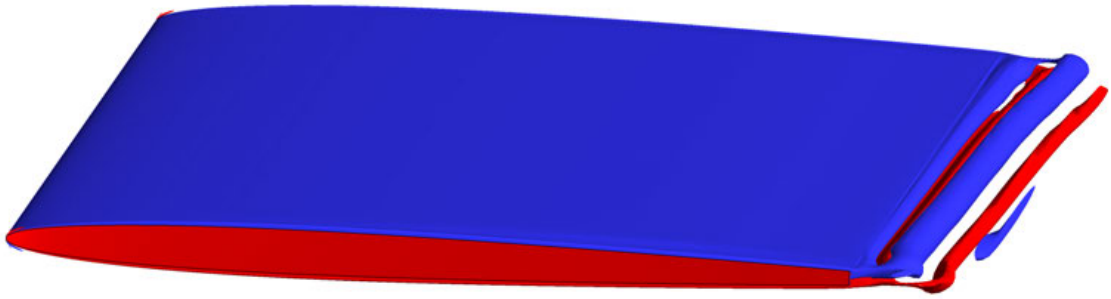

A 1.14 Vortex shedding at $v_{inlet} = 12.5\ ms^{-1}$ visualised by iso-surface of vorticity component perpendicular to the mean flow (-3500 s^{-1} is blue, 3500 s^{-1} in red)

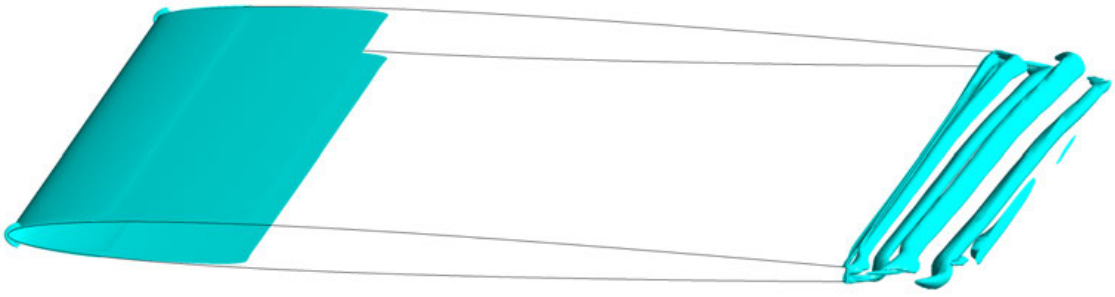

A 1.15 Vortex shedding at $v_{inlet} = 12.5\ ms^{-1}$ visualised by iso-surface of Q-criterion for value $2.5 \cdot 10^6\ s^{-2}$

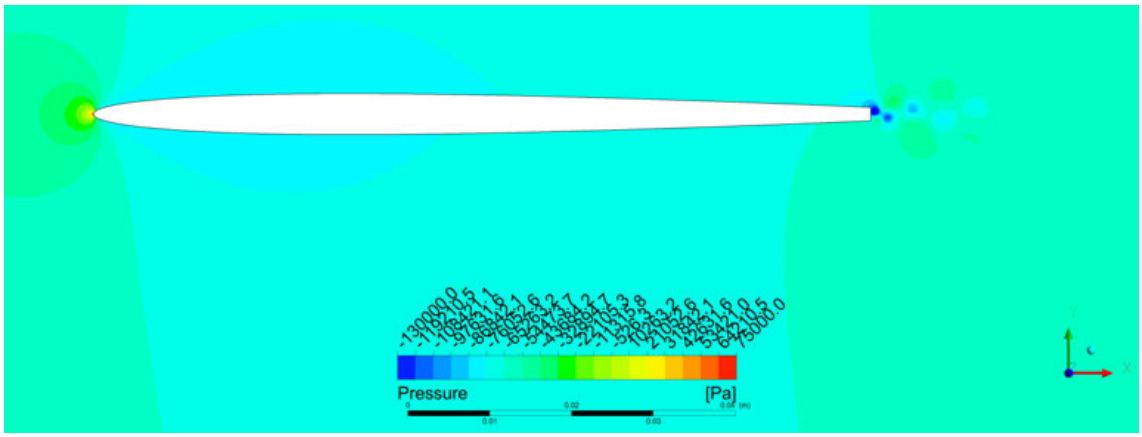

A 1.16 Pressure field around hydrofoil at $v_{inlet} = 15\ ms^{-1}$

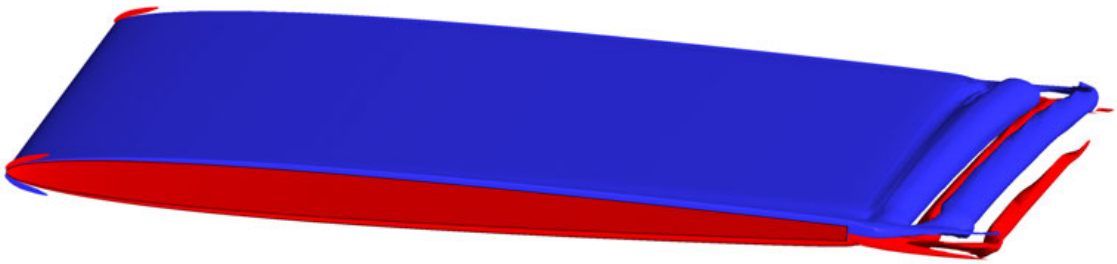

A 1.17 Vortex shedding at $v_{inlet} = 15\ ms^{-1}$ visualised by iso-surface of vorticity component perpendicular to the mean flow (-2500 s^{-1} is blue, 2500 s^{-1} in red)

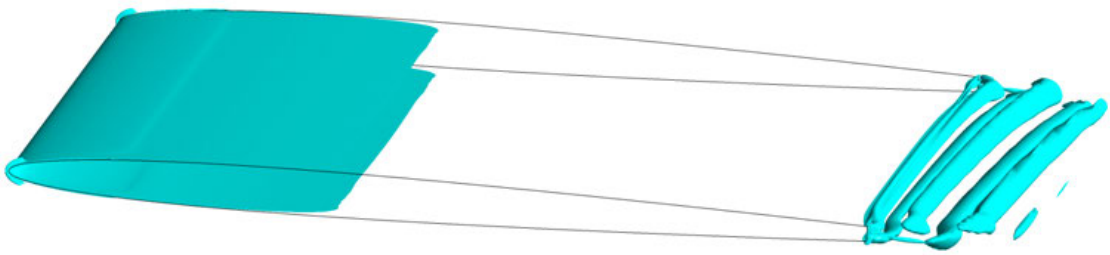

A 1.18 Vortex shedding at $v_{inlet} = 15\ ms^{-1}$ visualised by iso-surface of Q-criterion for value $2.5 \cdot 10^6\ s^{-2}$

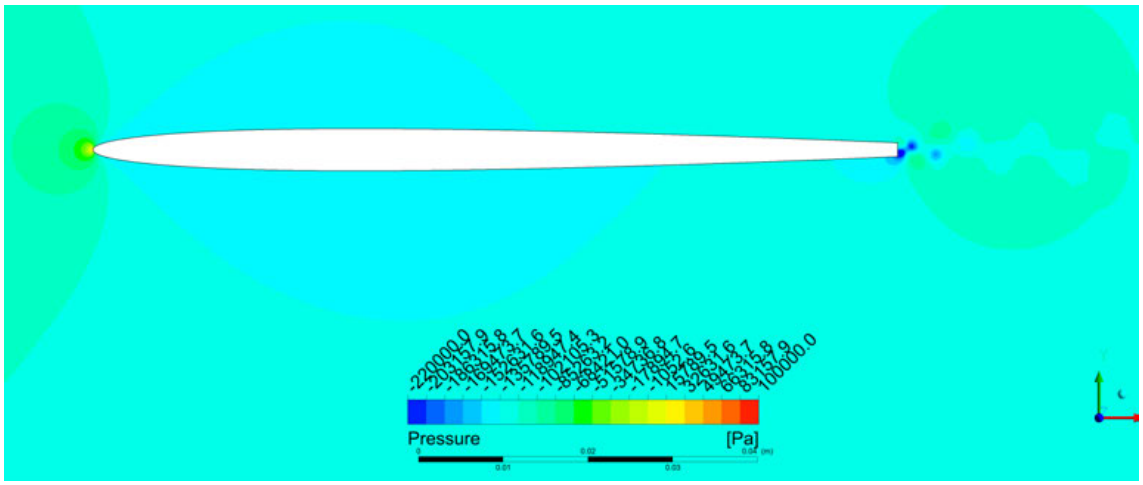

A 1.19 Pressure field around hydrofoil at $v_{inlet} = 17.5\ ms^{-1}$

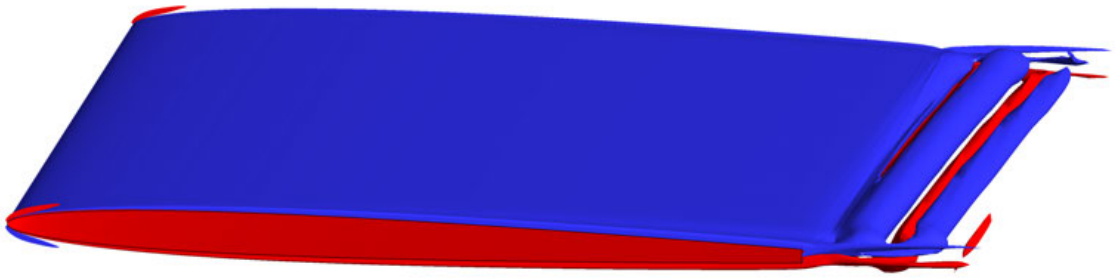

A 1.20 Vortex shedding at $v_{inlet} = 17.5\ ms^{-1}$ visualised by iso-surface of vorticity component perpendicular to the mean flow (-2500 s^{-1} is blue, 2500 s^{-1} in red)

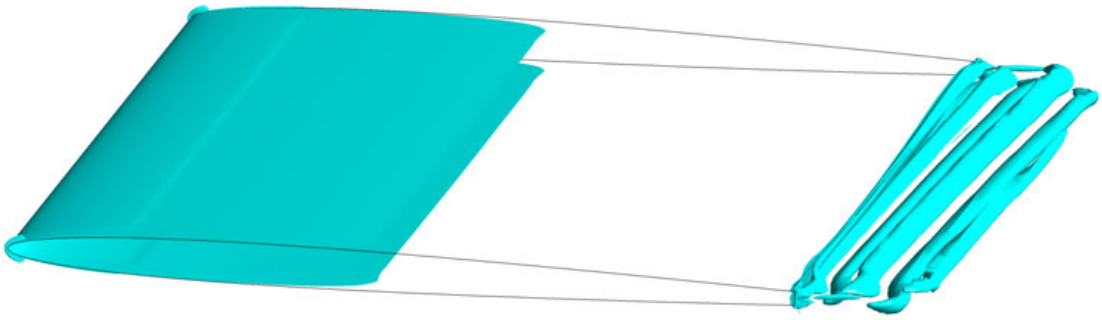

A 1.21 Vortex shedding at $v_{inlet} = 17.5\ ms^{-1}$ visualised by iso-surface of Q-criterion for value $2.5 \cdot 10^6\ s^{-2}$

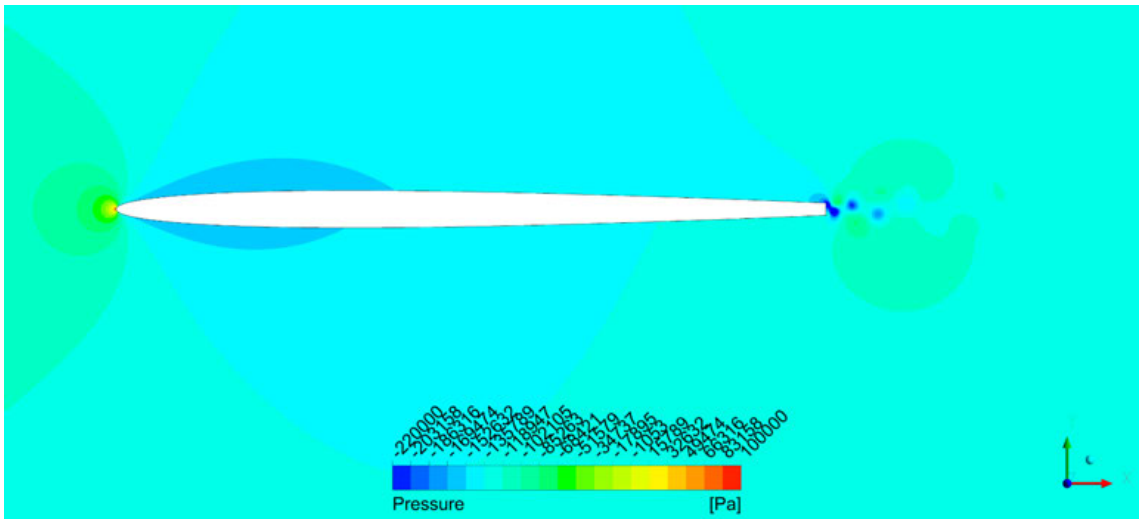

A 1.22 Pressure field around hydrofoil at $v_{inlet} = 20\ ms^{-1}$

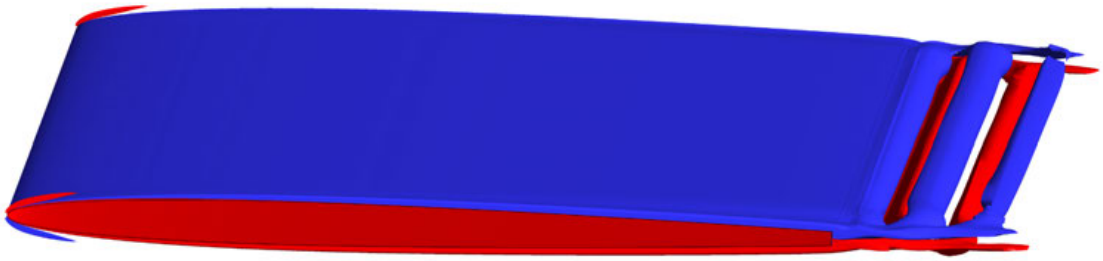

A 1.23 Vortex shedding at $v_{inlet} = 20\ ms^{-1}$ visualised by iso-surface of vorticity component perpendicular to the mean flow (-2500 s^{-1} is blue, 2500 s^{-1} in red)

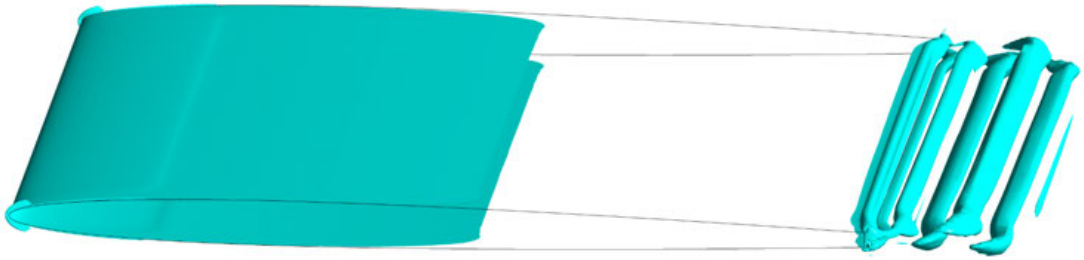

A 1.24 Vortex shedding at $v_{inlet} = 20\ ms^{-1}$ visualised by iso-surface of Q-criterion for value $2.5 \cdot 10^6\ s^{-2}$

A.2 Vortex Shedding Frequency Calculated by FFT from CFD

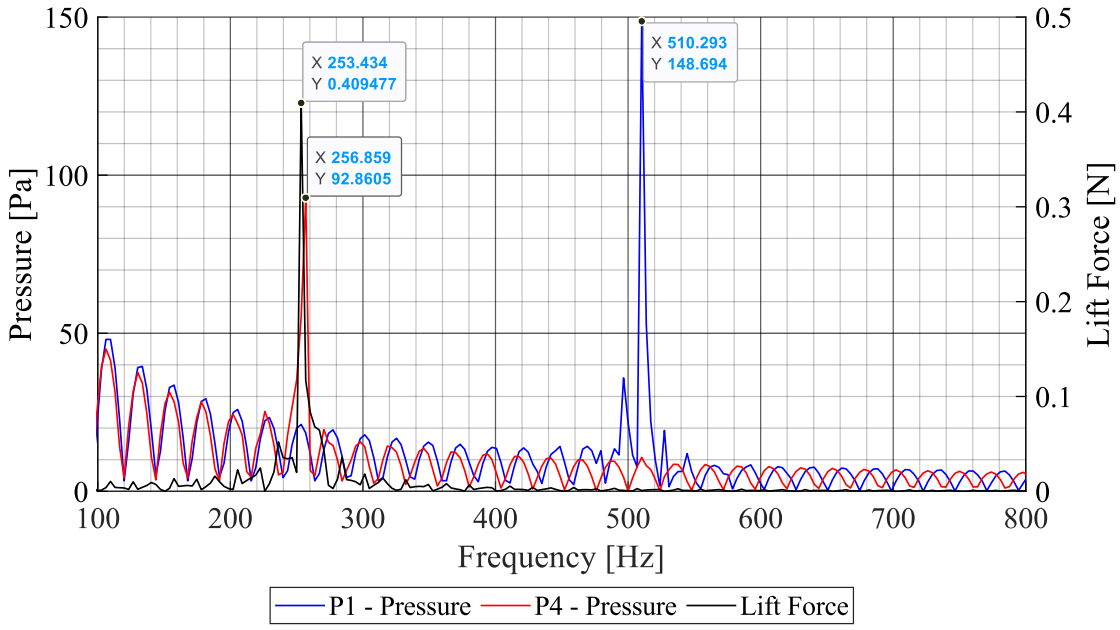

A 2.1 Amplitude-frequency spectra of vortex shedding at $v_{inlet} = 2.5\ ms^{-1}$

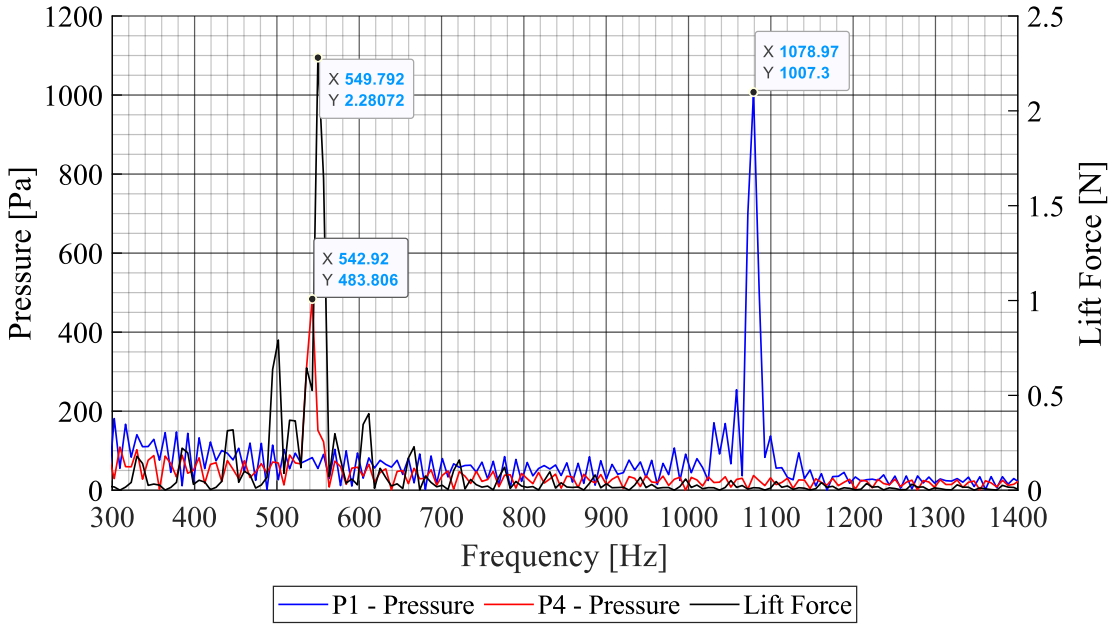

A 2.2 Amplitude-frequency spectra of vortex shedding at $v_{inlet} = 5\ ms^{-1}$

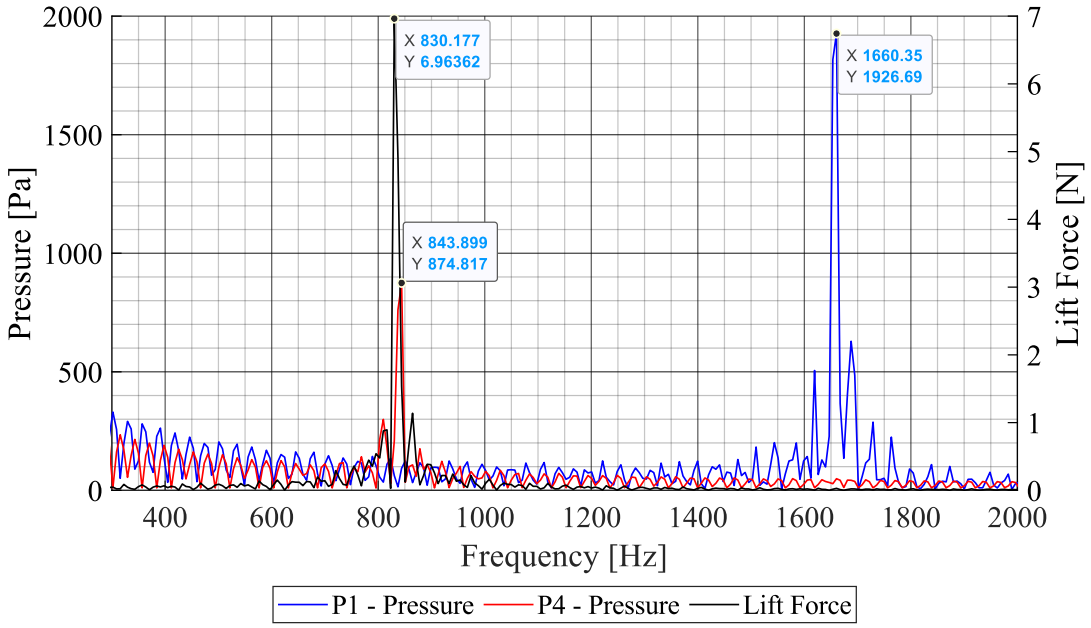

A 2.3 Amplitude-frequency spectra of vortex shedding at $v_{inlet} = 7.5\ ms^{-1}$

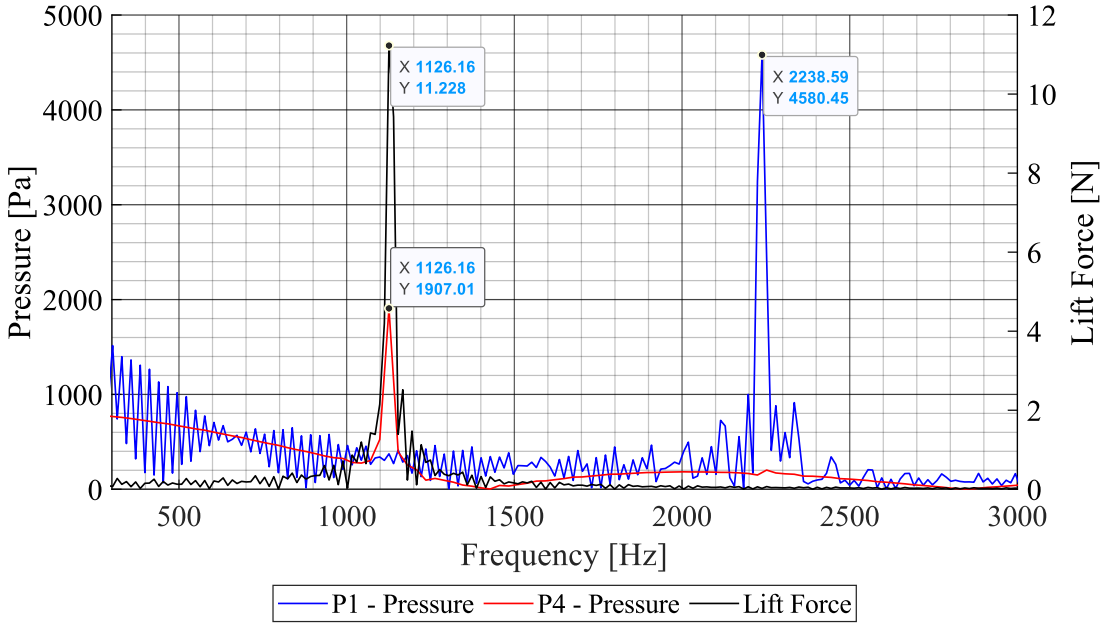

A 2.4 Amplitude-frequency spectra of vortex shedding at $v_{inlet} = 10\ ms^{-1}$

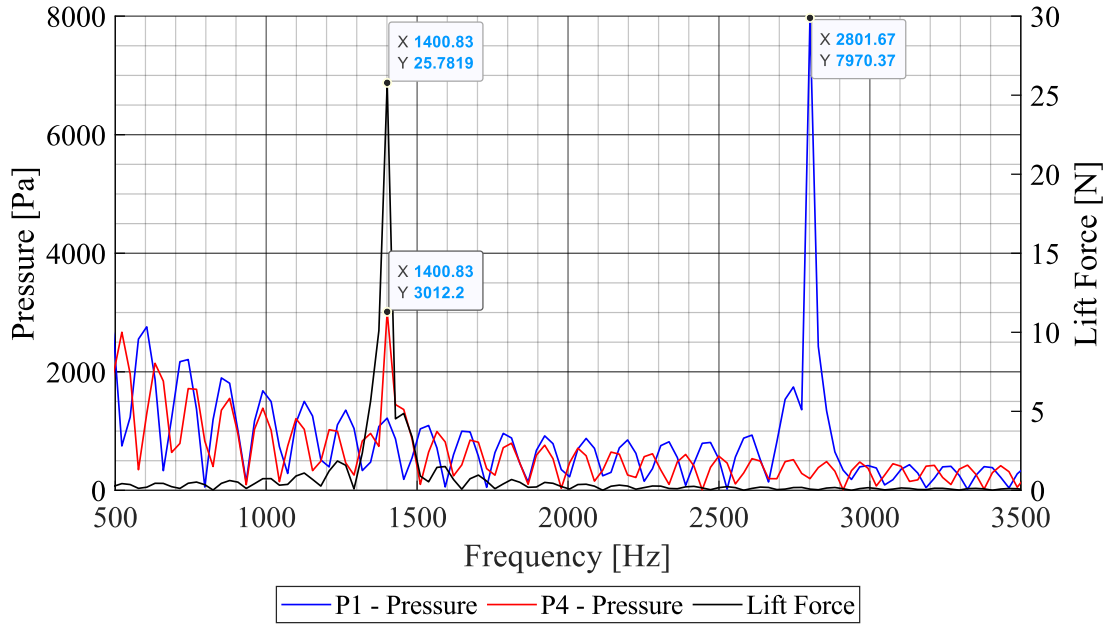

A 2.5 Amplitude-frequency spectra of vortex shedding at $v_{inlet} = 12.5\ ms^{-1}$

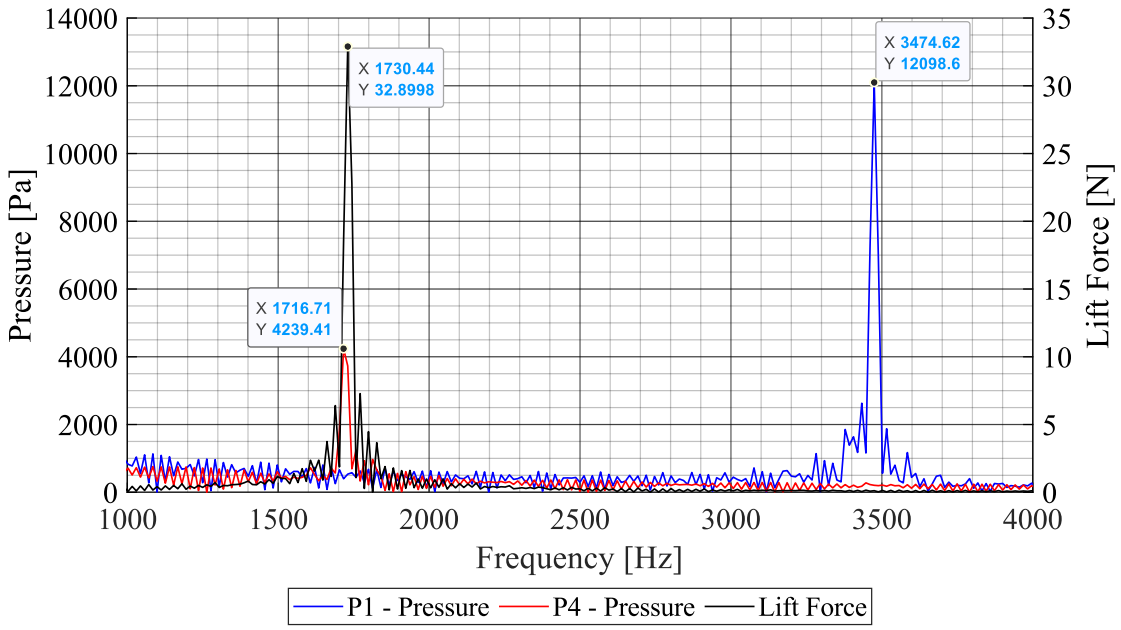

A 2.6 Amplitude-frequency spectra of vortex shedding at $v_{inlet} = 15\ ms^{-1}$

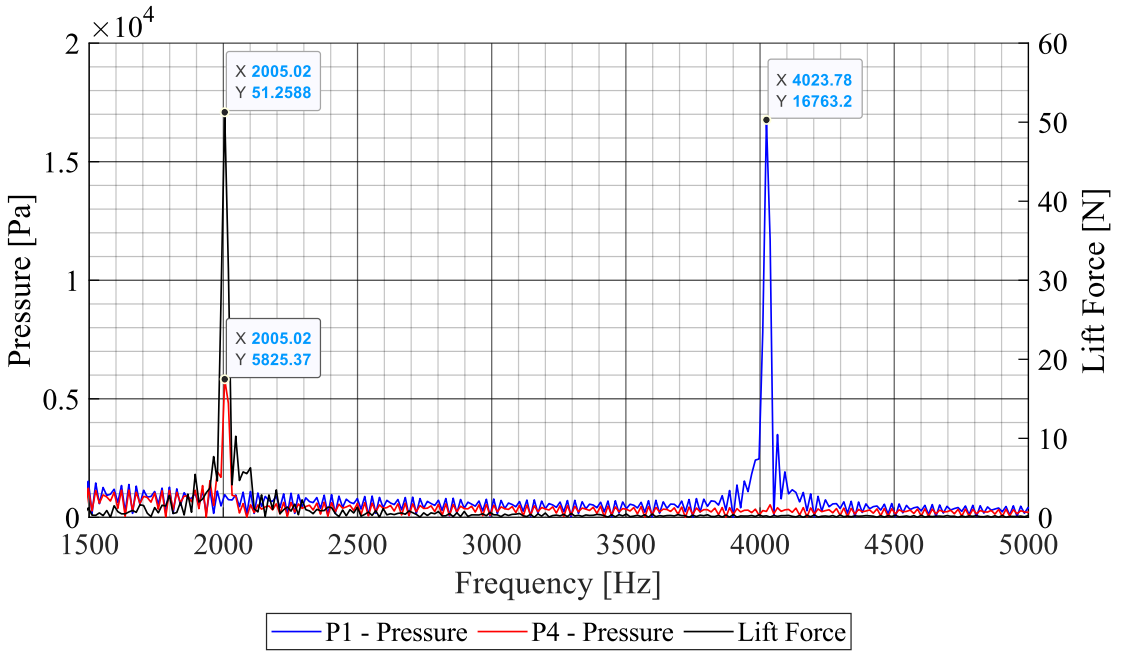

A 2.7 Amplitude-frequency spectra of vortex shedding at $v_{inlet} = 17.5\ ms^{-1}$

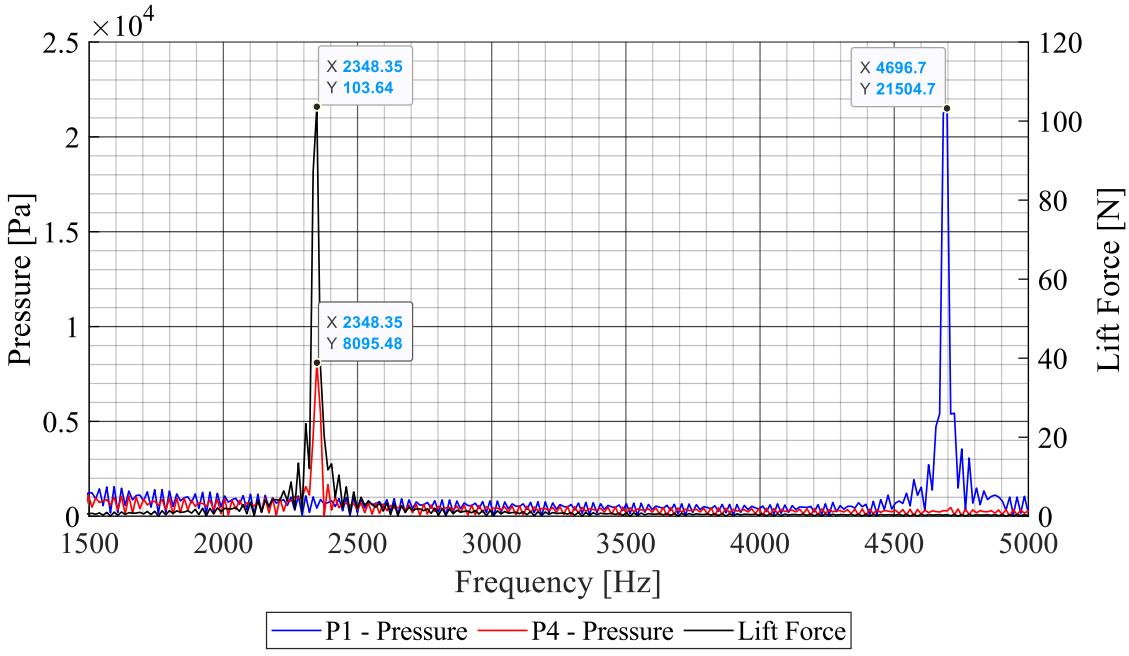

A 2.8 Amplitude-frequency spectra of vortex shedding at $v_{inlet} = 20\ ms^{-1}$

A.3 Comparison of Kármán Frequencies from Experiment and CFD

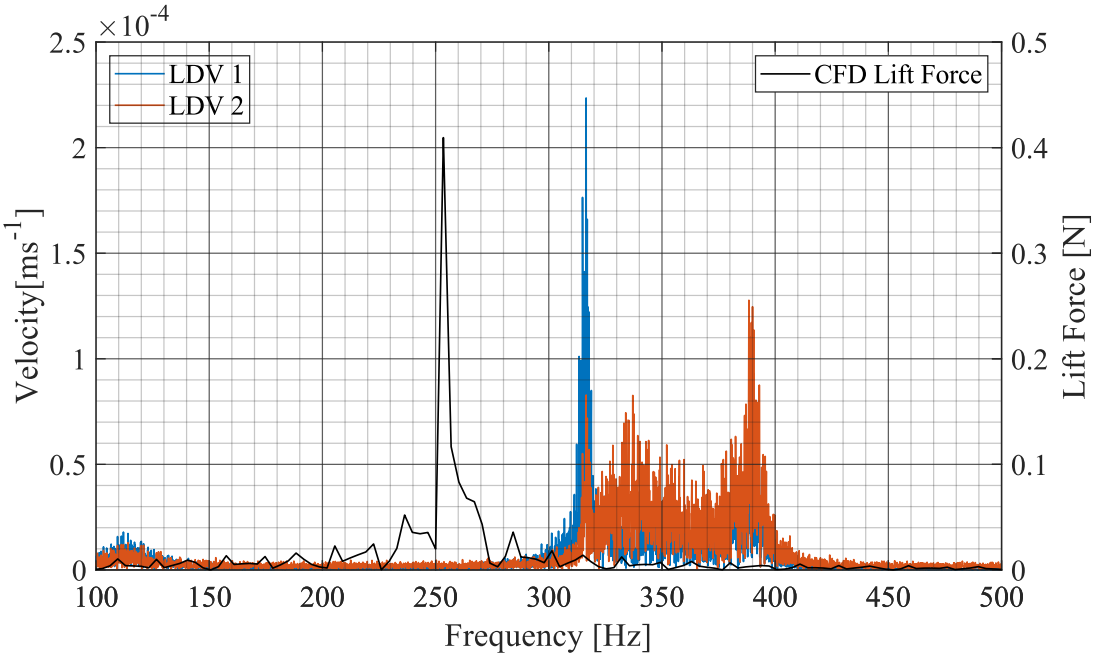

A 3.1 Amp.-freq. spectra: CFD lift force and vibrometers at $v_{inlet} = 2.5\ ms^{-1}$

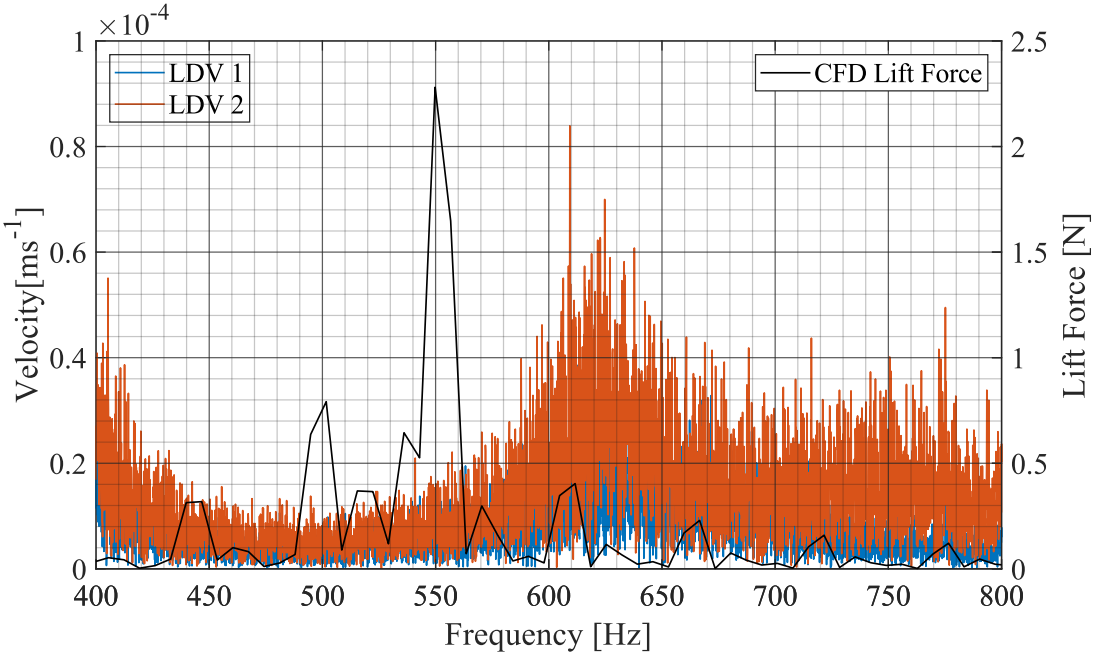

A 3.2 Amp.-freq. spectra: CFD lift force and vibrometers at $v_{inlet} = 5\ ms^{-1}$

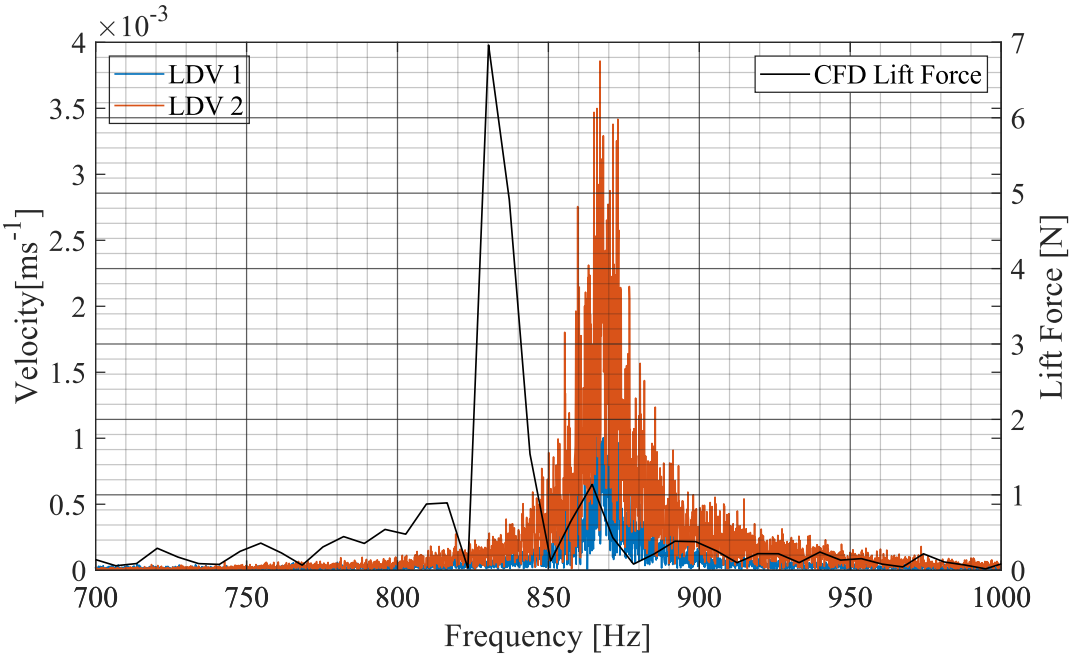

A 3.3 Amp.-freq. spectra: CFD lift force and vibrometers at $v_{inlet} = 7.5\ ms^{-1}$

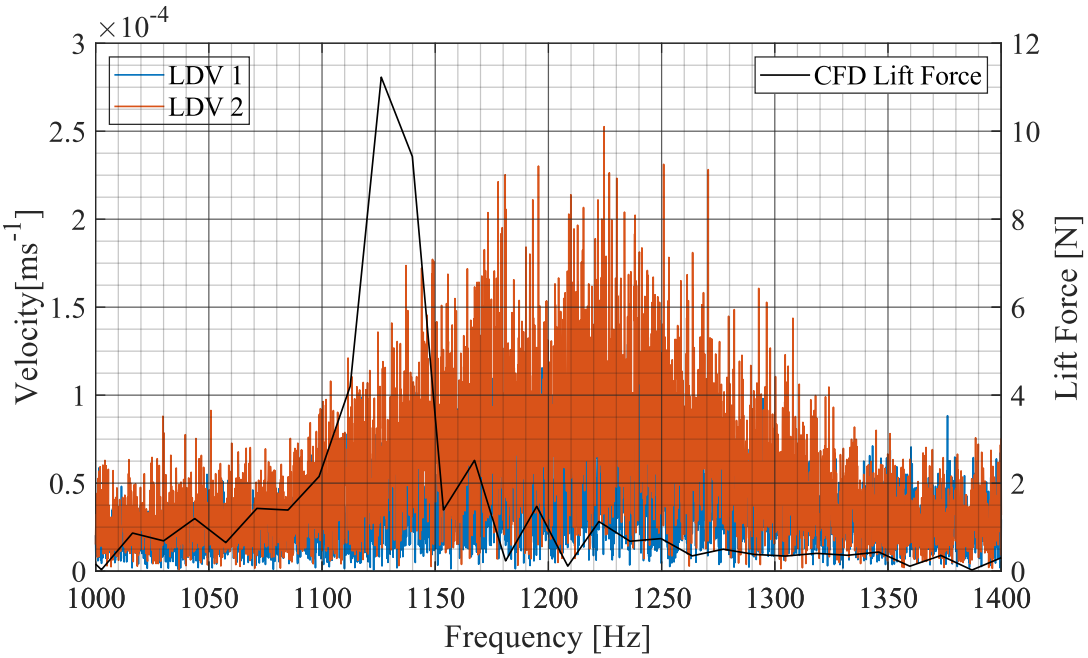

A 3.4 Amp.-freq. spectra: CFD lift force and vibrometers at $v_{inlet} = 10\ ms^{-1}$

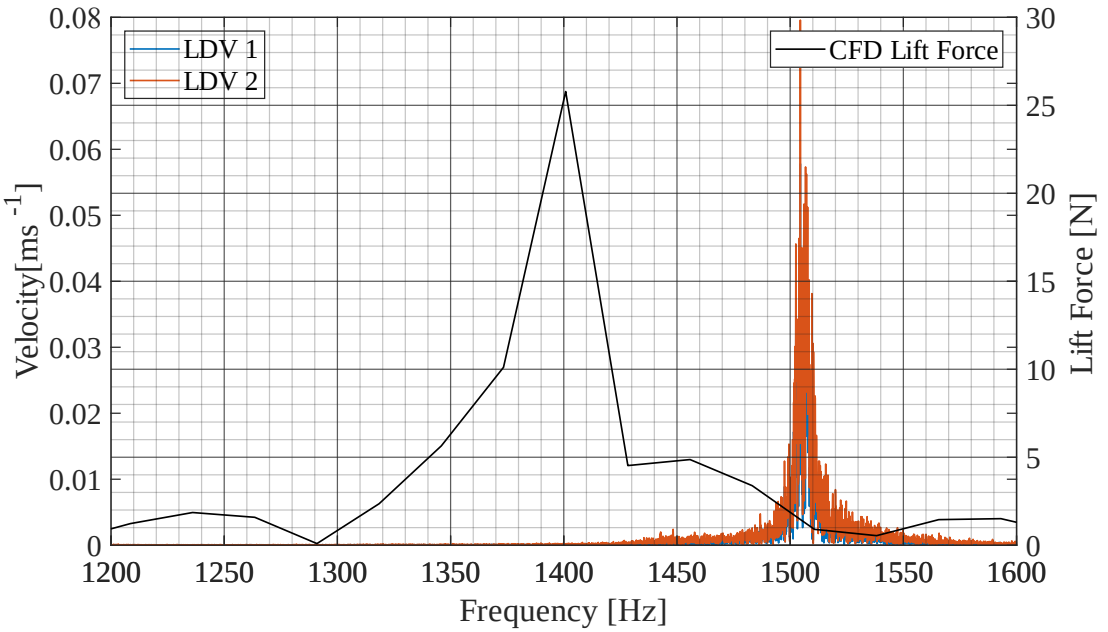

A 3.5 Amp.-freq. spectra: CFD lift force and vibrometers at $v_{inlet} = 12.5\ ms^{-1}$

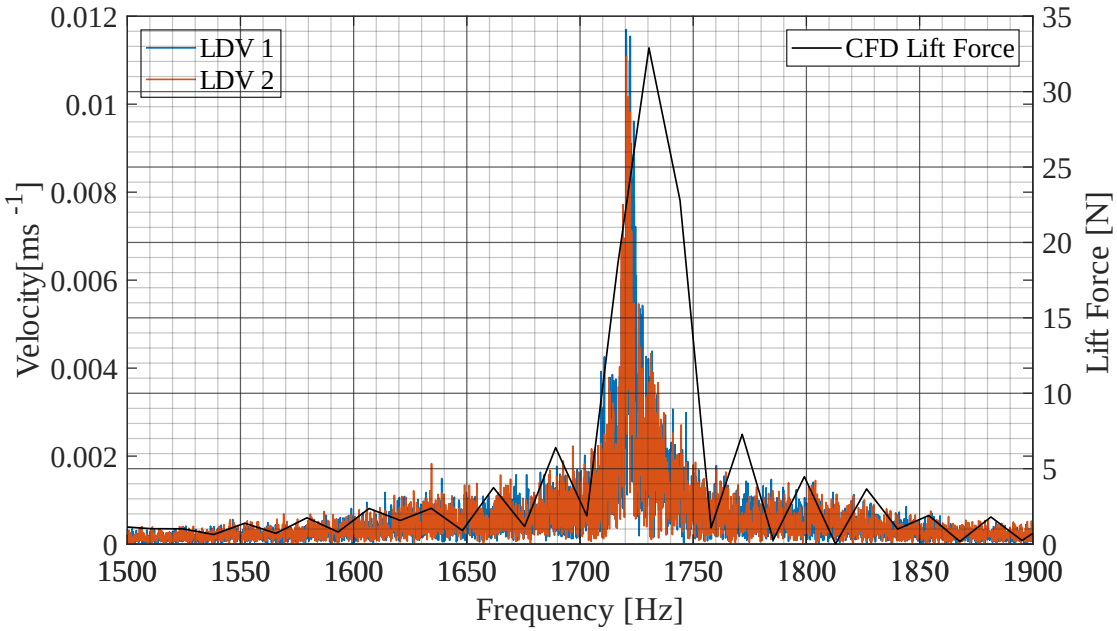

A 3.6 Amp.-freq. spectra: CFD lift force and vibrometers at $v_{inlet} = 15\ ms^{-1}$

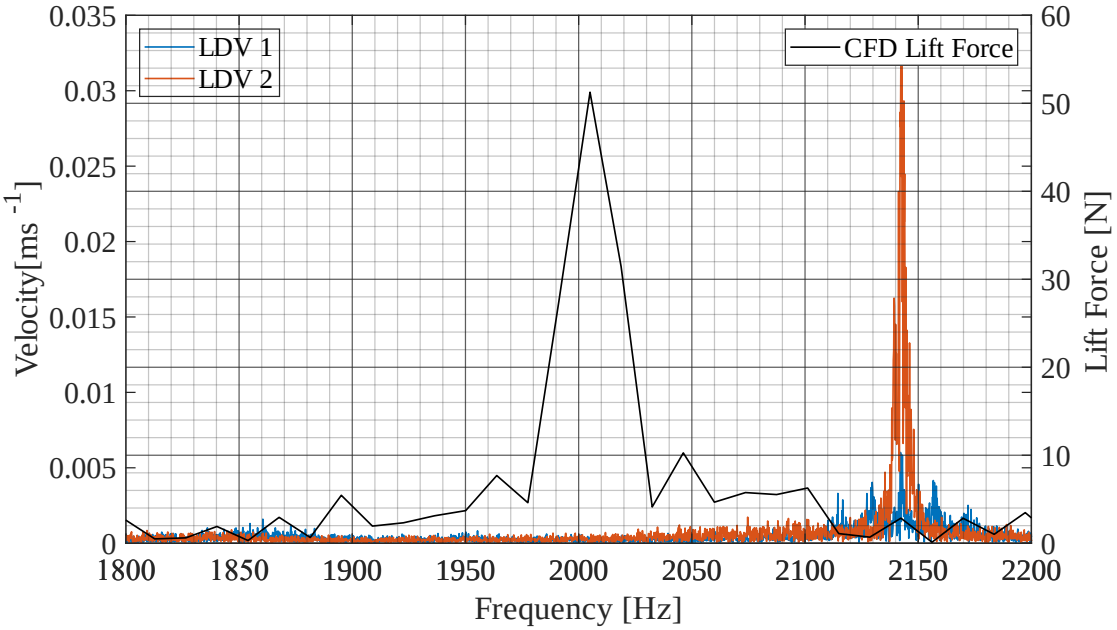

A 3.7 Amp.-freq. spectra: CFD lift force and vibrometers at $v_{inlet} = 17.5\ ms^{-1}$

A.4 FRF of Hydrofoil with Angle of Attack 0°

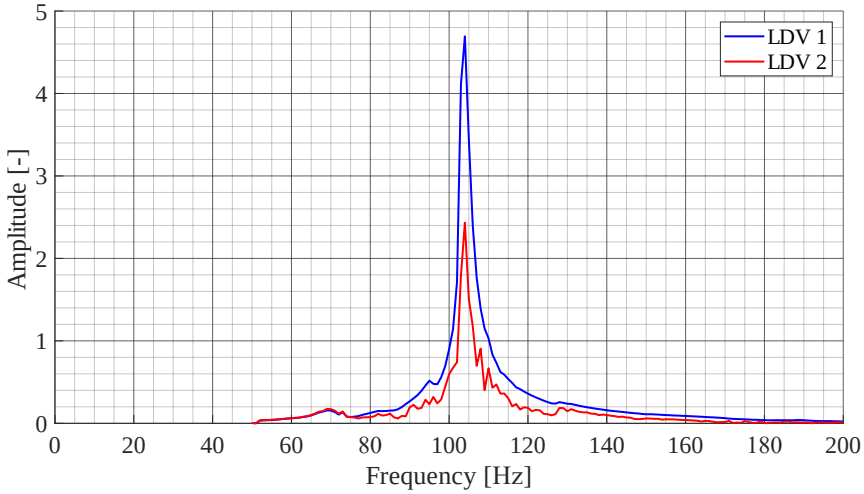

A 4.1 FRF of hydrofoil at $v_{inlet} = 0\ ms^{-1}$ ($\alpha_{inc} = 0°$)

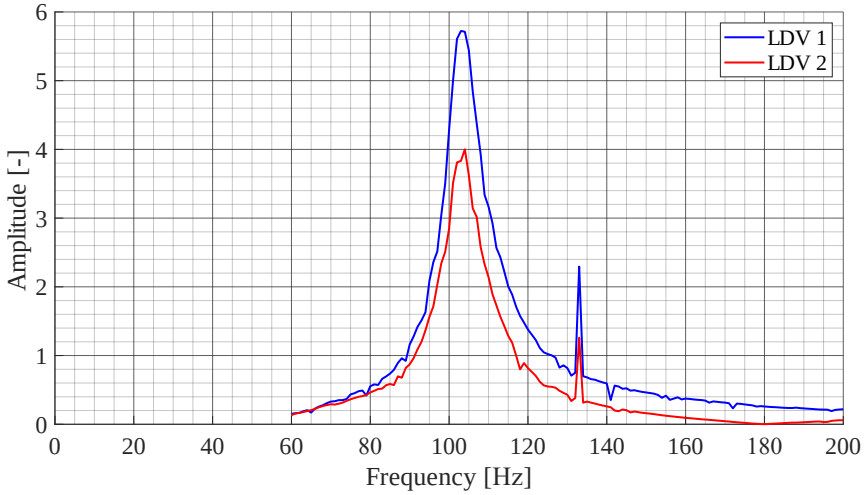

A 4.2 FRF of hydrofoil at $v_{inlet} = 1\ ms^{-1}$($\alpha_{inc} = 0°$)

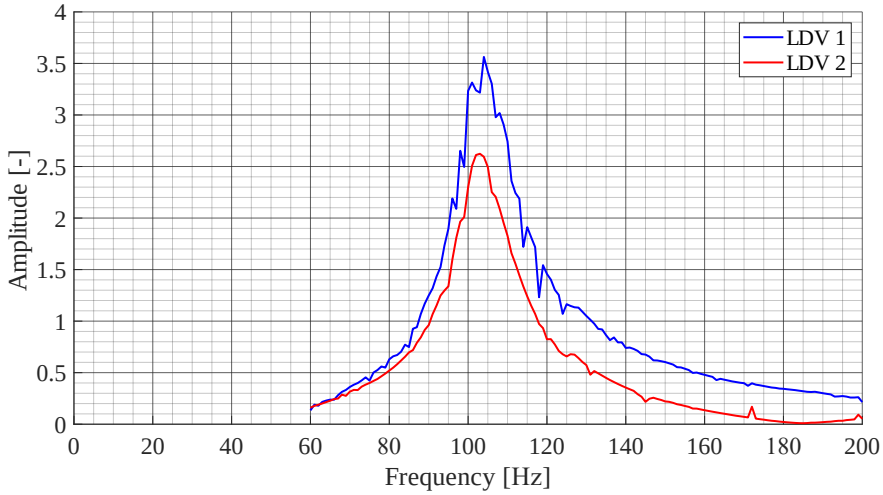

A 4.3 FRF of hydrofoil at $v_{inlet} = 2\ ms^{-1}$ ($\alpha_{inc} = 0°$)

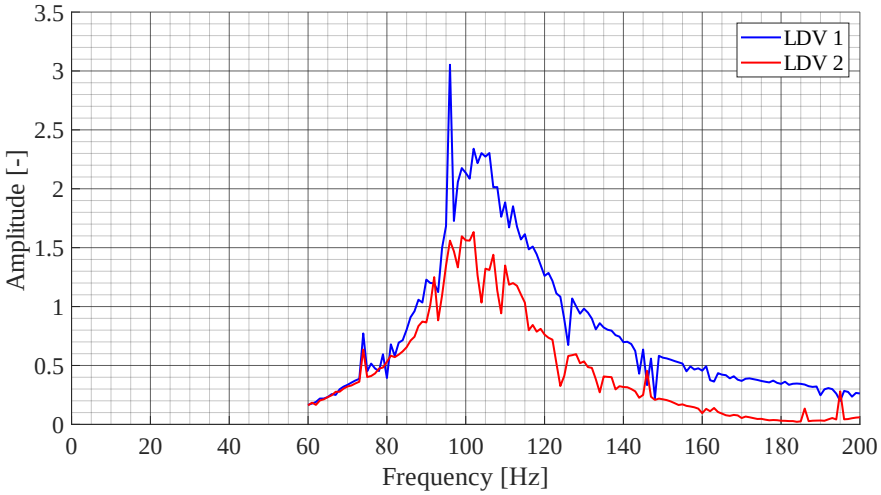

A 4.4 FRF of hydrofoil at $v_{inlet} = 3\ ms^{-1}$ ($\alpha_{inc} = 0°$)

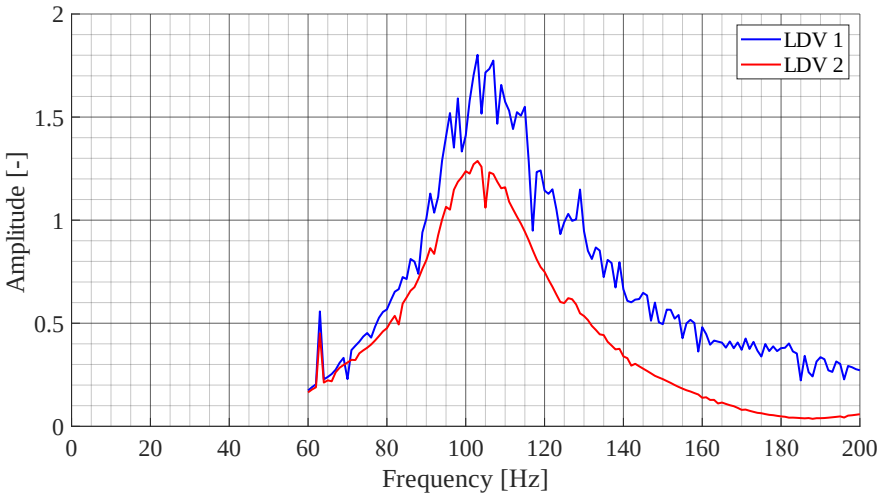

A 4.5 FRF of hydrofoil at $v_{inlet} = 4\ ms^{-1}$ ($\alpha_{inc} = 0°$)

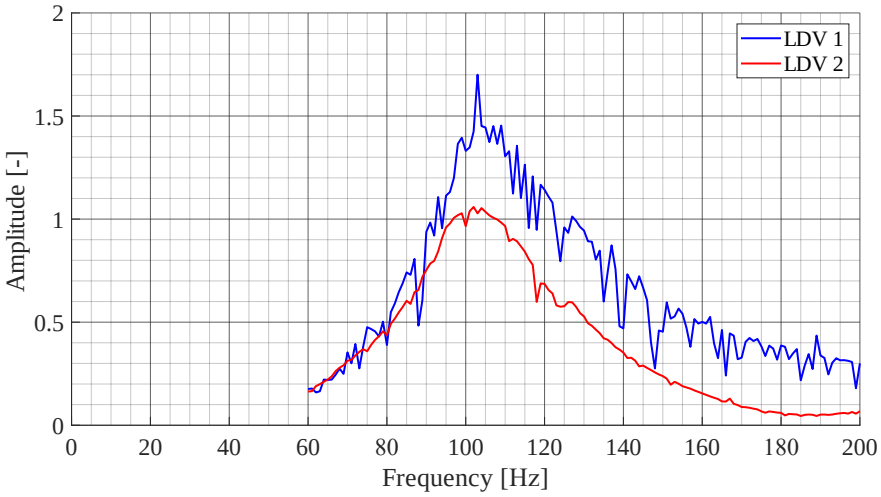

A 4.6 FRF of hydrofoil at $v_{inlet} = 5\ ms^{-1}$ ($\alpha_{inc} = 0°$)

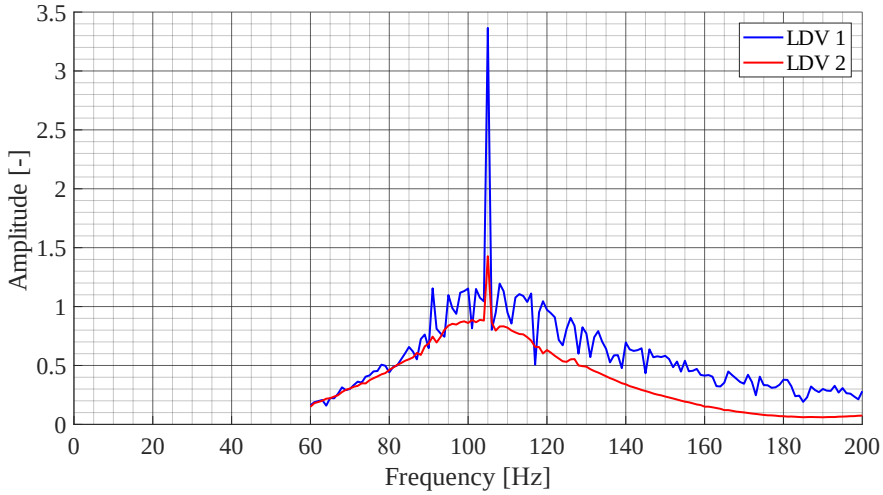

A 4.7 FRF of hydrofoil at $v_{inlet} = 6\ ms^{-1}$ ($\alpha_{inc} = 0°$)

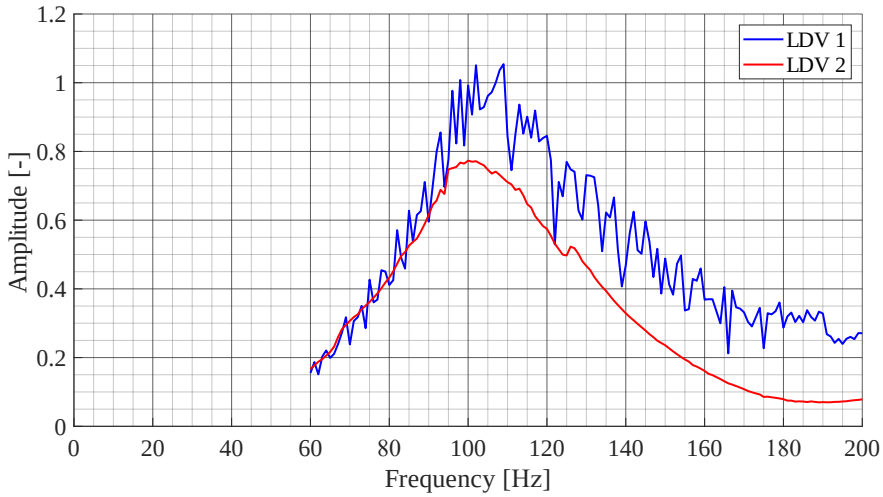

A 4.8 FRF of hydrofoil at $v_{inlet} = 7\ ms^{-1}$ ($\alpha_{inc} = 0°$)

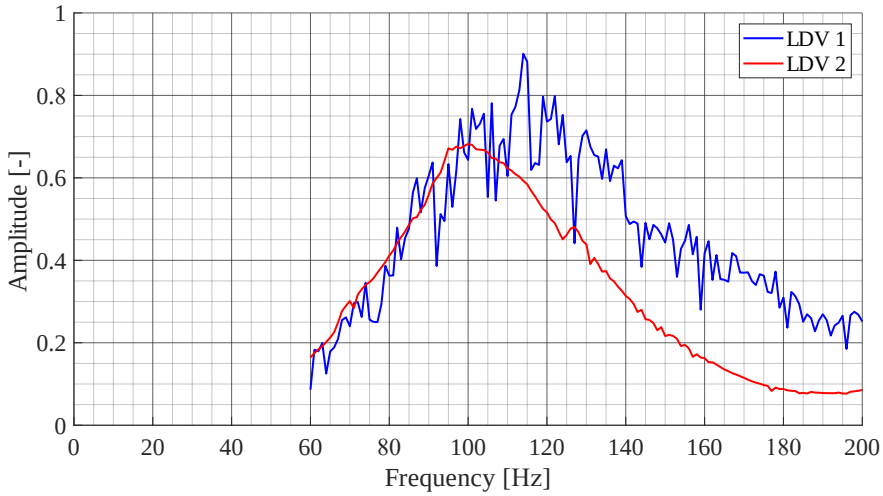

A 4.9 FRF of hydrofoil at $v_{inlet} = 8\ ms^{-1}$ ($\alpha_{inc} = 0°$)

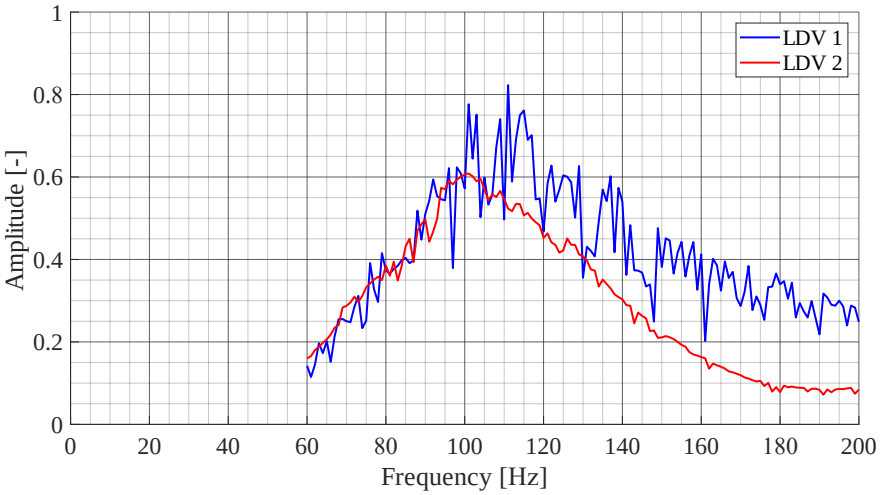

A 4.10 FRF of hydrofoil at $v_{inlet} = 9\ ms^{-1}$ ($\alpha_{inc} = 0°$)

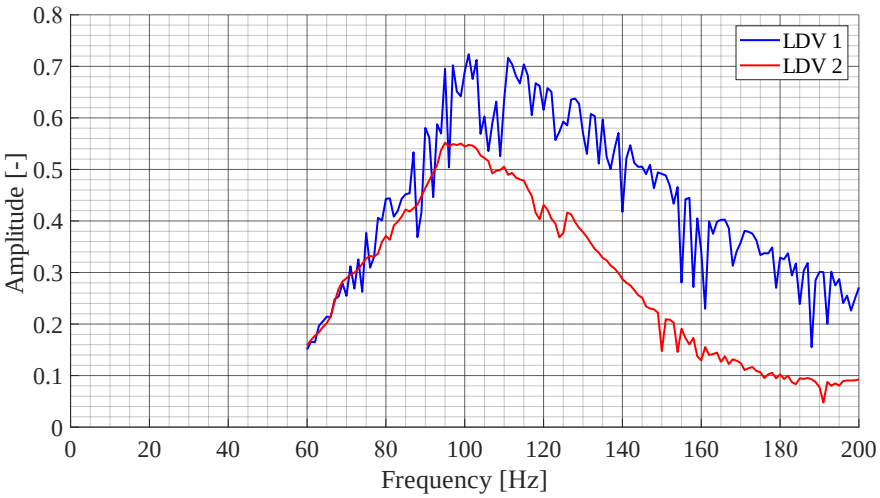

A 4.11 FRF of hydrofoil at $v_{inlet} = 10\ ms^{-1}$ ($\alpha_{inc} = 0°$)

A.5 FRF Approximation by SDOF Response Fit Method (Angle of Attack 0°)

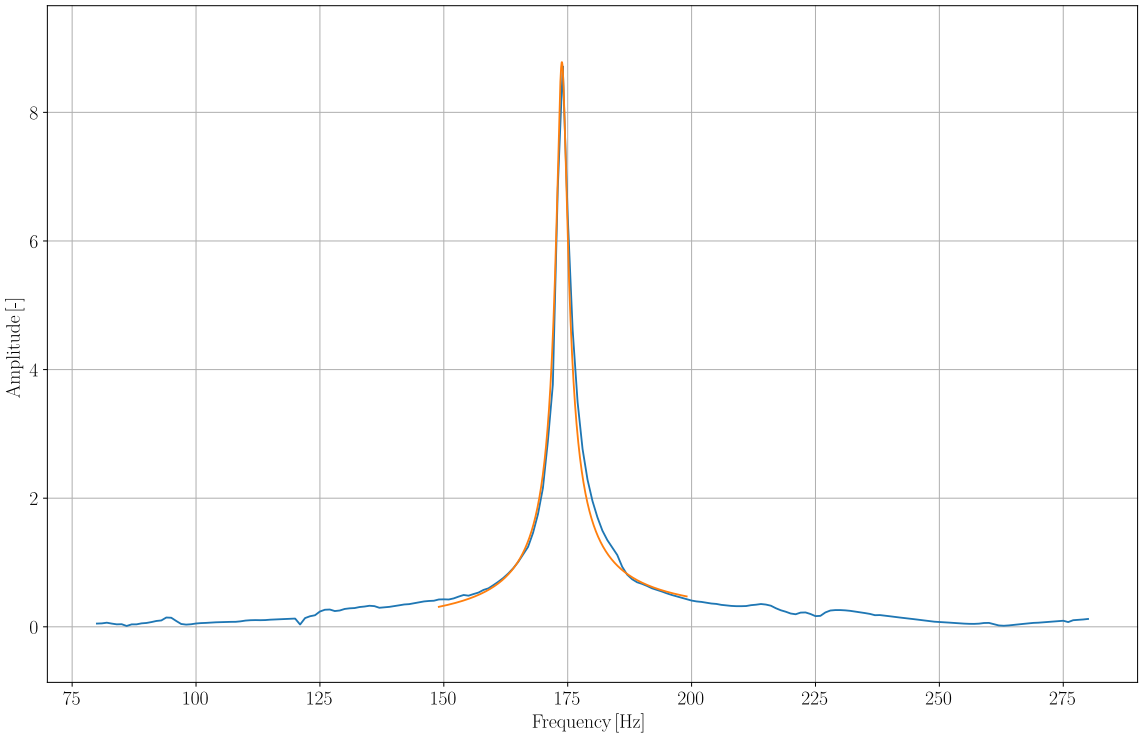

A 5.1 Approximated FRF from vibrometer LDV 1: hydrofoil in air ($\alpha_{inc} = 0°$)

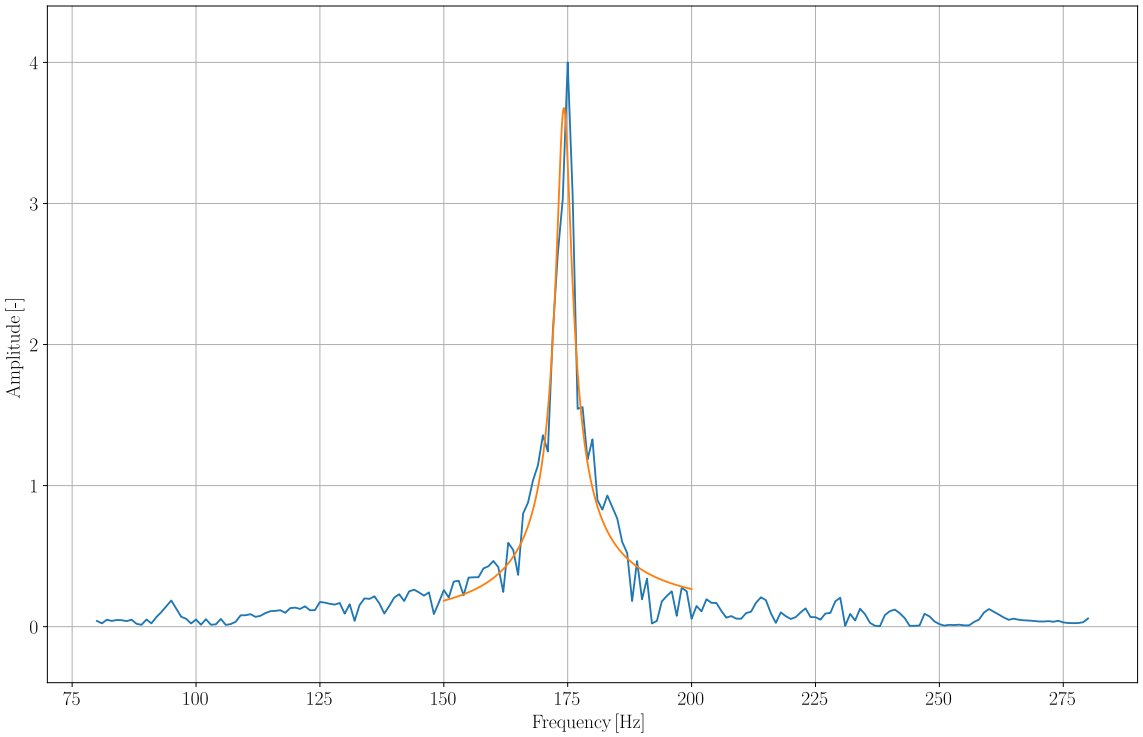

A 5.2 Approximated FRF from vibrometer LDV 2: hydrofoil in air ($\alpha_{inc} = 0°$)

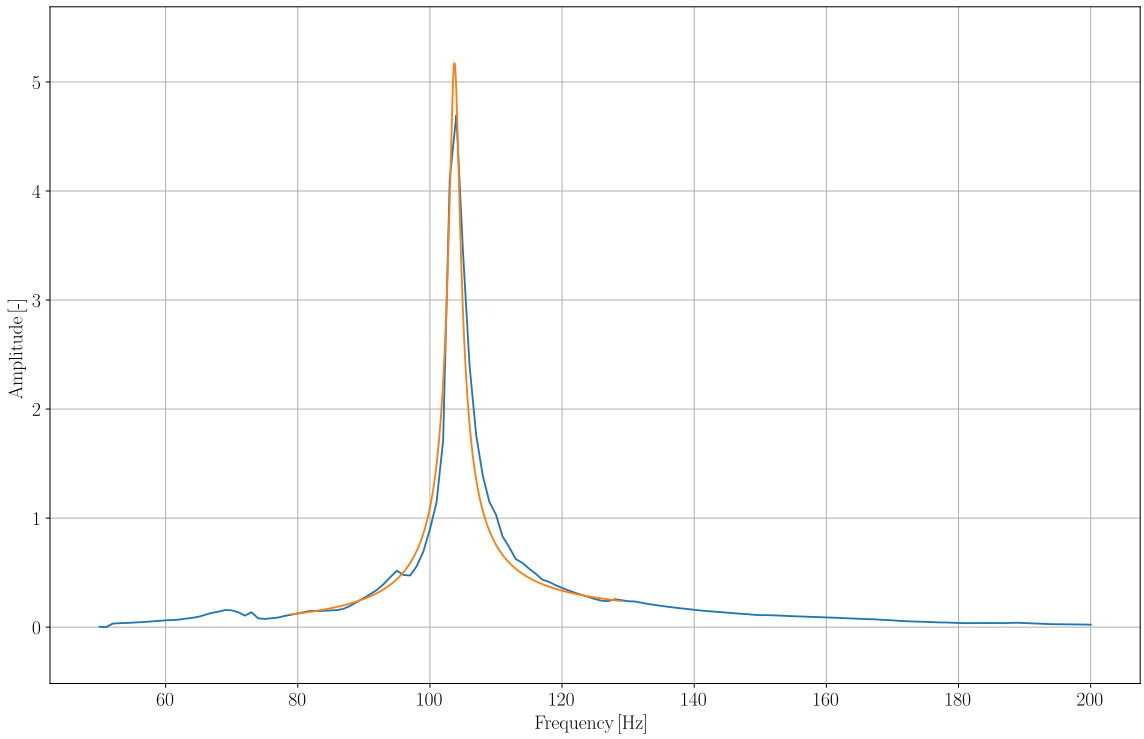

A 5.3 Approximated FRF from vibrometer LDV 1 at $v_{inlet} = 0\ ms^{-1}$ ($\alpha_{inc} = 0°$)

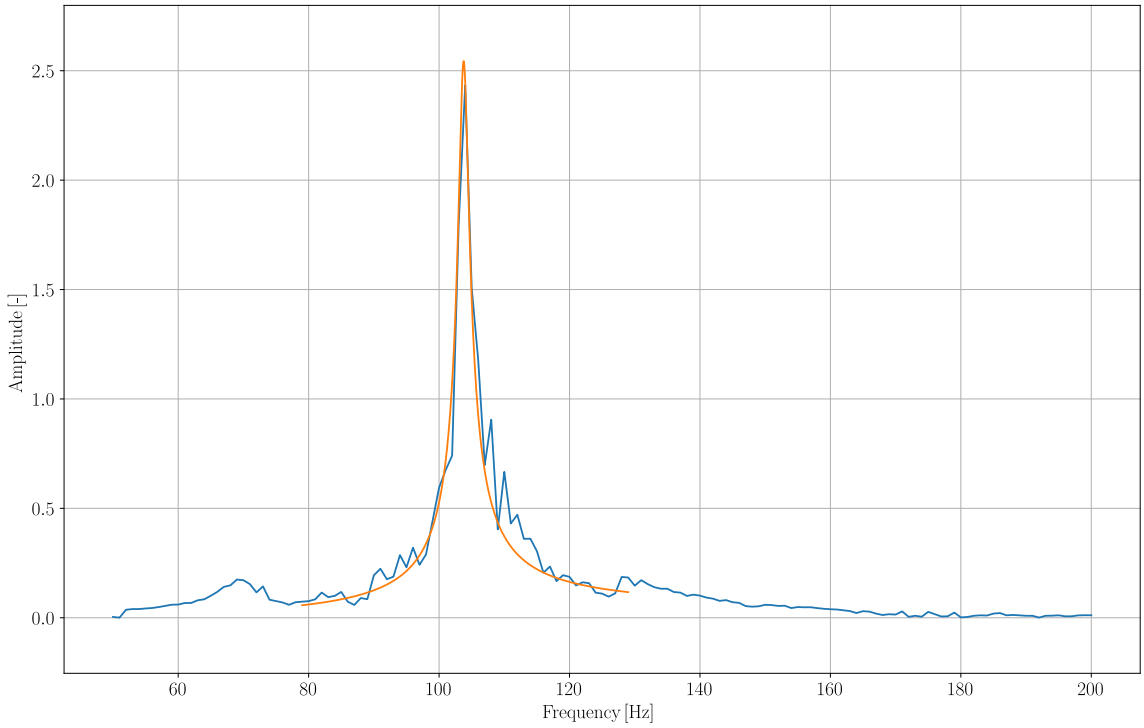

A 5.4 Approximated FRF from vibrometer LDV 2 at $v_{inlet} = 0\ ms^{-1}$ ($\alpha_{inc} = 0°$)

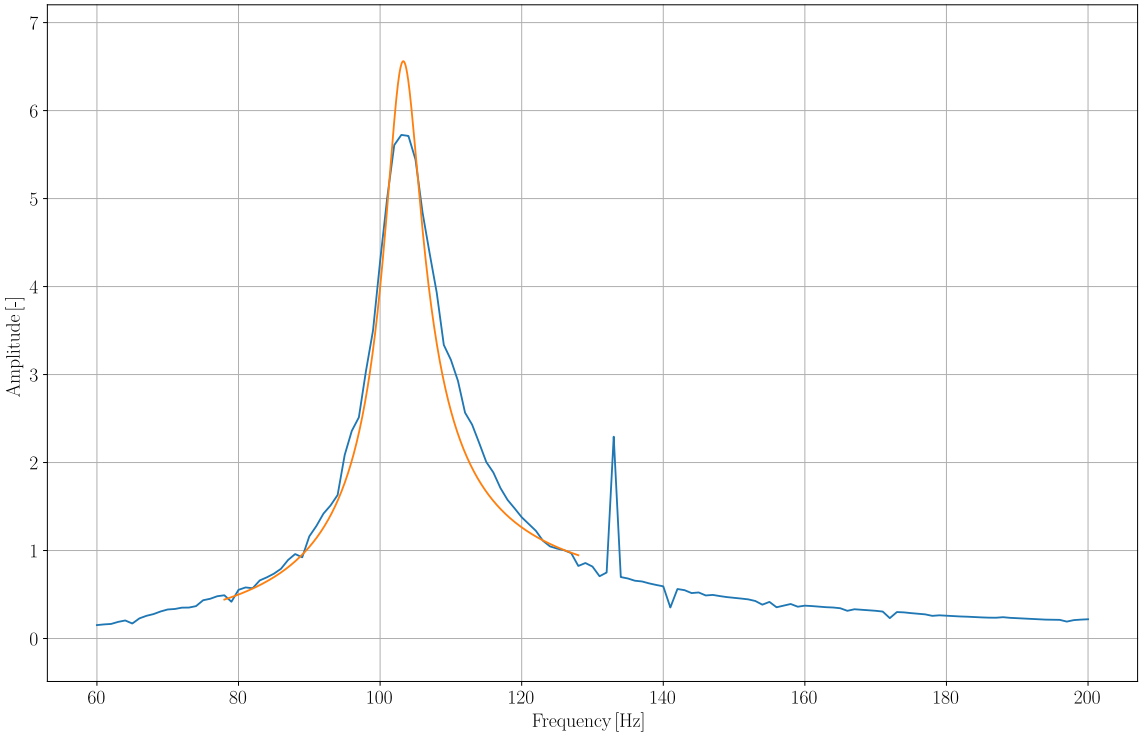

A 5.5 Approximated FRF from vibrometer LDV 1 at $v_{inlet} = 1\ ms^{-1}$ ($\alpha_{inc} = 0°$)

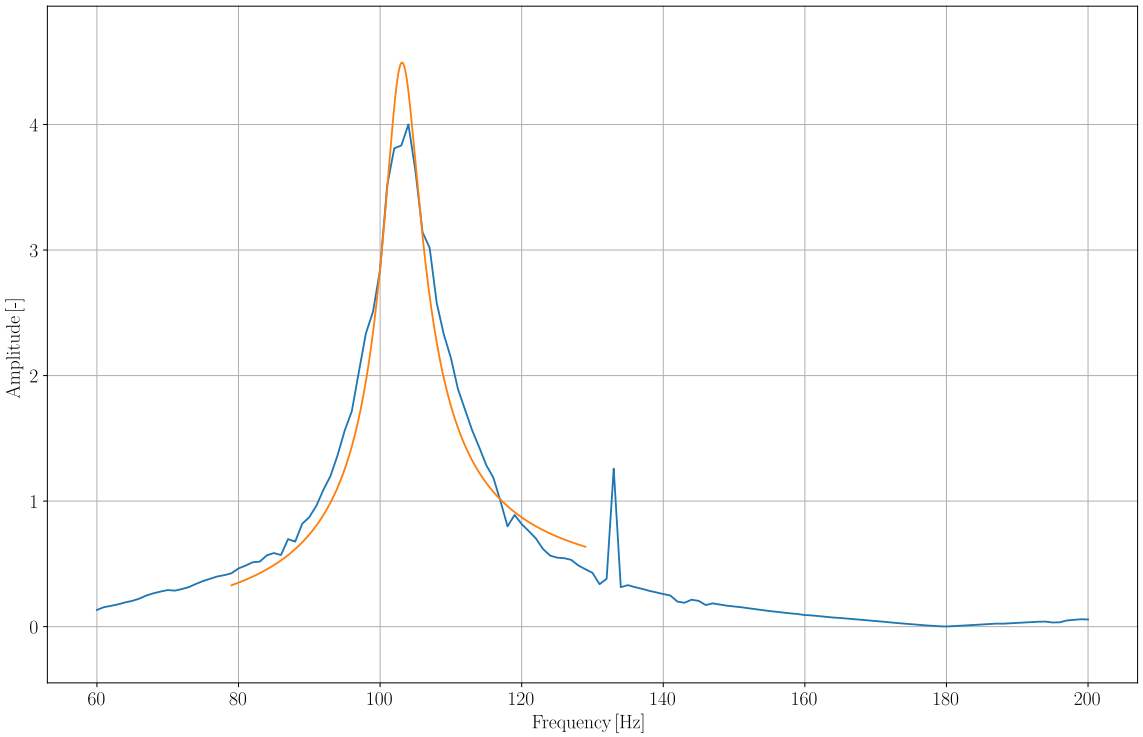

A 5.6 Approximated FRF from vibrometer LDV 2 at $v_{inlet} = 1\ ms^{-1}$ ($\alpha_{inc} = 0°$)

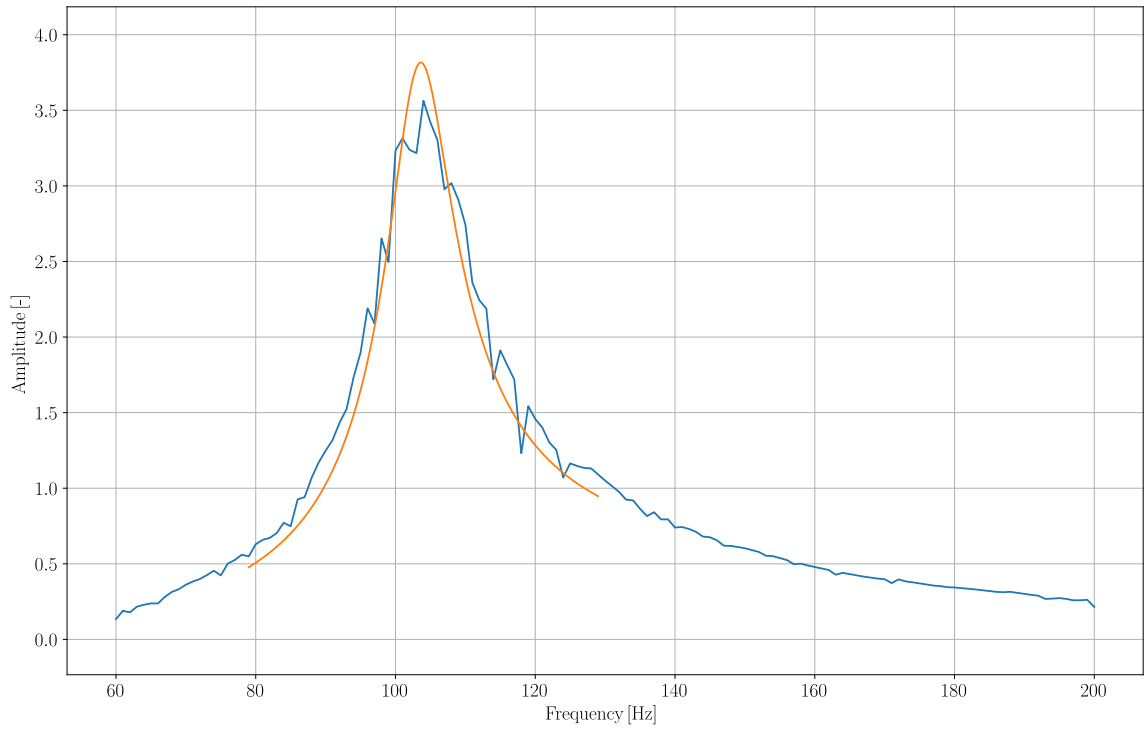

A 5.7 Approximated FRF from vibrometer LDV 1 at $v_{inlet} = 2\ ms^{-1}$ ($\alpha_{inc} = 0°$)

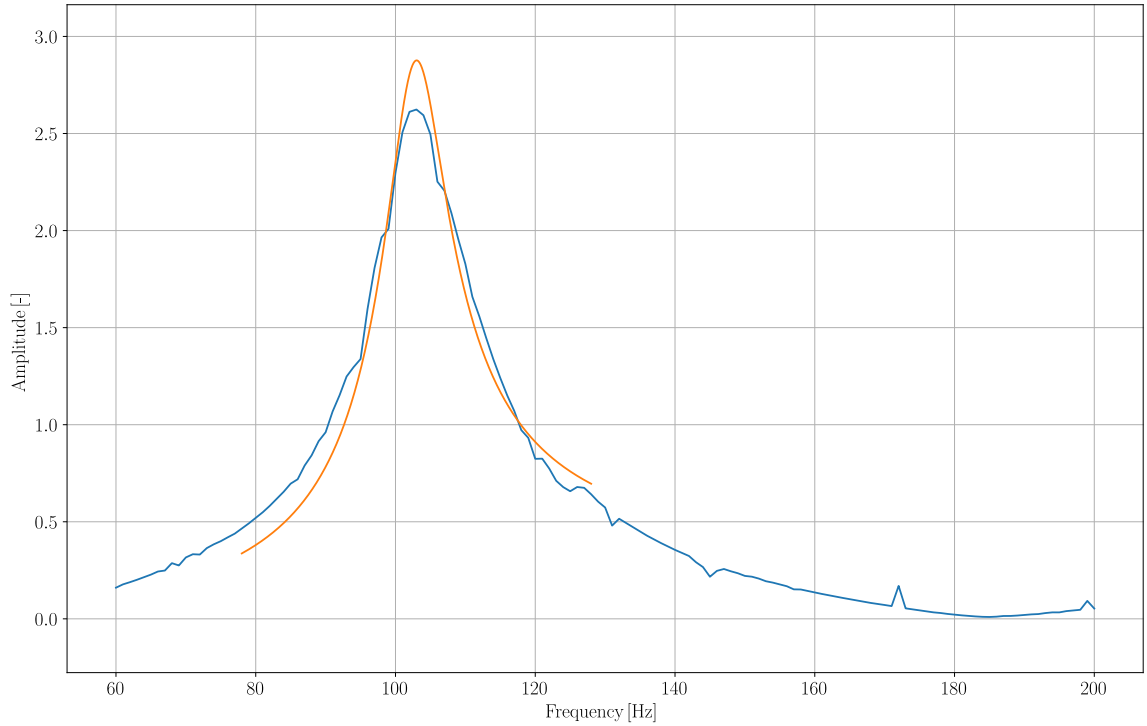

A 5.8 Approximated FRF from vibrometer LDV 2 at $v_{inlet} = 2\ ms^{-1}$ ($\alpha_{inc} = 0°$)

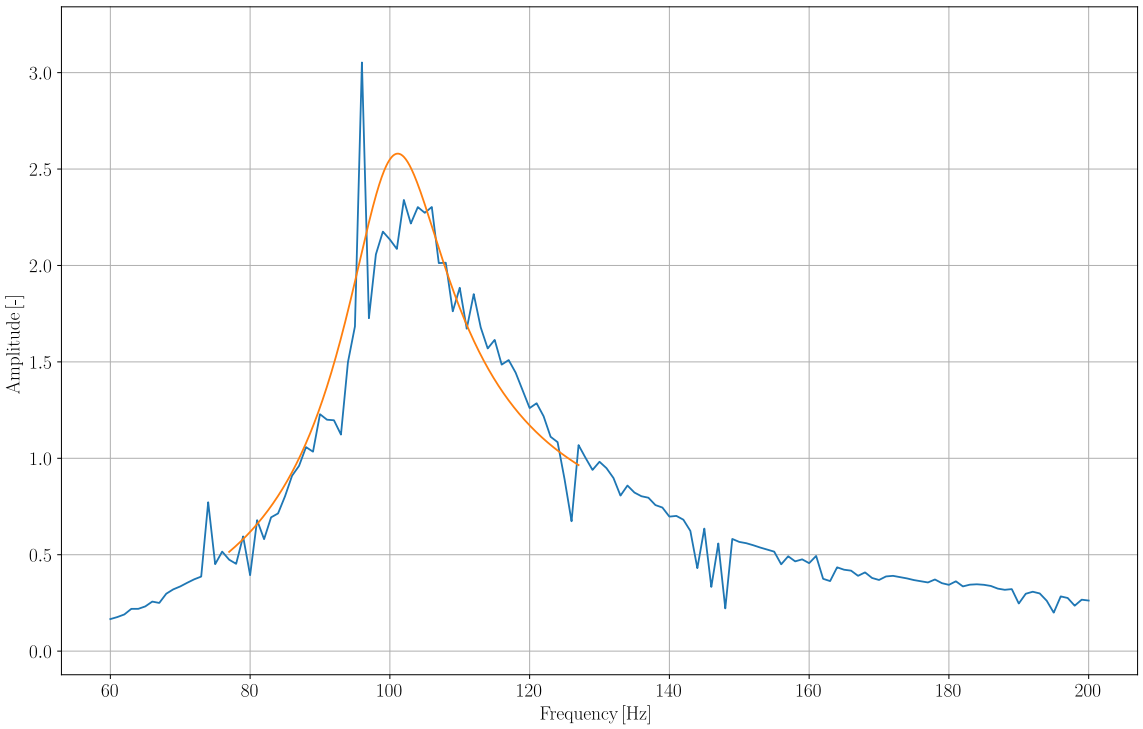

A 5.9 Approximated FRF from vibrometer LDV 1 at $v_{inlet} = 3\ ms^{-1}$ ($\alpha_{inc} = 0°$)

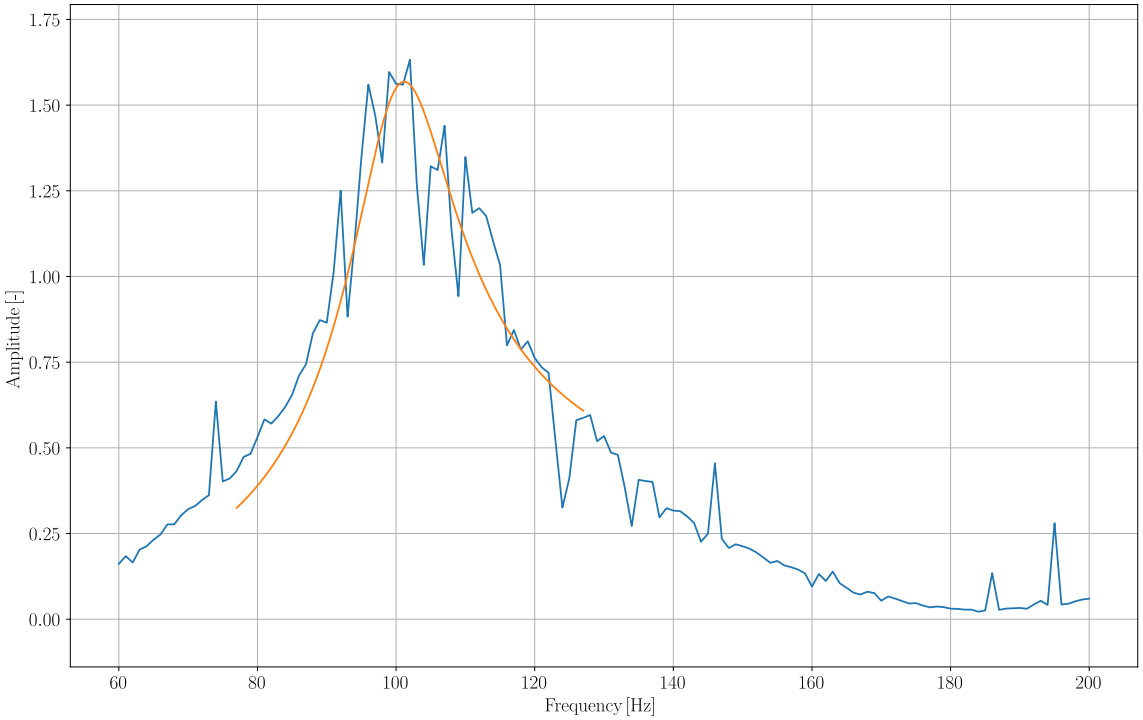

A 5.10 Approximated FRF from vibrometer LDV 2 at $v_{inlet} = 3\ ms^{-1}$ ($\alpha_{inc} = 0°$)

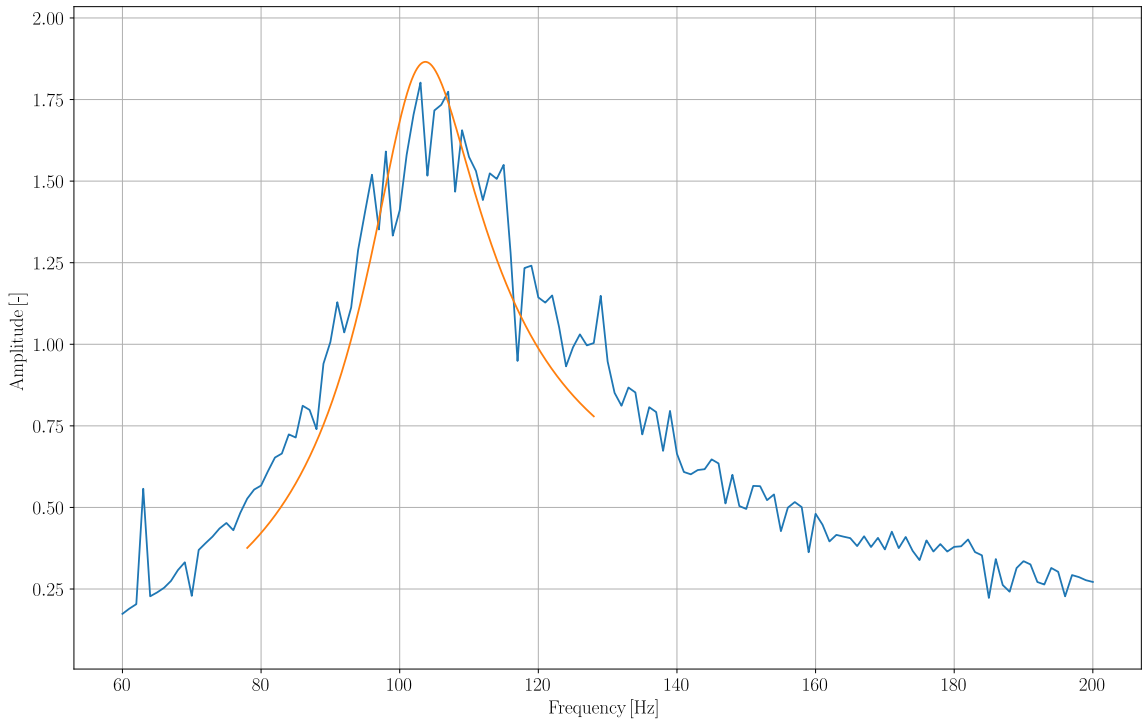

A 5.11 Approximated FRF from vibrometer LDV 1 at $v_{inlet} = 4\ ms^{-1}$ ($\alpha_{inc} = 0°$)

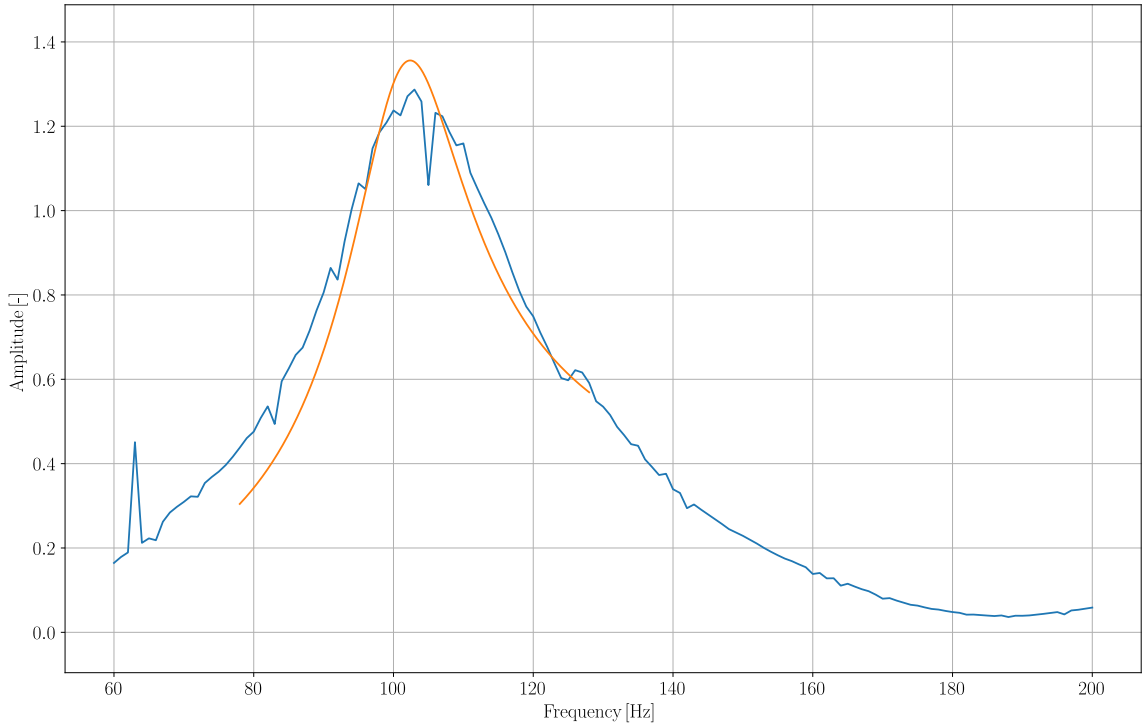

A 5.12 Approximated FRF from vibrometer LDV 2 at $v_{inlet} = 4\ ms^{-1}$ ($\alpha_{inc} = 0°$)

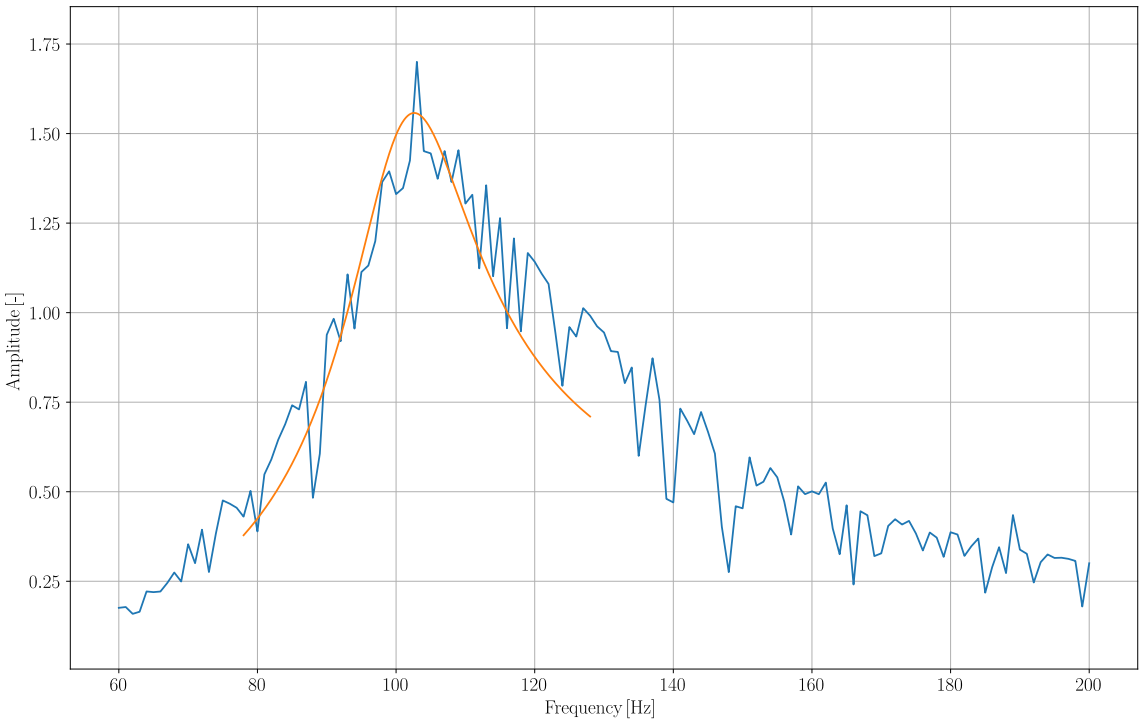

A 5.13 Approximated FRF from vibrometer LDV 1 at $v_{inlet} = 5\ ms^{-1}$ ($\alpha_{inc} = 0°$)

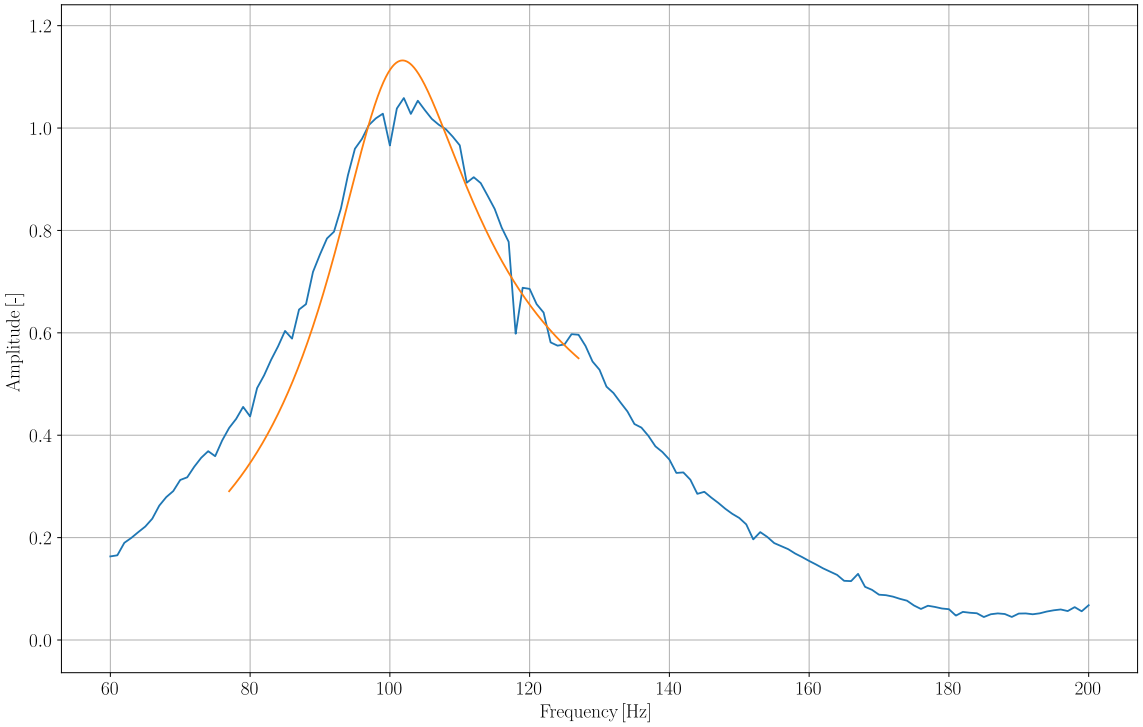

A 5.14 Approximated FRF from vibrometer LDV 2 at $v_{inlet} = 5\ ms^{-1}$ ($\alpha_{inc} = 0°$)

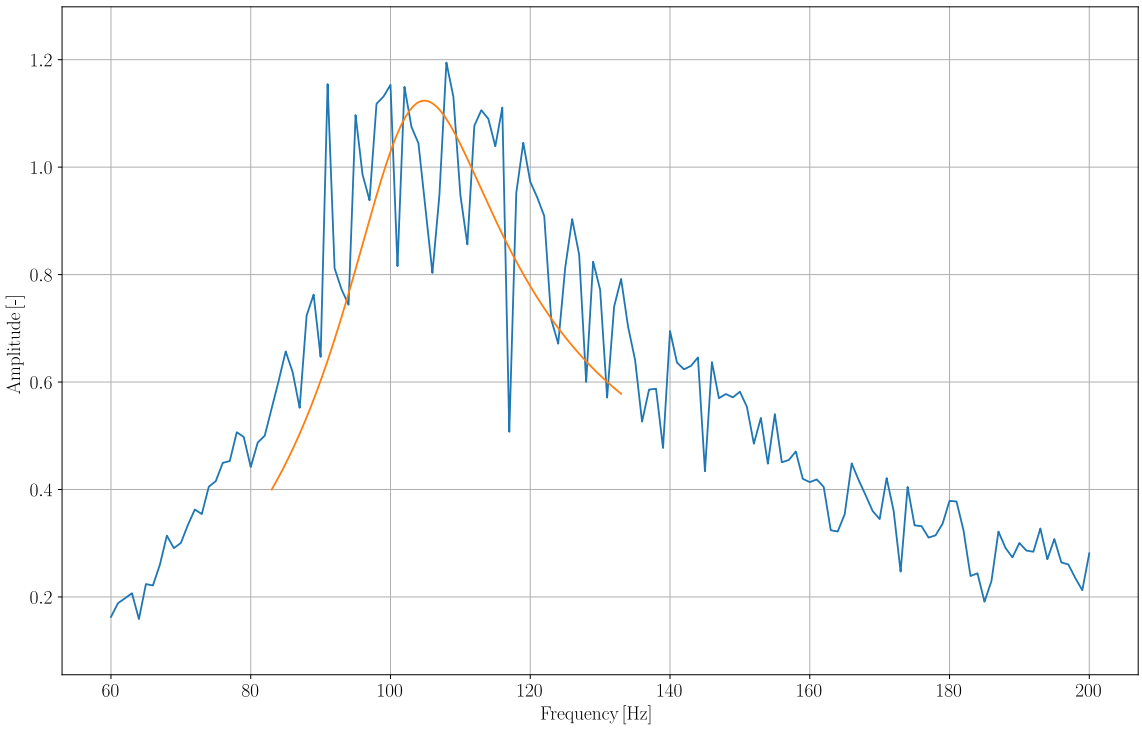

A 5.15 Approximated FRF from vibrometer LDV 1 at $v_{inlet} = 6\ ms^{-1}$ ($\alpha_{inc} = 0°$)

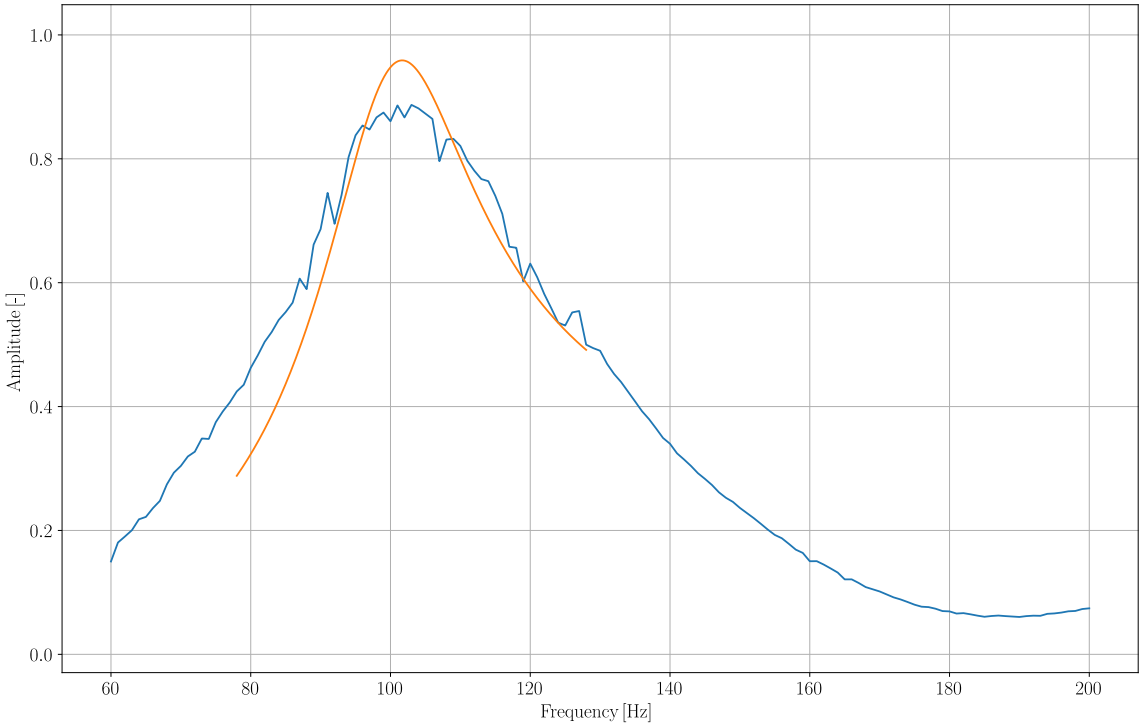

A 5.16 Approximated FRF from vibrometer LDV 2 at $v_{inlet} = 6\ ms^{-1}$ ($\alpha_{inc} = 0°$)

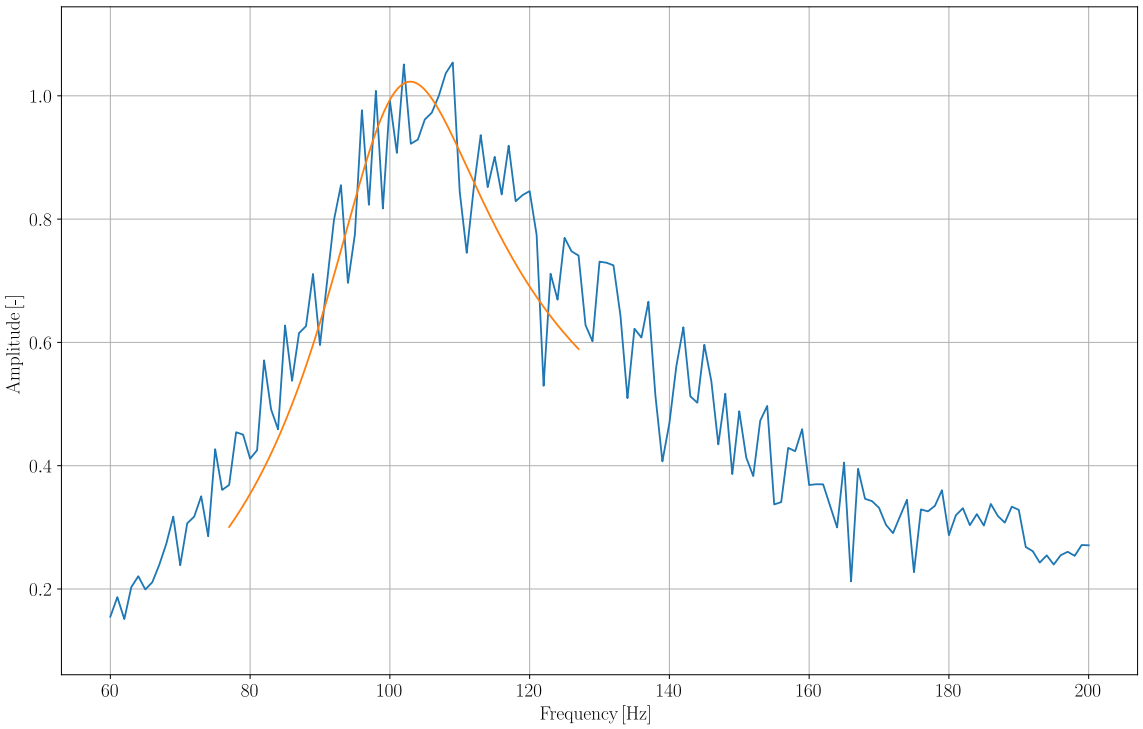

A 5.17 Approximated FRF from vibrometer LDV 1 at $v_{inlet} = 7\ ms^{-1}$ ($\alpha_{inc} = 0°$)

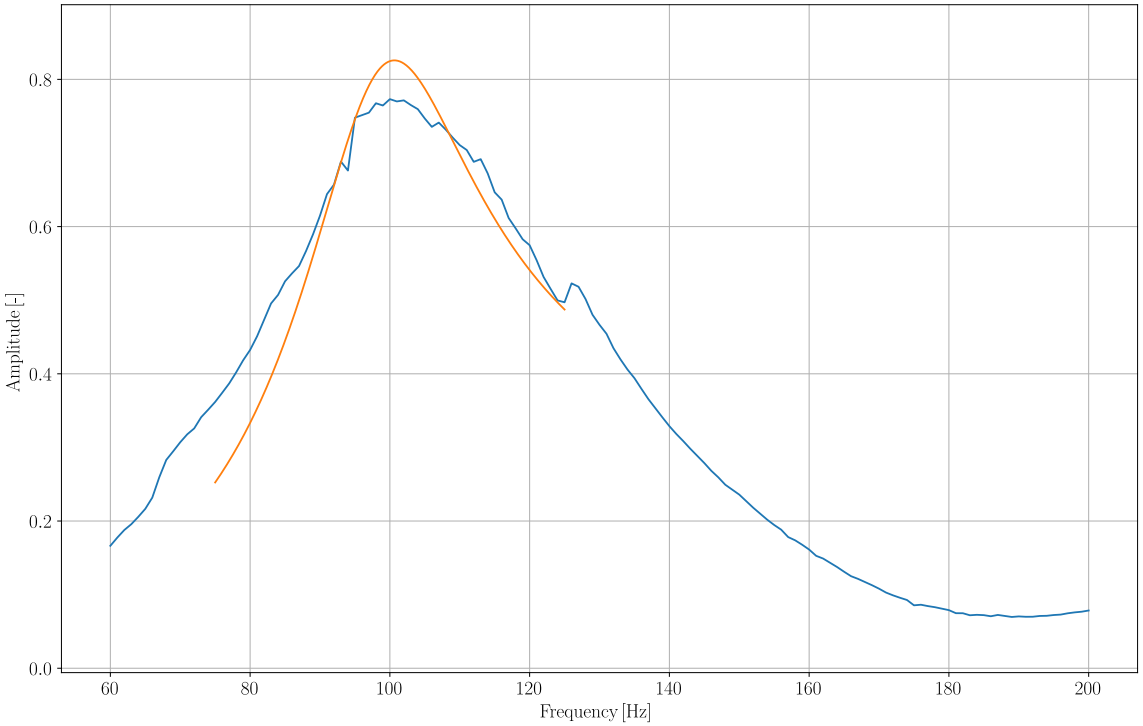

A 5.18 Approximated FRF from vibrometer LDV 2 at $v_{inlet} = 7\ ms^{-1}$ ($\alpha_{inc} = 0°$)

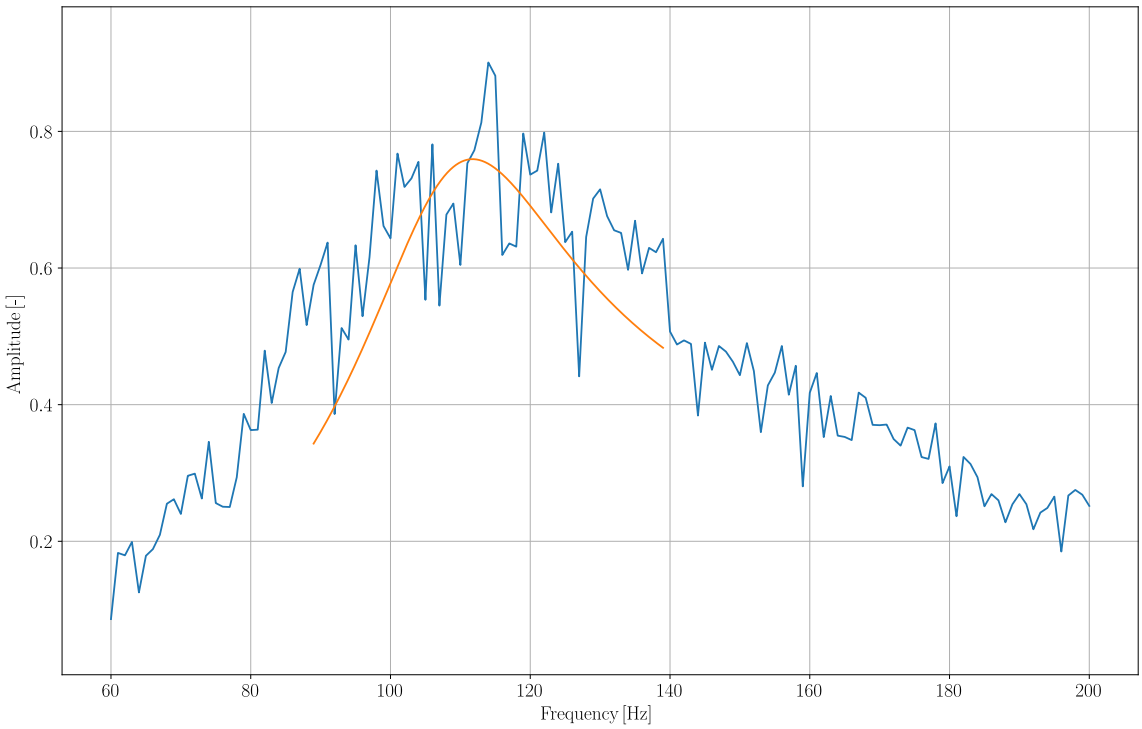

A 5.19 Approximated FRF from vibrometer LDV 1 at $v_{inlet} = 8\, ms^{-1}$ ($\alpha_{inc} = 0°$)

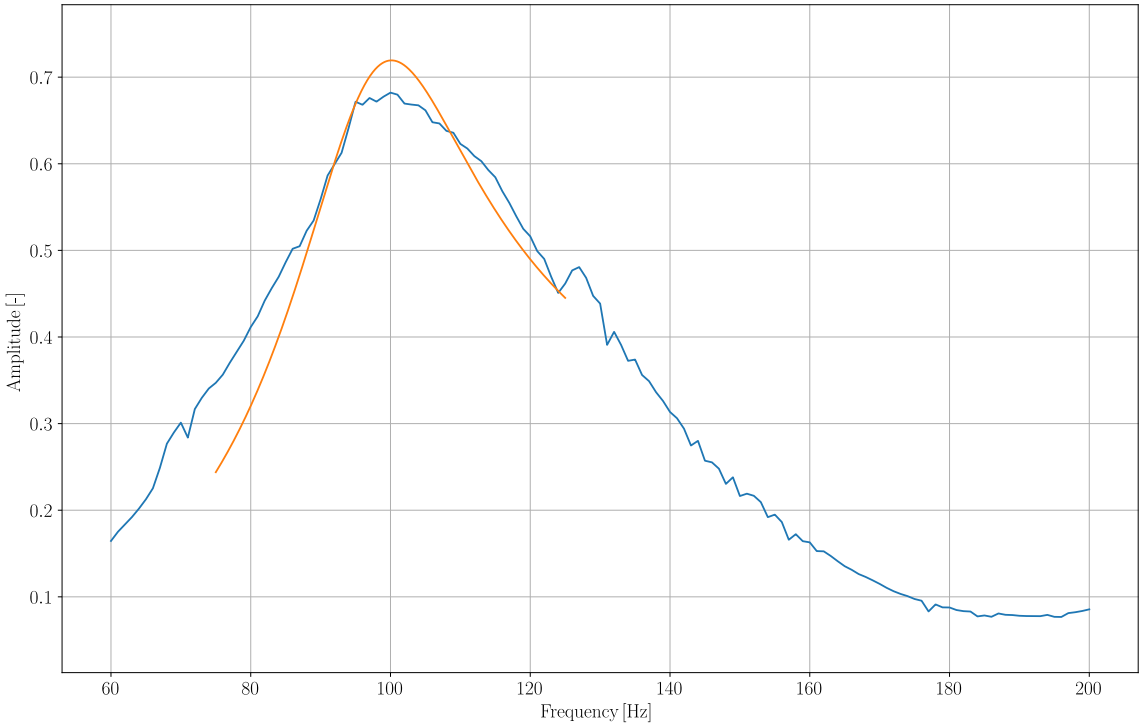

A 5.20 Approximated FRF from vibrometer LDV 2 at $v_{inlet} = 8\, ms^{-1}$ ($\alpha_{inc} = 0°$)

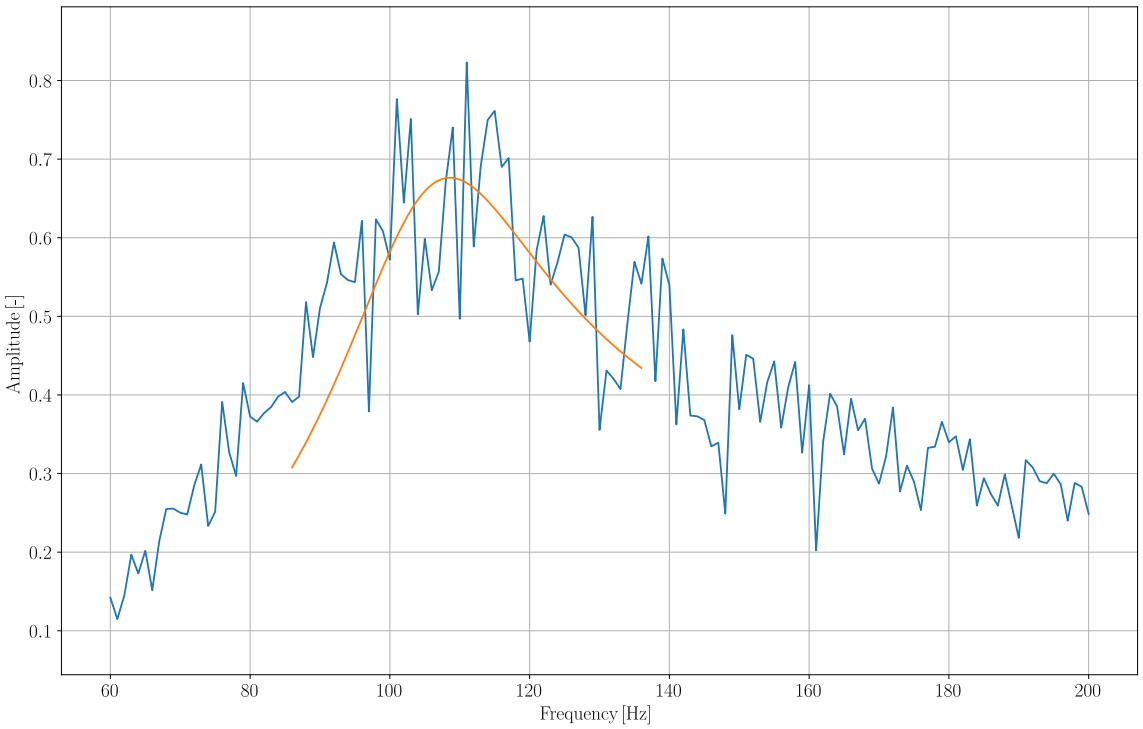

A 5.21 Approximated FRF from vibrometer LDV 1 at $v_{inlet} = 9\ ms^{-1}$ ($\alpha_{inc} = 0°$)

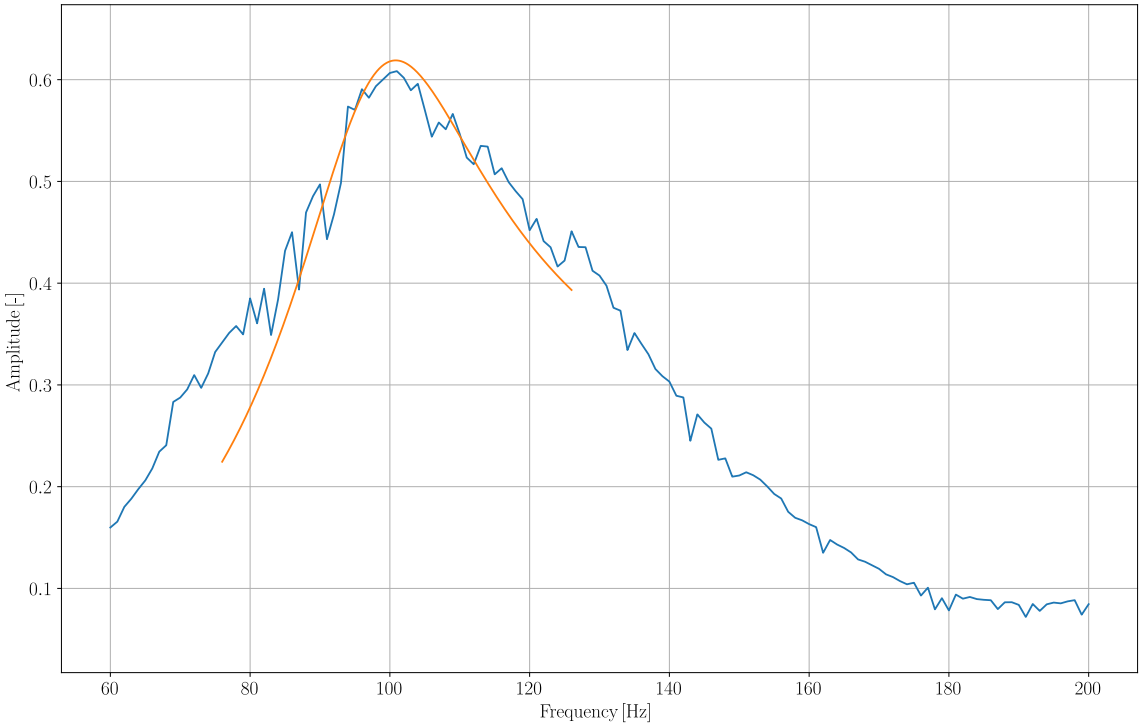

A 5.22 Approximated FRF from vibrometer LDV 2 at $v_{inlet} = 9\ ms^{-1}$ ($\alpha_{inc} = 0°$)

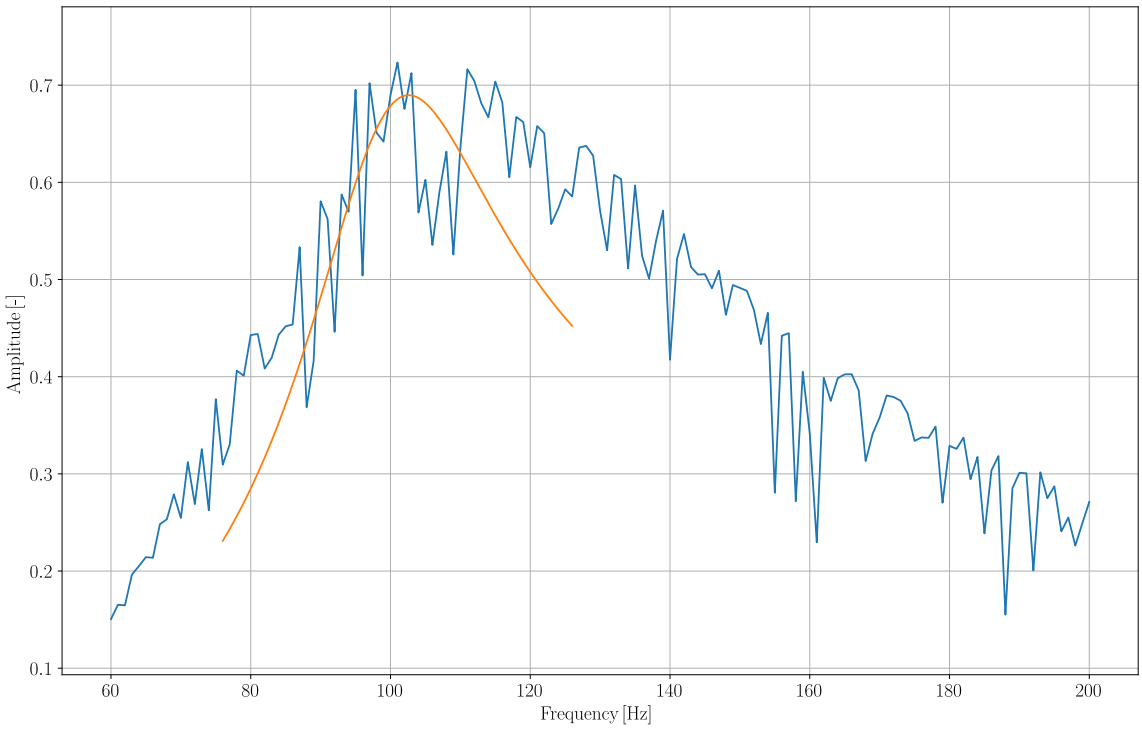

A 5.23 Approximated FRF from vibrometer LDV 1 at $v_{inlet} = 10\ ms^{-1}$ ($\alpha_{inc} = 0°$)

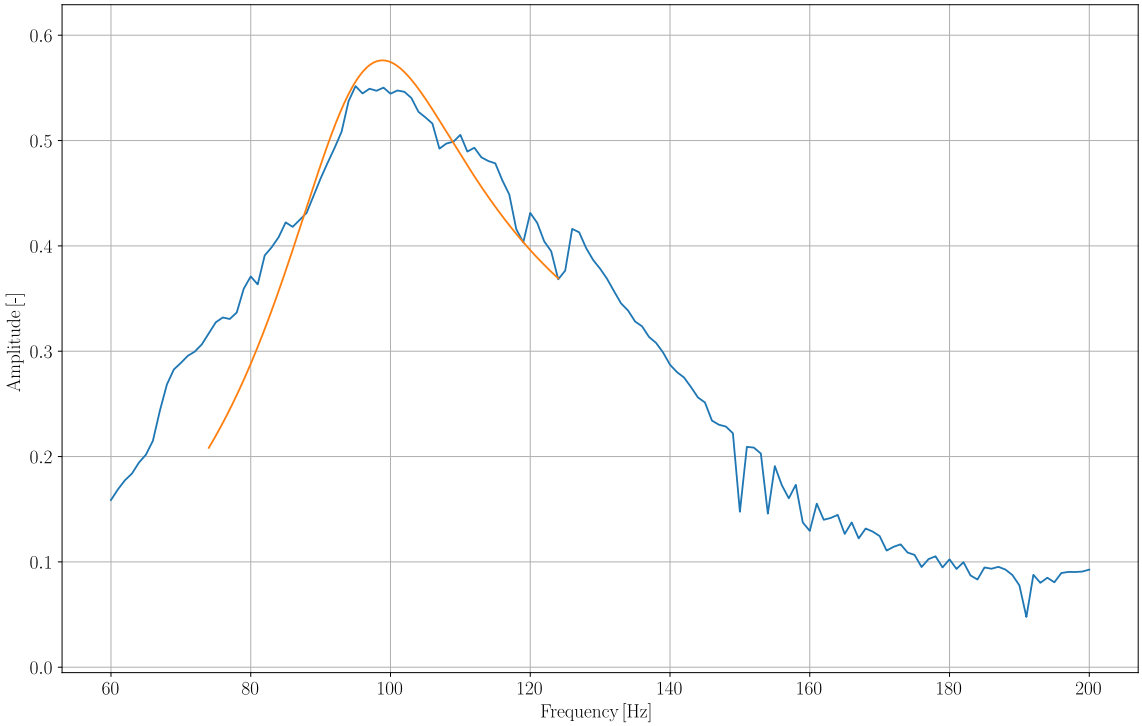

A 5.24 Approximated FRF from vibrometer LDV 2 at $v_{inlet} = 10\ ms^{-1}$ ($\alpha_{inc} = 0°$)

A.6 FRF Approximation by SDOF Response Fit Method (Angle of Attack 5°)

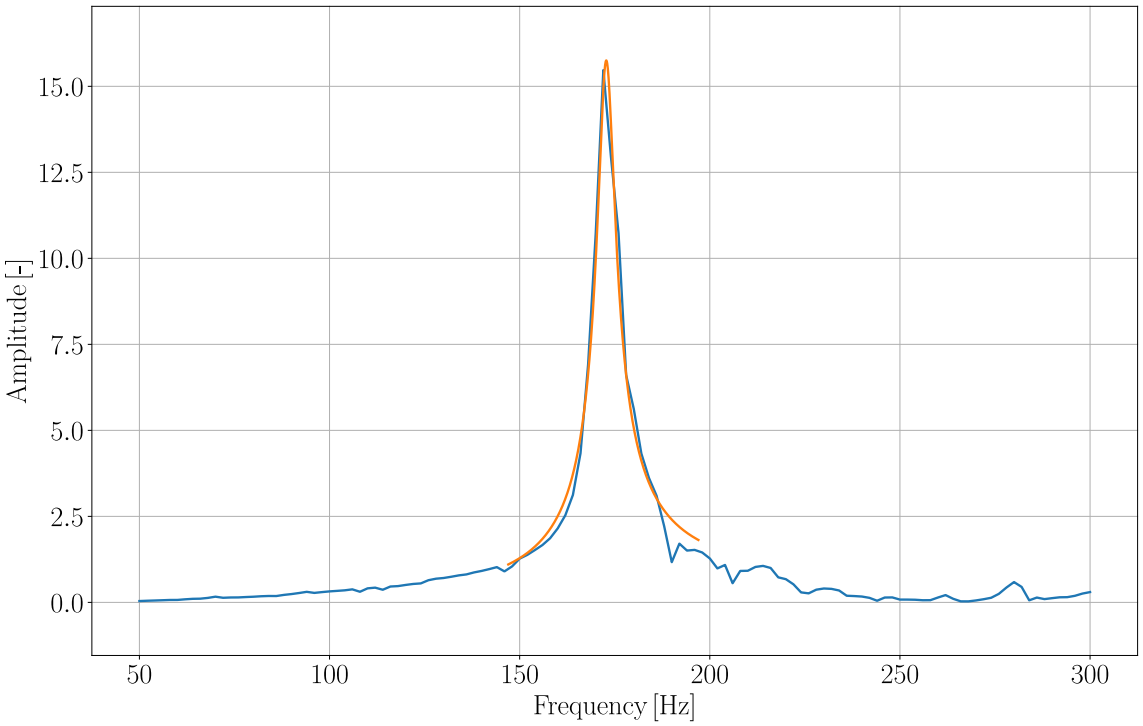

A 6.1 Approximated FRF from vibrometer LDV 1: hydrofoil in air ($\alpha_{inc} = 5°$)

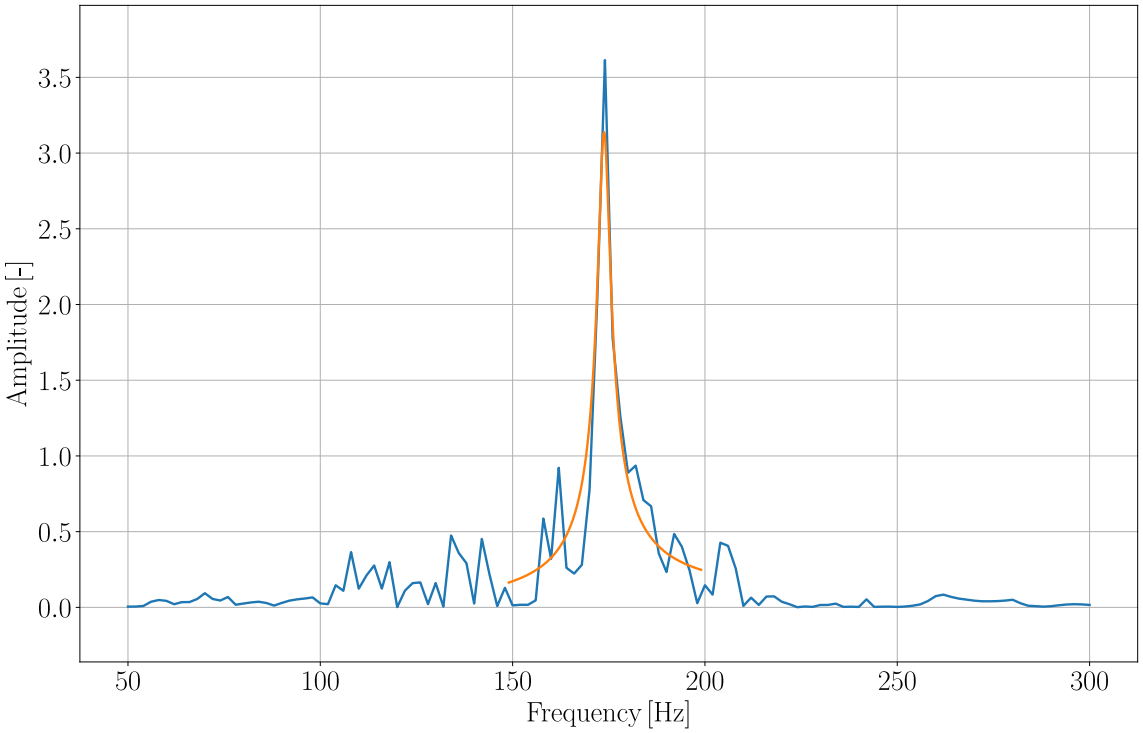

A 6.2 Approximated FRF from vibrometer LDV 1: hydrofoil in air ($\alpha_{inc} = 5°$)

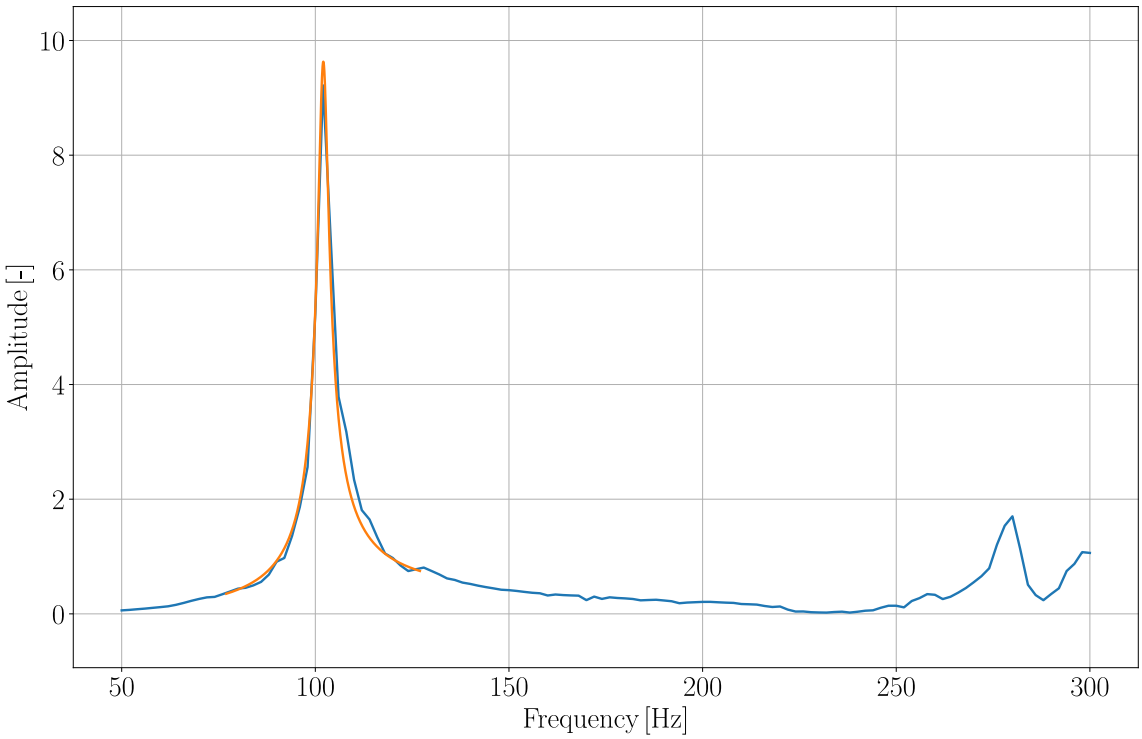

A 6.3 Approximated FRF from vibrometer LDV 1 at $v_{inlet} = 0\ ms^{-1}$ ($\alpha_{inc} = 5°$)

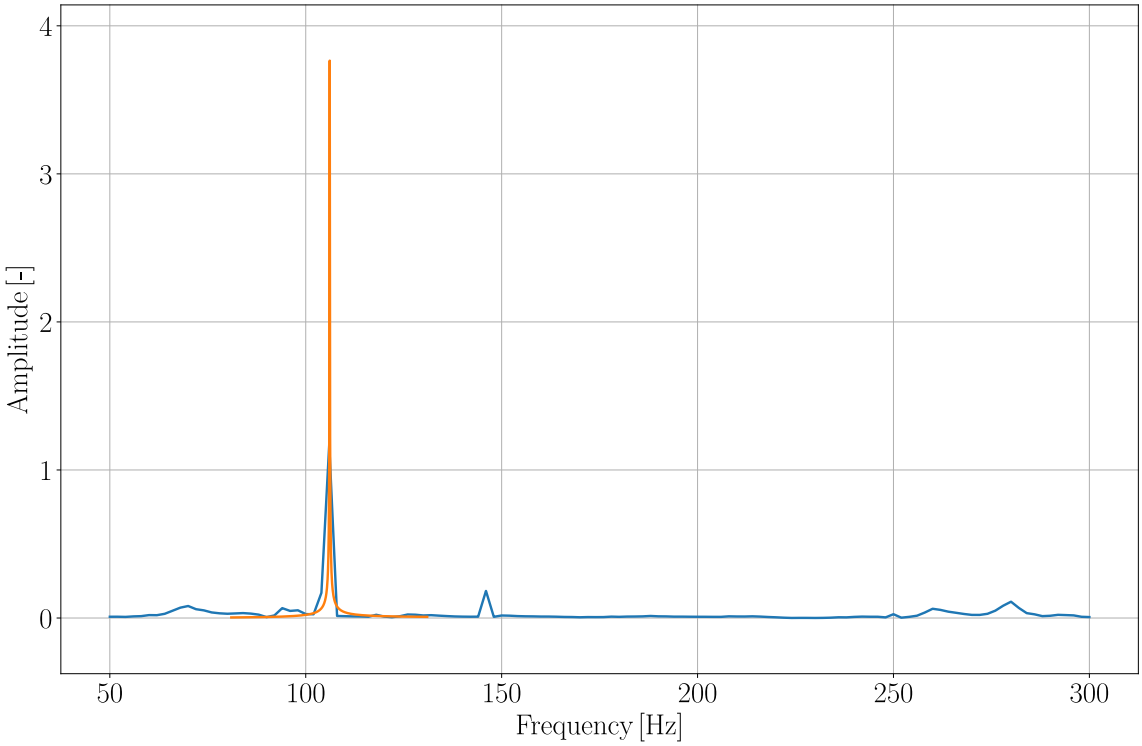

A 6.4 Approximated FRF from vibrometer LDV 2 at $v_{inlet} = 0\ ms^{-1}$ ($\alpha_{inc} = 5°$)

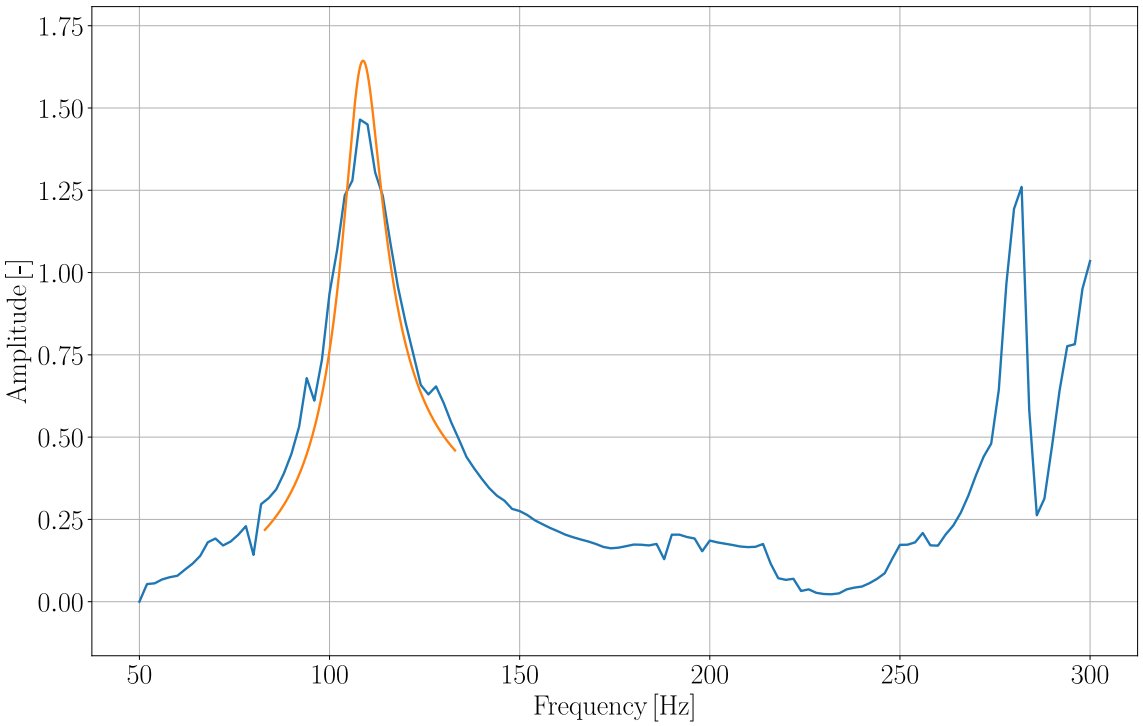

A 6.5 Approximated FRF from vibrometer LDV 1 at $v_{inlet} = 2.5\ ms^{-1}$ ($\alpha_{inc} = 5°$)

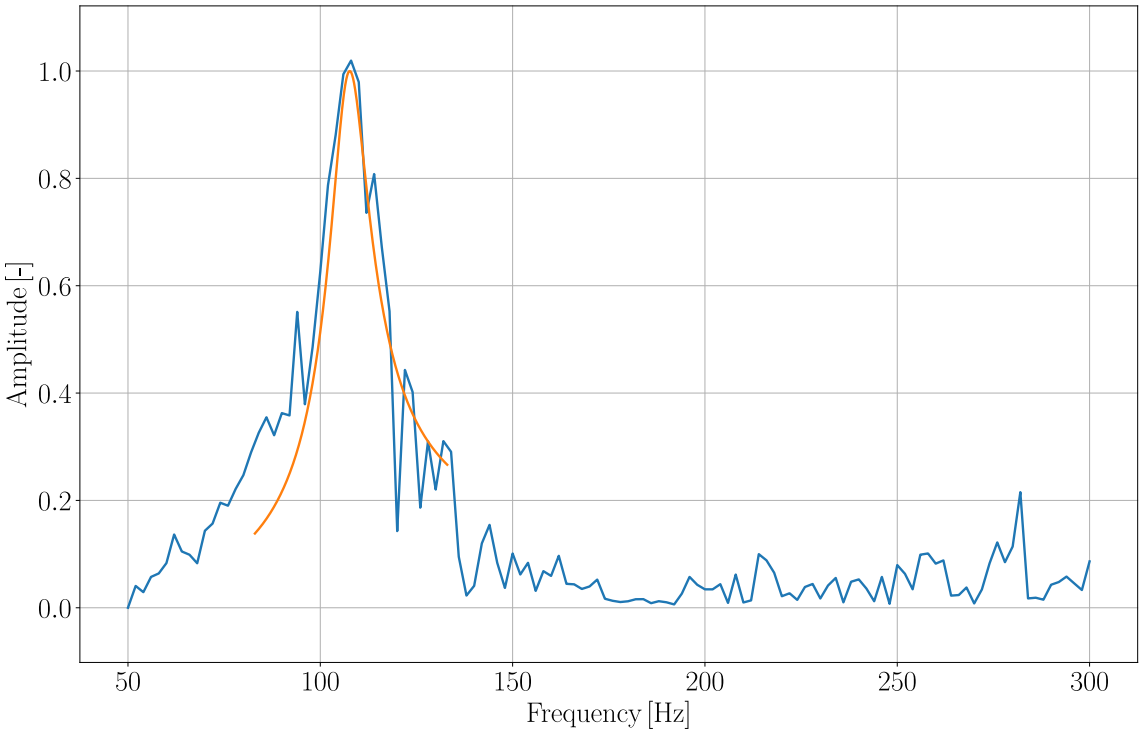

A 6.6 Approximated FRF from vibrometer LDV 2 at $v_{inlet} = 2.5\ ms^{-1}$ ($\alpha_{inc} = 5°$)

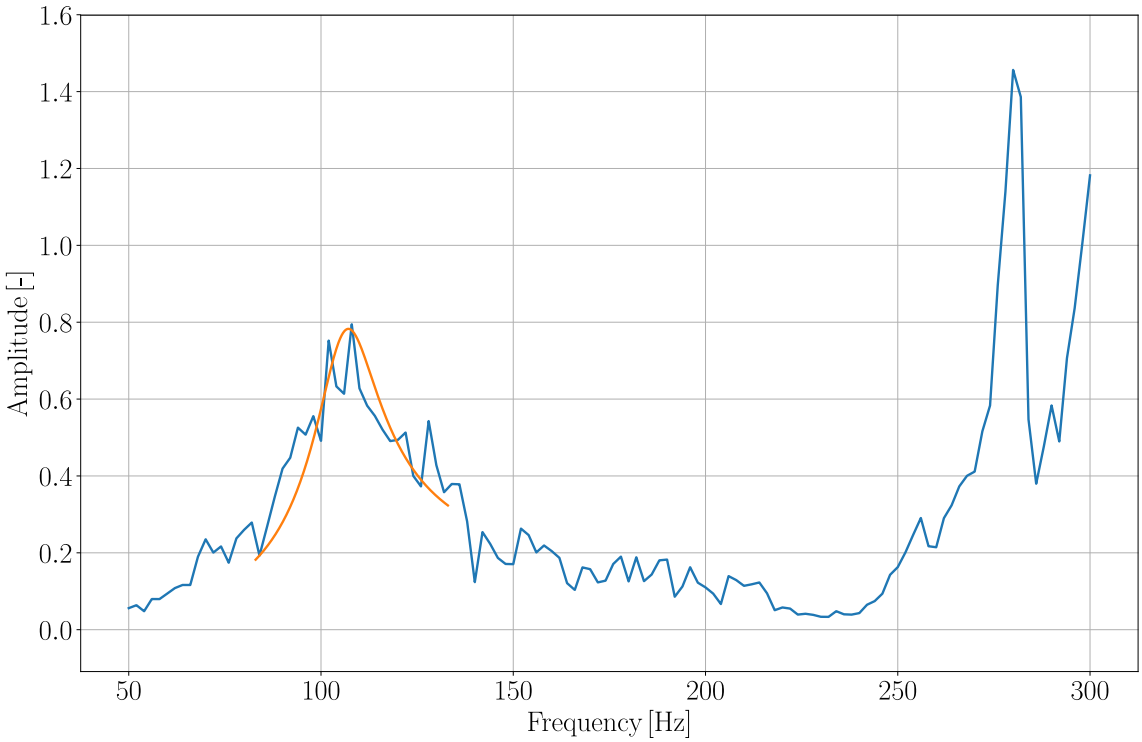

A 6.7 Approximated FRF from vibrometer LDV 1 at $v_{inlet} = 5\ ms^{-1}$ ($\alpha_{inc} = 5°$)

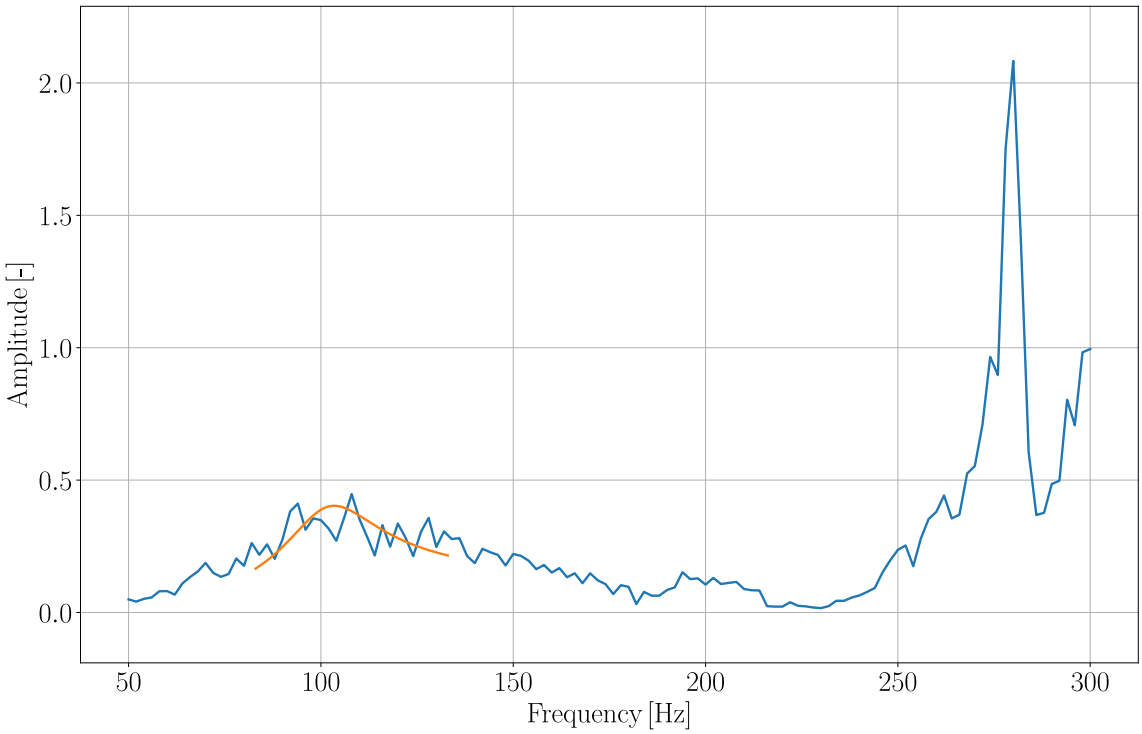

A 6.8 Approximated FRF from vibrometer LDV 1 at $v_{inlet} = 7.5\ ms^{-1}$ ($\alpha_{inc} = 5°$)

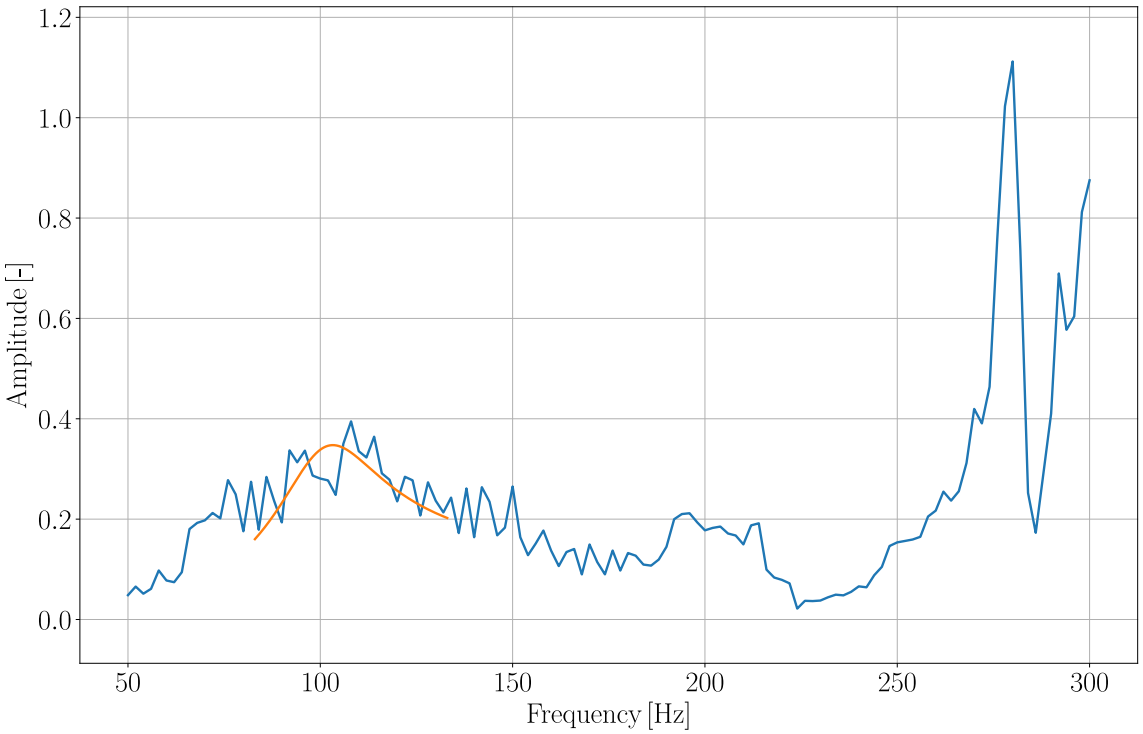

A 6.9 Approximated FRF from vibrometer LDV 1 at $v_{inlet} = 10\ ms^{-1}$ ($\alpha_{inc} = 5°$)

A.7 Pressure Field from Unsteady CFD with Prescribed Motion

A 7.1 Pressure field from unsteady CFD with prescribed motion at $v_{inlet} = 0\ ms^{-1}$

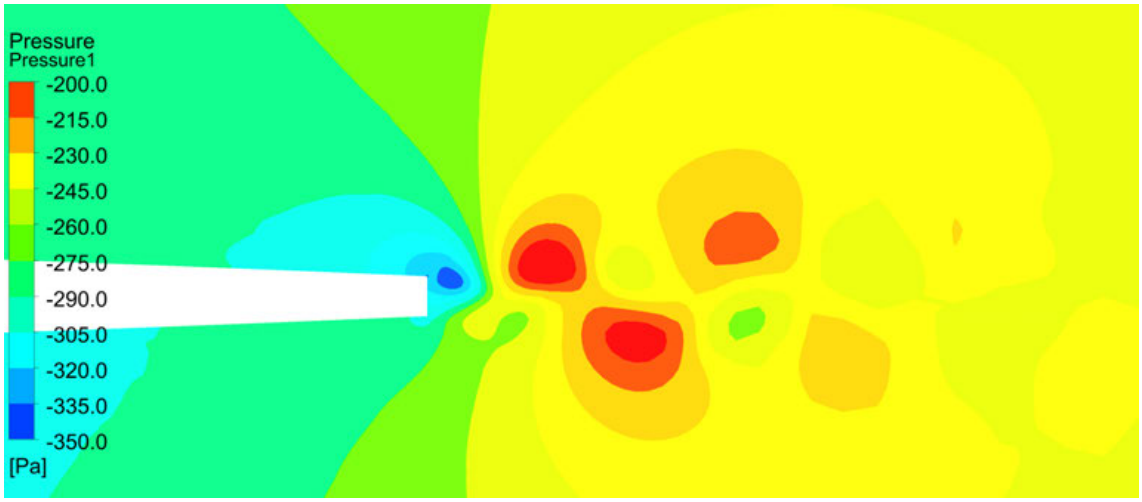

A 7.2 Pressure field from unsteady CFD with prescribed motion at $v_{inlet} = 1\ ms^{-1}$

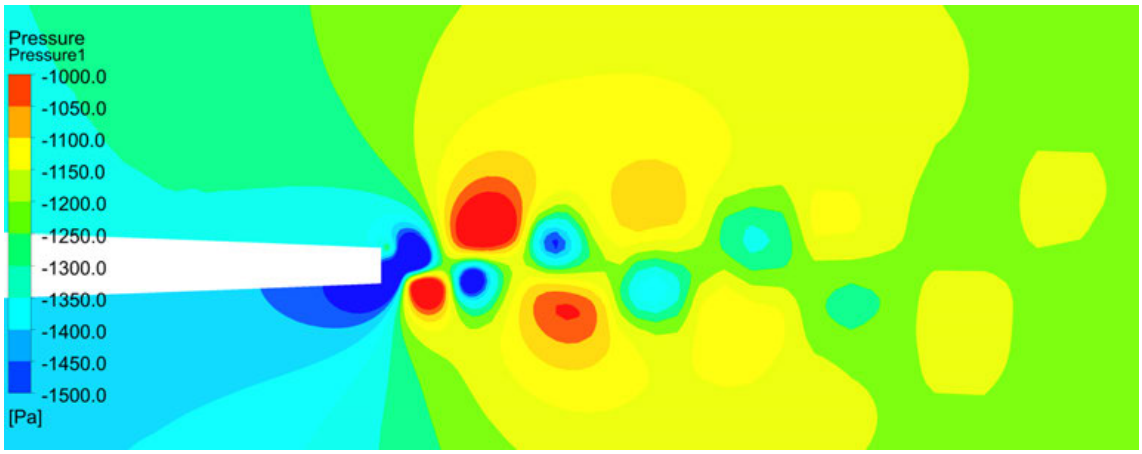

A 7.3 Pressure field from unsteady CFD with prescribed motion at $v_{inlet} = 2\ ms^{-1}$

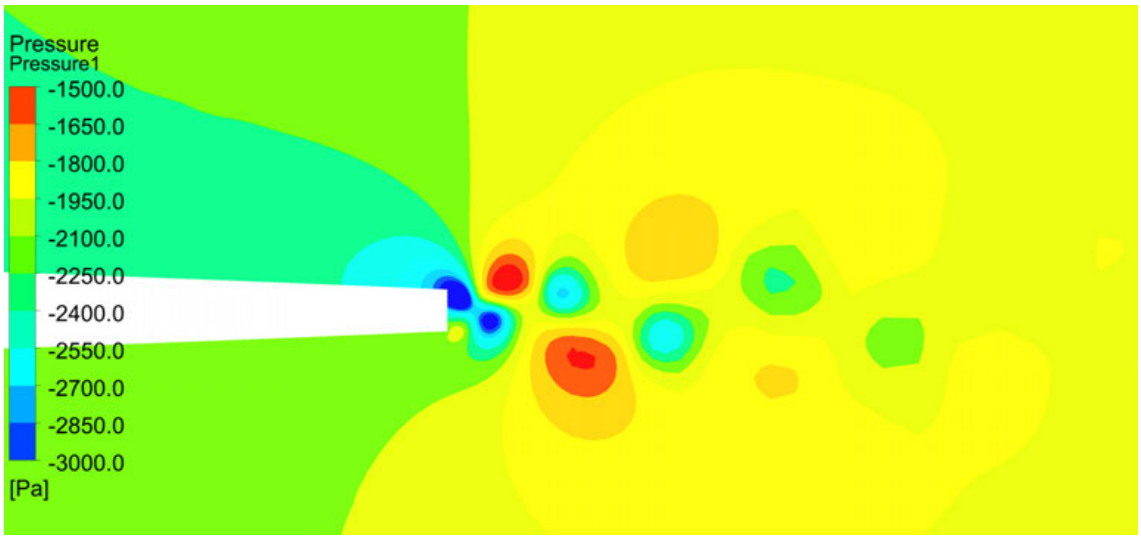

A 7.4 Pressure field from unsteady CFD with prescribed motion at $v_{inlet} = 2.5\ ms^{-1}$

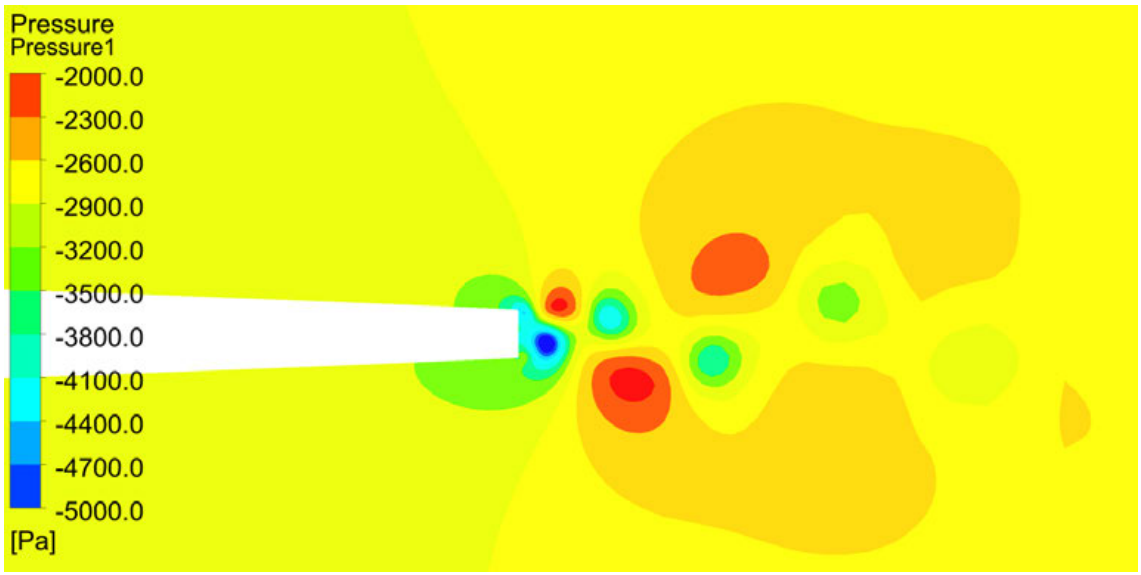

A 7.5 Pressure field from unsteady CFD with prescribed motion at $v_{inlet} = 3\ ms^{-1}$

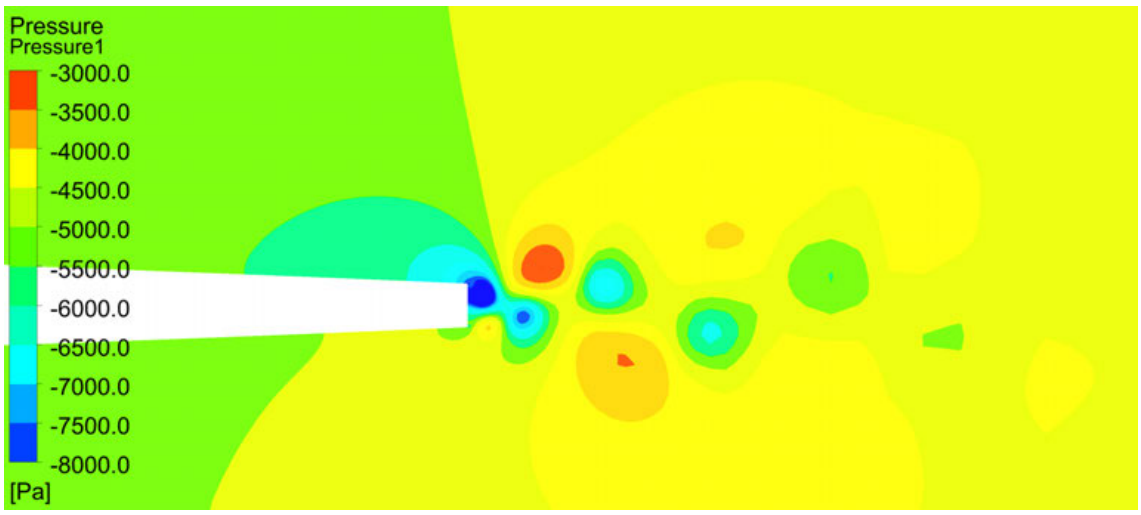

A 7.6 Pressure field from unsteady CFD with prescribed motion at $v_{inlet} = 4\ ms^{-1}$

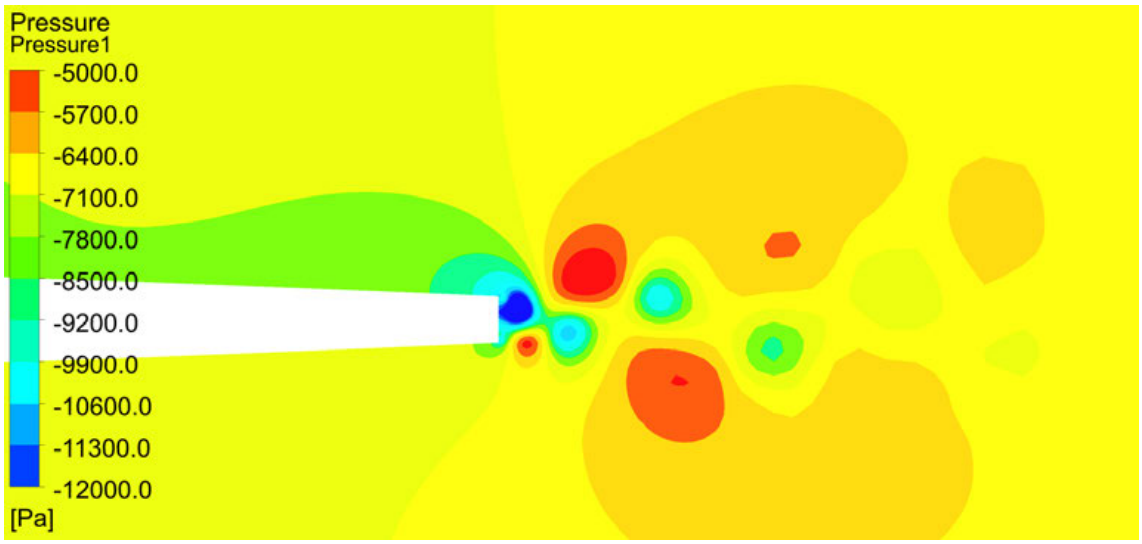

A 7.7 Pressure field from unsteady CFD with prescribed motion at $v_{inlet} = 5\ ms^{-1}$

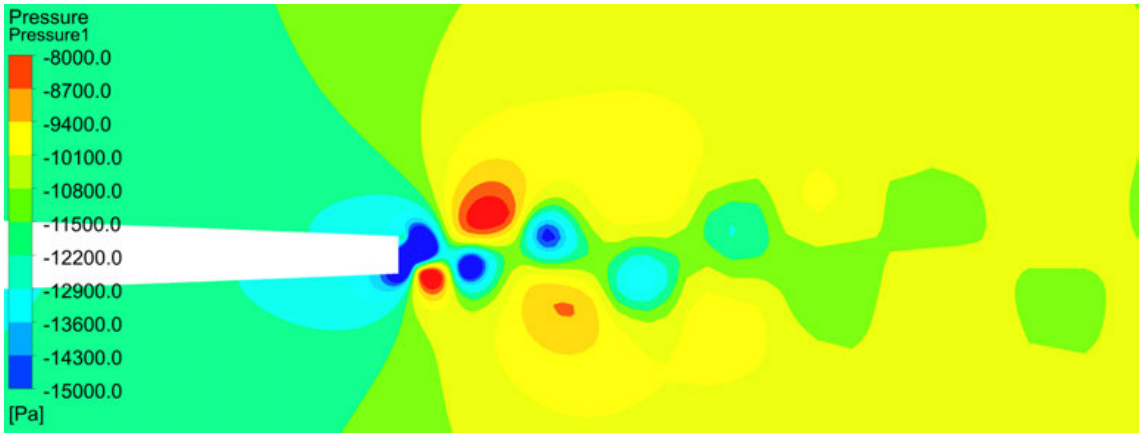

A 7.8 Pressure field from unsteady CFD with prescribed motion at $v_{inlet} = 6\ ms^{-1}$

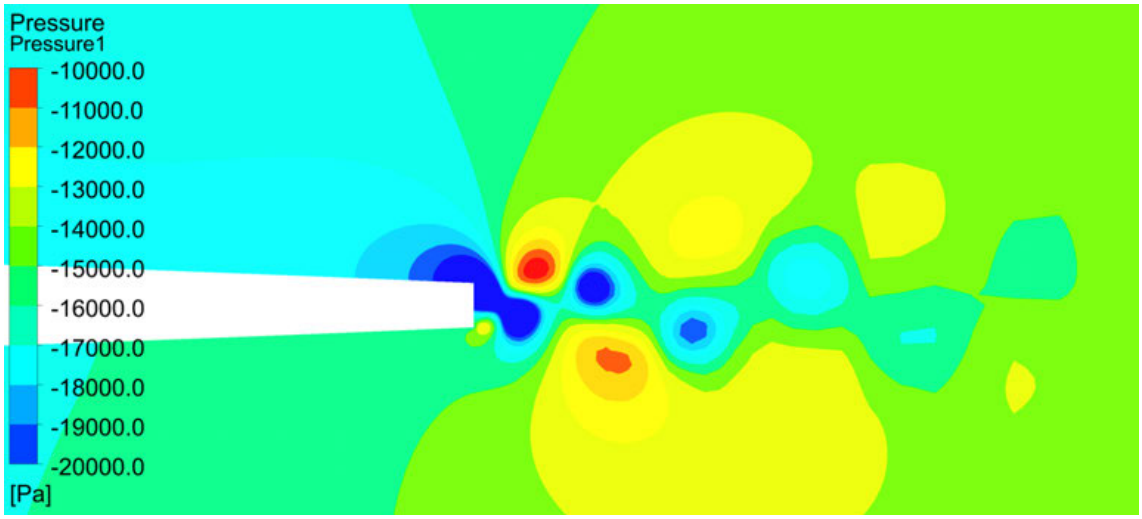

A 7.9 Pressure field from unsteady CFD with prescribed motion at $v_{inlet} = 7\ ms^{-1}$

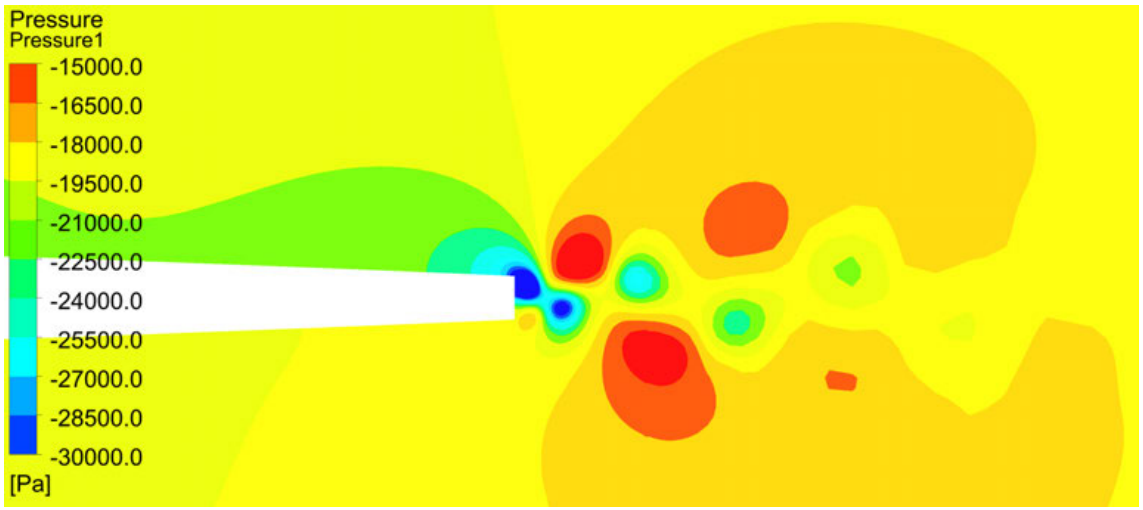

A 7.10 Pressure field from unsteady CFD with prescribed motion at $v_{inlet} = 7.5\ ms^{-1}$

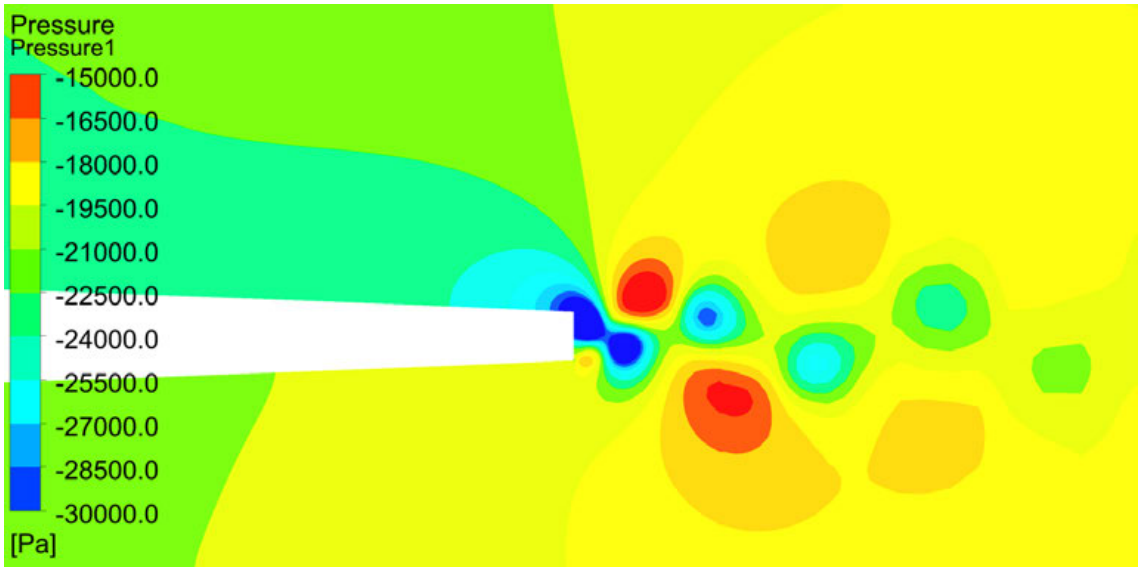

A 7.11 Pressure field from unsteady CFD with prescribed motion at $v_{inlet} = 8\ ms^{-1}$

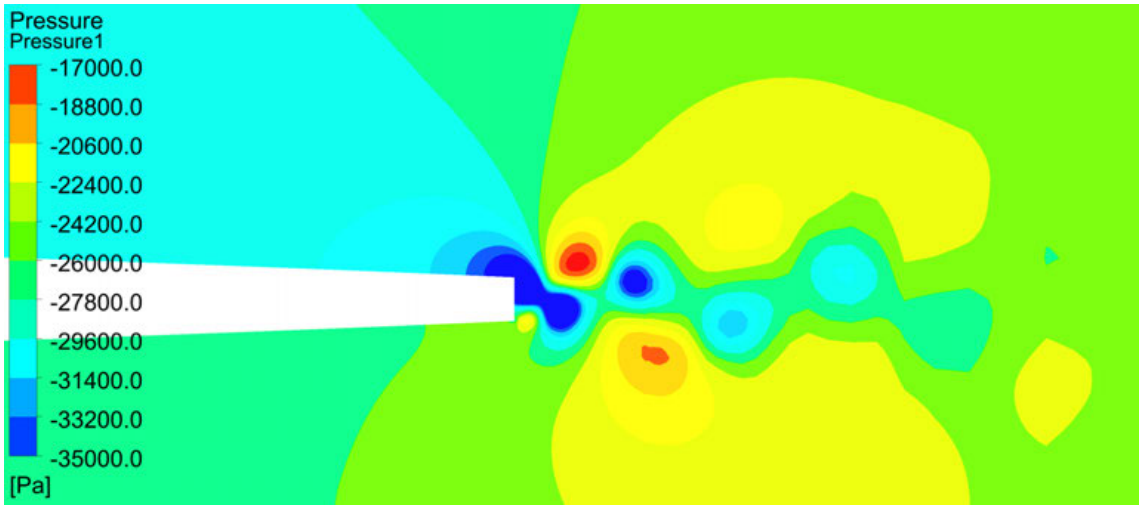

A 7.12 Pressure field from unsteady CFD with prescribed motion at $v_{inlet} = 9\ ms^{-1}$

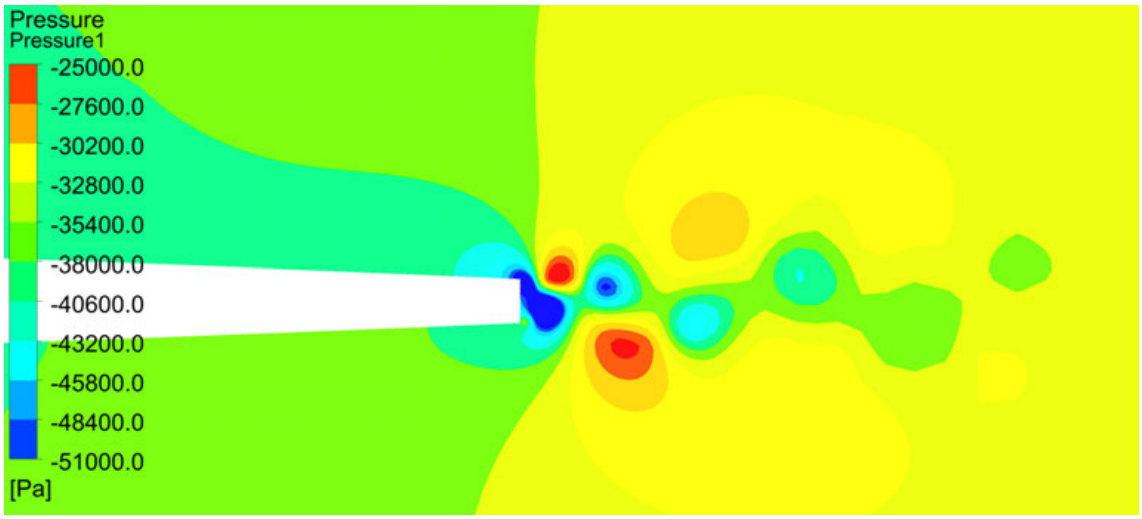

A 7.13 Pressure field from unsteady CFD with prescribed motion at $v_{inlet} = 10\ ms^{-1}$

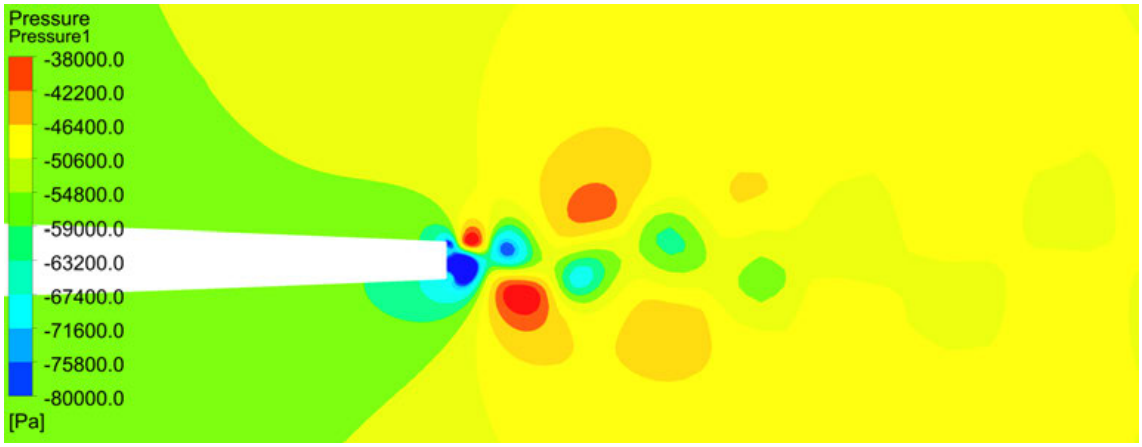

A 7.14 Pressure field from unsteady CFD with prescribed motion at $v_{inlet} = 12.5\ ms^{-1}$

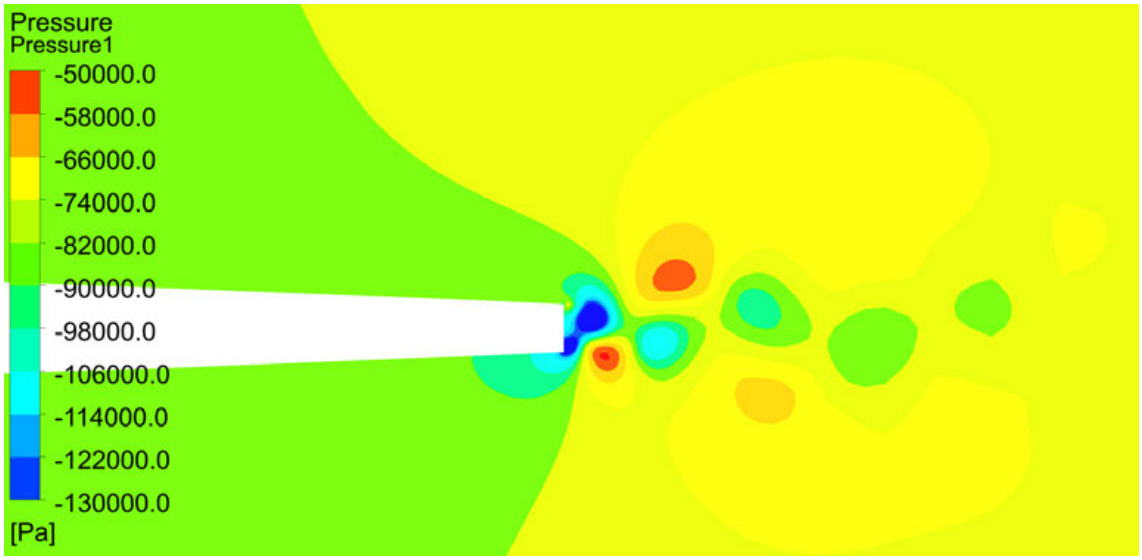

A 7.15 Pressure field from unsteady CFD with prescribed motion at $v_{inlet} = 15\ ms^{-1}$

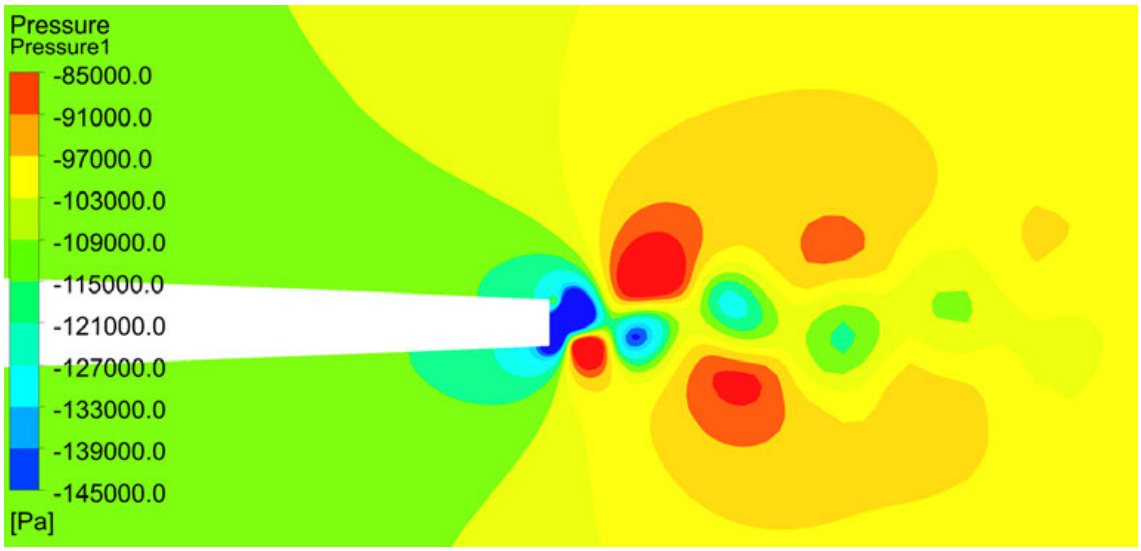

A 7.16 Pressure field from unsteady CFD with prescribed motion at $v_{inlet} = 17.5\ ms^{-1}$

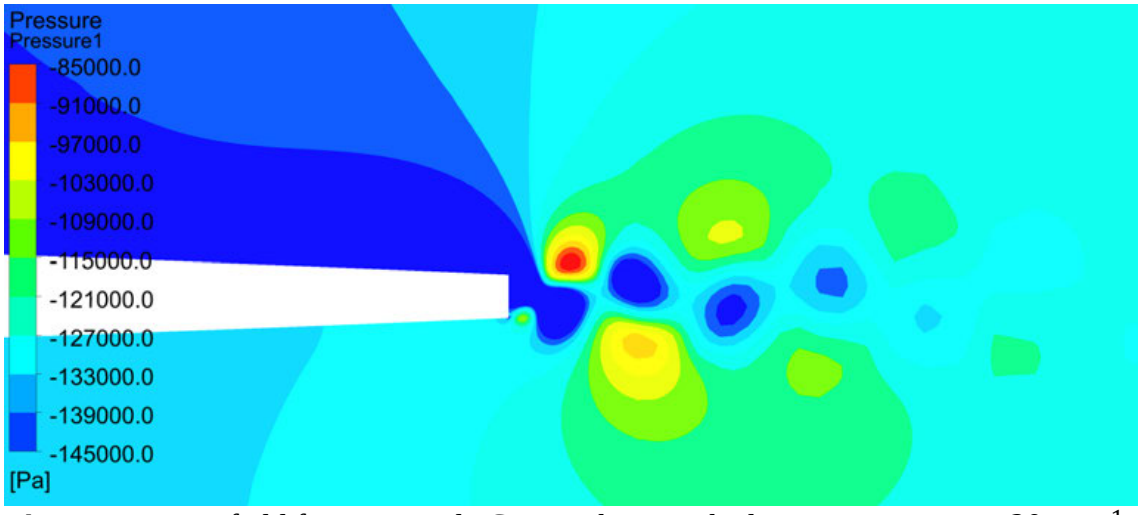

A 7.17 Pressure field from unsteady CFD with prescribed motion at $v_{inlet} = 20\ ms^{-1}$

A.8 Flow Induced Vibrations under Cavitation Conditions

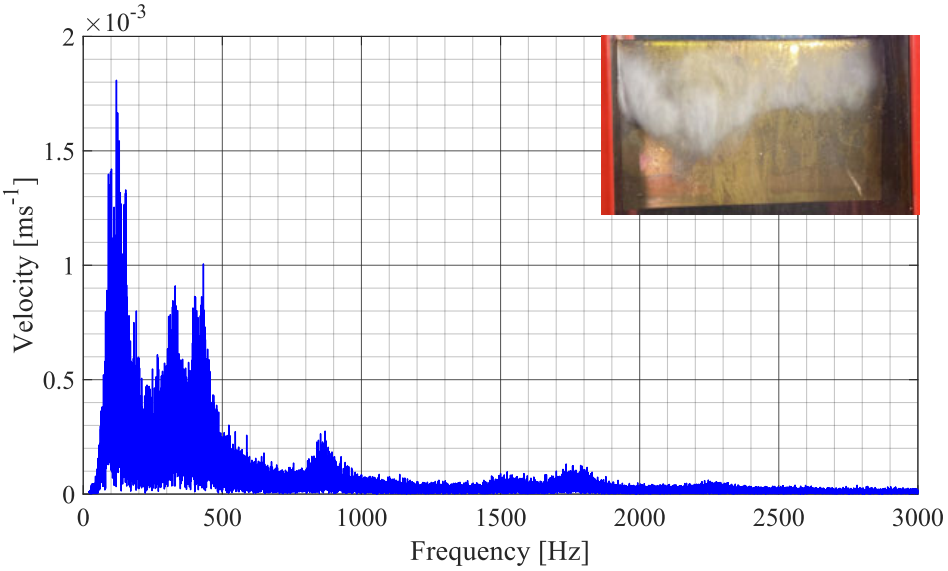

A 8.1 Flow induced vibrations at $v_{inlet} = 5.0\ ms^{-1}$ σ = 1.860 (LDV 1)

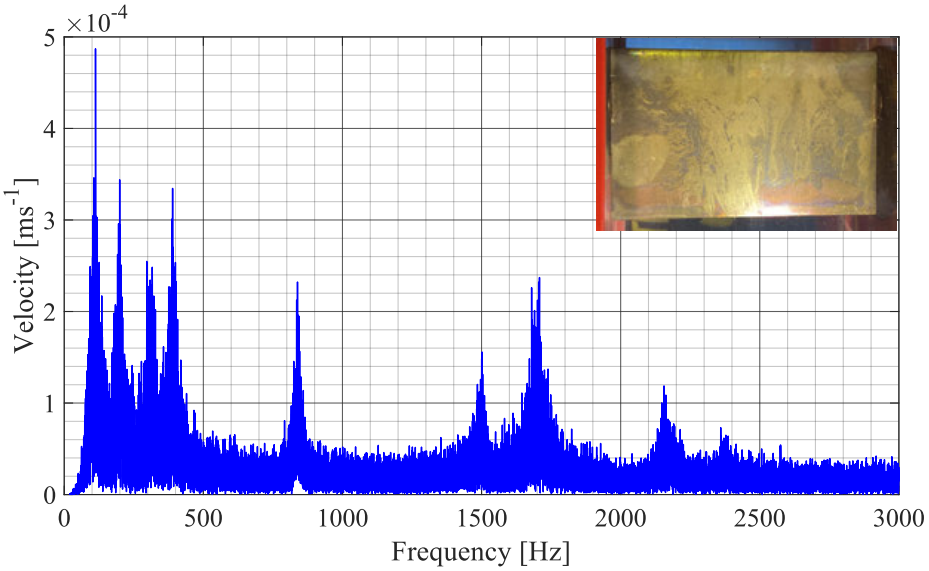

A 8.2 Flow induced vibrations at $v_{inlet} = 5.0\ ms^{-1}$ σ = 2.583 (LDV 1)

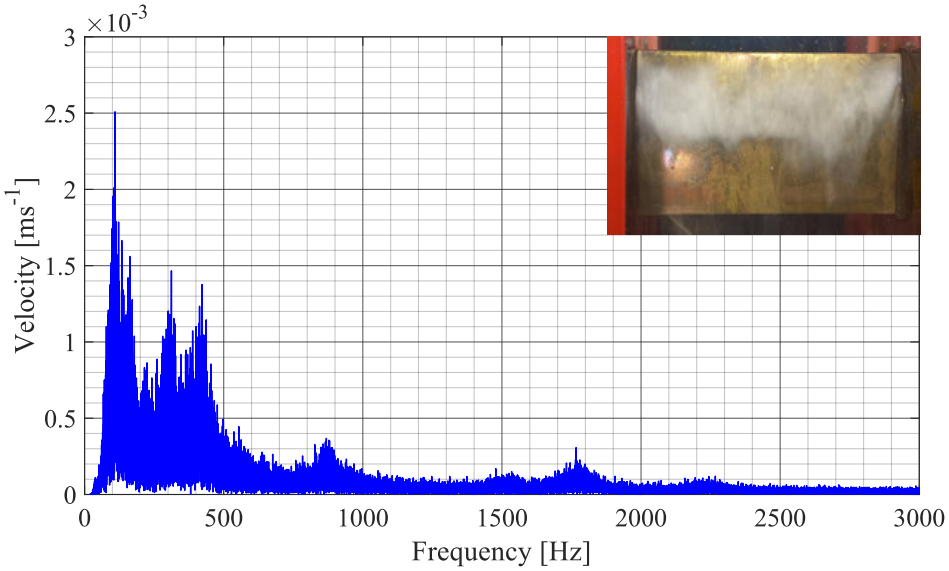

A 8.3 Flow induced vibrations at $v_{inlet} = 6.0\ ms^{-1}$ σ = 1.768 (LDV 1)

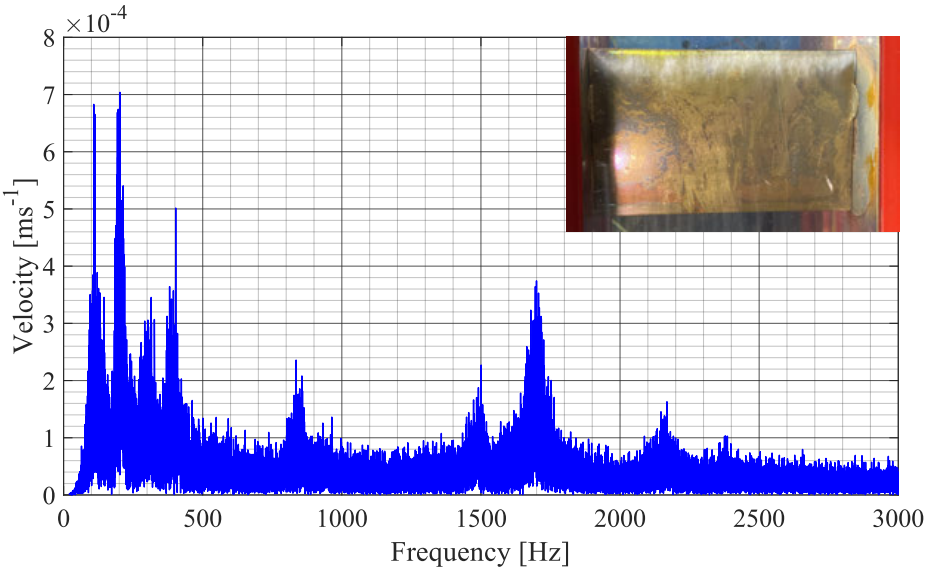

A 8.4 Flow induced vibrations at $v_{inlet} = 6.0\ ms^{-1}$ σ = 2.480 (LDV 1)

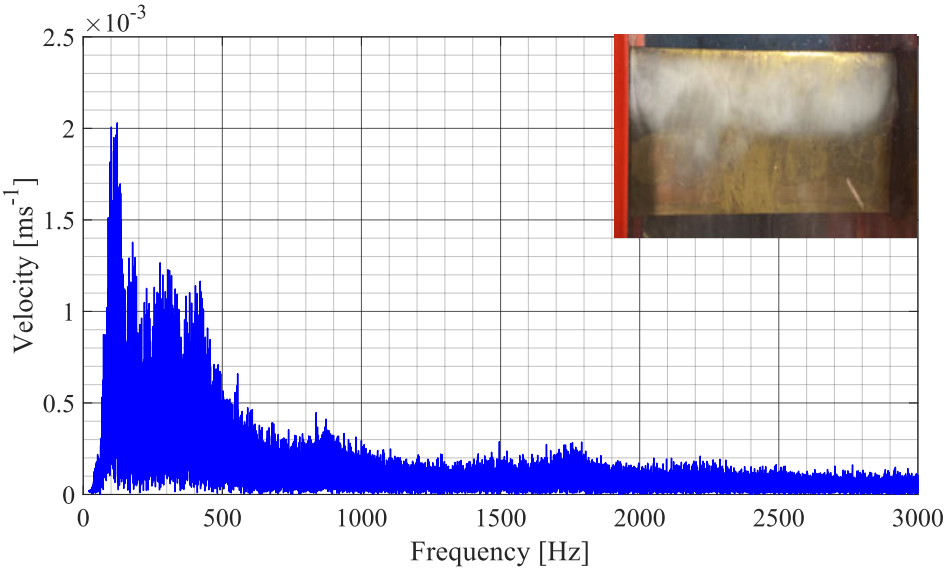

A 8.5 Flow induced vibrations at $v_{inlet} = 7.0\ ms^{-1}$ σ = 1.813 (LDV 1)

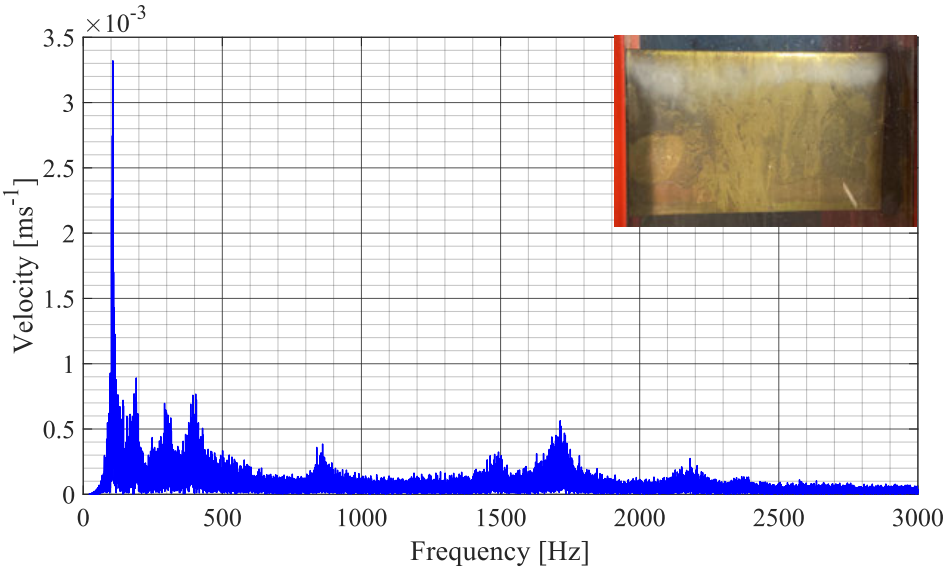

A 8.6 Flow induced vibrations at $v_{inlet} = 7.0\ ms^{-1}$ σ = 2.326 (LDV 1)

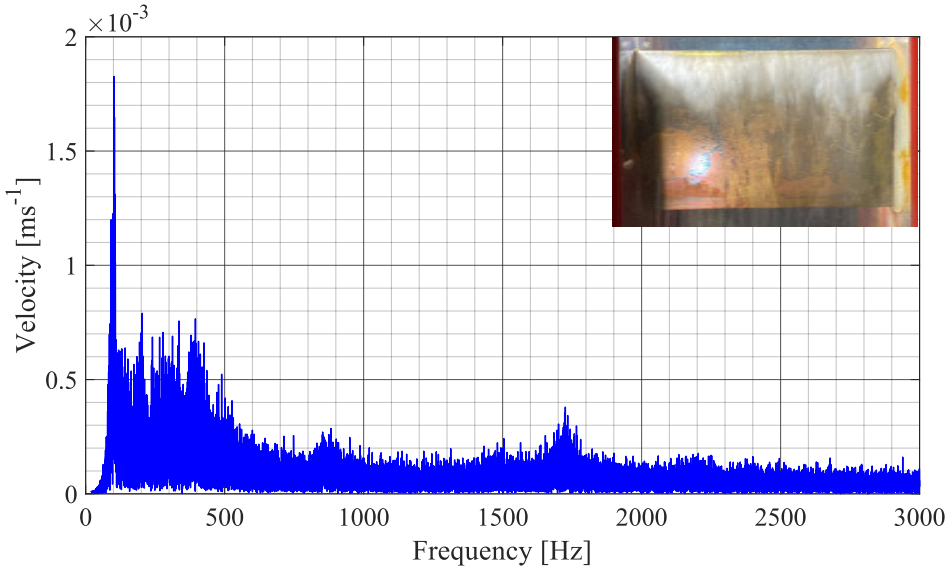

A 8.7 Flow induced vibrations at $v_{inlet} = 7.5\ ms^{-1}$ σ = 2.181 (LDV 1)

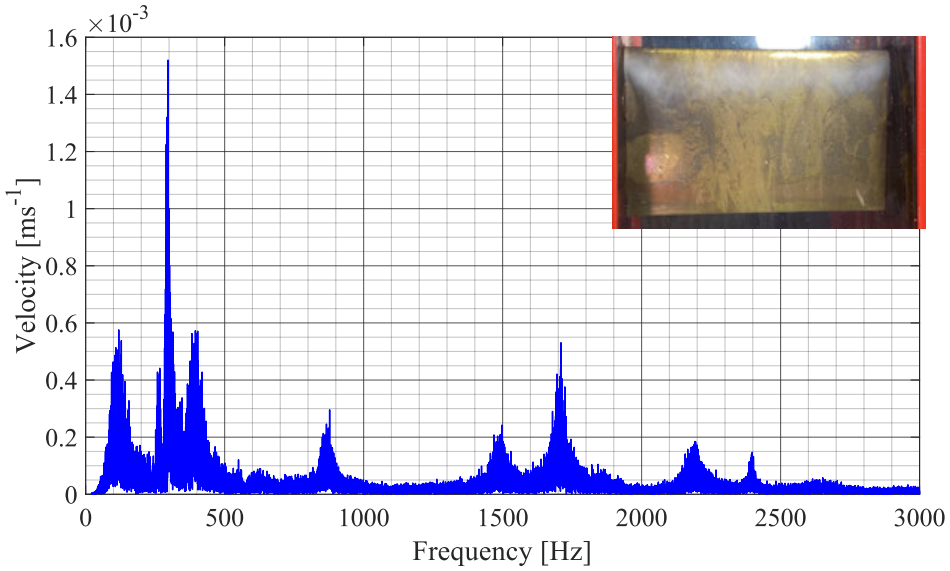

A 8.8 Flow induced vibrations at $v_{inlet} = 7.5\ ms^{-1}$ σ = 2.823 (LDV 1)

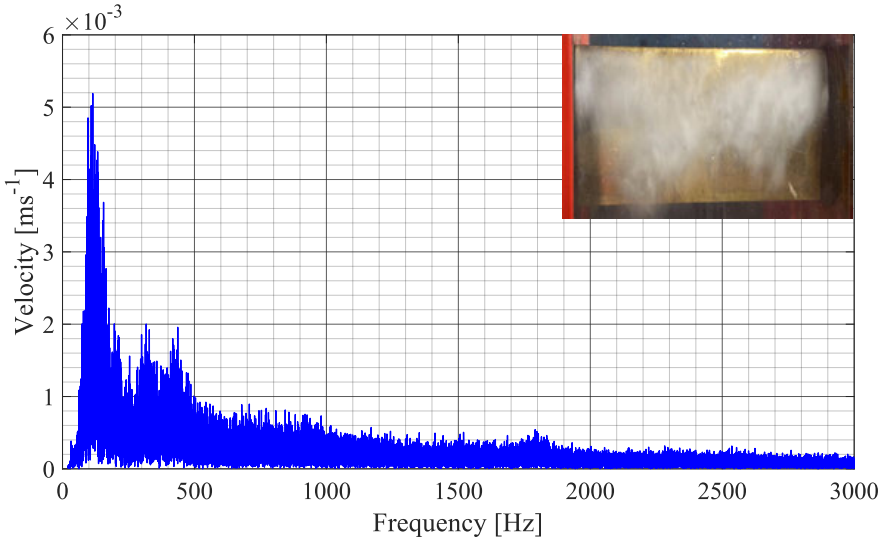

A 8.9 Flow induced vibrations at $v_{inlet} = 8.0\ ms^{-1}$ σ = 1.538 (LDV 1)

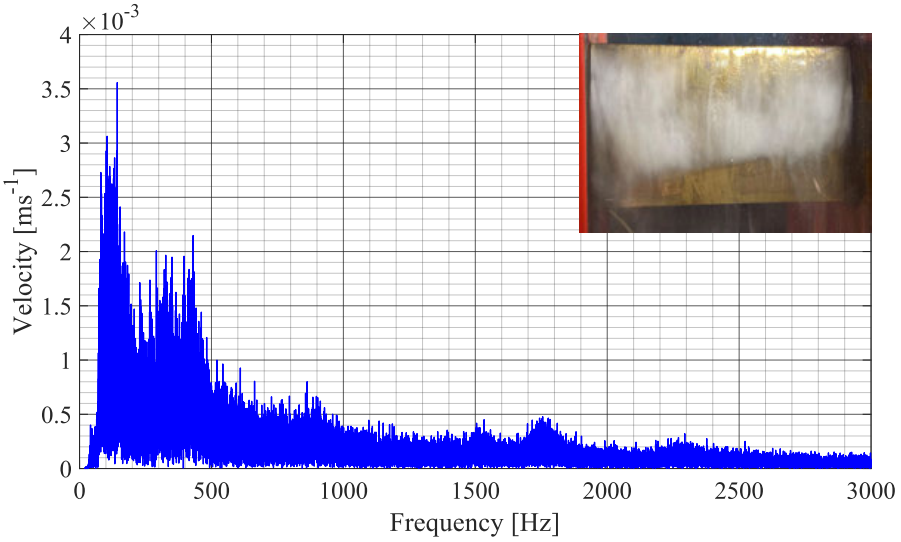

A 8.10 Flow induced vibrations at $v_{inlet} = 8.0\ ms^{-1}$ σ = 1.751 (LDV 1)

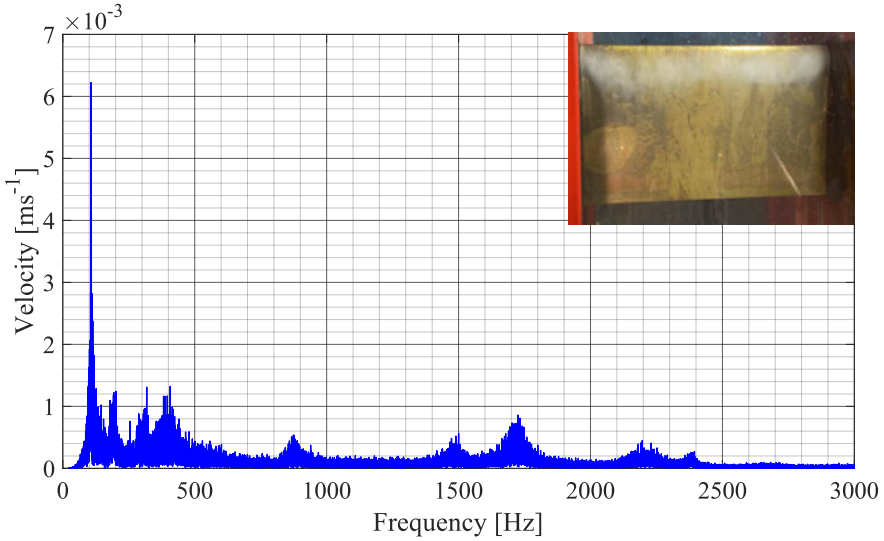

A 8.11 Flow induced vibrations at $v_{inlet} = 8.0\ ms^{-1}$ σ = 2.295 (LDV 1)

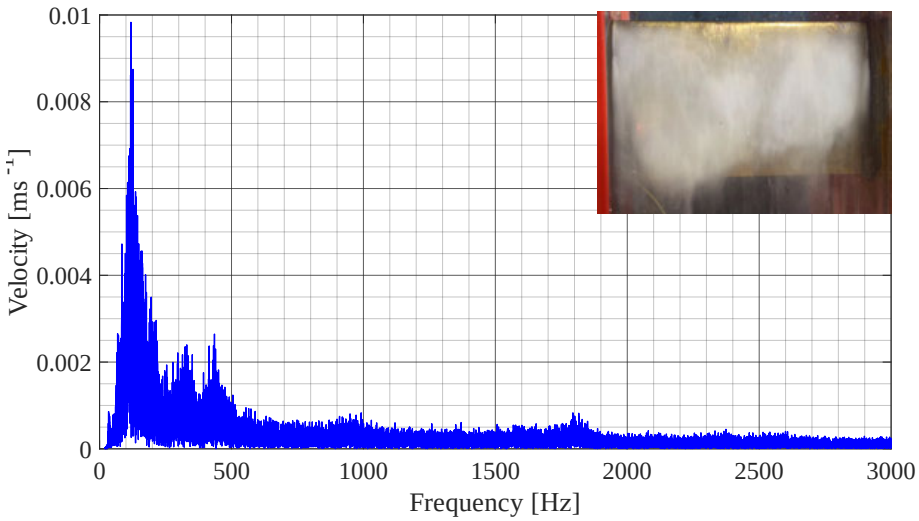

A 8.12 Flow induced vibrations at $v_{inlet} = 9.0\ ms^{-1}$ σ = 1.458 (LDV 1)

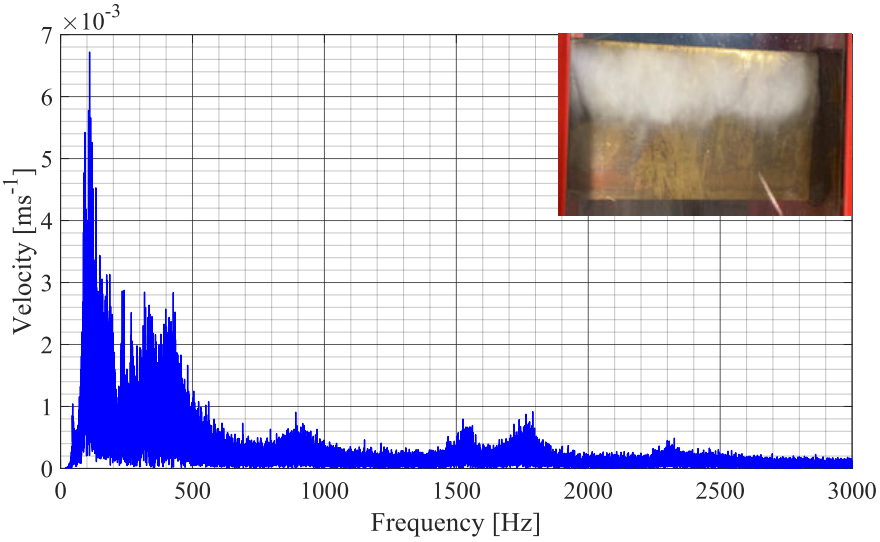

A 8.13 Flow induced vibrations at $v_{inlet} = 9.0\ ms^{-1}$ σ = 1.761 (LDV 1)

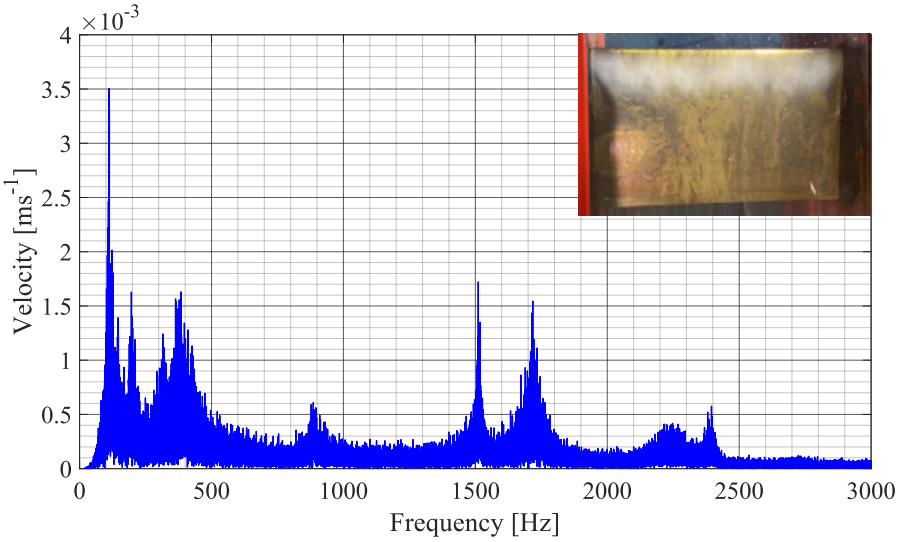

A 8.14 Flow induced vibrations at $v_{inlet} = 9.0\ ms^{-1}$ σ = 2.301 (LDV 1)

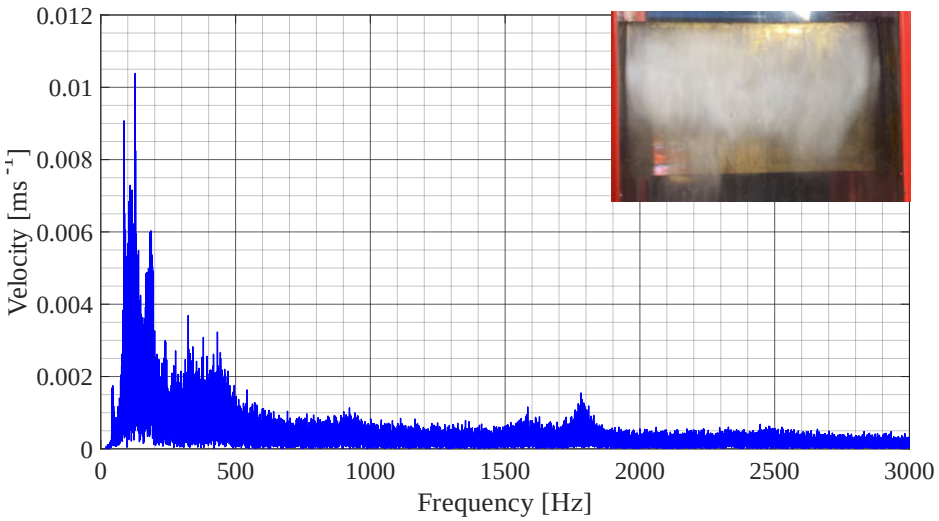

A 8.15 Flow induced vibrations at $v_{inlet} = 10.0\ ms^{-1}$ σ = 1.615 (LDV 1)

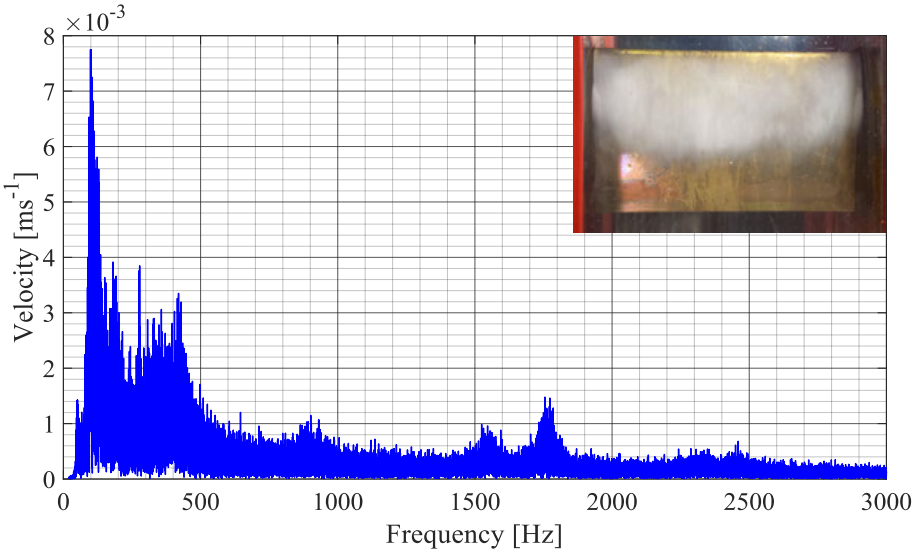

A 8.17 Flow induced vibrations at $v_{inlet} = 10.0\ ms^{-1}$ σ = 1.770 (LDV 1)

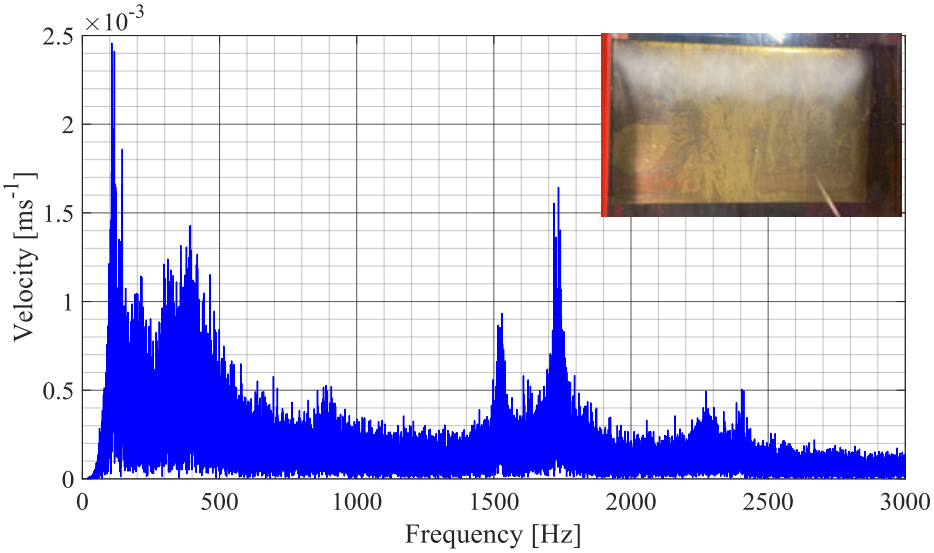

A 8.16 Flow induced vibrations at $v_{inlet} = 10.0\ ms^{-1}$ σ = 2.198 (LDV 1)

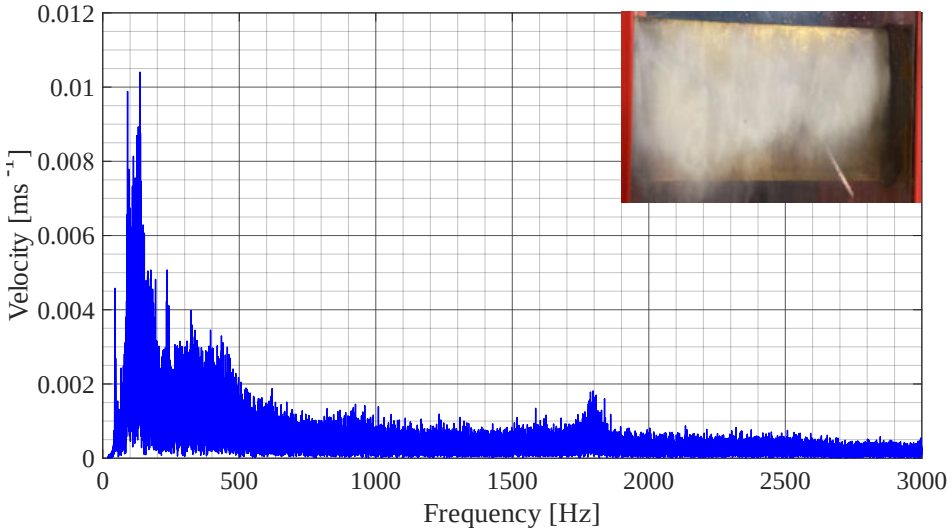

A 8.18 Flow induced vibrations at $v_{inlet} = 11.0\ ms^{-1}$ σ = 1.497 (LDV 1)

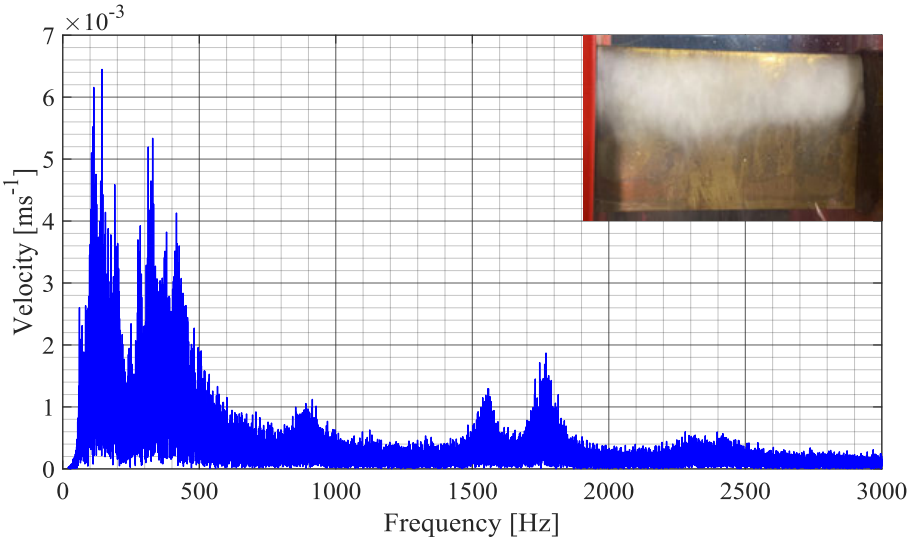

A 8.19 Flow induced vibrations at $v_{inlet} = 11.0\ ms^{-1}$ σ = 1.850 (LDV 1)

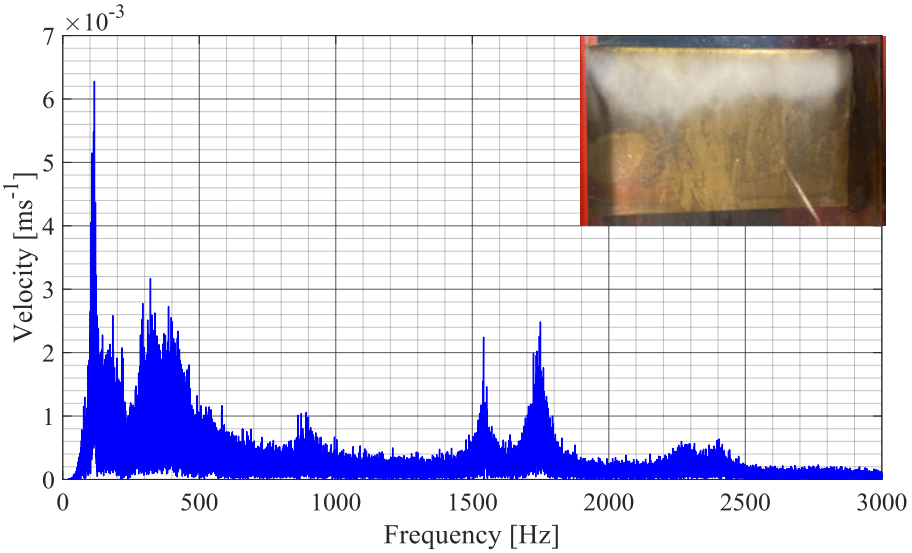

A 8.20 Flow induced vibrations at $v_{inlet} = 11.0\ ms^{-1}$ σ = 2.134 (LDV 1)

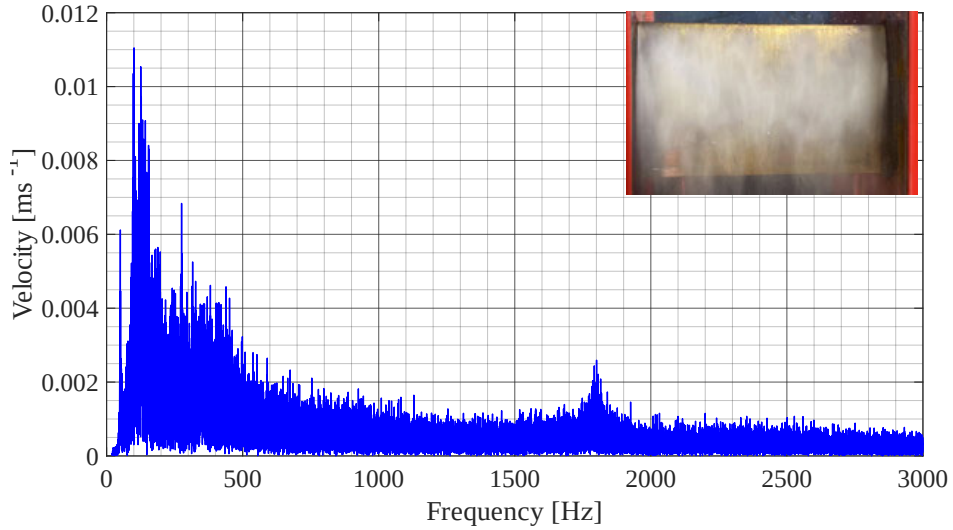

A 8.21 Flow induced vibrations at $v_{inlet} = 12.0\ ms^{-1}$ σ = 1.514 (LDV 1)

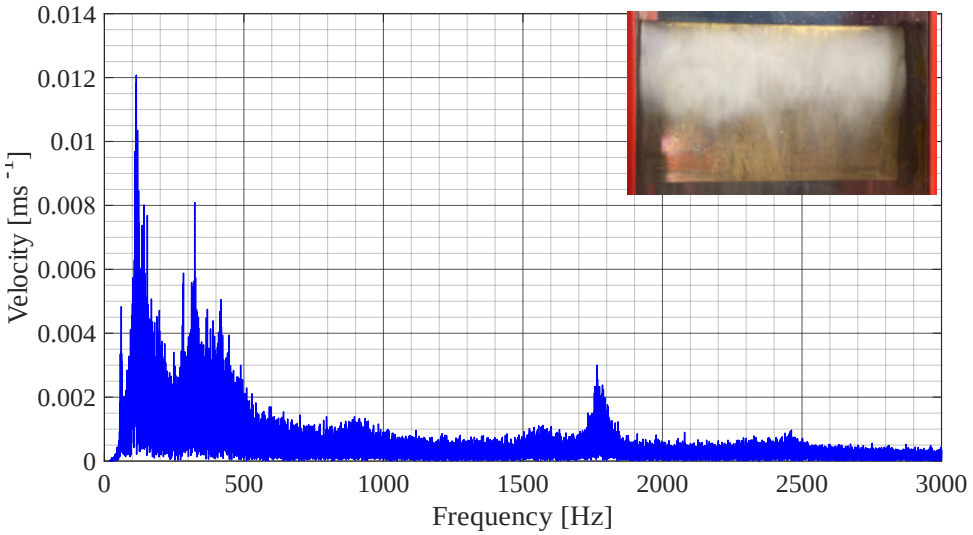

A 8.22 Flow induced vibrations at $v_{inlet} = 12.0\ ms^{-1}$ σ = 1.774 (LDV 1)

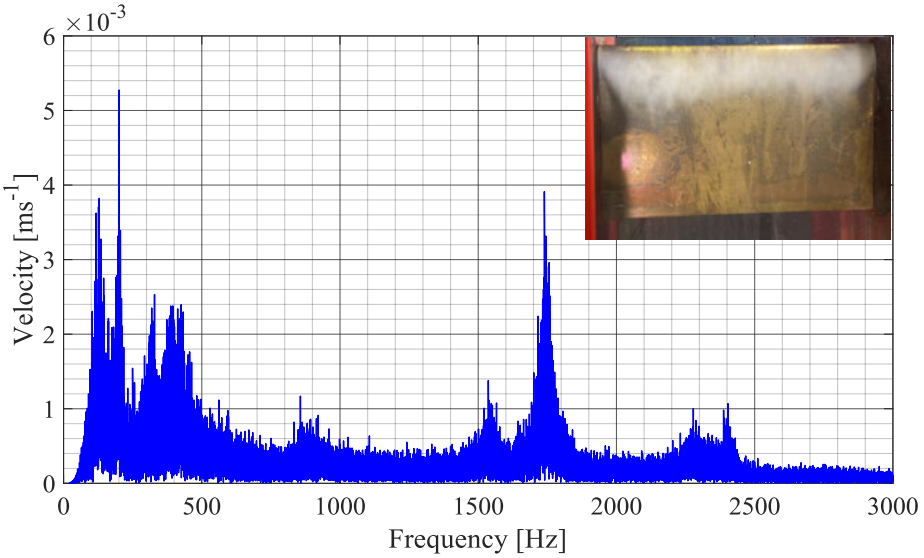

A 8.23 Flow induced vibrations at $v_{inlet} = 12.0\ ms^{-1}$ σ = 2.241 (LDV 1)

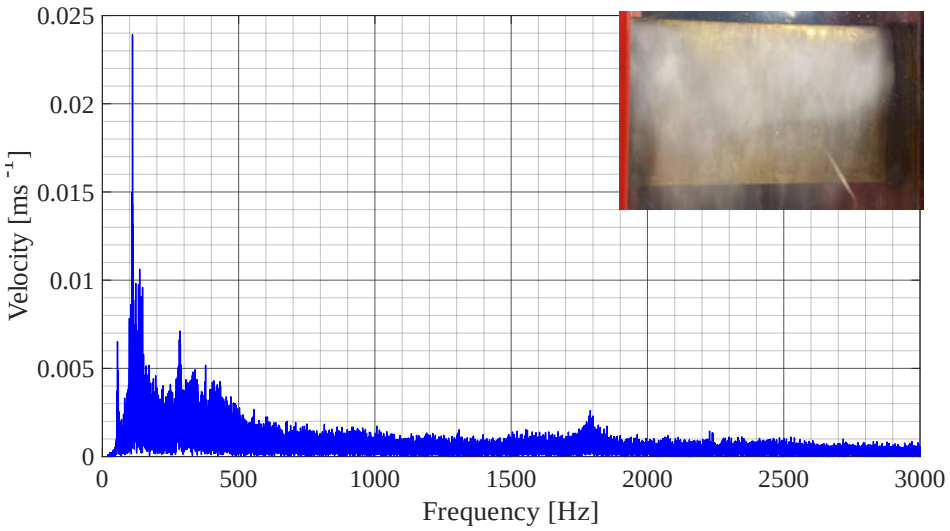

A 8.24 Flow induced vibrations at $v_{inlet} = 12.5\ ms^{-1}$ σ = 1.664 (LDV 1)

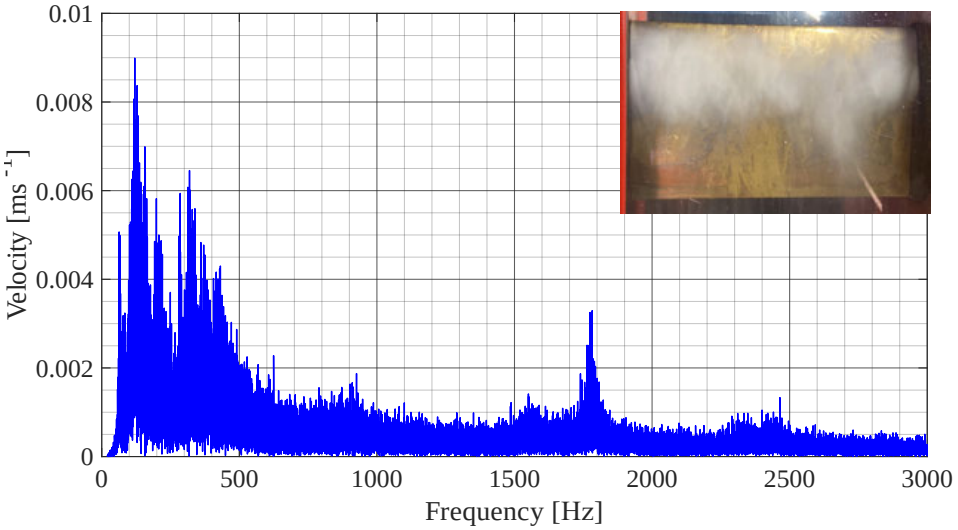

A 8.25 Flow induced vibrations at $v_{inlet} = 12.5\ ms^{-1}$ σ = 1.806 (LDV 1)

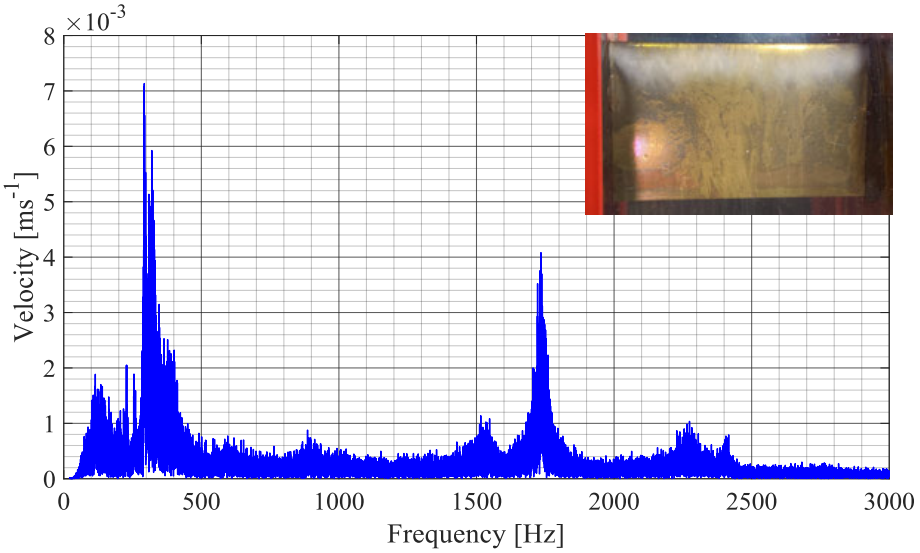

A 8.26 Flow induced vibrations at $v_{inlet} = 12.5\ ms^{-1}$ σ = 2.533 (LDV 1)

A.9 Forced Vibrations of Hydrofoil under Cavitation Conditions

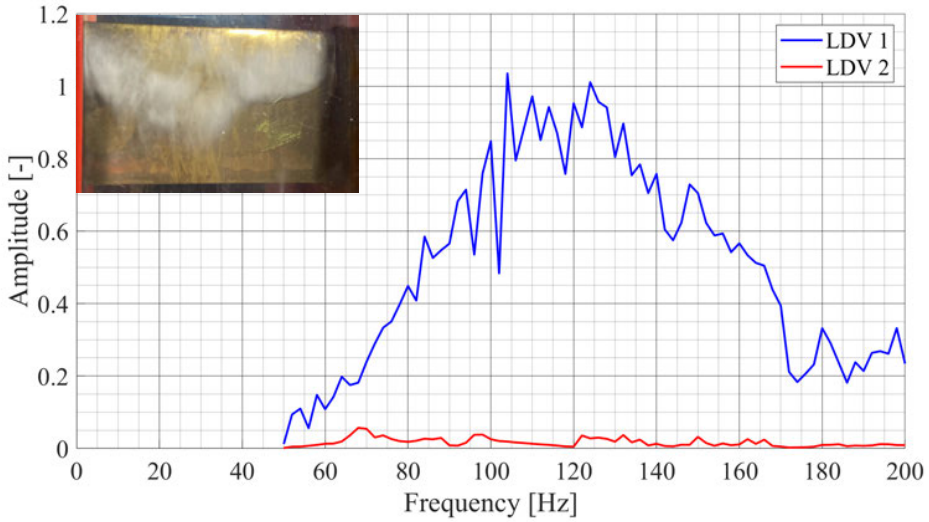

A 9.1 FRF under cavitation conditions at $v_{inlet} = 5.0\ ms^{-1}$ σ = 1.942 ($\alpha_{inc} = 5°$)

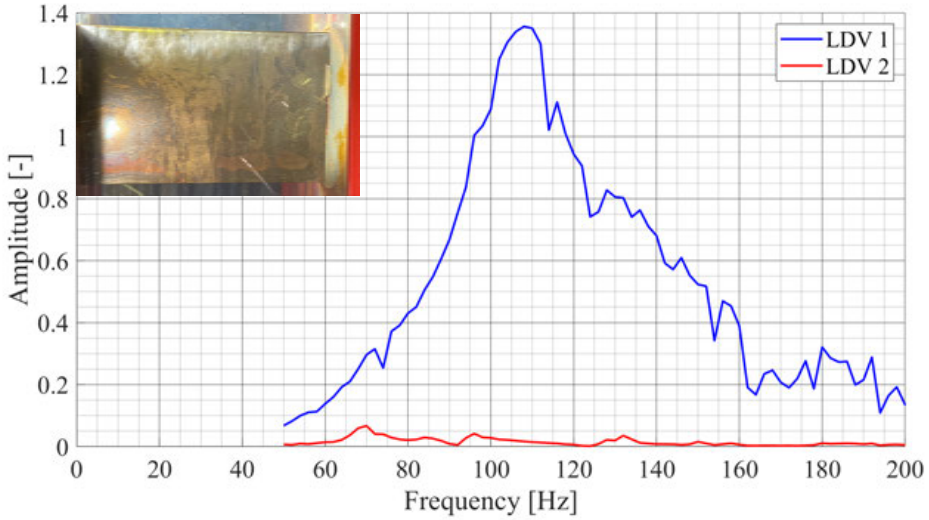

A 9.2 FRF under cavitation conditions at $v_{inlet} = 5.0\ ms^{-1}$ σ = 2.690 ($\alpha_{inc} = 5°$)

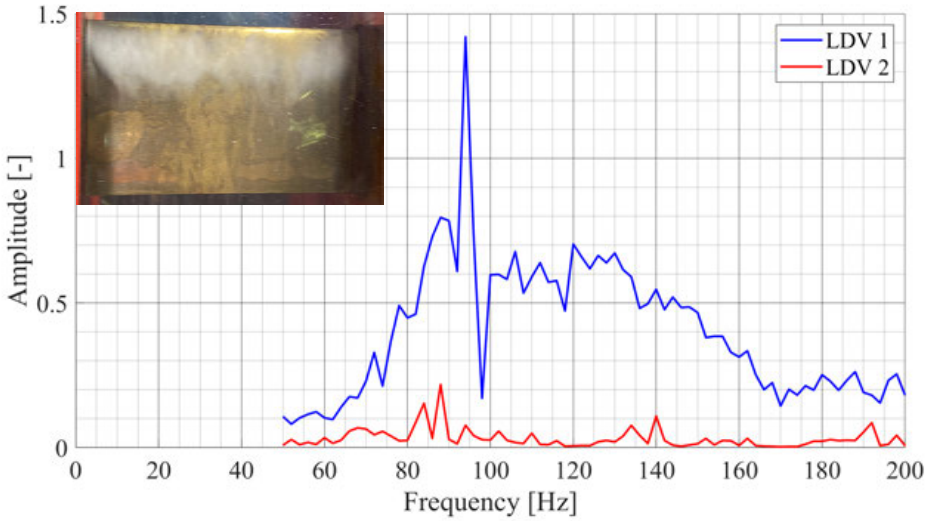

A 9.3 FRF under cavitation conditions at $v_{inlet} = 7.5\ ms^{-1}$ σ = 2.114 ($\alpha_{inc} = 5°$)

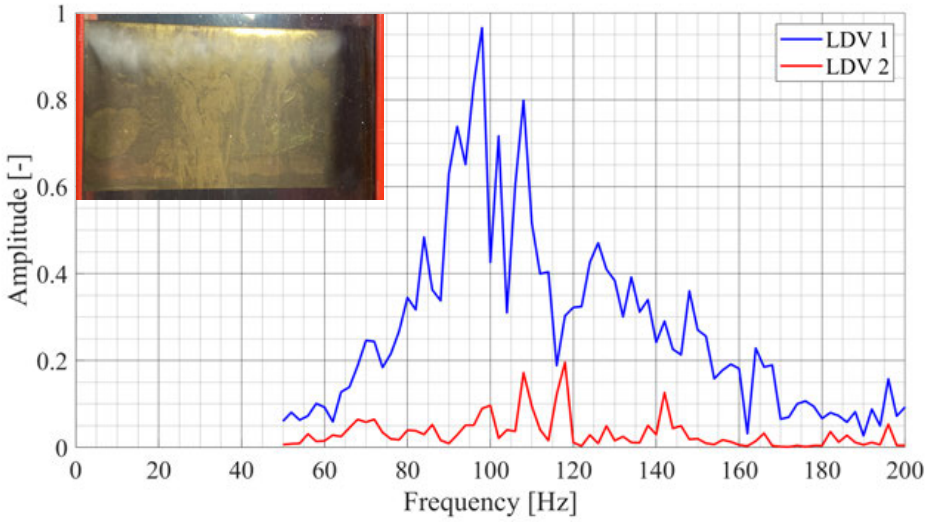

A 9.4 FRF under cavitation conditions at $v_{inlet} = 7.5\ ms^{-1}$ σ = 2.430 ($\alpha_{inc} = 5°$)

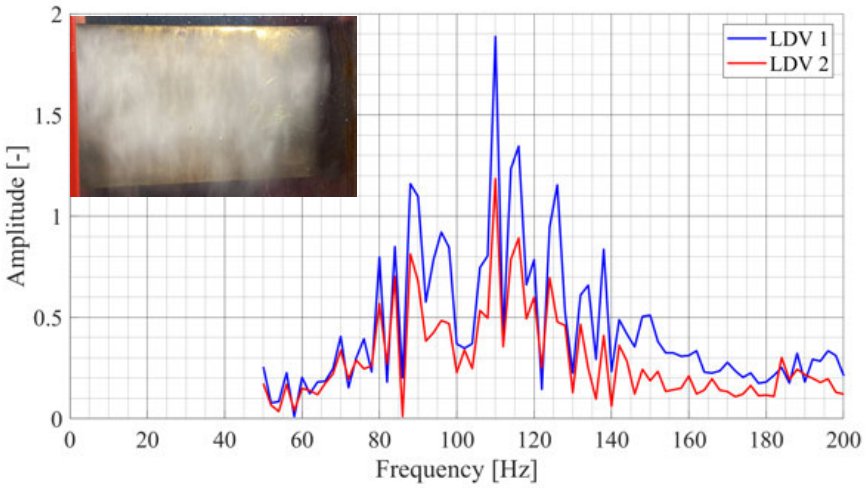

A 9.5 FRF under cavitation conditions at $v_{inlet} = 10.0\ ms^{-1}$ σ = 1.651 ($\alpha_{inc} = 5°$)

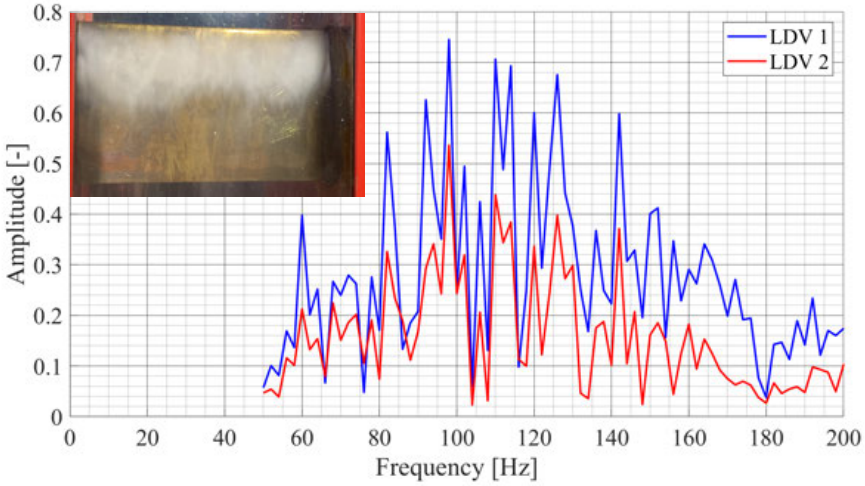

A 9.6 FRF under cavitation conditions at $v_{inlet} = 10.0\ ms^{-1}$ σ = 1.970 ($\alpha_{inc} = 5°$)

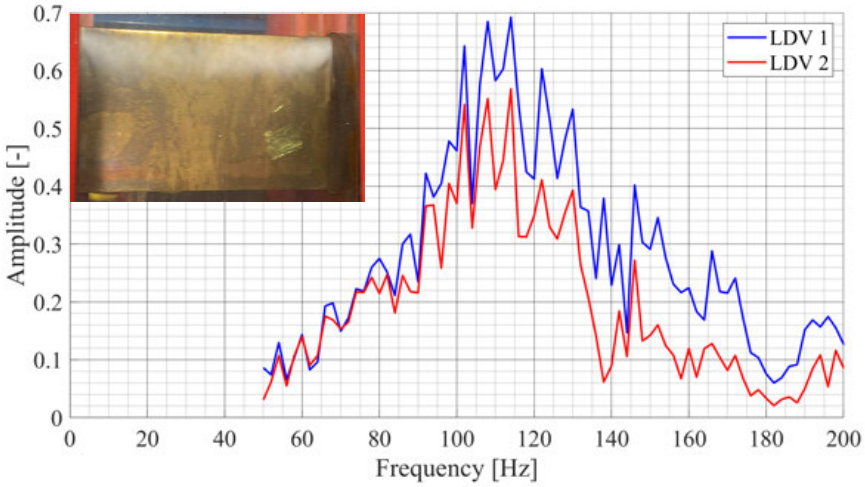

A 9.7 FRF under cavitation conditions at $v_{inlet} = 10.0\ ms^{-1}$ σ = 2.398 ($\alpha_{inc} = 5°$)

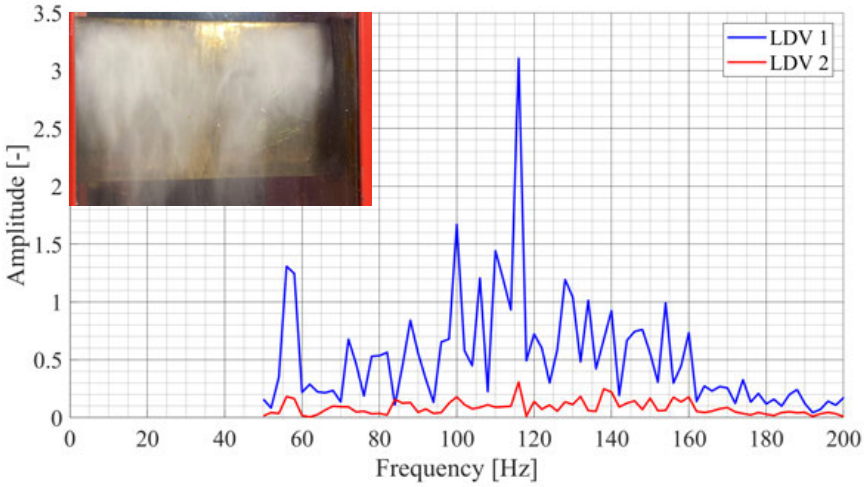

A 9.8 FRF under cavitation conditions at $v_{inlet} = 12.5\ ms^{-1}$ σ = 1.718 ($\alpha_{inc} = 5°$)

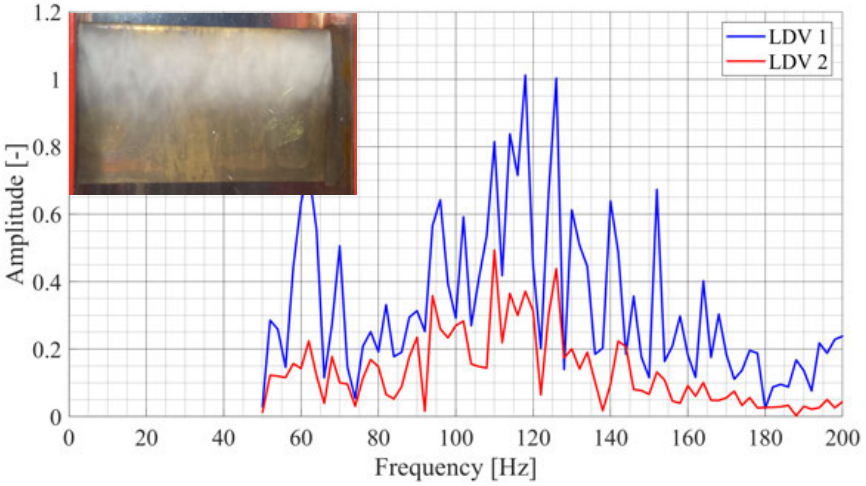

A 9.9 FRF under cavitation conditions at $v_{inlet} = 12.5\ ms^{-1}$ σ = 1.830 ($\alpha_{inc} = 5°$)

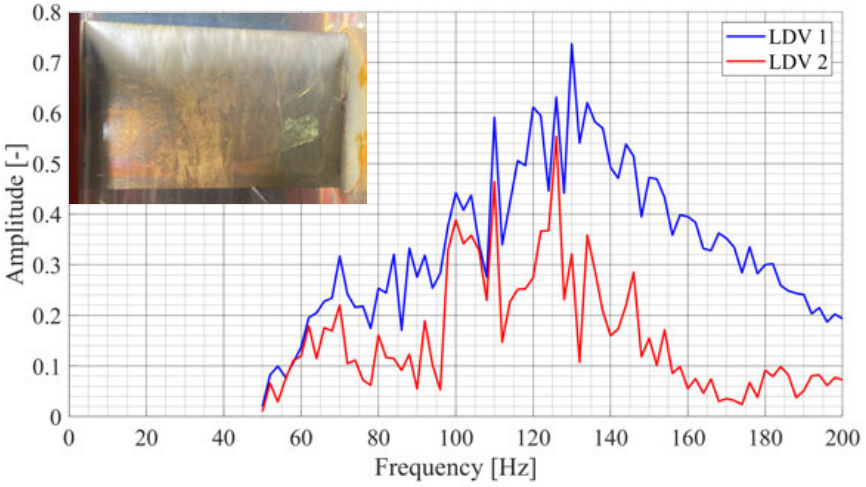

A 9.10 FRF under cavitation conditions at $v_{inlet} = 12.5\ ms^{-1}$ σ = 2.533 ($\alpha_{inc} = 5°$)

A.10 FRF Approximation by SDOF Response Fit Method (Cavitation)

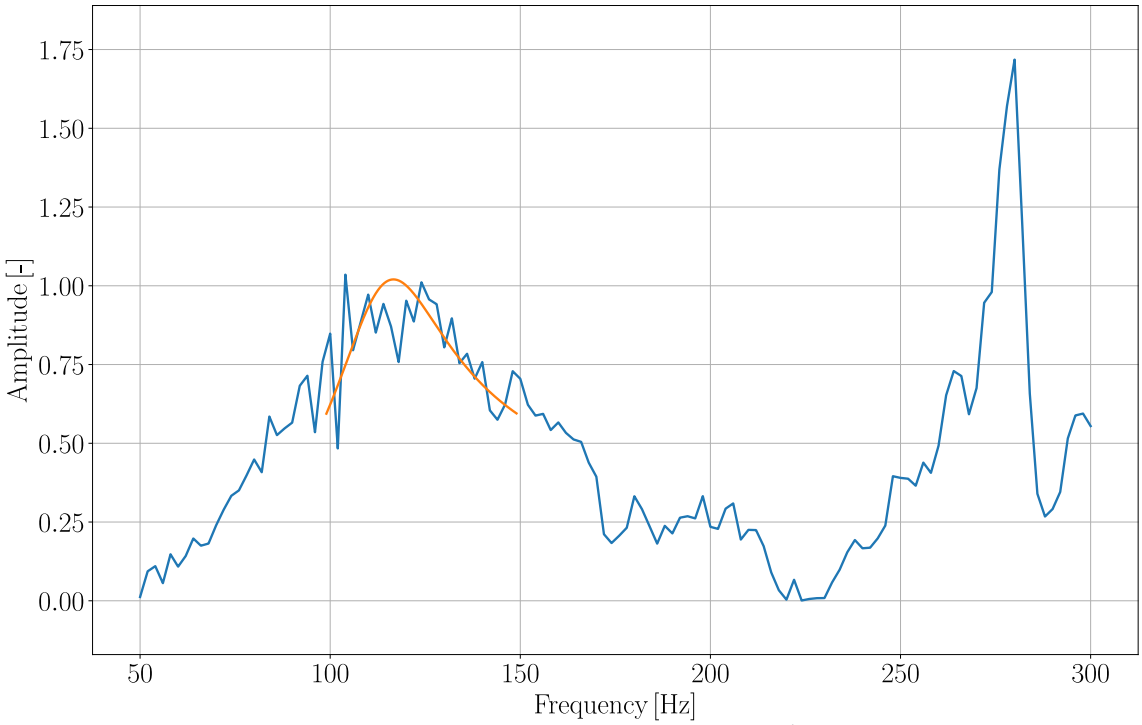

A 10.1 Approximated FRF from LDV 1 at $v_{inlet} = 5.0\, ms^{-1}$; $\sigma = 1.942$ ($\alpha_{inc} = 5°$)

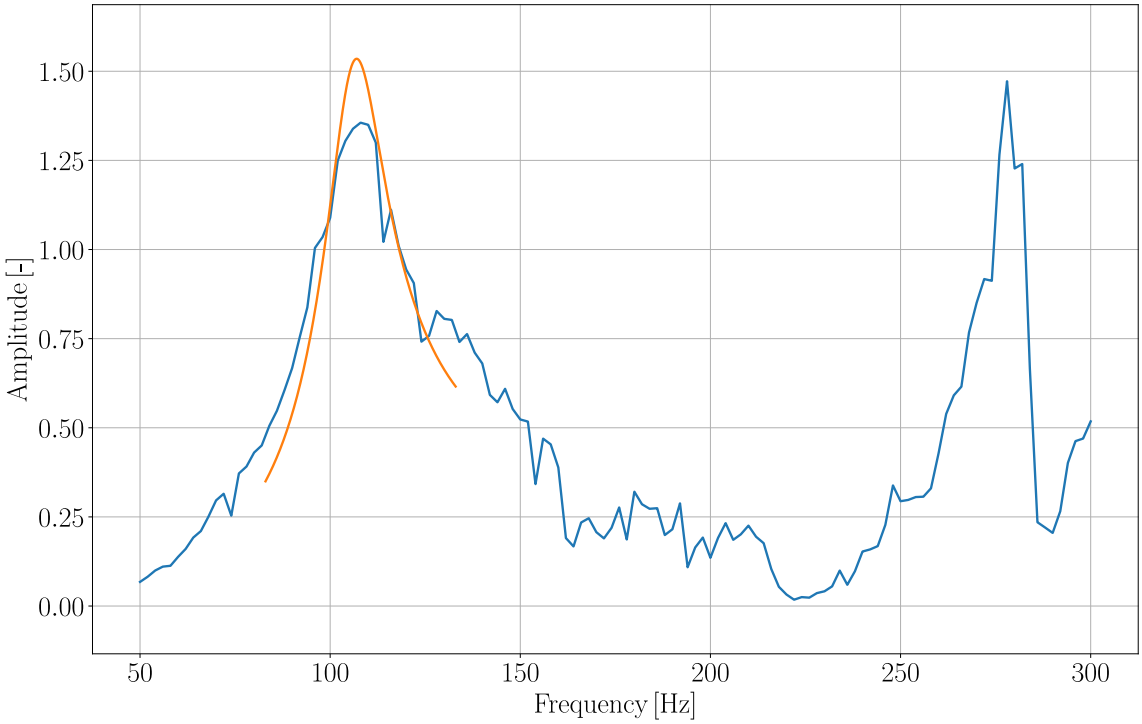

A 10.2 Approximated FRF from LDV 1 at $v_{inlet} = 5.0\, ms^{-1}$; $\sigma = 2.690$ ($\alpha_{inc} = 5°$)

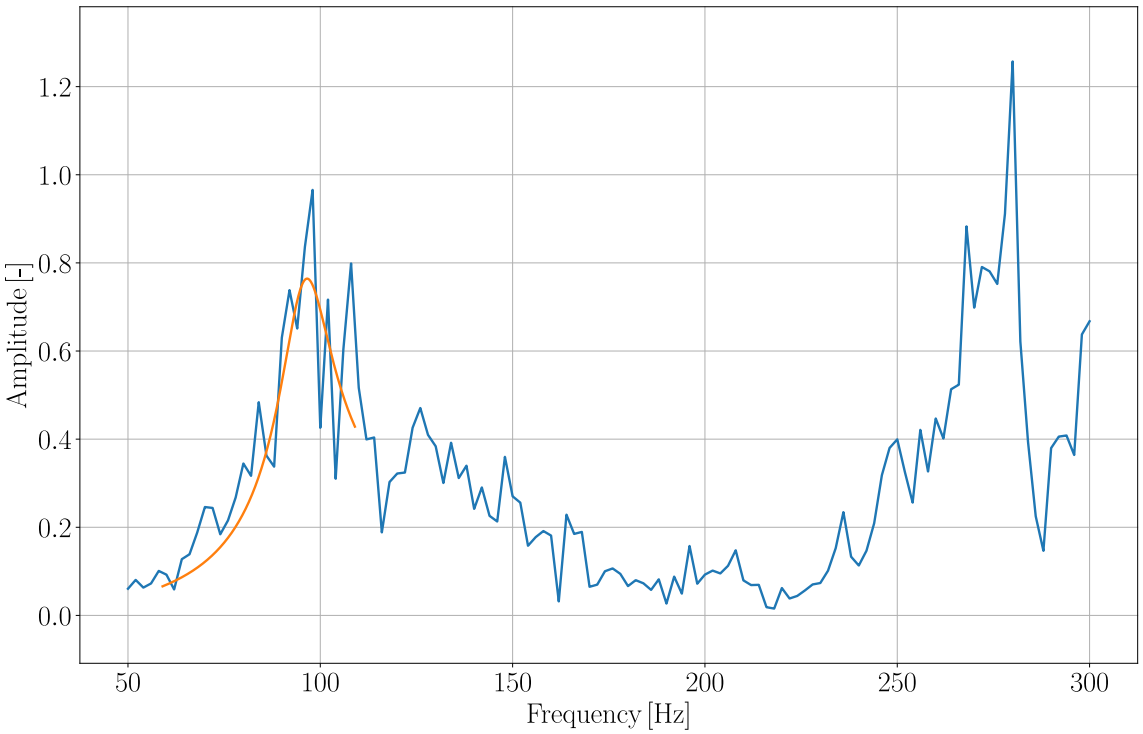

A 10.3 Approximated FRF from LDV 1 at $v_{inlet} = 7.5\ ms^{-1}$; $\sigma = 2.430$ ($\alpha_{inc} = 5°$)

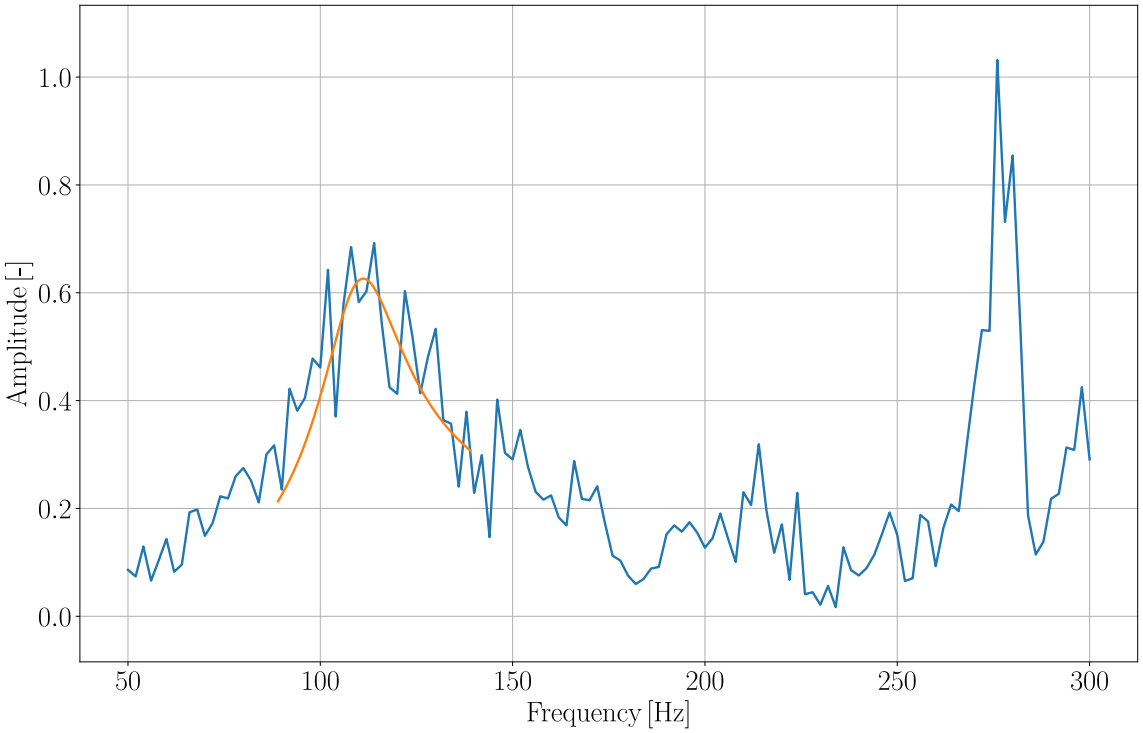

A 10.4 Approximated FRF from LDV 1 at $v_{inlet} = 10.0\ ms^{-1}$; $\sigma = 2.398$ ($\alpha_{inc} = 5°$)

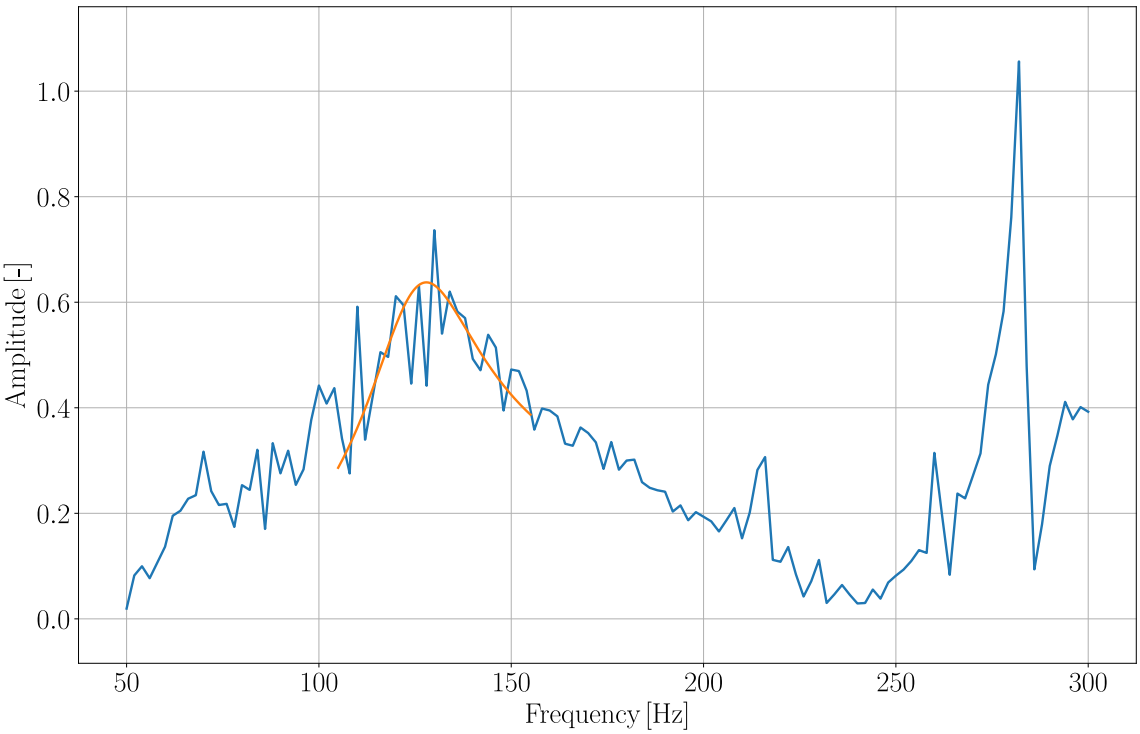

A 10.5 Approximated FRF from LDV 1 at $v_{inlet} = 12.5\ ms^{-1}$; $\sigma = 2.533$ ($\alpha_{inc} = 5°$)

A.11 Sensitivity of Natural Frequencies on Speed of Sound

c_{mix}	ρ_{mix}	f_1	f_2	f_3	f_4	f_5
$[ms^{-1}]$	$[kgm^{-3}]$	$[Hz]$	$[Hz]$	$[Hz]$	$[Hz]$	$[Hz]$
1450	0.17	105.2	344.1	409.0	472.5	901.0
1400	0.17	105.2	340.4	407.8	463.0	901.0
1300	0.17	105.2	330.7	404.4	447.4	900.9
1200	0.17	105.2	316.9	400.0	436.6	900.9
1150	0.17	105.2	308.4	397.6	433.0	900.9
1100	0.17	105.2	299.0	395.2	430.2	900.9
1050	0.17	105.2	288.7	393.0	428.1	900.9
1000	0.17	105.2	277.6	391.0	426.6	900.9
980	0.17	105.2	273.0	390.3	426.1	900.9
960	0.17	105.1	268.3	389.6	425.6	900.9
940	0.17	105.1	263.5	388.9	425.2	900.9
920	0.17	105.1	258.6	388.3	424.8	900.9
900	0.17	105.1	253.7	387.7	424.4	900.9
880	0.17	105.1	248.6	387.2	424.1	900.8
860	0.17	105.1	243.6	386.7	423.8	900.8
840	0.17	105.1	238.4	386.2	423.6	900.8
820	0.17	105.1	233.2	385.7	423.3	900.8
800	0.17	105.1	228.0	385.3	423.1	900.8
780	0.17	105.1	222.7	384.9	422.9	900.8
760	0.17	105.1	217.4	384.5	422.7	900.8
740	0.17	105.1	212.0	384.1	422.5	900.8
720	0.17	105.1	206.6	383.8	422.4	900.8
700	0.17	105.1	201.2	383.5	422.2	900.8
680	0.17	105.0	195.7	383.2	422.1	900.8
660	0.17	105.0	190.2	382.9	421.9	900.8
640	0.17	105.0	184.7	382.6	421.8	900.8
620	0.17	105.0	179.2	382.4	421.7	900.8
600	0.17	105.0	173.6	382.2	421.6	900.8
580	0.17	104.9	168.1	381.9	421.5	900.8
560	0.17	104.9	162.5	381.7	421.4	900.8
540	0.17	104.9	156.9	381.5	421.3	900.8
520	0.17	104.8	151.3	381.3	421.2	900.8
500	0.17	104.7	145.7	381.2	421.2	900.8
480	0.17	104.7	140.1	381.0	421.1	900.8
460	0.17	104.5	134.5	380.8	421.0	900.8
440	0.17	104.3	129.0	380.7	421.0	900.8
420	0.17	104.1	123.5	380.6	420.9	900.8
400	0.17	103.5	118.3	380.4	420.9	900.8
390	0.17	103.1	115.8	380.4	420.8	900.8
380	0.17	102.5	113.6	380.3	420.8	900.8
370	0.17	101.6	111.6	380.3	420.8	900.8

360	0.17	100.3	110.0	380.2	420.8	900.8
350	0.17	98.6	108.8	380.2	420.7	900.8
340	0.17	96.6	108.0	380.1	420.7	900.8
330	0.17	94.2	107.4	380.1	420.7	900.8
320	0.17	91.7	107.0	380.0	420.7	900.8
310	0.17	89.1	106.8	380.0	420.7	900.8
300	0.17	86.4	106.6	379.9	420.6	900.7
290	0.17	83.7	106.4	379.9	420.6	876.4
280	0.17	80.9	106.3	379.8	420.6	846.4
270	0.17	78.1	106.2	379.8	420.6	816.4
260	0.17	75.3	106.1	379.8	420.6	786.2
250	0.17	72.4	106.1	379.7	420.6	756.1
240	0.17	69.6	106.0	379.7	420.5	726.0
230	0.17	66.7	106.0	379.7	420.5	695.8
220	0.17	63.8	105.9	379.6	420.5	665.6
210	0.17	61.0	105.9	379.6	420.5	635.4
200	0.17	58.1	105.9	379.6	420.5	605.2
190	0.17	55.2	105.8	379.5	420.5	575.0
180	0.17	52.3	105.8	379.5	420.5	544.8
170	0.17	49.4	105.8	379.5	420.4	514.5
160	0.17	46.5	105.8	379.5	420.4	484.3
150	0.17	43.6	105.8	379.4	420.4	454.1
140	0.17	40.7	105.7	379.4	419.6	424.7
130	0.17	37.8	105.7	379.3	393.4	420.6
120	0.17	34.9	105.7	363.1	379.5	420.5
110	0.17	32.0	105.7	332.9	379.4	420.5
100	0.17	29.1	105.7	302.7	379.4	420.5
90	0.17	26.2	105.7	272.4	379.3	420.4
80	0.17	23.3	105.7	242.2	379.3	420.4
70	0.17	20.4	105.7	211.9	379.3	420.3
60	0.17	17.5	105.7	181.6	379.0	402.1
50	0.17	14.6	105.7	151.4	334.8	379.5
40	0.17	11.7	105.7	121.1	267.9	379.4
30	0.17	8.7	90.8	105.7	201.0	296.6
20	0.17	5.8	60.5	105.7	134.0	197.7
10	0.17	2.9	30.3	67.0	98.9	105.7

A.12 Mode Shapes of Hydrofoil under Cavitation Conditions

- **Mode shapes for parameters:** $L_{cloud} = 25\ mm; H_{cloud} = 0.5\ mm; \alpha_{vap} = 0.5$

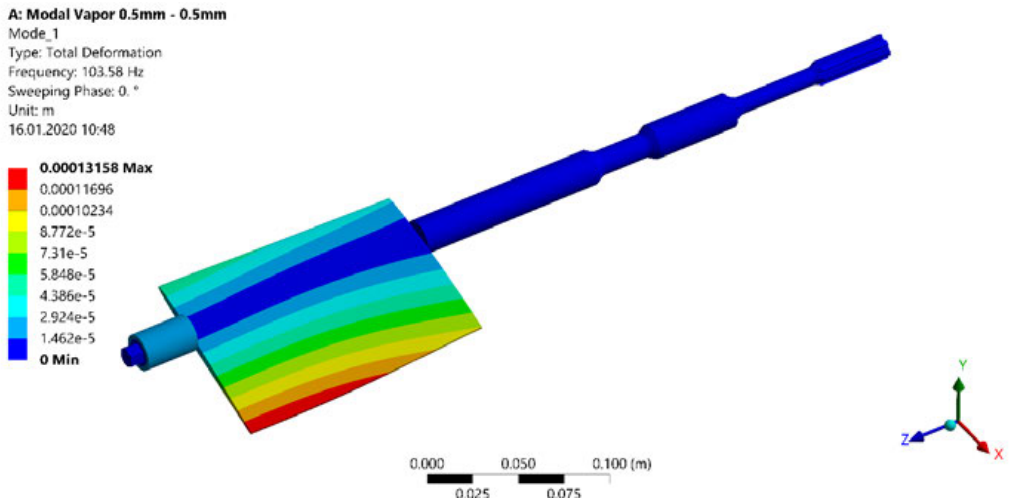

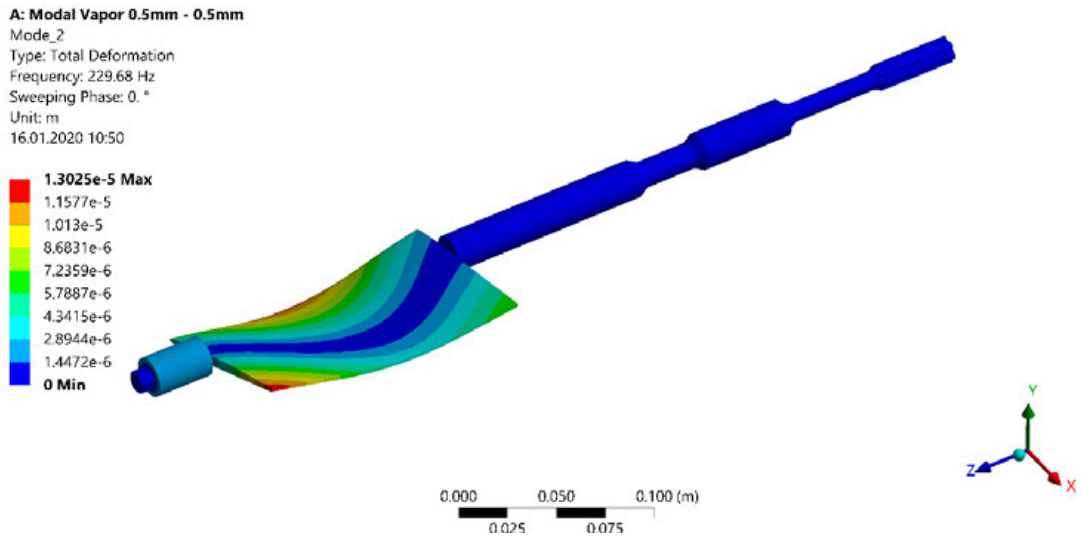

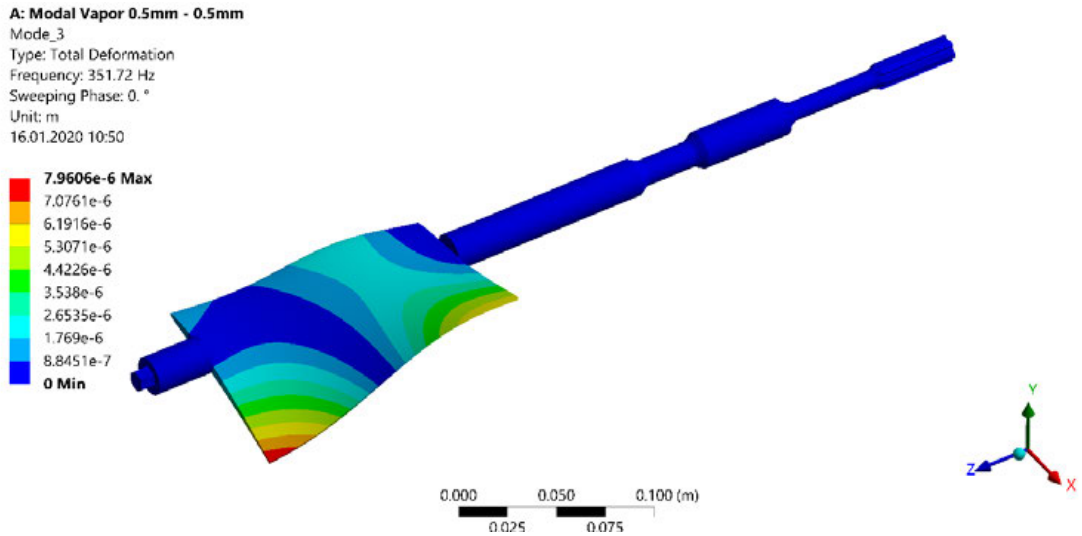

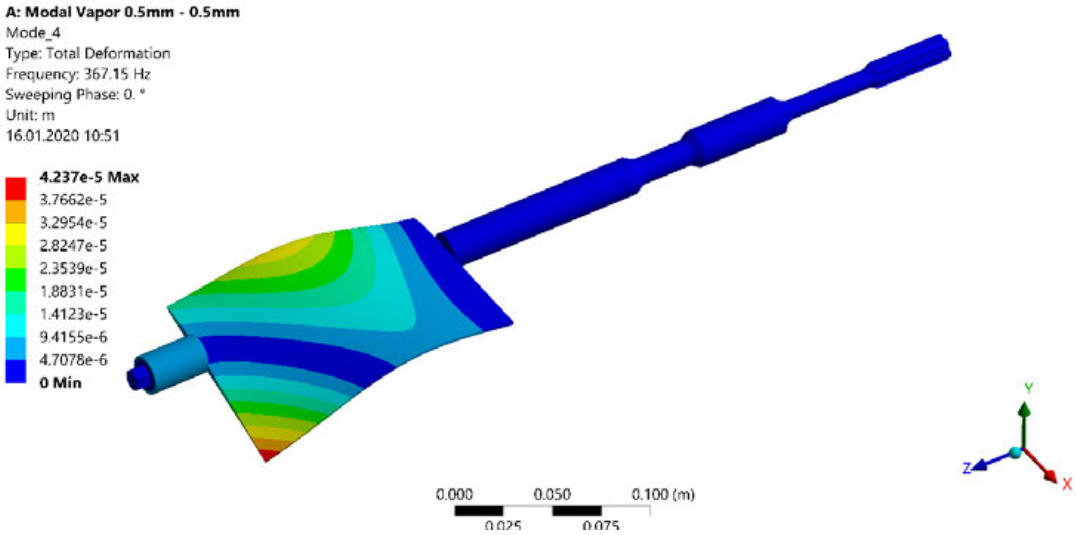
A: Modal Vapor 0.5mm - 0.5mm
Mode_4
Type: Total Deformation
Frequency: 367.15 Hz
Sweeping Phase: 0. °
Unit: m
16.01.2020 10:51
4.237e-5 Max
3.7662e-5
3.2954e-5
2.8247e-5
2.3539e-5
1.8831e-5
1.4123e-5
9.4155e-6
4.7078e-6
0 Min
0.000
0.050
0.100 (m)
0.025
0.075
Y
Z
X

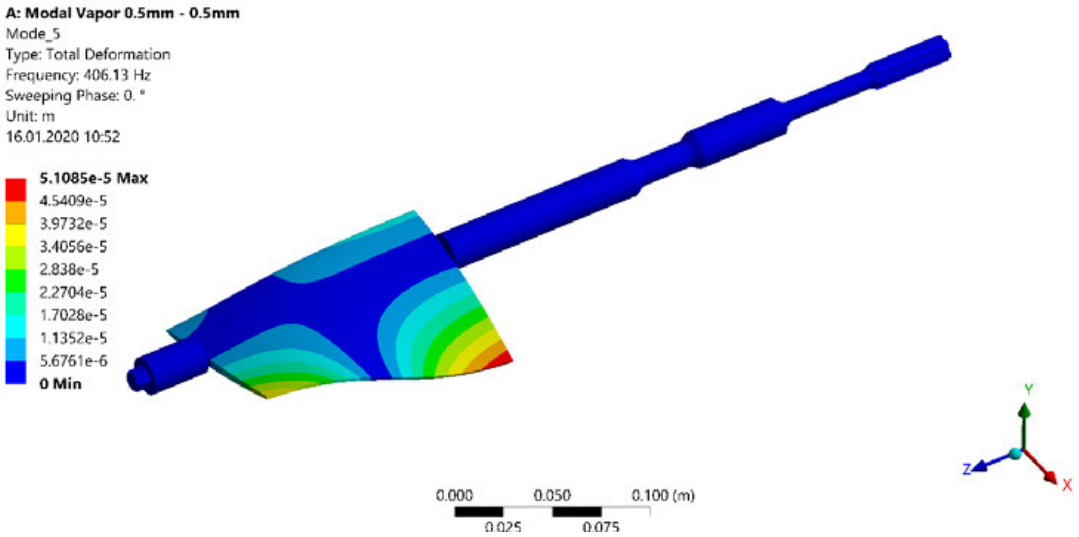
A: Modal Vapor 0.5mm - 0.5mm
Mode_5
Type: Total Deformation
Frequency: 406.13 Hz
Sweeping Phase: 0. °
Unit: m
16.01.2020 10:52
5.1085e-5 Max
4.5409e-5
3.9732e-5
3.4056e-5
2.838e-5
2.2704e-5
1.7028e-5
1.1352e-5
5.6761e-6
0 Min
0.000
0.050
0.100 (m)
0.025
0.075
Y
Z
X

- **Mode shapes for parameters:** $L_{cloud} = 25\ mm; H_{cloud} = 0.5\ mm; \alpha_{vap} = 1.0$

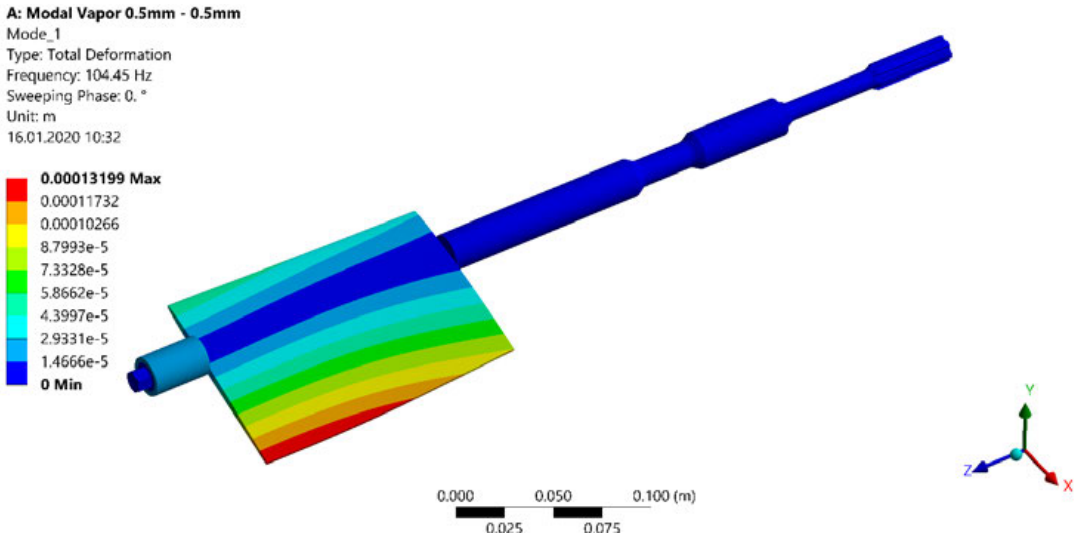

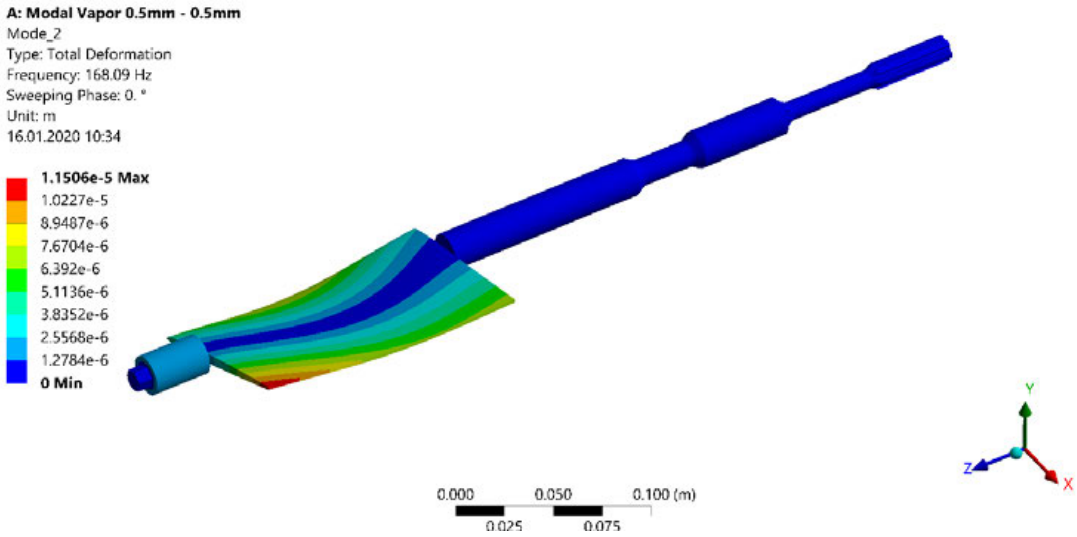

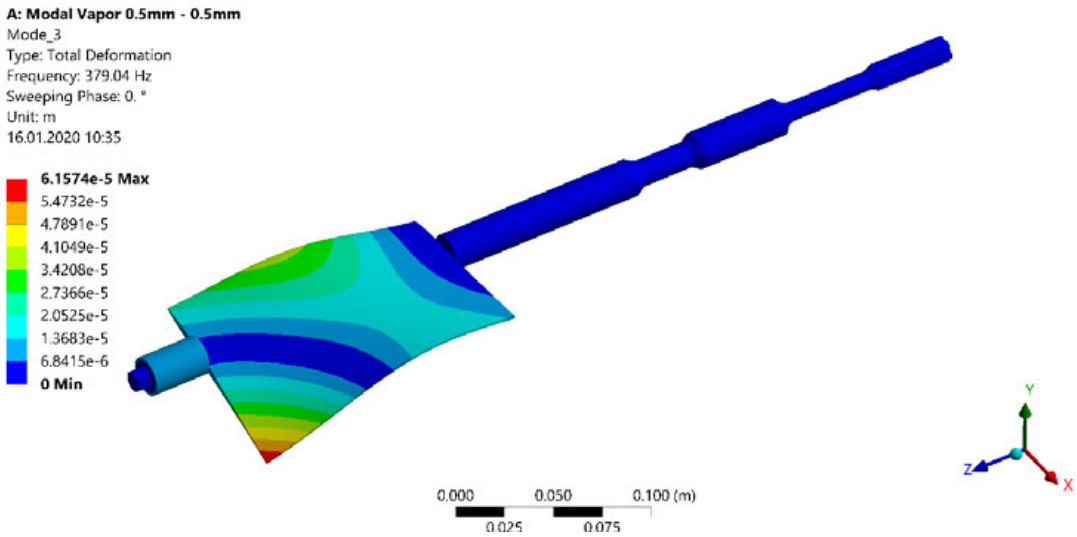

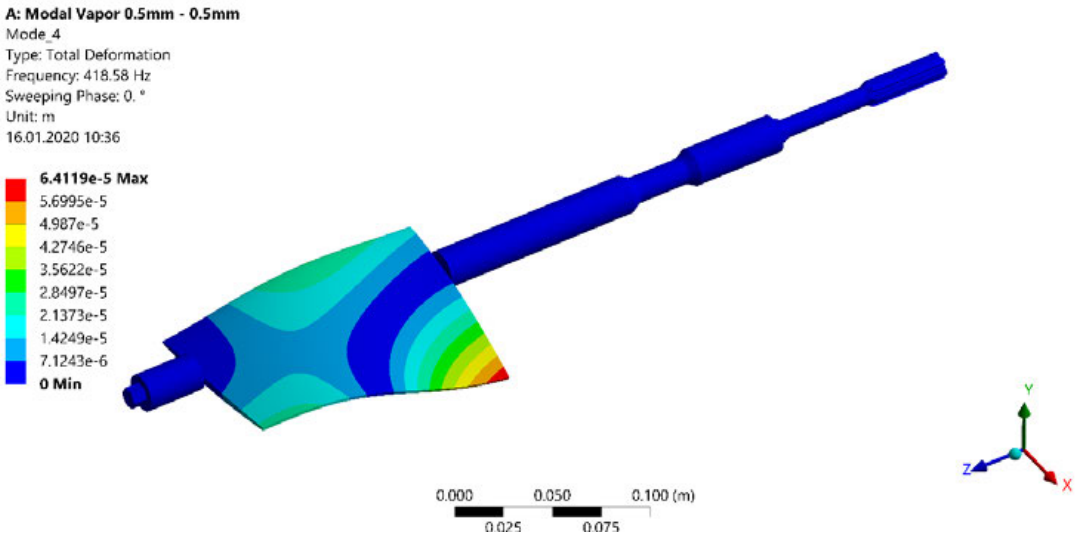
A: Modal Vapor 0.5mm - 0.5mm
Mode_4
Type: Total Deformation
Frequency: 418.58 Hz
Sweeping Phase: 0. °
Unit: m
16.01.2020 10:36
6.4119e-5 Max
5.6995e-5
4.987e-5
4.2746e-5
3.5622e-5
2.8497e-5
2.1373e-5
1.4249e-5
7.1243e-6
0 Min
0.000
0.050
0.100 (m)
0.025
0.075
Y
Z
X

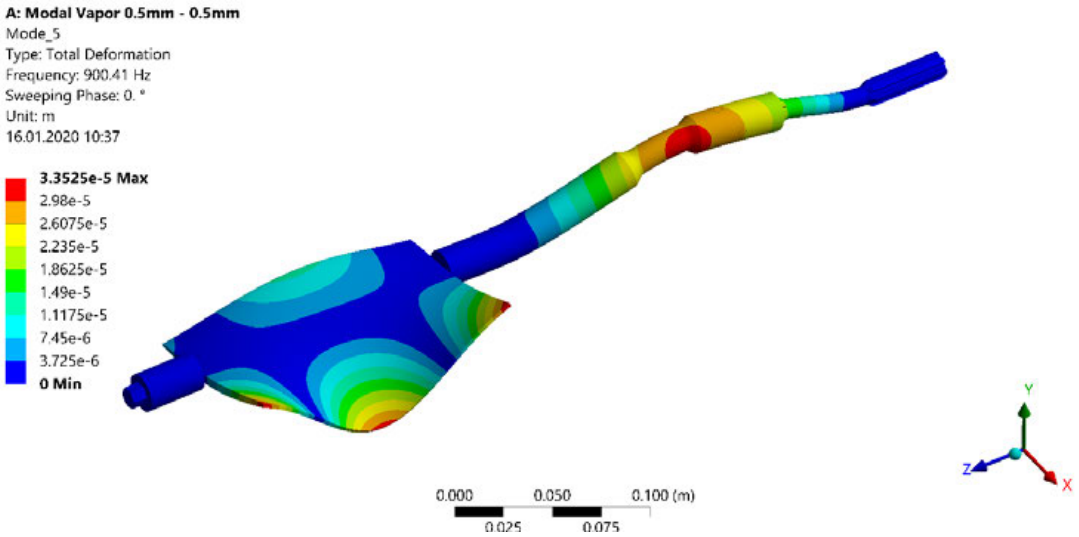
A: Modal Vapor 0.5mm - 0.5mm
Mode_5
Type: Total Deformation
Frequency: 900.41 Hz
Sweeping Phase: 0. °
Unit: m
16.01.2020 10:37
3.3525e-5 Max
2.98e-5
2.6075e-5
2.235e-5
1.8625e-5
1.49e-5
1.1175e-5
7.45e-6
3.725e-6
0 Min
0.000
0.050
0.100 (m)
0.025
0.075
Y
Z
X

- **Mode shapes for parameters:** $L_{cloud} = 25\ mm; H_{cloud} = 2.0\ mm; \alpha_{vap} = 0.5$

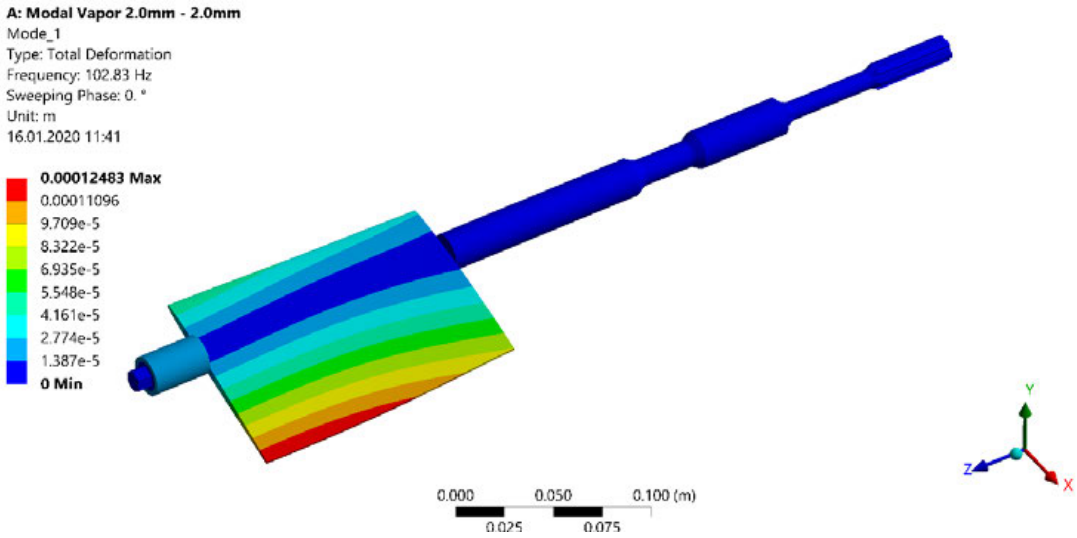

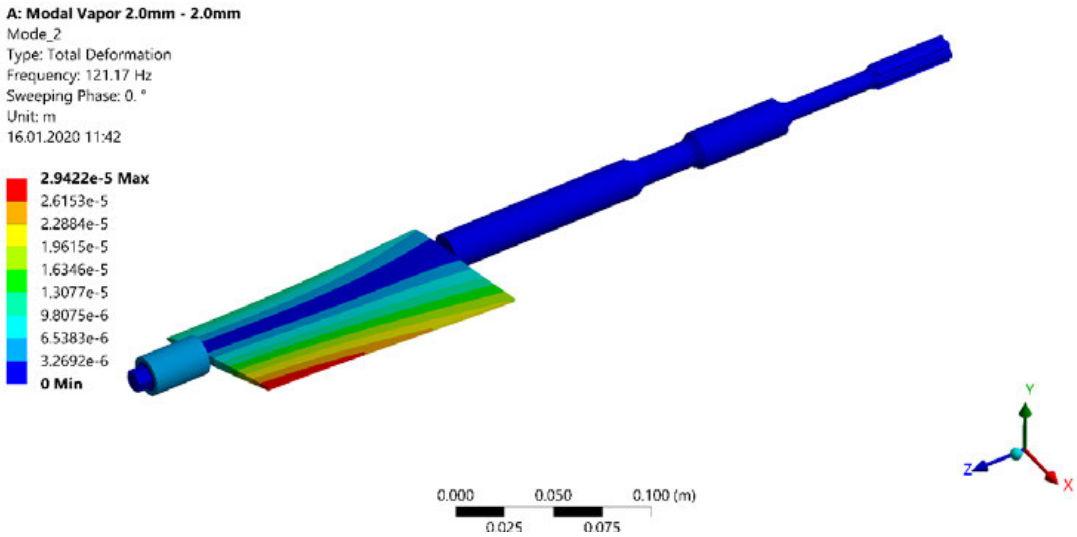

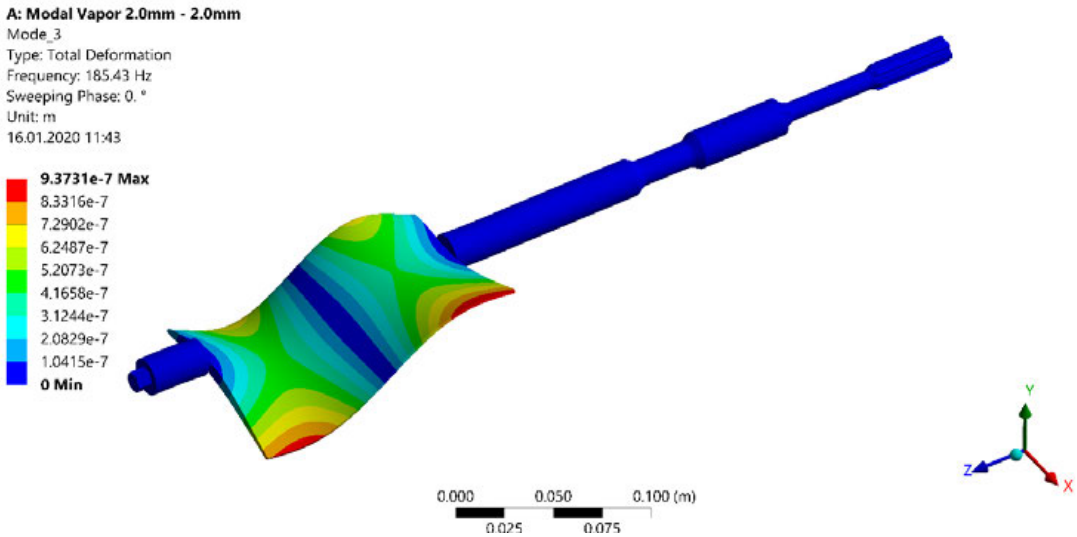

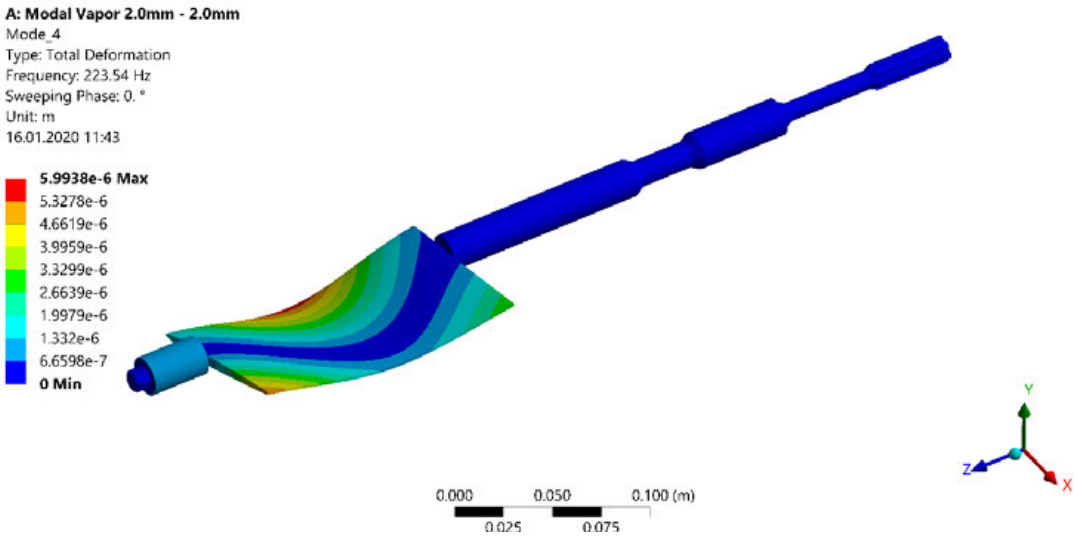
A: Modal Vapor 2.0mm - 2.0mm
Mode_4
Type: Total Deformation
Frequency: 223.54 Hz
Sweeping Phase: 0. °
Unit: m
16.01.2020 11:43
5.9938e-6 Max
5.3278e-6
4.6619e-6
3.9959e-6
3.3299e-6
2.6639e-6
1.9979e-6
1.332e-6
6.6598e-7
0 Min
0.000
0.050
0.100 (m)
0.025
0.075
Y
Z
X

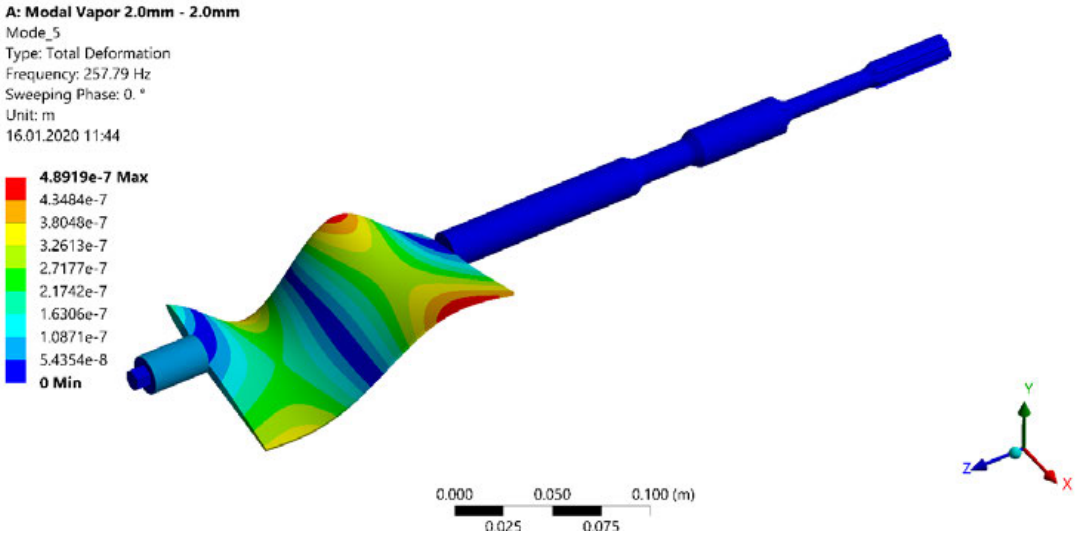
A: Modal Vapor 2.0mm - 2.0mm
Mode_5
Type: Total Deformation
Frequency: 257.79 Hz
Sweeping Phase: 0. °
Unit: m
16.01.2020 11:44
4.8919e-7 Max
4.3484e-7
3.8048e-7
3.2613e-7
2.7177e-7
2.1742e-7
1.6306e-7
1.0871e-7
5.4354e-8
0 Min
0.000
0.050
0.100 (m)
0.025
0.075
Y
Z
X

- **Mode shapes for parameters:** $L_{cloud} = 25\ mm; H_{cloud} = 2.0\ mm; \alpha_{vap} = 1.0$

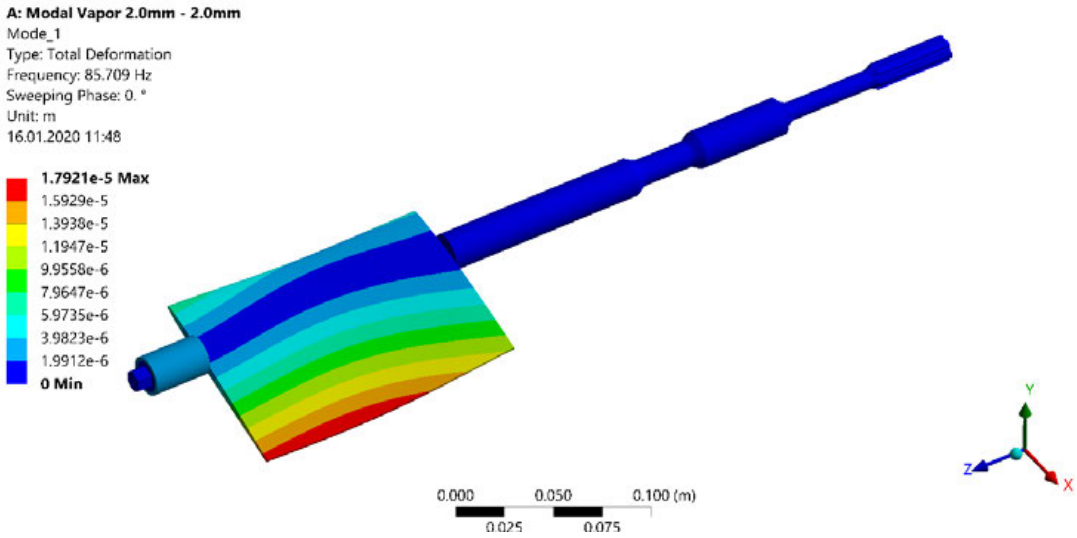

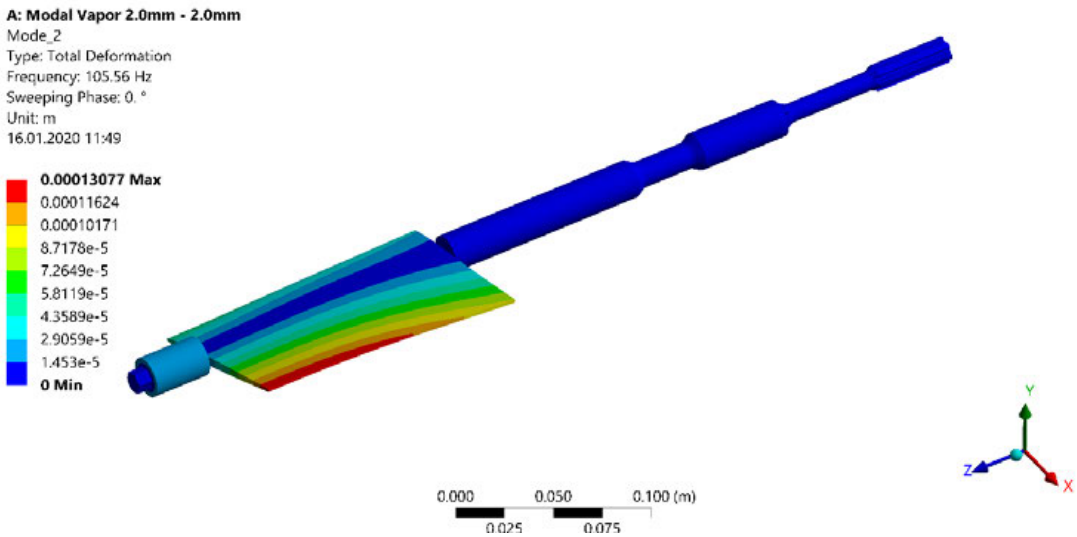

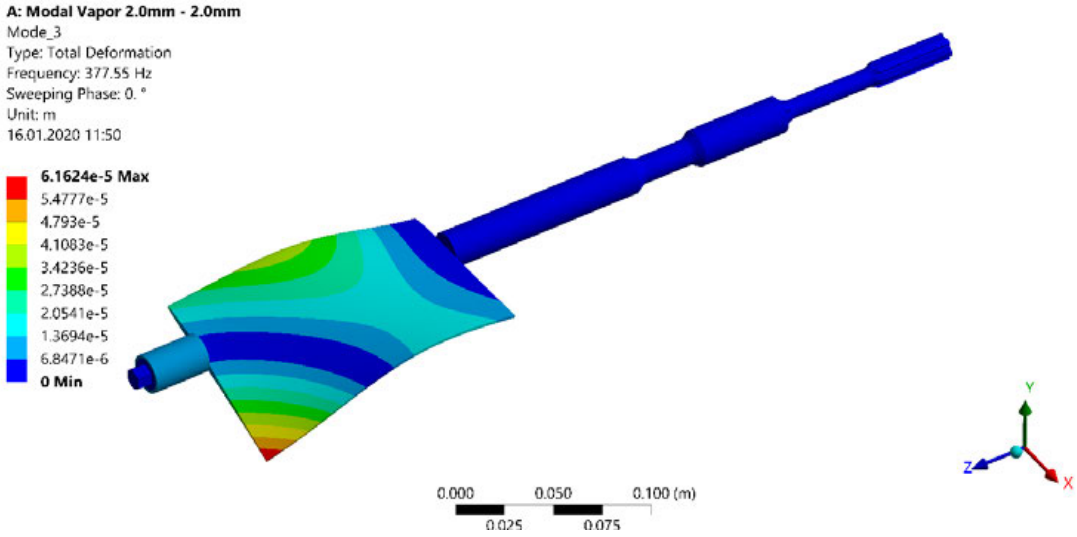

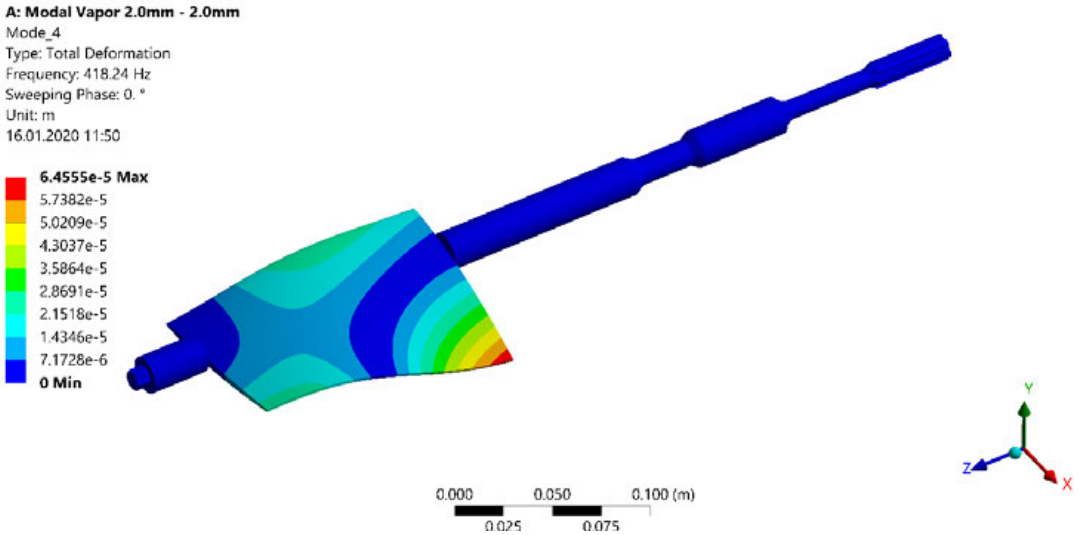
A: Modal Vapor 2.0mm - 2.0mm
Mode_4
Type: Total Deformation
Frequency: 418.24 Hz
Sweeping Phase: 0. °
Unit: m
16.01.2020 11:50
6.4555e-5 Max
5.7382e-5
5.0209e-5
4.3037e-5
3.5864e-5
2.8691e-5
2.1518e-5
1.4346e-5
7.1728e-6
0 Min
0.000
0.050
0.100 (m)
0.025
0.075
Y
Z
X

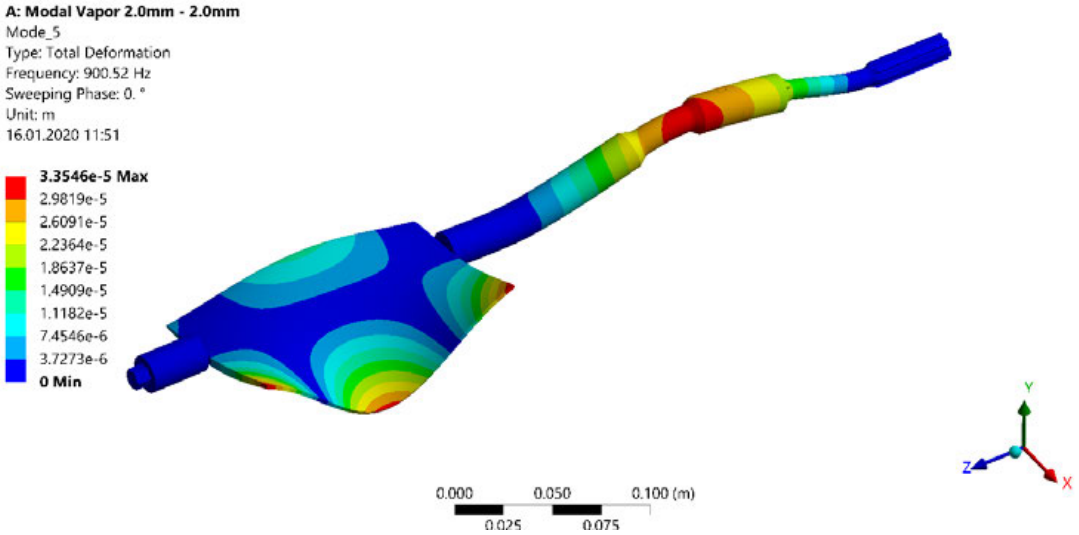
A: Modal Vapor 2.0mm - 2.0mm
Mode_5
Type: Total Deformation
Frequency: 900.52 Hz
Sweeping Phase: 0. °
Unit: m
16.01.2020 11:51
3.3546e-5 Max
2.9819e-5
2.6091e-5
2.2364e-5
1.8637e-5
1.4909e-5
1.1182e-5
7.4546e-6
3.7273e-6
0 Min
0.000
0.050
0.100 (m)
0.025
0.075
Y
Z
X

- **Mode shapes for parameters:** $L_{cloud} = 60\ mm; H_{cloud} = 0.5\ mm; \alpha_{vap} = 0.5$

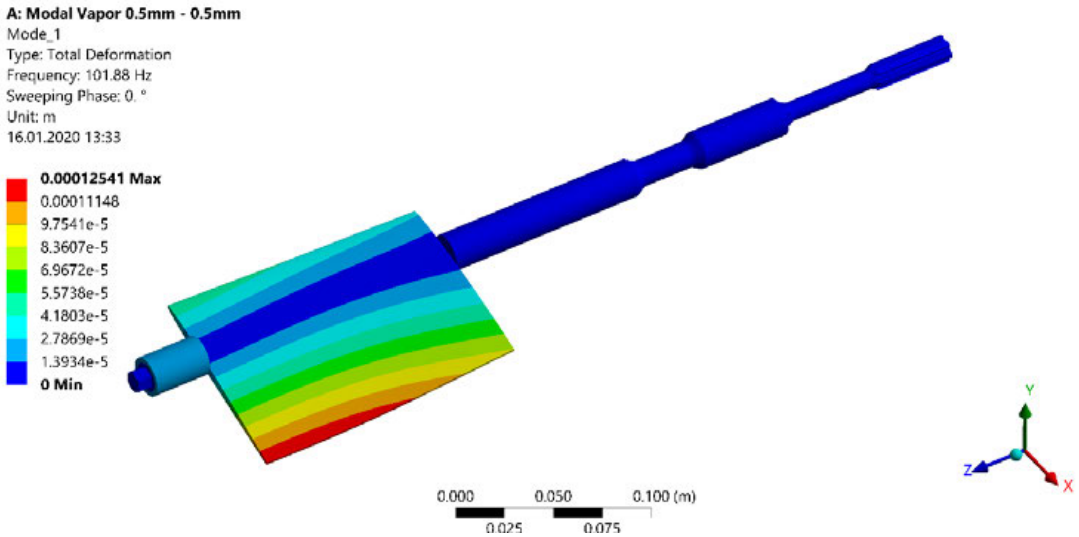

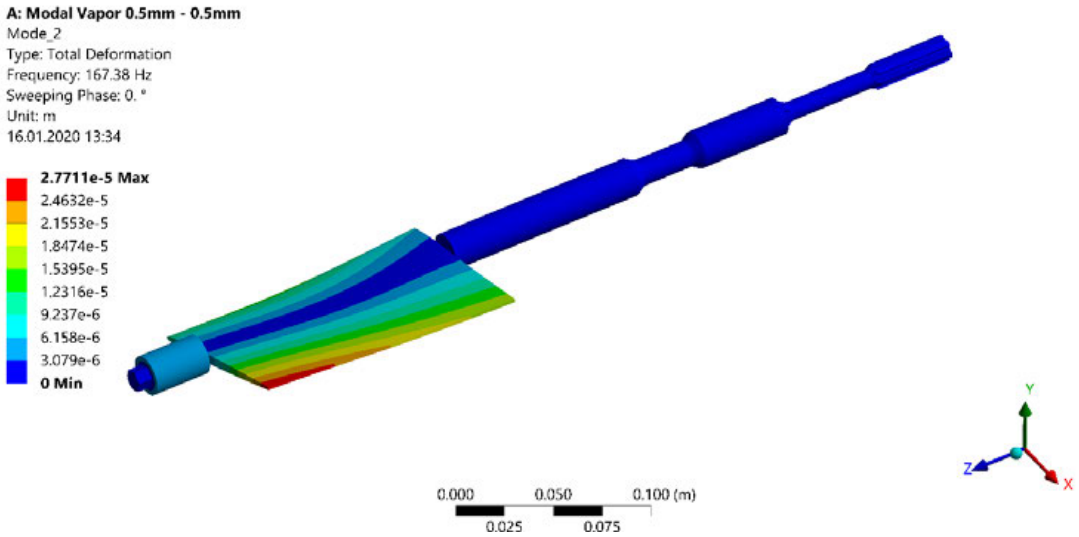

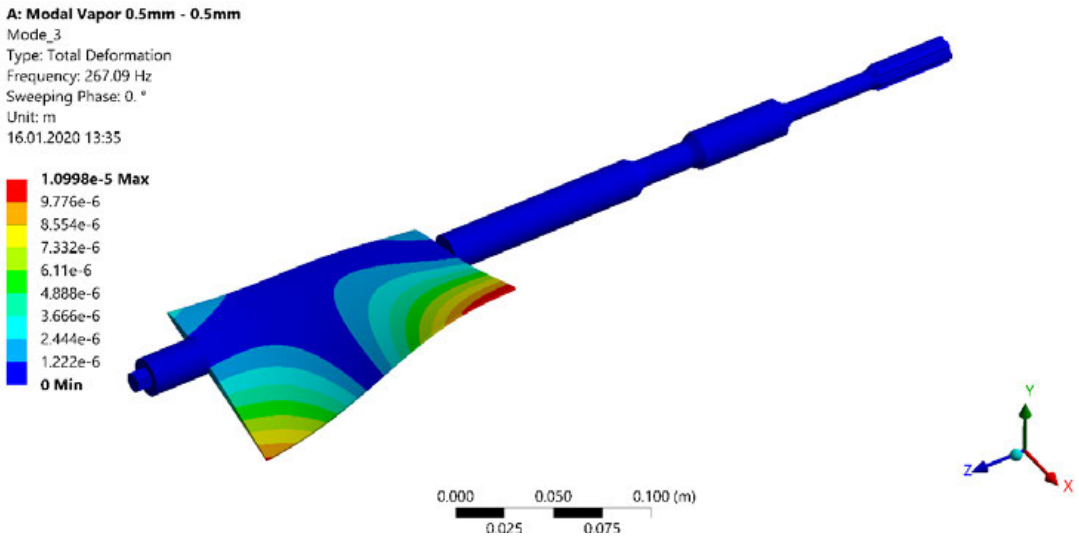

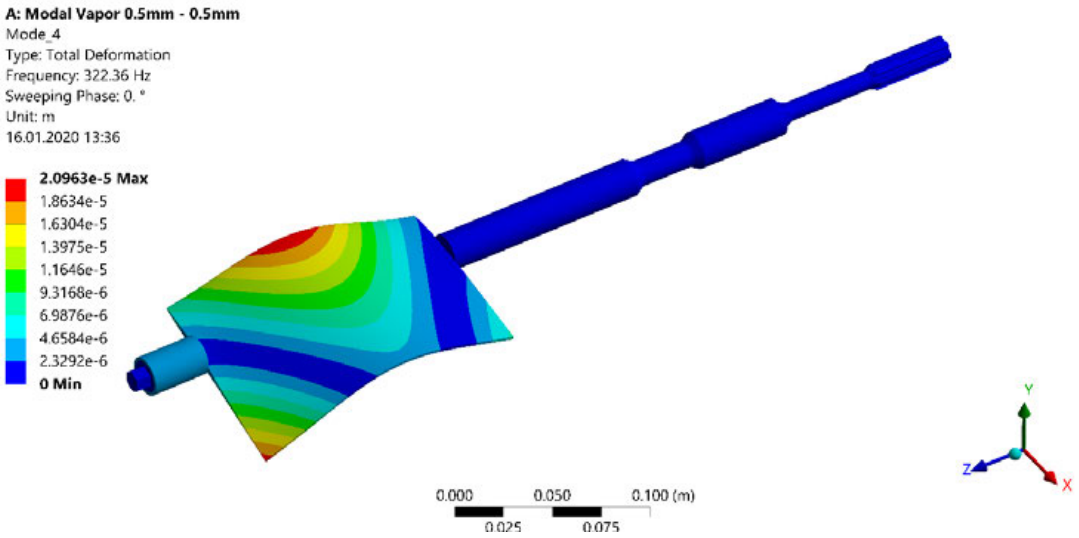
A: Modal Vapor 0.5mm - 0.5mm
Mode_4
Type: Total Deformation
Frequency: 322.36 Hz
Sweeping Phase: 0. °
Unit: m
16.01.2020 13:36
2.0963e-5 Max
1.8634e-5
1.6304e-5
1.3975e-5
1.1646e-5
9.3168e-6
6.9876e-6
4.6584e-6
2.3292e-6
0 Min
0.000
0.050
0.100 (m)
0.025
0.075
Y
Z
X

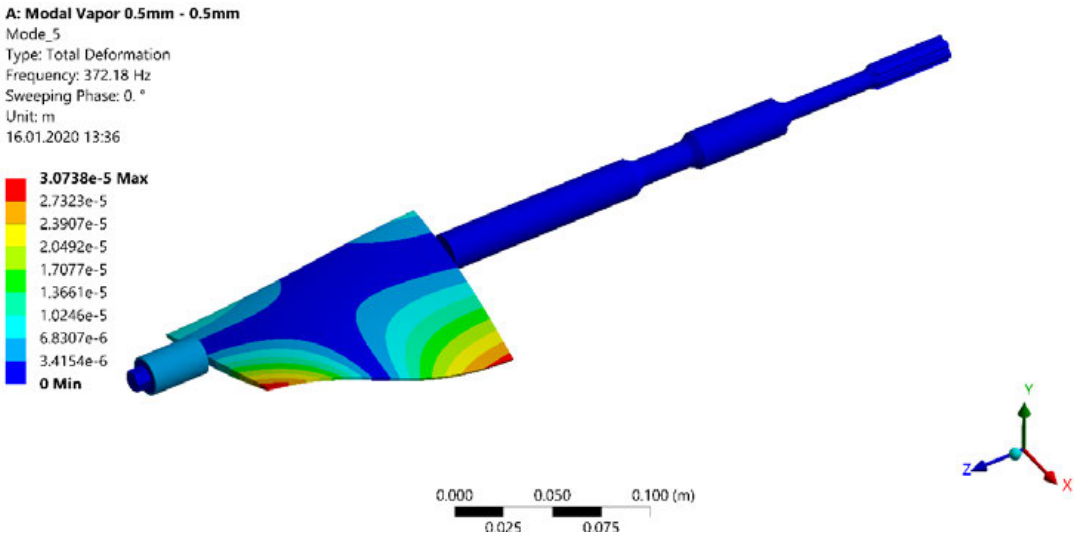
A: Modal Vapor 0.5mm - 0.5mm
Mode_5
Type: Total Deformation
Frequency: 372.18 Hz
Sweeping Phase: 0. °
Unit: m
16.01.2020 13:36
3.0738e-5 Max
2.7323e-5
2.3907e-5
2.0492e-5
1.7077e-5
1.3661e-5
1.0246e-5
6.8307e-6
3.4154e-6
0 Min
0.000
0.050
0.100 (m)
0.025
0.075
Y
Z
X

- **Mode shapes for parameters:** $L_{cloud} = 60\ mm; H_{cloud} = 0.5\ mm; \alpha_{vap} = 1.0$

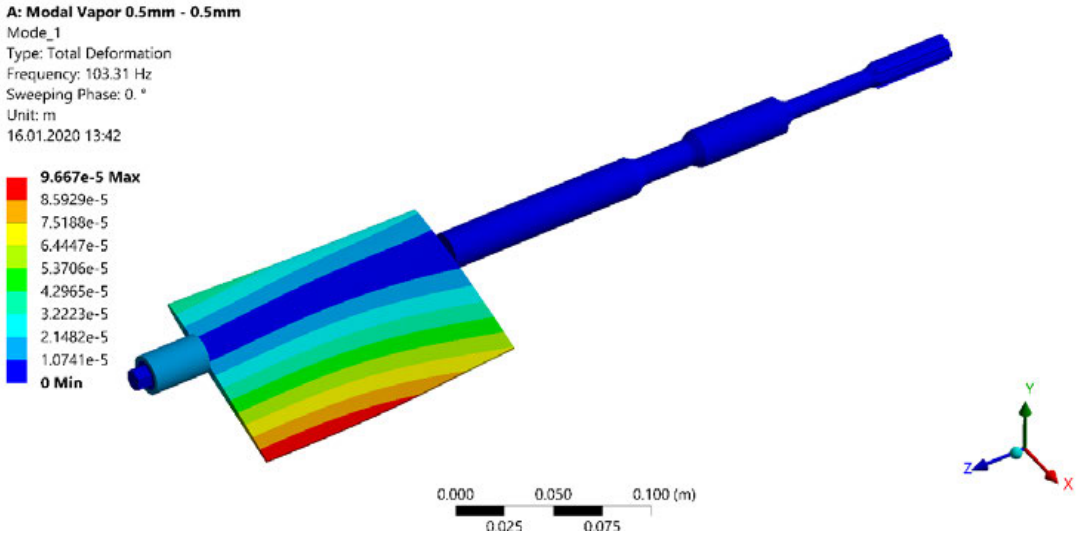

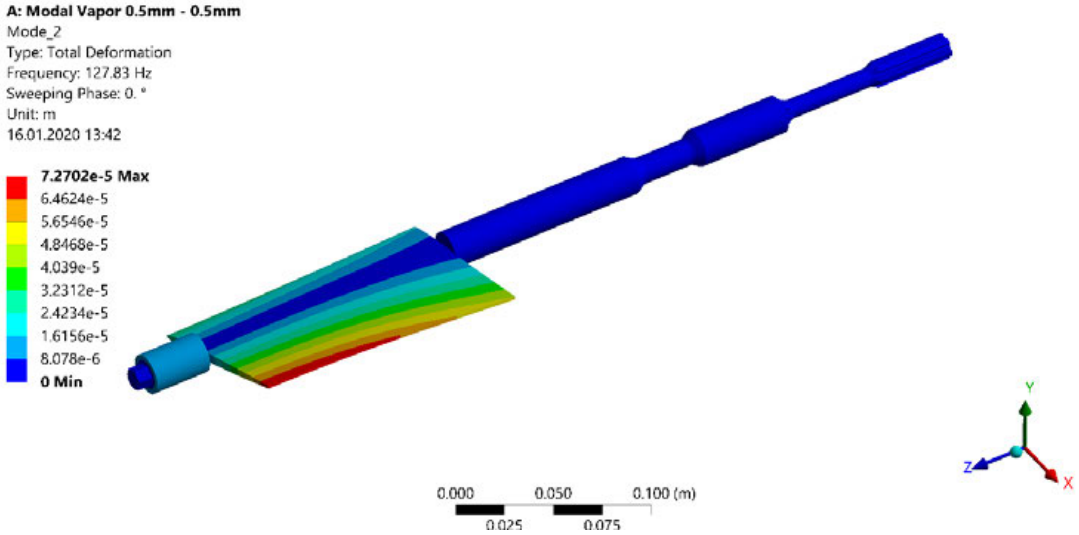

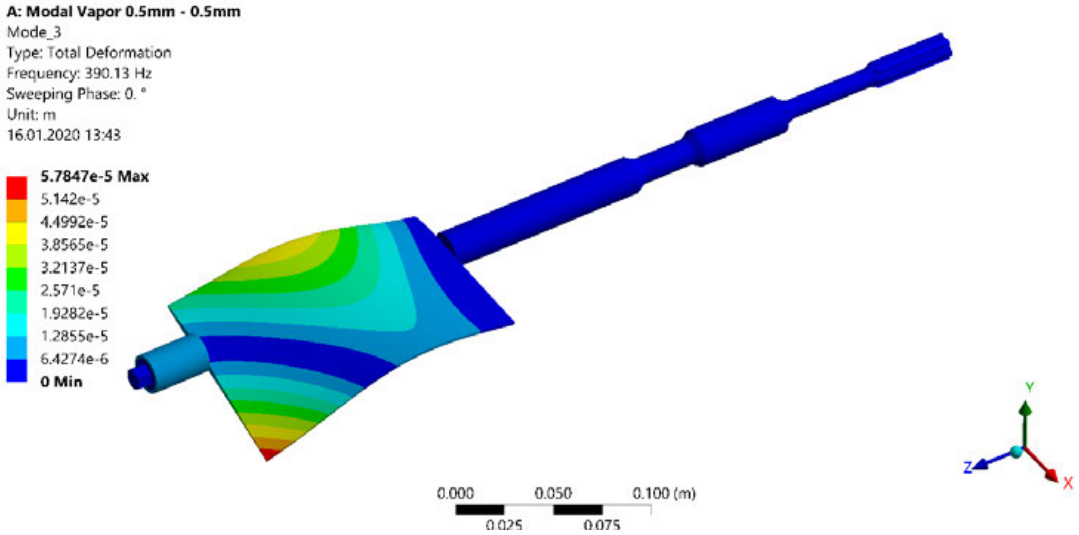

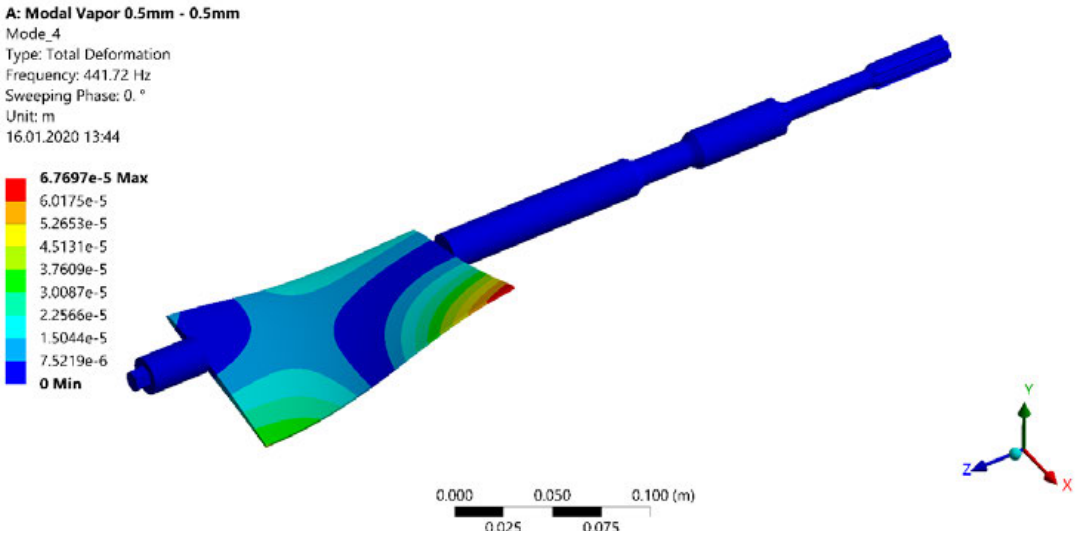
A: Modal Vapor 0.5mm - 0.5mm
Mode_4
Type: Total Deformation
Frequency: 441.72 Hz
Sweeping Phase: 0. °
Unit: m
16.01.2020 13:44
6.7697e-5 Max
6.0175e-5
5.2653e-5
4.5131e-5
3.7609e-5
3.0087e-5
2.2566e-5
1.5044e-5
7.5219e-6
0 Min
0.000
0.050
0.100 (m)
0.025
0.075
Y
Z
X

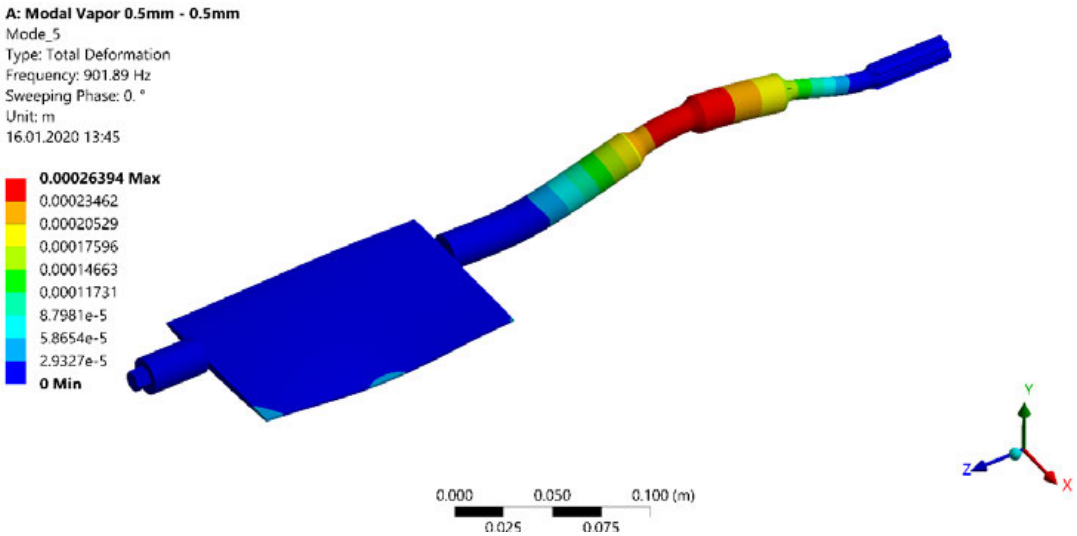
A: Modal Vapor 0.5mm - 0.5mm
Mode_5
Type: Total Deformation
Frequency: 901.89 Hz
Sweeping Phase: 0. °
Unit: m
16.01.2020 13:45
0.00026394 Max
0.00023462
0.00020529
0.00017596
0.00014663
0.00011731
8.7981e-5
5.8654e-5
2.9327e-5
0 Min
0.000
0.050
0.100 (m)
0.025
0.075
Y
Z
X

- **Mode shapes for parameters:** $L_{cloud} = 60\ mm; H_{cloud} = 2.0\ mm; \alpha_{vap} = 0.5$

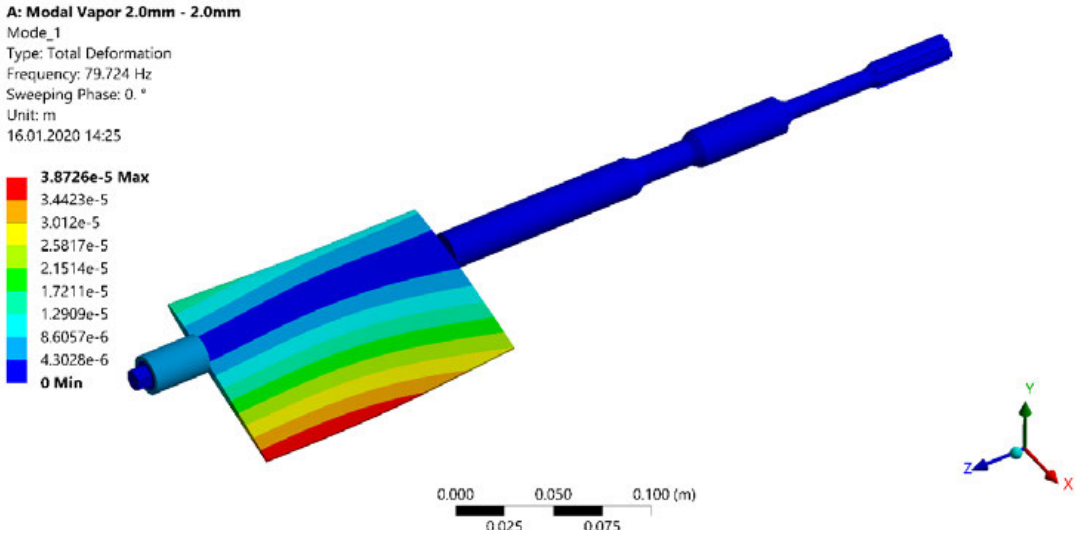

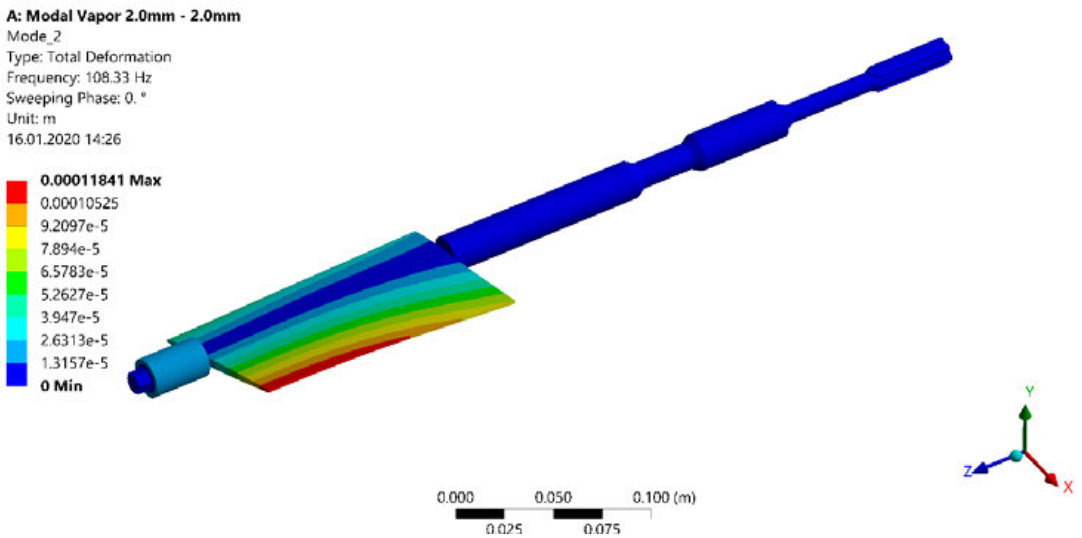

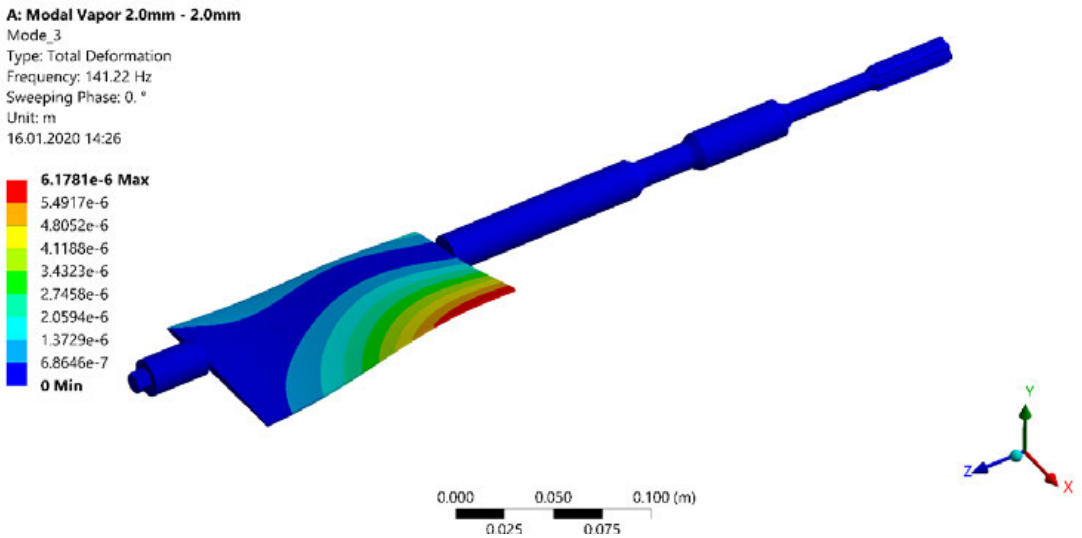

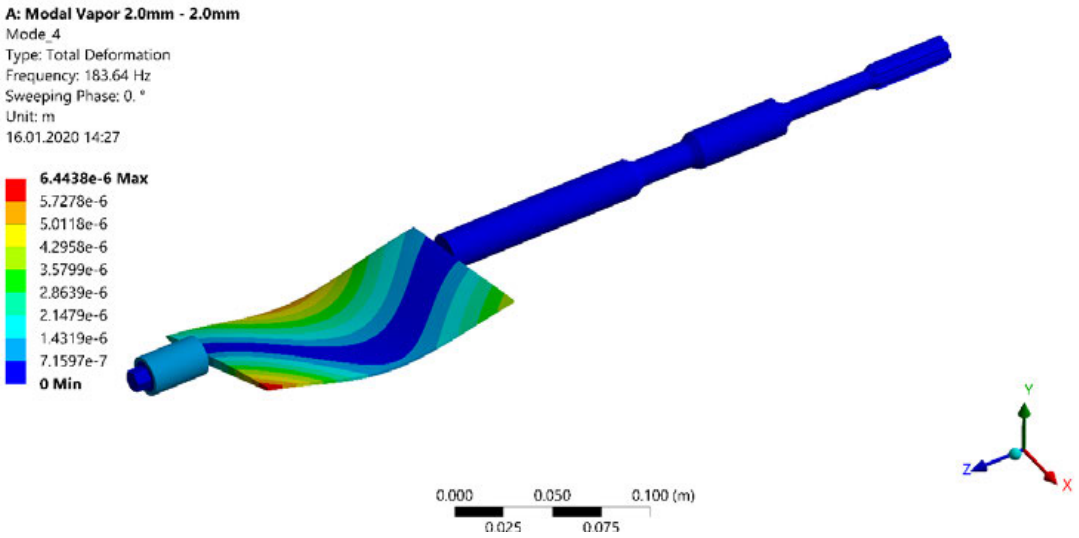
A: Modal Vapor 2.0mm - 2.0mm
Mode_4
Type: Total Deformation
Frequency: 183.64 Hz
Sweeping Phase: 0. °
Unit: m
16.01.2020 14:27
6.4438e-6 Max
5.7278e-6
5.0118e-6
4.2958e-6
3.5799e-6
2.8639e-6
2.1479e-6
1.4319e-6
7.1597e-7
0 Min
0.000
0.050
0.100 (m)
0.025
0.075
Y
Z
X

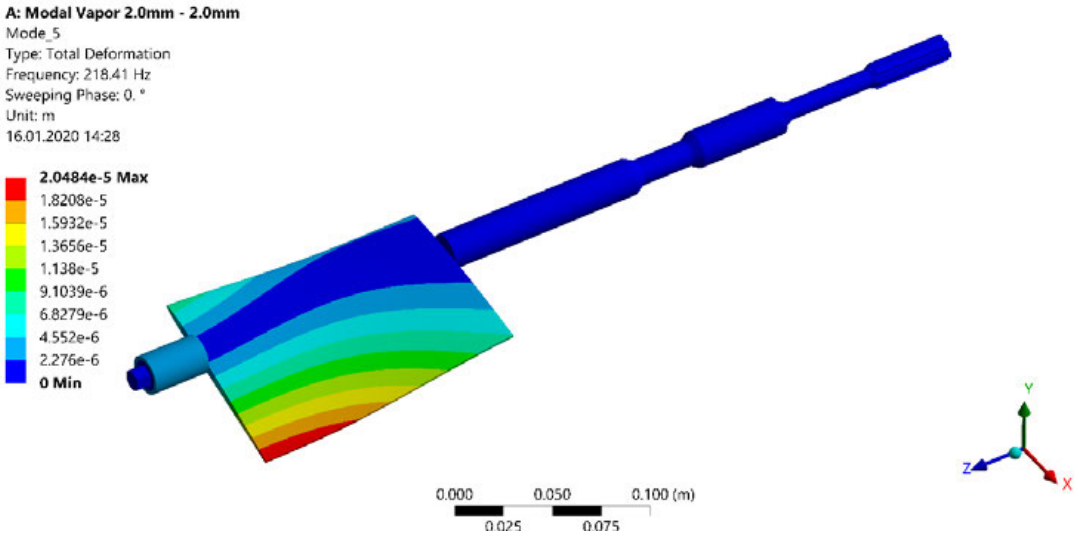
A: Modal Vapor 2.0mm - 2.0mm
Mode_5
Type: Total Deformation
Frequency: 218.41 Hz
Sweeping Phase: 0. °
Unit: m
16.01.2020 14:28
2.0484e-5 Max
1.8208e-5
1.5932e-5
1.3656e-5
1.138e-5
9.1039e-6
6.8279e-6
4.552e-6
2.276e-6
0 Min
0.000
0.050
0.100 (m)
0.025
0.075
Y
Z
X

- **Mode shapes for parameters:** $L_{cloud} = 60\ mm; H_{cloud} = 2.0\ mm; \alpha_{vap} = 1.0$

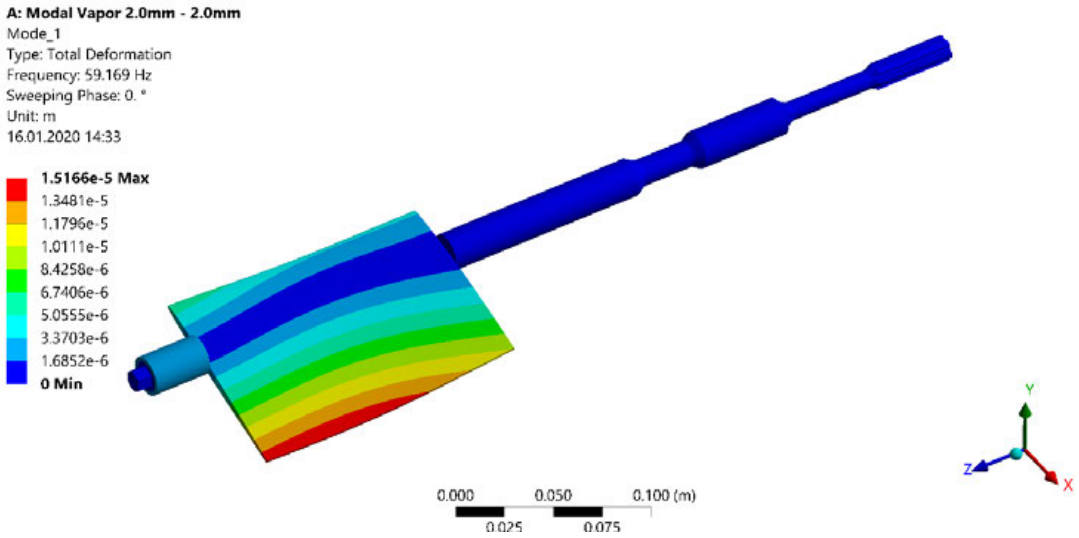

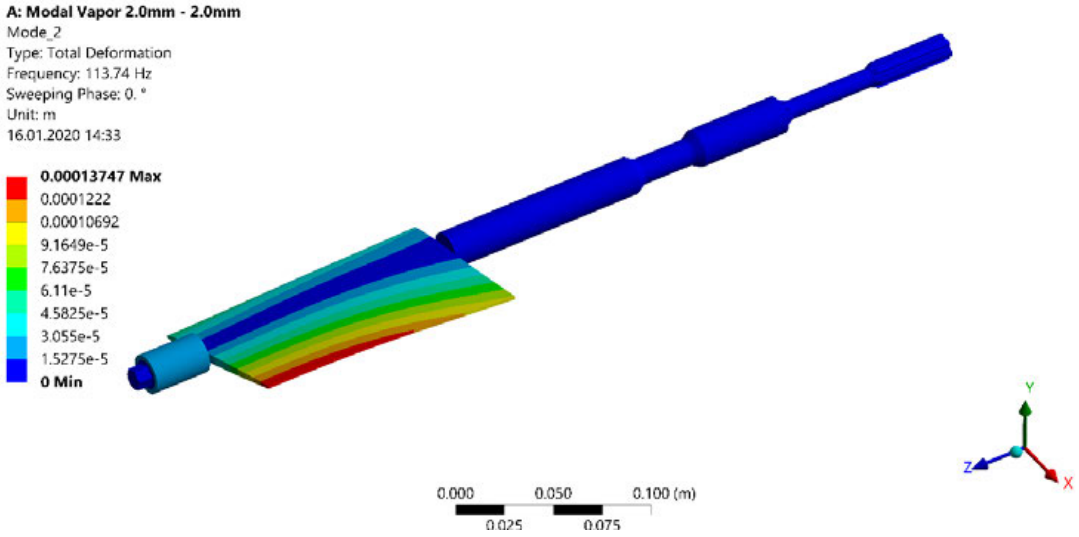

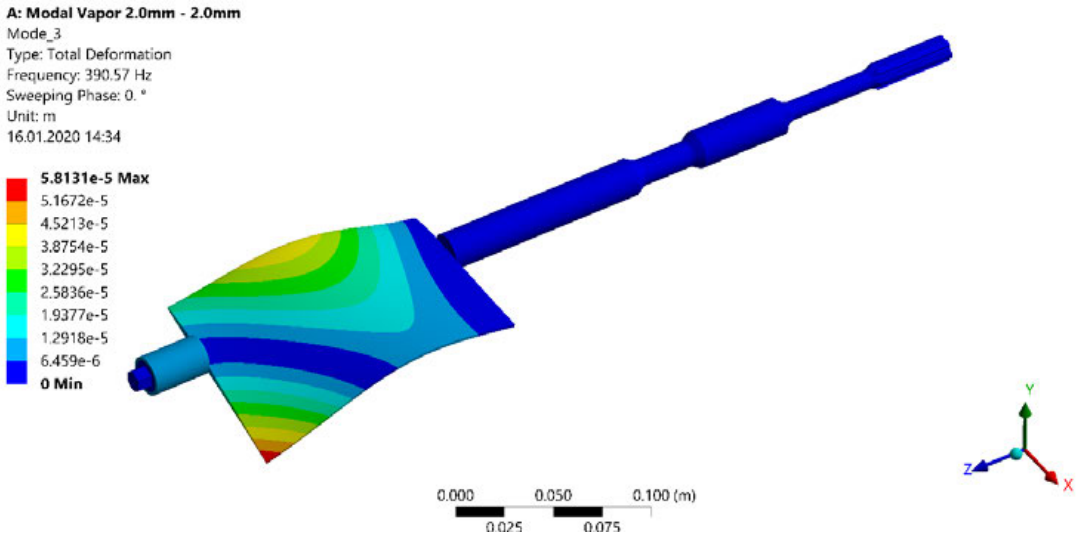

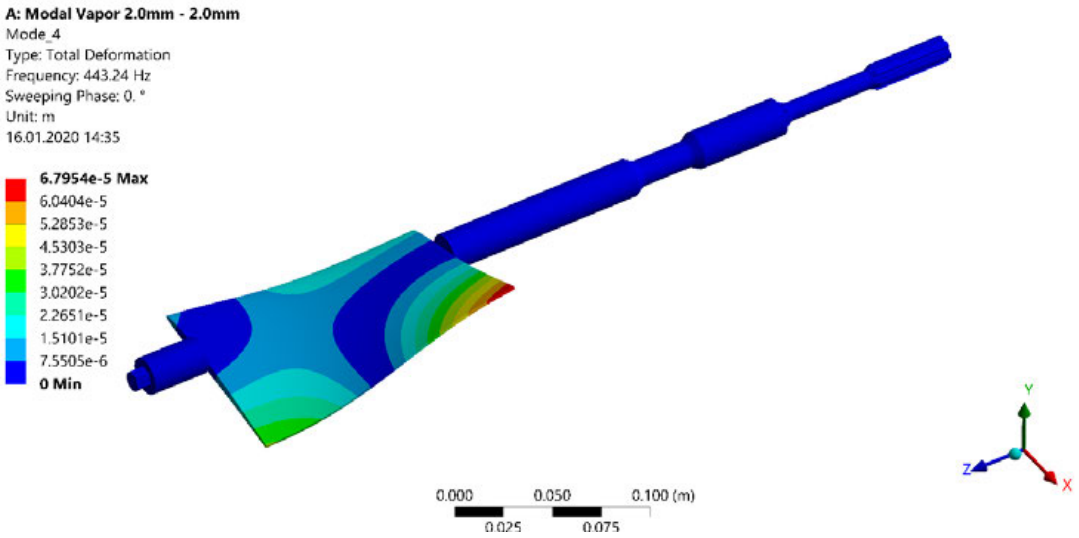
A: Modal Vapor 2.0mm - 2.0mm
Mode_4
Type: Total Deformation
Frequency: 443.24 Hz
Sweeping Phase: 0. °
Unit: m
16.01.2020 14:35
6.7954e-5 Max
6.0404e-5
5.2853e-5
4.5303e-5
3.7752e-5
3.0202e-5
2.2651e-5
1.5101e-5
7.5505e-6
0 Min
0.000
0.050
0.100 (m)
0.025
0.075
Y
Z
X

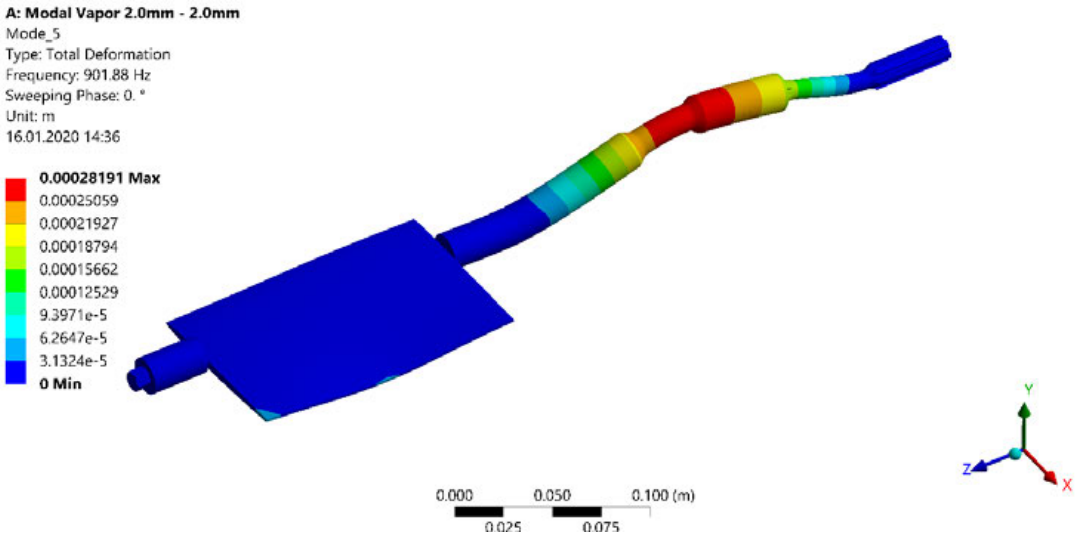
A: Modal Vapor 2.0mm - 2.0mm
Mode_5
Type: Total Deformation
Frequency: 901.88 Hz
Sweeping Phase: 0. °
Unit: m
16.01.2020 14:36
0.00028191 Max
0.00025059
0.00021927
0.00018794
0.00015662
0.00012529
9.3971e-5
6.2647e-5
3.1324e-5
0 Min
0.000
0.050
0.100 (m)
0.025
0.075
Y
Z
X

- **Mode shapes for "real" cavitation cloud ($\alpha_{vap} = 0.5$)**

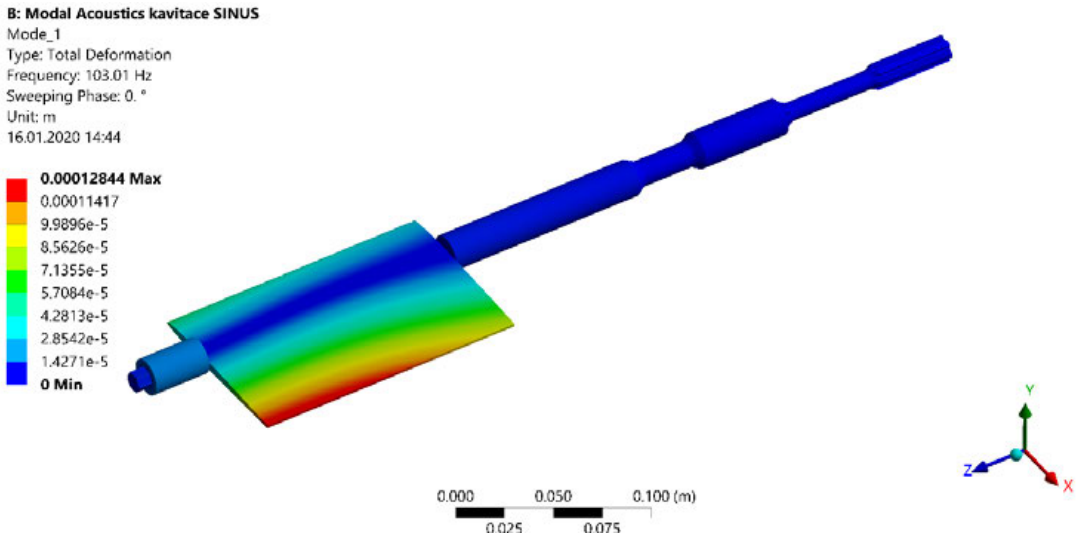

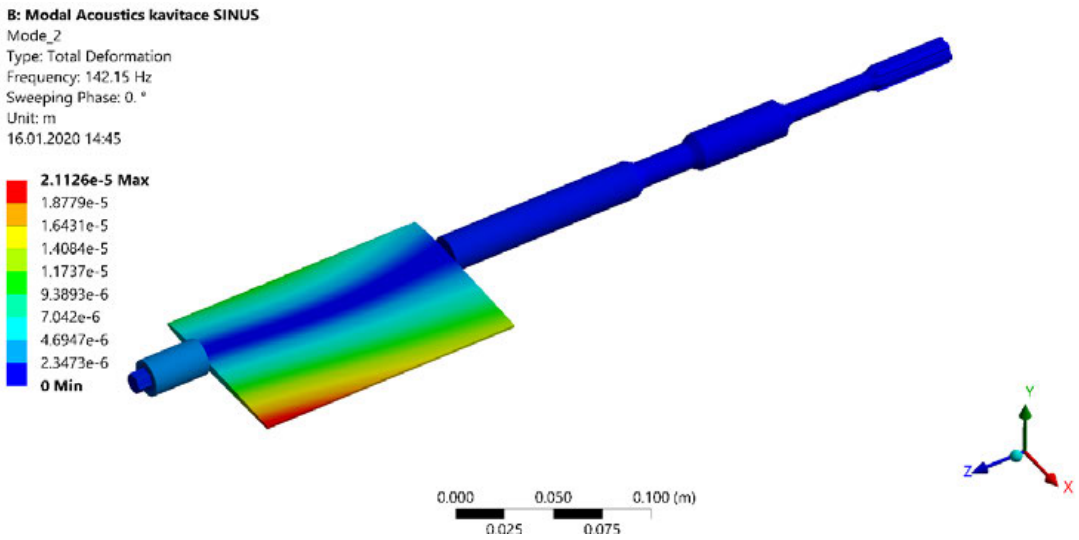

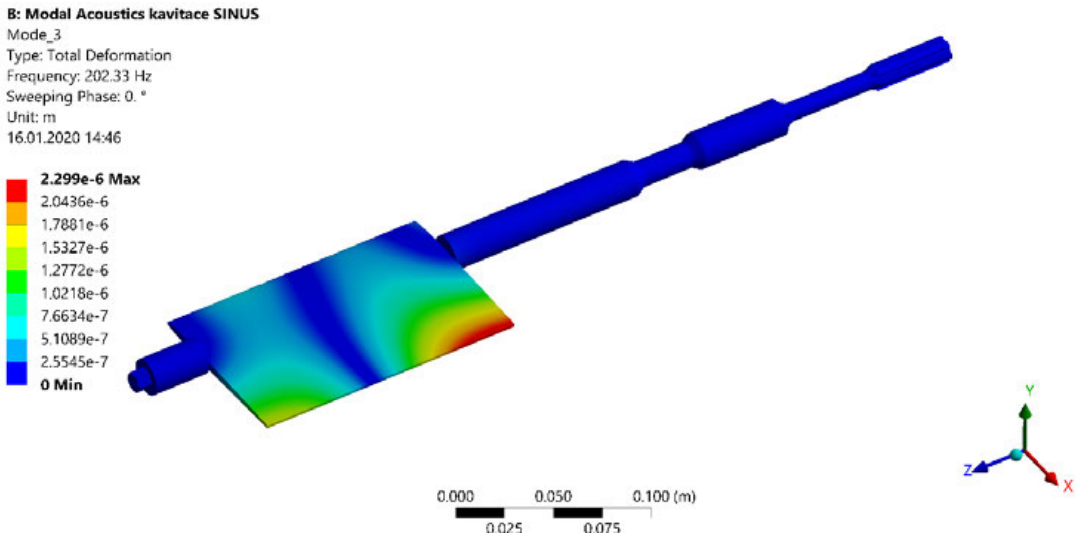

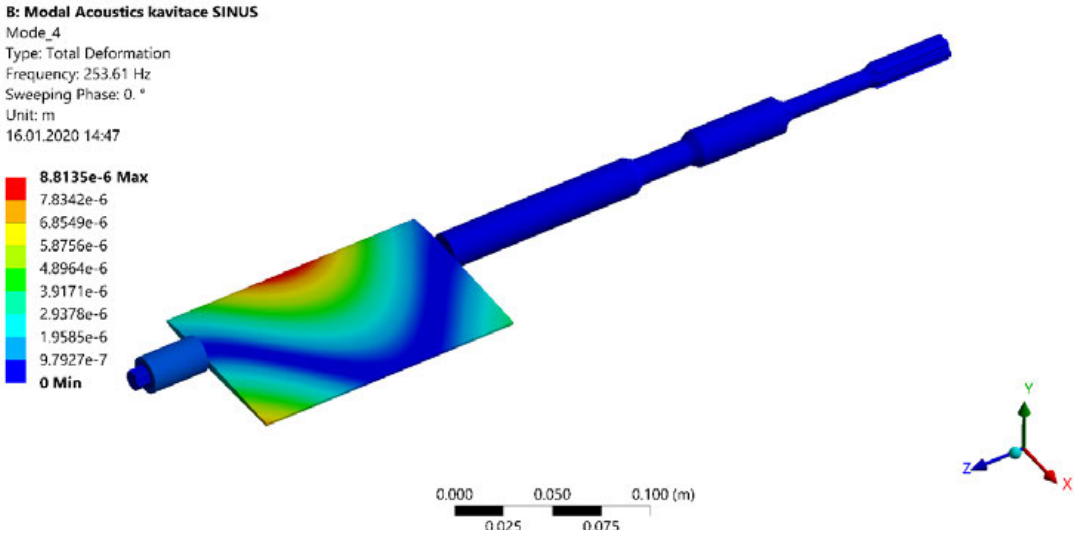
B: Modal Acoustics kavitace SINUS
Mode_4
Type: Total Deformation
Frequency: 253.61 Hz
Sweeping Phase: 0. °
Unit: m
16.01.2020 14:47
8.8135e-6 Max
7.8342e-6
6.8549e-6
5.8756e-6
4.8964e-6
3.9171e-6
2.9378e-6
1.9585e-6
9.7927e-7
0 Min
0.000
0.050
0.100 (m)
0.025
0.075
Y
Z
X

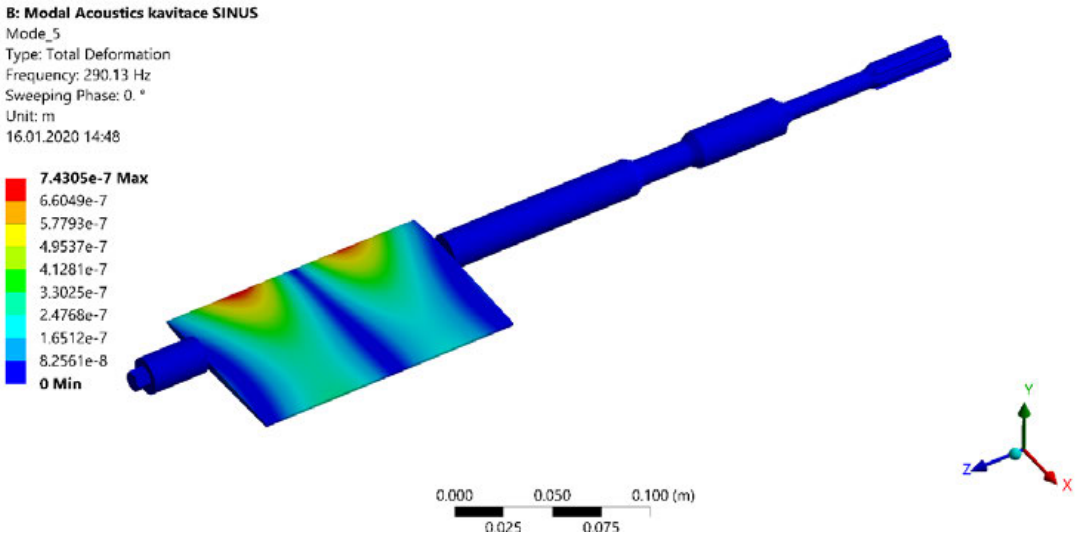
B: Modal Acoustics kavitace SINUS
Mode_5
Type: Total Deformation
Frequency: 290.13 Hz
Sweeping Phase: 0. °
Unit: m
16.01.2020 14:48
7.4305e-7 Max
6.6049e-7
5.7793e-7
4.9537e-7
4.1281e-7
3.3025e-7
2.4768e-7
1.6512e-7
8.2561e-8
0 Min
0.000
0.050
0.100 (m)
0.025
0.075
Y
Z
X

- **Mode shapes for "real" cavitation cloud ($\alpha_{vap} = 1.0$)**

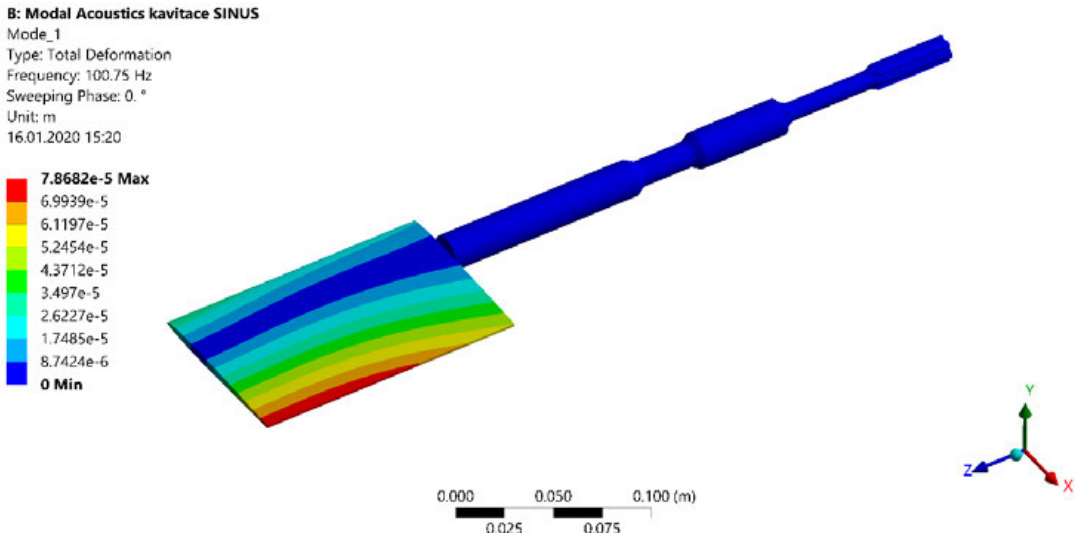

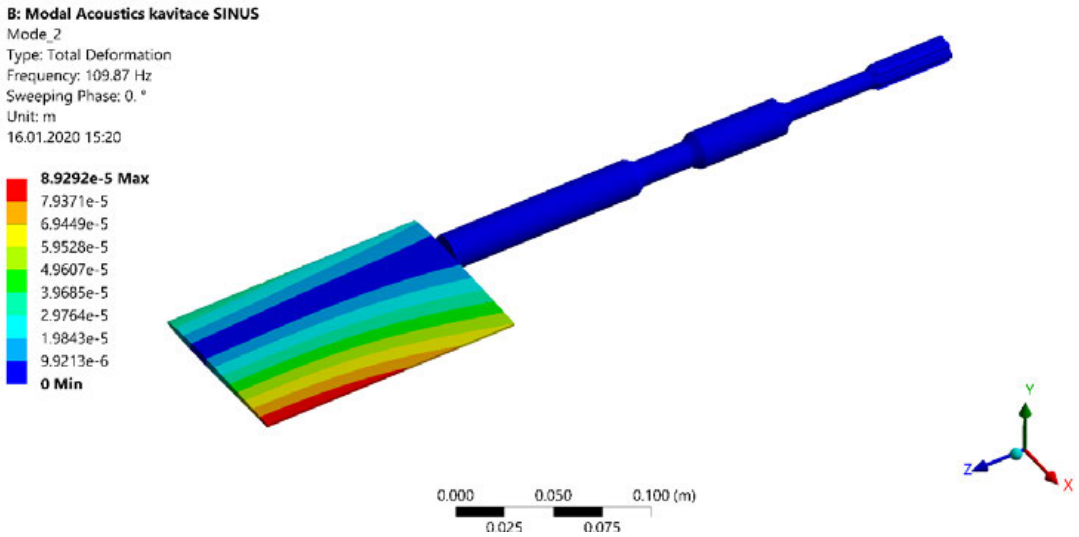

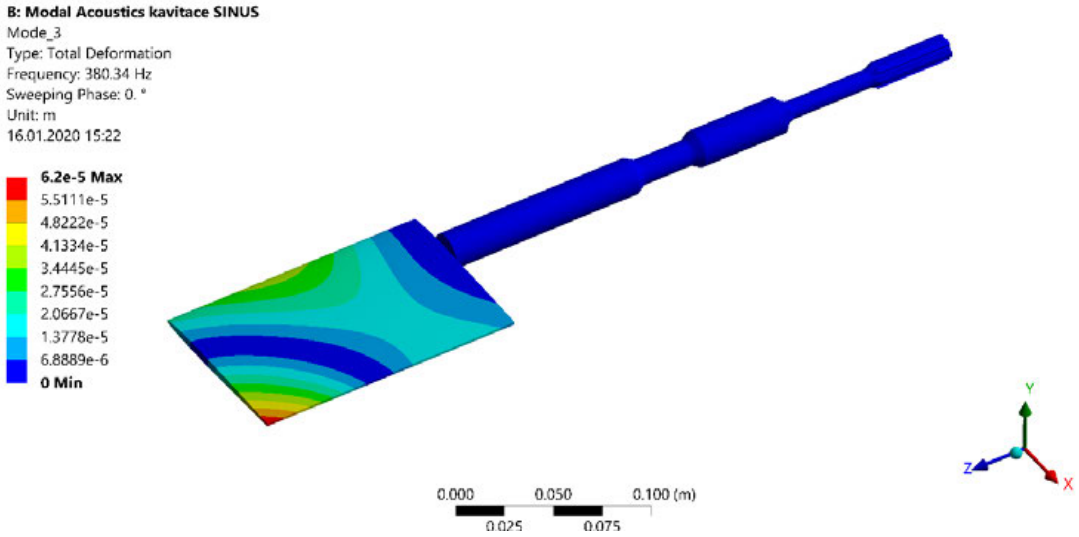

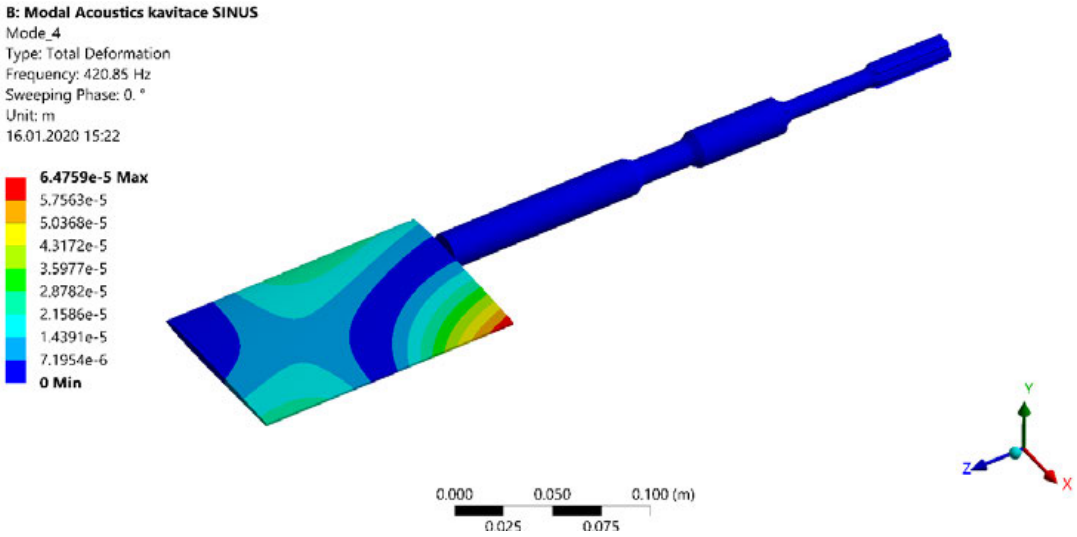
B: Modal Acoustics kavitace SINUS
Mode_4
Type: Total Deformation
Frequency: 420.85 Hz
Sweeping Phase: 0. °
Unit: m
16.01.2020 15:22
6.4759e-5 Max
5.7563e-5
5.0368e-5
4.3172e-5
3.5977e-5
2.8782e-5
2.1586e-5
1.4391e-5
7.1954e-6
0 Min
0.000
0.050
0.100 (m)
0.025
0.075
Y
Z
X

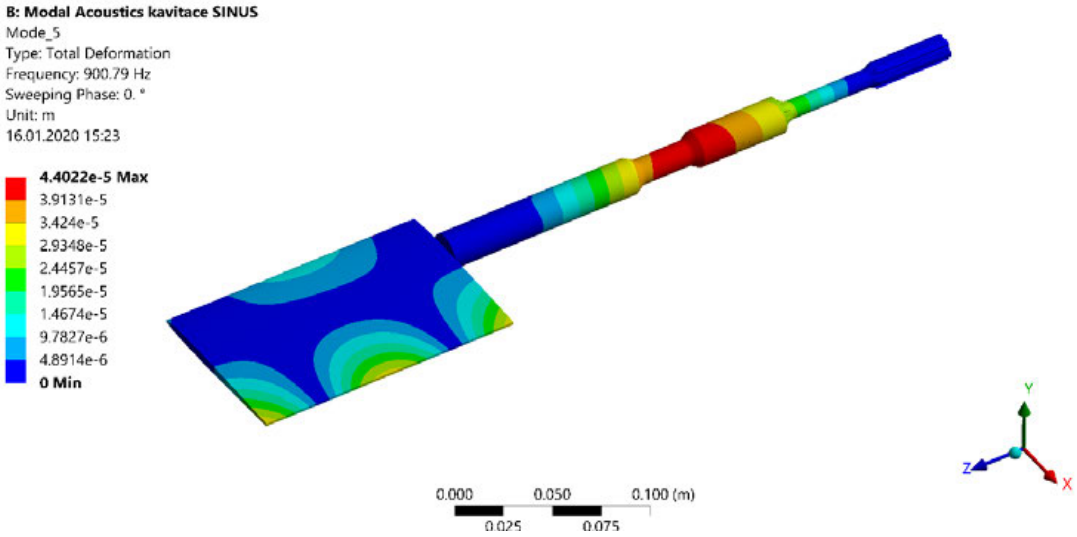
B: Modal Acoustics kavitace SINUS
Mode_5
Type: Total Deformation
Frequency: 900.79 Hz
Sweeping Phase: 0. °
Unit: m
16.01.2020 15:23
4.4022e-5 Max
3.9131e-5
3.424e-5
2.9348e-5
2.4457e-5
1.9565e-5
1.4674e-5
9.7827e-6
4.8914e-6
0 Min
0.000
0.050
0.100 (m)
0.025
0.075
Y
Z
X